QUENCH - SAFEST: Scientific Report NUSAFE 3576

Results of the QUENCH-20 experiment with BWR test bundle

J. Stuckert, S. Bechta, M. Große, P. Isaksson,
J. Laier, J. Moch, U. Peters, U. Stegmaier, M. Steinbrück

Karlsruher Institut für Technologie

Karlsruher Institut für Technologie

in der Helmholtz-Gemeinschaft

Wissenschaftliche Berichte

NUSAFE 3576

Results of the QUENCH-20 experiment with BWR test bundle

J. Stuckert, S. Bechta*, M. Große, P. Isaksson**,
J. Laier, J. Moch, U. Peters, U. Stegmaier, M. Steinbrück

Institut für Angewandte Materialien:
Angewandte Werkstoffphysik (IAM-AWP)

Programm Nukleare Sicherheitsforschung

*Kungliga Tekniska högskolan (KTH), Sweden
**Strålsäkerhetsmyndigheten (SSM), Sweden

Karlsruher Institut für Technologie

2022

DOI: 10.5445/IR/1000149400

Impressum

Karlsruher Institut für Technologie (KIT)
Institut für Angewandte Materialien
Angewandte Werkstoffphysik IAM-AWP
Nukleare Sicherheitsforschung
Hermann-von-Helmholtz-Platz 1
76344 Eggenstein-Leopoldshafen
www.iam.kit.edu/awp/163.php

Abstract

The experiment QUENCH-20 with BWR geometry simulation bundle was successfully conducted at KIT on 9th October 2019. This test was performed in the framework of EU SAFEST project and its international access to European SA research infrastructure of the users from Swedish Radiation Safety Authority (SSM) in cooperation with Westinghouse Sweden, GRS and KTH.

The test objective was the investigation of the BWR fuel assembly degradation including a B_4C control blade. The test bundle mock-up represented one quarter of a BWR fuel assembly. 24 electrically heated fuel rod simulators were filled separately with krypton (overpressure of 4 bar).

According to the pre-test calculations performed with ATHLET-CD, the bundle was heated to a temperature of 1230 K at the cladding of the central rod at the hottest elevation of 950 mm. This pre-oxidation phase in steam lasted 4 hours. Towards the end of this phase, one reference rod was extracted from the test bundle for determination of the oxide thickness axial distribution.

During the transient stage, the bundle was heated to a maximal temperature of 2000 K. The cladding failures were observed at temperatures about 1700 K and lasted about 200 s. Massive absorber melt relocation was observed 50 s before the end of the transient stage.

The test was terminated by the injection of quench water with a flow rate of 50 g/s into the bundle bottom. Fast temperature escalation from 2000 to 2300 K during 20 s was observed. The mass spectrometer measured release of CO_x and little CH_4 during the reflood as products of absorber oxidation; corresponding production of B_2O_3 should be about 97 g. Hydrogen production during the reflood amounted to 32 g (57.4 g during the whole test) including 10 g from B_4C oxidation.

Contents

List of Tables

List of Figures

Introduction

The main objective of the QUENCH program at KIT is the investigation of the hydrogen source term and materials interactions during LOCA and the early phase of severe accidents including reflood [1-3]. Bundle experiments as well as separate-effects tests are conducted to provide data for the development of models and the validation of severe accident codes. The QUENCH bundle facility is an out-of-pile bundle facility with electrically heated fuel rod simulators and extensive instrumentation. So far, 20 experiments with various severe accident scenarios (Table 1) as well as a series of 7 DBA LOCA experiments were conducted. Two of the bundle tests on severe accident were performed with PWR geometry containing a central B_4C neutron absorber rod: QUENCH-07 [4] and QUENCH-09 [5]. Numerous accompanying single control rod tests were performed at KIT and showed a complicated eutectic interaction between B_4C, stainless steel and zirconium with formation of different borides [6, 7].

The latest severe accident test QUENCH-20 was the first test performed in the QUENCH facility with BWR geometry simulation bundle.

1 Test facility

The general scheme of the test section is given in Figure 1; the flow diagram of facility, containment, and test section are shown in Figure 2 - Figure 4. The test rods were arranged within the QUENCH-20 bundle as shown in the schematic cross section of Figure 5. Composition characteristics of the QUENCH-20 bundle are presented in Table 2. The rod cladding of the fuel rod has 9.84 mm outside diameter and 8.63 mm inner diameter. The cladding tubes used in this test consisted of Zircaloy-2 with inner liner (LK3/L). The composition of the LK3 and L materials can be found in Table 3.

The test bundle is approximately 2.5 m long and is made up of 24 heated fuel rod simulators. Heating is electric by 5.25 mm diameter tungsten heaters installed in the rod centers, and the bundle section heated by tungsten heaters between bundle elevations 0 and 1024 mm (Figure 6). Molybdenum heaters and copper electrodes are connected to the tungsten heaters at one end and to the cable leading to the DC electrical power supply at the other end. Two DC generators were applied; the corresponding bundle partitioning (12+12 rods) between two generators is marked in Figure 5 with two transparent colors. The tungsten heaters are surrounded by annular ZrO_2 pellets simulating UO_2 fuel (Table 4). The Mo heaters and Cu electrodes are coated with a ZrO_2 layer (about 200 µm thickness) to avoid electrical contact to the cladding inner surface. After assembling of the bundle, the total electrical resistance of each rod (summary resistance of W, Mo, Cu parts and gilded slide contacts) was measured separately (Table 5). The rod resistances were measured also after the test. The resistance of rods #4 and #20 turned out to be somewhat increased; the most likely reason for this may be a change in the resistance of the threaded connection between the tungsten and molybdenum heaters as a result of a change in their lengths during heating and cooling. The post-test total resistance (resistance of the corresponding twelve rods connected in parallel) was slightly higher for the second rod group connected to the GS2 generator. A corresponding increase in the resistance of the second current circuit was observed at the end of the transient (Figure 19). Since the control program was configured to maintain the same power in both circuits, the voltage value of the second generator was automatically correspondingly increased. In this case, of course, there is a slight redistribution of power between the rods of the second circuit (decrease in heat release for rods #4 and #20).

All the test rods were filled with Kr at an overpressure of approximately 0.6 MPa after bundle heating to cladding peak temperature of 900 K. The system pressure maintained at about 0.2 MPa.

The fuel rod simulators are held in position by five grid spacers at bundle elevations -200, 50, 550, 1050 and 1410 mm. All five grid spacers were the standard Westinghouse Inconel X750 spacers (Figure 7). Two steel blades with horizontal *B_4C absorber pins* (Figure 8) were filled with helium (0.12 MPa) and inserted between channel box and shroud (Figure 9). The composition of the steel blade is the following (low carbon alloy *AISI 316L* SS): *Fe, Cr (17%), Ni (11%), Mo (2.5%), [Si, P, S (<1%)]*.

One corner rod was installed in the water channel and was designed to be withdrawn from the bundle to check the amount of oxidation and hydrogen absorption at a specific time. This corner rod was withdrawn at the end of the pre-oxidation stage.

The test bundle is surrounded by an octagonal shroud made of Zr 702, then by ZrO_2 fiber insulation (Table 6) extending from the bottom (-300 mm) to the upper end of the heated zone (+1024 mm) and a double-walled cooling jacket made of Inconel 600 (inner)/stainless steel (outer) over the entire length.

The annulus between shroud and cooling jacket with the fiber insulation is purged (after several cycles of evacuation) and then filled with stagnant argon. This annulus is connected to a flow- and pressure-controlled argon feeding system in order to keep the pressure constant at the target of 0.3 MPa (beyond this pressure gas is released by the feeding system). It must prevent an access of steam from the test bundle to the annulus after a possible shroud failure, after which argon is supplied continuously.

The 6.7 mm annulus of the cooling jacket is cooled by argon from the upper end of the heated zone to the bottom of the bundle and by water in the upper electrode zone. Both the absence of ZrO_2 insulation above the heated region and the water cooling are to avoid too high temperatures of the bundle in that region.

2 Instrumentation and data acquisition

All measurement devices used in QUENCH-20 and connected to the MERSY/Siemens measurement system are listed in Table 7. The readings of pressure transducers connected to each rod were recorded separately by the DELPHIN measurement system. For temperature measurements the test bundle, shroud, and cooling jackets are equipped with thermocouples (Figure 10 - Figure 13). The thermocouples attached to the outer surface of the rod cladding at elevations between -250 and 1350 mm are designated “TFS” for all heated rods (Table 8). The shroud thermocouples (designation “TSH”) are mounted at the outer surface between -250 and 1250 mm. The thermocouples installed at the blade side at the bundle elevations 250, 350 and 450 mm are designated as TBL. The thermocouples mounted at the channel box at elevations 350 and 450 mm are designated as TCH.

The thermocouples in the lower bundle region, i.e. up to 550 mm elevation, were NiCr/Ni thermocouples with stainless steel sheath/MgO insulation and an outside diameter of 1.0 mm, used for measurements of the rod cladding and shroud temperatures. The thermocouples in the hot zone and above were high-temperature thermocouples with W5Re/W26Re wires, HfO_2 insulation, and two sheaths of tantalum (inner sheath) and zirconium (outer sheath), Figure 14 and Table 9. The material properties of the HfO2 insulator are presented in Table 10. The high temperature thermocouples have an outer diameter of about 2.3 mm and were welded to the outer surface of claddings and shroud with Zr clamps (Figure 15).

The thermocouple measurement accuracies are:

at bundle elevations between 0 and 500 mm (NiCr/Ni thermocouples): ± 2 K (up to 600 K), ± 0.005*T K (above 600 K);

at bundle elevations between 600 and +1300 mm (W/Re thermocouples): ± 5 K (up to 700 K), ± 0.01*T K (above 700 K).

The hydrogen release is analyzed by a quadrupole mass spectrometer Balzers “GAM300” with the sampling position at the off-gas pipe of the test facility (Figure 16, Figure 17). The ion currents representing the concentrations of the respective gases are determined. From these data the mass production rate of hydrogen as well as of the other gases is calculated with the ratio of the concentrations of the particular gas and that one of argon (carrier gas) and multiplied by the argon flow rate through the test bundle. The uncertainty for the hydrogen release rate is about 0.004 mol/m²/s. The delay time for the gas transfer from the hottest bundle elevation to the mass spectrometer is about 5 s.

The operational data, e.g. voltage, current, electric power, pressure, and temperatures are recorded by a data acquisition system as are the temperatures of the test section.

3 Test performance and results of online measurements

The detailed sequence of the test events is described in Table 11.

In the QUENCH-20 experiment the test sequence can be distinguished in the following stages:

Pre-oxidation	0 – 14416 s,
Heat-up	14416 – 15882 s,
Quench	15882 – 16375 s with water flow rate 50 g/s.

The scheme of test performance is depicted in Figure 18. The electrical parameters (current, voltage, resistance) of two bundle groups connected to two DC generators are presented in Figure 19.

The histories of system pressure and gas flow rates are depicted in Figure 20, and Figure 21 correspondingly.

Figure 22 - Figure 38 show the TFS, TBL, TCH and TSH thermocouple readings separately for each bundle elevation. The hottest elevation of QUENCH-20 was the level 950 mm similar to most former QUENCH bundle tests. Figure 39 and Figure 40 present change of temperatures behind the heat insulation due to radial heat transport in the test section.

To determine the axial temperature profile at a certain time, the average values of all thermocouple readings of certain bundle elevations were calculated separately for claddings and shroud. Figure 41 presents these axial temperature distributions at the end of the pre-oxidation stage and at the end of the transient stage. For both time points, the hottest region was close to the elevation 950 mm.

Figure 42 shows readings of pressure transducers connected to heated rods pressurized with Kr to about 0.6 MPa. According to pressure drops, the cladding failures occurred during the transient stage, probably at a temperature of about 1700 K measured at the failure time at the elevation 950 mm. Simultaneous release of Kr was registered by mass spectrometer, which has shown seven Kr peaks corresponding to seven rod groups failing over a period of about 200 s. In the first group, the rods 8, 1, and 4 of the internal group failed. The last group consists of rods 17 and 12 located at bundle periphery. The failure sequence from internal to outer rods (Table 12) is due to the radial temperature profile, decreasing from the center rod to the shroud.

The Zr elasticity decreases significantly at temperatures above 700 °C, consequently the shroud was ductile deformed during the pre-oxidation stage due to overpressure in the annulus behind the shroud (absolute pressure 3 bar) in comparison to the bundle pressure of 2 bar (Figure 43). The shroud failure was registered

by Ar flow through the shroud breach into the bundle (Figure 44) and occurred during the cladding failures about 200 s before the quench initiation.

The absorber blade failures were registered by He release (Figure 45). The corresponding absorber melt relocations to the elevations of 250…450 mm were indicated during the transient stage by the TBL thermocouples installed at these elevations (Figure 46).

The quench water injection was initiated at 15891 s, the flow rate of 50 g/s was registered by the flow controller Fm 104 a few seconds later (Figure 47). The maximum cladding temperature achieved during the test was recorded with the TFS 1/13 thermocouple at the time of quenching and was 2098 K. Previously, the bundle foot had been filled within about 9 s by fast injection of 4 L water, which is indicated by a jump registered by the differential pressure transducer L501. The following oscillation readings of this transducer (Figure 48) indicate intensive evaporation of quench water also registered by mass spectrometer (Figure 49). The sequence of thermocouple wettings in Figure 48 shows, that the bundle was cooled during about 450 s.

During the quench stage, the mass spectrometer registered release of the following products of B_4C oxidation by steam (Figure 50, Figure 51): significant amounts of CO (12.6 g), and CO_2 (9.7 g) as well as a relatively small mass of CH_4 (0.4 g). This corresponds to the following chemical reactions:

$$B_4C(s)+7H_2O(g)=2B_2O_3(l)+CO(g)+7H_2+[732\ kJ/mol\ \&\ 1600\ K] \quad (1)$$

$$B_4C(s)+8H_2O(g)=2B_2O_3(l)+CO_2(g)+8H_2+[761\ kJ/mol\ \&\ 1600\ K] \quad (2)$$

$$B_4C(s)+6H_2O(g)=2B_2O_3(l)+CH_4(g)+4H_2+[959\ kJ/mol\ \&\ 1600\ K] \quad (3)$$

Steam reacts with liquid boron oxide to form volatile boric acids:

$$B_2O_3(l)+H_2O(g)=2HBO_2-[329\ kJ/mol\ \&\ 1600\ K] \quad (4)$$

$$B_2O_3(l)+3H_2O(g)=2H_3BO_3+[42\ kJ/mol\ \&\ 1600\ K] \quad (5)$$

Boron oxide itself directly evaporates at temperatures above 1500 °C

Theoretically, two additional reactions are possible:

$$CO + H_2O \rightleftharpoons CO_2 + H_2 - [11\ kJ/mol\ \&\ 1273\ K] \quad (6)$$

$$CH_4 + H_2O \rightleftharpoons CO + 3H_2 - 206\ kJ/mol \quad (7)$$

The reaction (6), is so a called water-gas shift reaction (WGSR), which is endothermic at high temperatures (above 800 °C) and shifted towards reactants. I.e. at high temperatures (QUENCH-conditions), the production of a noticeable amount of hydrogen significantly decreases. . The reaction (7) is also a (strongly) endothermic reaction, which is possible between 700 and 1100 °C only in the presence of nickel as catalyst. The probability of production of additional hydrogen due to this reaction is also low for the QUENCH conditions (only the Inconel spacers have a noticeable content of Ni).

The calculations, based on the equations (1)…(3) and measured data, show that the corresponding mass of reacted B_4C was 38.4 g (4.3% of the total mass of B_4C pins). Additionally to the released gases CO (12.6 g), CO_2 (9.7 g) and CH_4 (0.4 g) 96.8 g B_2O_3 were formed and 10 g hydrogen were released. The total energy release due to boron carbide oxidation is about 500 kJ. The integral hydrogen release registered by mass spectrometer during the whole test was 57.4 g, of which 32 g thereof during the quench stage (Figure 52).

4 Posttest investigations

4.1 Inspection of corner rods

The oxidation status of the corner rod withdrawn at the end of the pre-oxidation stage was measured by means of eddy current method. Figure 53 shows the integral thickness of ZrO_2 and α-Zr(O) layers measured along the corner rod. The oxide layer was partially spalled at elevations between 930 and 1030 mm due to the breakaway effect [8], which is typical for these temperatures (about 1250 K at hottest elevations during pre-oxidation). On the basis of these data, it could be suggested that maximum integral thickness was reached at elevations between 950 and 1000 mm and was between 60 and 70 µm. The thicknesses of the layers at different levels were refined metallographically, which showed that a maximum oxide layer of 60...65 µm was formed after the pre-oxidation stage at bundle elevations 850...950 mm (Figure 54). At the same time - due to the relatively low temperatures and the breakaway oxidation - the maximum thickness of the alpha layer was only 5…7 µm. Since the corner rod was in a well-cooled water channel, the obtained values of the layer thicknesses reached at the end of the pre-oxidation stage can serve as a lower estimate for the layers formed before transient on the claddings of the heated rods. It is possible that a breakaway at the end of pre-oxidation took place also on the cladding surface of heated rods (if any), but the thicknesses of the spalled scales (less than 25 µm) are small compared to the final thicknesses of the oxide layers at these hot elevations (from 110 to 650 µm).

4.2 Visual inspection

Visual inspection of the bundle after being freed from the ZrO_2 thermal insulation showed severe damage of the shroud and the channel box between elevations 600 and 950 mm at the angle positions of the absorber blades (Figure 55, Figure 56). At these bundle elevations, the B_4C pins reacted eutectically with the stainless steel blades. Figure 57 shows part of the absorber blade that spalled from the bundle at an elevation of about 800 mm. This part was encapsulated in epoxy resin and metallographically investigated. Partial dissolution of B_4C pins occurred due to the interaction with the surrounding stainless steel. The formed melt has attacked the channel box and partially relocated to lower elevations inside the gaps between the rods and the channel box as well as between the channel box and the shroud.

4.3 Metallographic examination

The test bundle was encapsulated in epoxy resin Epotec 320 with the pertinent hardener Epikure 350 and modifier. The mixture of these three components gives a good result concerning formation of hardened mass without cracks and pores. After epoxy hardening during about three weeks, the bundle was cut into slices according to Table 13. The homogeneous state of the epoxy resin and its transparency is illustrated in Figure 58, showing a top view at the elevation of 55 mm. Here, also the four point contacts between each cladding and the Inconel grid spacer are clearly visible, resulting in eutectic interaction at higher elevations. Figure 59 shows top views of ground and polished cross sections between elevations 50 and 1150 mm. The cladding melt was partially released into the space between rods at the bundle elevations 555…950 mm, whereas eutectic absorber melt is seen at elevations 450…950 mm.

At the elevations of 450...950 mm, detailed measurements of all characteristic layers of each cladding were carried out. The corresponding data are collected in Table 14…Table 19. Figure 199 presents a comparison of the thicknesses of the oxide layers of all claddings at these bundle elevations.

The shroud was ductile deformed at the angular positions 90° and 180° at bundle elevations above 350 mm due to higher gas pressure outside the shroud (Figure 43). This caused the bundle and two grid spacers (at 550 and 1050 mm) to be crushed in the 0° and 270° directions and led to the narrowing of the cooling channels between the rods.

At elevations 1050 and 555 mm, only small fragments of Inconel spacer grids remained on the periphery of the bundle. At four contact points of the spacer cell to the cladding, the spacer grids at these elevations could melt locally due to the eutectic interaction of Ni of the grids with Zr of the claddings at about 1480 K. However, the main part of the spacers was melted at the end of the transient (melting point of Inconel X-750 is 1610 K).

Elevation 1050 mm

A peak cladding temperature of about 1530 K was measured at the claddings of intermediate rods at the beginning of the quench stage. The absorber blades were partially melted due to eutectic interaction with the B_4C pins (Figure 60). Due to the deformation of the bundle, the gap between the central rod and some rods surrounding it turned out to be minimal, which led to steam starvation in these places and the formation of only relatively thin oxide layers on the outer surface of the cladding (Figure 61). Due to the low heat removal, the inner part of the β-Zr layer of the cladding is partially melted here. Due to high temperatures, oxygen diffused deep into the cladding, forming a thick alpha layer, and when cooled during flooding, α-Zr(O) lamellas precipitated inside the β-Zr layer.

In other circumferential places with a large gap between the rods, a relatively thick oxide layer was formed on the outer surface of the cladding, comparable in thickness to the α-Zr(O) layer (Figure 62). The oxide layer here was also formed on the inside of the cladding due to the penetration of steam into the gap between the cladding and the pellets at the lower bundle elevations. A similar layer structure without partial melting of the β-Zr layer is characteristic of most claddings that are cooled well by steam. In this case, a number of claddings exhibit wall thinning, which occurred due to the radial plastic strain of the cladding under elevated internal pressure (Figure 63).

However, melting of the inner part of the cladding also occurred in some peripheral rods at locations that were in contact with adjacent rods (and, accordingly had poor heat removal at these locations) (Figure 64). On the other hand, the relatively well cooled part of such cladding did not melt (Figure 65).

Elevation 950 mm

The peak cladding temperature about 2100 K was measured at the central rod during the quench stage. The absorber blade at the angle position 0° is heavily damaged due to eutectic interactions (Figure 66). The B_4C pin is practically absent at this position, whereas the B_4C pin at the angle position 270° was slightly attacked by the melt formed due to interaction of the stainless steel blade with the Zr-based channel box and the shroud.

Small molten pools were formed around the central rod by cladding melt released through the failed oxide layers of claddings. This cladding melt is mixed with the spacer melt relocated from 1050 mm and the steel melt from absorber blades. The degree of oxidation of the claddings is very inhomogeneous across the bundle (Figure 67). The distribution of oxide layers shows that the lowest temperatures were on those peripheral sides of the assembly where there were no absorber blades (bundle sides 90° and 180°). The highest cladding temperatures were reached in the corner region between the two absorber blades.

The gap between the pellets and the cladding was increased during the pre-oxidation stage due to the overpressure by the Kr filling gas (lift-off). The cladding melt was partially released outside the claddings of the inner rods 1…9 and mixed with the spacer melt and the absorber steel melt (Figure 68…Figure 73). The spacer melt from 1050 mm and from the steel absorber plate has penetrated between the α-Zr(O) layers of

the rods (Figure 69…Figure 70). The inner cladding surface of several rods was also partially oxidized due to steam penetration in the gap or due to interaction with the ZrO_2 pellets.

The claddings of peripheral hot rods along the absorber blades were strongly oxidized and partially melted (e.g. rod #12, Figure 74). The claddings of rods 13, 14 and 15 failed at the contact with the water channel and the absorber blade. The corresponding Zr/(stainless steel) eutectic melt, containing ZrB_2 and (Fe, Cr) chunks, penetrated underneath the cladding and distributed along the entire perimeter of the cladding under the outer oxide layer. Part of the oxide layer was dissolved and formed ceramic precipitates in the melt (Figure 76, Figure 77).

The claddings of the relatively cold peripheral rods (e.g. rod #20, Figure 81) were only moderately oxidized without melting. The water wings and the shroud were also only moderately oxidized in this relatively cold region (Figure 82).

Elevation 850 mm

Because of the failure of the cladding surface thermocouples on the inner rods at the end of transient stage, the highest cladding temperature of about 2230 K was measured during the quench stage on the surface of peripheral rod #20. Very strong melting of the absorber blade at 270° was observed (Figure 85). The absorber blade at 0° was spalled during the bundle dismounting. The degree of oxidation of claddings is higher in comparison to the elevation 950 mm, whereas the bundle oxidation gradient is similar to the 950 mm elevation: the region along the absorber blades was hotter than along the two bundle sides without absorber blades (Figure 86). The oxide layer thickness of the central rod is relatively low due to dissolution of this layer in the melting pools formed in the bundle center.

The surrounding of the inner rods #1…#4 contains relatively few metal melt because this melt was relocated downwards (Figure 87, Figure 88). The claddings of the other five inner rods #5…#9 consists of α-Zr(O) layers and segments of frozen metal melt (Figure 89…Figure 91). The hot peripheral rods #10…#17 along the absorber blades lost a significant part of the cladding metal melt, which relocated downward (Figure 91…Figure 96). The small residues of the α-Zr(O) layer began to actively oxidize (Figure 93). The melting of the cladding metal at the boundary to the oxide layer led to the dissolution of the oxide by molten metal with the formation of ceramic precipitates (Figure 97). The phenomenology of this process was investigated and described in [9]. Additionally, the metal precipitates are formed in the oxide due to oxygen transport to the metal [10]. The claddings of the relatively cold peripheral rods #18…#22 were not melted (Figure 98…Figure 101). The prior β-Zr layers of rods #23 and #24 were partially melted and include ceramic precipitates formed due to dissolution of the oxide layers by molten Zr (Figure 102…Figure 104).

Elevation 750 mm

Due to disturbances of the cladding thermocouples, the highest temperature of 2400 K was measured by thermocouples installed at the outer surface of the shroud behind the absorber blades. Similar to 850 mm, the part of the absorber blade at the angle position 0° was spalled during the bundle dismounting, whereas the B_4C pin inside the absorber blade at 270° reacted with the stainless steel of the absorber blade and was partially dissolved (Figure 105, Figure 106). The detailed SEM/EDX analysis of the eutectic melt around the B_4C pin revealed the formation of equiaxed (Fe, Cr) borides near to the pins and the needle-shape ZrB_2 near to the Zr-based channel box (Figure 107…Figure 109), in full accordance with the structures observed in [7].

A very detailed analysis of all bundle elements was performed. The thicknesses of oxide layers of ZIRLO water wings and Zr shroud were measured at the positions far from contacts with other bundle elements (no steam starvation) (Figure 110). The oxide layer thickness of the water wings was 130 µm and that of the shroud 85 µm. The thicknesses of all cladding layers for each rod were measured with a circumferential step of 45° (Figure 111). The distribution of cladding oxide layer thicknesses (averaged values for each rod) across the bundle has the similar gradient as for the elevations 950 and 850 mm: the degree of oxidation at the bundle sides along the absorber blades is higher in comparison to the bundle sides without blades (Figure 112).

The cladding melt released inside the group of the inner rods #1…#9 formed several molten pools with steam channels with oxidized edges. The pellet-cladding gaps of the inner rods #1…#4 were filled with molten metal or voids were formed here due to downwards relocation of the melt (Figure 113…Figure 115). For the colder inner rods #5…#9, the gaps were mostly free of melt (Figure 116…Figure 118). For the hot peripheral rods #10…#17, the metal melt filled the entire gap and contacted the pellet (Figure 118…Figure 124). The gap (formed during the lift-off of the cladding due to Kr overpressure) was free from melt for the relatively cold peripheral rods #18…#22 (Figure 123…Figure 127). The claddings of the last two peripheral rods #23 and #24, which are in turn in the hot bundle area, were partially melted (especially for rod #24), and the melt contacted the pellets and the outer oxide layer (Figure 128).

Elevation 650 mm

A peak cladding temperature of about 1800 K was measured at the claddings of intermediate rods on the beginning of the quench stage. The absorber blades were significantly melted. Part of the melt was relocated also from upper elevations and attacked the B_4C pins, which were partially dissolved (Figure 129, Figure 130). Intense interaction of the stainless steel blade with the elements of the ZIRLO channel box and the Zr shroud was also observed (Figure 131, Figure 132, and Figure 133).

While the claddings of the peripheral rods show moderate oxidation, the claddings of the central and intermediate rods were oxidized significantly (Figure 134, Figure 135). Due to rather high temperatures, the oxide layer was partially dissolved by the molten β-Zr formed here and partially displaced from above.

For rods 1, 4, 7, and 8, the molten β-Zr partially moved along the pellets to lower elevations, leaving voids in their place (Figure 136, Figure 139, Figure 142, and Figure 143). The molten cladding β-Zr of other intermediate rods 2, 3, 5, 6, and 9 filled the gap between the outer layers and either the pellet or inner oxide layer without forming voids (Figure 137, Figure 138, Figure 140, Figure 141, and Figure 144). In some cases, due to the lift-off of the cladding under the action of internal pressure, an increased cladding-pellet gap was formed even before the formation of the melt.

Due to the limited heat loss through the absorber blades, the temperatures of the claddings of the peripheral rods 10-27, located on the azimuth sides 270° and 0° of the bundle, reached the melting points of the β-Zr phase in many places (Figure 145…Figure 152). The melt formed here, together with the melt relocated from above, filled the space between the outer α-Zr(O) layer and the pellet (or inner α-Zr(O) or oxide layer). Part of the oxygen from the pellet material diffused into the melt at the points of contact between the melt and the pellet. As a result, the corresponding parts of the pellet acquired a characteristic dark shade, which indicates the sub-stoichiometry of the pellet material - the corresponding effect was revealed in single effect tests [9]. The dark and light parts of the pellets are clearly visible in the overview image Figure 129 of this section. At the points of contact between the melt and the inner oxide layer, oxygen also diffused from the oxide into the melt, and alpha precipitates formed in the oxide. The latter effect is typical for oxide layers under steam starvation conditions [10].

The claddings of the peripheral rods 18-24, located along the azimuth sides of the bundle 90º and 180º, did not melt and have a standard solid-state layer structure ZrO_2 - α-Zr(O) - β-Zr (with α lamellas) - α-Zr(O) - ZrO_2 (Figure 153…Figure 160). These rods are located on two sides of the assembly, where there are no absorber blades - here the heat losses towards the shroud were higher than at the sides of the assembly with absorbers, and, respectively, the temperatures inside the rods did not reach the melting point of the cladding metal.

Elevation 555 mm

Temperature peaks on the shroud (azimuthal side 0°) during the transient stage indicate the relocation of the Zr-SS eutectic melt here from the upper bundle elevations (Figure 161). The interaction of the melt with the B_4C pins was minimal. Cladding oxidation was moderate and more pronounced in the center of the bundle (Figure 162).

Only small fragments of Inconel spacer grids (about 70% Ni) remained on the periphery of the bundle. In the center of the bundle, the spacer grids at these elevations were melted firstly due to the eutectic interaction of the nickel of the grids with the zirconium of the claddings: the deepest eutectic temperature in the Zr-Ni system is 1233 K (Figure 163). At a later stage of the transient, the melting point of the Inconel spacer (1610 K) was exceeded. The melt was partially relocated down, and partially penetrated under the damaged claddings.

For the central rod, even the melting point of the beta layer of cladding was exceeded. The corresponding melt partially dissolved the outer oxide layer, resulting in the formation of ceramic precipitates in the melt (Figure 164). Similar processes were observed for the shell of rod #4 (Figure 168). The melt also went beyond the oxide layer and formed molten pools in the inter-rod space (Figure 165). For other internal rods with strong damaged claddings, the formation of an eutectic melt occurred as a result of the interaction of the Inconel spacer melt with the residual β-Zr layer of the cladding (Figure 166…Figure 172). This melt is characterized by the formation of Zr precipitates distributed over the eutectic melt. The claddings of the outer rods were less damaged than those of the inner ones, but the eutectic melt formed not only in the in the gap between the cladding and the pellet, but also between inner and outer α-Zr(O) layers (Figure 174…Figure 189). It is interesting to note that if the zirconium-nickel eutectic prevails in the melt for the more damaged inner rods, then the zirconium-iron eutectic dominates in the less damaged outer rods. This is clearly seen from the comparison of the SEM/EDX analysis of rods 9 (Figure 173) and 10 (Figure 177). Sometimes for the outer rods, the formation of (Fe, Cr) chunks in the (Zr, Ni) eutectic melt is observed (Figure 182).

Elevation 450 mm

At this elevation, the outer layers of all claddings were not damaged (Figure 190). The degree of oxidation of the claddings can be characterized as medium (Figure 191). Despite this, on the inner surface of almost all claddings, a eutectic nickel-containing melt is observed, which has relocated from the elevation of 550 mm along the gap between the pellets and the outer layers of the claddings (Figure 192…Figure 198).

Elemental composition of different melt regions presented in Table 20.Comparison of cladding oxidation degrees between bundle elevations 450 and 950 mm is presented in Figure 199.

5 Summary and Conclusions

The experiment QUENCH-20 with BWR geometry simulation bundle was successfully conducted at KIT on 9th October 2019 in the framework of the international SAFEST project. The test bundle mock-up represented one quarter of a BWR fuel assembly with 24 electrically heated fuel rod simulators and two B_4C control blades. The rod simulators were filled with Kr to an inner pressure of 5.5 bar at peak cladding temperature of 900 K.

The pre-oxidation stage in a flowing gas mixture of steam and argon (each 3 g/s) and system pressure of 2 bar lasted 4 hours at the peak cladding temperature of 1250 K. The Zry-4 corner rod, withdrawn at the end of this stage, showed the maximal oxidation at elevations between 930 and 1020 mm with signs of breakaway.

During the transient stage, the bundle was heated to a maximum temperature of 2000 K. The coolability of the bundle was decreased by its squeezing due to the shroud ductile deformation caused by an overpressure outside the shroud. The cladding radial strain and failures due to inner overpressure (about 4 bar) were observed at temperature about 1700 K and lasted about 200 s.

During the period of rod failures also the first absorber melt relocation accompanied by shroud failure were registered. The interaction of B_4C with the steel blade and the ZIRLO channel box were observed at elevations 650…950 mm with the formation of eutectic melt. The typical components of this melt are (Fe, Cr) borides

and ZrB_2 precipitated in steel or in Zr-steel eutectic melt. Massive absorber melt relocation was observed 50 s before the end of transition stage. Small fragments of the absorber melt moved down to the elevation of 50 mm.

The melting point of Inconel spacer grids at 500 and 1050 mm was also reached at the end of the transition stage. The Inconel melt from the elevation 1050 mm relocated downwards through hot bundle regions to the Inconel grid spacer at 550 mm and later (during the escalation caused by quench) to 450 mm. This melt penetrated also under the damaged cladding oxide layer and formed molten eutectic mixtures between elevations 450 and 550 mm.

The test was terminated by quench water injection with a flow rate of 50 g/s from the bundle bottom. Fast temperature escalation from 2000 to 2300 K during 20 s was observed due to the strongly exothermic oxidation reactions. As result, the metal part (prior β-Zr) of the claddings between 550 and 950 mm was melted, partially released into space between rods and partially relocated in the gap between pellet and outer oxide layer to 450 mm. In this case, the positive role of the oxide layer should be noted, which does not allow the melt to completely escape into the inter-rod space. It is thereby limiting the possibility of interactions of a large amount of melt with steam, which could significantly increase the exothermic oxidation processes and the escalation of temperatures.

The distribution of the oxidation rate within each bundle cross section is very inhomogeneous: whereas the average outer ZrO_2 layer thickness for the central rod (#1) at the elevation of 750 mm is 465 µm, the same parameter for the peripheral rod #24 is only 108 µm. The average oxidation rate of the inner cladding surface (due to interaction with steam and with ZrO_2 pellets) is about 20% in comparison to the outer cladding oxidation. The bundle elevations 850 and 750 mm are mostly oxidized with average cladding ECR 33% due to: 1) downwards shift of the temperature maximum from 950 mm (ECR 31%) during the transient and the quench stages, and 2) due to cladding melt relocation inside and outside the rods from 800…1000 mm to lower bundle elevations. The oxidation of the melt relocated inside the rods was observed at elevations 550…950 mm.

The mass spectrometer measured release of CO (12.6 g), CO_2 (9.7 g) and CH_4 (0.4 g) during the reflood as products of absorber oxidation; the corresponding B_4C reacted mass was 41 g or 4.6% of the total B_4C inventory. It is significantly lower than in the PWR bundle tests QUENCH-07 and QUENCH-09 containing central absorber rod with B_4C pellets inserted into a *thin* stainless steel cladding and Zry-4 guide tubes (20% and 50% reacted B_4C correspondingly [5]).

Hydrogen production during the reflood amounted to 32 g during the reflood (57.4 g during the whole test) including 10 g from B_4C oxidation.

6 Acknowledgments

The QUENCH-20 experiment was performed in the framework of the SAFEST project in cooperation with Swedish Radiation Safety Authority (SSM), Westinghouse Sweden, GRS/Germany and KTH/Sweden and supported by the KIT program NUSAFE. Special thanks goes to Ms. Korske (Westinghouse), Mr. Hollands (GRS) for their help and fruitful cooperation. The bundle materials and absorbers were provided by Westinghouse Sweden.

The authors would like to thank all colleagues involved in the pre-test calculations.

7 References

1. J. Stuckert, M. Steinbrueck, M. Grosse, “Experimental program QUENCH at KIT on core degradation during reflooding under LOCA conditions and in the early phase of a severe accident,” Proceedings of Meeting on Modelling of Water Cooled Fuel Including Design Basis and Severe Accidents, Chengdu/China, 28 October–1 November 2013, IAEA-TECDOC-CD-1775, pp. 281-297, https://www-pub.iaea.org/MTCD/Publications/PDF/TE-1775_CD_web.pdf (2013).

2. T. Haste, M. Steinbrück, M. Barrachin, O. de Luze, M. Grosse, J. Stuckert, “A comparison of core degradation phenomena in the CORA, QUENCH, Phébus SFD and Phébus FP experiments,” *Nuclear Engineering and Design*, 283, pp. 8–20 (2015), https://doi.org/10.1016/j.nucengdes.2014.06.035.

3. M. Steinbrück, M. Große, L. Sepold, J. Stuckert. “Synopsis and outcome of the QUENCH experimental program”, *Nuclear Engineering and Design*, 240 (7), pp. 1714-1727, (2010), https://doi.org/10.1016/j.nucengdes.2010.03.021.

4. M. Steinbrück, C. Homann, A. Miassoedov, G. Schanz, L. Sepold, U. Stegmaier, H. Steiner, J. Stuckert. „Results of the B_4C control rod test QUENCH-07“, FZKA-6746 (2004), https://doi.org/10.5445/IR/270058023.

5. M. Steinbrück, A. Miassoedov, G. Schanz, L. Sepold, U. Stegmaier, H. Steiner, J. Stuckert. „Results of the QUENCH-09 experiment with a B_4C control rod”, FZKA-6829 (2004), https://doi.org/10.5445/IR/270059406.

6. P. Hofmann, M. Markiewicz, J. Spino. “Reaction Behaviour of B_4C Absorber Material with Stainless Steel and Zircaloy in Severe LWR Accidents”, KfK 4598, CNEA NT -10/89, (1989), https://doi.org/10.5445/IR/270027893.

7. M. Steinbrück. “Degradation and oxidation of B_4C control rod segments at high temperatures”, *Journal of Nuclear Materials*, 400 (2), pp. 138-150, (2010), https://doi.org/10.1016/j.jnucmat.2010.02.022.

8. Jong Hyuk Baek, Yong Hwan Jeong. “Breakaway phenomenon of Zr-based alloys during a high-temperature oxidation”, *Journal of Nuclear Materials*, 372 (2008), pp. 152-159, https://doi.org/10.1016/j.jnucmat.2007.02.011.

9. P. Hofmann, J. Stuckert, A. Miassoedov, M.S. Veshchunov, A.V. Berdyshev, A.V. Boldyrev. “ZrO_2 dissolution by molten zircaloy and cladding oxide shell failure. New experimental results and modelling”, FZKA-6383, https://doi.org/10.5445/IR/270046616.

10. J. Stuckert, M. S. Veshchunov. “Behaviour of Oxide Layer of Zirconium-Based Fuel Rod Cladding under Steam Starvation Conditions”, FZKA-7373, https://doi.org/10.5445/IR/270071587.

Tables and Figures

Table 1 QUENCH Test Matrix 1997 – 2019

Test	Quench medium and injection rate	Temp. at onset of flooding[1)]	Max. ZrO_2 before transient[2)]	Max. ZrO_2 (*X s*) before flooding[2)]	Posttest average ZrO_2 thickness[3)]	H_2 production before / during cooldown	Remarks, objectives
QUENCH-00 Oct. 9 - 16, 97	Water 80 g/s	≈ 1800 K			completely oxidized		Commissioning tests.
QUENCH-01 Feb. 26, 98	Water 52 g/s	≈ 1830 K	312 µm		500 µm at 913 mm	36 / 3	COBE Project; partial fragmentation of pre-oxidized cladding.
QUENCH-02 July 7, 98	Water 47 g/s	≈ 2400 K			completely oxidized	20 / 140	COBE Project; no additional pre-oxidation; quenching from high temperatures.
QUENCH-03 January 20, 99	Water 40 g/s	≈ 2350 K			completely oxidized	18 / 120	No additional pre-oxidation, quenching from high temperatures.
QUENCH-04 June 30, 99	Steam 50 g/s	≈ 2160 K	82 µm		280 µm	10 / 2	Cool-down behavior of slightly pre-oxidized cladding by cold steam injection.
QUENCH-05 March 29, 2000	Steam 48 g/s	≈ 2020 K	160 µm		420 µm	25 / 2	Cool-down behavior of pre-oxidized cladding by cold steam injection.
QUENCH-06 Dec 13 2000	Water 42 g/s	≈ 2060 K	207 µm[5)]	300 µm, (60 s), SVECHA modeling	630 µm[4)]	32 / 4	OECD-ISP 45; prediction of H_2 source term by different code systems.
QUENCH-07 July 25, 2001	Steam 15 g/s	≈ 2100 K	230 µm		completely oxidized	66 / 120	COLOSS Project; impact of B_4C absorber rod failure on H_2, CO, CO_2, and CH_4 generation.
QUENCH-09 July 3, 2002	Steam 49 g/s	≈ 2100 K			completely oxidized	60 / 400	As QUENCH-07, steam-starved conditions prior to cooldown.
QUENCH-08 July 24, 2003	Steam 15 g/s	≈ 2090 K	274 µm		completely oxidized	46 / 38	As QUENCH-07, no absorber rod.

Table 1. QUENCH Test Matrix 1997 – 2019 (continue)

Test	Quench medium and injection rate	Temp. at onset of flooding[1)]	Max. ZrO_2 before transient[2)]	Max. ZrO_2 (*X s*) before flooding[2)]	Posttest average ZrO_2 thickness[3)]	H_2 production before / during cooldown	Remarks, objectives
QUENCH-10 July 21, 2004	Water 50 g/s	≈ 2200 K	514 µm	613 µm (at 850 mm)	completely oxidized	48 / 5	LACOMERA Project; Air ingress.
QUENCH-11 Dec 08, 2005	Water 18 g/s	≈ 2040 K		170 µm	completely oxidized	9 / 132	LACOMERA Project; Boil-off.
QUENCH-12 Sept 27, 2006	Water 48 g/s	≈ 2100 K	160 µm, breakaway	300 µm, (110 s), breakaway	completely oxidized	34 / 24	ISTC Project #1648.2; VVER bundle with E110 claddings.
QUENCH-13 Nov 7, 2007	Water 52 g/s	≈ 1820 K		400 µm, after AgInCd rod failure	750 µm	42 / 1	SARNET; impact of AgInCd absorber rod failure on aerosol generation.
QUENCH-14 July 2, 2008	Water 41 g/s	≈ 2100 K	170 µm[6)]	470 µm[6)] (30 s)	900 µm	34 / 6	ACM series: M5® cladding
QUENCH-15 May 27, 2009	Water 48 g/s	≈ 2100 K	145 µm[6)]	380 µm[6)] (30 s)	620 µm	41 / 7	ACM series: ZIRLO™ cladding.
QUENCH-16 July 27, 2011	Water 53 g/s	≈ 1870 K*	135 µm	130 µm at 450-950 mm, breakaway	1075 µm at 550-650 mm	144 / 128	LACOMECO Project; Air ingress.
QUENCH-17 Jan. 31, 2013	Water 10 g/s	≈ 1800 K		completely oxidized	completely oxidized	110 / 1	SARNET-2; Debris formation and coolability.
QUENCH-18 Sept. 27, 2017	Water 53 g/s	≈ 1950 K	80 µm	completely oxidized	completely oxidized	57 / 238	ALISA Project; air ingress; AgInCd absorber rods
QUENCH-19 Aug. 29, 2018	Water 48 g/s	≈ 1800 K	-	-	-	8 / 1.2	Bundle with FeCrAl materials; cooperation with ORNL
QUENCH-20 Oct. 9, 2019	Water 50 g/s	≈ 2000 K	55 µm breakaway		completely oxidized at 850 mm	57 / 32	SAFEST Project

[1)] Maximum measured bundle temperature at 950 mm elevation.
[2)] Measured at the withdrawn corner rod at 950 mm elevation.
[3)] Measured posttest at the bundle elevation of maximum temperature.
[4)] Some claddings were completely oxidized at 950 mm elevation.
[5)] Oxide thickness during transient stage.
[6)] Zircaloy-4 corner rods.

Revised: June 2021

Table 2 Design characteristics of the QUENCH-20 test bundle

Bundle type		BWR
Bundle size (heated rods)		24 rods
Pitch		12.898 mm
Coolant channel area		46.18 cm^2
Cladding outside/inside diameter, thickness		9.84 / 8.63 mm, 605 µm
Cladding material		Zry-2 with inner ZrSn-liner (70 µm)
Cladding length (elevations)		2280 mm (-595 to 1685 mm)
Cladding thickness		605 µm
Full rod length (elevations)		2480 mm (-690 to 1790 mm)
Material of main heater		Tungsten (W)
surface roughness		Ra = 1.6 µm
W heater length		1024 mm
W heater diameter		5.25 ± 0.025 mm
Annular pellet	material	ZrO_2; Y_2O_3-stabilized
	dimensions	∅ 8.48 ± 0.05/5.45 ± 0.01 mm; L=11 mm
Pellet stack		0…≈1020 mm
Internal rod pressure (gas)		0.55 ± 0.05 MPa abs. (Kr)
Stainless steel blade (Figure 8)		2 blades
	material	AISI 316 L (Fe17Cr12Ni2Mo1.5Mn)
	length	1560 mm
	width	67 mm (6 mm of which are milled)
	thickness	8.05 mm
	hole center spacing	8 mm
	hole depth/diameter	59 (65 with steel strip channel)/6.03 mm
	mass of 1 blade (without/with steel strip)	3573/3700 g
B_4C pins		
	length	53 ± 1.4 mm
	diameter	4.7 ± 0.6 mm
	quantity	190/blade (5 lower holes not filled)
	total mass (390 pins)	897 g
Fuel channel box		
	material	low tin ZIRLO
	length (extension)	1560 mm (-300…+1260 mm)
	wall thickness	1.4 mm
	material	ZIRLO
Water channel box and	length (extension)	1560 mm (-300…+1260 mm)
wings	wall thickness	0.8 mm

Corner rod (1)	material not instrumented (A)	Zry-4 rod ∅ 6 mm (-1350…+1155 mm)
Grid spacers sleeve type	material length sheet thickness elevation of lower side	Inconel X750 (70Ni15Cr7Fe2.5Ti0.7Al) 11.8 mm 0.2 mm -200; 50; 550; 1050, 1410 mm
Shroud octagon with 4 short and 4 long sides	material wall thickness small clearance large clearance length (extension)	Zr 702 3 mm 90 mm 114 mm 1600 mm (-300…+1300 mm)
Shroud insulation	material insulation thickness elevation	ZrO_2 fiber ≈34 mm -300…≈+1000 mm
Molybdenum heaters and copper electrodes	length of upper parts length of lower parts diameter of electrodes: - prior to coating - after coating with ZrO_2 coating surface roughness	766 mm (576 mm Mo, 190 mm Cu) 690 mm (300 mm Mo, 390 mm Cu) 7.85 mm 8.25 mm Ra = 6-12 µm
Cooling jacket	Material: inner/outer tube inner tube outer tube	Inconel 600 (2.4816) / SS (1.4571) ∅ 158.3 / 168.3 mm ∅ 181.7 / 193.7 mm

Table 3 ASTM B-811 specification (weight %) of the Zircaloy-2 material and respective liner used for QUENCH-20

	Sn	**Fe**	**Cr**	**Ni**	**O**	**Si**	**Zr**
LK3 (Zry-2)	1.20–1.70	0.07–0.20	0.05–0.15	0.03–0.08	0.10–0.14	max. 0.009	bal.
Liner	max. 0.3	max. 0.07	-	-	-	-	bal.

Table 4 Main characteristics of the ZrO_2 pellet material, yttria-stabilized (type ZYK3)

Property	Data
Y_2O_3 content	5 %
Density	6.07 ± 0.03 g/cm^3
Open porosity	0
Average crystallite size	0.8 µm
Specific heat at 20 °C	400 J/kg K
Thermal conductivity at 100 °C	2.5 W/m K
Linear expansion, 20-1000 °C	11 x 10^{-6}/K
Vickers Hardness HV10	> 12000 N/mm^2
Bending strength	> 1150 MPa
Elastic modulus	> 200 GPa
Weibull modulus	20
Fracture toughness K_{1C}	12 MPa•m$^{1/2}$

According to Barat Ceramics GmbH, 07955 Auma

Table 5 QUENCH-20; Electrical resistances of rod circuits measured at 20 °C [mΩ]; two rod groups connected to two DC generators: GS1 and GS2

Rod #	1	2	3	4	5	6	7	8	9	10	11	12	*ave-rage*	*12 rods parallel*
Pre-test	4.1	4.2	4.2	4.1	4.1	4.1	4.1	4.1	4.1	4.2	4.2	4.2	*4.14*	***0.35***
Post-test	3.9	4.2	4.3	5.6	4.8	5.3	4.3	4.1	4.6	4.3	4.4	4.2	*4.48*	***0.37***

Rod #	13	14	15	16	17	18	19	20	21	22	23	24	*ave-rage*	*12 rods parallel*
Pre-test	4.2	4.1	4.1	4.1	4.2	4.1	4.1	4.2	4.1	4.1	4.2	4.2	*4.14*	***0.35***
Post-test	4.5	4.2	4.2	4.6	4.4	4.6	4.4	**6.9**	4.2	4.4	5.9	4.2	*4.73*	***0.39***

Table 6 Properties of zirconia fiber insulating boards of type ZYFB3

Chemical composition

Oxide	ZrO_2	Y_2O_3	HfO_2	TiO_2	SiO_2	CaO	MgO	Fe_2O_3	Al_2O_3	Na_2O
typical wt%	88	10	2	0.14	0.12	0.09	0.03	0.04	0.01	0.01

Physical properties

bulk density	porosity	shrinkage		thermal expansion coefficient @298-1453K	melting point	max service temperature	flexural strength	compressive strength @10% compression
		(1 hour @1925 K)	(24 hours @1925 K)					
g/cm³	%	%		1/K	K	K	MPa	MPa
0.48	92	1.2	2.8	$10.7*10^{-6}$	2866	2500	0.59	0.29

Thermal conductivity

temperature, K	673	1073	1373	1673	1923
conductivity, W/(m*K)	0.08	0.11	0.14	0.19	0.24

Specific heat capacity

temperature, K	366	2644
specific heat capacity, J/(kg*K)	544	754

According to specifications of manufacturer ZIRCAR PRODUCTS

Table 7 Measurement channels of the MERSY system for the QUENCH-20 test

Channel	Designation	Instrument, location	Unit
0	TFS 1/13	TC (W/Re) fuel rod simulator 1, 950 mm	K
1	TFS 9/13	TC (W/Re) fuel rod simulator 9, 950 mm	K
2	TFS 16/13	TC (W/Re) fuel rod simulator 16, 950 mm	K
3	TFS 18/13	TC (W/Re) fuel rod simulator 18, 950 mm	K
4	TFS 3/14	TC (W/Re) fuel rod simulator 3, 1050 mm	K
5	TSH 13/180	TC (W/Re) shroud outer surface, 950 mm, 180°, TC legs behind shroud insulation	K
6	TFS 5/12	TC (W/Re) fuel rod simulator 5, 850 mm	K
7	TFS 5/14	TC (W/Re) fuel rod simulator 5, 1050 mm	K
8	TFS 7/14	TC (W/Re) fuel rod simulator 7, 1050 mm	K
9	TFS 9/14	TC (W/Re) fuel rod simulator 9, 1050 mm	K
10	TFS 1/15	TC (W/Re) fuel rod simulator 1, 1150 mm	K
11	TFS 11/15	TC (W/Re) fuel rod simulator 11, 1150 mm	K
13	TFS 22/15	TC (W/Re) fuel rod simulator 22, 1150 mm	K
14	TFS 5/16	TC (W/Re) fuel rod simulator 5, 1250 mm	K
15	TFS 9/16	TC (W/Re) fuel rod simulator 9, 1250 mm	K
16	TFS 10/10	TC (W/Re) fuel rod simulator 10, 650 mm	K
17	TSH 13/270	TC (W/Re) shroud outer surface, 950 mm, 270°, TC legs behind shroud insulation	K
18	TSH 14/180	TC (W/Re) shroud outer surface, 1050 mm, 180°, TC legs behind shroud insulation	K
19	TSH 14/270	TC (W/Re) shroud outer surface, 1050 mm, 270°, TC legs behind shroud insulation	K
20	TSH 15/270	TC (W/Re) shroud outer surface, 1150 mm, 270°, TC legs behind shroud insulation	K
21	TSH 12/90	TC (W/Re) shroud outer surface, 850 mm, 90°, TC legs behind shroud insulation	K
22	TSH 5/270	TC (NiCr/Ni) shroud, 150 mm, 270°	K
23	TSH 4/180	TC (NiCr/Ni) shroud, 50 mm, 180°	K
26	TFS 23/10	TC (W/Re) fuel rod simulator23, 650 mm	K
27	TFS 5/9	TC (W/Re) fuel rod simulator 5, 550 mm	K
29	TFS 11/9	TC (W/Re) fuel rod simulator 11, 550 mm	K
30	TFS 22/9	TC (W/Re) fuel rod simulator 22, 550 mm	K
31	TFS 1/8	TC (W/Re) fuel rod simulator 1, 450 mm	K
35	TSH 15/0	TC (NiCr/Ni) shroud, 1150 mm, 0°	K
36	TSH 15/180	TC (NiCr/Ni) shroud, 1150 mm, 180°	K
38	T 320	temperature of the surface of the gas inlet pipe at the bundle bottom	K

Channel	Designation	Instrument, location	Unit
39	TSH 12/180	TC (W/Re) shroud outer surface, 850 mm, 180°, TC legs behind shroud insulation	K
40	TFS 7/10	TC (NiCr/Ni) fuel rod simulator 7, 650 mm	K
41	TFS 20/12	TC (W/Re) fuel rod simulator 20, 850 mm	K
42	TSH 4/270	TC (NiCr/Ni) shroud, 50 mm, 270°	K
43	TSH 3/180	TC (NiCr/Ni) shroud, -50 mm, 180°	K
44	TSH 2/90	TC (NiCr/Ni) shroud, -150 mm, 90°	K
45	TFS 9/8	TC (NiCr/Ni) fuel rod simulator 9 , 450 mm	K
46	TSH 1/0	TC (NiCr/Ni) shroud, -250 mm, 0°	K
47	TSH 9/180	TC (W/Re) shroud outer surface, 550 mm, 180°, TC legs behind shroud insulation	K
48	TSH 9/270	TC (W/Re) shroud outer surface, 550 mm, 270°, TC legs behind shroud insulation	K
49	TSH 10/270	TC (W/Re) shroud outer surface, 650 mm, 270°, TC legs behind shroud insulation	K
52	TSH 12/180	TC (W/Re) shroud outer surface, 850 mm, 180°, TC legs behind shroud insulation	K
53	TFS 9/9	TC (W/Re) fuel rod simulator 9, 550 mm	K
54	TSH 11/0	TC (W/Re) shroud outer surface, 750 mm, 0°, TC legs behind shroud insulation	K
55	TSH 11/180	TC (W/Re) shroud outer surface, 750 mm, 180°, TC legs behind shroud insulation	K
56	TFS 24/12	TC (W/Re) fuel rod simulator 24, 850 mm	K
57	TFS 1/11	TC (W/Re) fuel rod simulator 1, 750 mm	K
58	TSH 16/90	TC (NiCr/Ni) shroud outer surface, 1250 mm, 90°	K
59	TFS 5/11	TC (W/Re) fuel rod simulator 5, 750 mm	K
60	TFS 9/11	TC (W/Re) fuel rod simulator 9, 750 mm	K
61		Reserve	K
62		Reserve	bar
63		Reserve	g/s
64	T 402b	Temperature of the tube surface after gas heater	K
65	TFS 12/11	TC (W/Re) fuel rod simulator 12, 750 mm, °	K
66	TSH 11/270	TC (W/Re) shroud outer surface, 750 mm, 270°, TC legs behind shroud insulation	K
67	TSH 10/180	TC (W/Re) shroud outer surface, 650 mm, 180°, TC legs behind shroud insulation	K
68	T 512	Gas temperature bundle outlet	K
70	TFS 3/10	TC (W/Re) fuel rod simulator 3, 650 mm	K
71	Ref. T 01	Reference temperature 1	K
72	TBL 6/90	TC (NiCr/Ni), absorber blade, 250 mm, 90°	K
73	TBL 7/180	TC (NiCr/Ni), absorber blade, 350 mm, 180°	K

Channel	Designation	Instrument, location	Unit
74	TBL 8/90	TC (NiCr/Ni), absorber blade, 450 mm, 90°	K
75	TBL 2/180	TC (NiCr/Ni), absorber blade, -150 mm, 180°	K
76	TBL 2/90	TC (NiCr/Ni), absorber blade, -150 mm, 90°	K
77	TCH 7/180	TC (NiCr/Ni), water channel box, 350 mm, 180°	K
78	TCH 7/90	TC (NiCr/Ni), water channel box, 350 mm, 90°	K
79	TCH 8/90	TC (NiCr/Ni), water channel box, 450 mm, 90°	K
80	TCH 8/180	TC (NiCr/Ni), water channel box, 450 mm, 180°	K
81	TFS 3/7	TC (NiCr/Ni) fuel rod simulator 3, 350 mm	K
82	TFS 10/7	TC (NiCr/Ni) fuel rod simulator 10, 350 mm,	K
83	TSH 16/270	TC (NiCr/Ni) shroud outer surface, 1250 mm, 270°	K
84	TSH 9/0	TC (NiCr/Ni) shroud outer surface, 550 mm, 0°	K
85	TSH 9/90	TC (NiCr/Ni) shroud outer surface, 550 mm, 90°	K
86	TSH 8/90	TC (NiCr/Ni) shroud outer surface, 450 mm, 90°	K
87	TSH 8/180	TC (NiCr/Ni) shroud outer surface, 450 mm, 180°	K
88	TSH 7/90	TC (NiCr/Ni) shroud outer surface, 350 mm, 90°	K
89	TSH 6/180	TC (NiCr/Ni) shroud outer surface, 250 mm, 180°	K
90	TSH 6/270	TC (NiCr/Ni) shroud outer surface, 250 mm, 270°	K
91	TFS 7/17	TC (NiCr/Ni) fuel rod simulator 7, 1350 mm	K
92	TCI 11/270	TC (NiCr/Ni) cooling jacket inner tube wall, 750 mm, 270°	K
93	TCI 10/270	TC (NiCr/Ni) cooling jacket inner tube wall, 650 mm, 270°	K
95	TFS 1/6	TC (NiCr/Ni) fuel rod simulator 1, 250 mm, °	K
96	TCI 7/180	TC (NiCr/Ni) cooling jacket inner tube wall, 350 mm, 180°	K
97	TCI 4/180	TC (NiCr/Ni) cooling jacket inner tube wall, 50 mm, 180°	K
98	TCI 13/180	TC (NiCr/Ni) shroud outer surface, 950 mm, 296°	K
99	TFS 3/17	TC (W/Re) fuel rod simulator 3 (type), 1350 mm	K
100	TCI 1/180	TC (NiCr/Ni) cooling jacket inner tube wall, -250 mm, 180°	K
101	TCI 12/180	TC (NiCr/Ni) cooling jacket inner tube wall, 850 mm, 180°	K
102	TCI 15/180	TC (NiCr/Ni) cooling jacket inner tube wall, 1150 mm, 180°	K
103	T002 inlet	Cooling water, inlet of off-gas tube	K
104	TCI 7/90	TC (NiCr/Ni) cooling jacket inner tube wall, 350 mm, 90°	K
105	TCI 10/90	TC (NiCr/Ni) cooling jacket inner tube wall, 650 mm, 90°	K
108	TFS 3/4	TC (NiCr/Ni) fuel rod simulator 3, 50 mm	K
109	TCI 4/0	TC (NiCr/Ni) cooling jacket inner tube wall, 50 mm, 0°	K
110	TCI 11/0	TC (NiCr/Ni) cooling jacket inner tube wall, 750 mm, 0°	K
111	TCI 13/0	TC (NiCr/Ni) cooling jacket inner tube wall, 950 mm, 0°	K
112	TCI 7/0	TC (NiCr/Ni) cooling jacket inner tube wall, 350 mm, 0°	K
113	TCI 1/0	TC (NiCr/Ni) cooling jacket inner tube wall, -250 mm, 0°	K
114	TCI 12/0	TC (NiCr/Ni) cooling jacket inner tube wall, 850 mm, 0°	K

Channel	Designation	Instrument, location	Unit
115	TCI 15/0	TC (NiCr/Ni) cooling jacket inner tube wall, 1150 mm, 0°	K
116	T003	Cooling water, outlet of off-gas tube	K
117	TSH 7/180	TC (NiCr/Ni) shroud outer surface, 350 mm, 180°	K
118	TSH 5/180	TC (NiCr/Ni) shroud outer surface, 150 mm, 180°	K
119	TFS 24/6	TC (NiCr/Ni) fuel rod simulator 24, 250 mm	K
120	TCO 1/0	TC (NiCr/Ni) cooling jacket outer tube surface, -250 mm, 0°	K
121	TCO 7/0	TC (NiCr/Ni) cooling jacket outer tube surface, 350 mm, 0°	K
122	TCO 13/0	TC (NiCr/Ni) cooling jacket outer tube surface, 950 mm, 0°	K
123	T 310	TC (NiCr/Ni) aerosol extraction tube in off-gas pipe	K
124	T 513	Outer wall of bundle head	K
125	T 514	Cooling water bundle head	K
126	T307 off-gas	TC (NiCr/Ni) inner surface of inlet of off-gas pipe	K
128	T 104	Temperature quench water	K
129	T 201	Temperature steam generator heating pipe	K
130	T 204	Temperature before steam flow instrument location 50 g/s	K
131	T 205	Temperature before steam flow instrument location 10 g/s	K
132	T 301A	Temperature behind superheater	K
133	T 302	Temperature superheater heating pipe	K
134	T 303	Temperature before total flow instrument (orifice) location	K
135	T 401	Temperature before gas flow instrument (orifice) location	K
136	T 403	Temperature of Ar at inlet cooling jacket	K
137	T 404	Temperature of Ar at outlet cooling jacket	K
138	T 501 cont-t	Temperature in containment (close to bundle head)	K
139	T 502	Temperature at outer surface of containment, 0°, 2.4 m	K
140	TFS 5/1 F	TC (NiCr/Ni) fuel rod simulator 5, -250 mm, °	K
141	TFS 7/4	TC (NiCr/Ni) fuel rod simulator 7, 50 mm, °	K
142	T 505	Temperature at outer surface of containment, 90°, 3.2 m	K
143	T 506	Temperature at outer surface of containment, 270°, 3.6 m	K
144	TFS 9/3	TC (NiCr/Ni) fuel rod simulator 9, -50 mm	K
145	TFS 1/2	TC (NiCr/Ni) fuel rod simulator 1, -150 mm	K
147	T 510	Temperature at outer surface of containment, 270°, 4.4 m	K
148	T 511	Gas temperature at bundle inlet	K
149	TFS 11/5	TC (NiCr/Ni) fuel rod simulator 11, 150 mm	K
150	TFS 22/5	TC (NiCr/Ni) fuel rod simulator 22, 150 mm	K
152	P 201	Pressure steam generator	bar
154	P 205	Pressure at steam flow instrument location 10 g/s	bar
155	P 303	Pressure before total flow instrument (orifice) location	bar
156	P 401	Pressure before gas flow instrument location	bar

Channel	Designation	Instrument, location	Unit
157	P 511	Pressure at bundle inlet	bar
158	P 512	Pressure at bundle outlet	bar
159	P 601	Pressure before off-gas flow instrument (orifice) F 601	bar
160	P 901	Reserve	bar
161	L 201	Liquid level steam generator	mm
162	L 501	Liquid level quench water	mm
163	L 701	Liquid level condensation vessel	mm
164	Fm 401 Ar	Argon flow rate	g/s
165	P 411	Pressure Kr supply	bar
166	P 403	Pressure Ar cooling of cooling jacket	bar
167	P 406	Pressure insulation shroud/cooling jacket	bar
168	Fm 104	Flow rate quench water	l/h
169		Reserve	g/s
170	Fm 205_cor	Flow rate steam 10 g/s	g/s
171	F 303	Flow rate at bundle inlet (steam + argon), orifice; differential pressure measurement	mbar
173	F 403	Flow rate cooling gas	g/s
174	F 601	Flow rate off-gas (orifice); differential pressure measurement	mbar
175	Fm 406 Ar	Flow rate argon into room between shroud and cooling jacket	g/s
176	E 201	Electric current steam generator	A
177	E 301	Electric current superheater	A
178	E 501	Electric current inner ring of fuel rod simulators	A
179	E 502	Electric current outer ring of fuel rod simulators	A
180	E 503	Electric voltage inner ring of fuel rod simulators	V
181	E 504	Electric voltage outer ring of fuel rod simulators	V
182	Hub_V302	Gas supply valve lift	%
250	E 505	Electric power inner ring of fuel rod simulators	W
251	E 506	Electric power outer ring of fuel rod simulators	W

Indications:

TFS – TC at the surface of fuel rod simulators;
TSH – TC at the outer surface of shroud;
TBL – TC at absorber blade;
TCH – TC at water channel box.

Note: the data of additional 21 measurement channels (internal pressures of rods) of the DELPHIN system were recorded separately

Table 8 QUENCH-20; map of TFS thermocouples

elevation, mm	-250	-150	-50	50	150	250	350	450	550	650	750	850	950	1050	1150	1250	1350
elev. No. / rod No.	1	2	3	4	5	6	7	8	9	10	11	12	13	14	15	16	17
1		N				N		W			W		W		W		
2																	
3				N			N			W				W			N
4																	
5	N								W		W	W		W		W	
6																	
7				N						W				W			N
8																	
9			N					N	W		W		W	W		W	
10							N			W							
11					N				W		W				W		
12																	
13																	
14																	
15																	
16													W				
17																	
18													W				
19																	
20												W					
21																	
22					N				W						W		
23										W							
24						N						W					
TC quantity:	1	1	1	2	2	2	2	1, 1	4	4	4	3	4	4	3	2	2

TC to bundle bottom: 16 W/Re + 12 NiCr/Ni

TC to bundle top: 13 W/Re, 2 NiCr/Ni

N NiCr/Ni (totally 14)

W W/Re (totally 29)

Table 9 Diameters of the materials used for the manufacture of High-Temperature Thermocouples [mm]

Material	As-received	Final
W/Re wires	0.254	
HfO_2 insulation OD (see drawing below)	1.1	
Ta tube OD / ID	2.15 / 1.65	1.4 / 0.94
Zr tube OD / ID	2.5 / 1.65 ± 0.05	2.2-2.3 / ~1.4

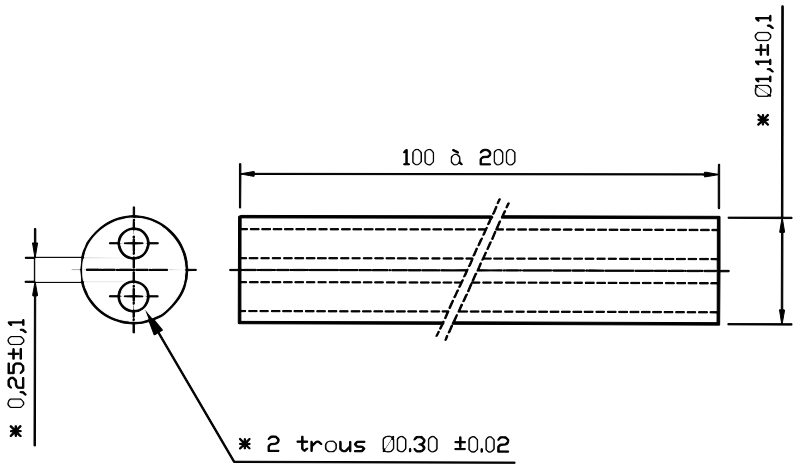

Table 10 Main characteristics of the HfO_2 thermocouple insulator

Property	Data
Composition of basic material	99 % HfO_2
Melting temperature	2840 °C
Max. use temperature	2500 °C
Density	8.4 g/cm^3
Thermal conductivity at 20-1000 °C	1.14 W/m K
Linear expansion	5.8 x 10^{-6}/K

Table 11 QUENCH-20; Sequence of events

Time, s	Event
0 (12:21:52)	Start data recording. TFS 1/13 = 902 K, el. power 3.4 kW, P 511=1.94 bar, internal rod pressure P_{rod1}=5.97 bar
158	El. power 7.15 kW
700	TFS 1/13 = 1075 K, interim maximum of rod internal pressure: P_{rod1}=6.08 bar; probable reason - decrease of the gap between heater and pellets due to thermal expansion of W, then beginning of gap increase between pellets and cladding due to ballooning effect
2286	El. power 7.9 kW; P 511=1.96 bar
4770…4815	Short-term pressure drop, P 511=1.93 bar
7177	Temperature plateau of TFS 1/13 = 1255 K reached
7500…14600	Ductile shroud deformation (implosion) (P 406 decrease) due to higher pressure outside shroud in comparison to system pressure (P 406 > P 511)
10000	Interim minimums of bundle temperatures and rod internal pressure, P_{rod1}=5.82 bar (probable reason: cessation of increase of the gap pellet-cladding due to thick oxide layer)
13000	Interim maximum of internal rod pressure P_{rod1}=5.88 bar
14412	Corner rod withdrawn
14406	Transient start, TFS 1/13=1258 K, P_{rod1}=5.85 bar
14406…15540	Linear increase of electrical power from 7.7 to 18.2 kW
14891	First He release (blade leakage)
15581	First *rod failures* (rods 1, 4, 8): drops of inner rod pressure, TFS 1/13=1718 K
15581…15768	7 Kr peaks during the rod failures (15587, 15602, 15639, 15668, 15693, 15739, 15774 s)
15625	Cessation of increase of resistance for heaters of the GS1 rod group (temperature escalation at cladding and stabilization of temperature inside heaters?)
15675	**First absorber melt relocation to 450 mm at 0°** (TBL 8/90 peak, He release, first **CH_4** production)
15668…15681	Shroud failure (pressure drop P 406, then start of *Ar flow Fm 406*)
15750	Decrease of resistance for heaters of the GS1 rod group (conductivity of pellets?)
15768	Last *rod failure* (rod 12); TFS 1/13=1832 K
15808	Cessation of increase of resistance for heaters of the GS2 rod group (temperature escalation at cladding and stabilization of temperature inside heaters?)
15835	Decrease of resistance for heaters of the GS2 rod group (conductivity of pellets?), TFS 1/13=1905 K
15882	Fast injection of 4 L water
15884…15901	Linear decrease of electric power from 18.2 to 3.97 kW
15891	Initiation of quench water injection; TFS 1/13=2098 K, maximum T reached during the test
16375	Last wetting of cladding thermocouple by two phase fluid
16475	Cessation of He release from blades
16851	El. power switch-off
17660 (17:16:12)	End of data recording.

Table 12 QUENCH-20; failures of 9 inner and 14 outer rods (1700 K < TFS 1/13 < 1850 K)

Time, s	15581	15582	15582	15588	15588	15590	15597	15598	15626
Rod #	8	1	4	7	6	2	9	5	3

Time, s	15631	15638	15662	15665	15670	15670	15681	15685	15695	15730	15734	15737	15762	15768
Rod #	15	22	11	19	10	21	16	20	23	13	24	18	17	12

Table 13 QUENCH-20; cross sections of the test bundle for metallographic examination

Sample	Sample length (mm)	Axial position (mm)		Remarks
		bottom	top	
			31	Remainder
Cut	4	31	35	
QUE-20-1	*20*	*35*	***55***	*Spacer 2, 55 mm polished*
Cut	4	55	59	
QUE-20-a	167	59	226	
Cut	4	226	230	
QUE-20-2	20	230	**250**	TC elevation 6, 250 mm polished
Cut	4	250	254	
QUE-20-b	72	254	326	
Cut	4	326	330	
QUE-20-3	20	330	**350**	TC elevation 7, 350 mm polished
Cut	4	350	354	
QUE-20-c	72	354	426	
Cut	4	426	430	
QUE-20-4	20	430	**450**	TC elevation 8, 450 mm polished
Cut	4	450	454	
QUE-20-d	77	454	531	
Cut	4	531	535	
QUE-20-5	*20*	*535*	***555***	*Spacer 3, 555 mm polished*
Cut	4	555	559	
QUE-20-e	67	559	626	
Cut	4	626	630	
QUE-20-6	16	630	**650**	TC elevation 10, 650 mm polished
Cut	4	650	654	
QUE-20-f	72	654	726	
Cut	4	726	730	
QUE-20-7	20	730	**750**	TC elevation 11, 750 mm polished
Cut	4	750	754	
QUE-20-g	72	754	826	
Cut	4	826	830	
QUE-20-8	20	830	**850**	TC elevation 12, 850 mm polished
Cut	4	850	854	
QUE-20-h	76	854	930	
Cut	4	930	934	
QUE-20-9	20	930	**950**	TC elevation 13, 950 mm polished
Cut	4	950	954	
QUE-20-i	77	954	1031	
Cut	4	1031	1035	
QUE-20-10	*20*	*1035*	***1055***	*Spacer 4, 1055 mm polished*
Cut	4	1055	1059	
QUE-20-j	67	1059	1126	
Cut	4	1126	1130	
QUE-20-11	20	1130	**1150**	
		1150		Remainder

Table 14 Cladding layer thicknesses at elevation 950 mm

rod #	angle, °	0	45	90	135	180	225	270	315
1	ZrO_2								360
	α-Zr(O)								350
	β-Zr/melt								0
	inn. α-Zr(O)								0
	inn. ZrO2								75
2	ZrO_2		350				225	370	420
	α-Zr(O)		300				380	320	280
	β-Zr/melt		0				0	0	0
	inn. α-Zr(O)		0				0	0	0
	inn. ZrO_2		0				0	15	15
3	ZrO_2	450	340	370	320		370	420	500
	α-Zr(O)	210	150	180	305		115	220	190
	β-Zr/melt	80	0	0	65		0	0	0
	inn. α-Zr(O)	120	70	0	0		150	0	10
	inn. ZrO2	90	160	175	50		135	115	80
4	ZrO_2	380	450				540	390	430
	α-Zr(O)	350	190				0	0	0
	β-Zr/melt	0	0				0	0	0
	inn. α-Zr(O)	0	0				0	0	0
	inn. ZrO_2	150	70				230	300	250
5	ZrO_2	440	340	320	345	350			425
	α-Zr(O)	250	360	350	325	300			250
	β-Zr/melt	0	0	0	0	0			0
	inn. α-Zr(O)	0	0	0	0	0			0
	inn. ZrO_2	0	0	20	40	60			20
6	ZrO_2		340	300	290				
	α-Zr(O)		360	320	440				
	β-Zr/melt		0	0	0				
	inn. α-Zr(O)		110	0	80				
	inn. ZrO_2		50	0	30				

rod #	angle, °	0	45	90	135	180	225	270	315
7	ZrO_2		240	160	95	165	230	260	
	α-Zr(O)		310	310	190	280	340	390	
	β-Zr/melt		70	90	205	150	0	0	
	inn. α-Zr(O)		60	80	30		80	0	
	inn. ZrO_2		45	35	25	25	40	50	
8	ZrO_2				280		330		
	α-Zr(O)				400		210		
	β-Zr/melt				0		200		
	inn. α-Zr(O)				0		90		
	inn. ZrO2				20		50		
9	ZrO_2			350			150	250	190
	α-Zr(O)			340			390	400	440
	β-Zr/melt			0			0	0	0
	inn. α-Zr(O)			0			0	0	0
	inn. ZrO_2			55			0	60	70
10	ZrO_2	220	205		210	165	155	140	210
	α-Zr(O)	270	240		265	155	190	165	230
	β-Zr/melt	200	150		280	200	240	350	320
	inn. α-Zr(O)	110	40		70	40	90	75	85
	inn. ZrO_2	10	65		25	25	50	70	60
11	ZrO_2	370	350	205	220	230	220	230	280
	α-Zr(O)	225	310	180	270	240	230	145	175
	β-Zr/melt	160	60	0	220	310	130	150	130
	inn. α-Zr(O)	70	70	165	105	55	65	30	95
	inn. ZrO_2	65	65	105	30	15	70	75	30
12	ZrO_2	415	490	360	420	400	340	285	300
	α-Zr(O)	0	215	280	0	0	25	0	0
	β-Zr/melt	300	0	80	210	370	180	312	750
	inn. α-Zr(O)	105	0	0	0	0	0	0	0
	inn. ZrO2	35	35	40	85	75	130	130	50

rod #	angle, °	0	45	90	135	180	225	270	315
13	ZrO_2		450	455	475	420	340	0	0
	α-Zr(O)		0	0	200	150	140	0	0
	β-Zr/melt		0	65	650	230	95	0	0
	inn. α-Zr(O)		0	0	0	35	115	0	0
	inn. ZrO_2		30	200	45	65	35	45	0
14	ZrO_2			390	350	280	470		
	α-Zr(O)			0	0	170	0		
	β-Zr/melt			420	470	600	350		
	inn. α-Zr(O)			0	0	0	0		
	inn. ZrO_2			55	80	35	65		
15	ZrO_2		350	380	480	400	410	350	
	α-Zr(O)		0	0	190	280	0	0	
	β-Zr/melt		0	0	0	0	430	0	
	inn. α-Zr(O)		0	0	90	0	0	0	
	inn. ZrO2		45	0	60	50	90	70	
16	ZrO_2	250	240	260	315	340	450	435	335
	α-Zr(O)	380	360	380	280	155	300	115	280
	β-Zr/melt	0	0	0	0	0	0	0	0
	inn. α-Zr(O)	0	0	0	0	0	0	0	0
	inn. ZrO_2	60	65	73	130	305	35	250	140
17	ZrO_2	180	165	150	135	165	195	205	175
	α-Zr(O)	340	180	175	185	230	250	250	210
	β-Zr/melt	0	220	260	300	150	130	75	0
	inn. α-Zr(O)	0	void	50	35	55	75	80	215
	inn. ZrO_2	60	25	45	0	35	35	60	55
18	ZrO_2	260	195	170	145	205	260	210	225
	α-Zr(O)	400	245	240	260	415	345	380	245
	β-Zr/melt	0	65	130	70	0	0	0	15
	inn. α-Zr(O)	0	125	110	90	0	0	0	95
	inn. ZrO_2	60	50	50	50	55	65	105	105

rod #	angle, °	0	45	90	135	180	225	270	315
19	ZrO_2	210	150	90	115	110	220	240	265
	α-Zr(O)	425	265	180	520	250	420	400	370
	β-Zr/melt	0	170	320	0	120	0	0	0
	inn. α-Zr(O)	0	35	150	0	55	0	0	0
	inn. ZrO_2	30	20	5	15	25	50	65	50
20	ZrO_2	100	75	65	120	125	55	75	160
	α-Zr(O)	230	180	130	145	175	240	145	260
	β-Zr/melt	260	360	360	330	285	230	330	140
	inn. α-Zr(O)	30	0	50	45	30	65	55	90
	inn. ZrO_2	20	10	25	20	25	30	25	20
21	ZrO_2	65	100	120	115	125	60	115	155
	α-Zr(O)	150	195	160	150	155	190	235	260
	β-Zr/melt	215	170	310	360	340	285	150	50
	inn. α-Zr(O)	150	90	25	0	0	65	95	120
	inn. ZrO_2	60	40	15	0	20	30	45	60
22	ZrO_2	220	215	150	115	65	125	210	290
	α-Zr(O)	325	425	270	210	200	205	410	350
	β-Zr/melt	0	0	130	220	220	240	0	0
	inn. α-Zr(O)	85	0	60	80	45	70	0	0
	inn. ZrO_2	50	50	30	20	20	25	45	55
23	ZrO_2	170	230	130	50	140	165	190	170
	α-Zr(O)	450	245	210	160	150	200	265	250
	β-Zr/melt	0	70	260	410	290	225	90	170
	inn. α-Zr(O)	0	75	60	20	40	45	60	140
	inn. ZrO_2	40	50	25	10	15	15	20	15
24	ZrO_2	155	145	125	115	115	115	105	130
	α-Zr(O)	190	190	180	155	145	155	155	180
	β-Zr/melt	330	270	280	310	350	355	330	330
	inn. α-Zr(O)	0	40	15	0	0	0	20	15
	inn. ZrO_2	0	25	15	0	0	0	15	15

Table 15 Cladding layer thicknesses at elevation 850 mm

rod #	angle, °	0	45	90	135	180	225	270	315
1	ZrO_2	460	350	0	320	0	0	480	300
	α-Zr(O)	0	0	400	340	585	0	0	0
	β-Zr/melt	0	190	0	0	0	475	0	0
	inn. α-Zr(O)	0	0	0	0	0	0	0	0
	inn. ZrO_2	110	310	90	90	115	50	70	90
2	ZrO_2	650	560	0	0	0	710	570	620
	α-Zr(O)	215	0	0	280	0	0	0	0
	β-Zr/melt	0	0	0	0	0	0	0	0
	inn. α-Zr(O)	0	0	0	0	480	0	60	0
	inn. ZrO_2	60	80	50	70	150	0	230	80
3	ZrO_2	725			635	0	560	630	695
	α-Zr(O)	0			0	0	0	0	0
	β-Zr/melt	0			240	0	215	0	100
	inn. α-Zr(O)	0			0	0	0	0	0
	inn. ZrO2	0			135	0	85	95	200
4	ZrO_2	380	730	630	290	0	550		610
	α-Zr(O)	0	0	230	0	0	0		0
	β-Zr/melt	void	910	550	210	360	0		0
	inn. α-Zr(O)	0	0	0	0	110	0		0
	inn. ZrO_2	0	160	140	45	90	220		0
5	ZrO_2	630	530	570		640	0	0	685
	α-Zr(O)	135	230	150		175	0	0	150
	β-Zr/melt	0	0	0		0	0	0	0
	inn. α-Zr(O)	0	0	0		0	330	0	0
	inn. ZrO_2	0	0	0		0	450	280	0
6	ZrO_2	0	615	0	525	0	0	0	0
	α-Zr(O)	790	200	0	260	280	450	530	200
	β-Zr/melt	0	0	0	0	360	0	0	0
	inn. α-Zr(O)	0	0	0	0	145	0	85	0
	inn. ZrO_2	90	95	65	40	40	70	65	70

rod #	angle, °	0	45	90	135	180	225	270	315
7	ZrO_2	0	410	300	175	350	360	380	350
	α-Zr(O)	500	260	300	325	295	275	230	290
	β-Zr/melt	0	0	0	70	0	0	0	0
	inn. α-Zr(O)	0	0	70	110	0	0	30	0
	inn. ZrO_2	115	80	45	35	40	60	75	60
8	ZrO_2	0		300	420	540	580	300	0
	α-Zr(O)	0		0	0	160	165	300	0
	β-Zr/melt	490		0	0	0	0	0	0
	inn. α-Zr(O)	100		0	0	0	70	0	500
	inn. ZrO_2	85		0	0	65	50	30	30
9	ZrO_2	0	0	575	540	0	0	445	420
	α-Zr(O)	0	0	0	190	0	0	220	0
	β-Zr/melt	550	450	70	0	790	330	0	50
	inn. α-Zr(O)	0	0	0	0	110	0	0	0
	inn. ZrO_2	100	75	235	170	70	50	75	310
10	ZrO_2	350	380	305				330	330
	α-Zr(O)	160	90	0				0	
	β-Zr/melt	420	220	0				0	590
	inn. α-Zr(O)		130	0				0	0
	inn. ZrO_2	50	60	0				0	70
11	ZrO_2	540	570	400	400	250	405	255	460
	α-Zr(O)	0	0	170	0	0	0	0	0
	β-Zr/melt	0	0	0	350	0	0	0	0
	inn. α-Zr(O)	0	0	0	0	0	0	0	0
	inn. ZrO_2	0	70	85	95	60	45	15	0
12	ZrO_2	460	580	930	560	590	645	350	390
	α-Zr(O)	0	0	0	0	0	0	0	0
	β-Zr/melt	260	0	0	250	200	0	0	0
	inn. α-Zr(O)	0	0	0	0	0	0	0	0
	inn. ZrO_2	55	0	0	90	35	0	0	0

rod #	angle, °	0	45	90	135	180	225	270	315
13	ZrO_2		395	600	580	550	400		
	α-Zr(O)		0	0	0	0	0		
	β-Zr/melt		800	340	430	0	0		
	inn. α-Zr(O)		0	0	0	0	0		
	inn. ZrO_2		60	90	50	0	0		
14	ZrO_2	520	500	430	380	530	640	660	645
	α-Zr(O)	0	0	0	0	0	0	65	0
	β-Zr/melt	0	0	0	0	340	0	0	310
	inn. α-Zr(O)	0	0	0	0	0	0	0	0
	inn. ZrO_2	0	95	75	80	150	0	60	100
15	ZrO_2		310	0	605	660	0	415	445
	α-Zr(O)		0	0	80	0	0	0	0
	β-Zr/melt		void	460	0	240	770	0	0
	inn. α-Zr(O)		0	0	0	0	0	0	0
	inn. ZrO_2		0	35	115	90	160	250	0
16	ZrO_2	430	455		570	480	510	620	340
	α-Zr(O)	0	0		150	0	0	0	0
	β-Zr/melt	0	200		170	0	0	0	0
	inn. α-Zr(O)	0	0		0	0	0	0	0
	inn. ZrO_2	65	50		150	270	280	0	160
17	ZrO_2		345		0	315	400	445	360
	α-Zr(O)		0		0	195	190	125	0
	β-Zr/melt		260		470	295	85	100	0
	inn. α-Zr(O)		0		170	155	160	135	0
	inn. ZrO_2		125		25	30	45	45	60
18	ZrO_2	515	395	345	270	395	520	0	0
	α-Zr(O)	215	310	275	275	290	160	570	440
	β-Zr/melt	0	0	0	105	0	0	0	0
	inn. α-Zr(O)	0	0	75	35	0	0	0	0
	inn. ZrO_2	25	25	30	35	45	70	70	50

rod #	angle, °	0	45	90	135	180	225	270	315
19	ZrO_2	485	340		230	300	455	420	515
	α-Zr(O)	190	330		405	330	215	75	170
	β-Zr/melt	0	0		0	50	0	0	0
	inn. α-Zr(O)	0	0		0	0	0	0	0
	inn. ZrO_2	55	25		30	40	60	80	30
20	ZrO_2	250	150	0	145	170	100	135	325
	α-Zr(O)	270	240	125	195	215	135	230	350
	β-Zr/melt	50	170	300	240	210	310	210	0
	inn. α-Zr(O)	70	70	100	45	55	80	75	0
	inn. ZrO_2	40	30	45	25	25	40	20	25
21	ZrO_2	135	180	145	125	140	130	235	285
	α-Zr(O)	185	245	190	170	185	240	255	255
	β-Zr/melt	55	0	260	320	255	190	30	25
	inn. α-Zr(O)	175	220	25	15	40	80	115	35
	inn. ZrO_2	115	45	15	10	15	40	55	125
22	ZrO_2	350	330	320	410	0	580	0	0
	α-Zr(O)	310	322	230	180	0	145	220	520
	β-Zr/melt	0	0	0	0	0	200	0	0
	inn. α-Zr(O)	0	0	0	0	0	50	0	0
	inn. ZrO_2	35	90	70	55	0	45	25	0
23	ZrO_2	180	445	290	50	235	270	305	60
	α-Zr(O)	0	175	220	140	230	160	0	0
	β-Zr/melt	0	330	160	440	240	110	225	0
	inn. α-Zr(O)	0	0	120	150	110	0	0	0
	inn. ZrO_2	40	220	90	5	35	20	30	0
24	ZrO_2	240	240	190	150	145	150	200	215
	α-Zr(O)	240	200	190	0	0	0	0	240
	β-Zr/melt	100	115	250	820	1220	640	700	70
	inn. α-Zr(O)	150	140	95	0	0	0	0	180
	inn. ZrO_2	10	10	10	0	45	25	55	20

Table 16 Cladding layer thicknesses at elevation 750 mm

rod #	angle, °	0	45	90	135	180	225	270	315
1	ZrO_2	525			410				460
	α-Zr(O)	255			245		350		150
	β-Zr/melt	0			650		350		0
	inn. α-Zr(O)	0			80		150		0
	inn. ZrO_2	95			90		55		85
2	ZrO_2	550	410	*65*	*65*	*40*	370	470	430
	α-Zr(O)	180	130	0	0	120	210	270	130
	β-Zr/melt	490	300	0	0	0	420	510	530
	inn. α-Zr(O)	80	80	0	0	0	55	0	0
	inn. ZrO_2	90	85	0	0	0	35	50	50
3	ZrO_2	505	415	450	430	530	540	440	505
	α-Zr(O)	0	0	0	0	0	290	700	450
	β-Zr/melt	620	820	330	0	0	0	0	0
	inn. α-Zr(O)	0	0	void	0	0	0	0	0
	inn. ZrO_2	85	65	70	75	55	110	55	60
4	ZrO_2	430	420	410	300	650	510	490	450
	α-Zr(O)	150	0	0	0	0	260	190	250
	β-Zr/melt	170	0	0	0	0	0	220	0
	inn. α-Zr(O)	120	0	0	150	0	0	230	0
	inn. ZrO_2	50	45	30	45	0	85	105	0
5	ZrO_2	380	200	330	400	410			445
	α-Zr(O)	290	280	240	250	220			330
	β-Zr/melt	0	150	60	60	0			0
	inn. α-Zr(O)	0	0	45	15	0			0
	inn. ZrO_2	70	0	10	10	0			85
6	ZrO_2		*40*		460		400		
	α-Zr(O)		175		250		290		
	β-Zr/melt		0		0		0		
	inn. α-Zr(O)		0		0		0		
	inn. ZrO_2		165		30		0		

rod #	angle, °	0	45	90	135	180	225	270	315
7	ZrO_2		400	260	200	260	350	380	340
	α-Zr(O)		150	290	380	370	270	210	290
	β-Zr/melt		0	0	0	0	0	0	0
	inn. α-Zr(O)		0	0	0	0	0	0	0
	inn. ZrO_2		280	160	65	50	95	110	35
8	ZrO_2				405	380	450		
	α-Zr(O)				280	310	200		
	β-Zr/melt				0	0	0		
	inn. α-Zr(O)				0	0	0		
	inn. ZrO_2				75	60	60		
9	ZrO_2			435	405	340	355	375	370
	α-Zr(O)			180	150	210	230	240	220
	β-Zr/melt			0	0	0	0	0	0
	inn. α-Zr(O)			0	0	0	0	0	0
	inn. ZrO_2			220	225	215	165	140	150
10	ZrO_2	280		275	215	180	150	155	215
	α-Zr(O)	135		190	235	175	155	220	190
	β-Zr/melt	580		105	210	435	780	610	610
	inn. α-Zr(O)	30		180	0	180	30	140	150
	inn. ZrO_2	45		25	205	35	0	30	10
11	ZrO_2	405	440	350	350	310	270	270	325
	α-Zr(O)	175	270	330	170	205	250	200	145
	β-Zr/melt	70	130	230	70	75	130	400	150
	inn. α-Zr(O)	15	95	95	205	205	220	200	25
	inn. ZrO_2	70	35	35	35	15	5	5	30
12	ZrO_2	470	430	440	480	460	390	340	430
	α-Zr(O)	0	70	0	0	0	0	0	0
	β-Zr/melt	490	450	590	400	620	100	1030	640
	inn. α-Zr(O)	0	0	0	0	0	0	0	0
	inn. ZrO_2	30	30	55	50	55	0	0	20

rod #	angle, °	0	45	90	135	180	225	270	315
13	ZrO_2	320	330	340	390	0	0	310	320
	α-Zr(O)	0	0	0	0	0	0	0	0
	β-Zr/melt	0	600	420	800	0	0	450	230
	inn. α-Zr(O)	0	0	0	0	0	0	0	0
	inn. ZrO_2	0	30	40	50	0	0	45	50
14	ZrO_2	380	400	410	400	390	410	430	400
	α-Zr(O)	115	90	80	0	205	120	0	0
	β-Zr/melt	133	240	330	470	0	90	750	0
	inn. α-Zr(O)	205	190	190	0	0	160	0	0
	inn. ZrO_2	40	45	50	55	75	80	70	0
15	ZrO_2		290	330	390	370	380	410	0
	α-Zr(O)		0	0	0	0	0	0	0
	β-Zr/melt		0	0	330	500	600	400	0
	inn. α-Zr(O)		0	0	0	0	0	0	0
	inn. ZrO_2		45	0	45	65	90	60	0
16	ZrO_2	310	300	310	350	230	300		
	α-Zr(O)	0	0	0	150	180	180		
	β-Zr/melt	0	0	490	210	400	110		
	inn. α-Zr(O)	0	0	0	180	130	70		
	inn. ZrO_2	0	0	75	35	30	50		
17	ZrO_2			240		245	270	280	220
	α-Zr(O)			0		0	0	0	0
	β-Zr/melt			475		600	500	520	0
	inn. α-Zr(O)			0		0	0	0	0
	inn. ZrO_2			25		40	40	0	0
18	ZrO_2	325	275	245	200	265	320		
	α-Zr(O)	0	0	225	230	360	340		
	β-Zr/melt	300	410	200	150	0	0		
	inn. α-Zr(O)	0	0	20	70	0	0		
	inn. ZrO_2	30	20	20	20	40	45		

rod #	angle, °	0	45	90	135	180	225	270	315
19	ZrO_2	350	260	195	100	240	380		390
	α-Zr(O)	345	270	225	170	0	0		260
	β-Zr/melt	0	160	180	295	390	230		0
	inn. α-Zr(O)	0	0	55	75	0	0		0
	inn. ZrO_2	25	10	20	30	40			40
20	ZrO_2	215	60	60	100	105		165	270
	α-Zr(O)	240	105	95	135	150		460	380
	β-Zr/melt	170	425	360	340	280		0	0
	inn. α-Zr(O)	35	0	60	40	50		0	0
	inn. ZrO_2	15	0	40	25	30		75	45
21	ZrO_2	145		100	90	105	70	155	225
	α-Zr(O)	180		130	115	125	130	200	190
	β-Zr/melt	70		355	400	370	340	130	60
	inn. α-Zr(O)	175		35	25	25	65	130	110
	inn. ZrO_2	90		20	10	20	35	55	110
22	ZrO_2			230	170		185	280	370
	α-Zr(O)			370	200		210	215	230
	β-Zr/melt			0	125		100	25	0
	inn. α-Zr(O)			0	145		140	120	0
	inn. ZrO_2			85	45		55	105	190
23	ZrO_2	320	285	210		130	165	185	100
	α-Zr(O)	250	200	205		160	160	190	140
	β-Zr/melt	100	30	75		410	290	180	0
	inn. α-Zr(O)	0	100	140		95	75	95	0
	inn. ZrO_2	0	115	60		30	25	35	0
24	ZrO_2	135	140	110	80	85	90	100	120
	α-Zr(O)	175	180	145	120	110	120	165	170
	β-Zr/melt	520	235	460	630	330	380	370	570
	inn. α-Zr(O)	100	130	85	0	0	0	150	95
	inn. ZrO_2	0	0	0	11	0	0	0	0

Table 17 Cladding layer thicknesses at elevation 650 mm

rod #	angle, °	0	45	90	135	180	225	270	315
1	ZrO_2	230	290	175	150	230	290	0	410
	α-Zr(O)	650	430	270	260	400	450	0	400
	β-Zr/melt	0	0	150	210	125	0	0	0
	inn. α-Zr(O)	0	0	0	0	110	0	600	0
	inn. ZrO_2	80	35	0	0	25	40	30	45
2	ZrO_2	195	170	240	170	180	160	150	200
	α-Zr(O)	480	470	206	530	230	220	210	420
	β-Zr/melt	580	200	170	840	400	570	410	120
	inn. α-Zr(O)	70	130	160	0	120	110	95	120
	inn. ZrO_2	20	30	20	10	0	0	0	25
3	ZrO_2	140		140		130		135	
	α-Zr(O)	200		400		300		180	
	β-Zr/melt	668		560		320		530	
	inn. α-Zr(O)	70		140		300		80	
	inn. ZrO_2	0		10		160		0	
4	ZrO_2	210		315	350	290	220		200
	α-Zr(O)	200		285	250	170	240		450
	β-Zr/melt	270		0	85	125	80		600
	inn. α-Zr(O)	70		0	120	210	195		0
	inn. ZrO_2	15		0	30	15	20		15
5	ZrO_2	295		270		395			305
	α-Zr(O)	290		260		305			290
	β-Zr/melt	135		135		0			0
	inn. α-Zr(O)	0		0		0			80
	inn. ZrO_2	0		0		0			0
6	ZrO_2	370	450		460	430	410		440
	α-Zr(O)	275	90		50	460	250		310
	β-Zr/melt	0	0		0	340	300		0
	inn. α-Zr(O)	140	120		70	140	220		120
	inn. ZrO_2	40	170		30	45	45		45

rod #	angle, °	0	45	90	135	180	225	270	315
7	ZrO_2	350	270	180	125	150	180	270	350
	α-Zr(O)	270	280	410	470	460	420	155	300
	β-Zr/melt	50	0	0	0	0	0	0	170
	inn. α-Zr(O)	150	0	0	0	0	0	0	100
	inn. ZrO_2	100	180	105	70	60	60	150	40
8	ZrO_2	250	440		235	180	205	235	300
	α-Zr(O)	500	70		210	240	245	420	310
	β-Zr/melt	0	0		50	50	55	150	420
	inn. α-Zr(O)	0	0		140	145	140	140	90
	inn. ZrO_2	0	370		90	45	40	15	20
9	ZrO_2	180	185	200	140	115	130	125	160
	α-Zr(O)	250	250	210	190	180	165	175	230
	β-Zr/melt	50	50	0	145	230	270	330	220
	inn. α-Zr(O)	155	160	200	155	120	90	30	45
	inn. ZrO_2	35	45	115	70	55	45	0	20
10	ZrO_2	90	110	110	90	72	65	65	72
	α-Zr(O)	160	180	205	125	105	88	95	105
	β-Zr/melt	750	560	0	425	400	520	790	900
	inn. α-Zr(O)	110	145	0	125	95	85	0	90
	inn. ZrO_2								
11	ZrO_2	110	135	130	110	90	75	65	80
	α-Zr(O)	150	180	180	170	135	105	95	120
	β-Zr/melt	250	150	290	330	350	400	460	430
	inn. α-Zr(O)	150	145	115	120	120	60	70	85
	inn. ZrO_2	50	50	0	0	0	0	0	45
12	ZrO_2	85	105	125	130	110	80	70	80
	α-Zr(O)	120	160	180	170	150	115	105	115
	β-Zr/melt	330	320	290	410	380	390	420	390
	inn. α-Zr(O)	30	25	35	40	90	125	100	20
	inn. ZrO_2	15	15	15	15	0	0	10	15

rod #	angle, °	0	45	90	135	180	225	270	315
13	ZrO_2	65	90	95		90	65	75	65
	α-Zr(O)	80	70	0		110	105	100	110
	β-Zr/melt	500	1050	1040		650	650	400	650
	inn. α-Zr(O)	55	0	0		75	120	110	100
	inn. ZrO_2	5	0	15		5	0	0	0
14	ZrO_2	110	130	160	180	160	125	110	105
	α-Zr(O)	180	180	180	195	240	180	165	170
	β-Zr/melt	210	240	330	360	230	390	720	450
	inn. α-Zr(O)	160	160	50	85	130	140	70	110
	inn. ZrO_2	15	15	0	0	30	0	0	0
15	ZrO_2	135	190	230	250	240	220	150	150
	α-Zr(O)	180	130	140	120	220	700	0	0
	β-Zr/melt	100	630	630	210	100	0	0	0
	inn. α-Zr(O)	150	90	110	160	210	0	0	0
	inn. ZrO_2	20	30	45	25	15	35	0	0
16	ZrO_2	130	135	145	180	190	235	190	155
	α-Zr(O)	180	140	390	230	500	255	250	185
	β-Zr/melt	560	200	0	300	0	55	230	550
	inn. α-Zr(O)	115	0	0	150	0	230	190	125
	inn. ZrO_2	10	15	25	15	10	10	0	5
17	ZrO_2	110	140	145	200	180	180	140	120
	α-Zr(O)	0	0	0	0	0	0	0	0
	β-Zr/melt	700	0	0	1000	1000	500	500	800
	inn. α-Zr(O)	0	0	0	0	0	0	0	0
	inn. ZrO_2	0	0	0	0	0	0	0	0
18	ZrO_2	165	145	130	140	150	210	180	200
	α-Zr(O)	170	135	135	170	175	210	180	200
	β-Zr/melt	300	335	360	250	205	80	70	130
	inn. α-Zr(O)	90	35	0	90	95	150	175	135
	inn. ZrO_2	30	20	0	25	35	55	95	40

rod #	angle, °	0	45	90	135	180	225	270	315
19	ZrO_2	270	165	140	115	160	280	0	320
	α-Zr(O)	220	185	170	160	190	120	0	215
	β-Zr/melt	55	175	280	280	75	65	130	40
	inn. α-Zr(O)	125	180	55	80	165	85	450	75
	inn. ZrO_2	65	40	30	25	75	180	125	50
20	ZrO_2	125	65	65	65	70	55	100	135
	α-Zr(O)	170	85	90	80	90	110	160	185
	β-Zr/melt	250	0	390	420	430	0	240	220
	inn. α-Zr(O)	75	0	70	25	30	0	95	85
	inn. ZrO_2	25	45	0	25	20	0	40	25
21	ZrO_2	80	80	65	60	60	75	100	125
	α-Zr(O)	140	105	90	65	70	80	120	145
	β-Zr/melt	280	380	450	490	460	420	335	225
	inn. α-Zr(O)	100	40	0	0	20	40	80	100
	inn. ZrO_2	60	20	0	0	15	25	35	65
22	ZrO_2	180	155	115	85	60	90	115	145
	α-Zr(O)	235	215	140	95	85	110	150	220
	β-Zr/melt	90	165	245	340	370	400	315	215
	inn. α-Zr(O)	140	130	120	0	60	60	75	85
	inn. ZrO_2	55	50	35	0	0	15	25	25
23	ZrO_2	110	100	105	75	95	100	105	100
	α-Zr(O)	155	135	125	90	115	119	130	140
	β-Zr/melt	370	330	510	470	570	544	480	325
	inn. α-Zr(O)	125	75	60	20	0	0	55	60
	inn. ZrO_2	50	35	25	15	10	13	20	30
24	ZrO_2	65	65	65	50	50	45	50	60
	α-Zr(O)	90	100	90	75	70	55	60	80
	β-Zr/melt	430	450	450	480	485	505	510	475
	inn. α-Zr(O)	0	0	0	0	0	0	0	0
	inn. ZrO_2	0	0	0	0	0	0	0	0

Table 18 Cladding layer thicknesses at elevation 555 mm

rod #	angle, °	0	45	90	135	180	225	270	315
1	ZrO_2	260	0	0	0	0	0	0	255
	α-Zr(O)								
	β-Zr/melt	550	0	0	0	0	0	0	520
	inn. α-Zr(O)								
	inn. ZrO_2	60	0	0	0	0	0	0	45
2	ZrO_2	205	0	0	0	250	170	0	165
	α-Zr(O)	0	0	0	0	70	0	0	95
	β-Zr/melt	90	0	0	0	740	140	0	350
	inn. α-Zr(O)	0	0	0	0	0	0	0	0
	inn. ZrO_2	20	0	0	0	50	105	0	30
3	ZrO_2	130	205	255	190	205	140	115	105
	α-Zr(O)	135	115	145	80	35	105	90	155
	β-Zr/melt	470	0	390	280	350	190	610	365
	inn. α-Zr(O)	140	0	35	105	90	0	30	145
	inn. ZrO_2	15	0	105	50	45	40	15	5
4	ZrO_2	175	225	265	205	230	240	270	300
	α-Zr(O)	190	45	0	0	0	0	0	0
	β-Zr/melt	110	850	750	425	570	0	0	0
	inn. α-Zr(O)	210	25	0	15	0	0	0	0
	inn. ZrO_2	20	30	35	30	35	0	0	0
5	ZrO_2	220	215	260	180	230	250	0	250
	α-Zr(O)	125	0	140	0	0	0	0	110
	β-Zr/melt	400	0	190	0	330	0	0	105
	inn. α-Zr(O)	35	0	170	0	150	0	0	135
	inn. ZrO_2	40	40	35	0	70	0	0	45
6	ZrO_2	245	225	0	0	240	265	0	270
	α-Zr(O)	90	0	0	0	280	0	0	140
	β-Zr/melt	310	0	0	0	750	420	0	330
	inn. α-Zr(O)	60	0	0	0	200	80	150	60
	inn. ZrO_2	20	0	0	0	60	40	50	20

rod #	angle, °	0	45	90	135	180	225	270	315
7	ZrO_2	0	0	120	0	0	80	225	420
	α-Zr(O)	0	0	55	0	0	120	175	160
	β-Zr/melt	0	0	0	0	0	210	180	130
	inn. α-Zr(O)	0	0	0	0	110	165	250	390
	inn. ZrO_2	0	0	0	0	25	20	0	75
8	ZrO_2	0	210	0	0	0	175	130	0
	α-Zr(O)	0	0	0	0	0	35	0	0
	β-Zr/melt	0	800	0	0	0	550	210	0
	inn. α-Zr(O)	230	0	0	0	170	25	155	0
	inn. ZrO_2	55	45	0	0	50	25	55	0
9	ZrO_2	225	0	0	125	130	0	115	190
	α-Zr(O)	50	0	0	120	125	0	130	60
	β-Zr/melt	135	0	0	150	125	0	270	void
	inn. α-Zr(O)	110	0	0	40	50	0	170	30
	inn. ZrO_2	25	0	55	90	85	0	10	25
10	ZrO_2	70	85	105	70	60	70	50	55
	α-Zr(O)	110	145	130	95	75	65	70	95
	β-Zr/melt	540	340	510	240	435	450	800	405
	inn. α-Zr(O)	110	145	90	45	40	30	65	50
	inn. ZrO_2	0	0	0	55	40	30	0	0
11	ZrO_2	90	115	240	105	80	65	60	0
	α-Zr(O)	85	110	1040	145	115	85	70	0
	β-Zr/melt	360	310	0	270	480	425	425	0
	inn. α-Zr(O)	55	35	0	135	95	45	50	0
	inn. ZrO_2	65	15	10	0	0	40	35	0
12	ZrO_2	65	75	90	90	80	65	55	55
	α-Zr(O)	90	105	125	115	105	80	75	80
	β-Zr/melt	435	390	355	325	320	390	450	475
	inn. α-Zr(O)	10	15	130	140	120	85	55	75
	inn. ZrO_2	5	15	0	0	0	35	0	0

rod #	angle, °	0	45	90	135	180	225	270	315
13	ZrO_2	50	55	70	70	70	60	60	45
	α-Zr(O)	75	85	75	75	95	85	75	75
	β-Zr/melt	590	440	490	650	670	700	890	370
	inn. α-Zr(O)	85	100	100	75	75	55	0	0
	inn. ZrO_2								
14	ZrO_2	65	70	100	140	145	95	75	65
	α-Zr(O)	100	115	120	0	220	120	85	95
	β-Zr/melt	305	505	475	550	145	470	430	550
	inn. α-Zr(O)	120	75	55	0	175	90	45	55
	inn. ZrO_2	0	0	5	20	0	15	35	0
15	ZrO_2	75	85	120	170	150	165	125	90
	α-Zr(O)	0	100	95	190	200	75	90	0
	β-Zr/melt	635	700	580	165	150	470	0	0
	inn. α-Zr(O)	25	55	35	230	210	25	0	0
	inn. ZrO_2	0	10	15	10	15	30	45	30
16	ZrO_2	75	95	125	145	0	175	115	85
	α-Zr(O)	130	115	160	95	0	180	145	150
	β-Zr/melt	200	790	910	290	0	390	580	430
	inn. α-Zr(O)	95	105	105	130	150	95	105	130
	inn. ZrO_2	0	5	3	15	30	10	15	10
17	ZrO_2	85	85	130	0	0	165	125	75
	α-Zr(O)	205	65	910	0	0	55	90	130
	β-Zr/melt	260	700	0	0	0	300	350	320
	inn. α-Zr(O)	125	40	0	0	0	35	55	125
	inn. ZrO_2	0	20	30	0	0	25	15	0
18	ZrO_2	185	0	0	270	0	0	275	210
	α-Zr(O)	185	0	0	0	0	0	45	115
	β-Zr/melt	590	0	0	0	0	0	310	35
	inn. α-Zr(O)	50	0	0	0	0	0	120	120
	inn. ZrO_2	25	0	0	0	0	0	20	60

rod #	angle, °	0	45	90	135	180	225	270	315
19	ZrO_2	300	260	275	0	0	0	0	305
	α-Zr(O)	0	0	150	0	0	0	0	0
	β-Zr/melt	0	730	0	0	0	0	0	435
	inn. α-Zr(O)	0	0	0	0	0	0	0	95
	inn. ZrO_2	45	75	195	0	0	0	0	35
20	ZrO_2	230	0	0	70	60	90	140	190
	α-Zr(O)	0	0	0	65	65	130	110	95
	β-Zr/melt	0	0	0	430	460	290	100	210
	inn. α-Zr(O)	0	0	0	35	30	140	125	50
	inn. ZrO_2	65	0	0	35	25	20	20	20
21	ZrO_2	60	65	50	43	50	60	105	130
	α-Zr(O)	100	85	65	60	65	0	95	120
	β-Zr/melt	210	460	600	465	450	0	430	230
	inn. α-Zr(O)	125	110	10	55	55	0	0	40
	inn. ZrO_2	10	0	0	0	0	0	70	105
22	ZrO_2	120	135	0	60	55	70	80	120
	α-Zr(O)	160	130	0	60	75	100	110	155
	β-Zr/melt	220	350	0	390	540	460	390	200
	inn. α-Zr(O)	150	120	0	0	75	95	110	150
	inn. ZrO_2	15	25	0	40	0	0	5	5
23	ZrO_2	75	90	55	60	50	60	60	80
	α-Zr(O)	110	95	60	65	65	700	90	95
	β-Zr/melt	650	255	780	250	420	0	500	300
	inn. α-Zr(O)	50	55	20	20	20	0	70	115
	inn. ZrO_2	30	45	0	15	15	0	0	5
24	ZrO_2	85	65	45	25	65	40	60	40
	α-Zr(O)	125	70	65	50	60	45	45	55
	β-Zr/melt	840	405	390	470	490	510	450	420
	inn. α-Zr(O)	185	80	90	70	30	20	60	50
	inn. ZrO_2	0	0	0	5	0	0	0	0

Table 19 Cladding layer thicknesses at elevation 450 mm

rod #	angle, °	0	45	90	135	180	225	270	315
1	ZrO_2	118	120	110	105	105	105	105	110
	α-Zr(O)	90	115	120	130	170	125	115	120
	β-Zr/melt	520	315	805	670	370	355	490	630
	inn. α-Zr(O)	125	120	0	90	175	135	65	70
	inn. ZrO_2	20	25	25	0	0	0	0	0
2	ZrO_2	85	85	90	85	85	75	65	65
	α-Zr(O)	115	130	130	125	120	115	95	95
	β-Zr/melt	630	480	370	370	515	730	855	840
	inn. α-Zr(O)	75	90	100	100	85	65	45	0
	inn. ZrO_2	0	0	0	0	0	0	0	0
3	ZrO_2	65		85		85		65	
	α-Zr(O)	105		105		120		95	
	β-Zr/melt	435		430		550		430	
	inn. α-Zr(O)	130		void		165		120	
	inn. ZrO_2	0		0		0		0	
4	ZrO_2	85	85	100	105	105	110	85	85
	α-Zr(O)	125	140	110	130	155	150	130	125
	β-Zr/melt	310	590	850	650	450	430	540	280
	inn. α-Zr(O)	140	120	60	85	125	130	110	125
	inn. ZrO_2	0	0	10	10	0	0	0	0
5	ZrO_2	75		75		85		95	
	α-Zr(O)	120		120		150		125	
	β-Zr/melt	450		415		440		865	
	inn. α-Zr(O)	140		135		145		15	
	inn. ZrO_2	0		0		0		0	
6	ZrO_2	95	90	85	90	95	100	120	115
	α-Zr(O)	135	125	100	120	125	125	190	150
	β-Zr/melt	460	350	450	470	540	780	310	720
	inn. α-Zr(O)	100	90	85	85	85	65	void	70
	inn. ZrO_2	0	0	0	0	0	0	0	0

rod #	angle, °	0	45	90	135	180	225	270	315
7	ZrO_2	85		65		65		85	
	α-Zr(O)	115		95		90		120	
	β-Zr/melt	360		400		470		655	
	inn. α-Zr(O)	60		100		100		65	
	inn. ZrO_2	45		0		0		0	
8	ZrO_2	95		85		75		85	
	α-Zr(O)	160		105		120		125	
	β-Zr/melt	255		380		350		675	
	inn. α-Zr(O)	void		25		130		45	
	inn. ZrO_2	0		10		0		0	
9	ZrO_2	75		80		65		60	
	α-Zr(O)	105		105		95		90	
	β-Zr/melt	390		680		390		635	
	inn. α-Zr(O)	35		0		95		60	
	inn. ZrO_2	15		0		0		0	
10	ZrO_2	30		45		25		15	
	α-Zr(O)	55		60		30		35	
	β-Zr/melt	580		480		530		535	
	inn. α-Zr(O)	30		30		20		15	
	inn. ZrO_2	20		0		15		15	
11	ZrO_2	40		60		50		30	
	α-Zr(O)	60		65		50		45	
	β-Zr/melt	460		505		510		490	
	inn. α-Zr(O)	35		20		25		30	
	inn. ZrO_2	30		10		10		25	
12	ZrO_2	45		50		40		25	
	α-Zr(O)	50		70		55		55	
	β-Zr/melt	420		450		480		490	
	inn. α-Zr(O)	0		20		15		15	
	inn. ZrO_2	20		15		10		15	

rod #	angle, °	0	45	90	135	180	225	270	315
13	ZrO_2	30	40	45	45	45	50	25	25
	α-Zr(O)	30	45	65	60	50	50	40	45
	β-Zr/melt	820	690	530	490	560	700	920	930
	inn. α-Zr(O)	55	60	60	55	55	45	40	30
	inn. ZrO_2	0	0	0	0	0	0	0	0
14	ZrO_2	40		55		55		50	
	α-Zr(O)	70		95		90		40	
	β-Zr/melt	420		450		575		530	
	inn. α-Zr(O)	90		95		110		void	
	inn. ZrO_2	0		0		0		0	
15	ZrO_2	55		65		85		70	
	α-Zr(O)	80		90		160		105	
	β-Zr/melt	375		900		270		850	
	inn. α-Zr(O)	90		80		120		70	
	inn. ZrO_2	0		0		0		0	
16	ZrO_2	50		65		80		60	
	α-Zr(O)	70		90		110		80	
	β-Zr/melt	420		560		565		295 (void)	
	inn. α-Zr(O)	95		105		95		void	
	inn. ZrO_2	0		0		0		0	
17	ZrO_2	60	50	55	55	55	60	65	60
	α-Zr(O)	90	90	80	80	85	80	90	85
	β-Zr/melt	470	405	490	600	660	735	720	620
	inn. α-Zr(O)	110	105	105	105	95	85	90	105
	inn. ZrO_2	0	0	0	0	0	0	0	0
18	ZrO_2	50		50		60		60	
	α-Zr(O)	60		75		70		70	
	β-Zr/melt	440		420		420		465	
	inn. α-Zr(O)	60		60		70		105	
	inn. ZrO_2	25		30		30		0	

rod #	angle, °	0	45	90	135	180	225	270	315
19	ZrO_2	60		45		60		75	
	α-Zr(O)	90		55		65		85	
	β-Zr/melt	490		490		455		540	
	inn. α-Zr(O)	85		35		35		75	
	inn. ZrO_2	0		20		15		0	
20	ZrO_2	50		30		30		57	
	α-Zr(O)	75		45		50		80	
	β-Zr/melt	230		250		510		435	
	inn. α-Zr(O)	void		void		55		75	
	inn. ZrO_2	0		0		0		0	
21	ZrO_2	45	40	30	25	25	35	45	50
	α-Zr(O)	70	55	35	35	35	40	60	75
	β-Zr/melt	420	475	505	530	510	495	445	430
	inn. α-Zr(O)	50	35	25	20	20	25	35	45
	inn. ZrO_2	35	30	20	15	15	15	20	25
22	ZrO_2	65		50		35		50	
	α-Zr(O)	95		65		50		70	
	β-Zr/melt	420		450		480		440	
	inn. α-Zr(O)	80		40		30		40	
	inn. ZrO_2	0		0		25		30	
23	ZrO_2	50		40		40		30	
	α-Zr(O)	65		50		45		45	
	β-Zr/melt	435		775		555		690	
	inn. α-Zr(O)	0		25		0		25	
	inn. ZrO_2	0		5		0		10	
24	ZrO_2	15	20	15	15	15	15	10	15
	α-Zr(O)	35	45	35	35	25	25	25	25
	β-Zr/melt	540	745	535	555	575	590	585	560
	inn. α-Zr(O)	0	0	0	0	0	0	0	0
	inn. ZrO_2	0	0	0	0	0	0	0	0

Table 20 Elemental composition of melt at different elevations (integral EDX analysis, Boron and Oxygen are not quantifiable)

Elevation, mm	Corresponding Figure in Report	Region of interest	Composition, at%
950	70	Melt with precipitates between rods 1 and 4	Cr 4%, Fe 14%, Ni 3%, Zr 77%, Sn 1 %
950	76	Melt inside rod 13	Cr 8%, Fe 26%, Ni 4%, Zr 62%, Sn <1 %
750	107	Three regions indicated by color rectangles between B_4C pin and ZrO_2 layer	brown: Cr 26%, Fe 60%, Ni 9%, Zr 3%, Mo 2%
			green: Cr 15%, Fe 39%, Ni 6%, Zr 38%, Mo 2%
			black: Cr 11%, Fe 43%, Ni 9%, Zr 35%, Mo 2%
750	108	Region indicated by red rectangle: interaction of B_4C with steel blade and ZIRLO channel box at 750 mm near to the rest of B_4C pin	grey region (Fe reach): Cr 23%, Fe 62%, Ni 10%, Zr 3%, Mo 2%
			light region (Zr reach): Cr 13%, Fe 50%, Ni 10%, Zr 25%, Mo 2%
750	109	Region indicated by blue rectangle: interaction of B_4C with steel blade and ZIRLO channel box at 750 mm near to the channel box	Cr 10%, Fe 34%, Ni 4%, Zr 52%
555	167	Melt inside rod 3	Cr 4%, Fe 2%, Ni 11%, Zr 74%, Sn <1 %, Ta 8 %
555	173	Melt inside rod 9	Cr 4%, Fe 2%, Ni 16%, Zr 77%, Sn <1 %
555	177	Melt inside rod 10	Cr 4%, Fe 13%, Ni 1%, Zr 81%, Sn <1 %
555	182	Melt inside rod 15	Cr 6%, Fe 21%, Ni 3%, Zr 69%, Sn 1 %
555	186	Melt inside rod 21	Cr 6%, Fe 2%, Ni 17%, Zr 74%, Sn <1 %
450	194	Melt inside rod 20	Cr 5%, Fe 10%, Ni 4%, Zr 80%, Sn <1%
450	196	Melt inside rod 23	Cr 5%, Fe 2%, Ni 14%, Zr 79%, Sn <1%

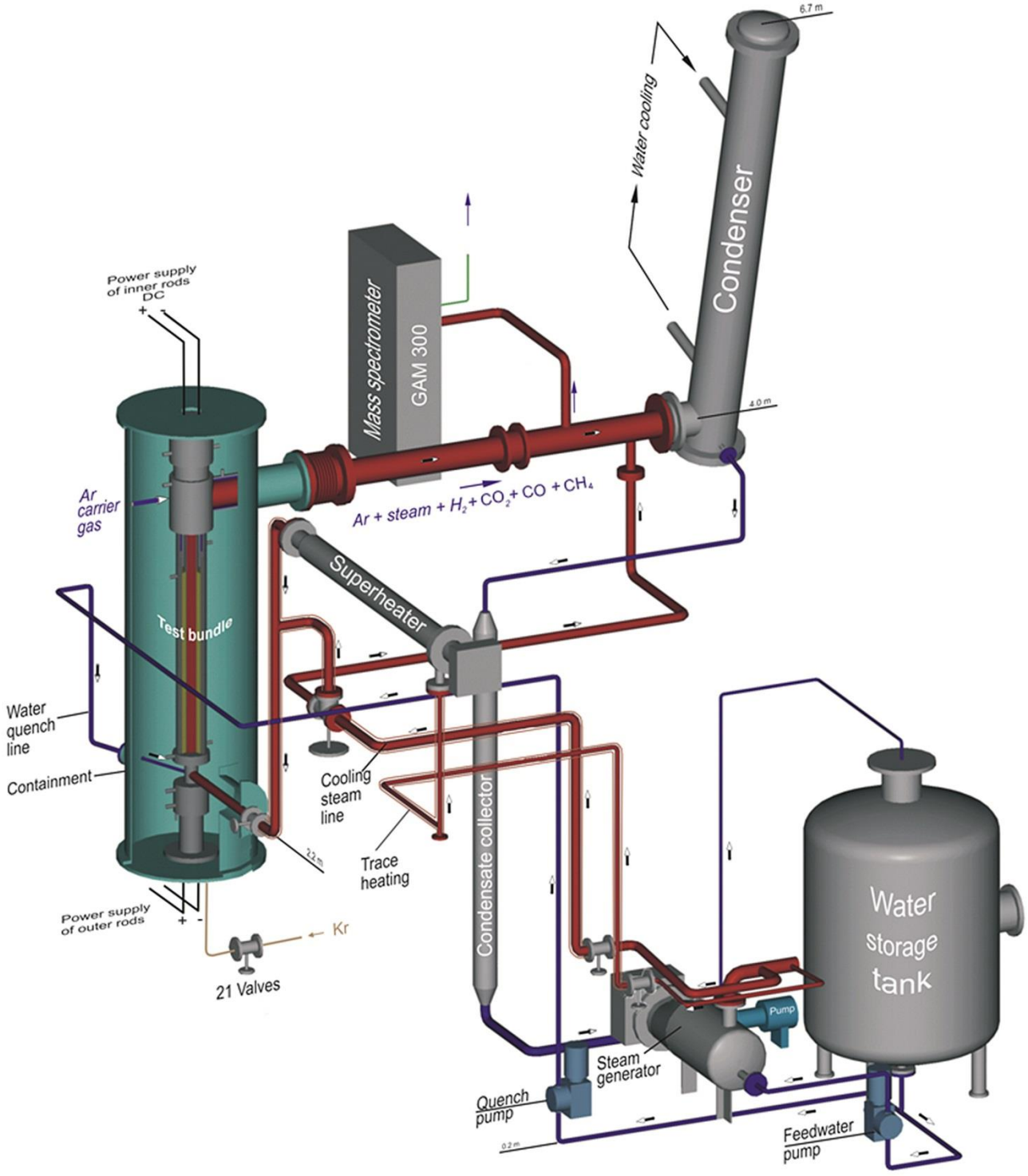

Figure 1 QUENCH Facility - Main components.

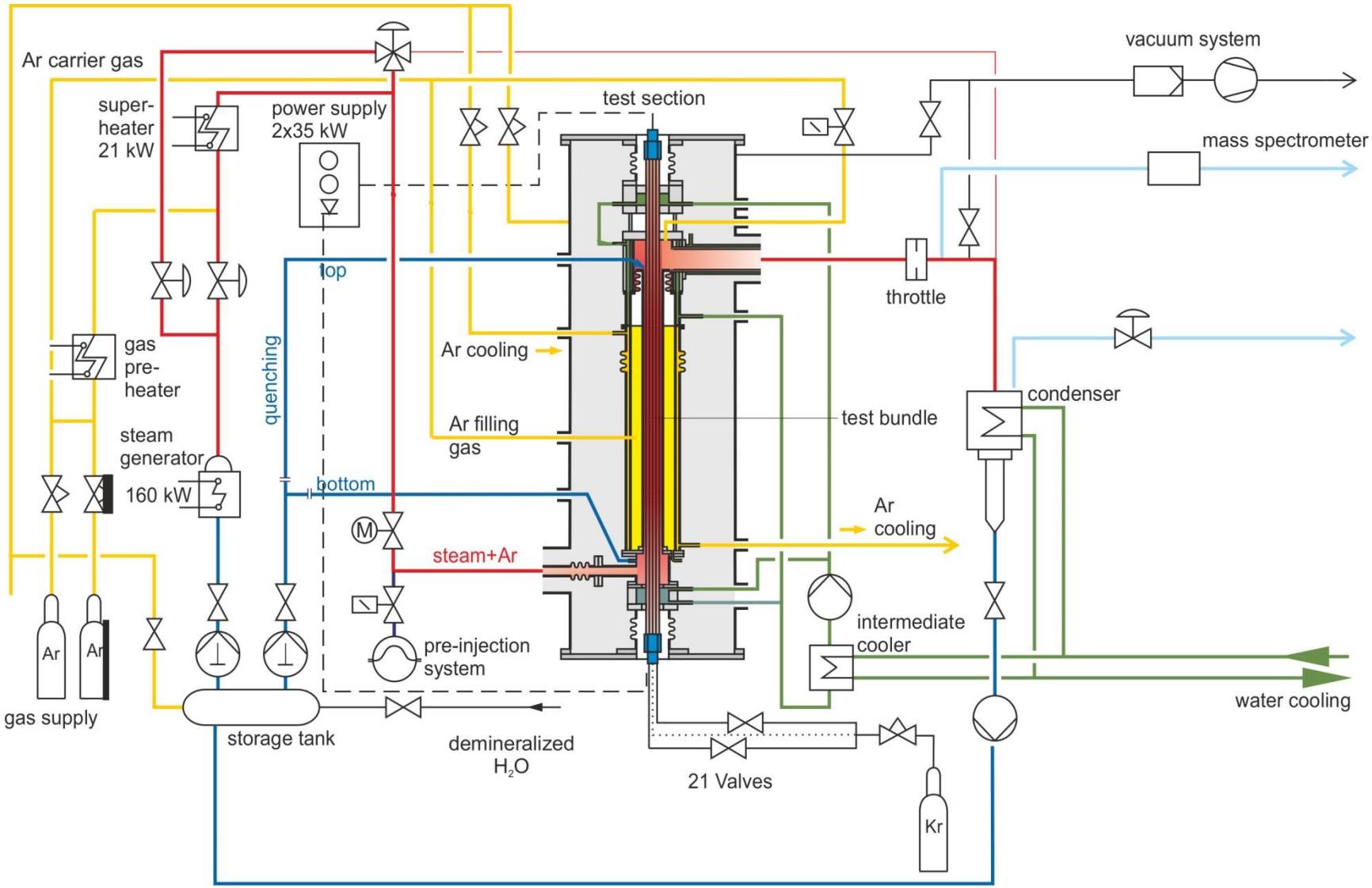

Figure 2 QUENCH-20; flow diagram of the QUENCH facility.

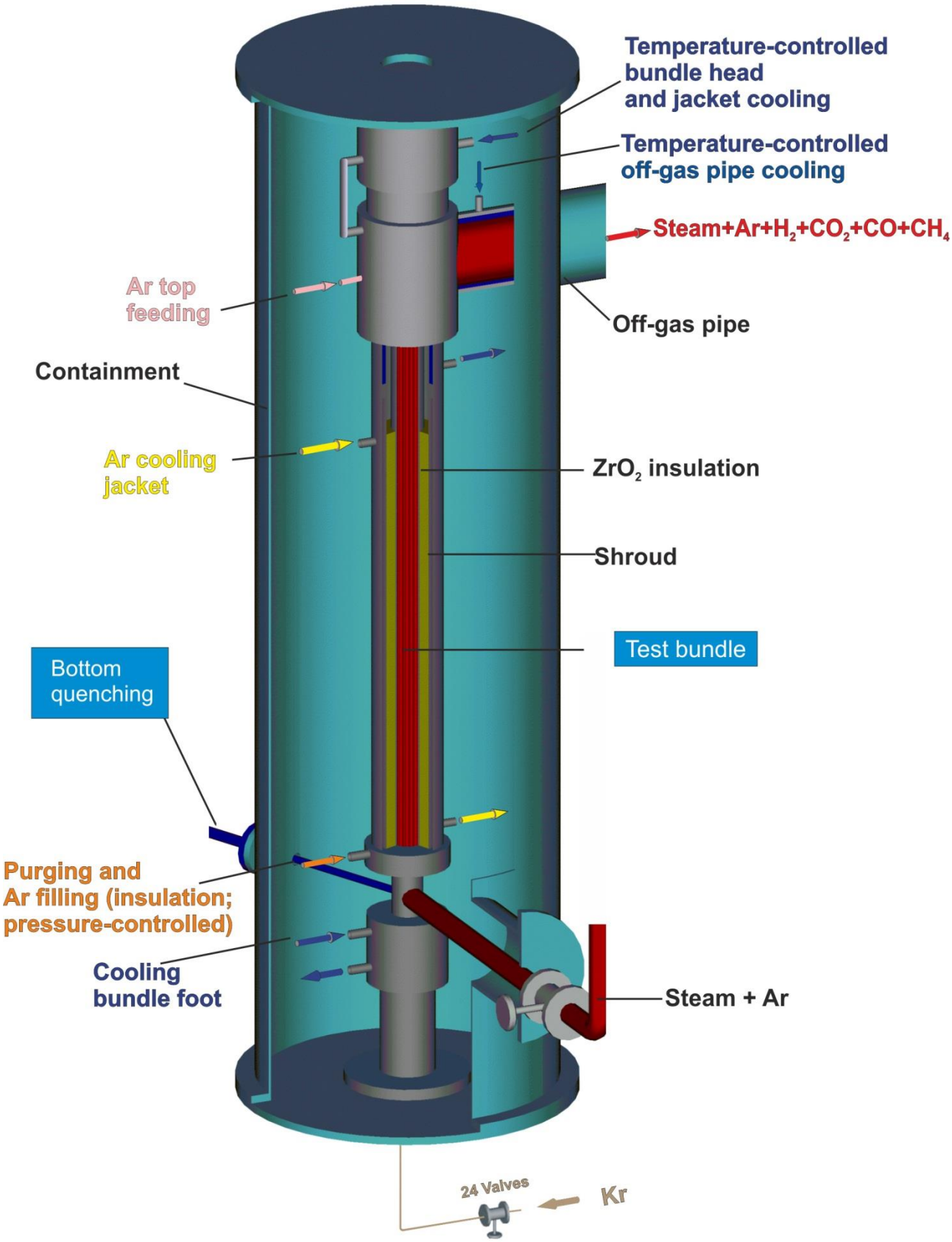

Figure 3 QUENCH-20; containment and test section.

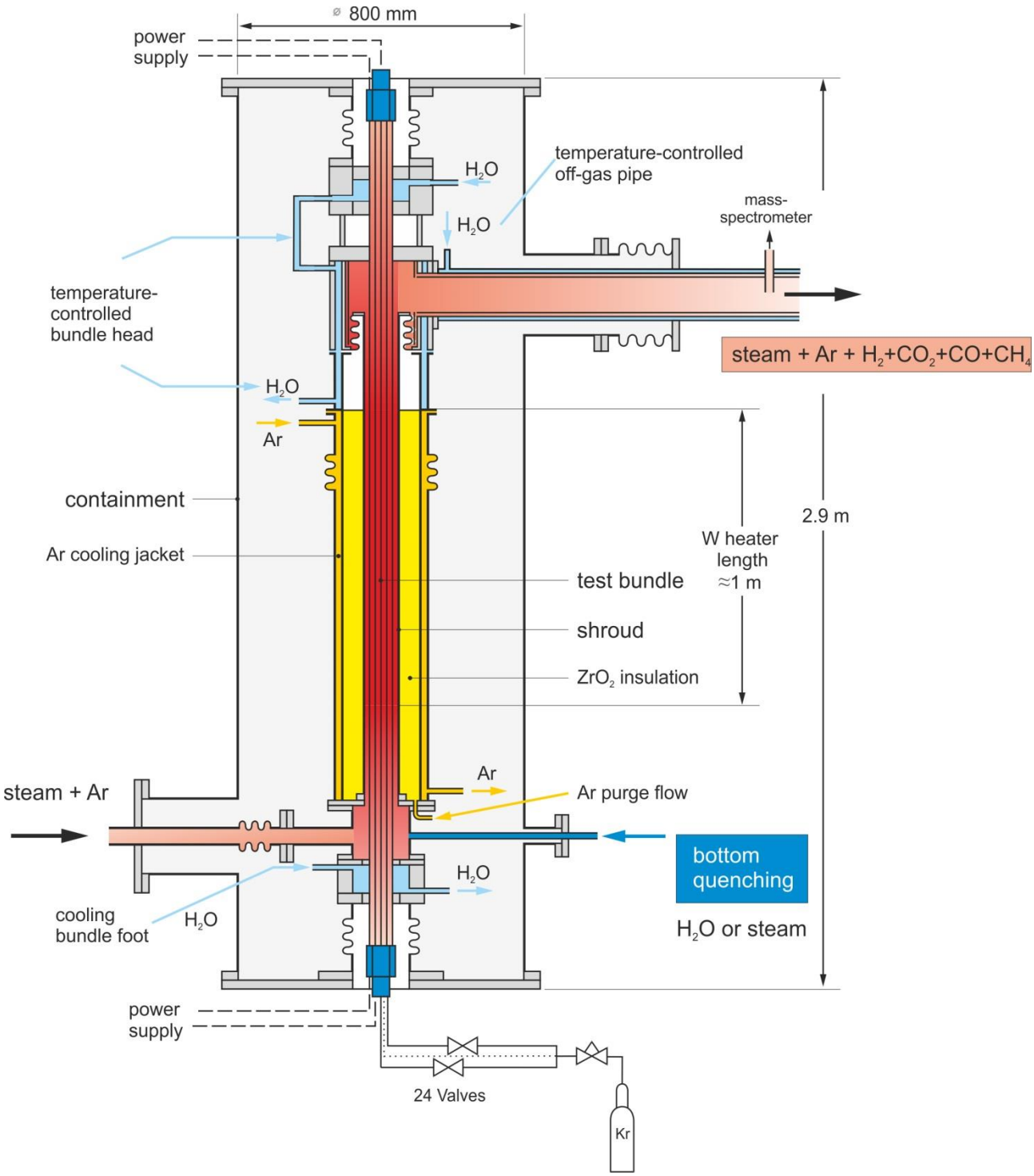

Figure 4 QUENCH-20; test section with flow lines.

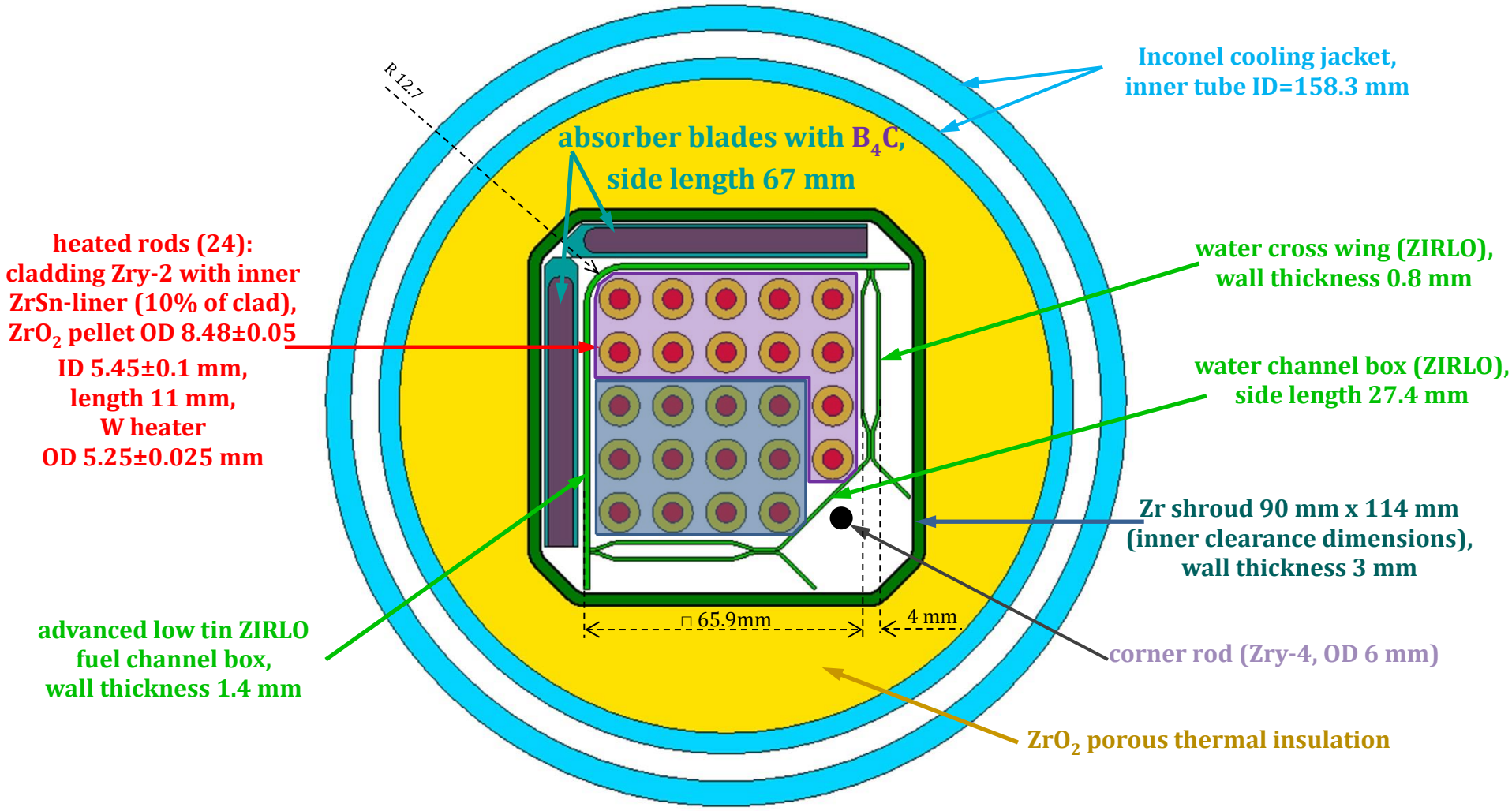

Figure 5 QUENCH-20; cross section of test section with ¼ SVEA-96 OPTIMA2 assembly; electrical partition of bundle (12+12) between two DC generators.

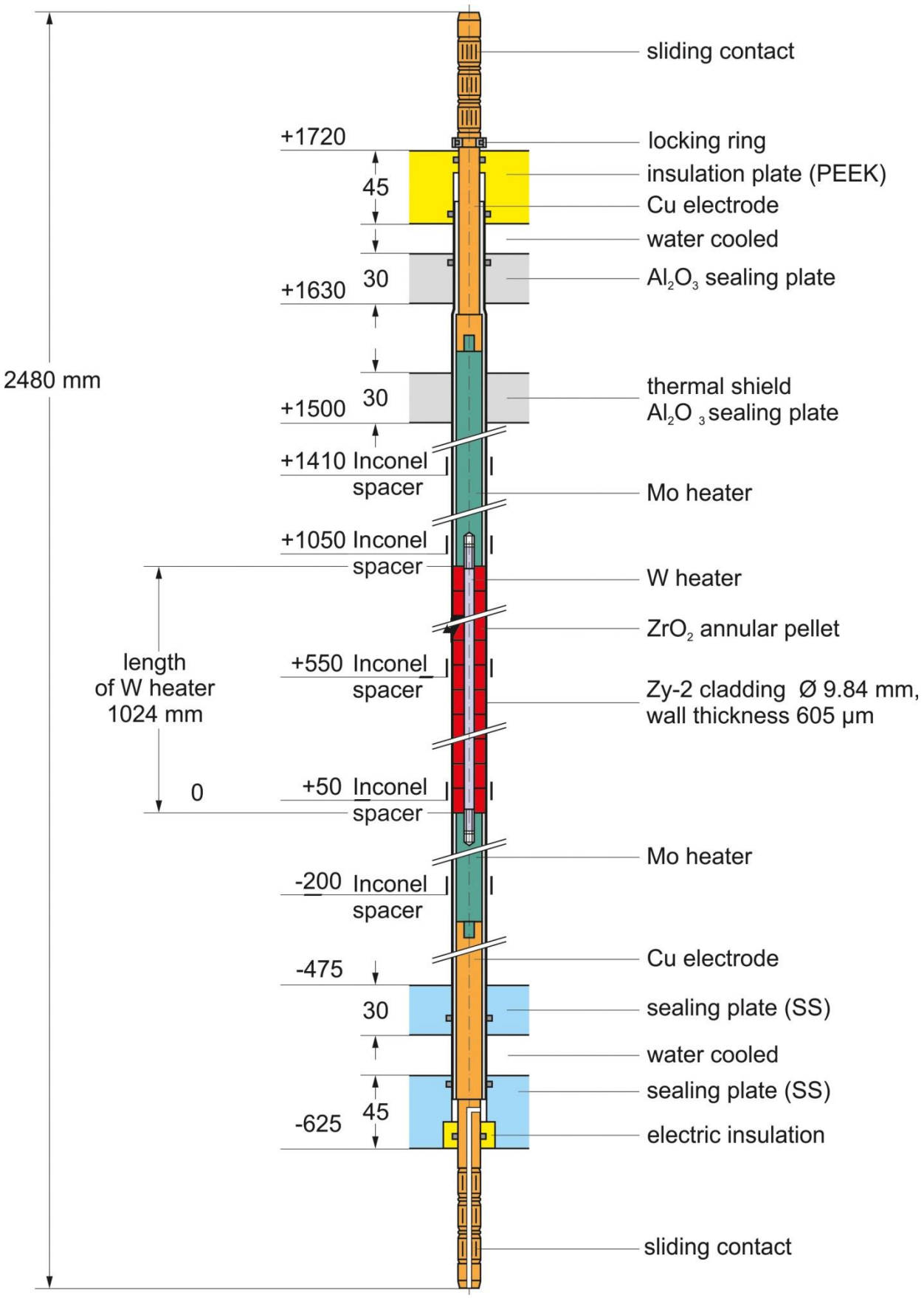

Figure 6 QUENCH-20; heated rod.

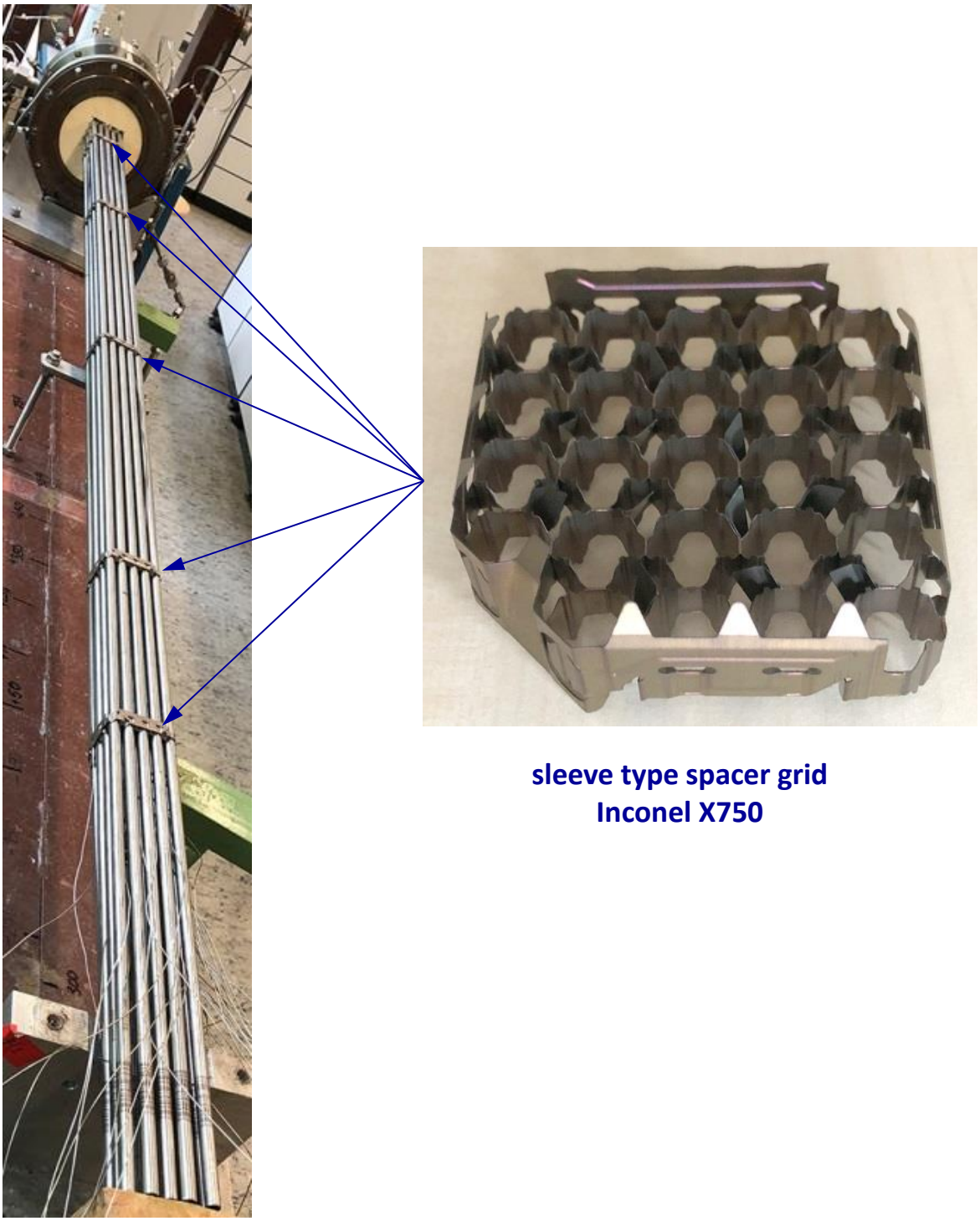

Figure 7 QUENCH-20; spacer grids.

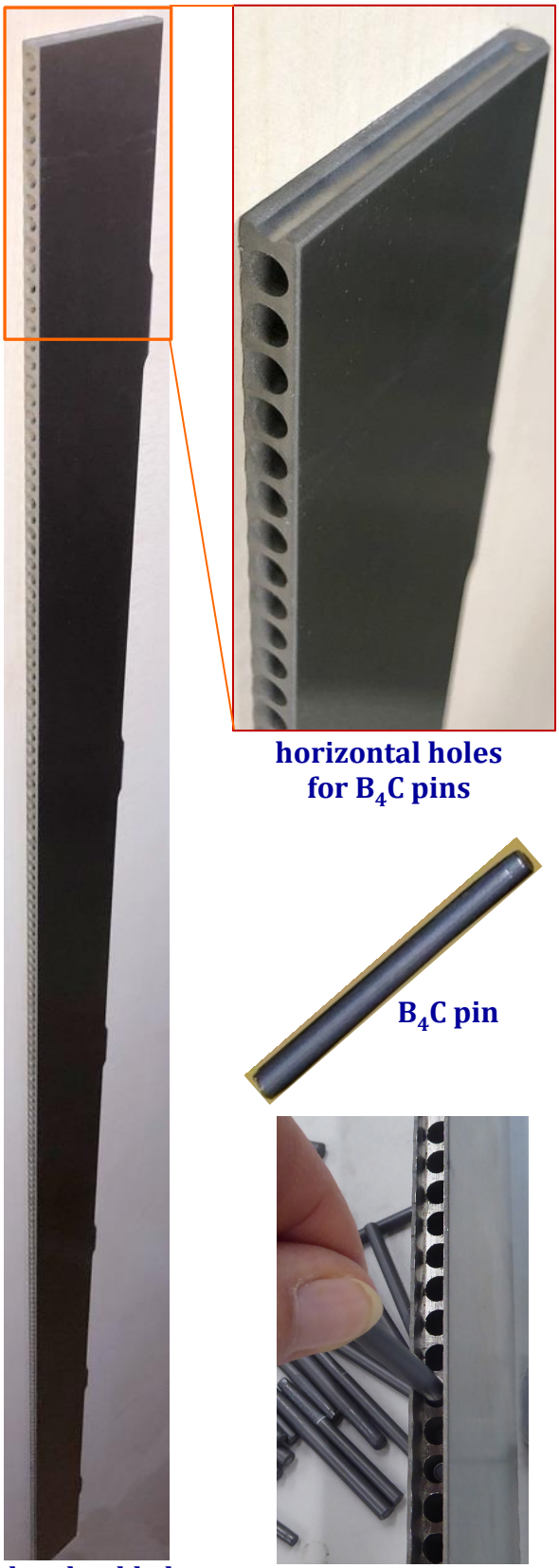

Figure 8 QUENCH-20; absorber blades and B_4C pins.

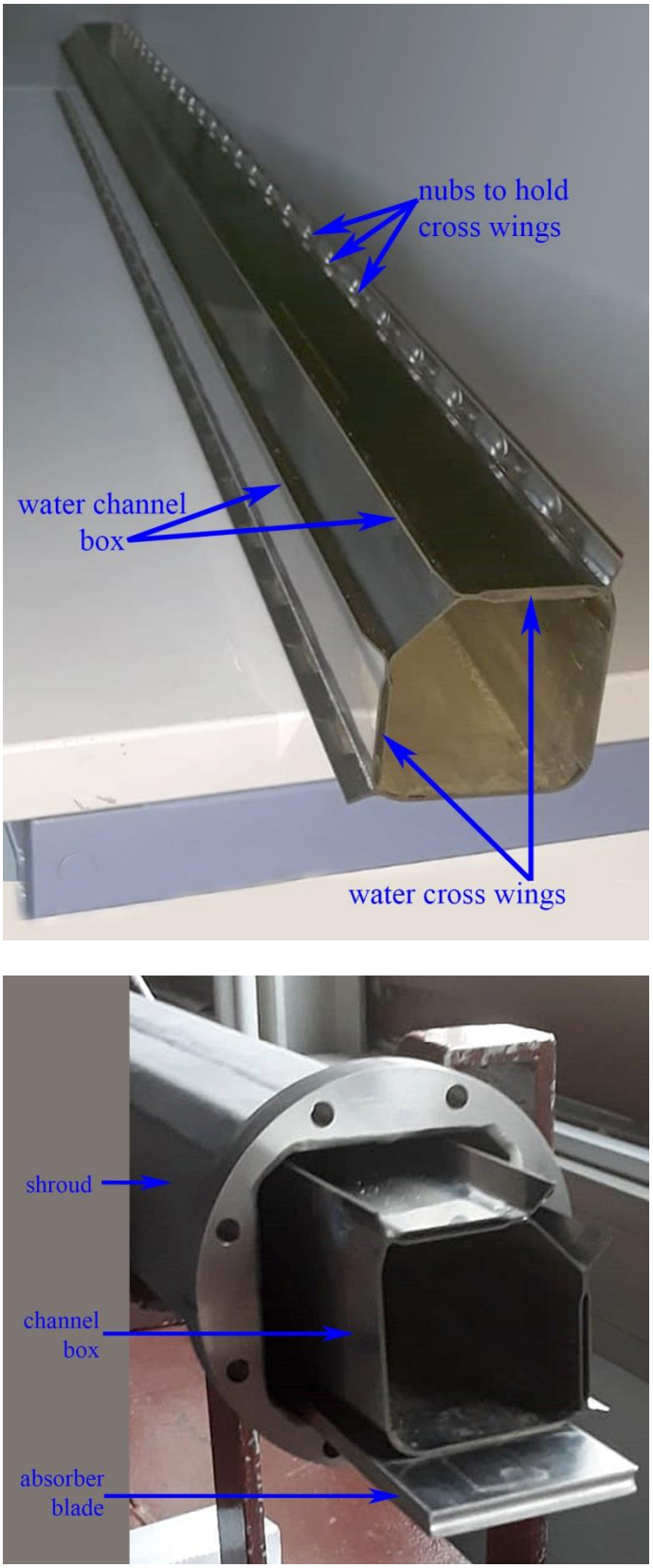

Figure 9 QUENCH-20; prepared channel box (top) and arrangement of channel box and blade inside shroud.

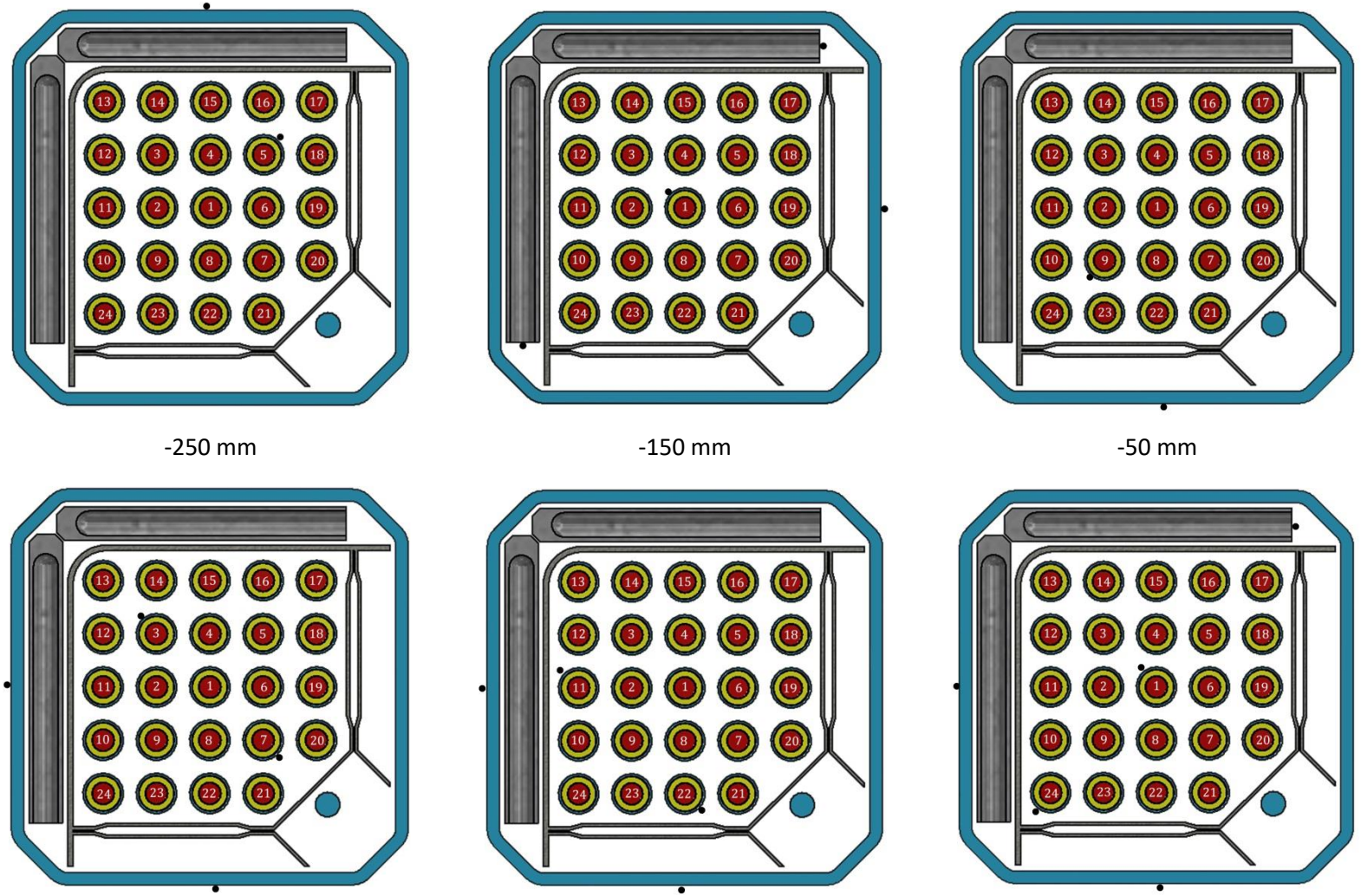

Figure 10 QUENCH-20; designation of the various thermocouples for cross sections between -250 mm and 250 mm.

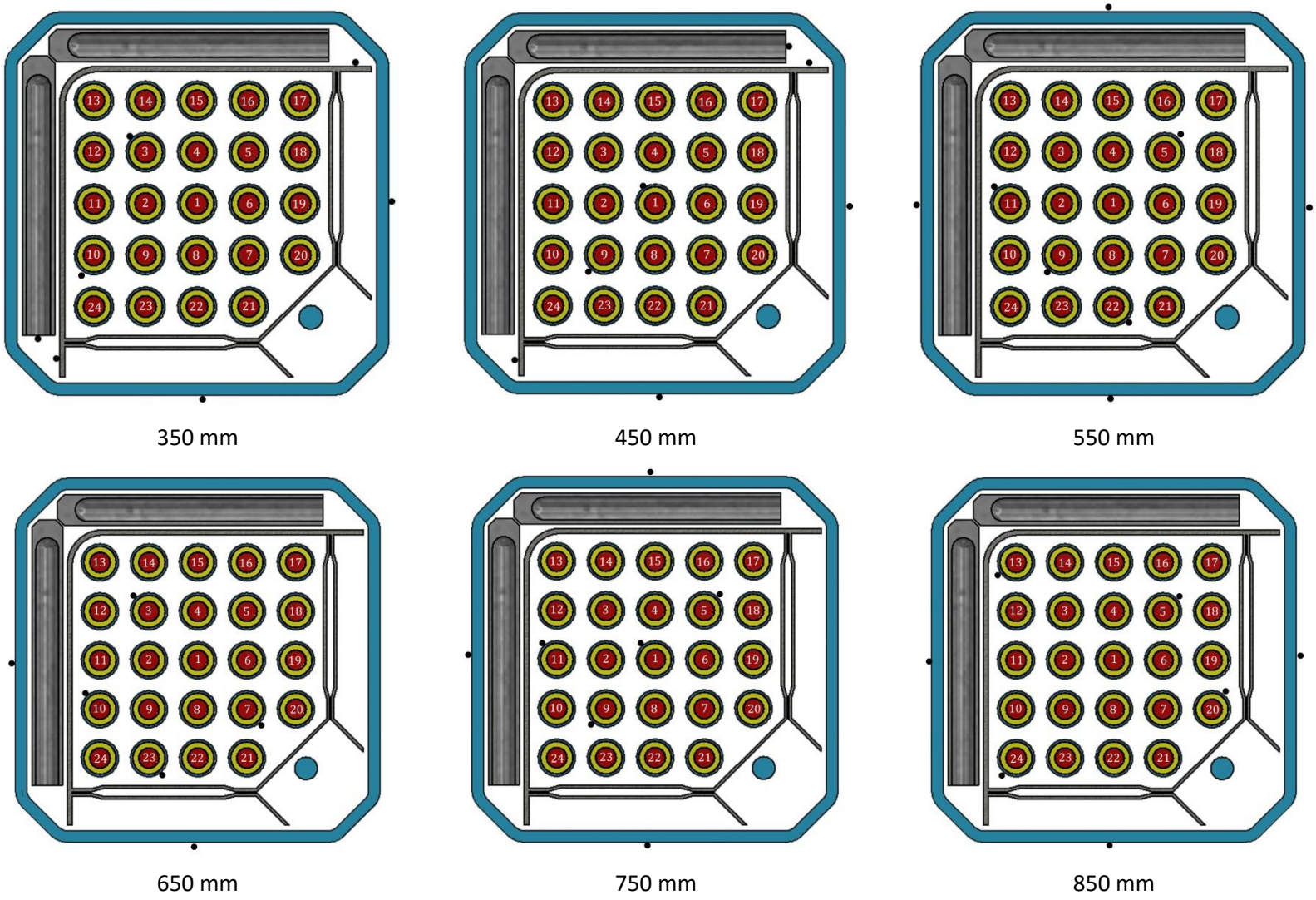

Figure 11 QUENCH-20; designation of the various thermocouples for cross sections between 350 mm and 850 mm.

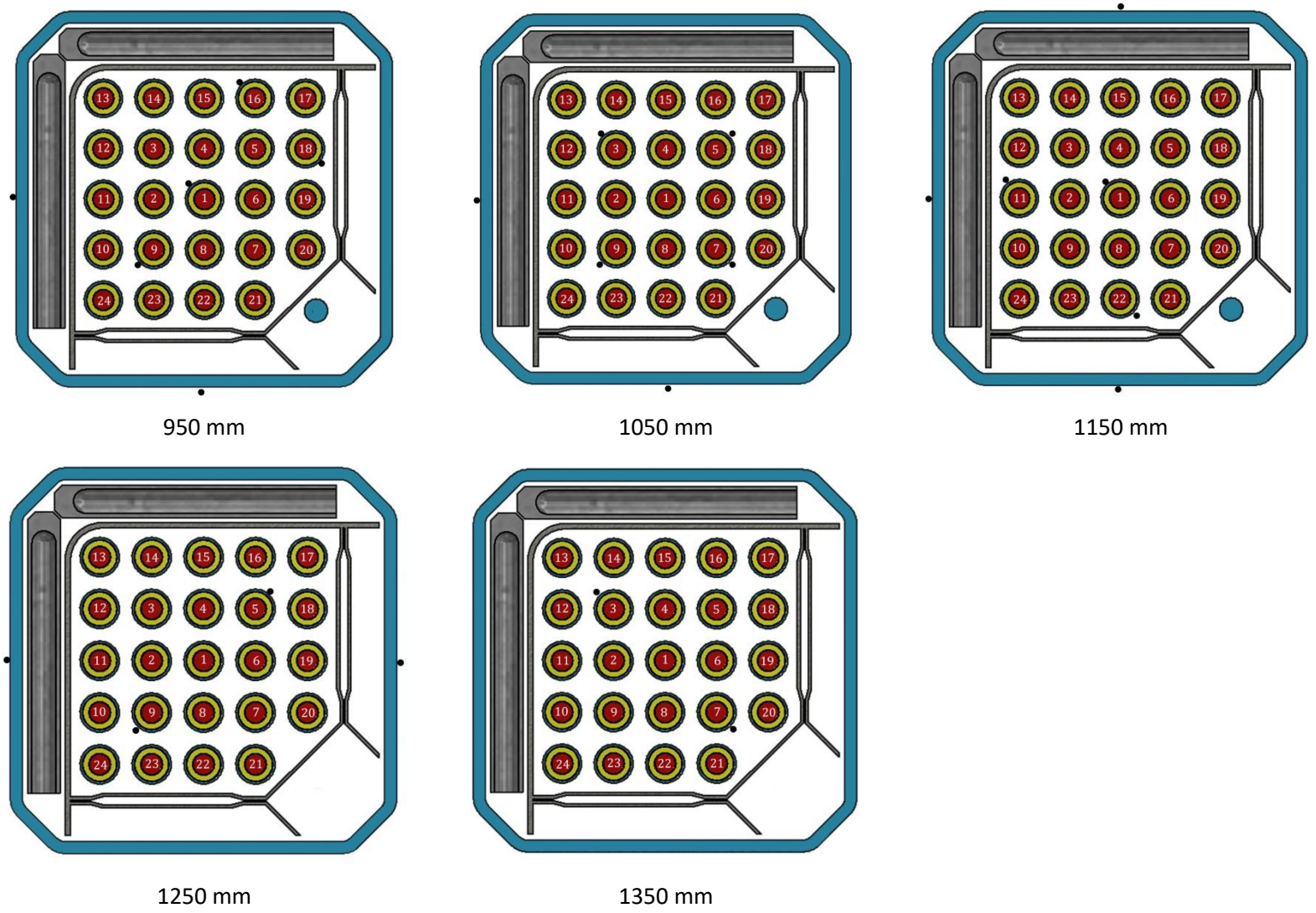

Figure 12 QUENCH-20; designation of the various thermocouples for cross sections between 950 mm and 1350 mm.

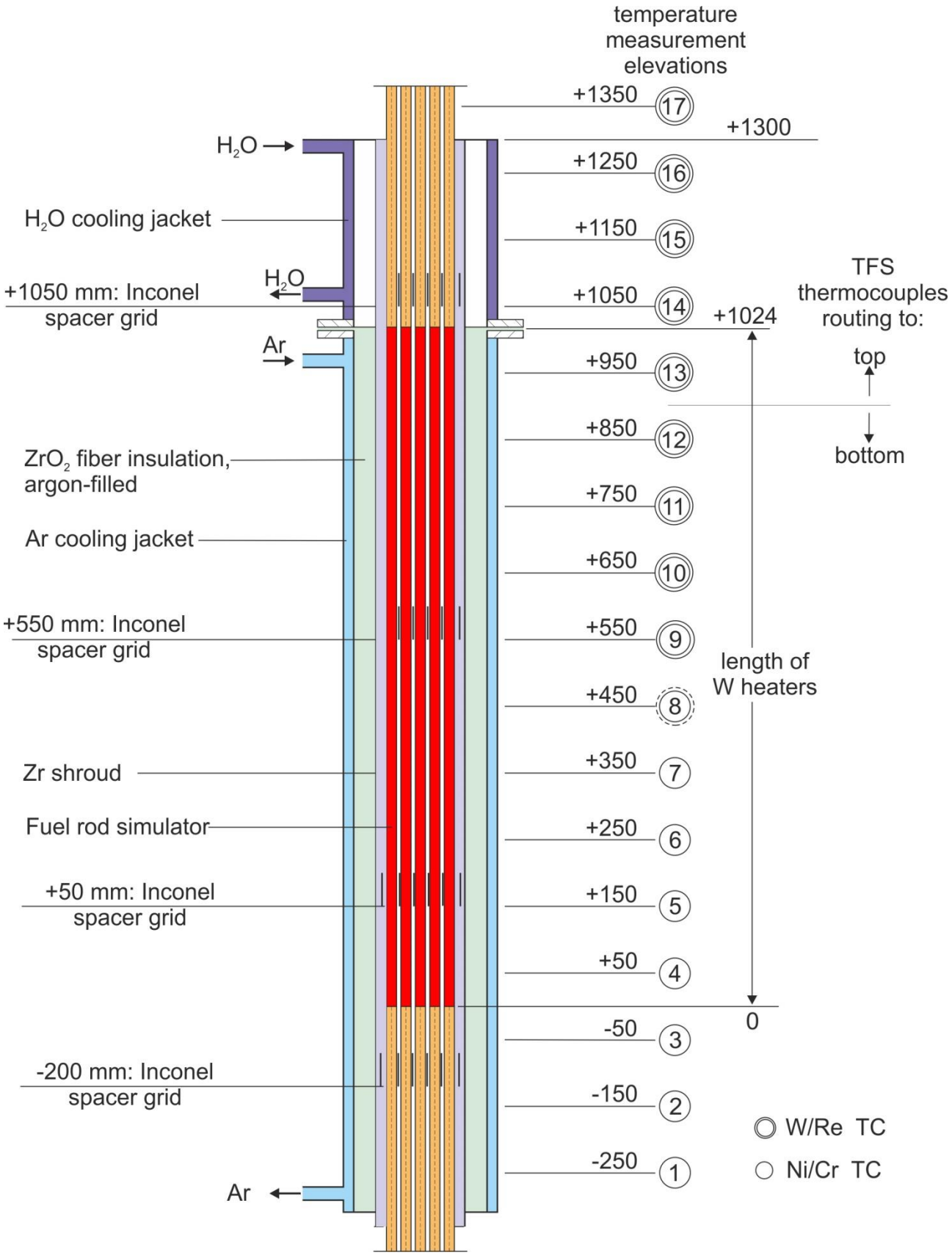

Figure 13 QUENCH-20; axial locations of thermocouples.

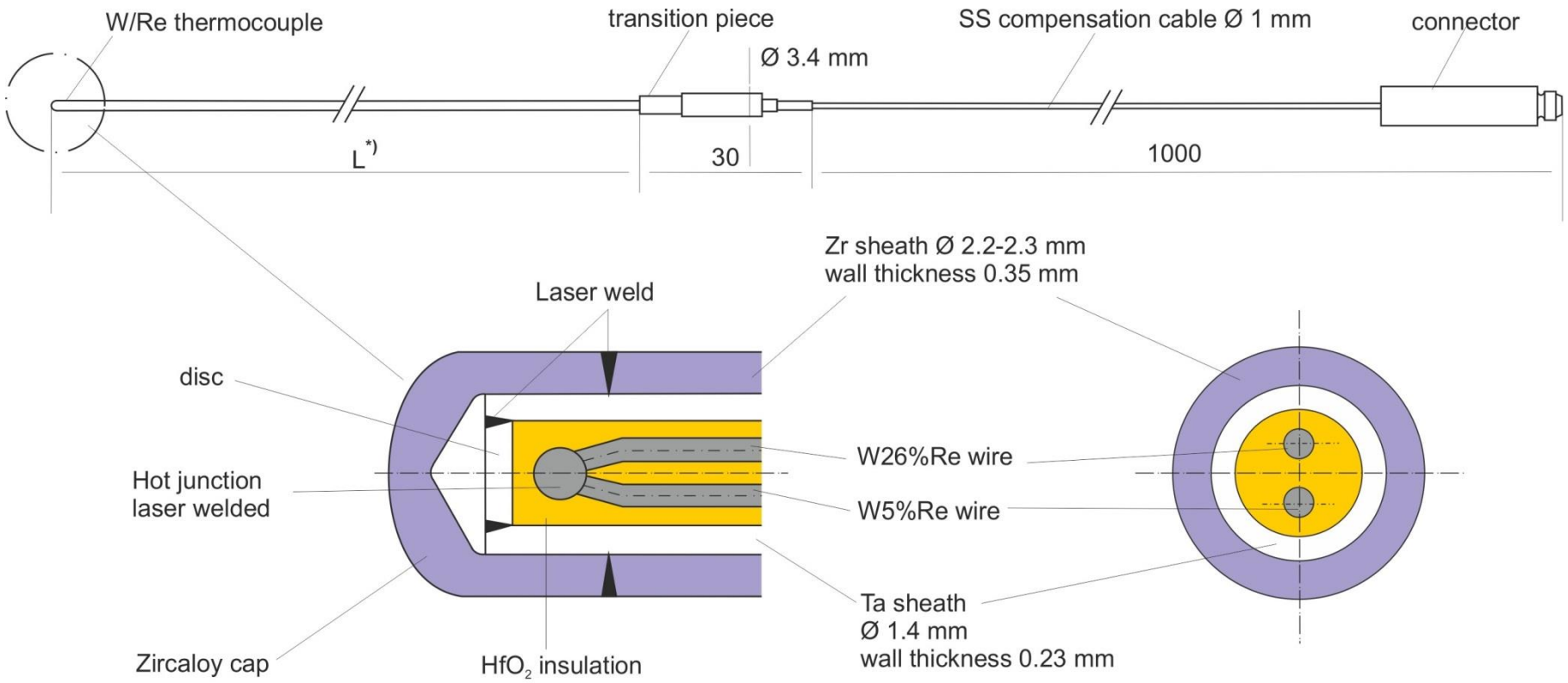

Figure 14 QUENCH-20; high temperature thermocouple.

high temperature TC at cladding surface

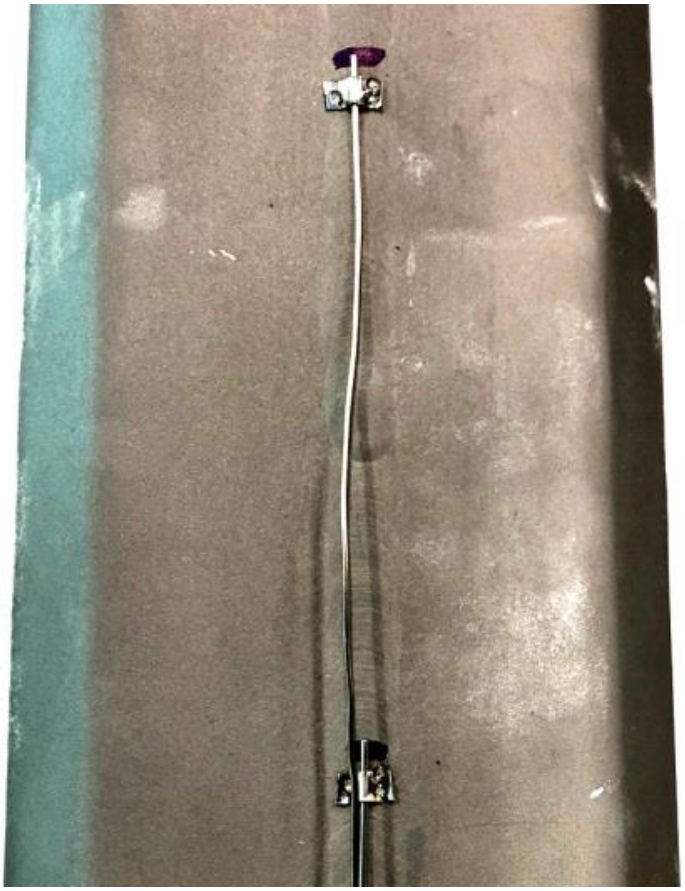

low temperature TC at shroud surface

Figure 15 QUENCH-20; TC fastening at the cladding outer surface and shroud outer surface

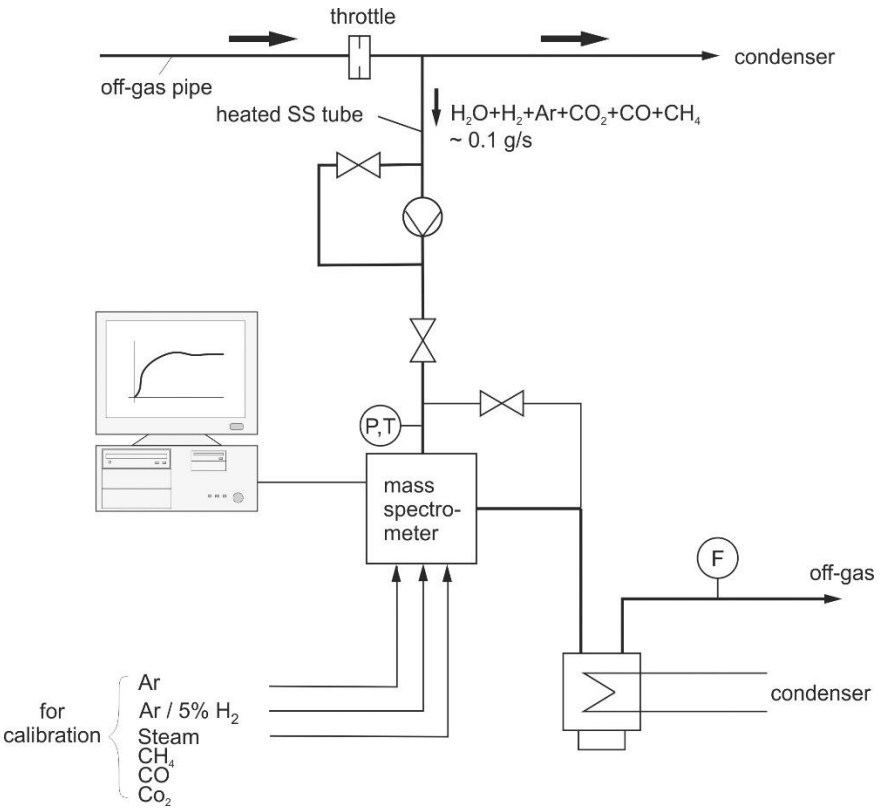

Figure 16 QUENCH-20; gas measurement with the GAM 300 mass spectrometer.

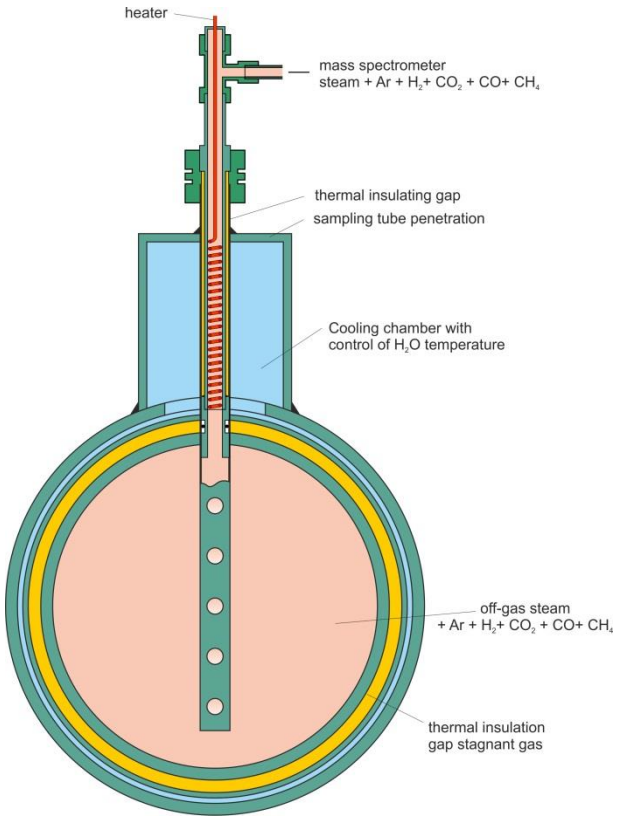

Figure 17 QUENCH-20; mass spectrometer sampling position at the off-gas pipe.

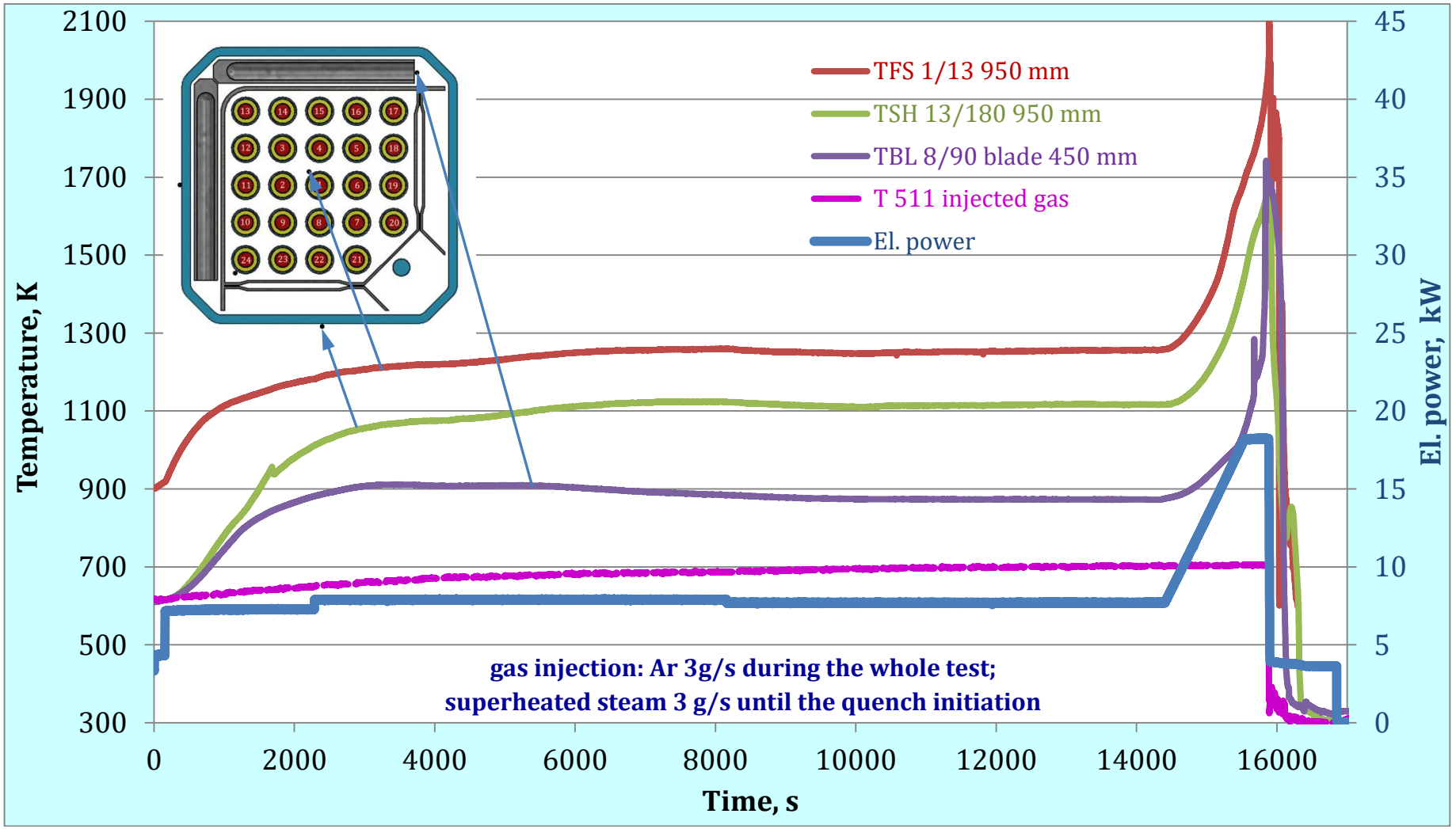

Figure 18 QUENCH-20; Test performance.

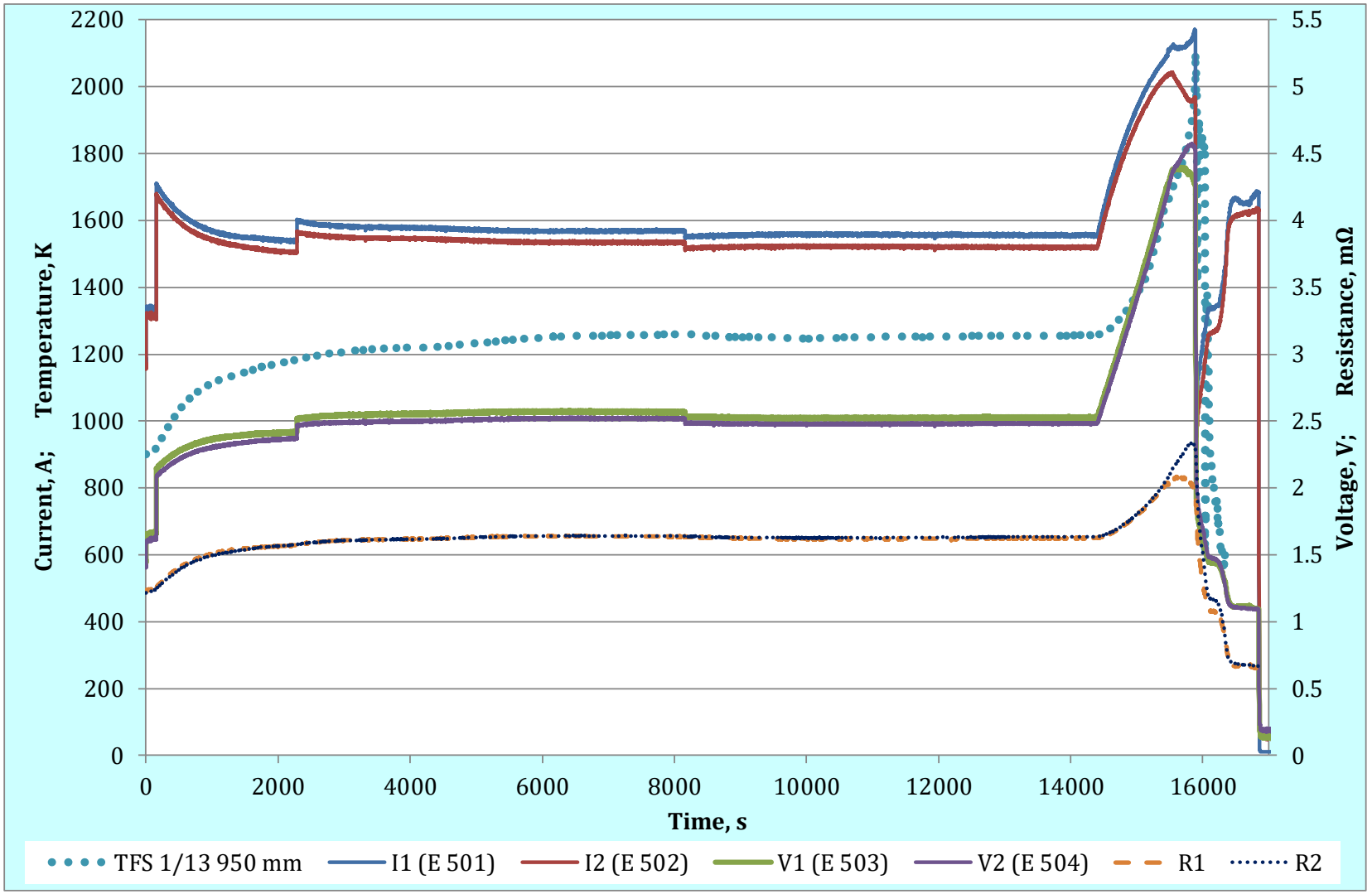

Figure 19 QUENCH-20; Electrical current I and voltage V for two rod groups, electrical resistance R=V/I for two rod groups.

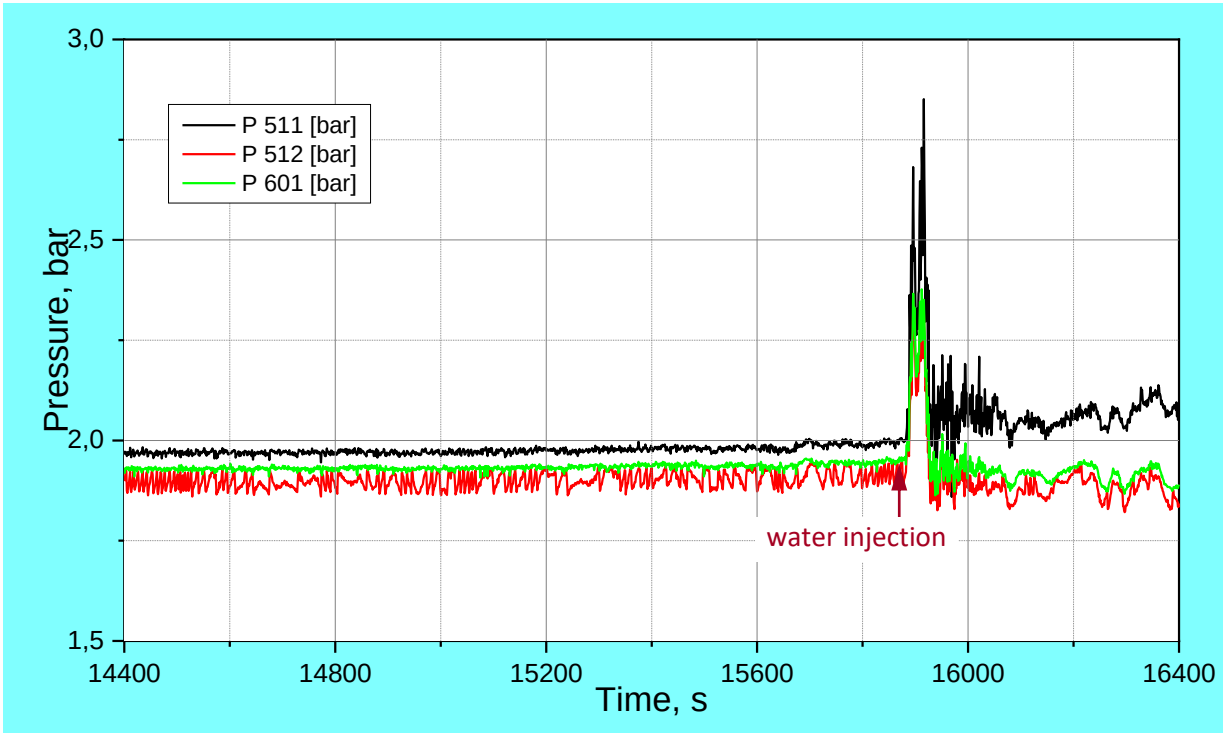

Figure 20 QUENCH-20; System pressure measured at test section inlet P 511, at outlet P 512, and in the off-gas pipe P 601.

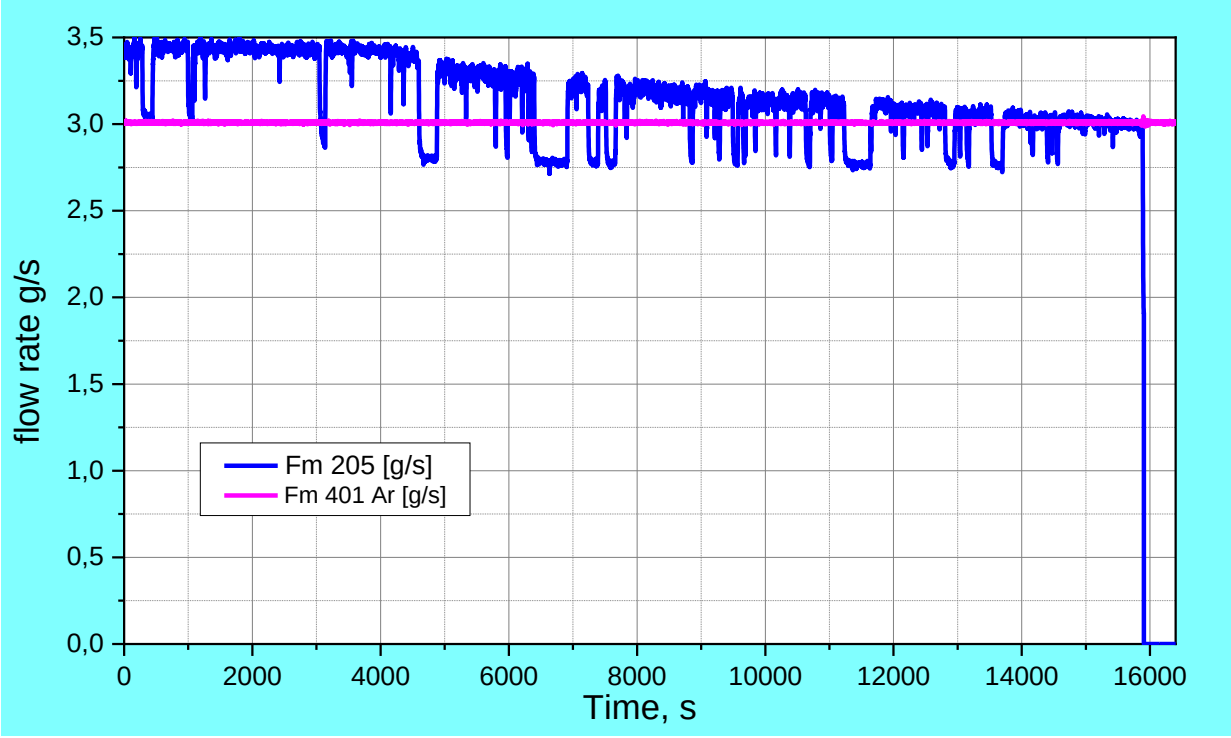

Figure 21 QUENCH-20; Argon and steam injection into the bundle.

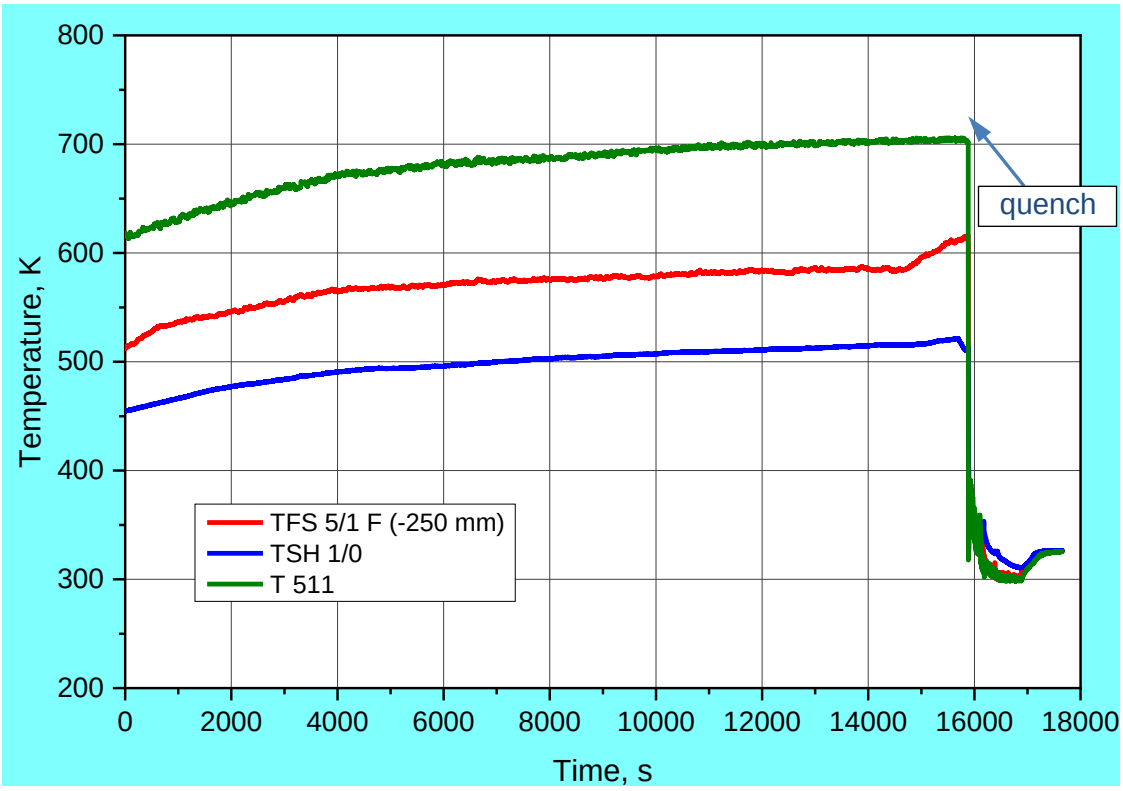

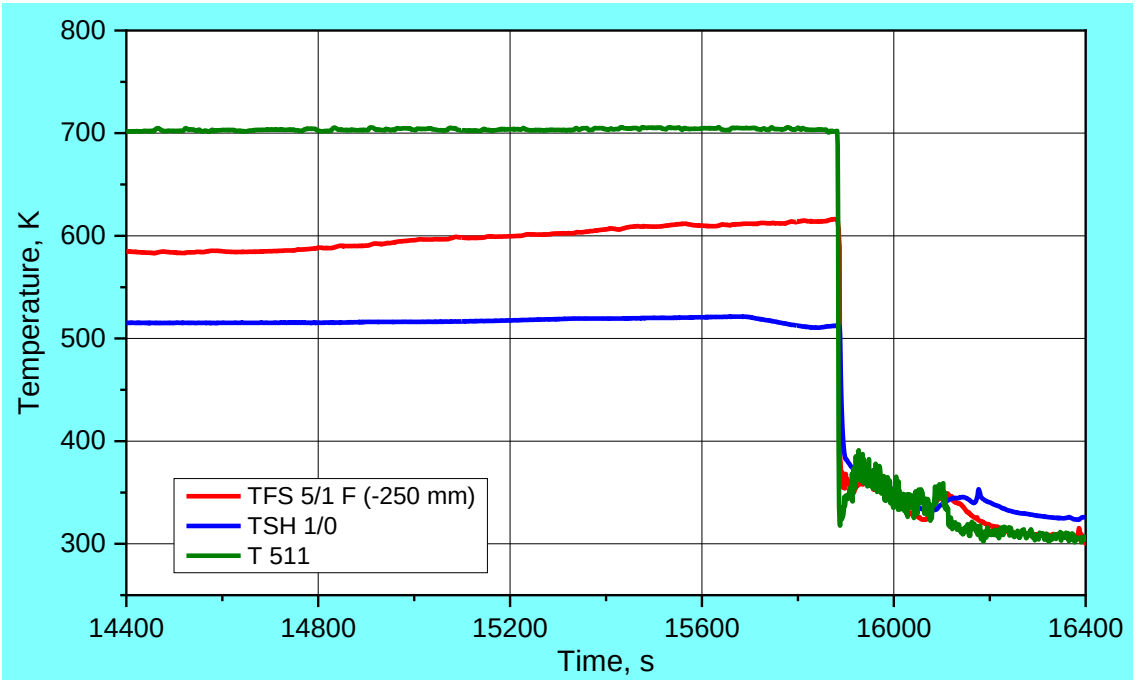

Figure 22 QUENCH-20: Temperatures measured by gas inlet thermocouple (T 511) at -412 mm, rod cladding thermocouple (TFS 5/1 F) and shroud (TSH 1/0) thermocouples at -250 mm elevation.

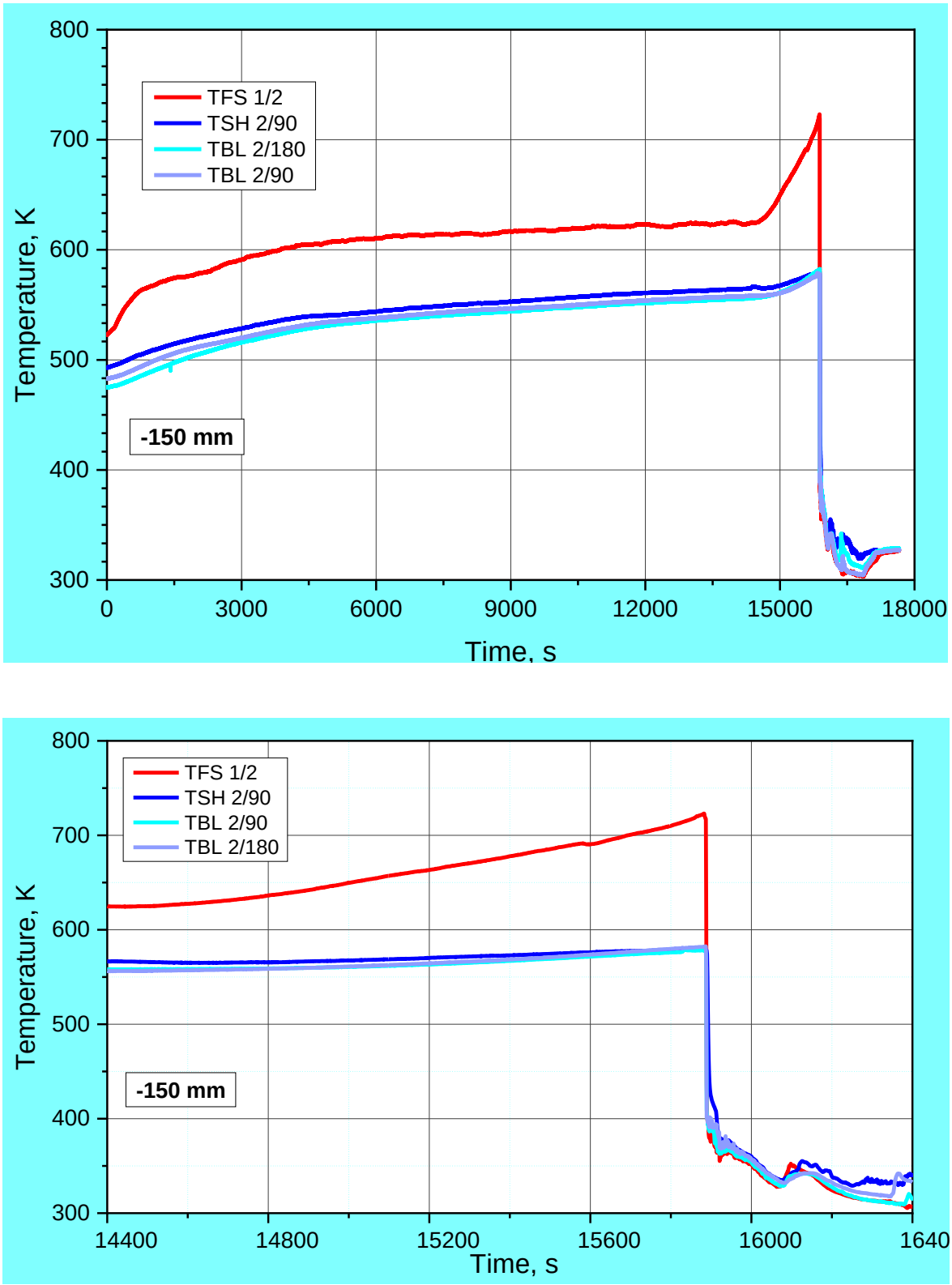

Figure 23 QUENCH-20; Temperatures measured by rod cladding (TFS 1/2) and shroud (TSH 2/90) and absorber blade (TBL) thermocouples thermocouple at -150 mm elevation.

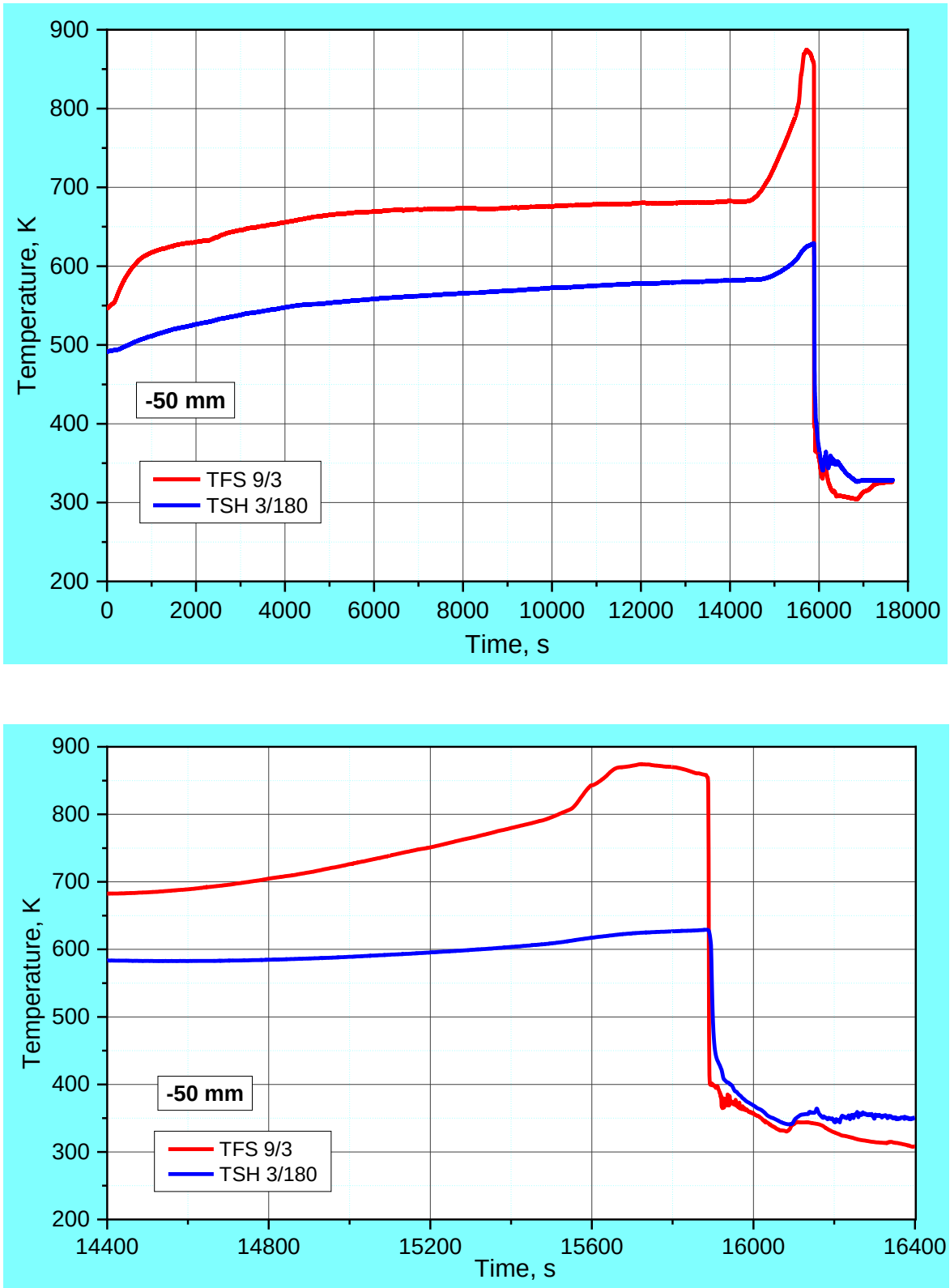

Figure 24 QUENCH-20; Temperatures measured by rod cladding (TFS 9/3) and shroud (TSH 3/180) thermocouples at -50 mm elevation.

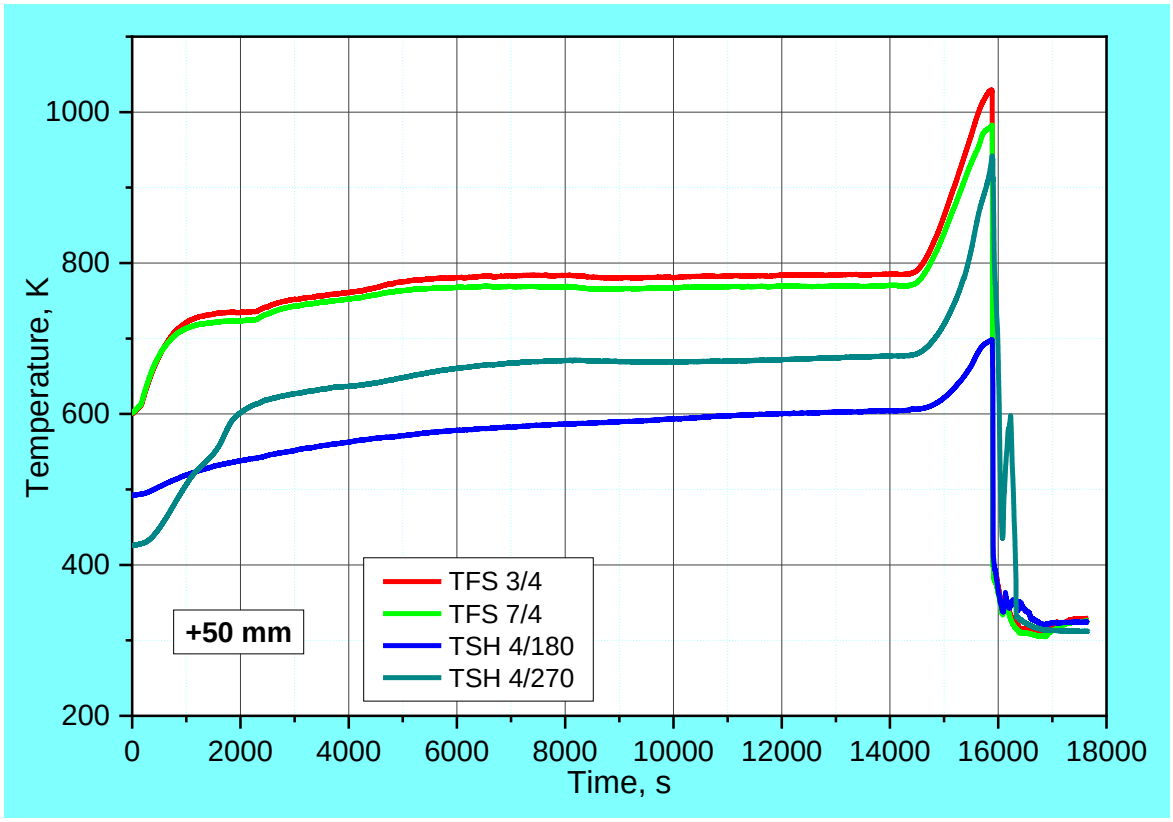

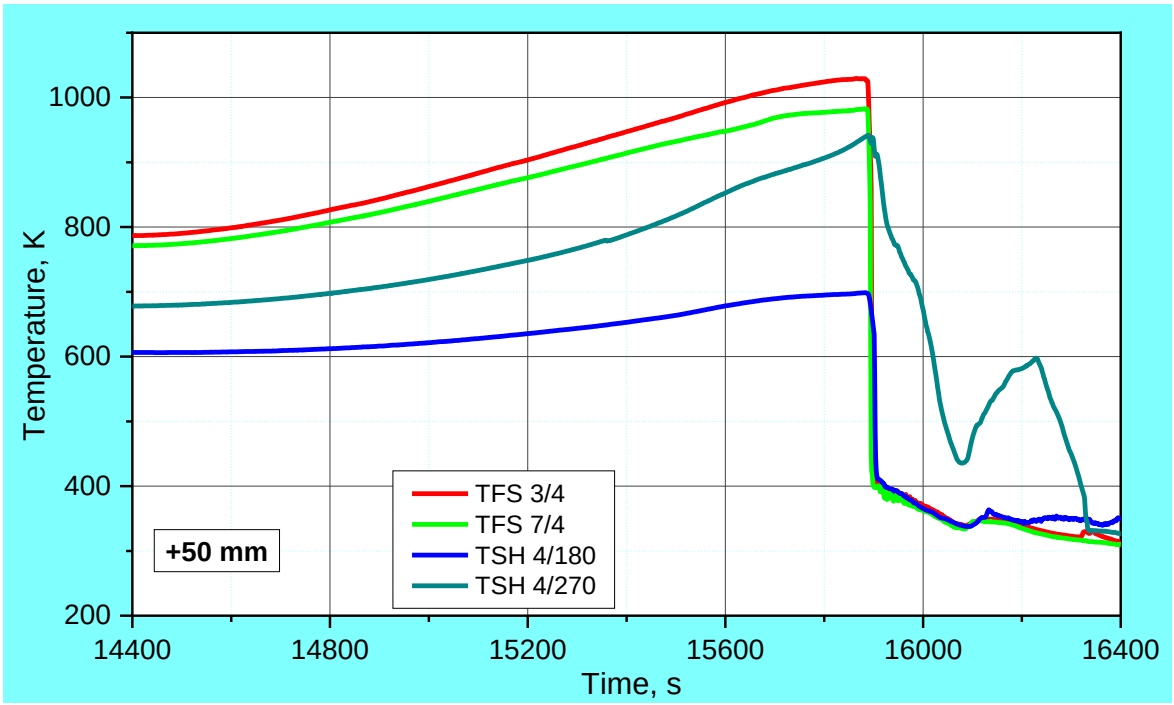

Figure 25 QUENCH-20; Temperatures measured by rod cladding (TFS) and shroud (TSH) thermocouples at 50 mm elevation.

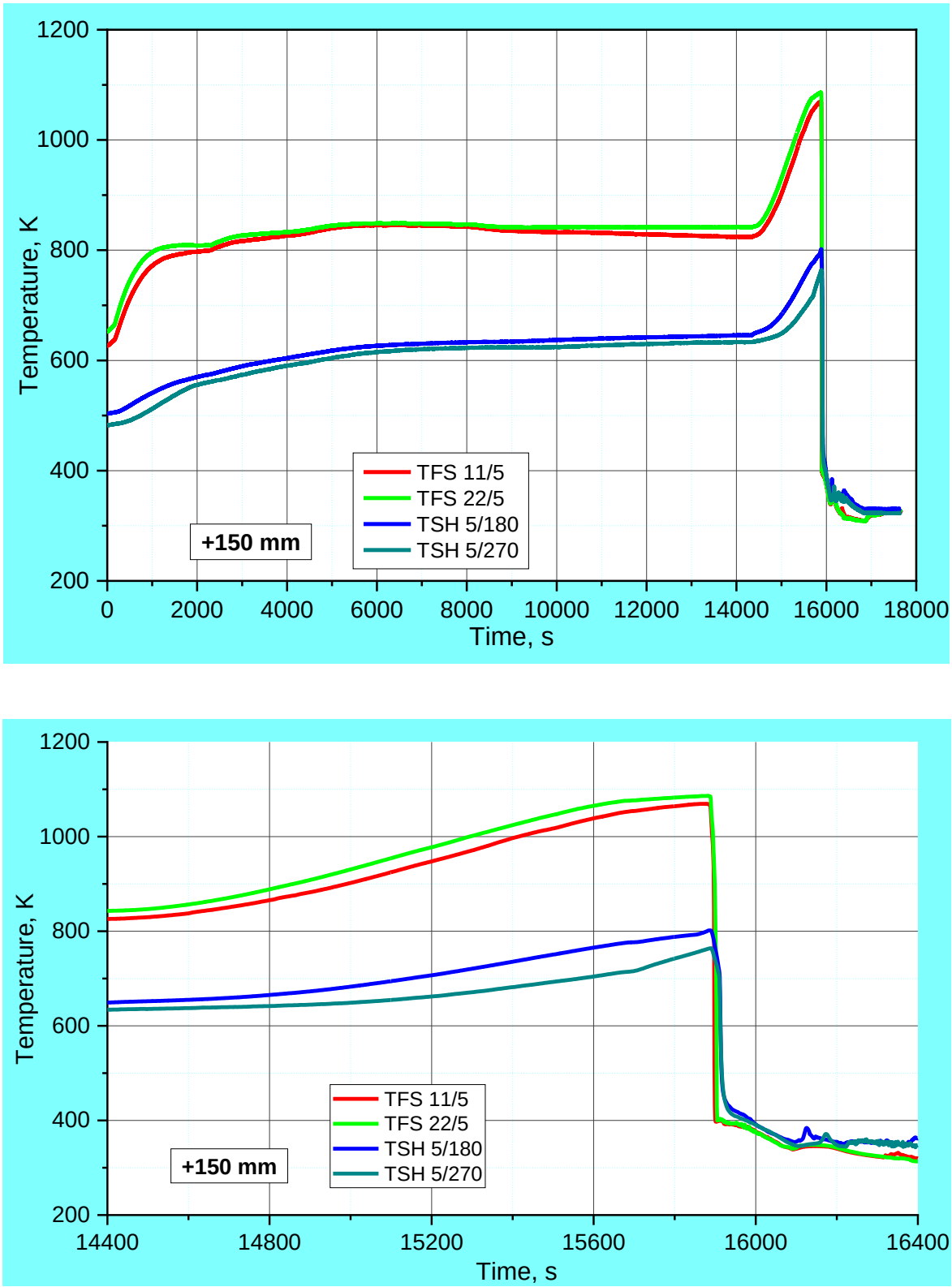

Figure 26 QUENCH-20; Temperatures measured by rod cladding (TFS) and shroud (TSH) thermocouples at 150 mm elevation.

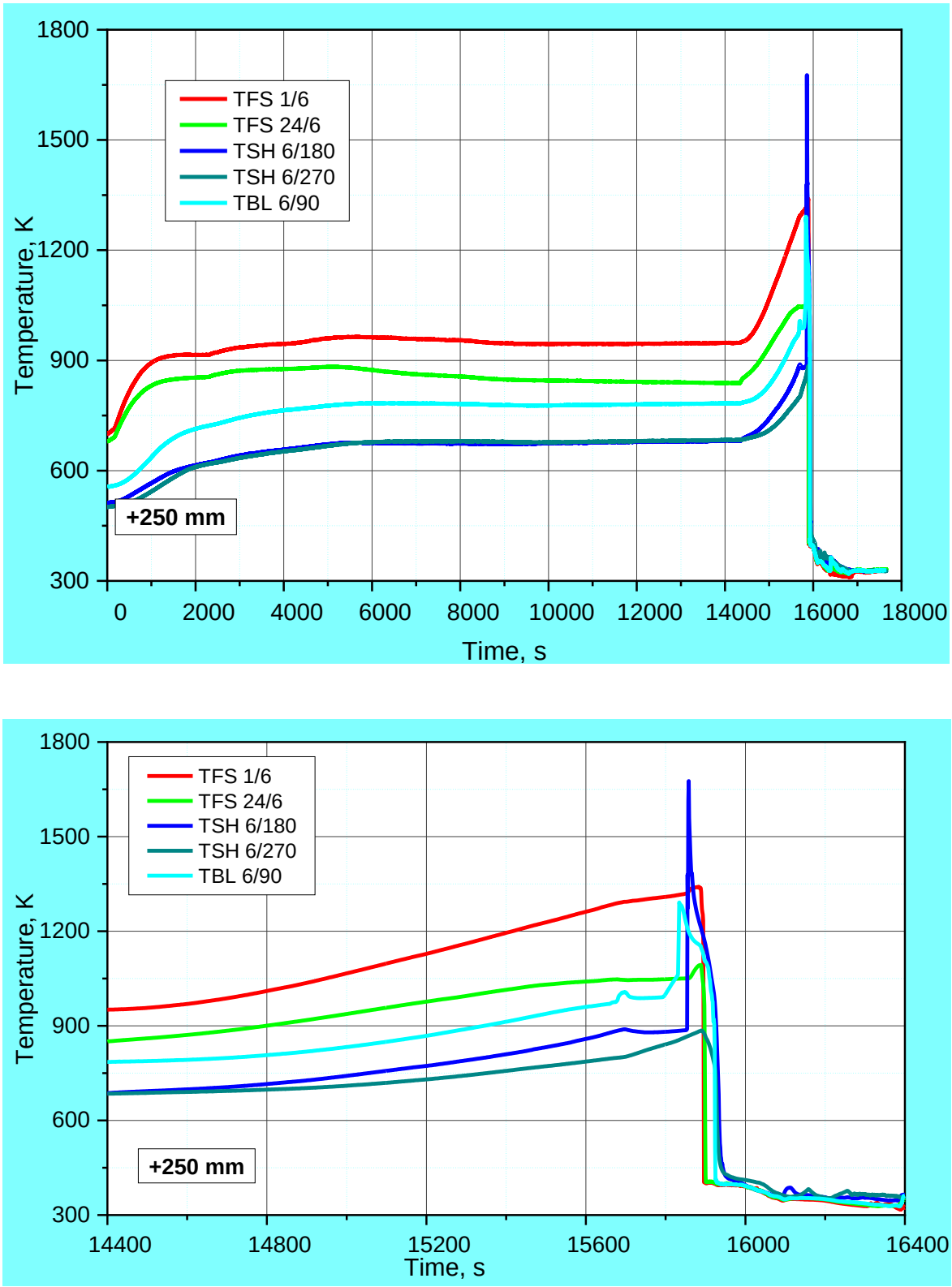

Figure 27 QUENCH-20; Temperatures measured by rod cladding (TFS), shroud (TSH) and (TBL) absorber blade thermocouples at 250 mm elevation.

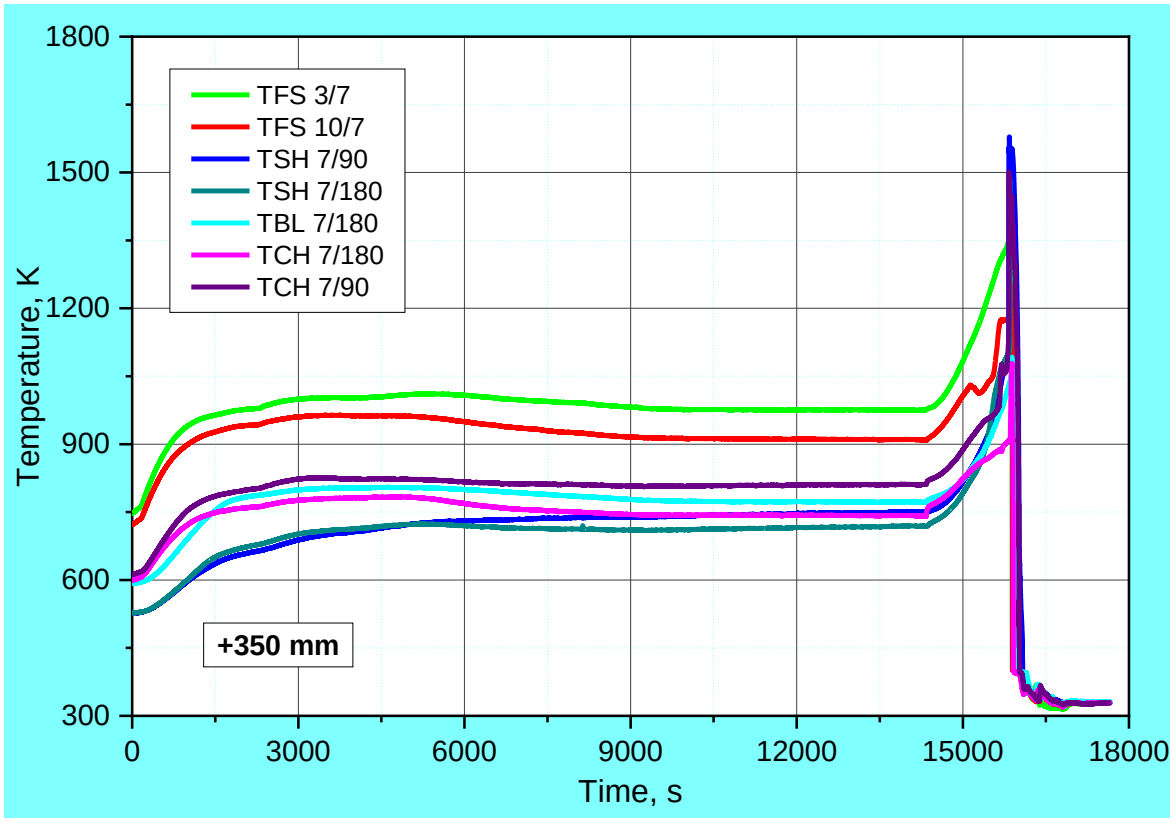

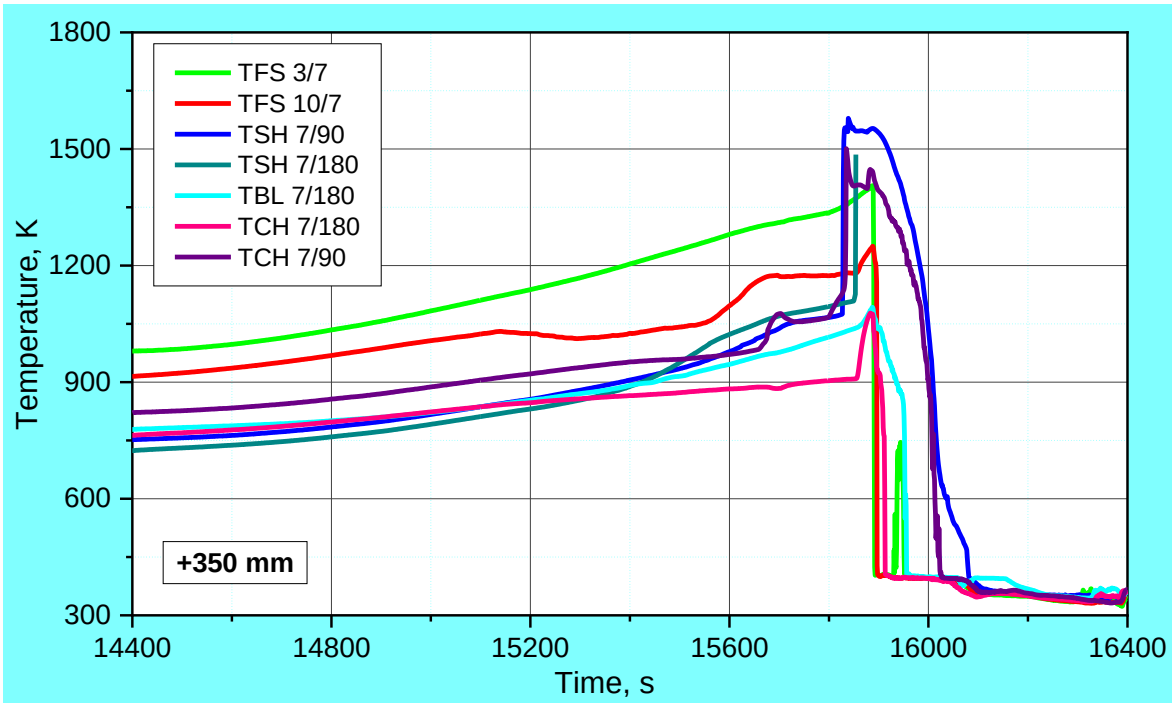

Figure 28 QUENCH-20; Temperatures measured by rod cladding (TFS), shroud (TSH) absorber blade (TBL) and water channel box (TCH) thermocouples at 350 mm elevation.

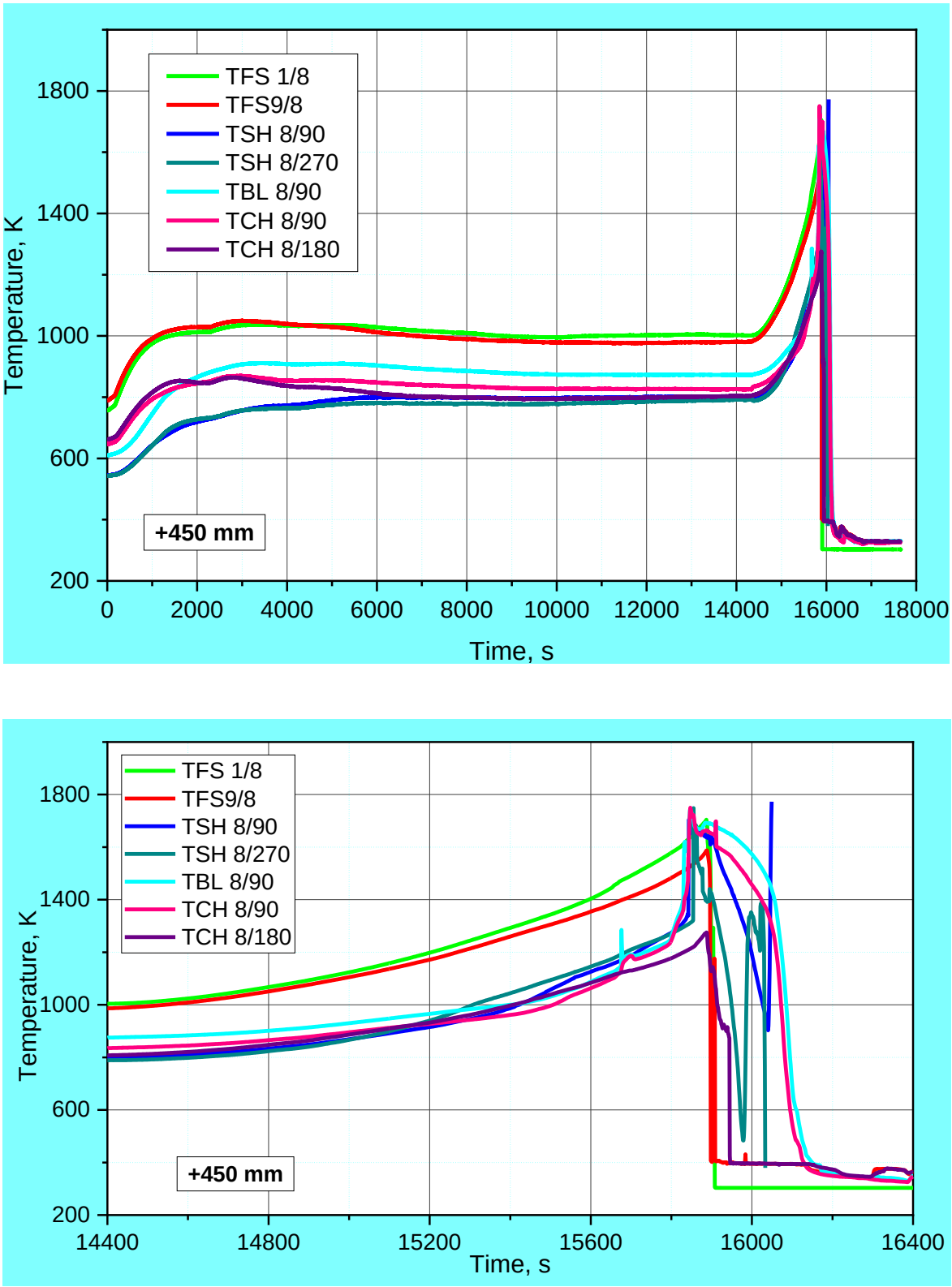

Figure 29 QUENCH-20; Temperatures measured by rod cladding (TFS), shroud (TSH) absorber blade (TBL) and water channel box (TCH) thermocouples at 450 mm elevation.

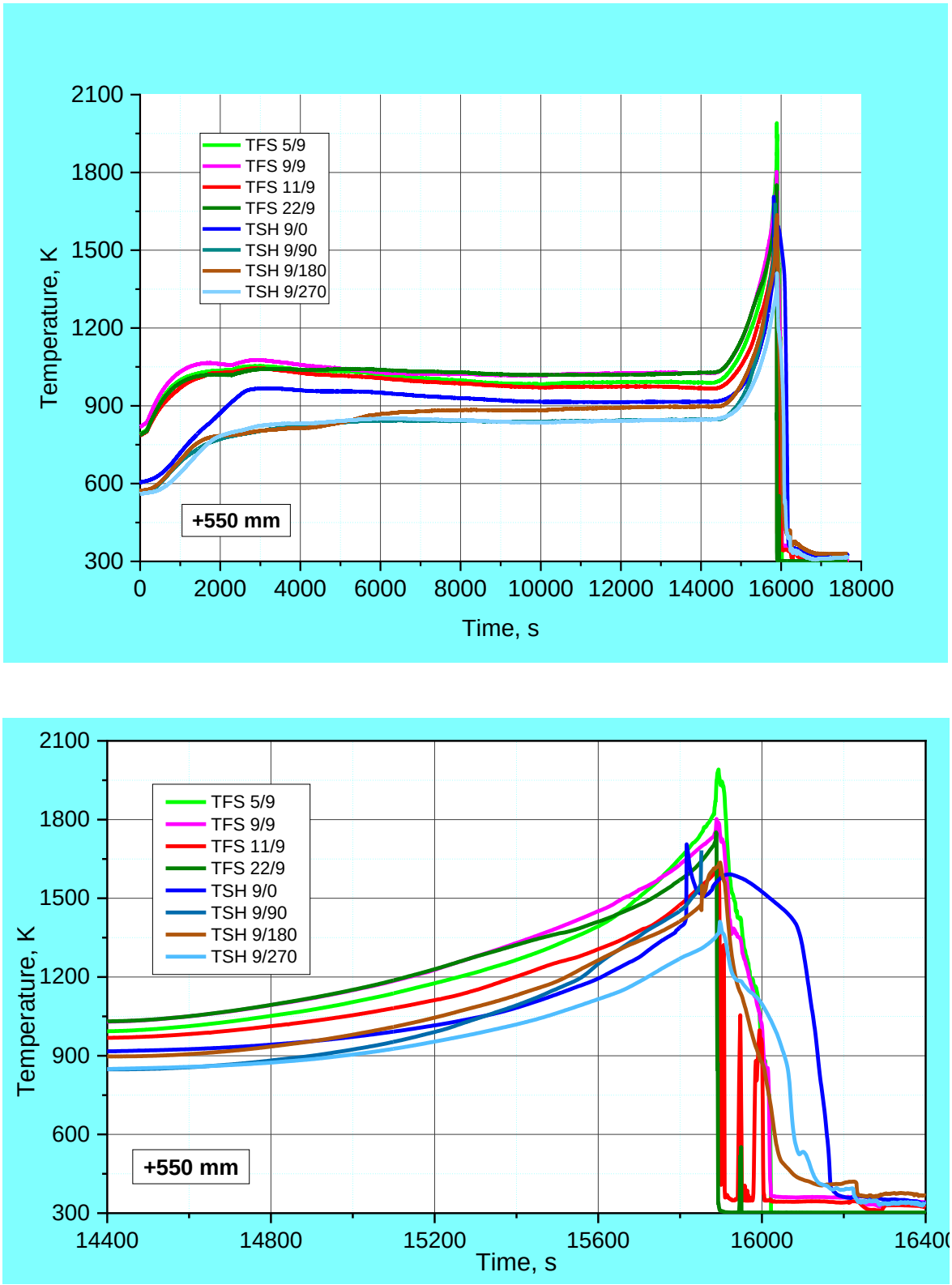

Figure 30 QUENCH-20; Temperatures measured by rod cladding (TFS) and shroud (TSH) thermocouples at 550 mm elevation.

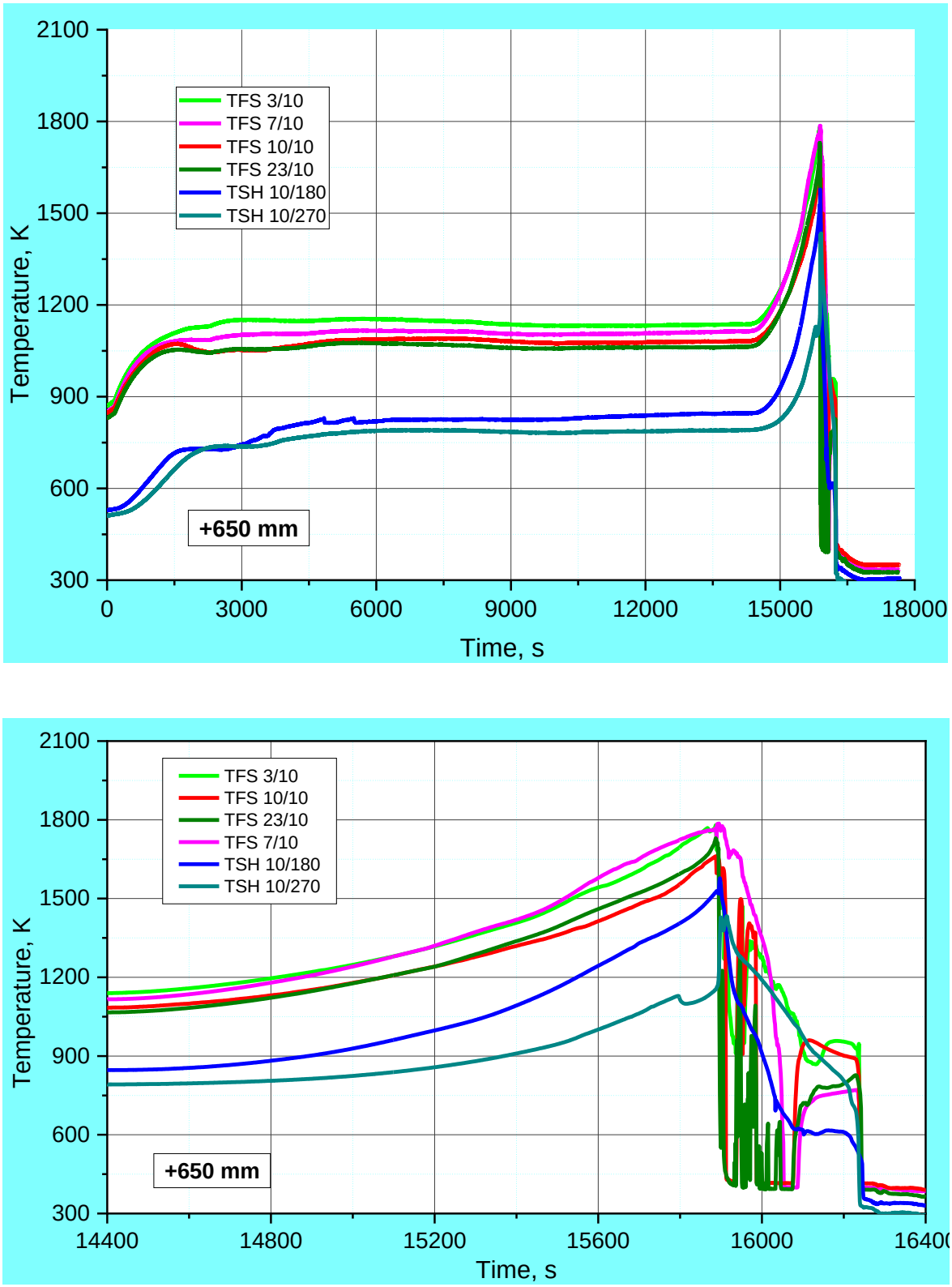

Figure 31 QUENCH-20; Temperatures measured by rod cladding (TFS) and shroud (TSH) thermocouples at 650 mm elevation.

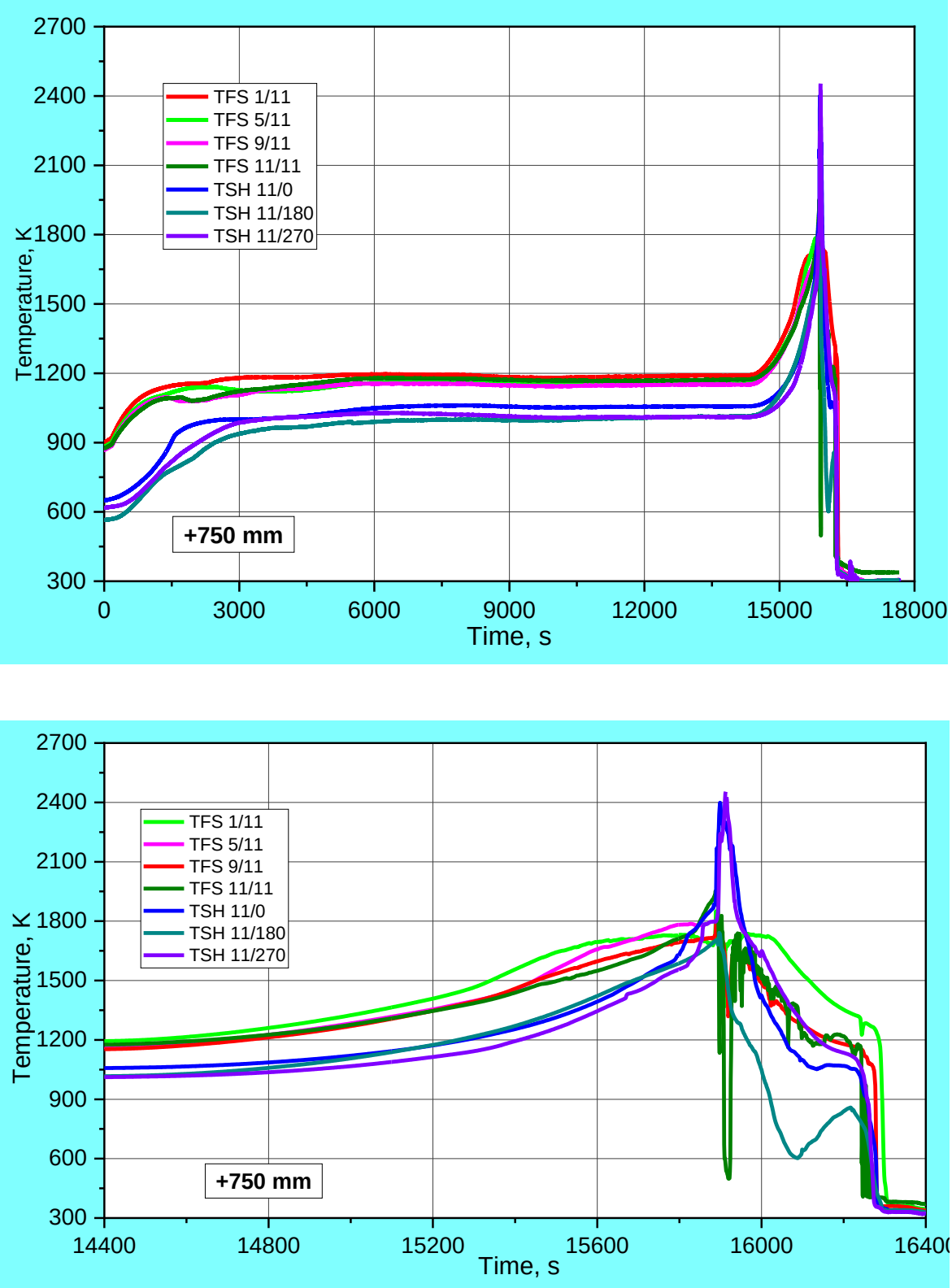

Figure 32 QUENCH-20; Temperatures measured by rod cladding (TFS) and shroud (TSH) thermocouples at 750 mm elevation.

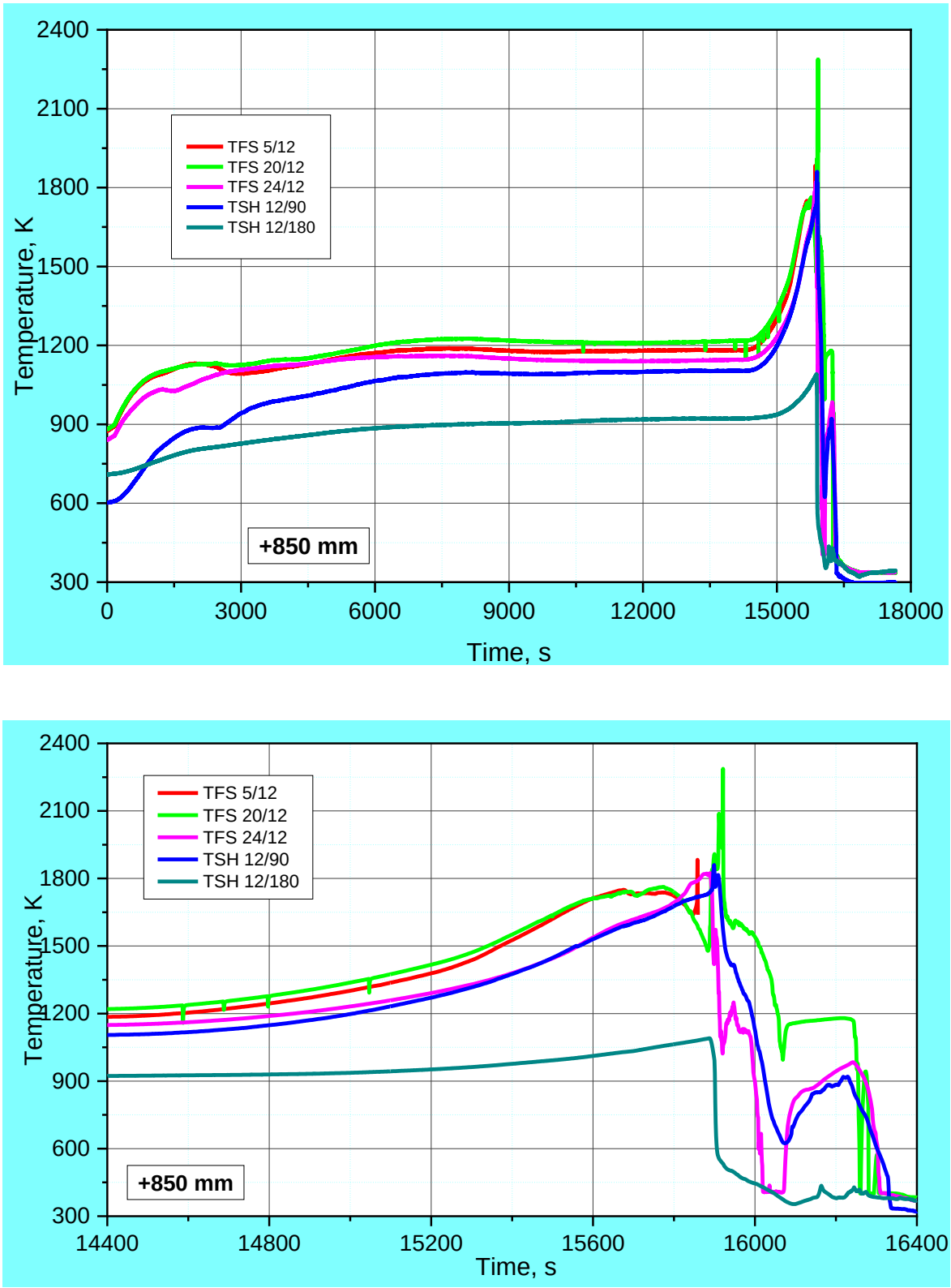

Figure 33 QUENCH-20; Temperatures measured by rod cladding (TFS) and shroud (TSH), thermocouples at 850 mm elevation.

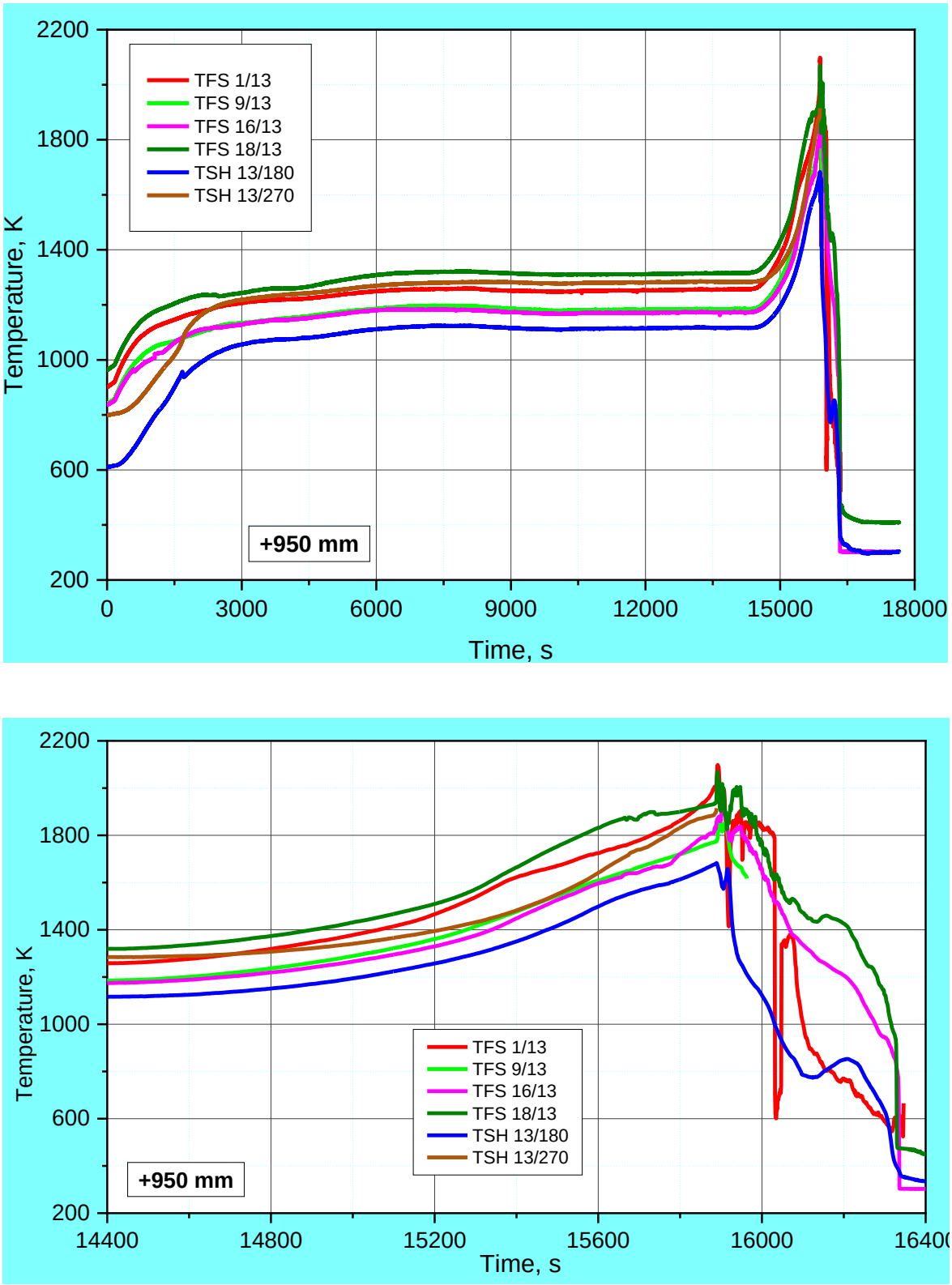

Figure 34 QUENCH-20; Temperatures measured by rod cladding (TFS) and shroud (TSH) thermocouples at 950 mm elevation.

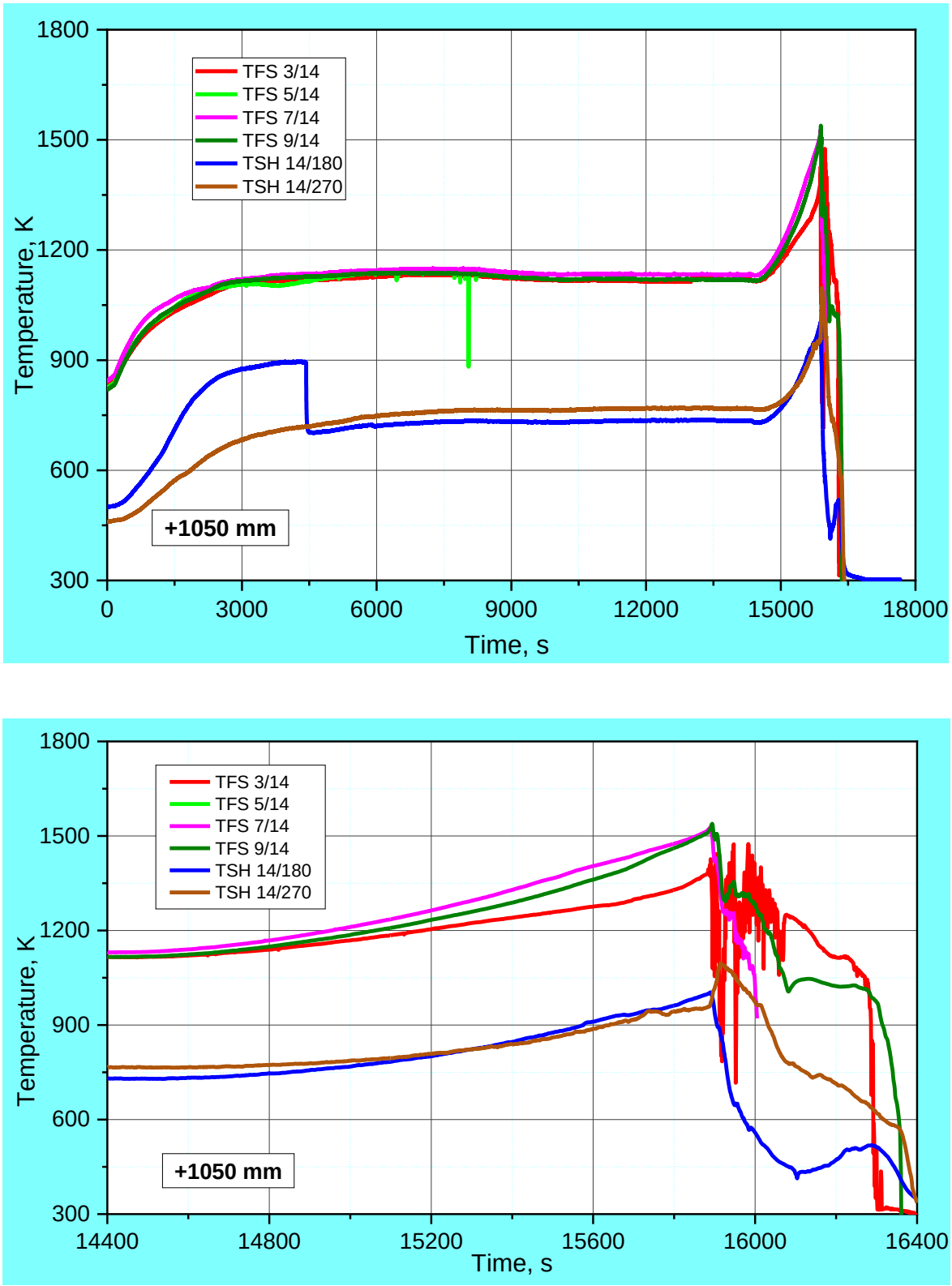

Figure 35 QUENCH-20; Temperatures measured by rod cladding (TFS) and shroud (TSH) thermocouples at 1050 mm elevation.

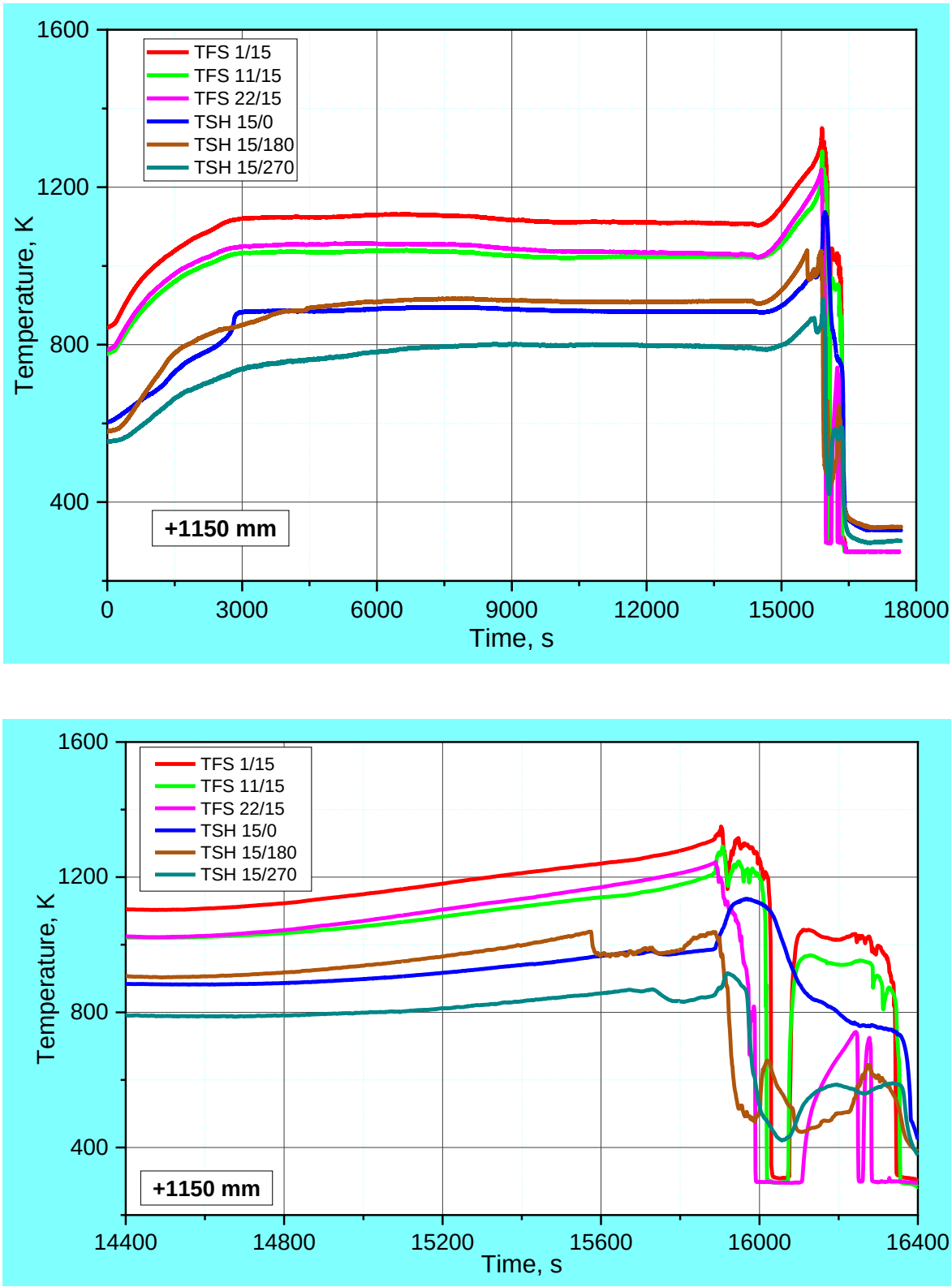

Figure 36 QUENCH-20; Temperatures measured by rod cladding (TFS) and shroud (TSH) thermocouples at 1150 mm elevation.

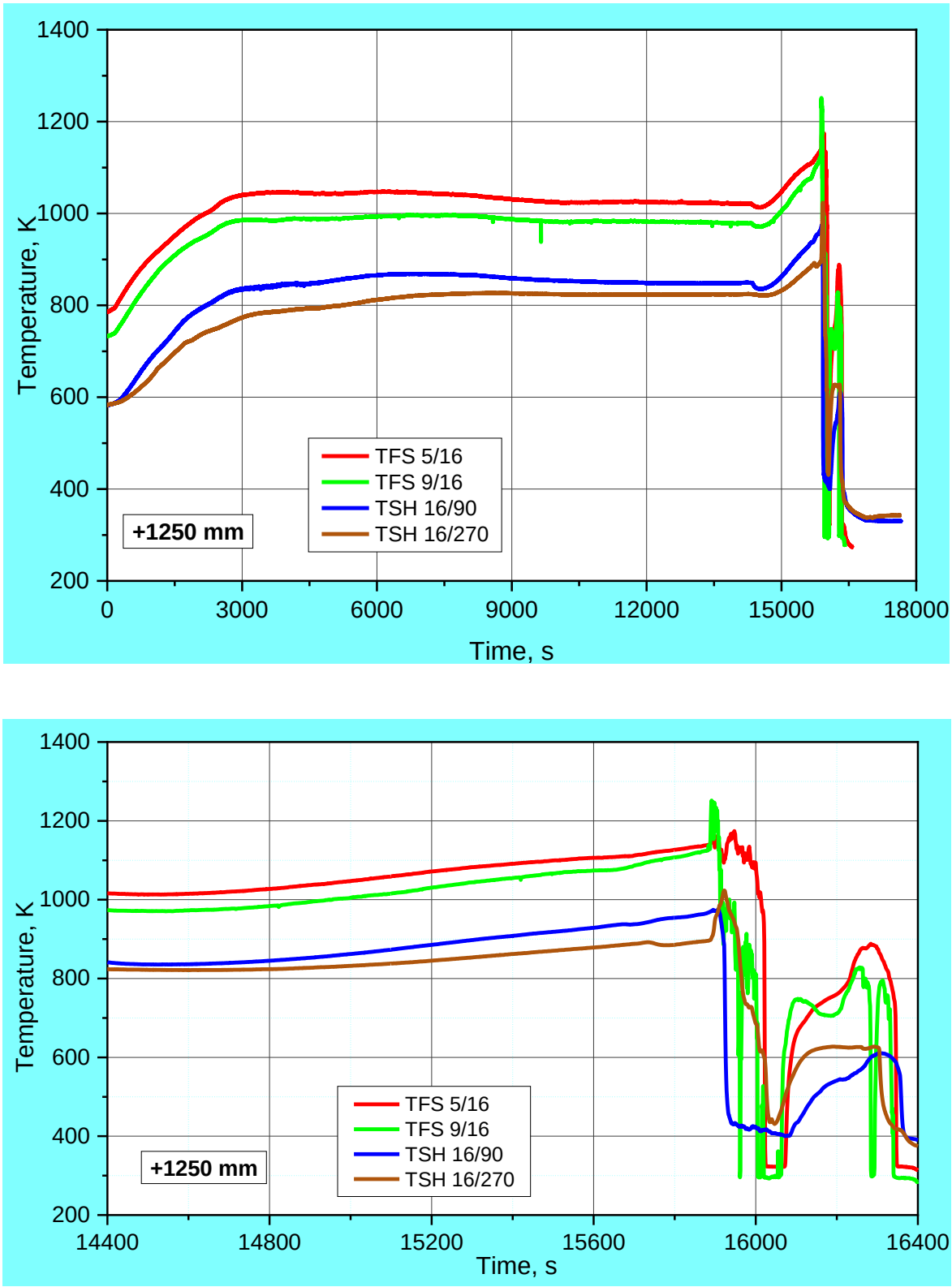

Figure 37 QUENCH-20; Temperatures measured by rod cladding (TFS) and shroud (TSH) thermocouples at 1250 mm elevation.

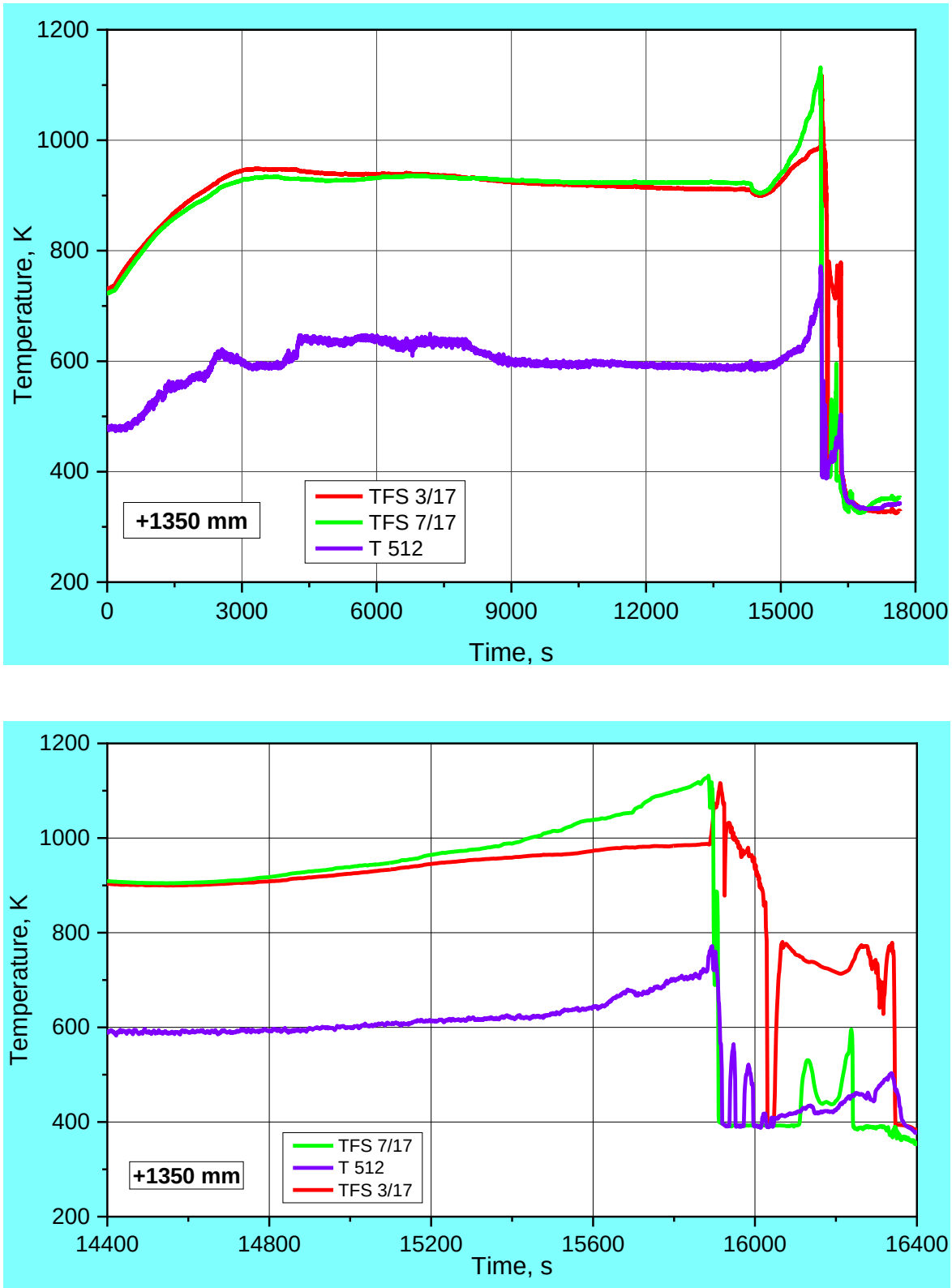

Figure 38 QUENCH-20; Temperature measured by rod cladding thermocouple at 1350 mm elevation (TFS) and gas temperature (T 512) at 1360 mm between shroud and rod #20.

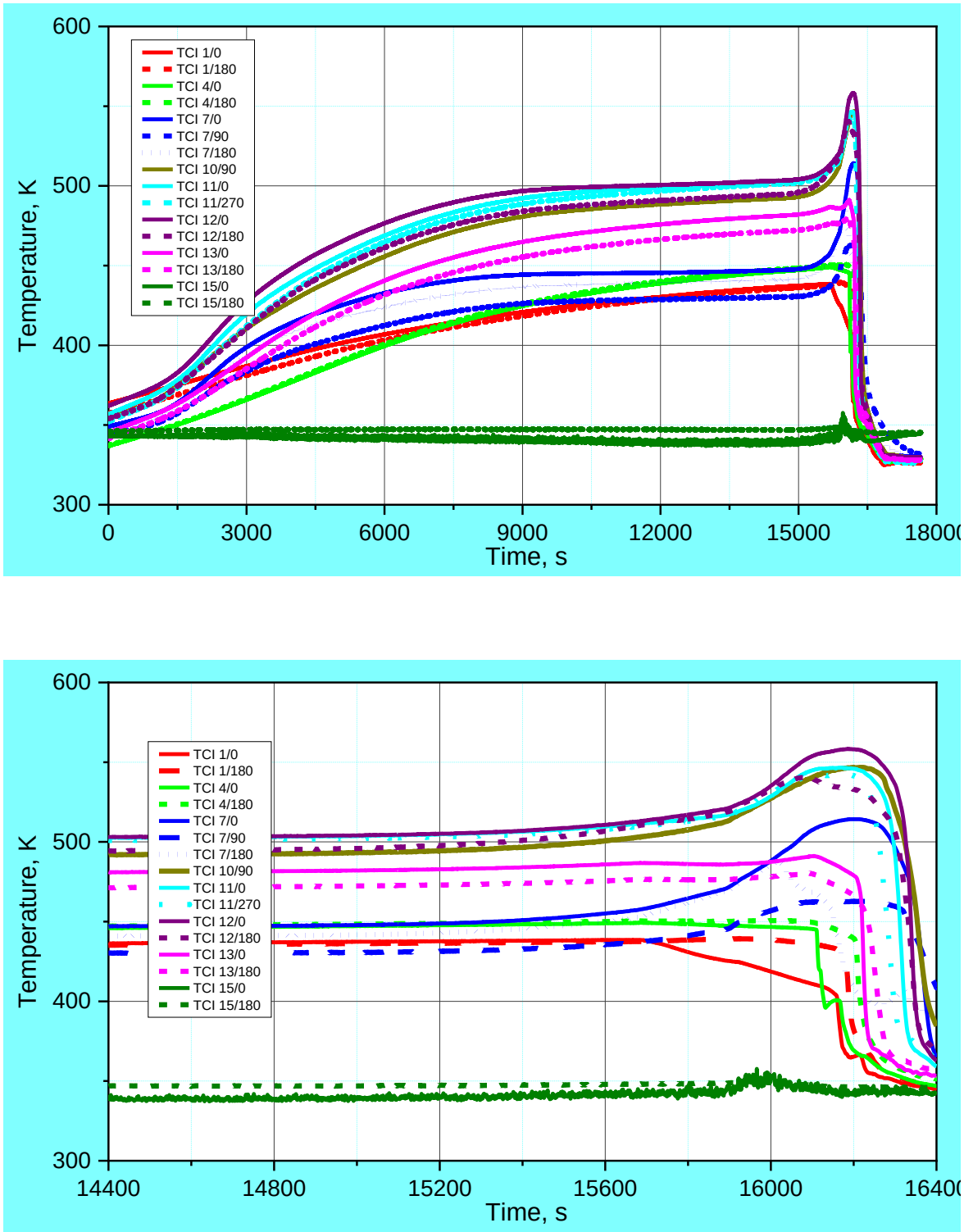

Figure 39 QUENCH-20; Overview of the TCI (inner cooling jacket).

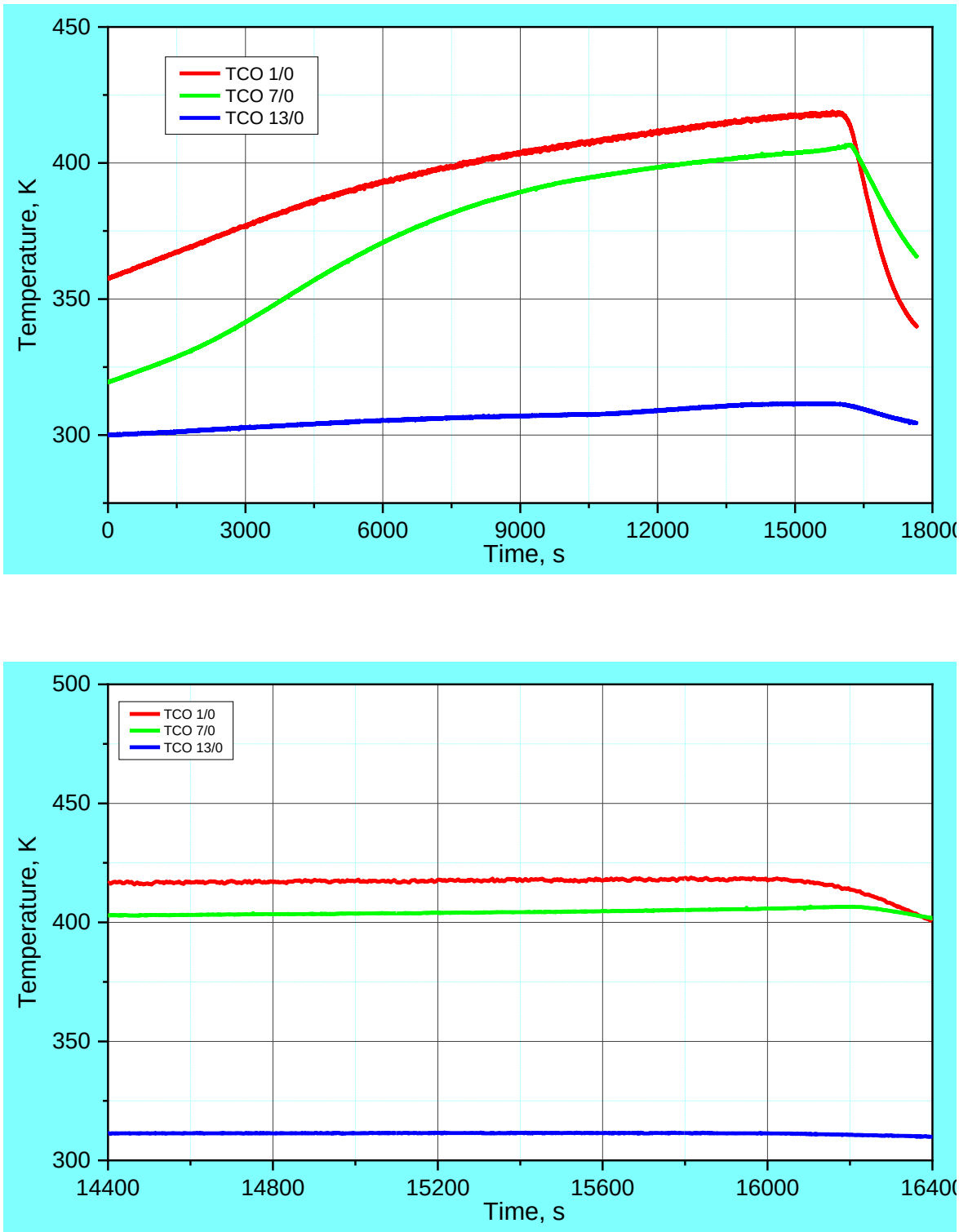

Figure 40 QUENCH-20; Overview of the TCO (outer cooling jacket).

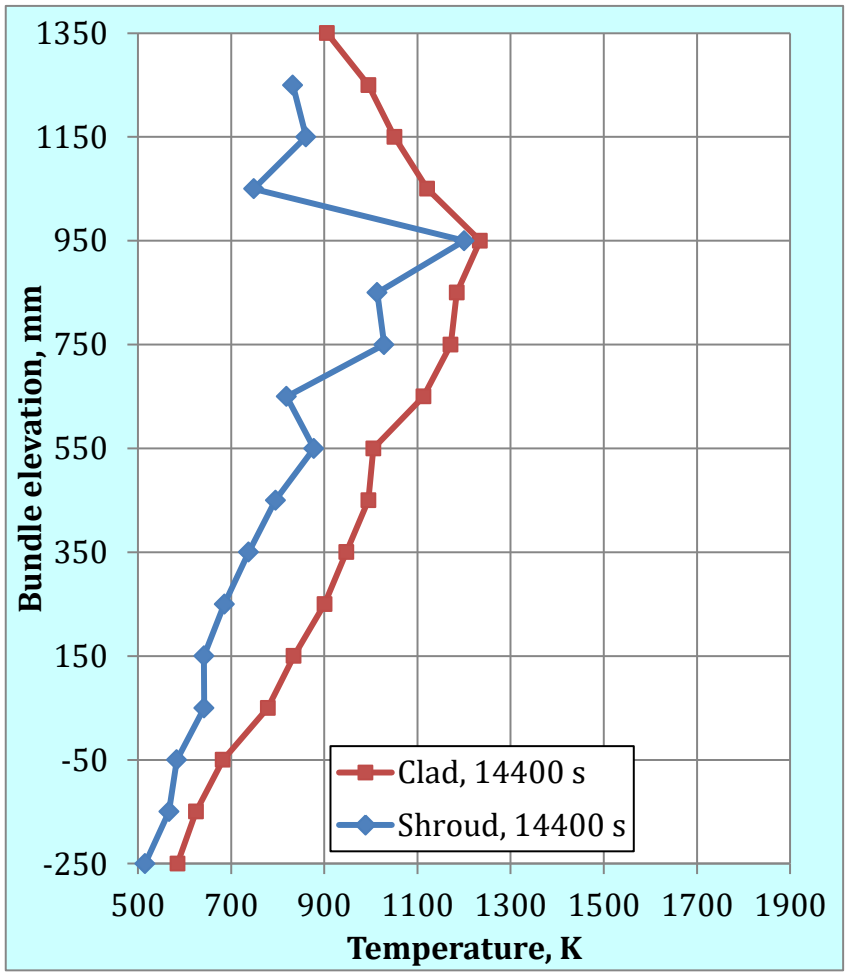

At the end of pre-oxidation (14400 s)

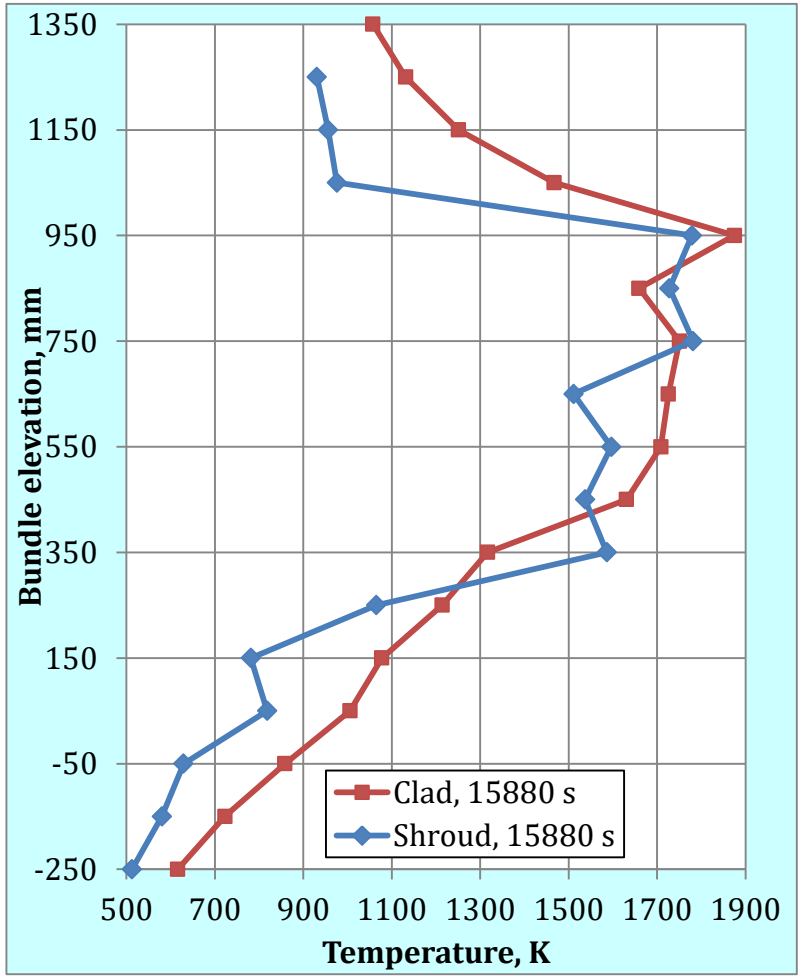

At the end of transient (15880 s)

Figure 41 QUENCH-20; axial temperature profiles of outer cladding surfaces and outer shroud surface (temperatures averaged over the cross-section for each elevation).

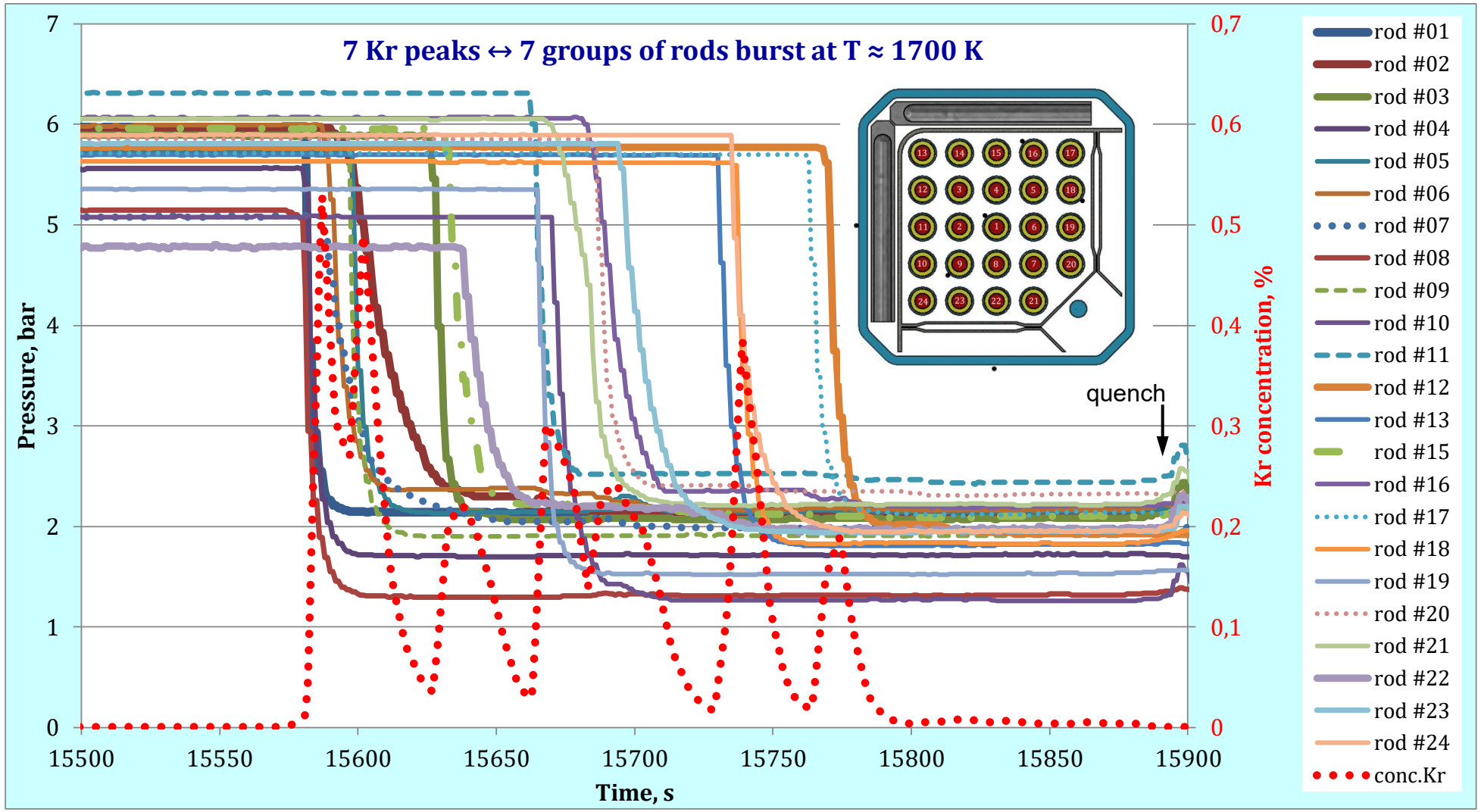

Figure 42 QUENCH-20; rod failure: indication by depressurization and Kr release.

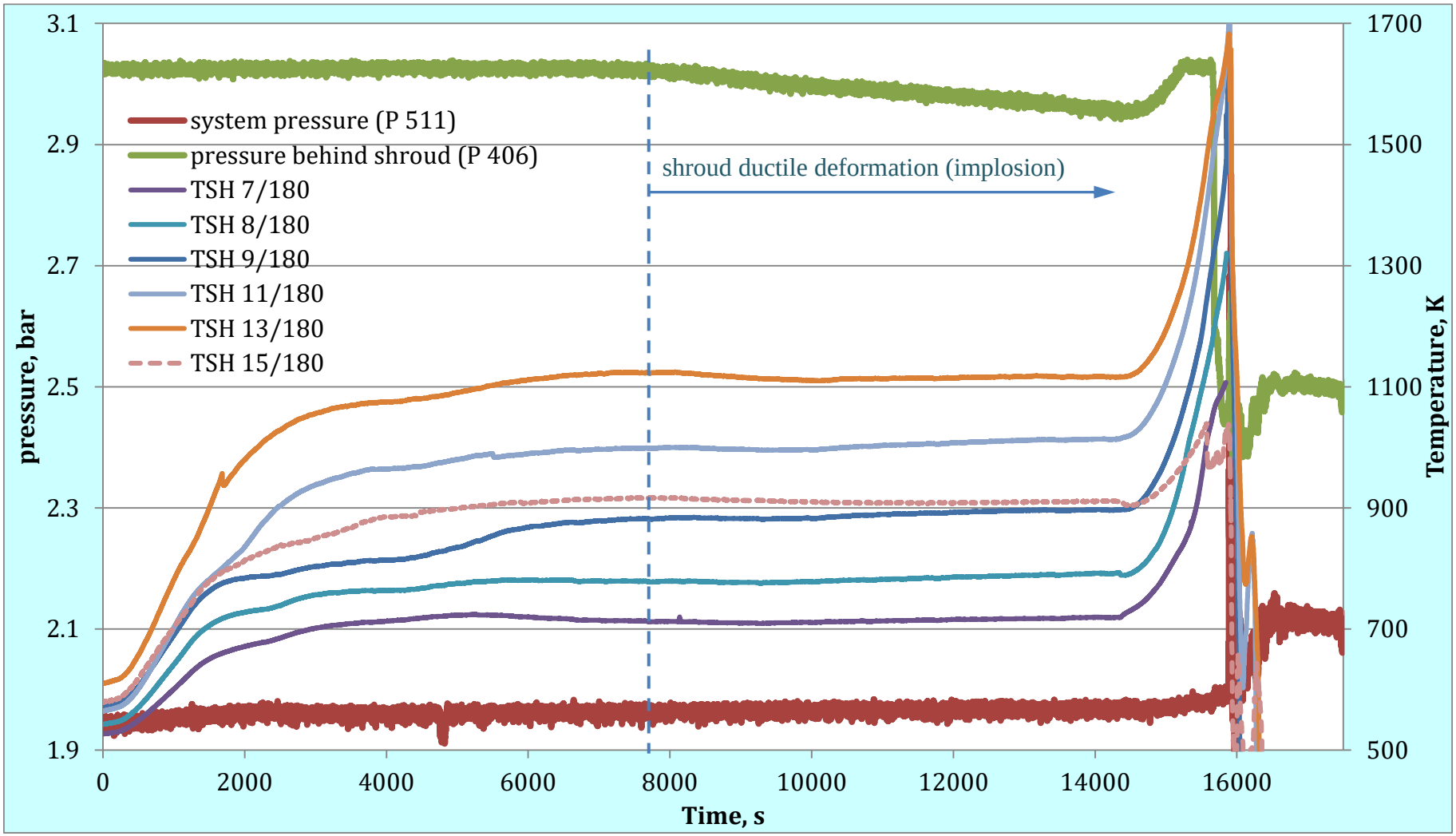

Figure 43 QUENCH-20; Ductile deformation of shroud between elevations 9 (550 mm) and 15 (1150 mm) at temperatures above 850 K (indicated by decrease of pressure in annulus between shroud and cooling jacket during increase of annulus volume).

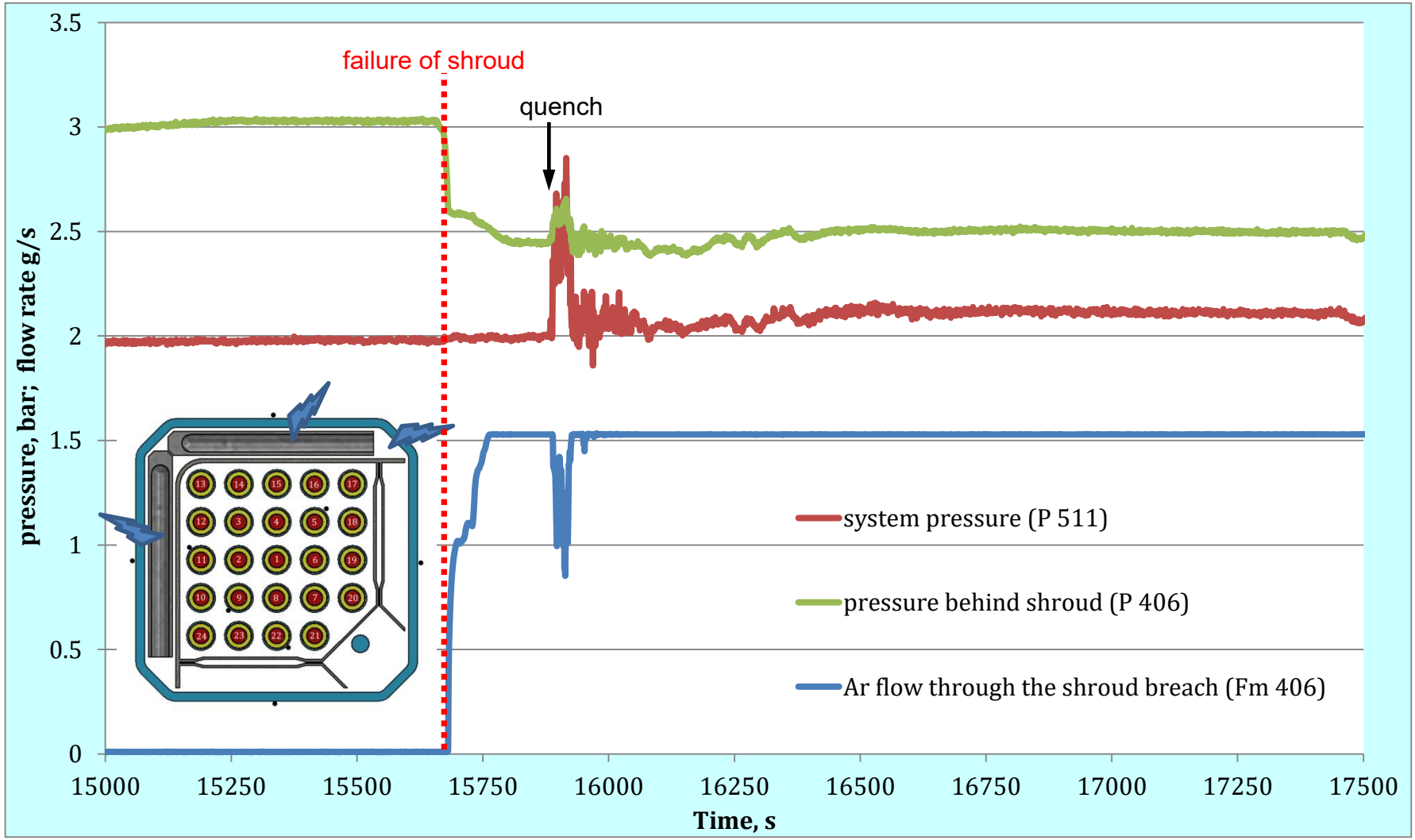

Figure 44 QUENCH-20; shroud failure: indication by decrease of annulus pressure and Ar flow through the breach.

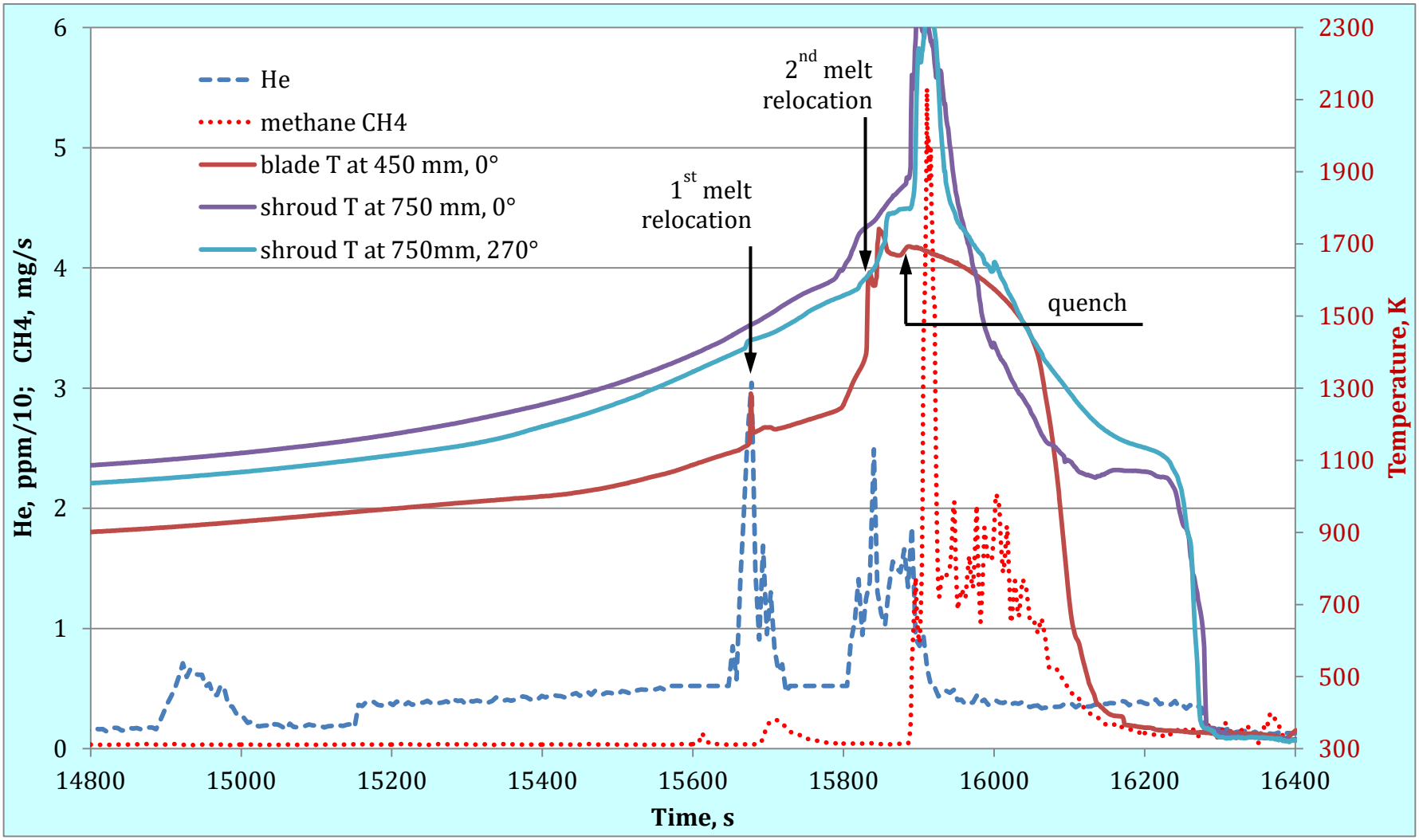

Figure 45 QUENCH-20, absorber melt formation above 750 mm and relocation to lower elevations.

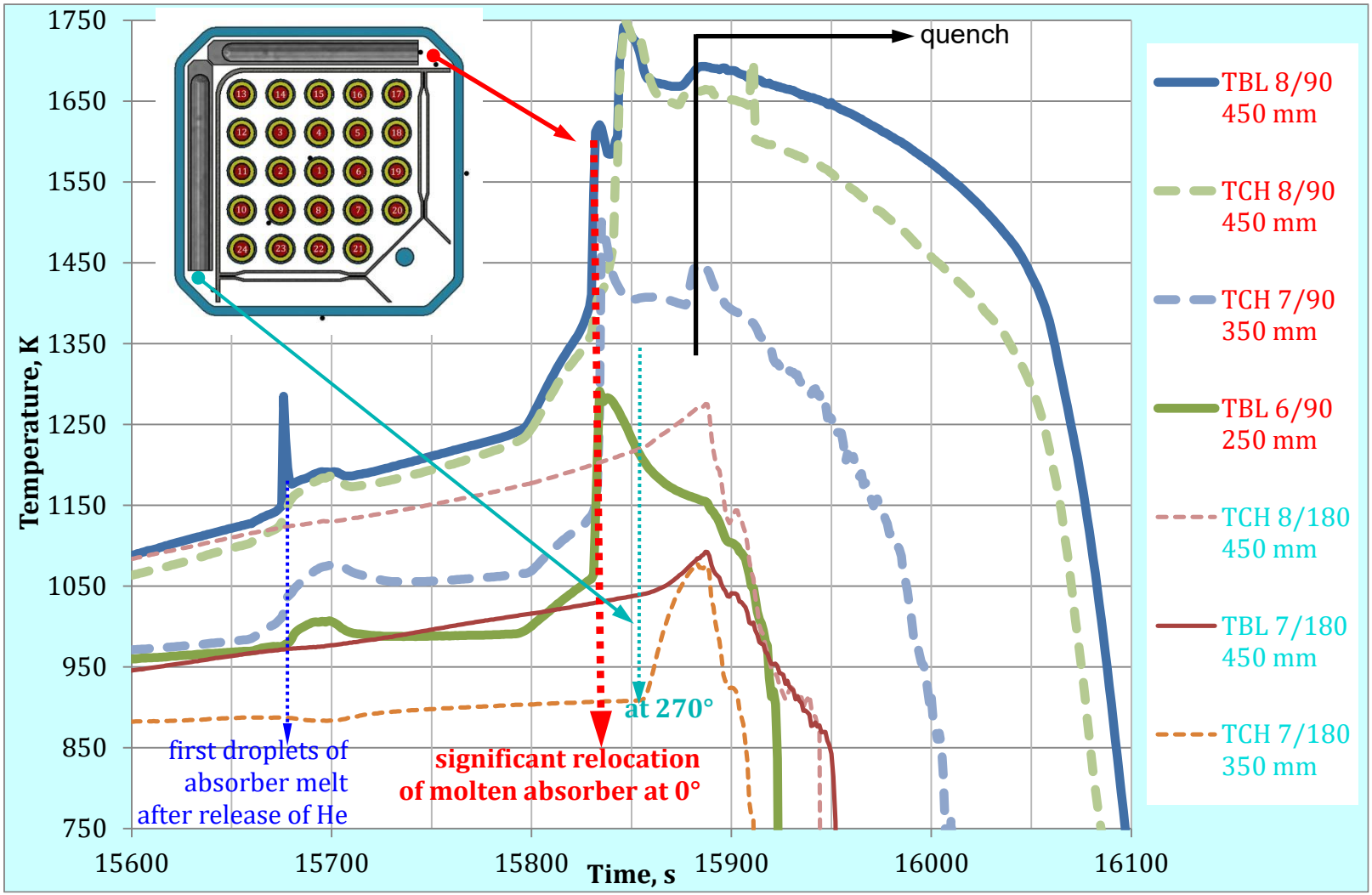

Figure 46 QUENCH-20; absorber melt relocation from hottest bundle elevations to elevations 250…450 mm.

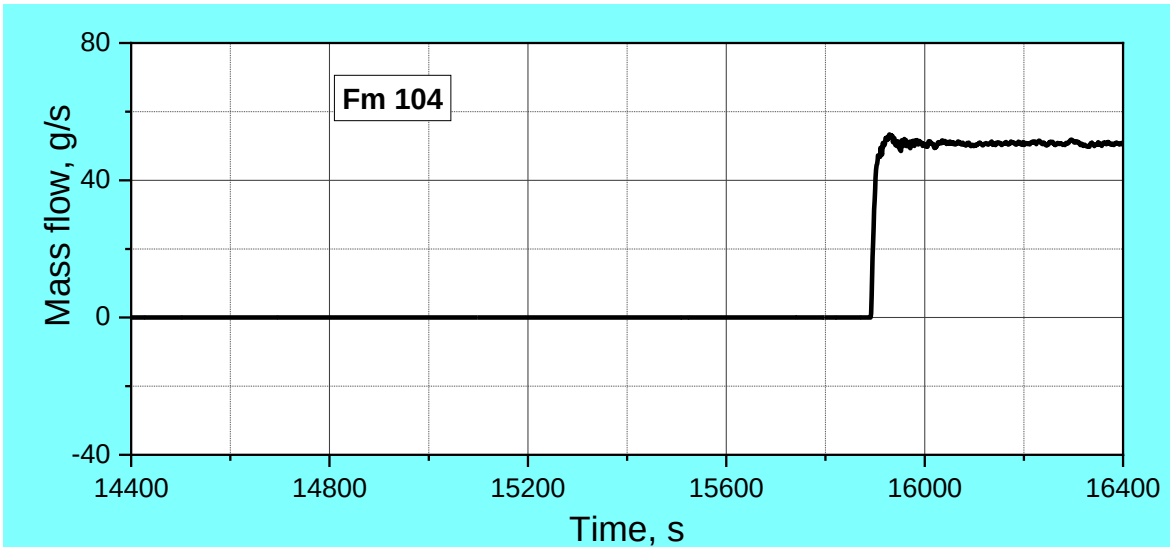

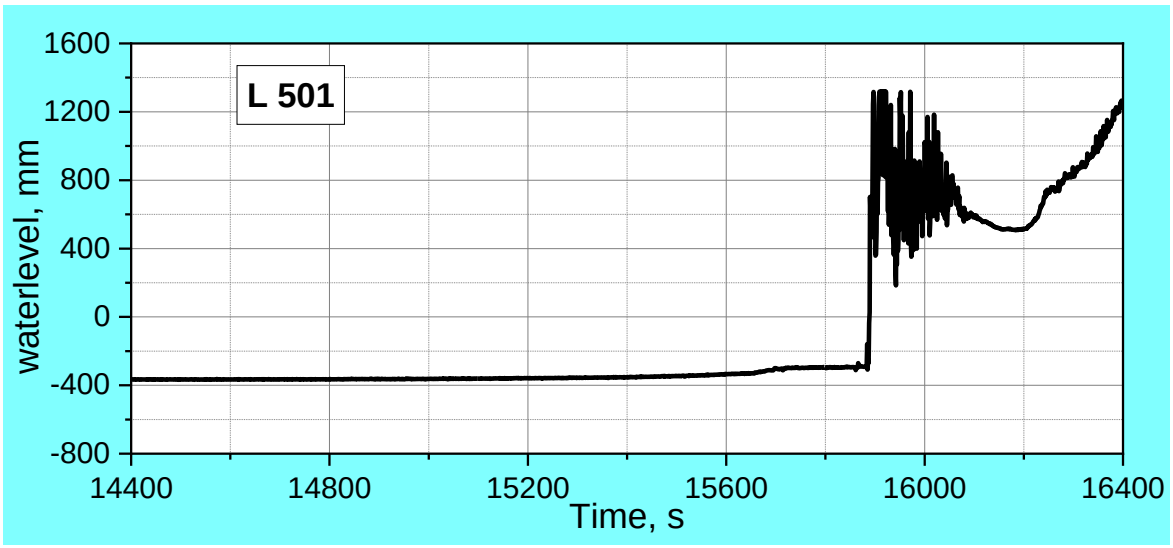

Figure 47 QUENCH-20; Quench measurement water mass flow rate (Fm 104), top; collapsed water level (L 501), bottom.

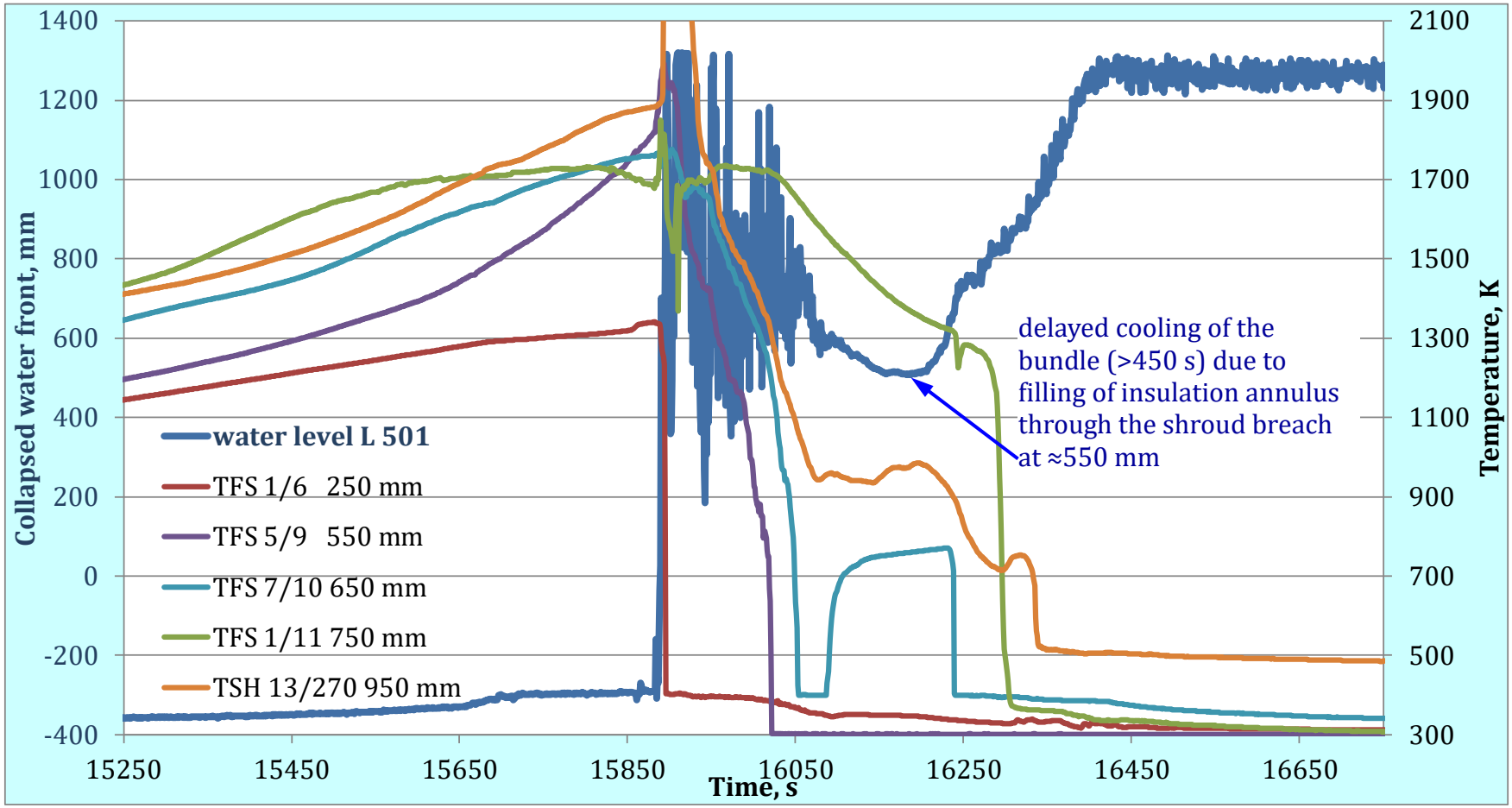

Figure 48 QUENCH-20; filling of bundle with quench water and wetting of thermocouples.

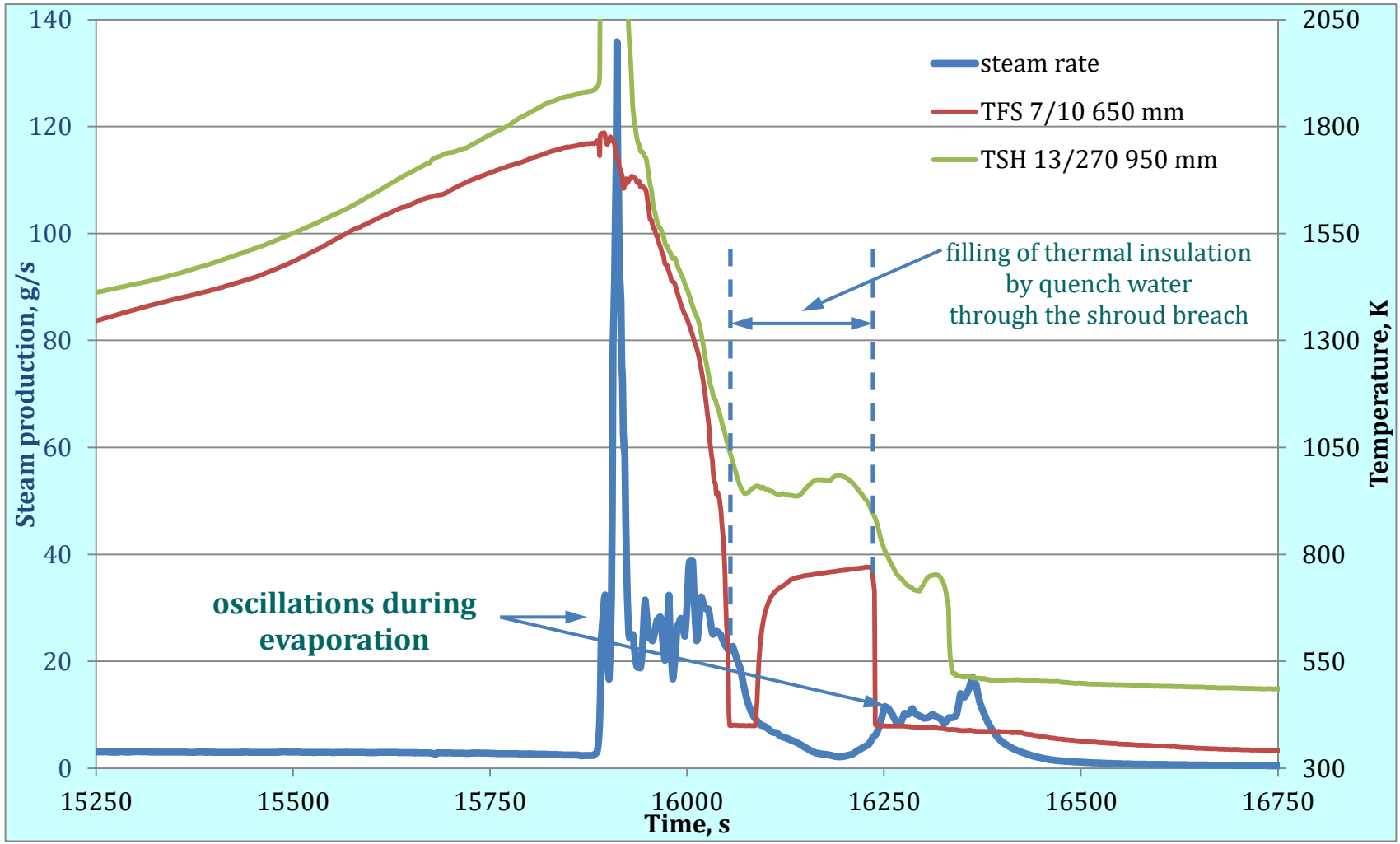

Figure 49 QUENCH-20; steam production (mass spectrometer data) during the quench stage.

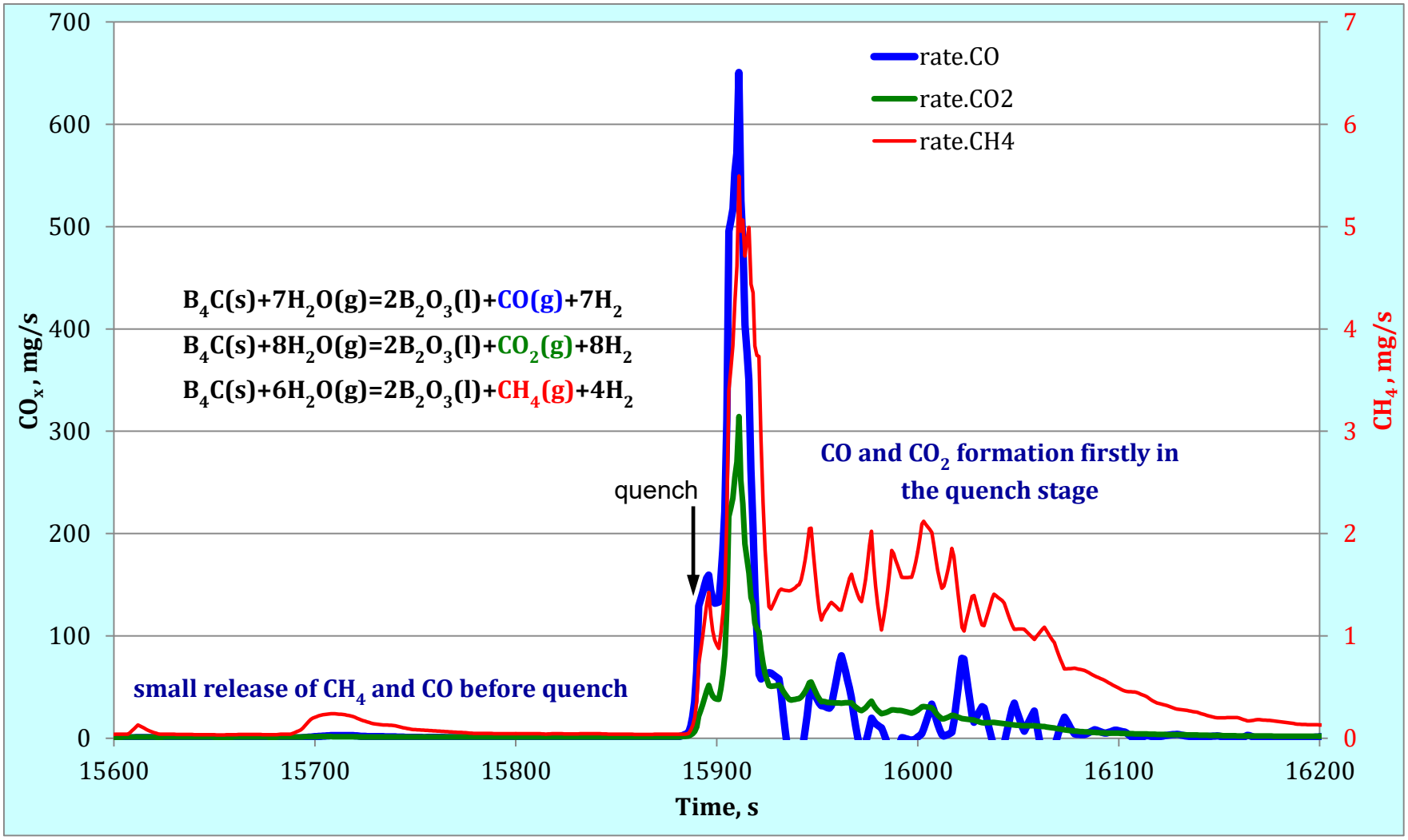

Figure 50 QUENCH-20, reaction of B_4C with steam.

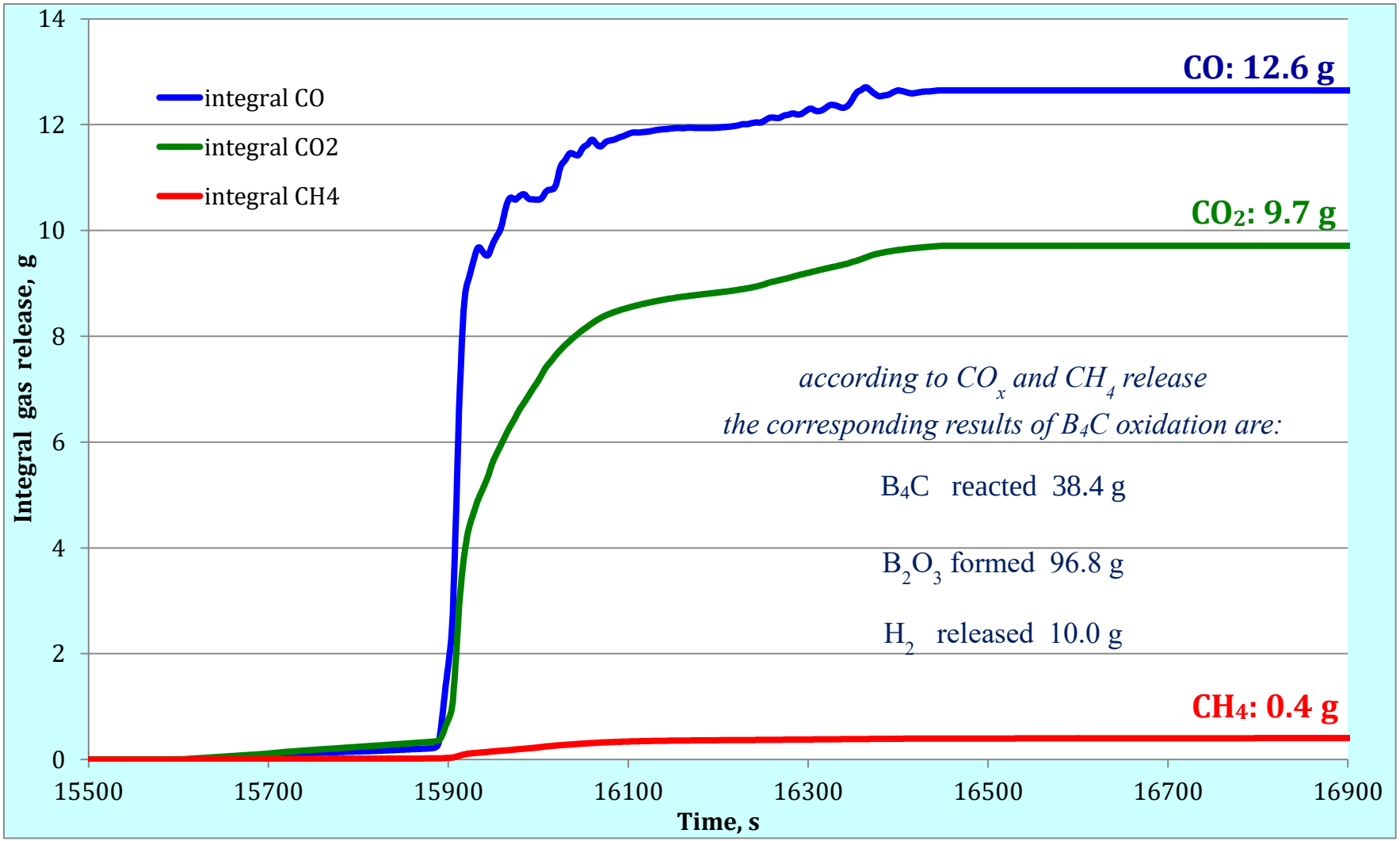

Figure 51 QUENCH-20, reaction of B_4C with steam, integral gas release.

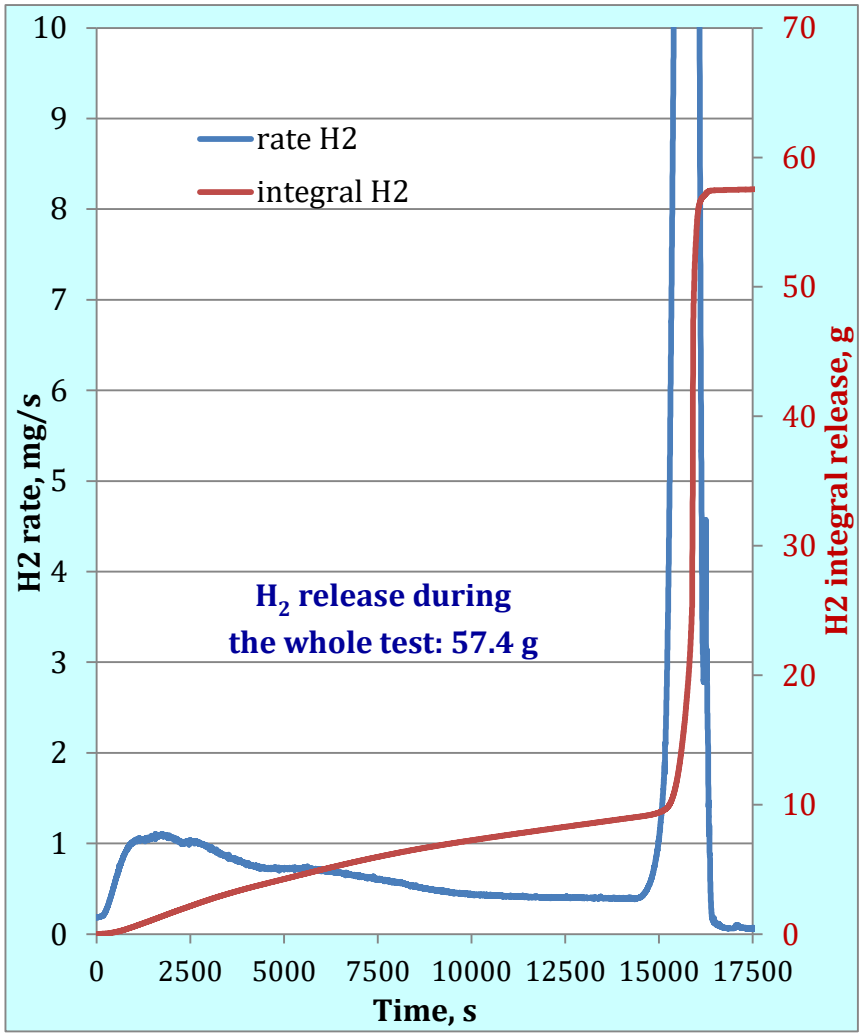

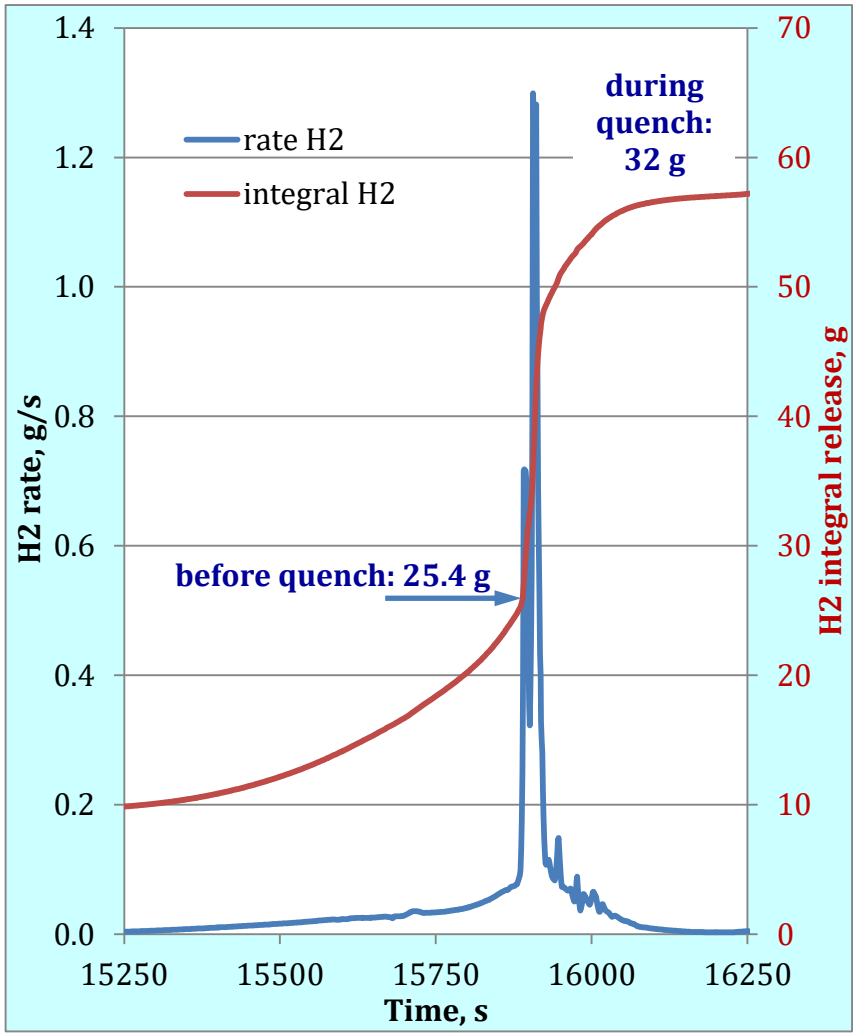

Figure 52 QUENCH-20; hydrogen release.

H_2 release during quench:
22 g (from Zry and molten steel) + 10 g (from B_4C)

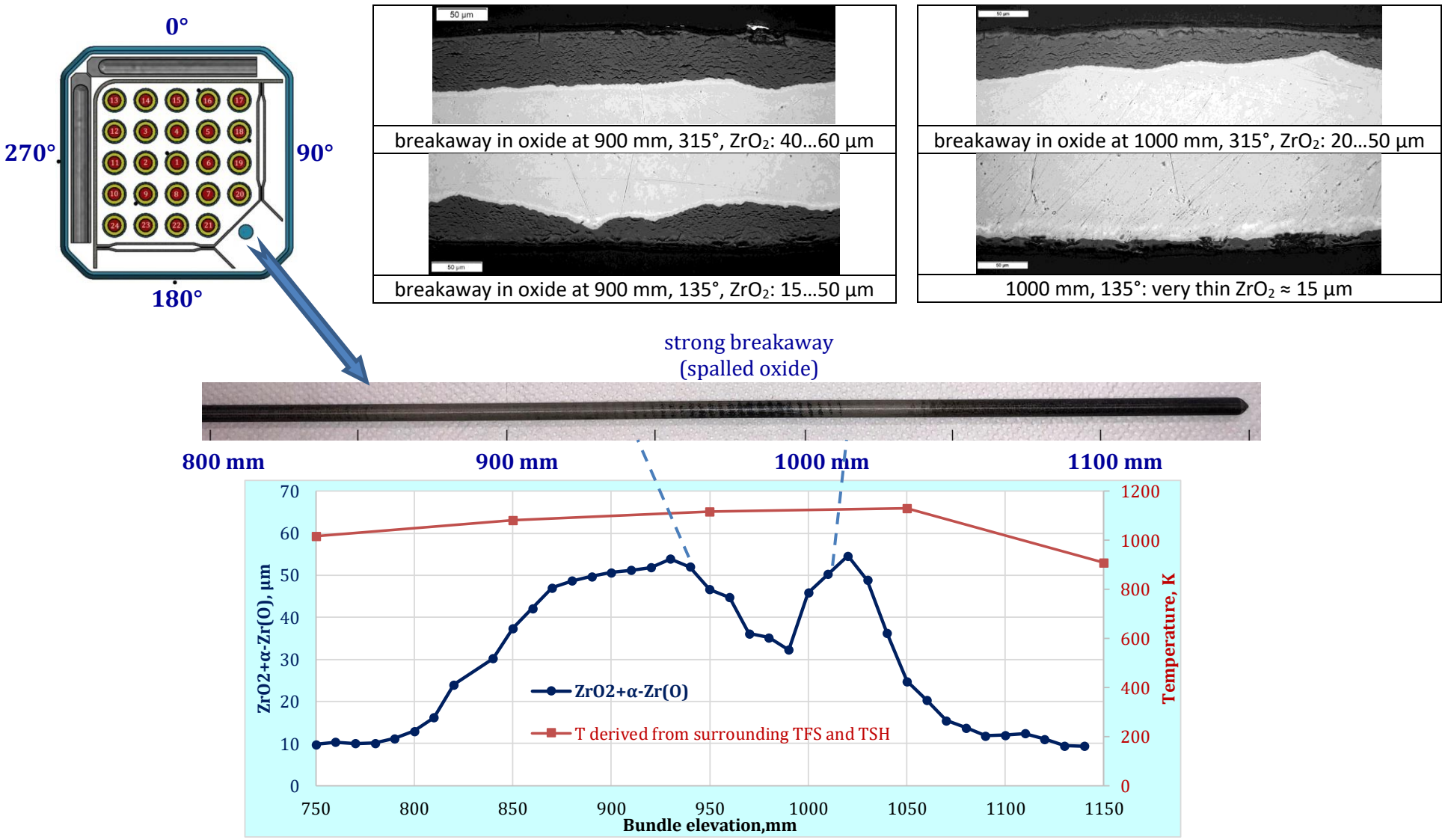

Figure 53 QUENCH-20; oxidation of Zry-4 corner rod withdrawn at the end of pre-oxidation (t=14412 s).

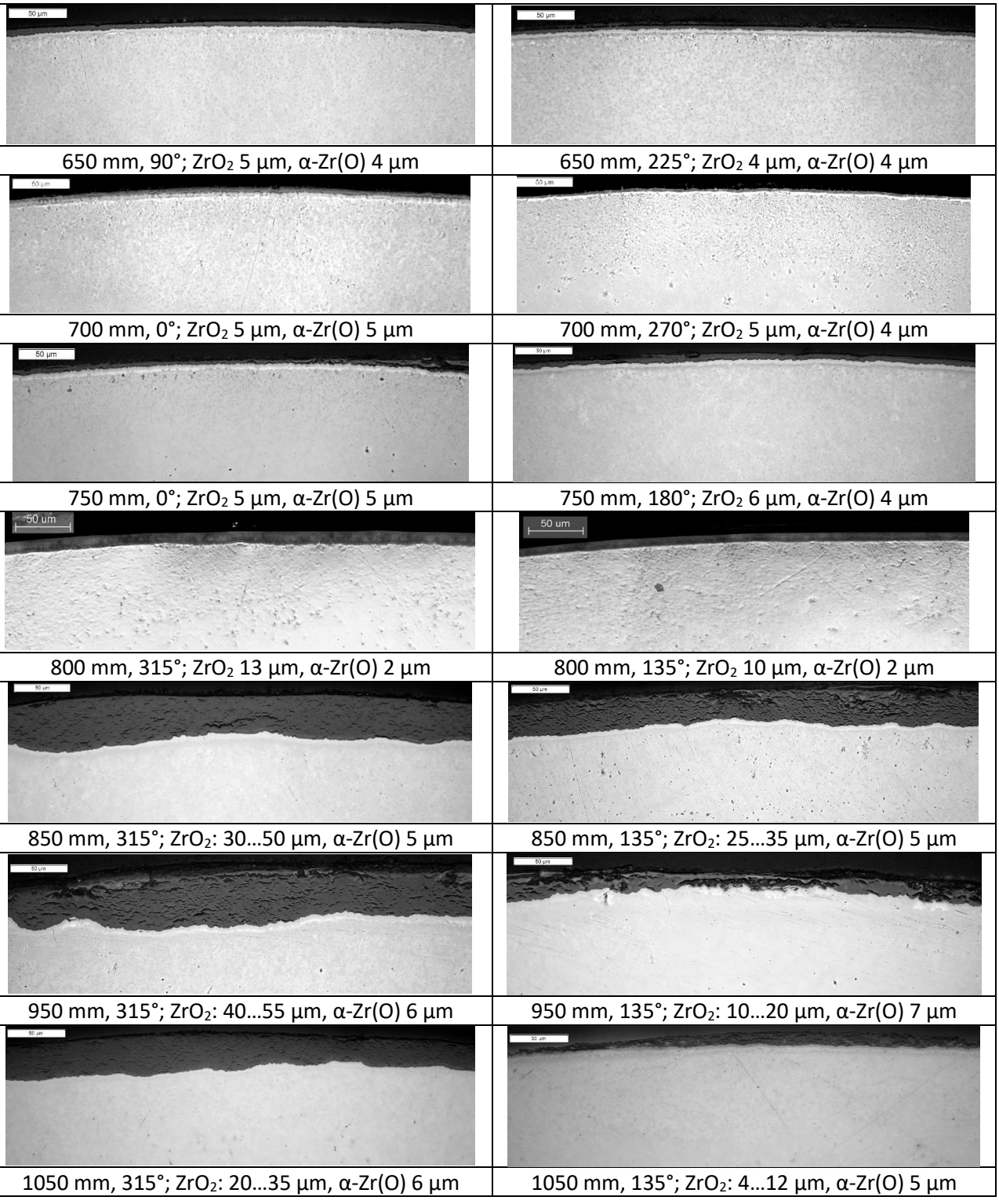

Figure 54 QUENCH-20; transition from regular to breakaway oxidation for the withdrawn Zry-4 corner rod.

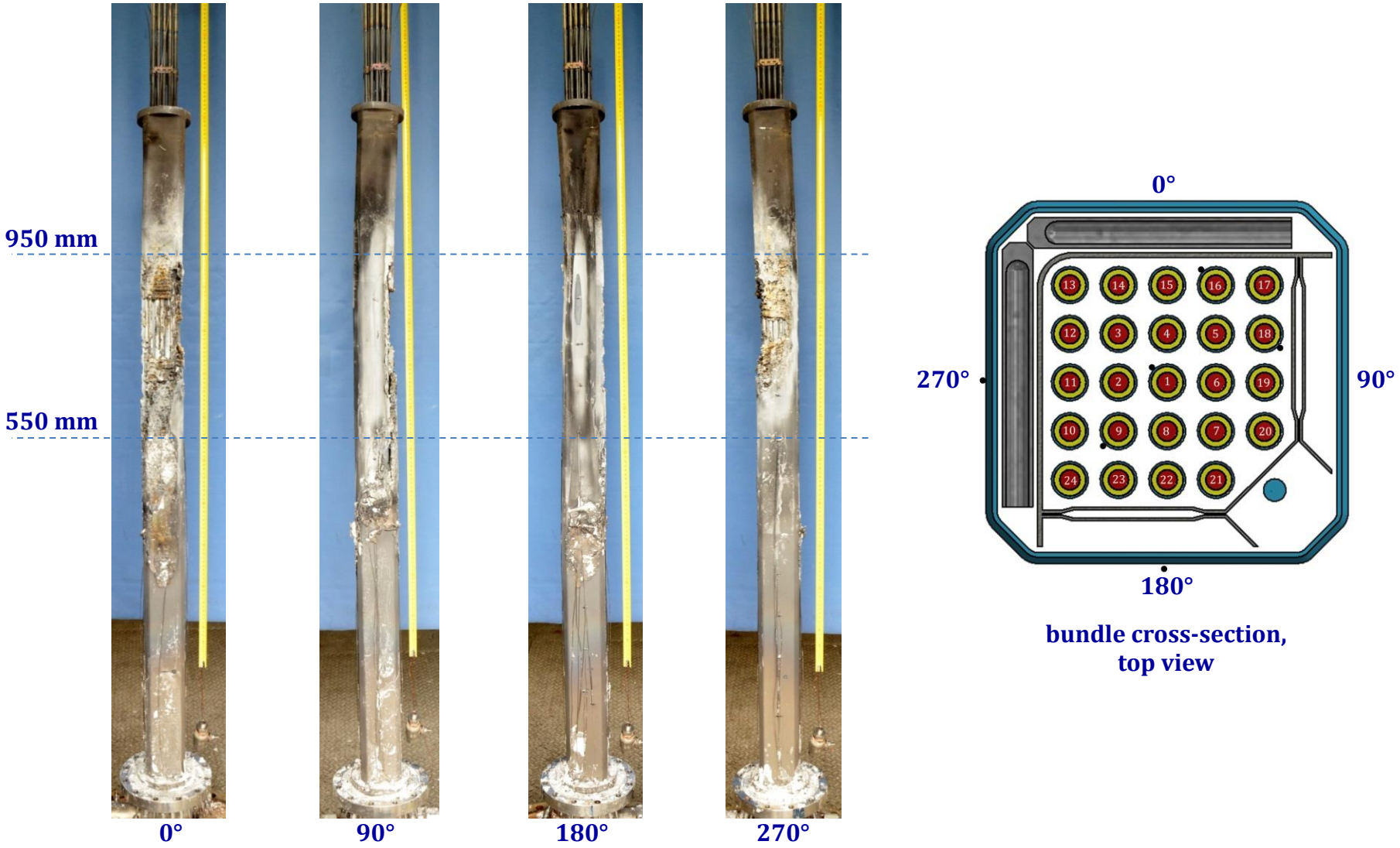

Figure 55 QUENCH-20; bundle surrounded by shroud: post-test view.

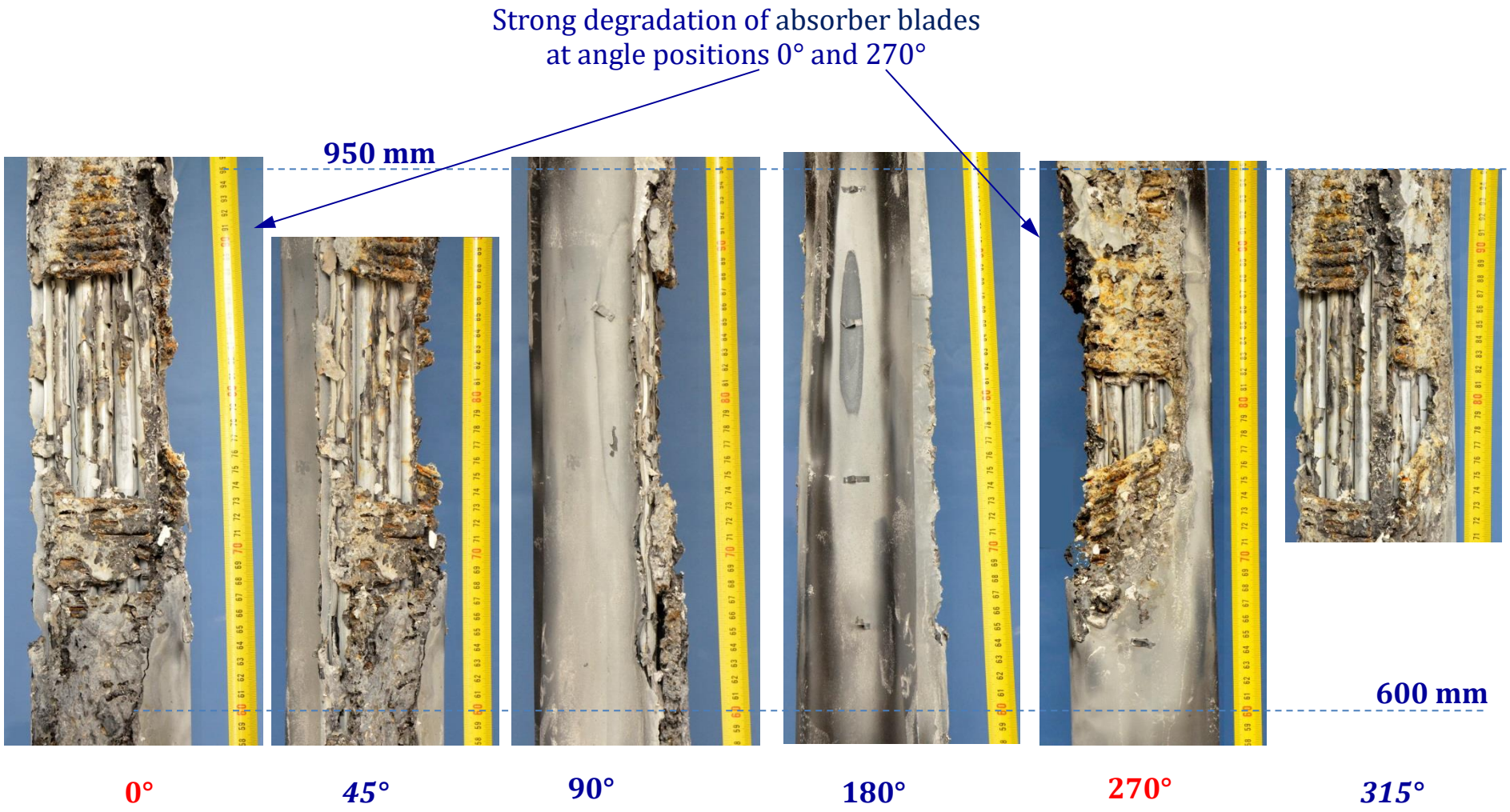

Figure 56 QUENCH-20; Degradation of absorber blades, channel box and shroud between elevations 650 and 950 mm.

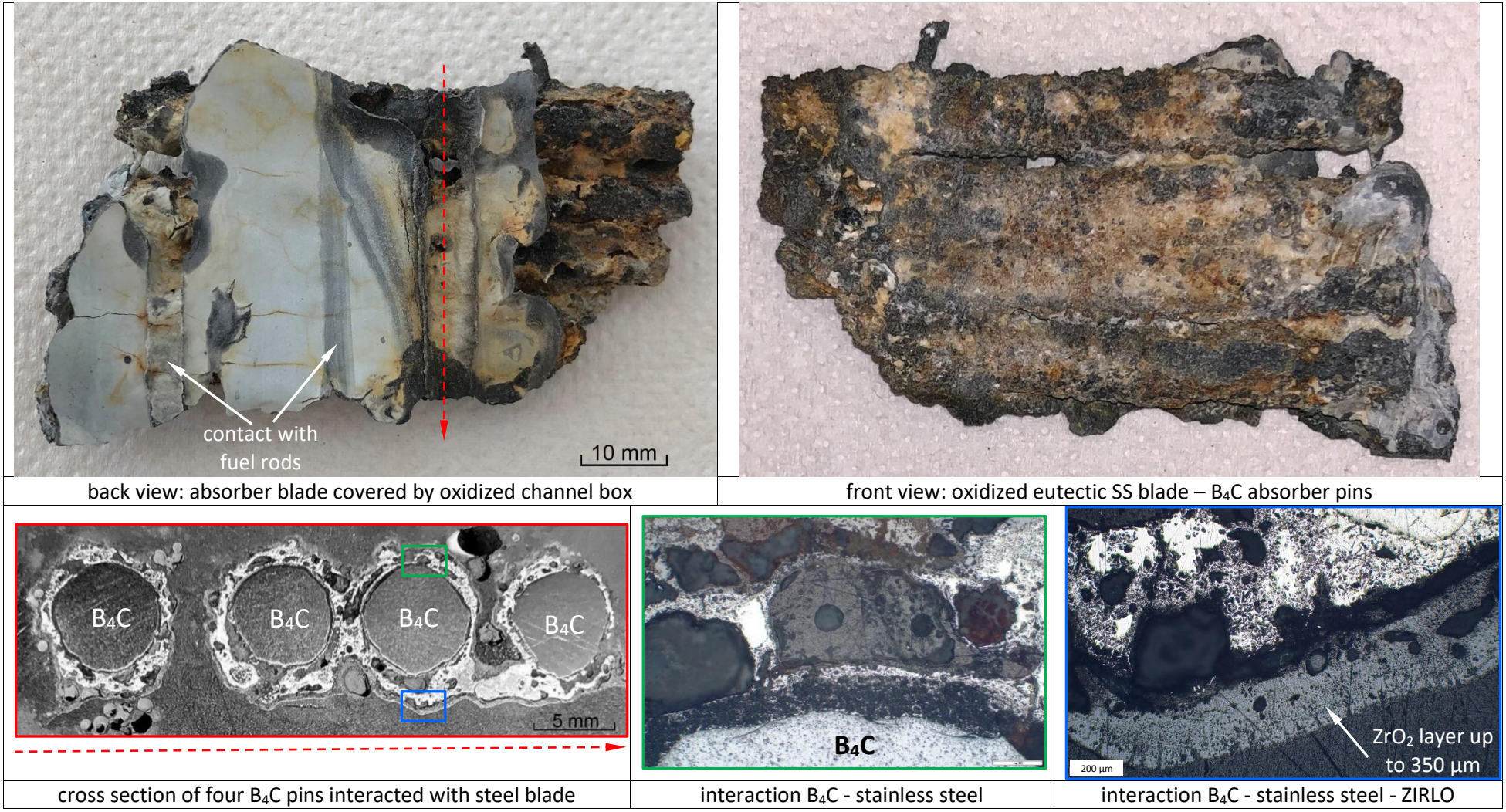

back view: absorber blade covered by oxidized channel box

front view: oxidized eutectic SS blade – B_4C absorber pins

cross section of four B_4C pins interacted with steel blade

interaction B_4C - stainless steel

interaction B_4C - stainless steel - ZIRLO

Figure 57 QUENCH-20; Piece of absorber blade broken away between 750 and 800 mm, 0°: eutectic interaction of B_4C pins with SS blade.

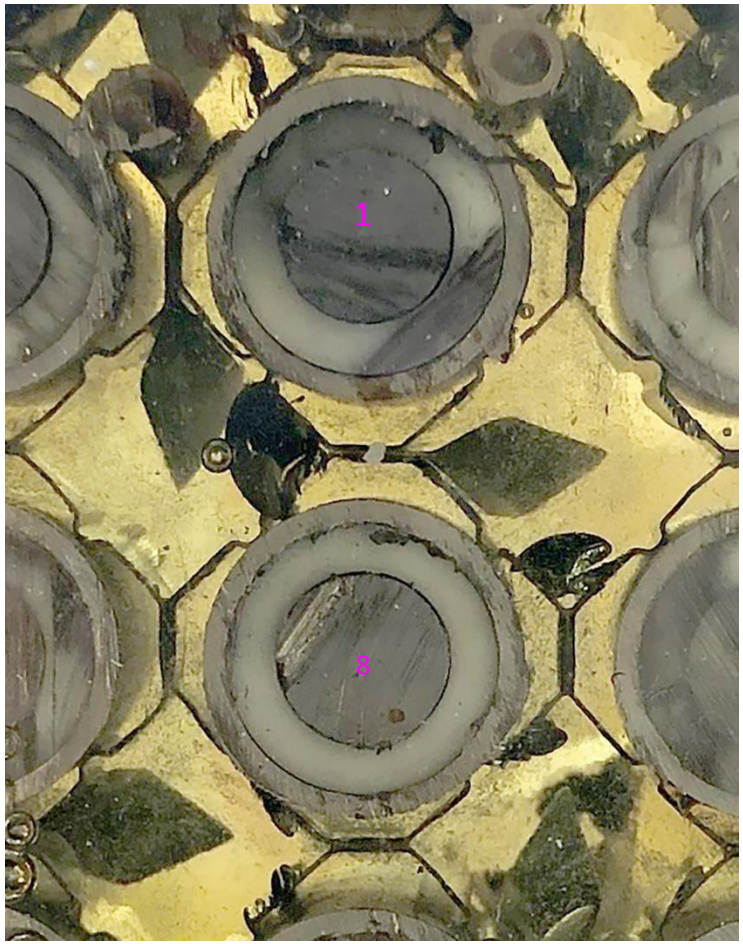

50 mm: bottom view, as ground

55 mm: top view, as polished

Figure 58 QUENCH-20; segment of bundle slice 50…55 mm embedded in resin: placement of rods inside grid spacer.

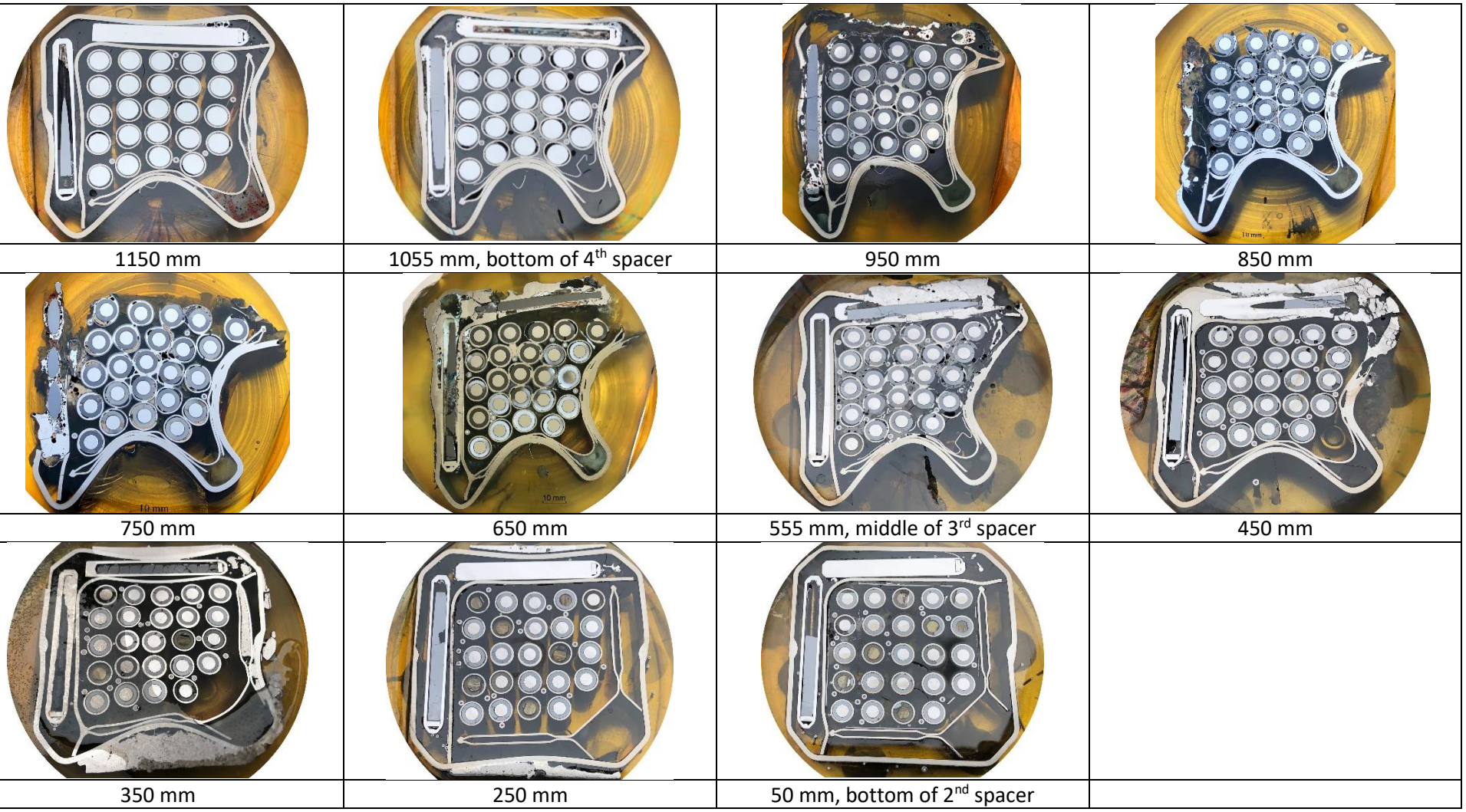

Figure 59 QUENCH-20; Overview of polished cross sections: formation of eutectic absorber melt at elevations 450…950 mm.

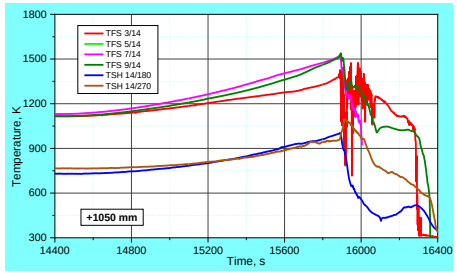

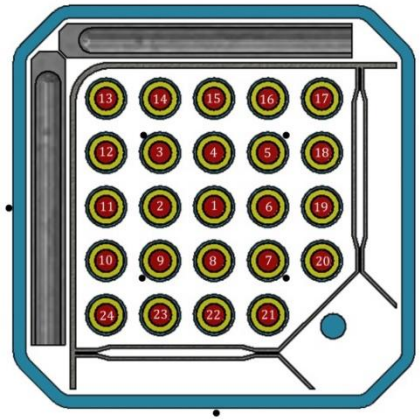

melt formation due to eutectic interaction between B_4C pin and SS blade

Figure 60 QUENCH-20; Bundle cross section at the elevation of 1055 mm: beginning of B_4C/SS eutectic melt formation.

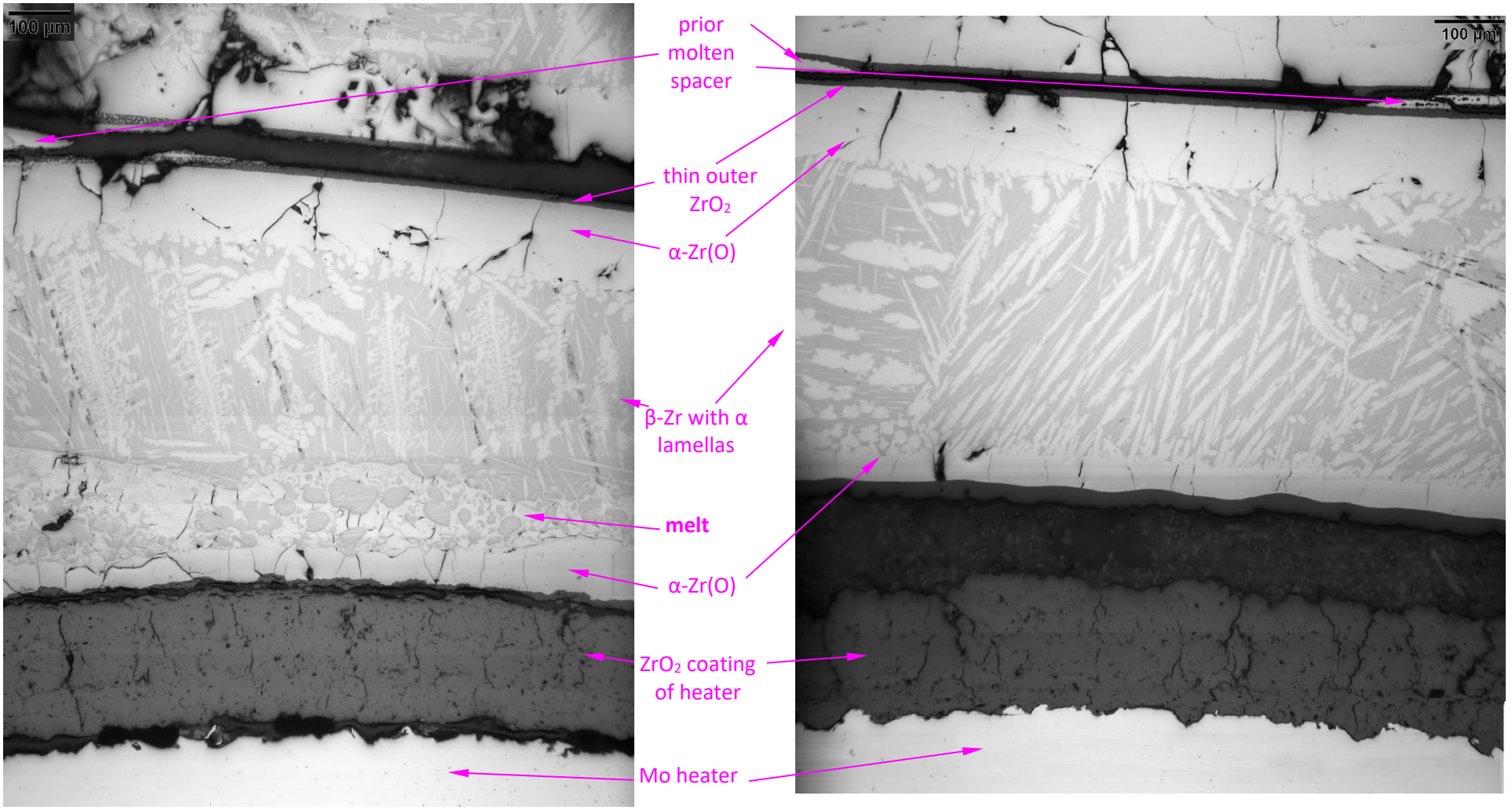

Figure 61 QUENCH-20; micro structure of rod #1 at 1055 mm at angle positions close to neighbour rods: thin outer oxide layer due to steam starvation.

90°

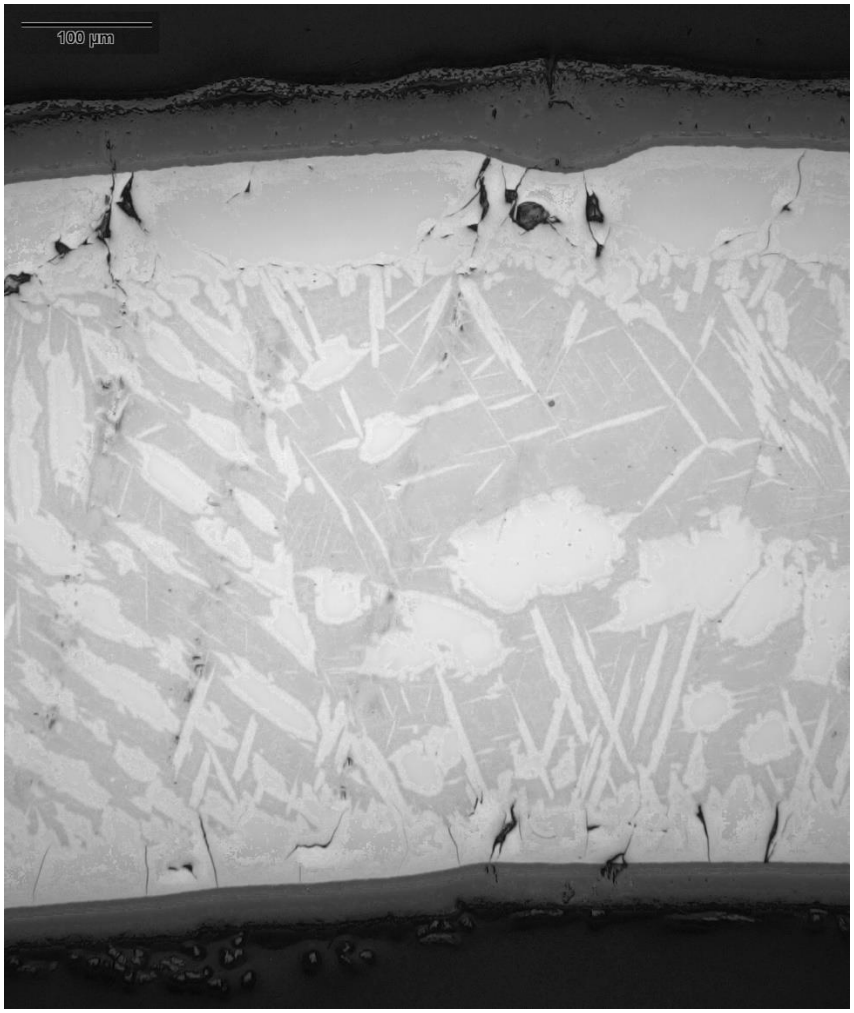

270°: outer oxide interacted with spacer grid

Figure 62 QUENCH-20; micro structure of rod #1 at 1055 mm at angle positions with thick outer oxide layer.

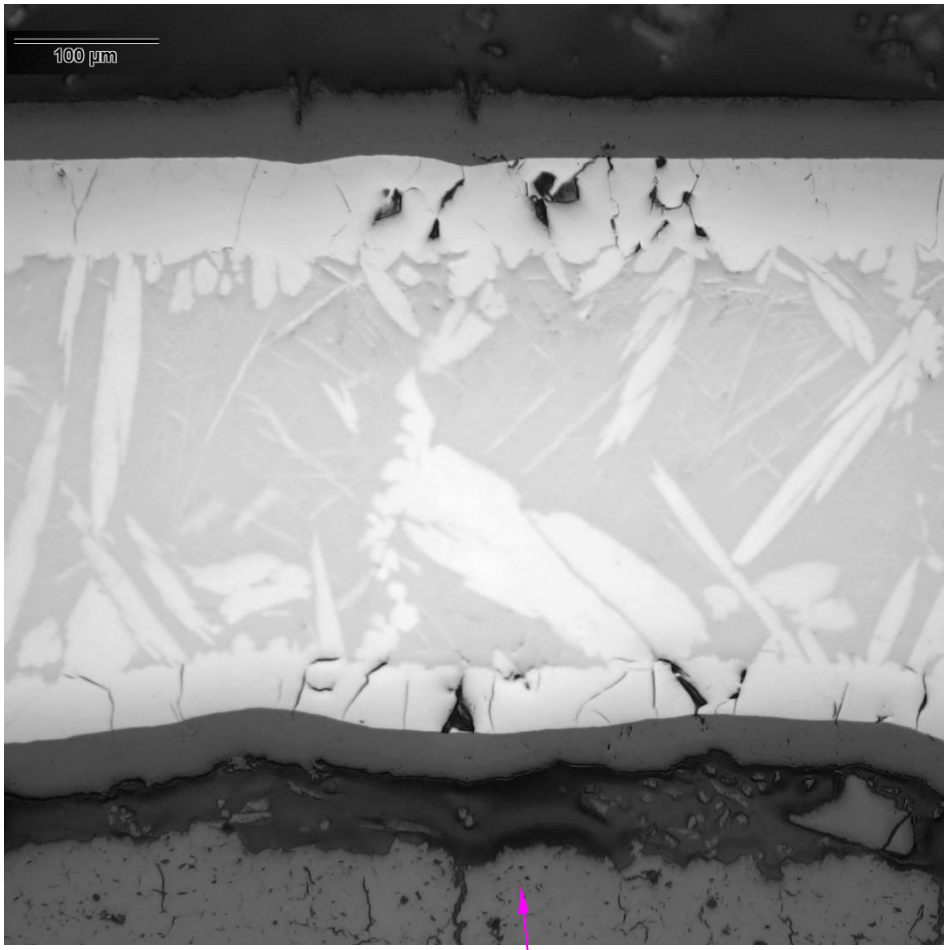

0°: thinning of cladding due to extension in the direction 90°-270°

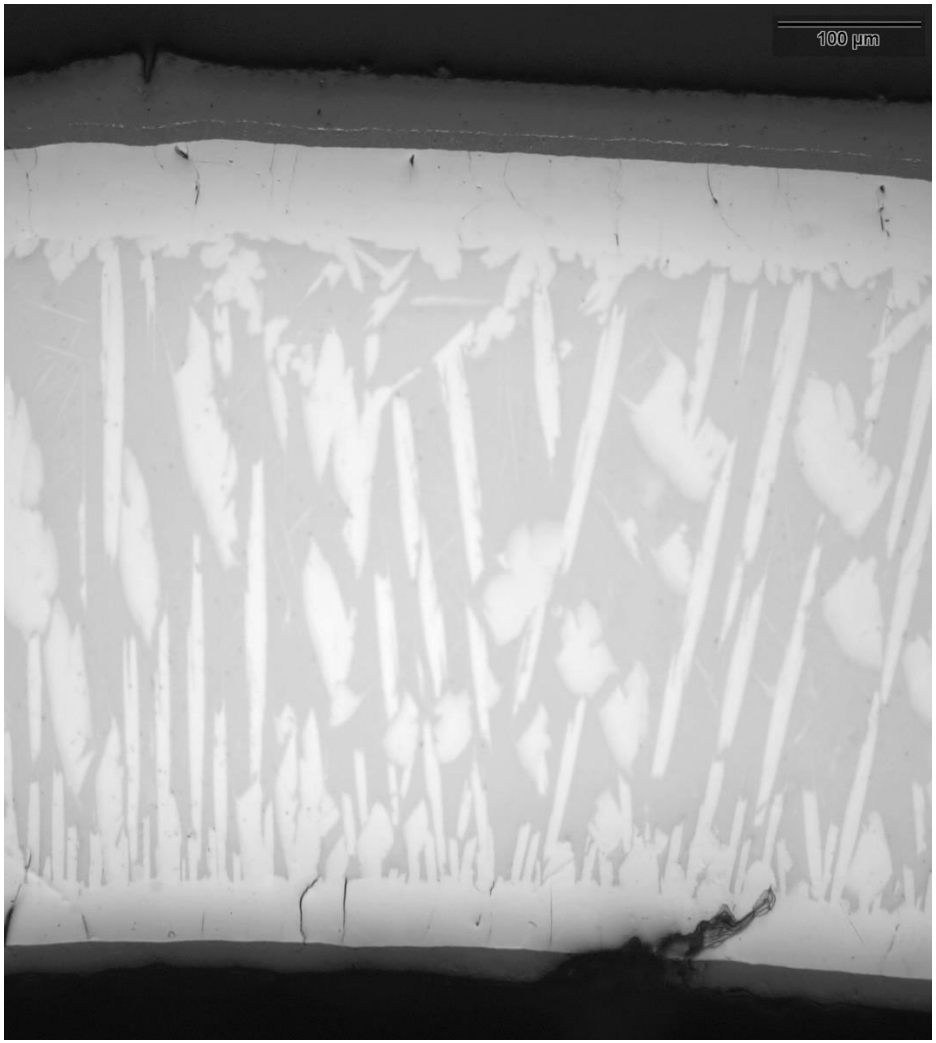

270°: original size of cladding at the lift-off position

Figure 63 QUENCH-20; micro structure of rod #15 at 1055 mm: ductile deformation of cladding during cladding extension under inner overpressure.

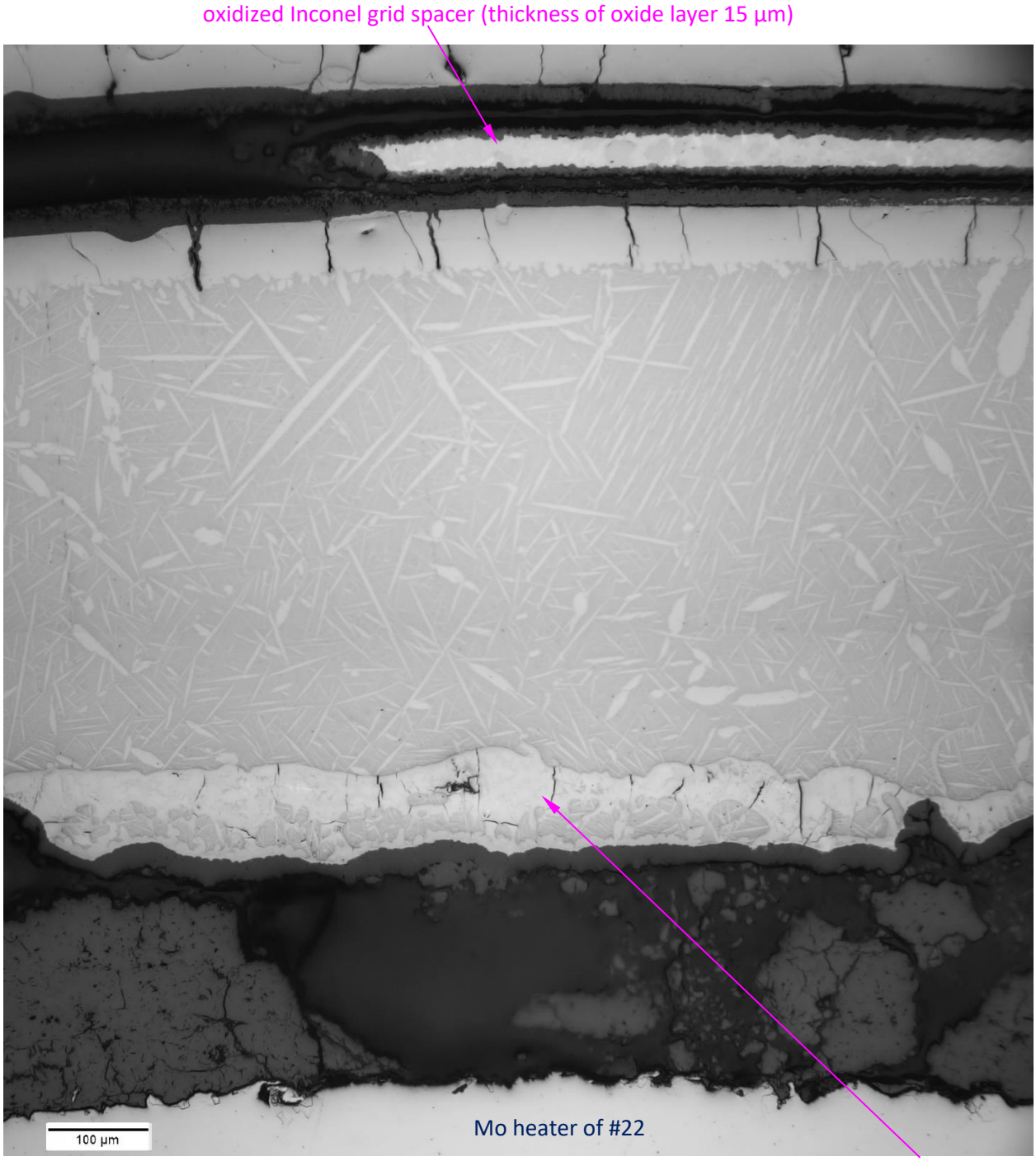

0°: oxidized partially molten Inconel grid spacer between rods #22 (down) and #8 (up); molten inner surface of cladding #22

Figure 64 QUENCH-20; micro structure of rod #22 at 1055 mm: partially molten grid spacer and molten inner surface of cladding.

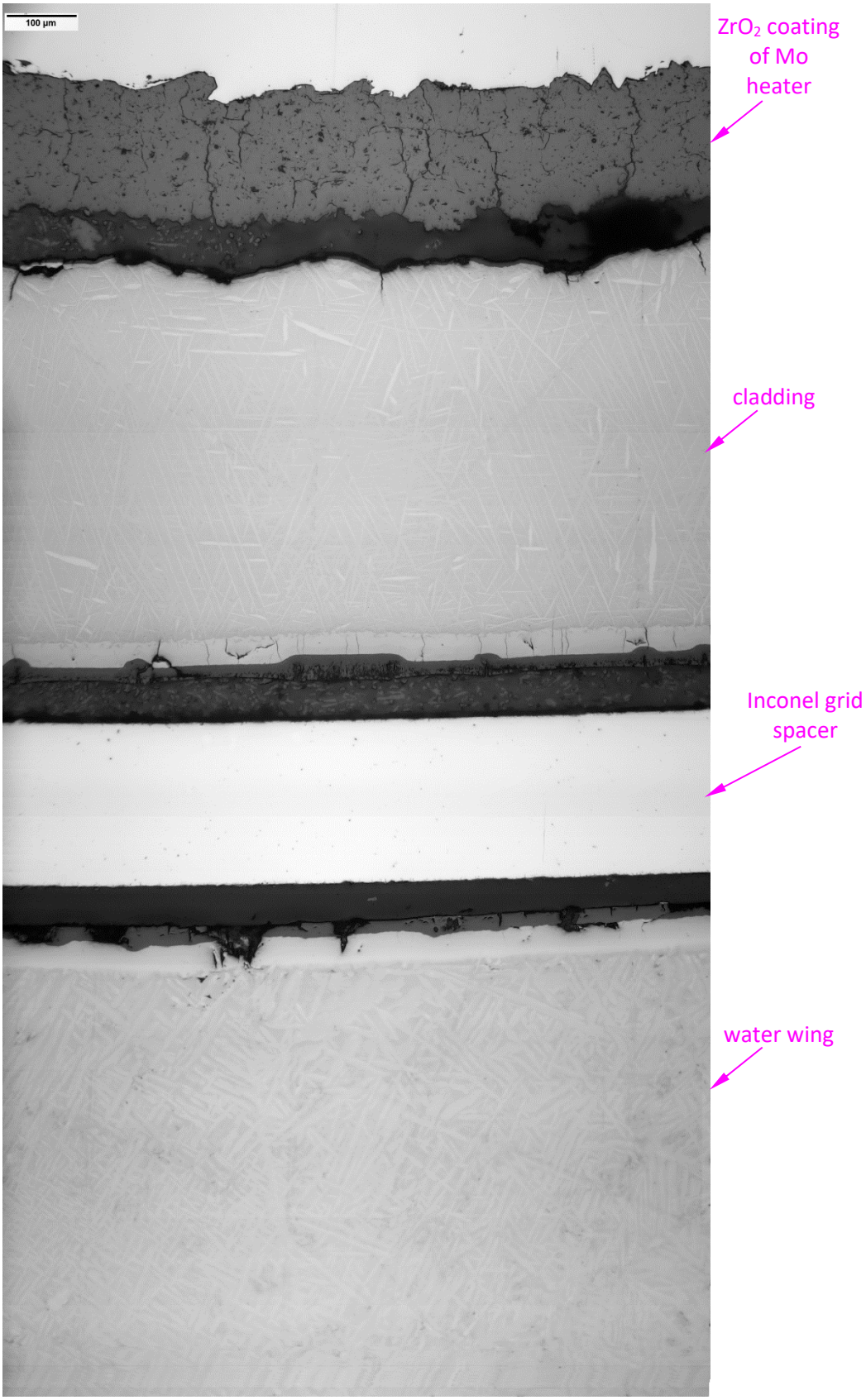

Figure 65 QUENCH-20; rod #22 at 1055 mm in contact with Inconel grid spacer and ZIRLO water wing.

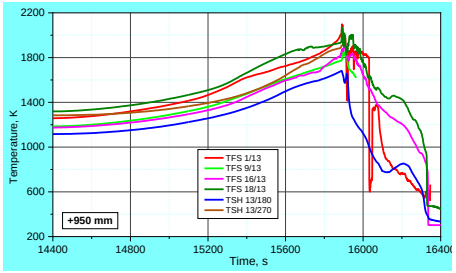

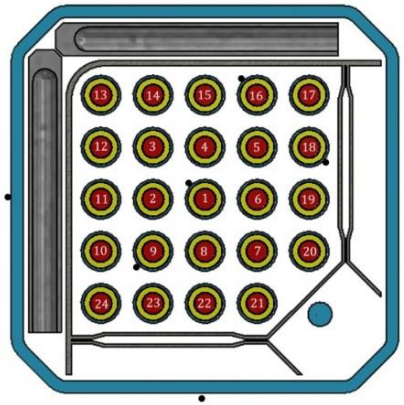

Figure 66 QUENCH-20; Bundle cross section at the elevation of 950 mm.

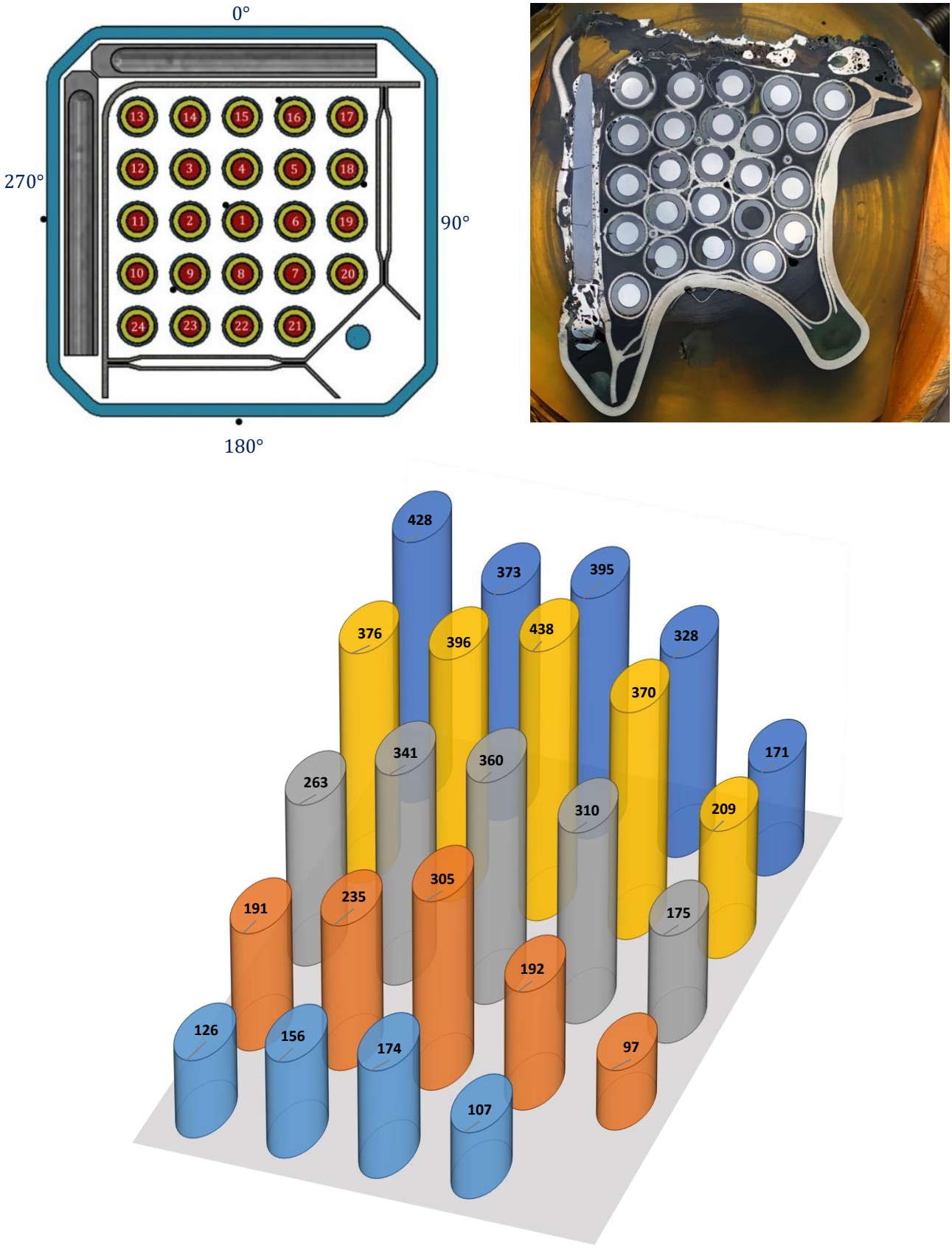

Figure 67 QUENCH-20; average thicknesses of outer ZrO_2 for each cladding at bundle elevation of 950 mm; indication of coldest bundle region at 180°.

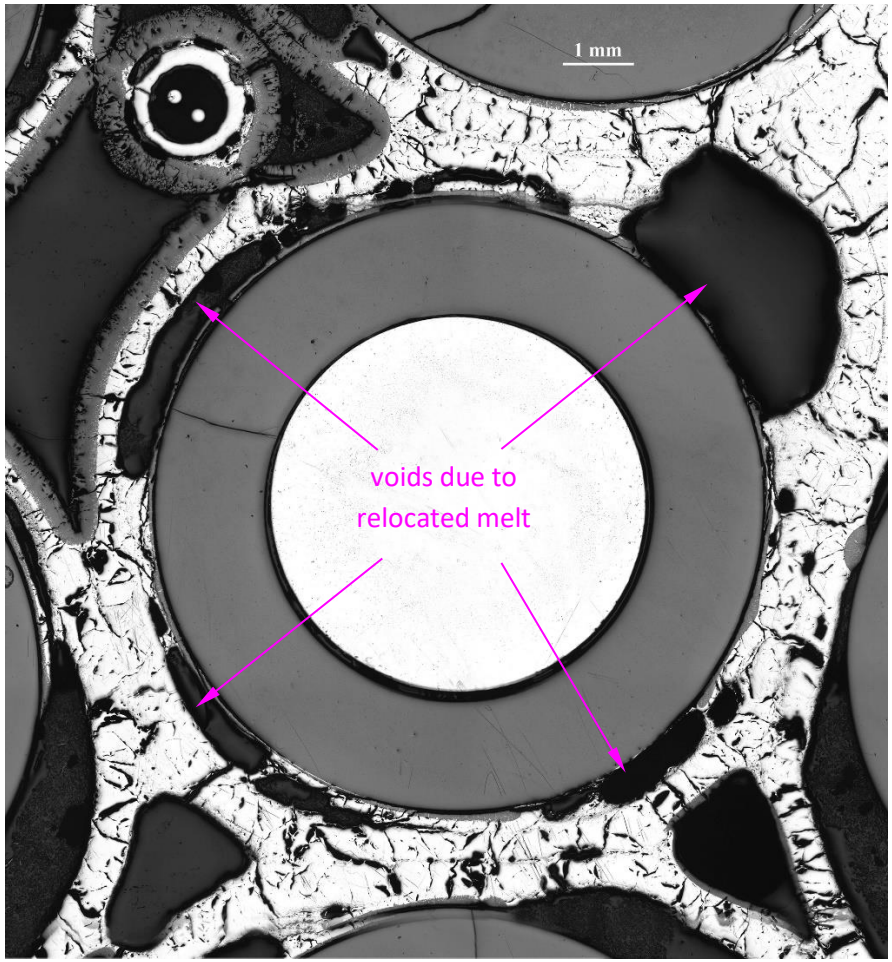

rod 1: extinction of oxide layer at positions of cladding contacts with rods 2, 6 and 8 (diffusion of oxygen from oxide to metal). The rod contact was caused by shroud implosion. Melting and relocation of β-Zr between pellet and α-Zr(O)

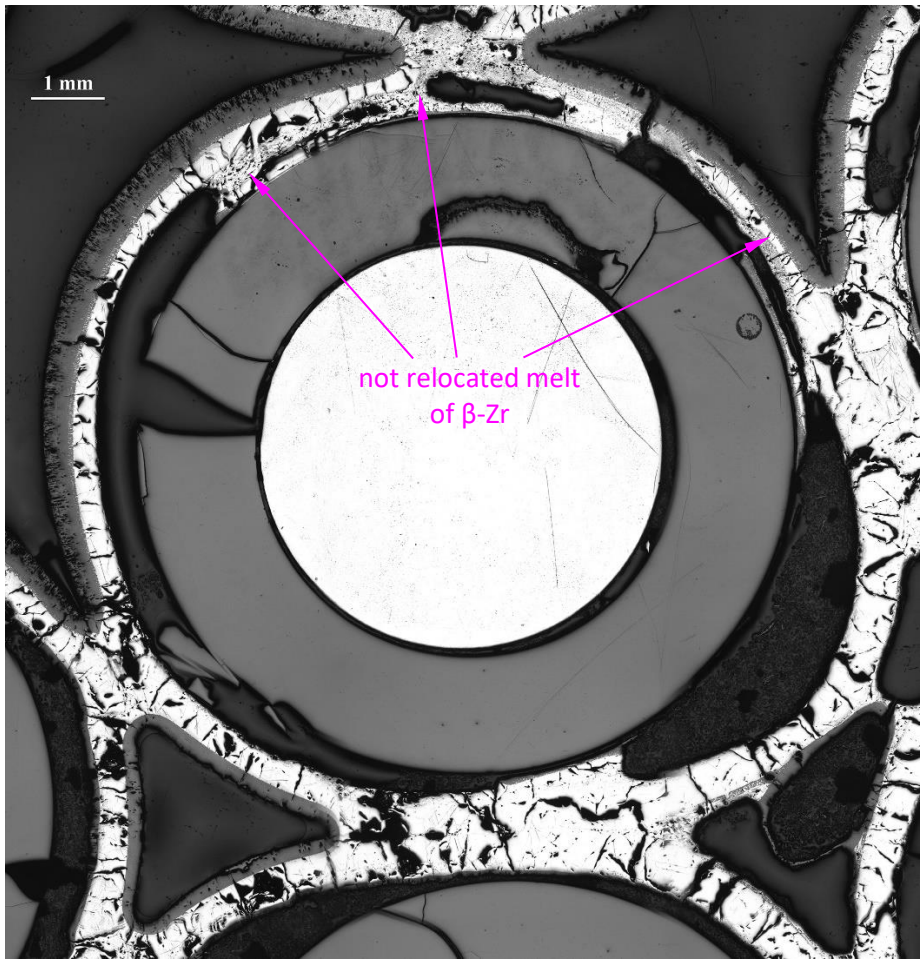

rod 2: contacts with claddings of rods 1, 9 and 11

Figure 68 QUENCH-20; Cross-sections of rods 1 and 2 at bundle elevation 950 mm: oxide extinction and melt formation.

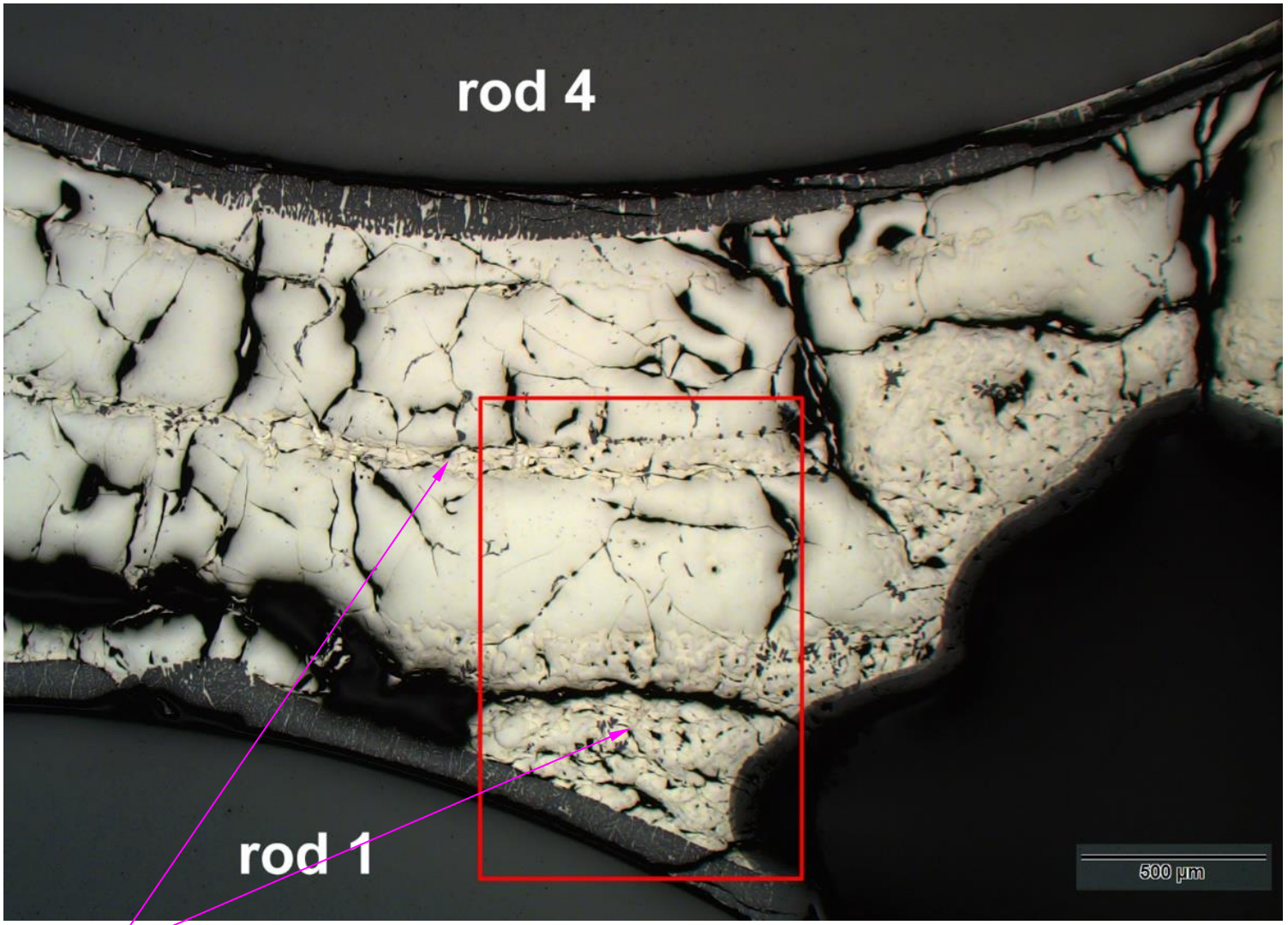

Figure 69 QUENCH-20; Melt penetrated between α-Zr(O) layers of rods 1 and 4 at 950 mm; red rectangle marks the region chosen for SEM/EDX analysis.

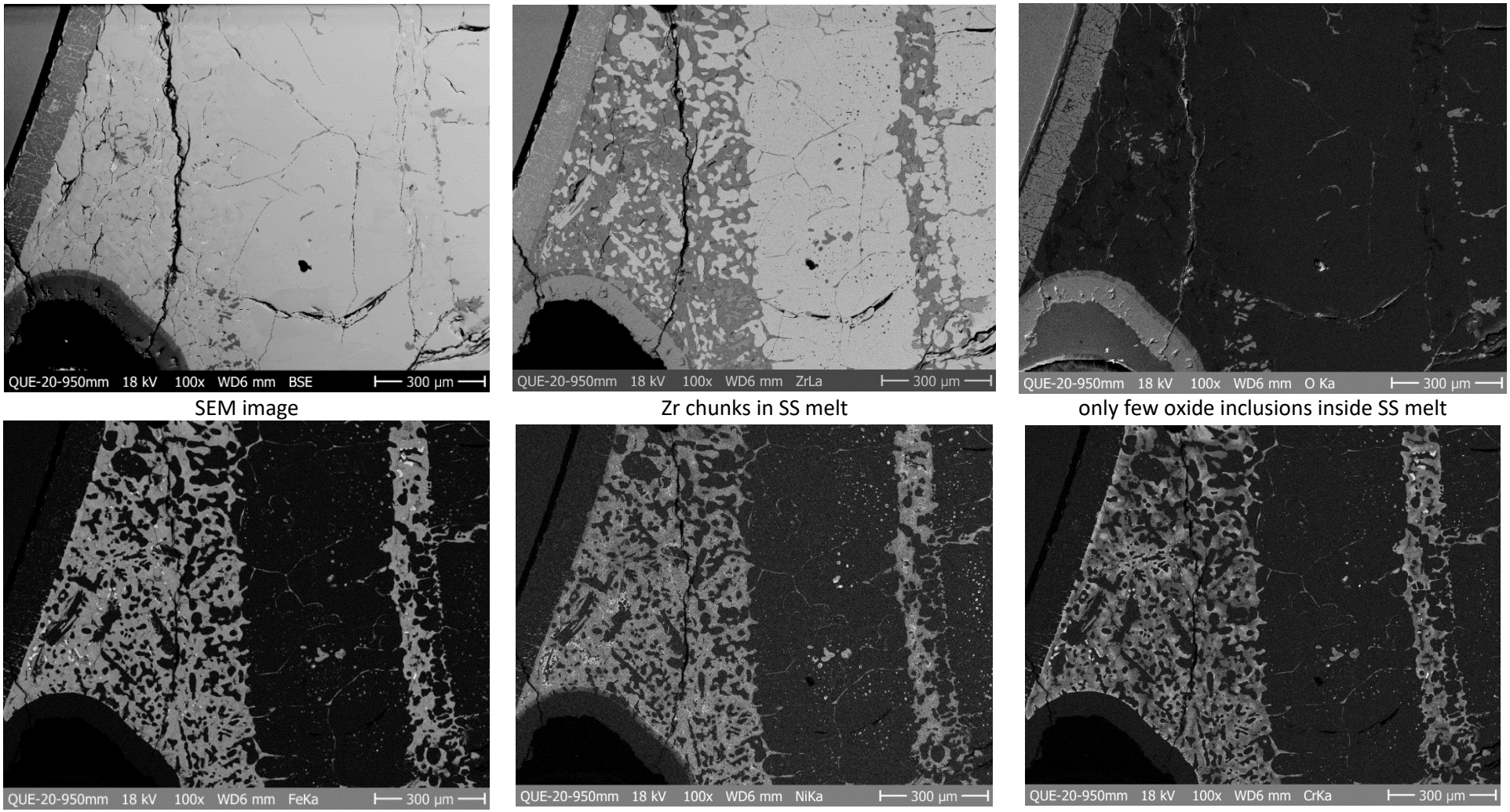

Figure 70 QUENCH-20; SEM/EDX mapping of melt between rods 1 and 4, marked as red rectangle in the previous Figure.

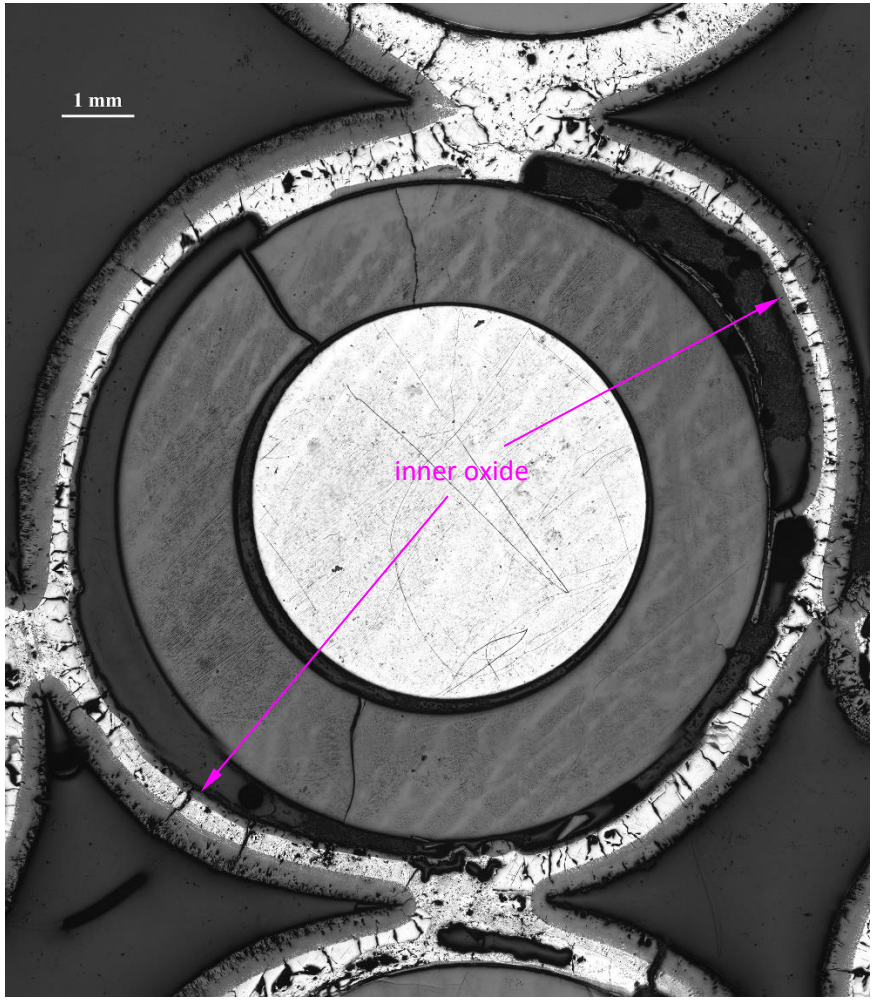

hot inner rod 3 with strong oxidation

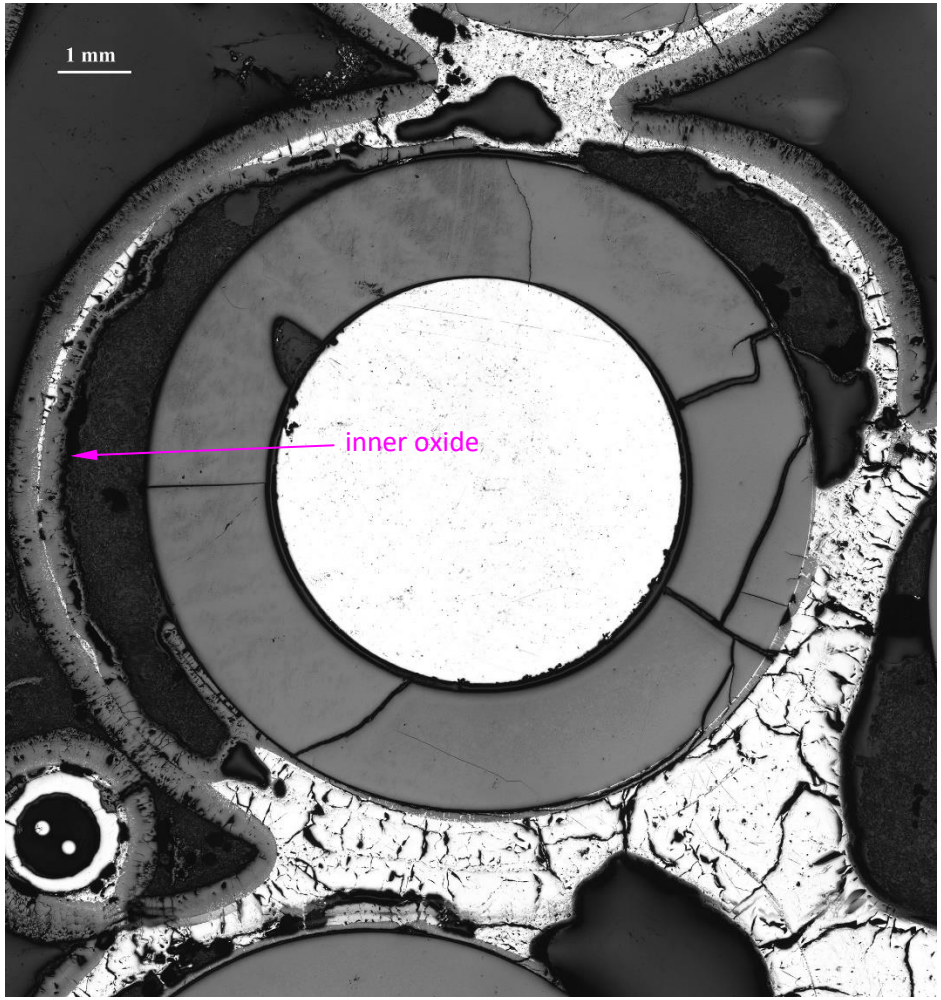

hot inner rod 4 with strong oxidation

Figure 71 QUENCH-20; Cross-sections of rods 3 and 4 at bundle elevation 950 mm: formation of inner oxide after downwards relocation of molten β-Zr.

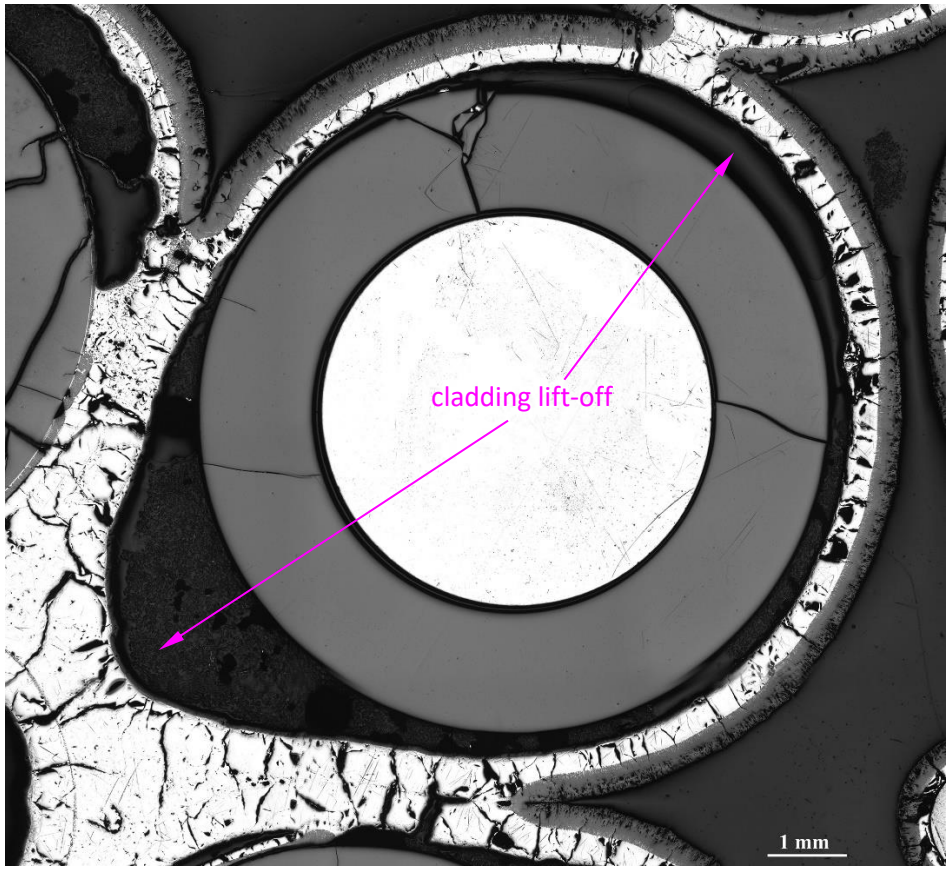

rod 5: β-Zr layer extinct before achievement of melting temperature

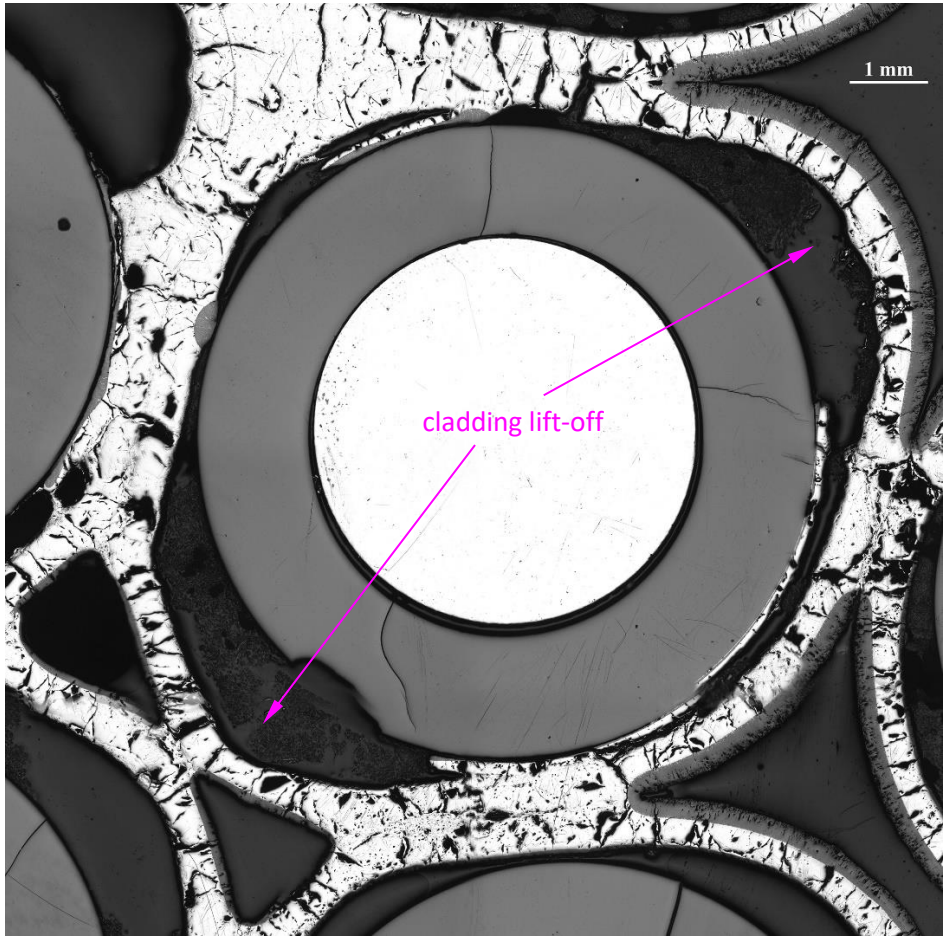

rod 6: β-Zr layer extinct before achievement of melting temperature

Figure 72 QUENCH-20; Cross-sections of rods 5 and 6 with not melted claddings at bundle elevation 950 mm: lift-off of claddings due to ballooning effect.

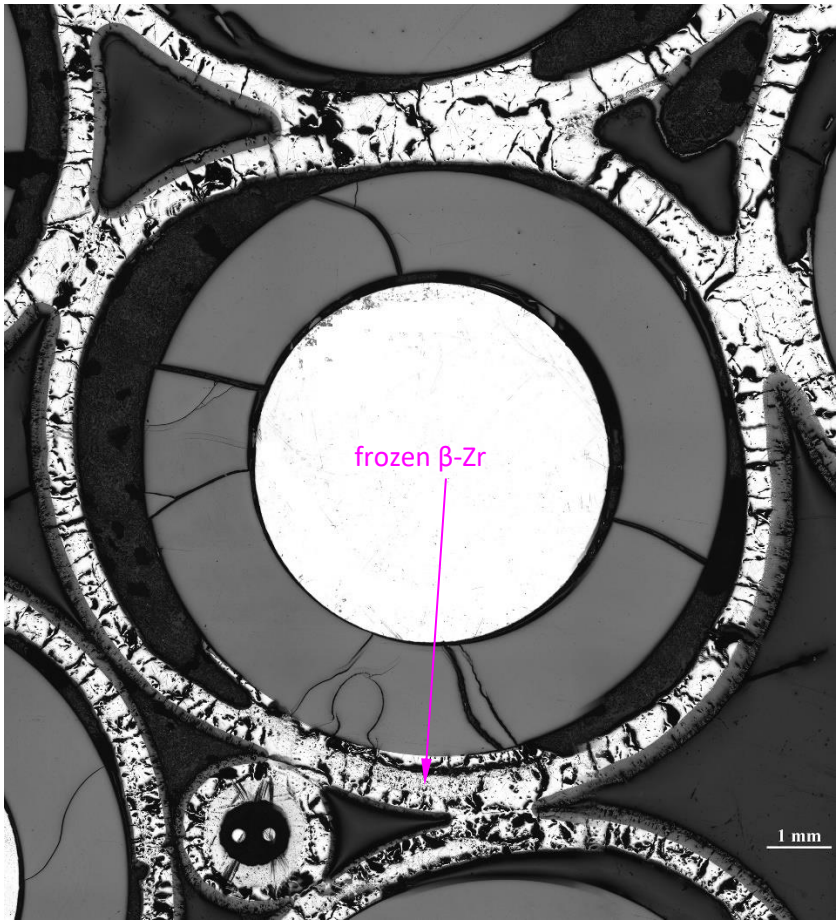

inner rod 9: β-Zr at the contact to relatively cold rod 23

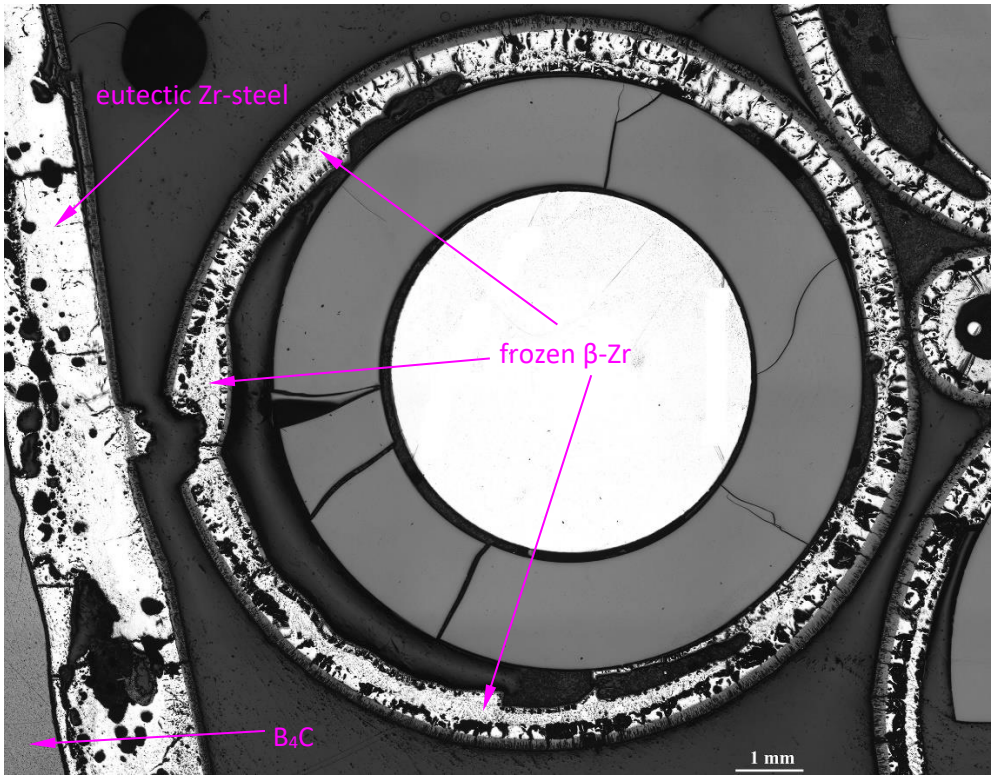

outer rod 10: loss of contact between cladding and water channel during quench

Figure 73 QUENCH-20; Cross-sections of rods 9 and 10 with not melted claddings at bundle elevation 950 mm: frozen molten β-Zr.

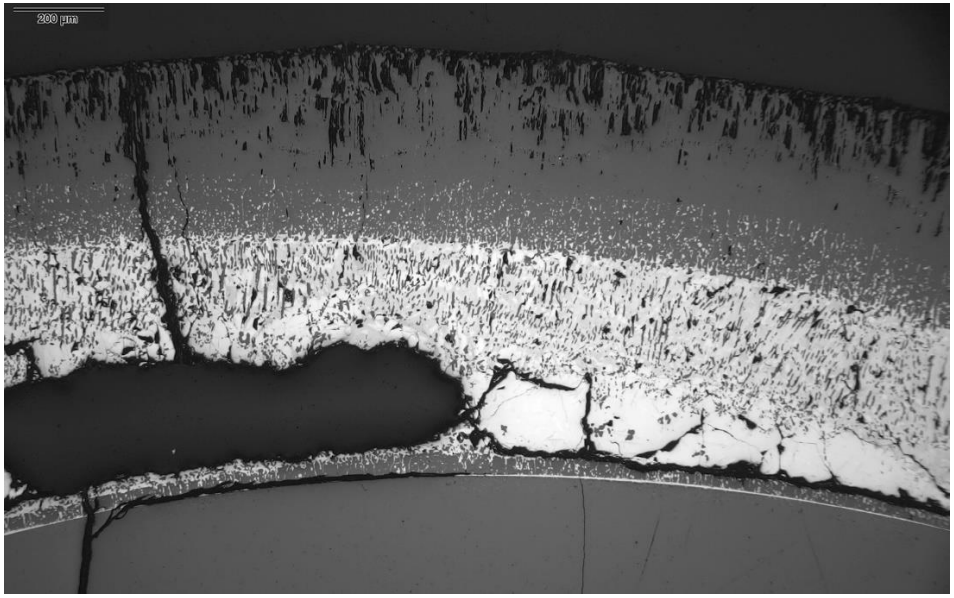

at 0°: ceramic precipitates inside molten metal layer

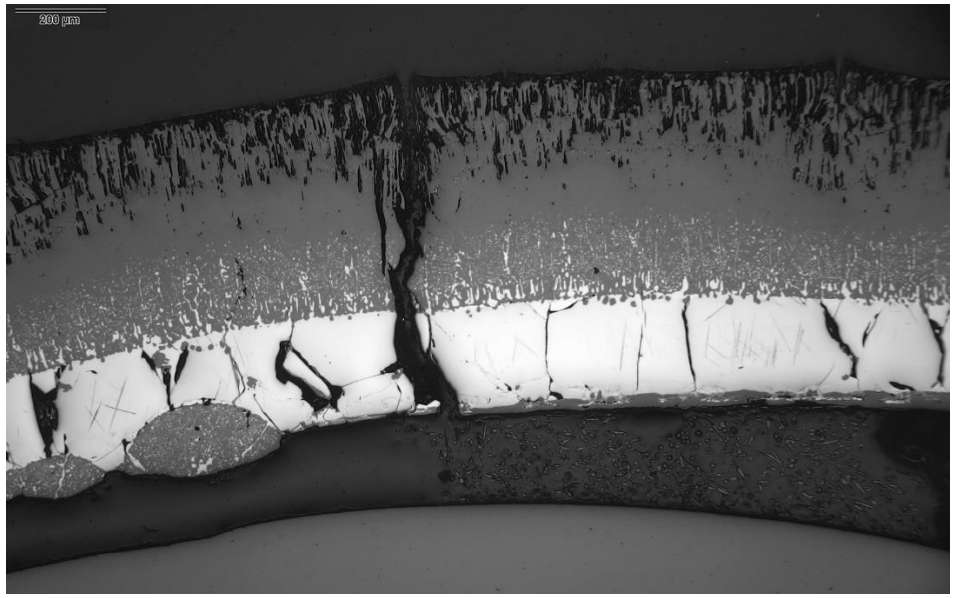

at 45°: not liquefied layers; local oxide spots at cladding inner surface due to cladding-pellet interaction before cladding lift-off

Figure 74 QUENCH-20; Microstructure of cladding for rod #12 at bundle elevation 950 mm.

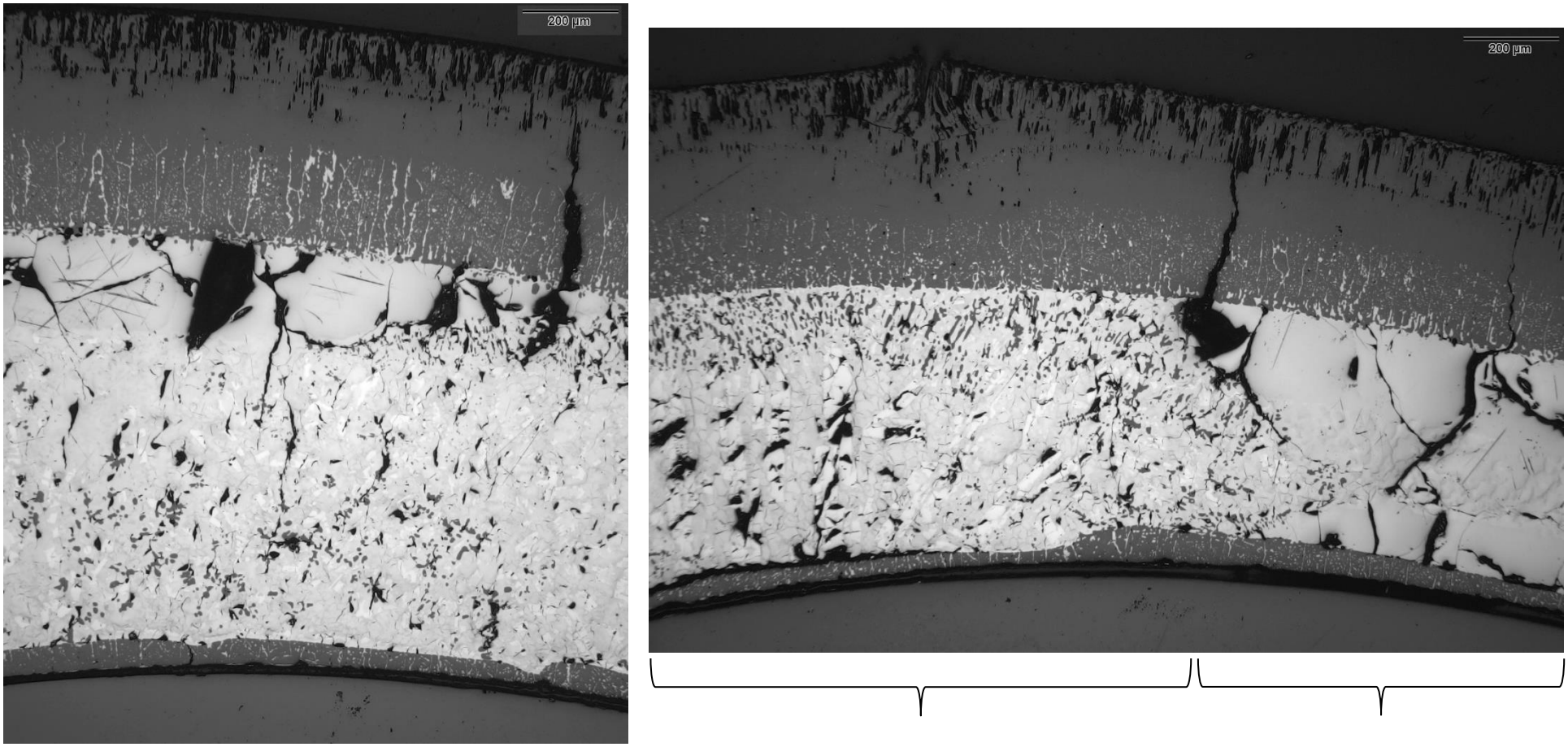

Figure 75 QUENCH-20; Microstructure of cladding for rod #13 at bundle elevation 950 mm: ceramic precipitates in melt.

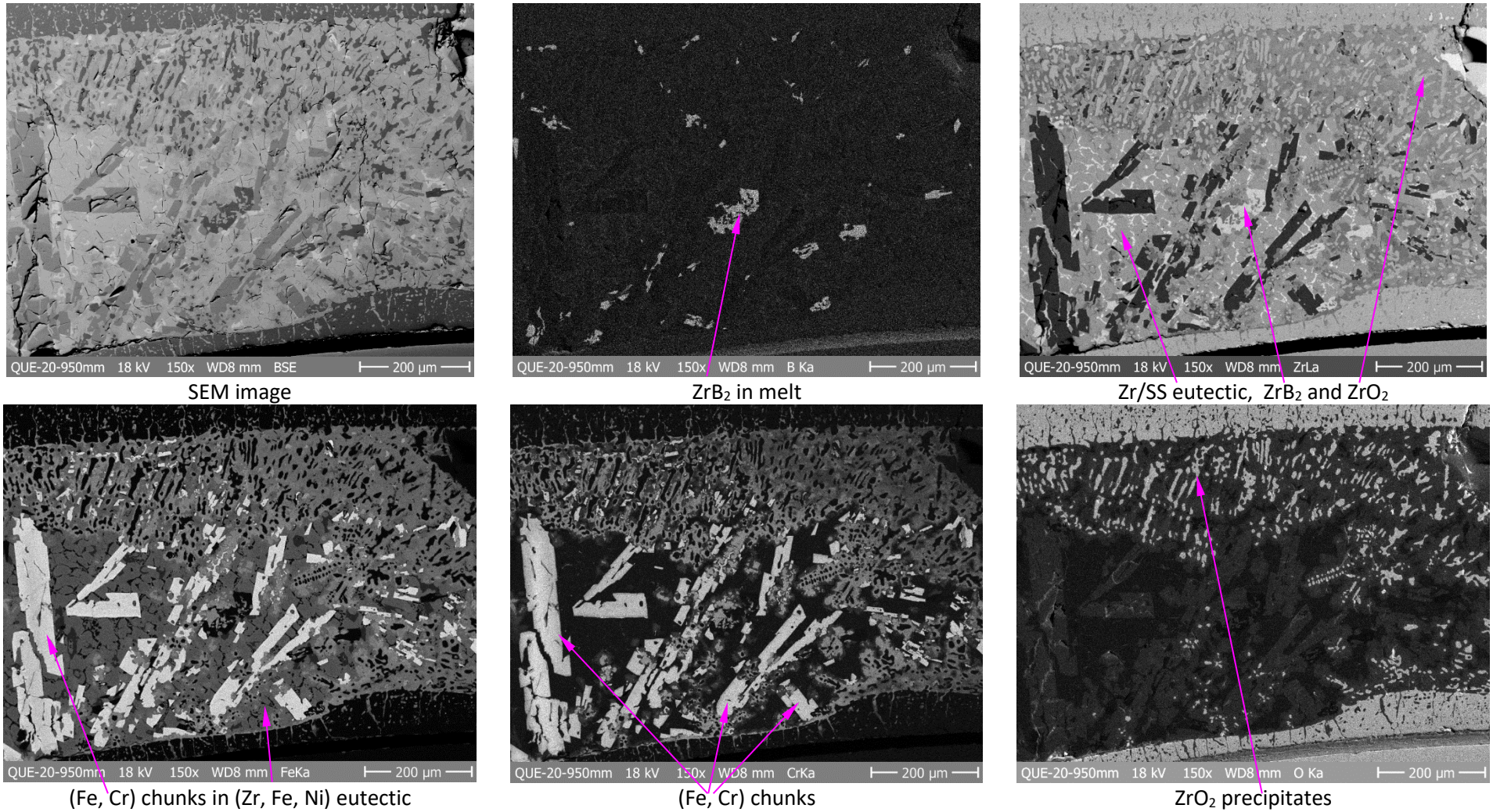

Figure 76 QUENCH-20; SEM/EDX mapping for rod #13 (angle 180°) at bundle elevation 950 mm: zirconium borides, Zr/SS eutectic, ceramic precipitates in melt.

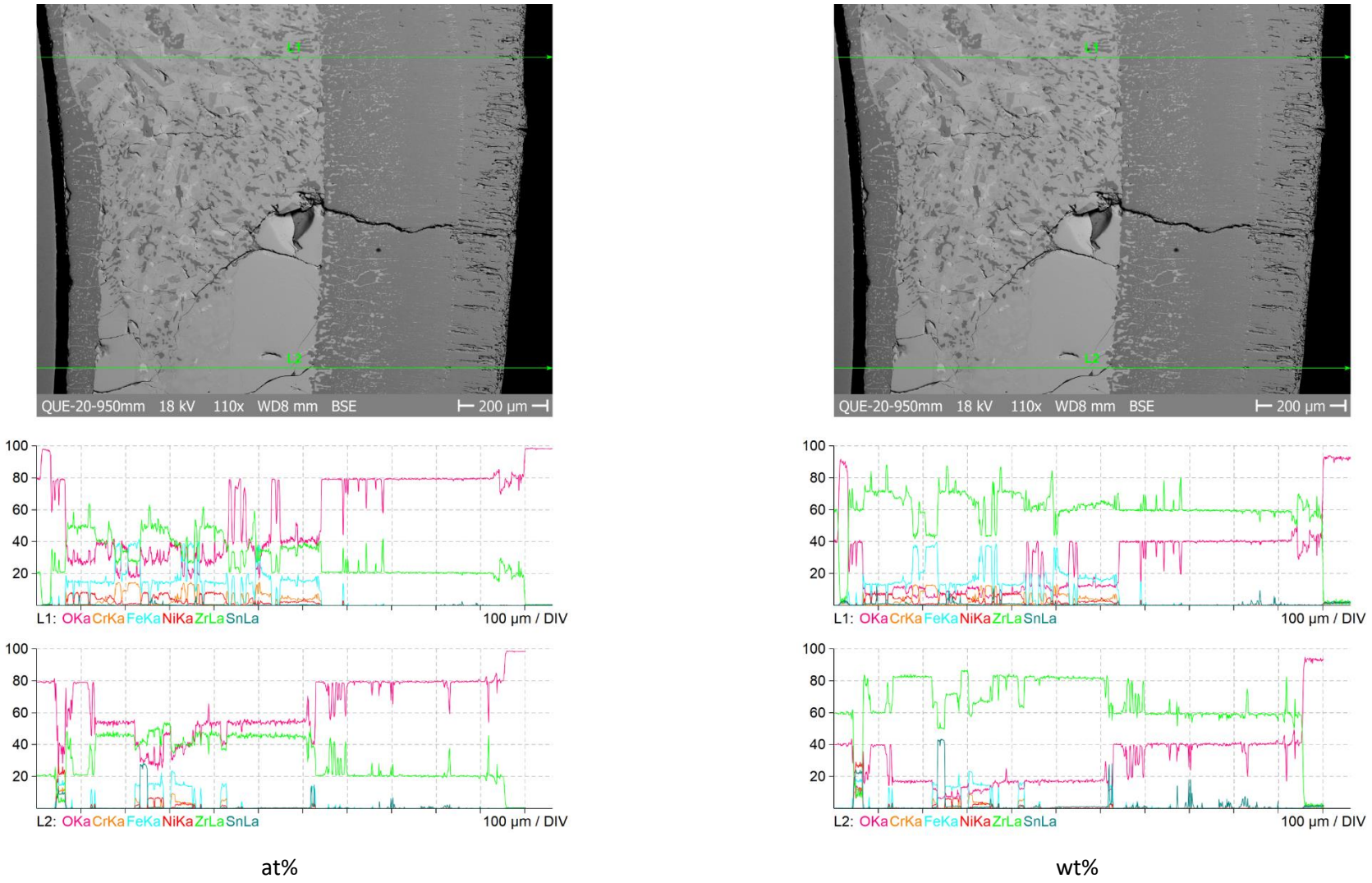

Figure 77 QUENCH-20; SEM/EDX line scan for rod #13 (angle 180°) at bundle elevation 950 mm.

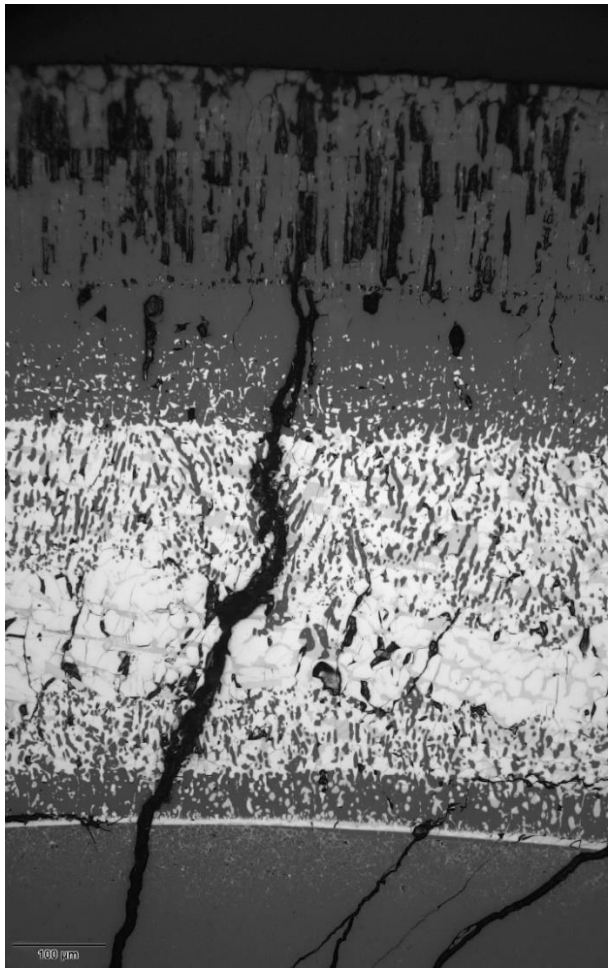

Rod 14, 90°

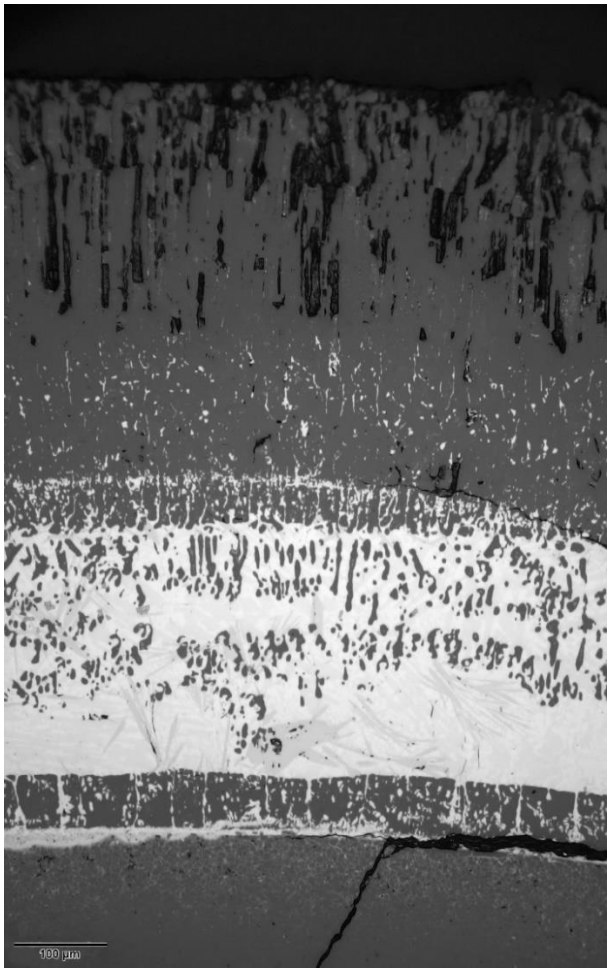

Rod 15, 135°

Figure 78 QUENCH-20; Interaction of cladding oxide layer and pellet with Zr/SS eutectic melt penetrated under cladding of rods 14 and 15 at bundle elevation 950 mm after cladding failure due to interaction of cladding, water channel and absorber blade: metallic precipitates in pellet and oxide layer as well as ceramic precipitates in melt.

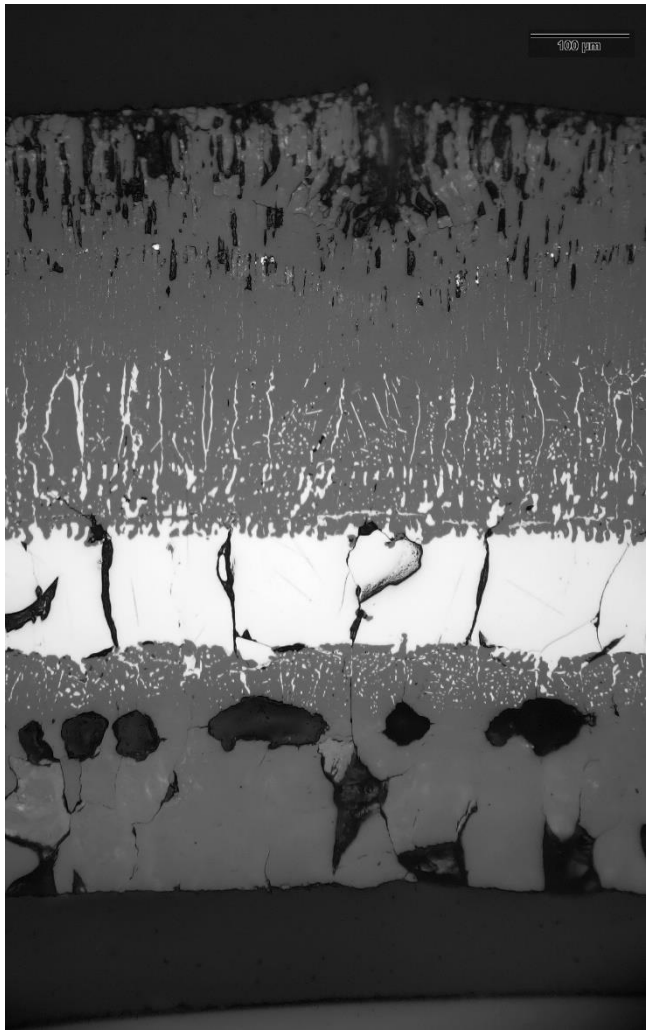

Rod 16, 270°: strong inner and outer oxidation

Rod 17, 135°: moderate outer oxidation close to similarly oxidized water wing

Figure 79 QUENCH-20; Structure of not melted rods 16 and 17 at bundle elevation 950 mm.

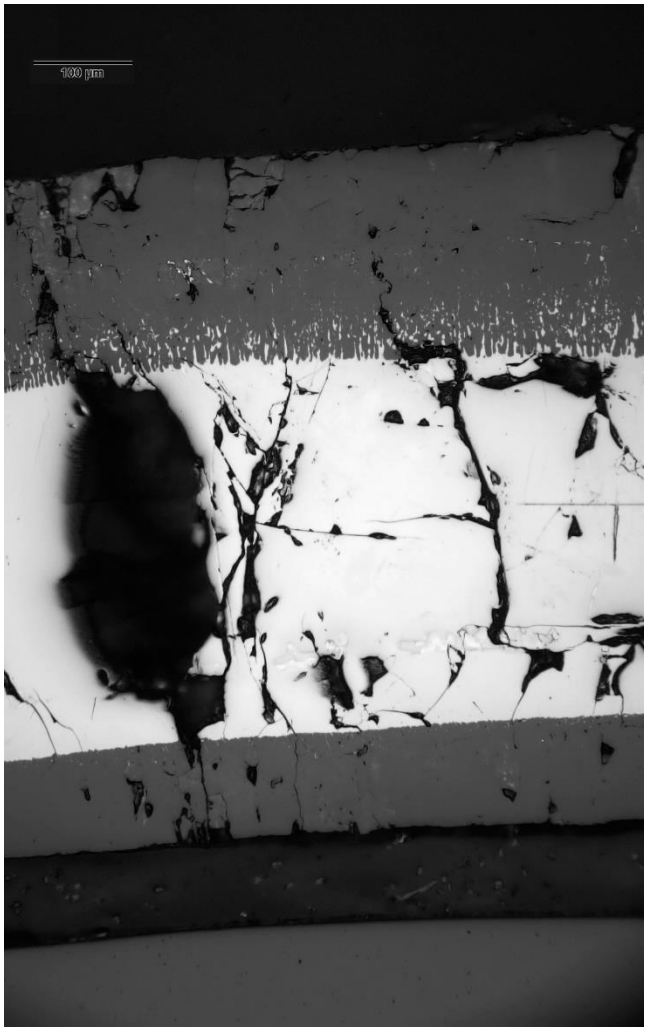

Rod 18, 270°

Rod 19, 135°

Figure 80 QUENCH-20; Structure of not melted rods 18 and 19 at bundle elevation 950 mm.

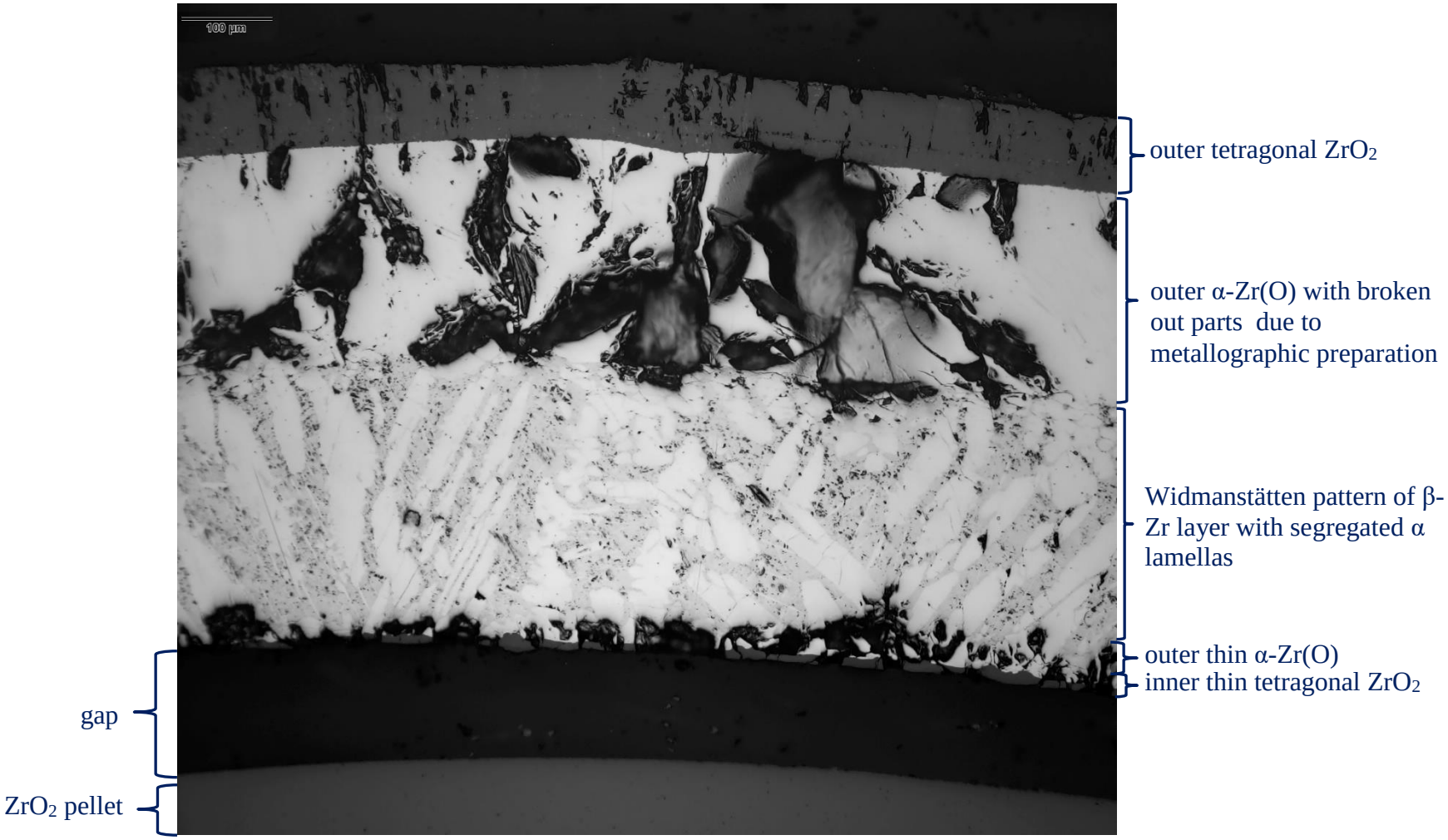

Figure 81 QUENCH-20; Microstructure of cladding for rod #20 at bundle elevation 950 mm and angle position 0°.

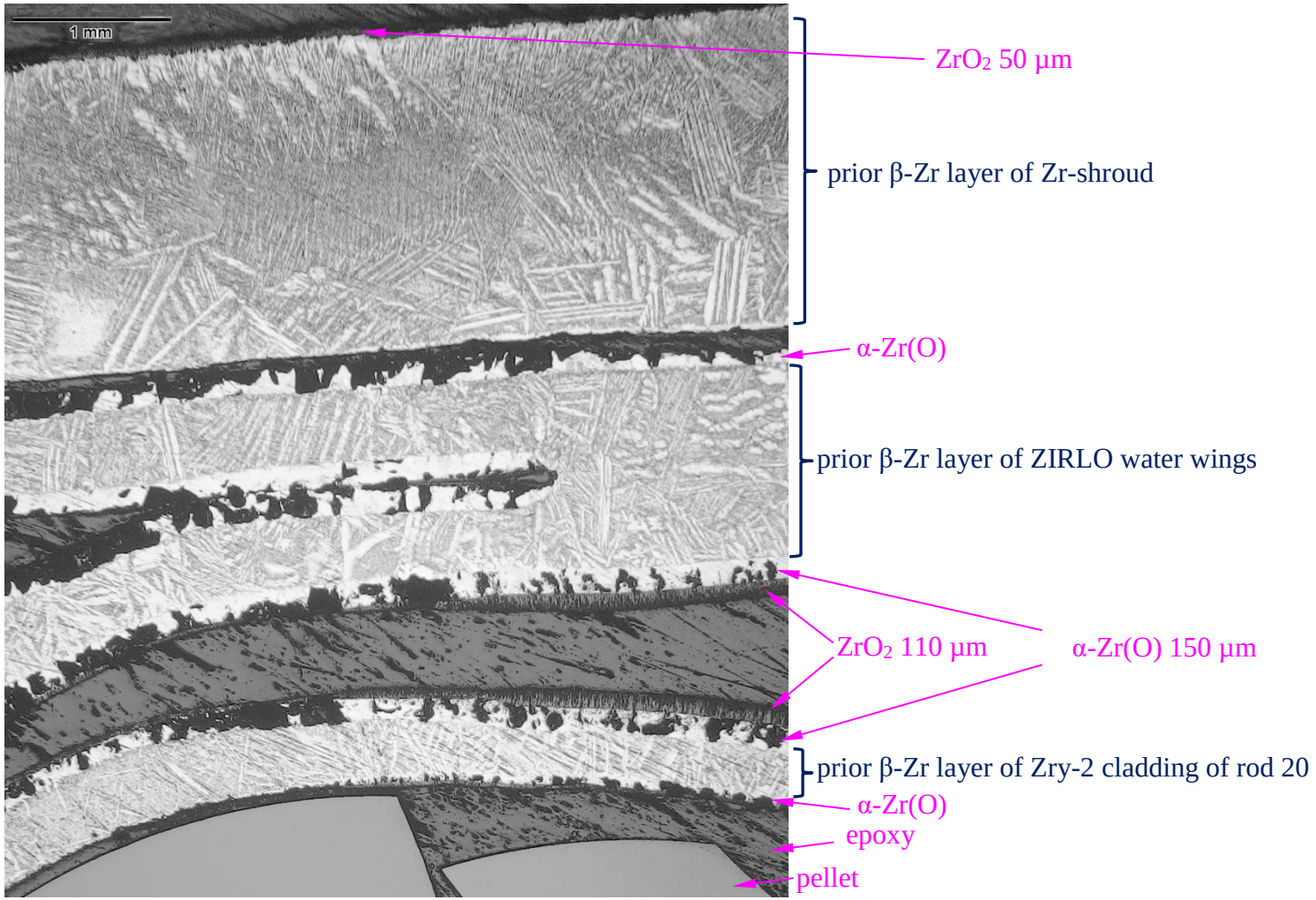

Figure 82 QUENCH-20; Microstructure of cladding #20 (angle 90°), water wings and shroud at bundle elevation 950 mm.

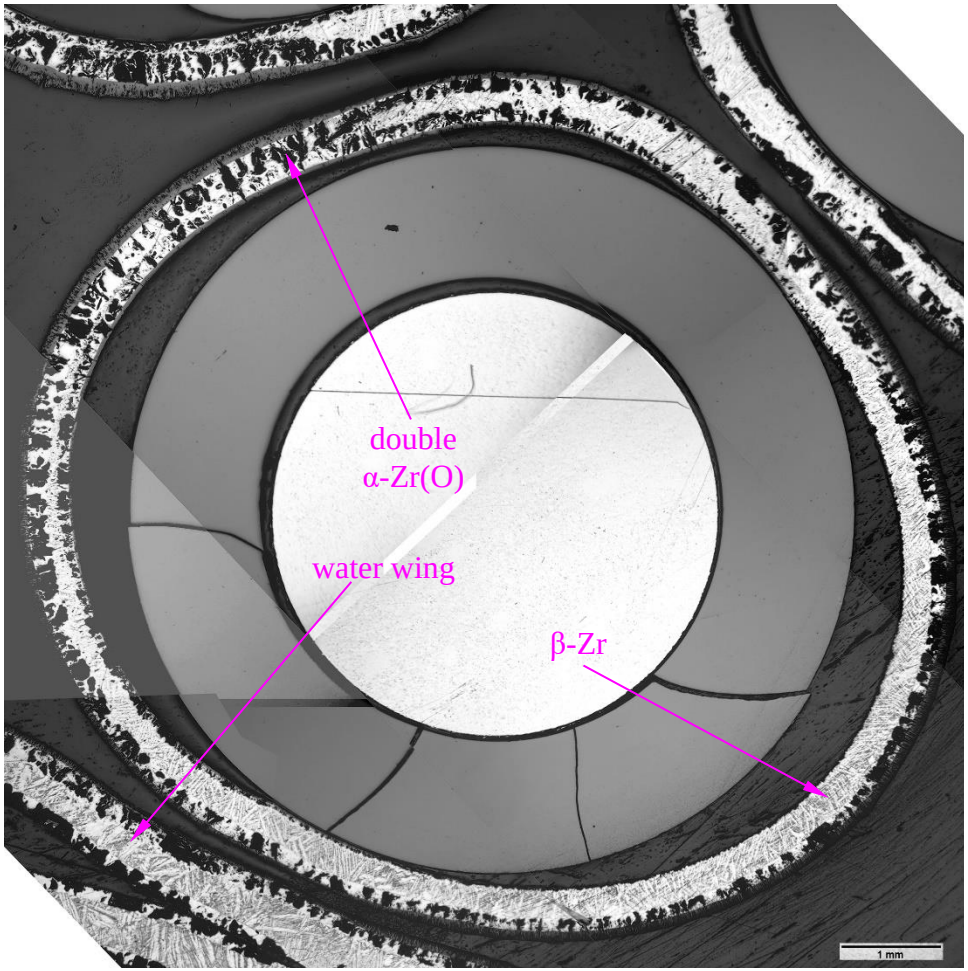

rod 21: thick β-Zr (lower oxidation degree of cladding) between 45° and 225°; very small gap between cladding and water wing at 225°

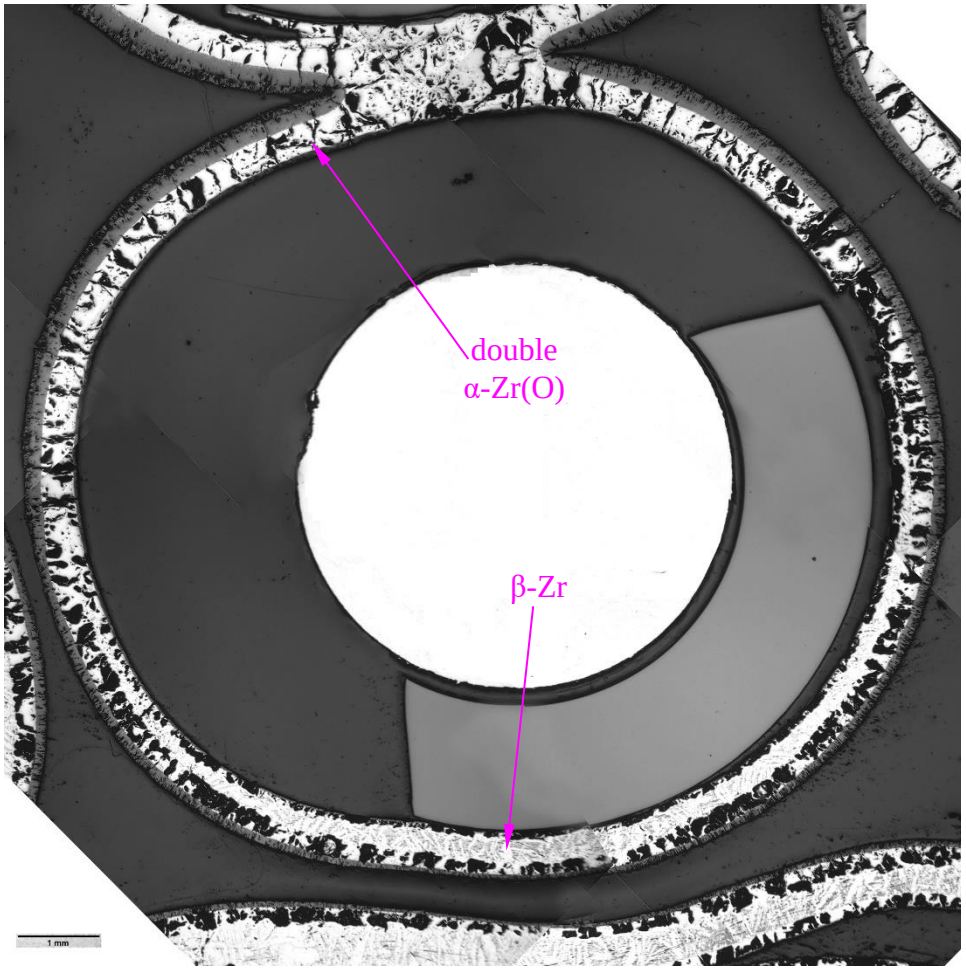

rod 22: thick β-Zr (lower oxidation degree of cladding) between 135° and 225°

Figure 83 QUENCH-20; Cross-sections of rods 21 and 22 with not melted claddings at bundle elevation 950 mm: typical outer and inner cladding oxidation.

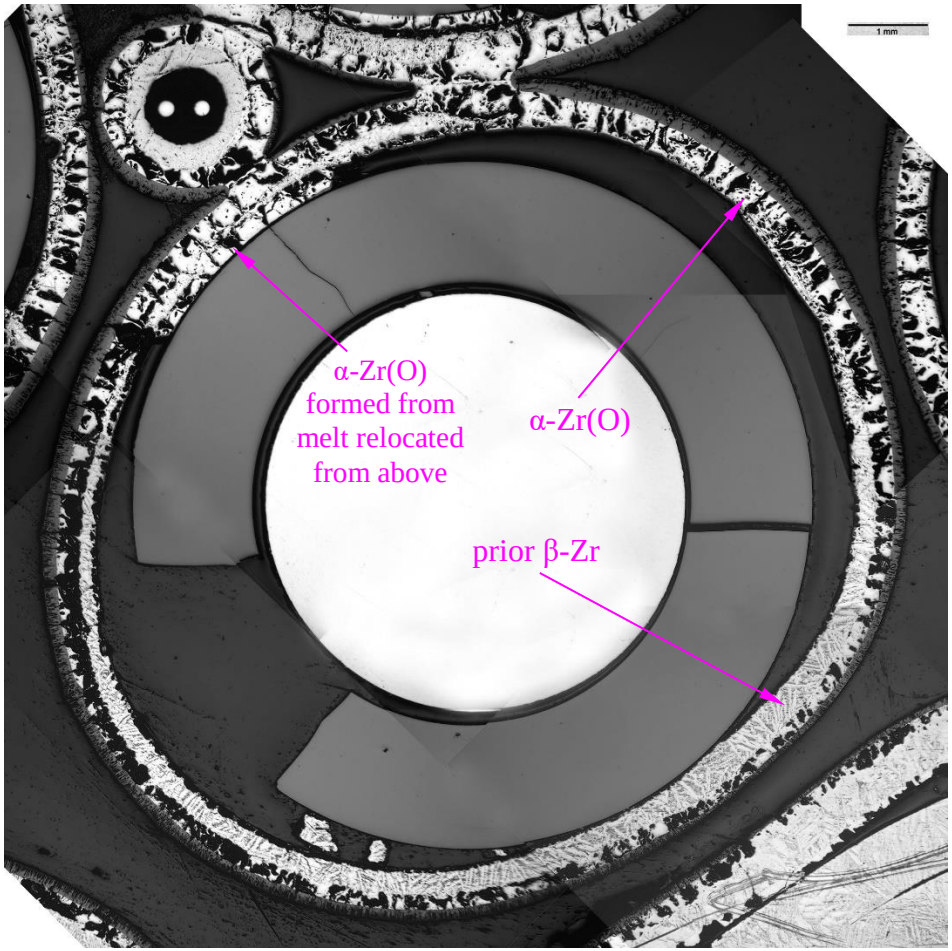

rod 23: thick β-Zr (lower oxidation degree of cladding) between 90° and 270

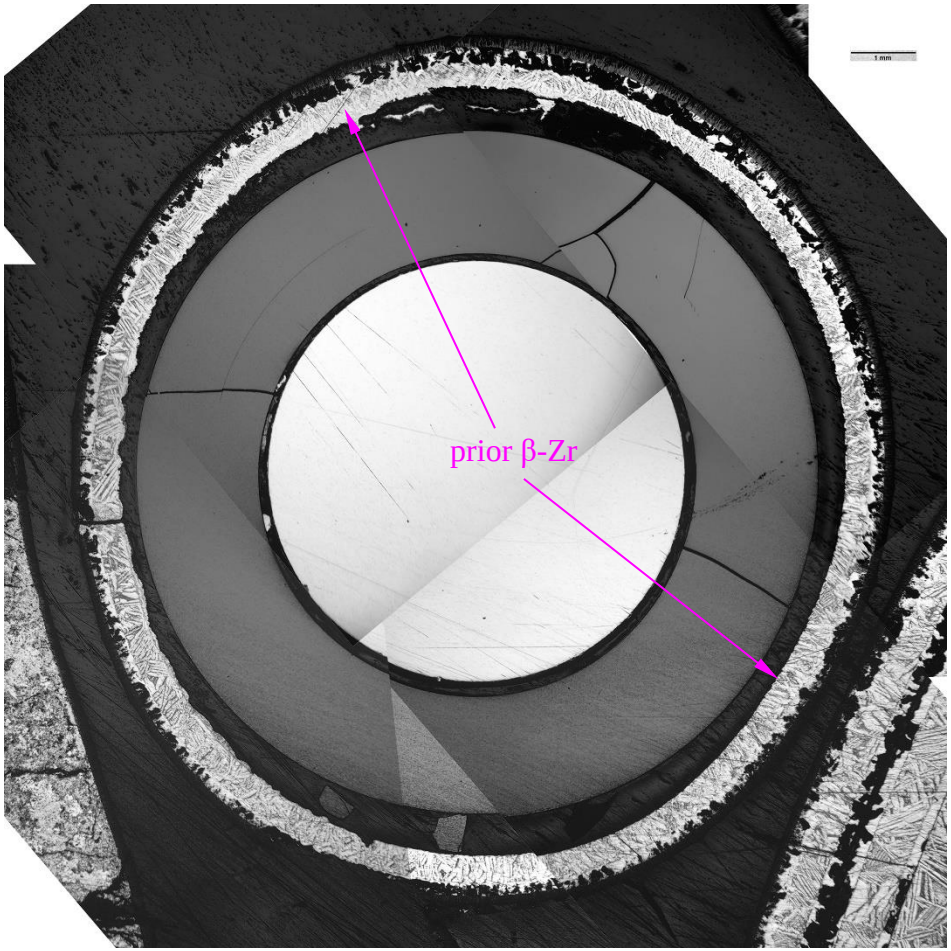

rod 24: thick β-Zr (lower oxidation degree of cladding)

Figure 84 QUENCH-20; Cross-sections of rods 23 and 24 with not melted claddings at bundle elevation 950 mm: typical outer cladding oxidation.

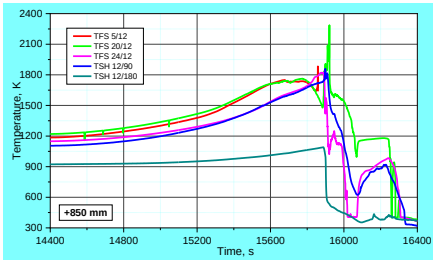

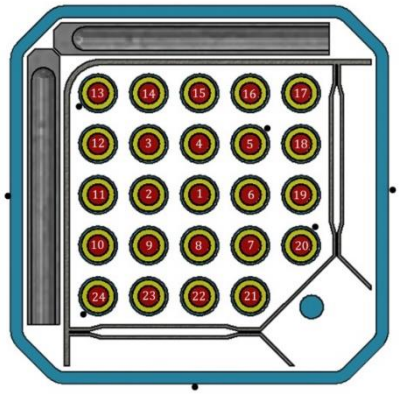

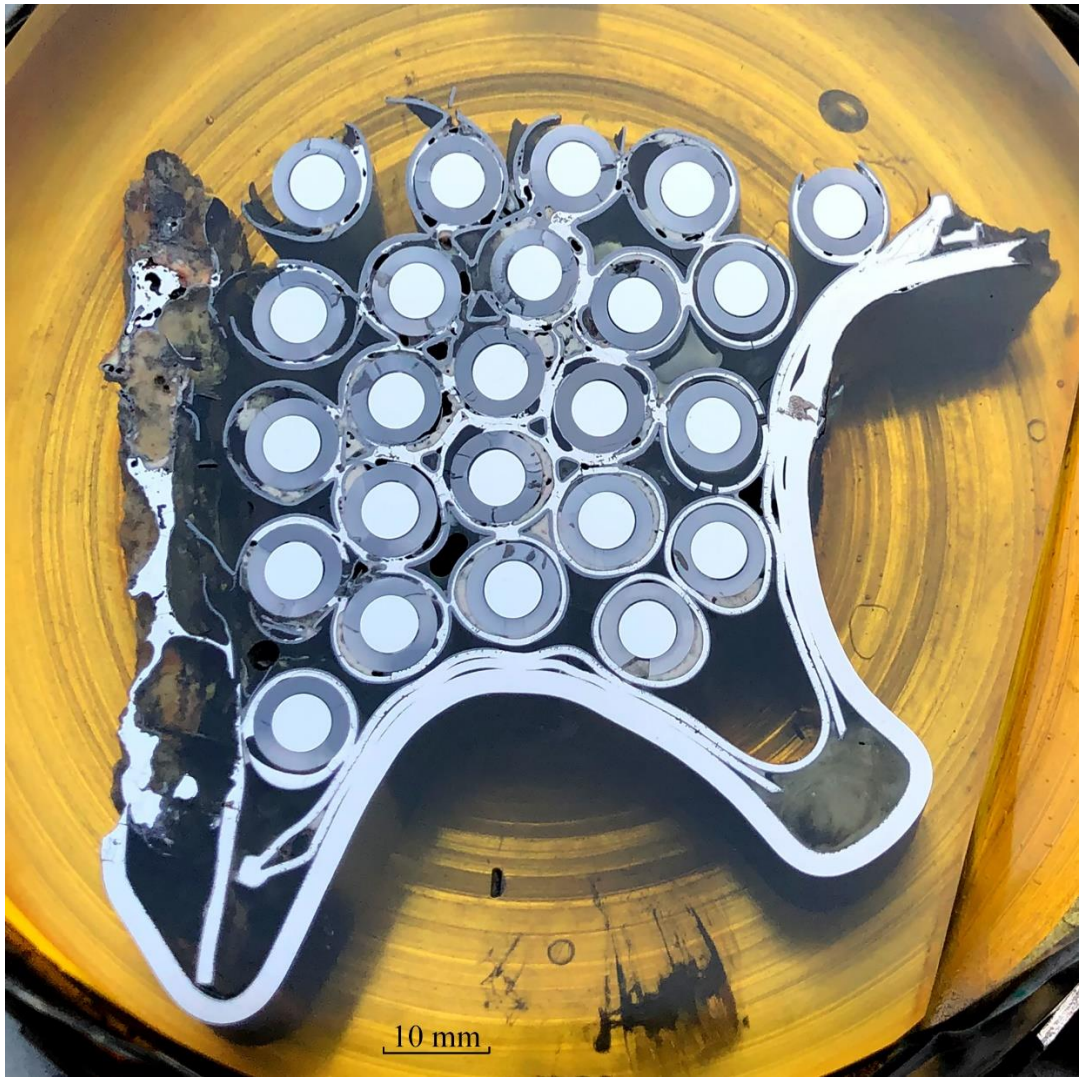

Figure 85 QUENCH-20; Bundle cross section at the elevation of 850 mm.

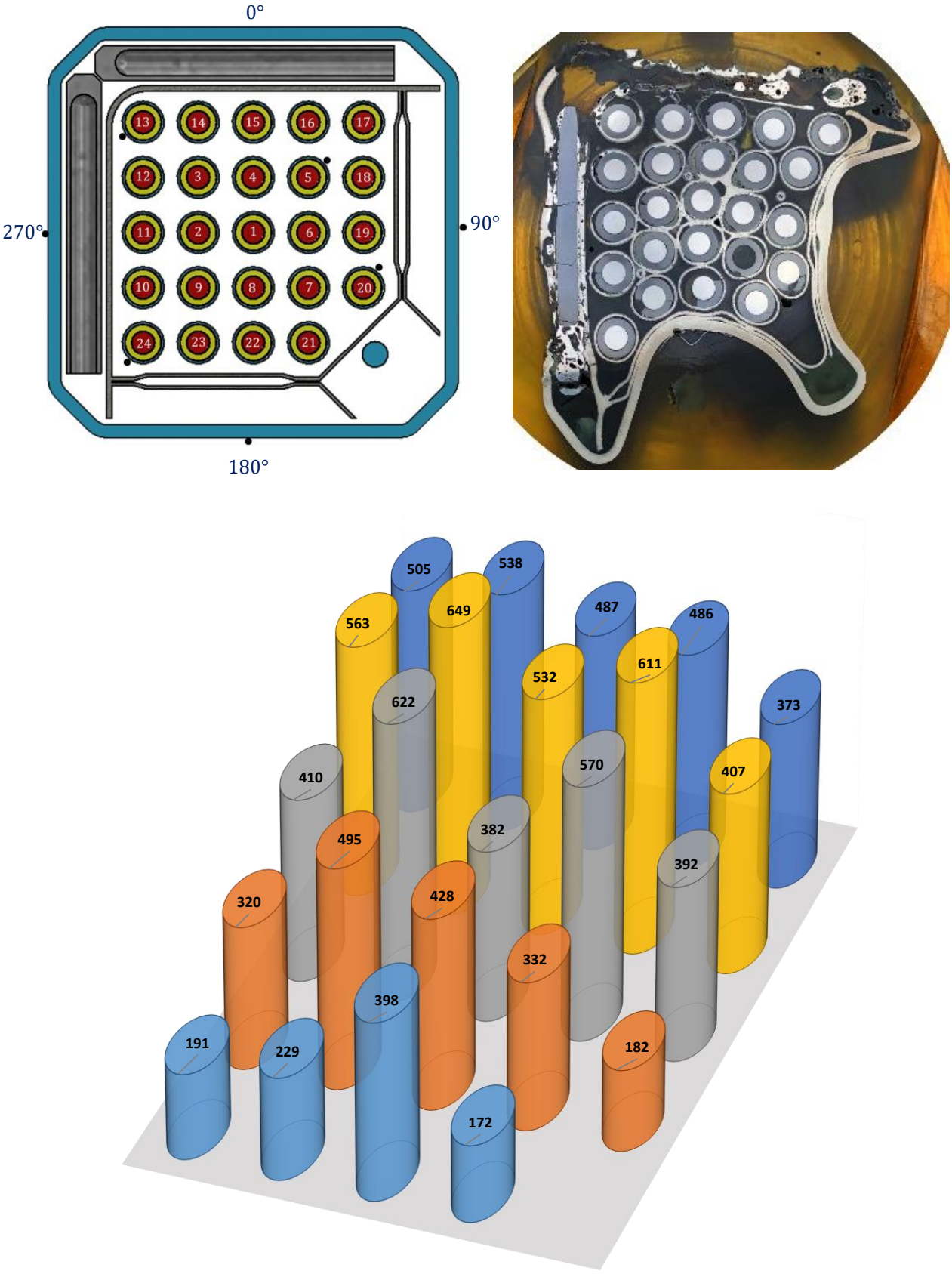

Figure 86 QUENCH-20; average thicknesses of outer ZrO_2 for each cladding at bundle elevation of 850 mm; indication of coldest bundle region at 180°.

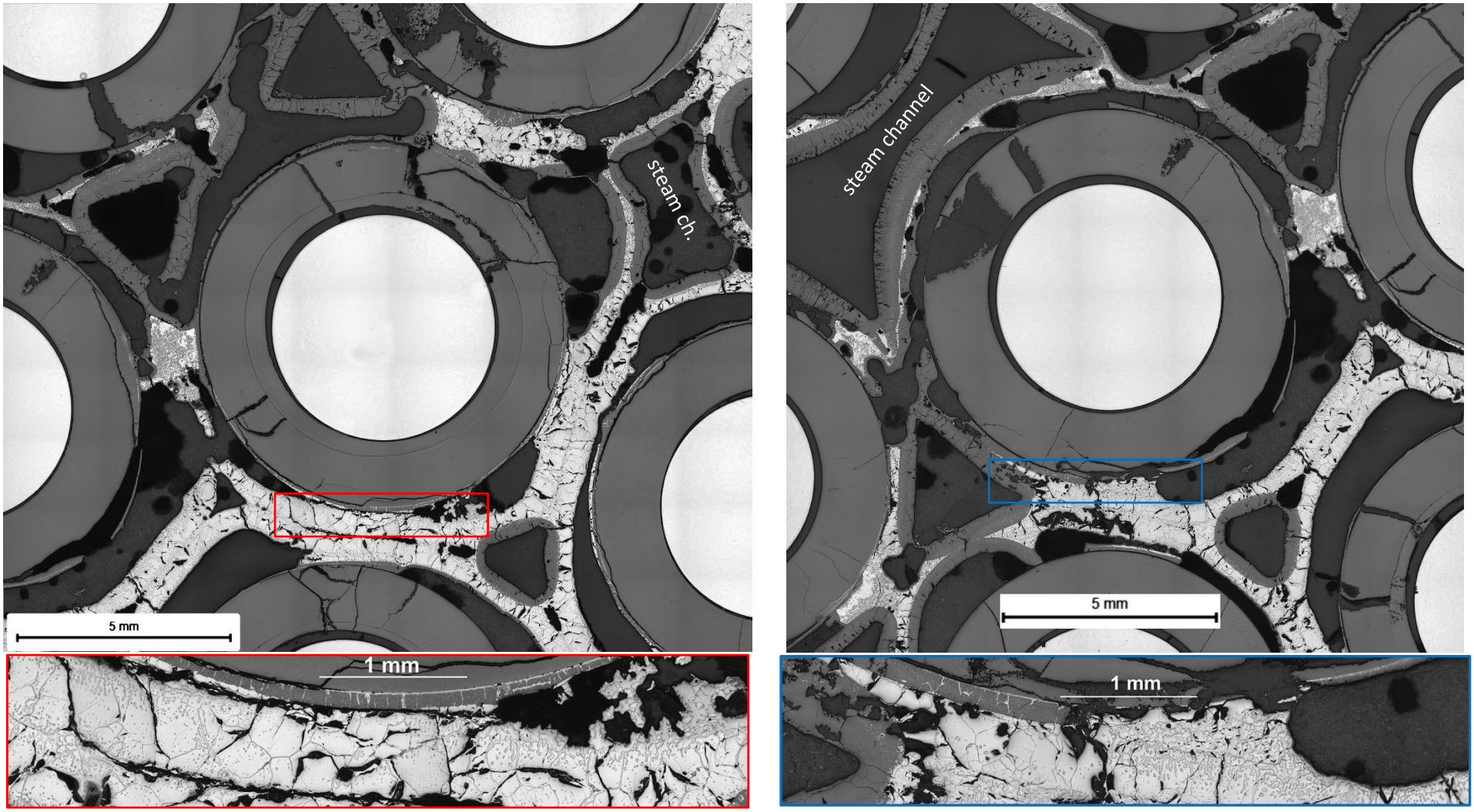

Figure 87 QUENCH-20; Melting of claddings for rods #1 and #2 at bundle elevation 850 mm, formation of steam channels.

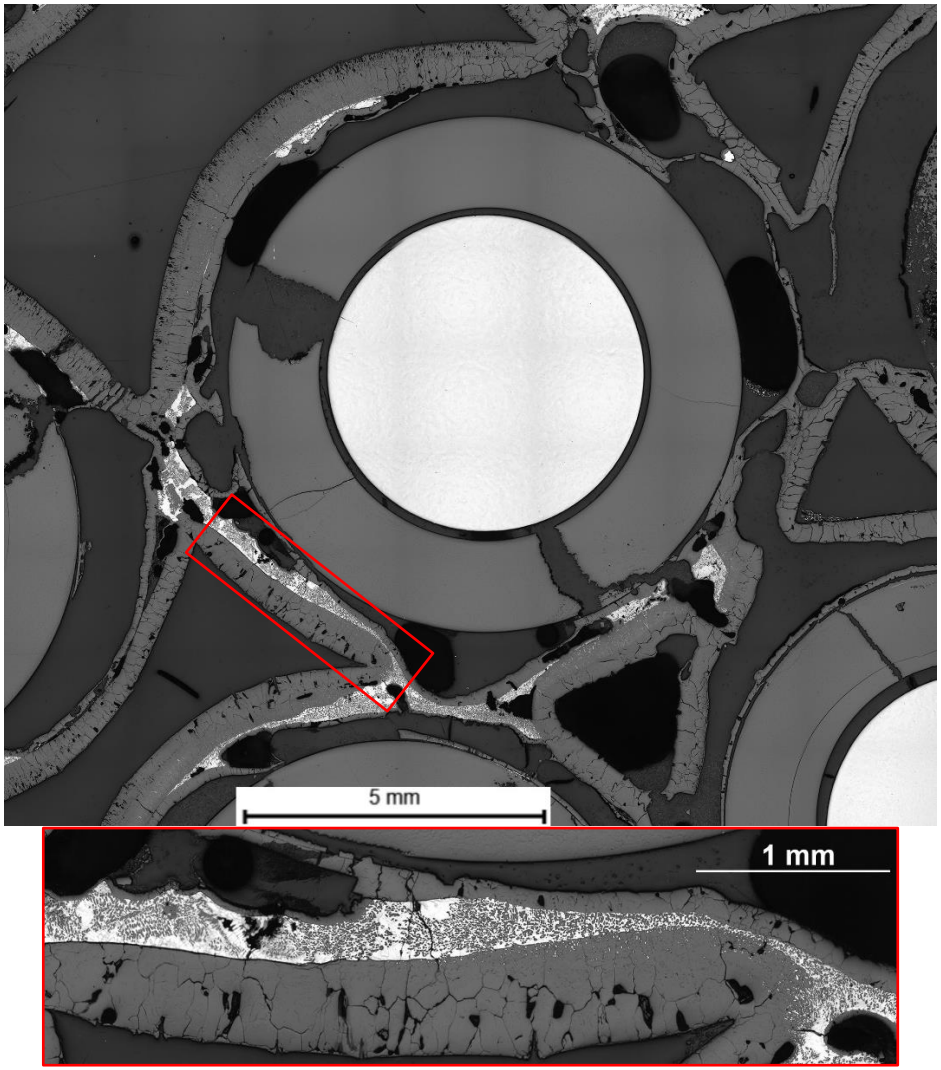

rod 3: ceramic precipitates in metal melt

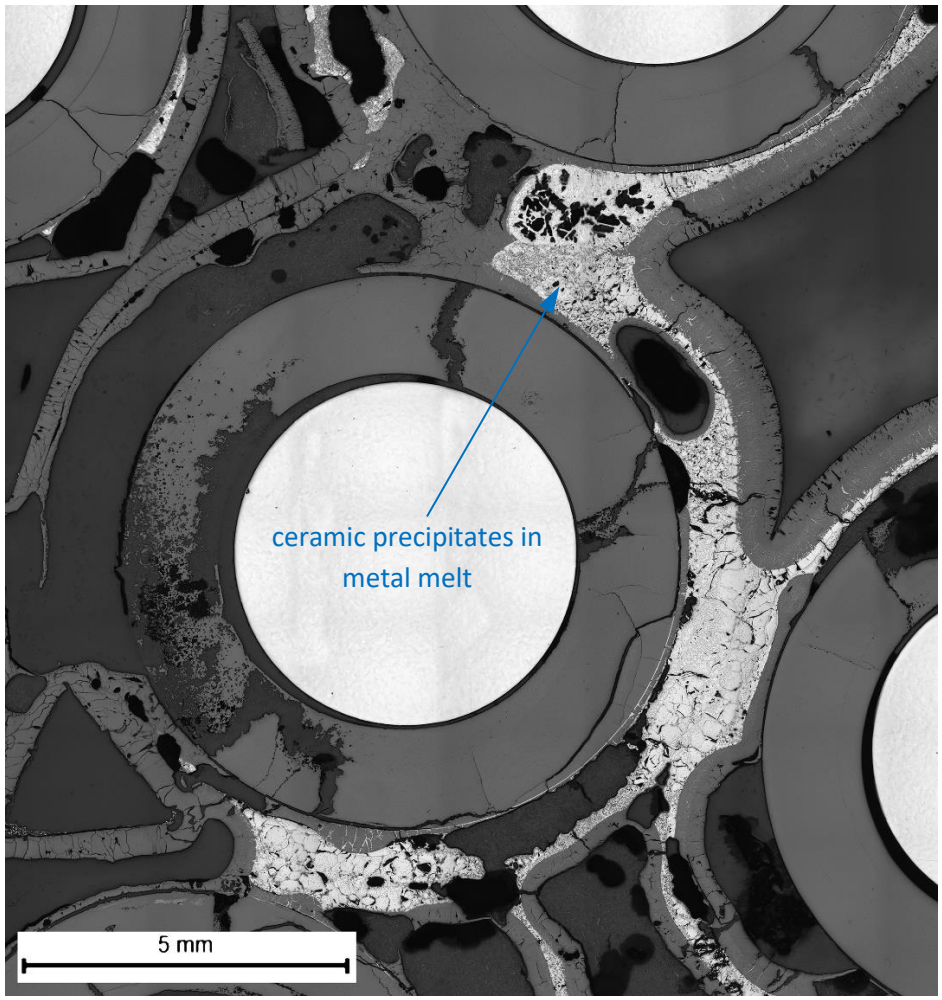

rod 4

Figure 88 QUENCH-20; Melting of claddings for rods #3 and #4 at bundle elevation 850 mm, ceramic precipitates in metallic melt.

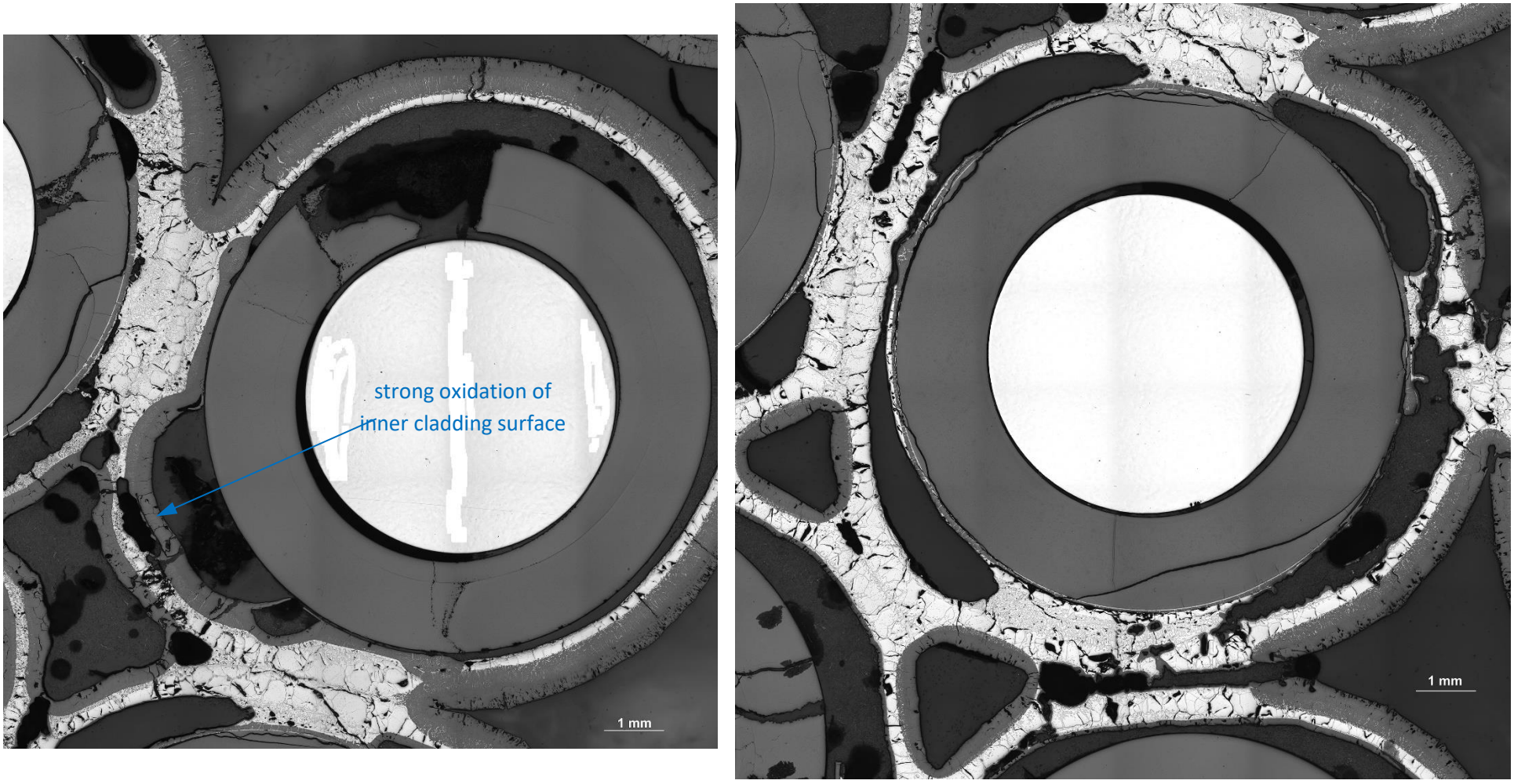

rod 5 rod 6

Figure 89 QUENCH-20; Oxidation and melting of claddings for rods #5 and #6 at bundle elevation 850 mm.

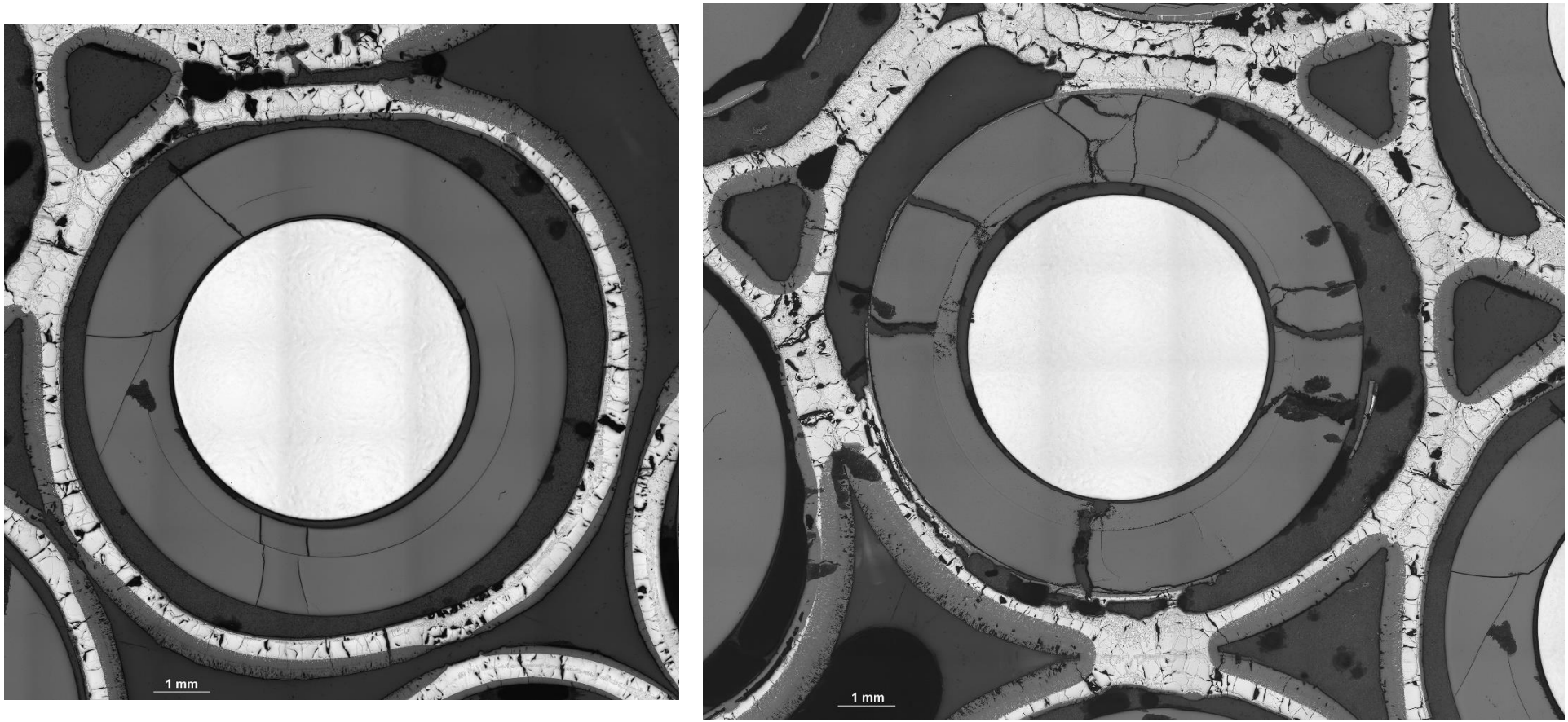

rod 7: complete lift-off of the cladding before cladding failure

rod 8

Figure 90 QUENCH-20; Oxidation and melting of claddings for rods #7 and #8 at bundle elevation 850 mm.

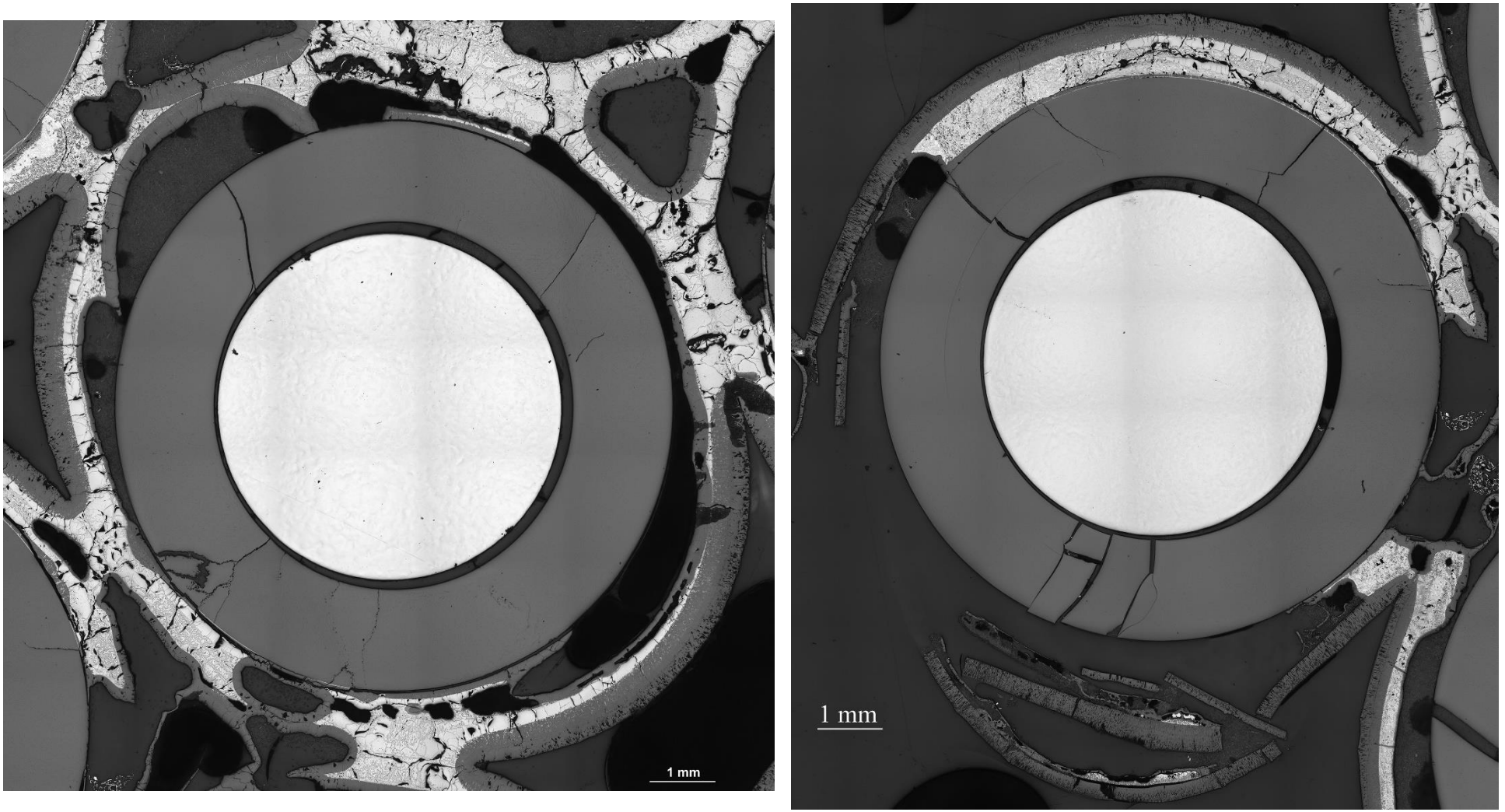

rod 9 rod 10

Figure 91 QUENCH-20; Oxidation and melting of claddings for rods #9 and #10 at bundle elevation 850 mm.

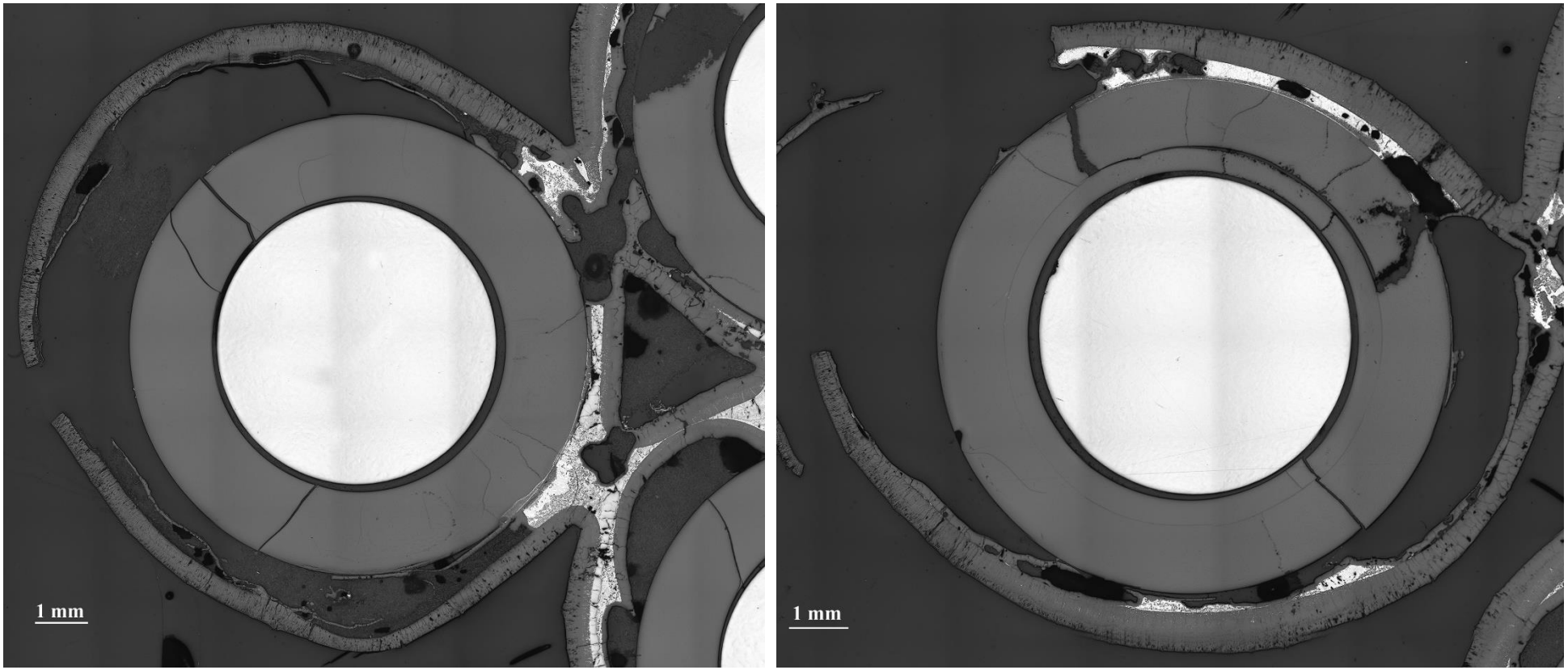

rod 11: almost complete metal melt relocation to lower elevations

rod 12

Figure 92 QUENCH-20; Oxidation and melting of claddings for rods #11 and #12 at bundle elevation 850 mm.

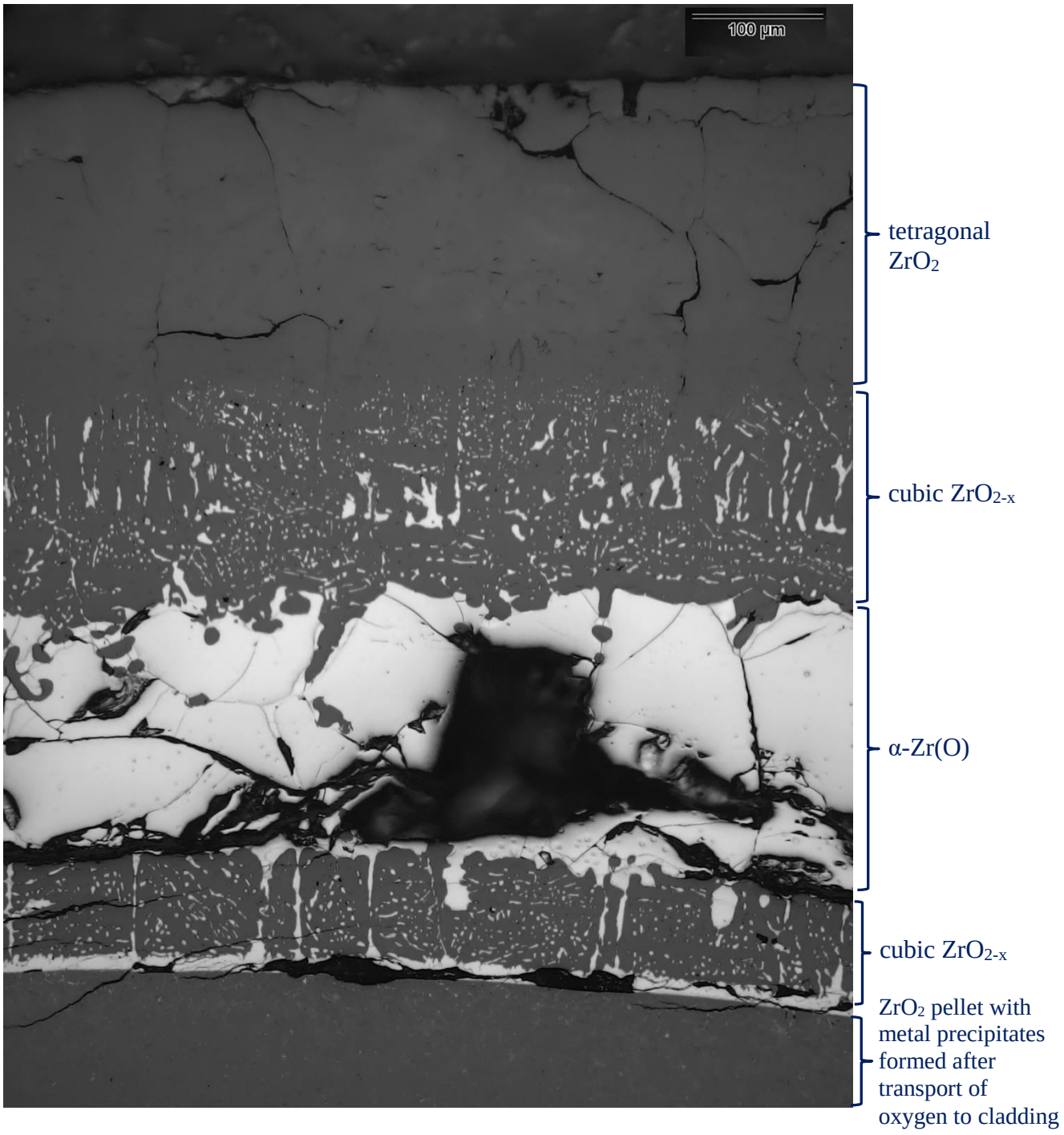

Figure 93 QUENCH-20; Oxidation of cladding for rods #11 at bundle elevation 850 mm, angle 90°.

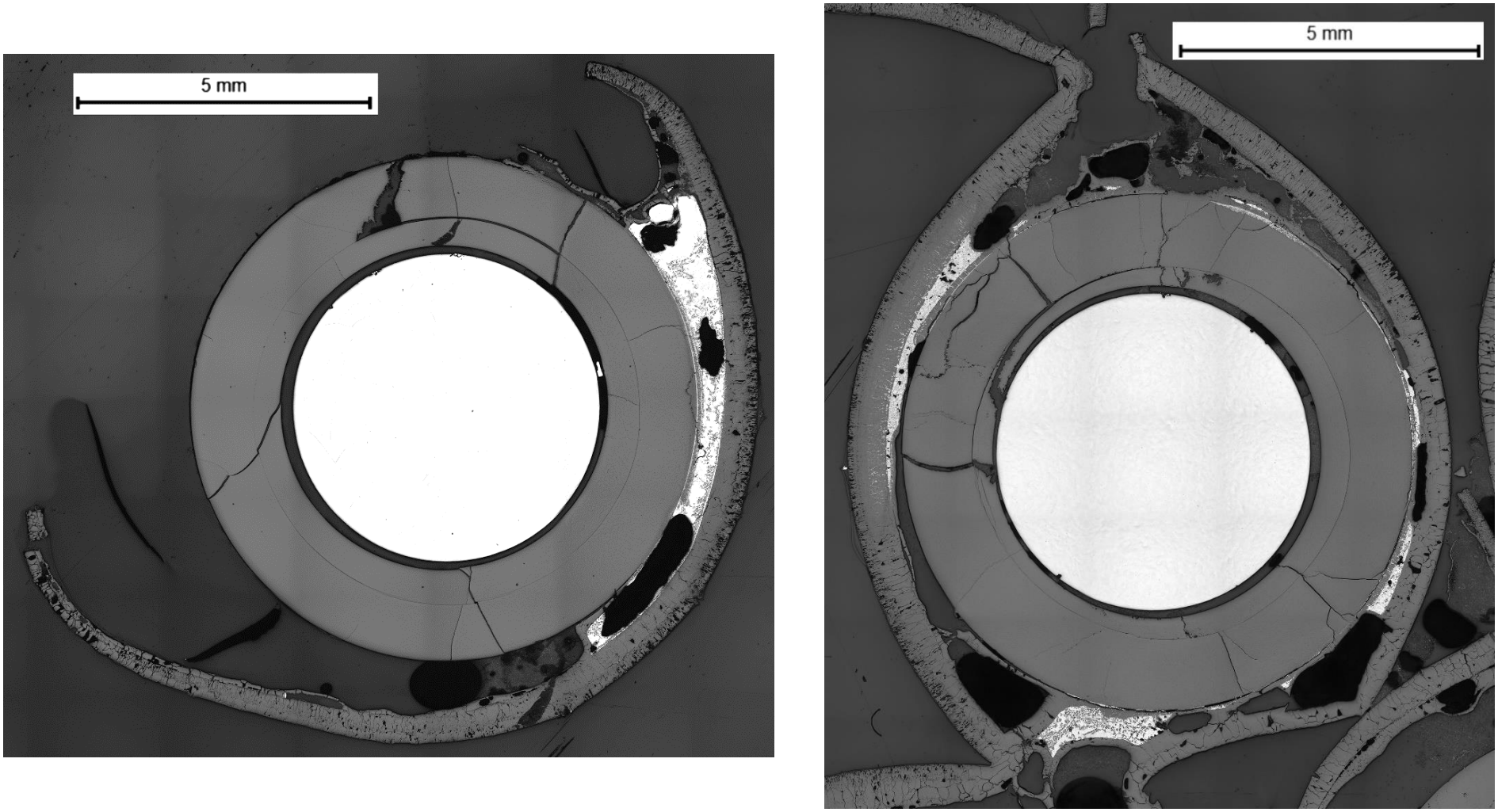

rod 13: flowering of cladding, strong cladding melting

rod 14: strong melting of cladding

Figure 94 QUENCH-20; Oxidation and melting of claddings for rods #13 and #14 at bundle elevation 850 mm.

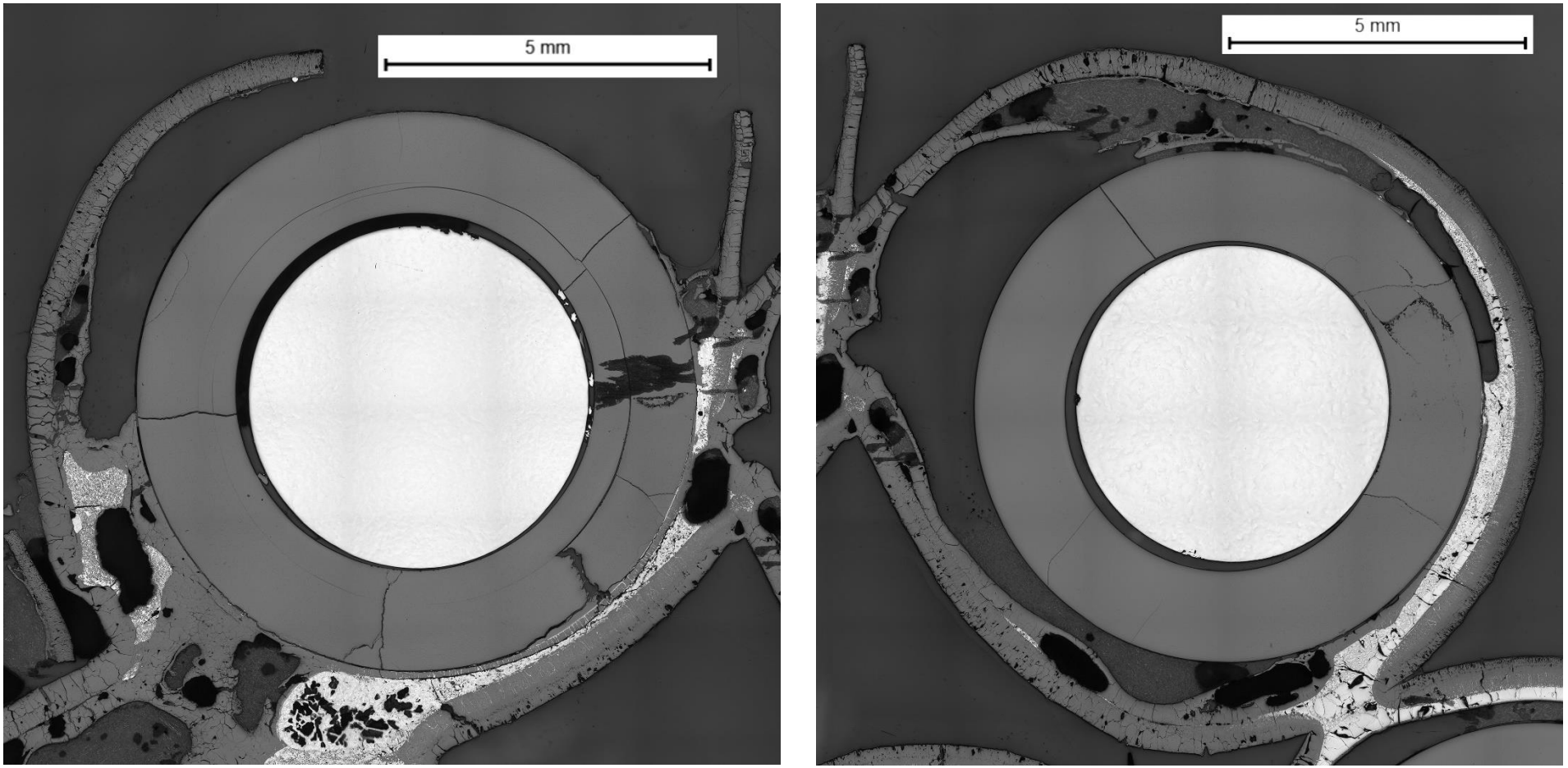

rod 15: strong cladding melting

rod 16: strong cladding melting

Figure 95 QUENCH-20; Oxidation and melting of claddings for rods #15 and #16 at bundle elevation 850 mm.

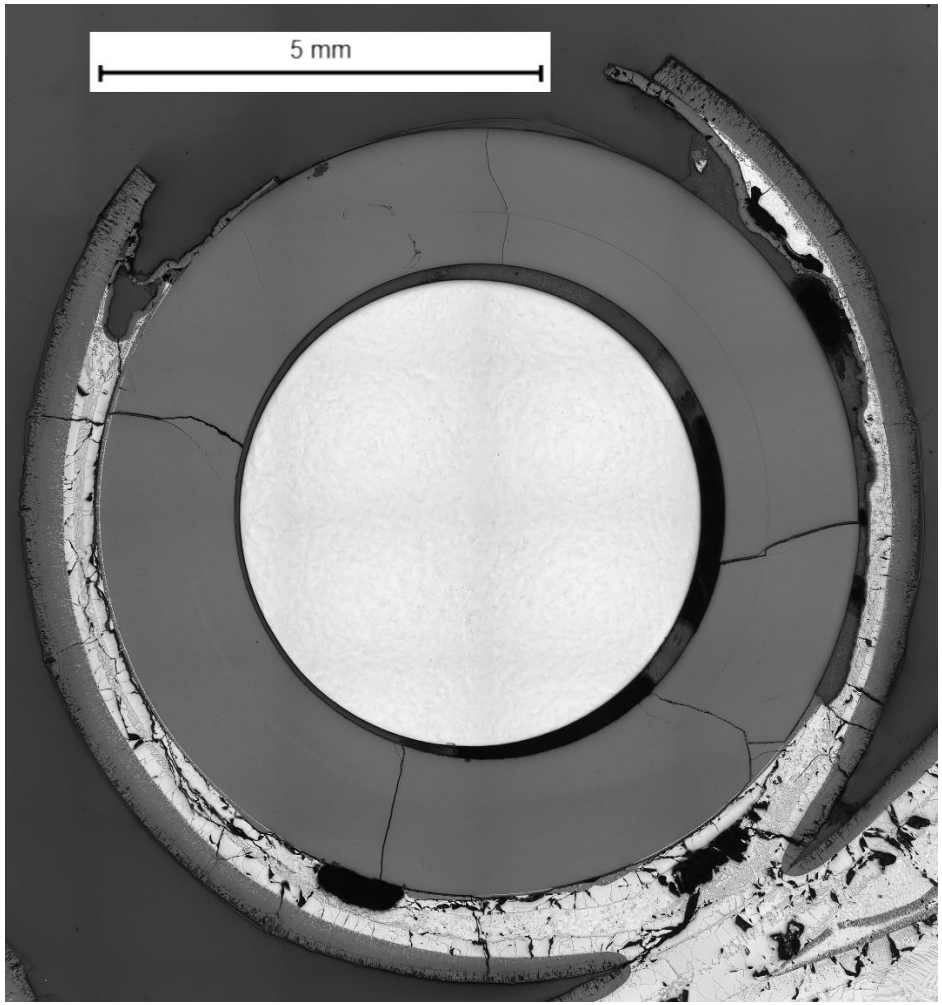

rod 17: cladding melt partially relocated from upper positions

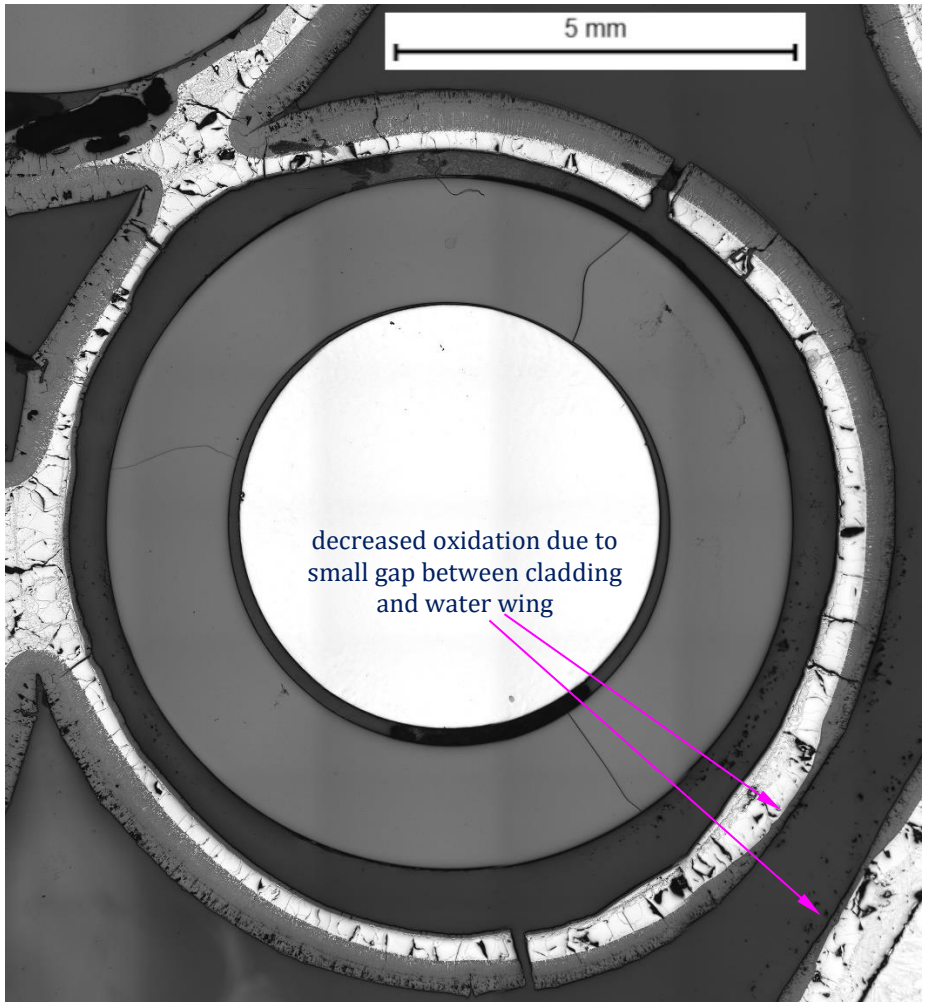

rod 18: clear lift-off of the cladding due to inner pressure; no cladding melting

Figure 96 QUENCH-20; Oxidation and melting of claddings for rods #17 and #18 at bundle elevation 850 mm.

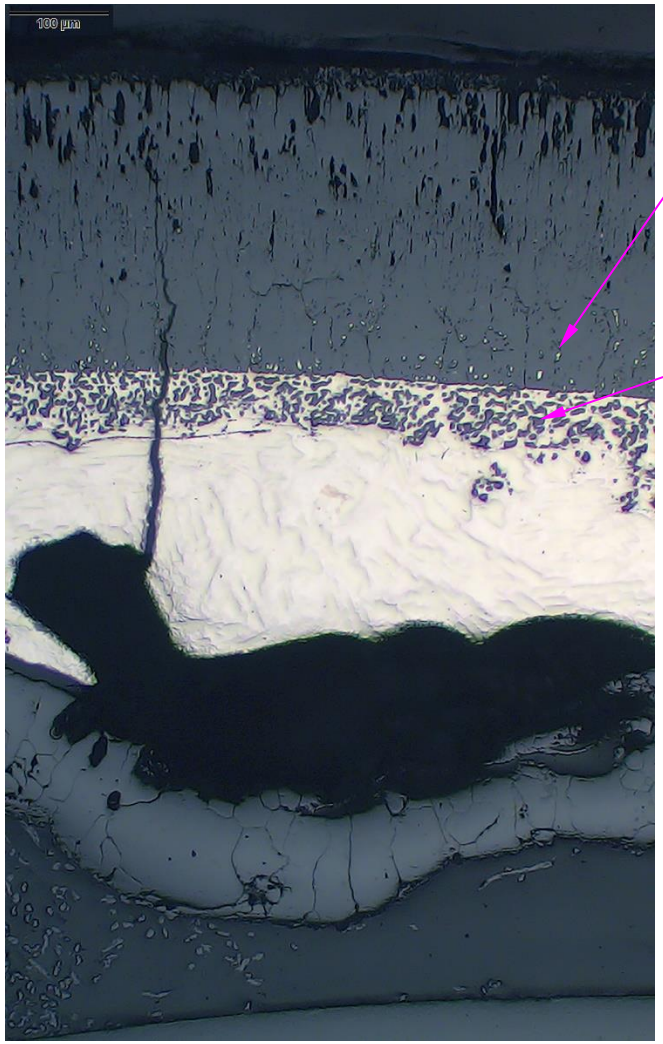

angle 45°: dissolution of oxide layer by metal melt

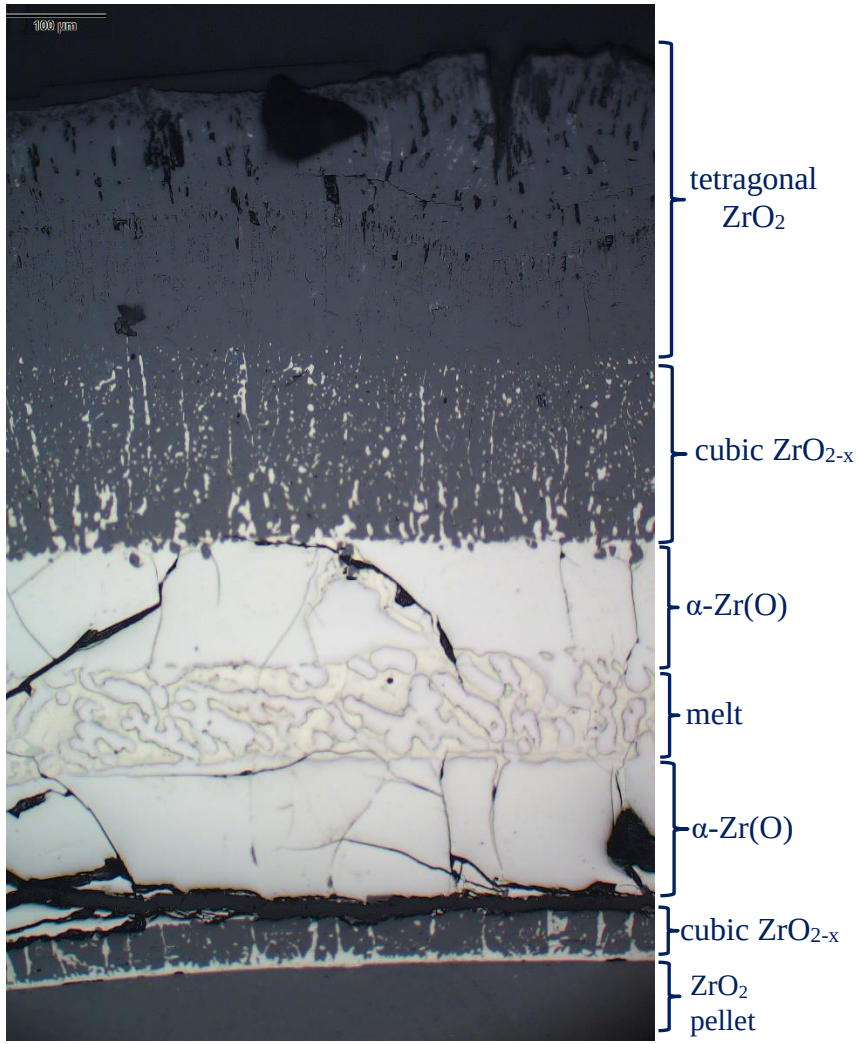

angle 270°: metal melt between outer and inner α-Zr(O) layers

Figure 97 QUENCH-20; Metal melt formed in the cladding of the rod #17 at bundle elevation 850 mm.

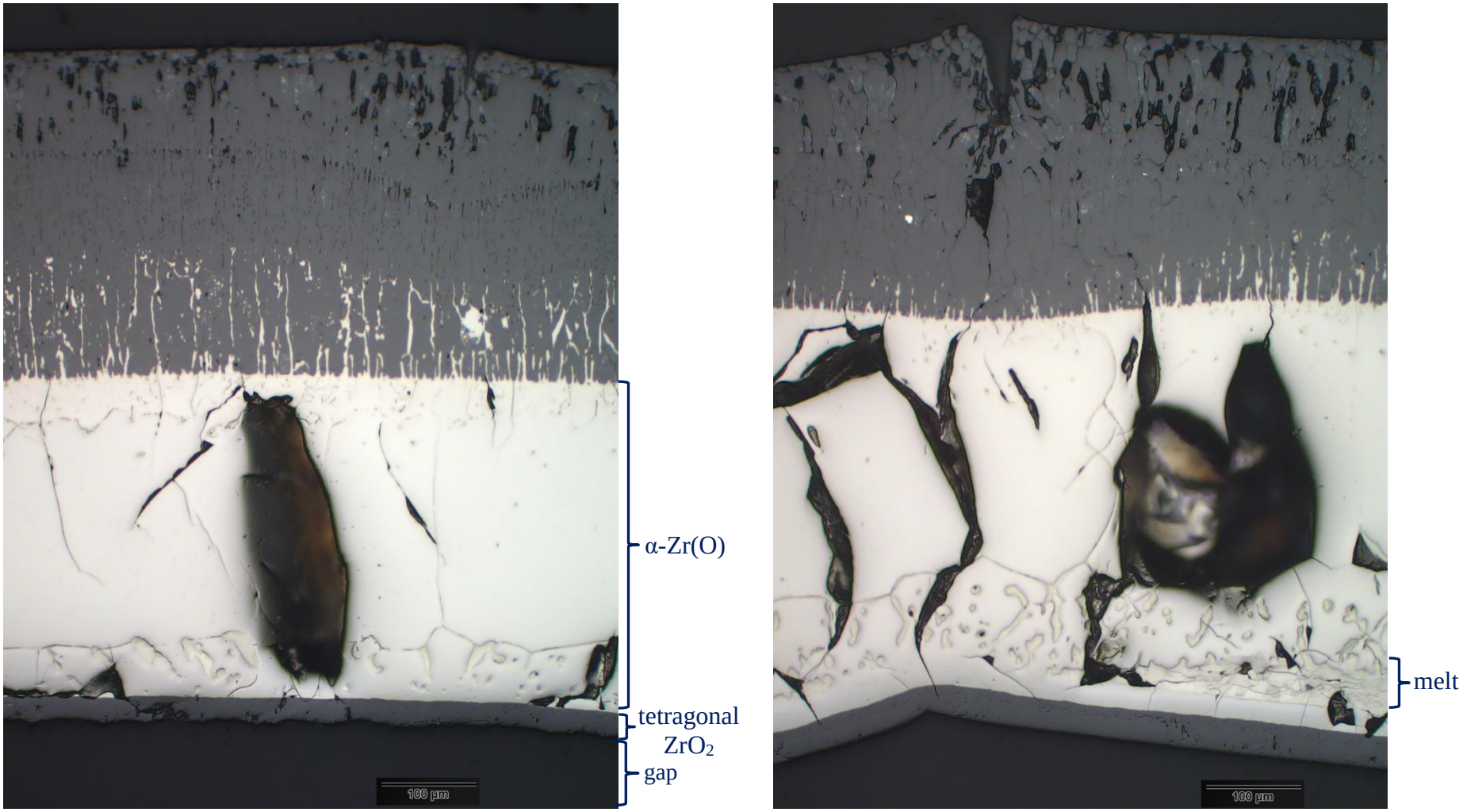

90°: thick outer and thin inner oxide layers

135°: thin molten layer

Figure 98 QUENCH-20; Layers of cladding #18 at bundle elevation 850 mm; only local cladding melting.

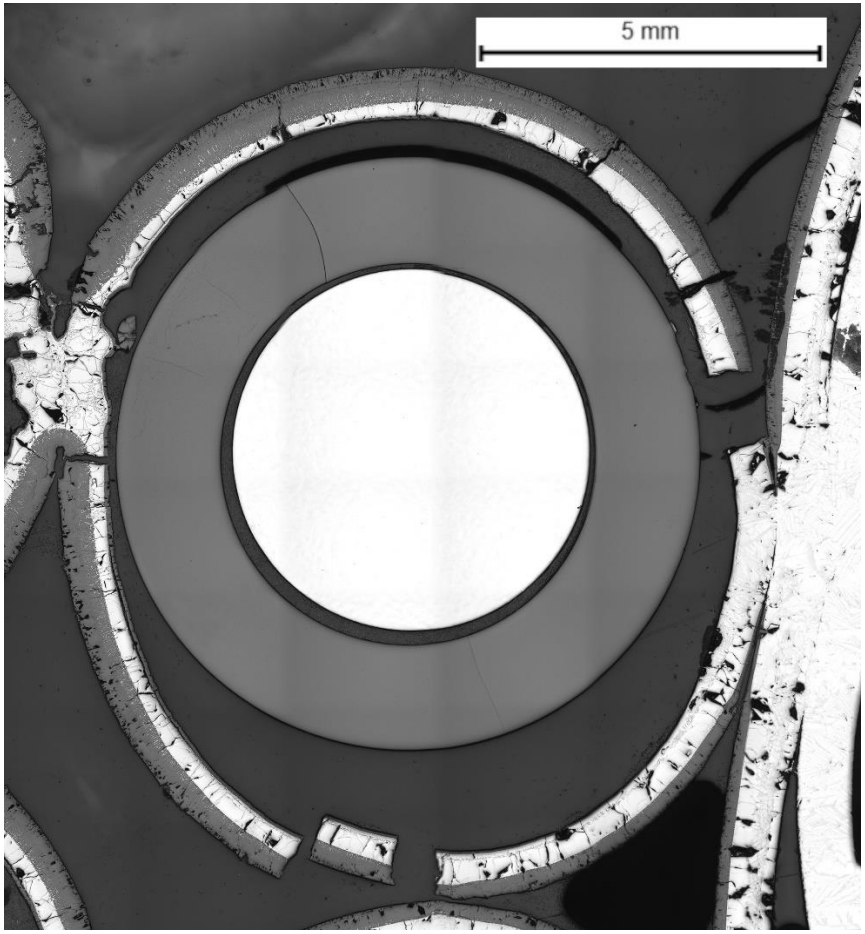

rod 19: cladding melted only locally at the contact to rod 6

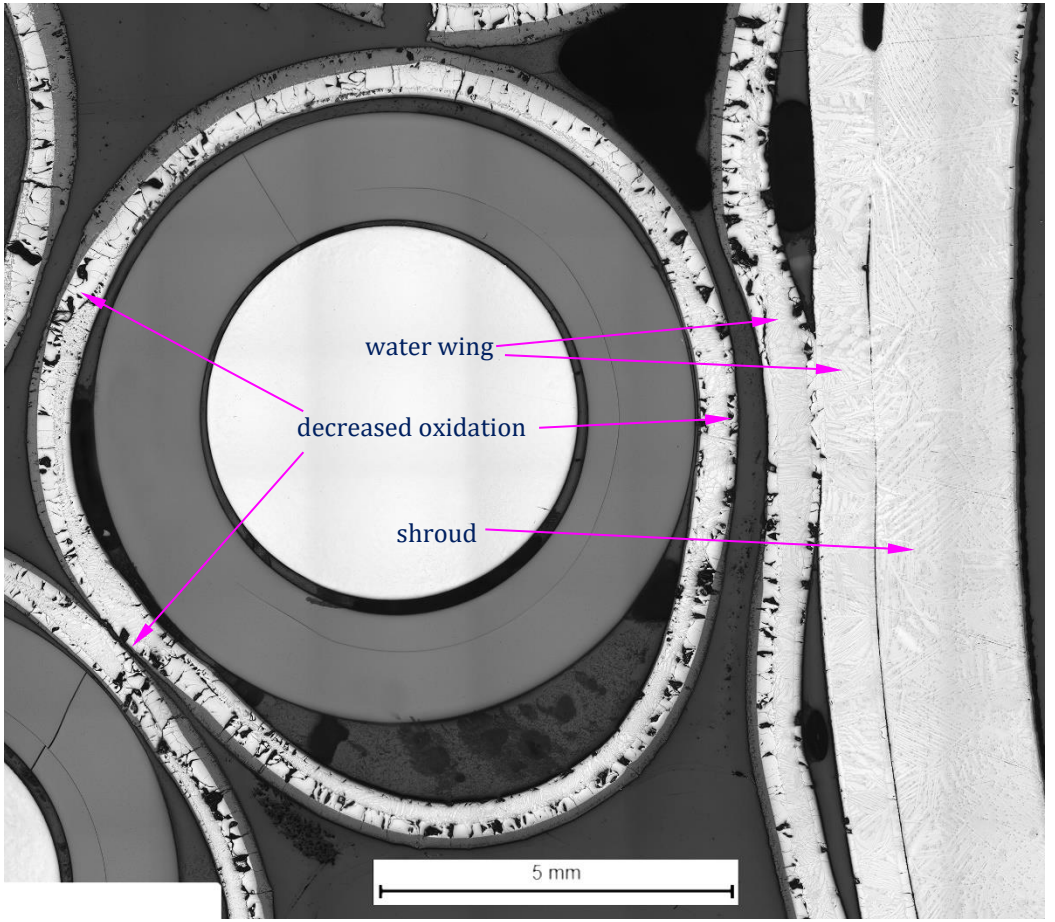

rod 20: decreased cladding oxidation due to small gap between cladding and neighbour bundle elements

Figure 99 QUENCH-20; Oxidation of claddings for rods #19 and #20 at bundle elevation 850 mm.

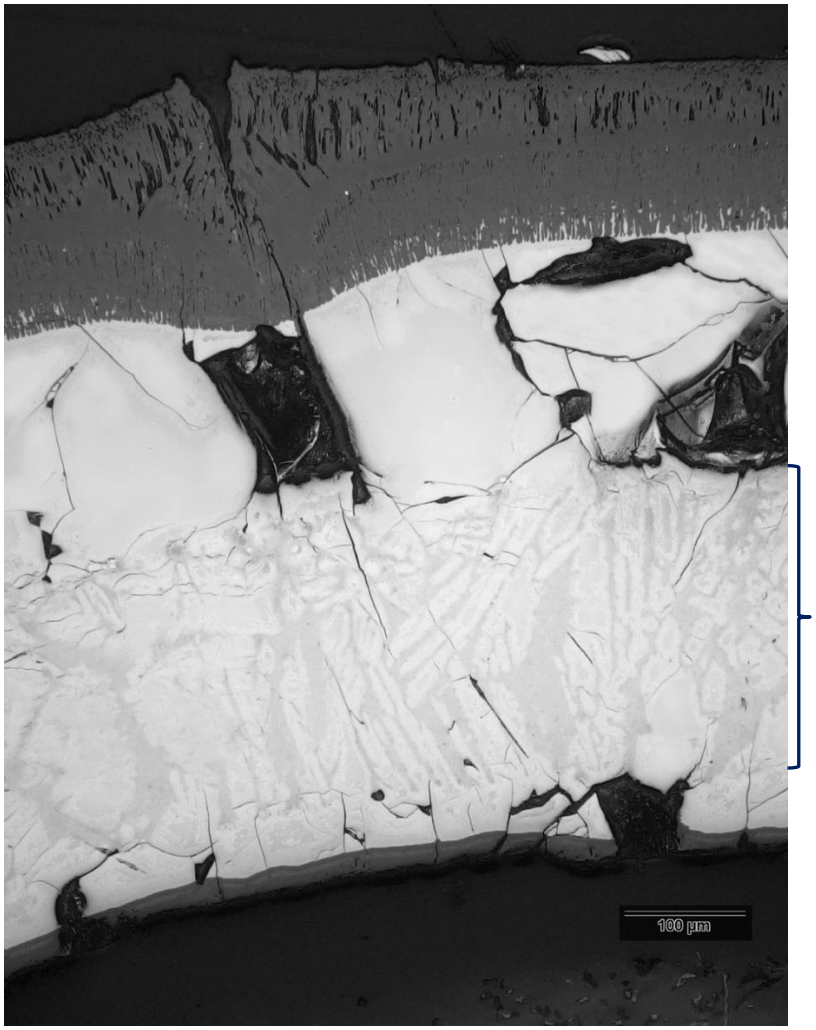

135°: thick prior β-Zr layer

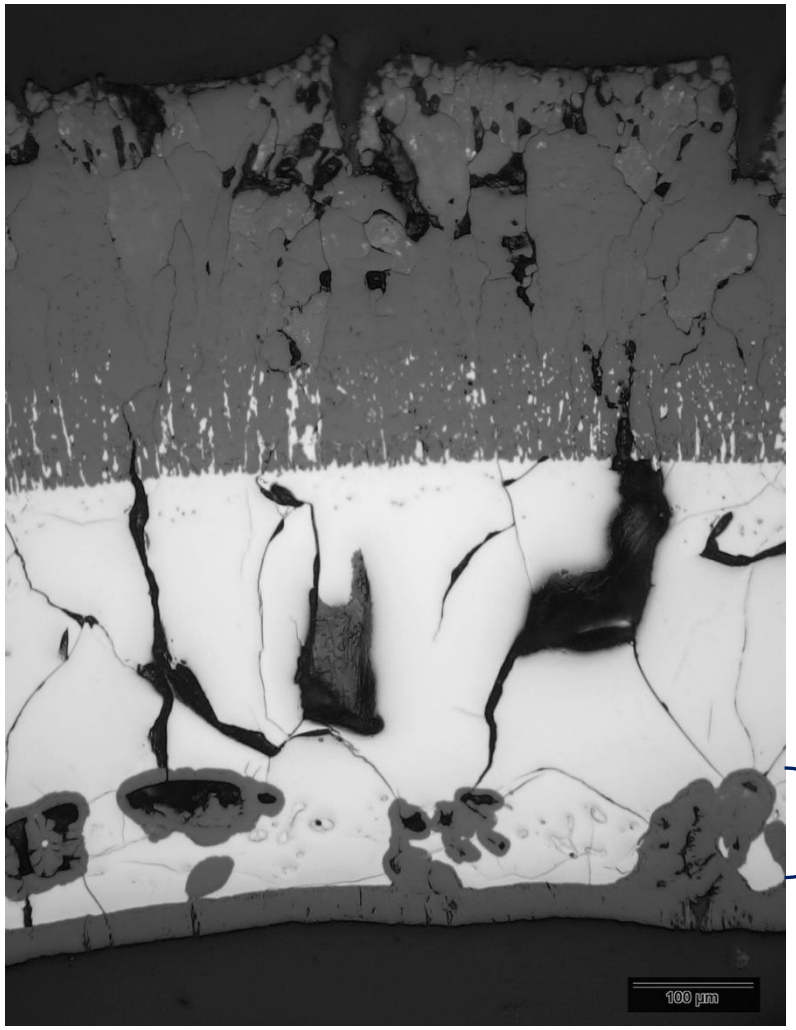

325°: closed outer and inner α-Zr(O) layers; penetration into voids

Figure 100 QUENCH-20; Layers of cladding #20 at bundle elevation 850 mm; absence of melt.

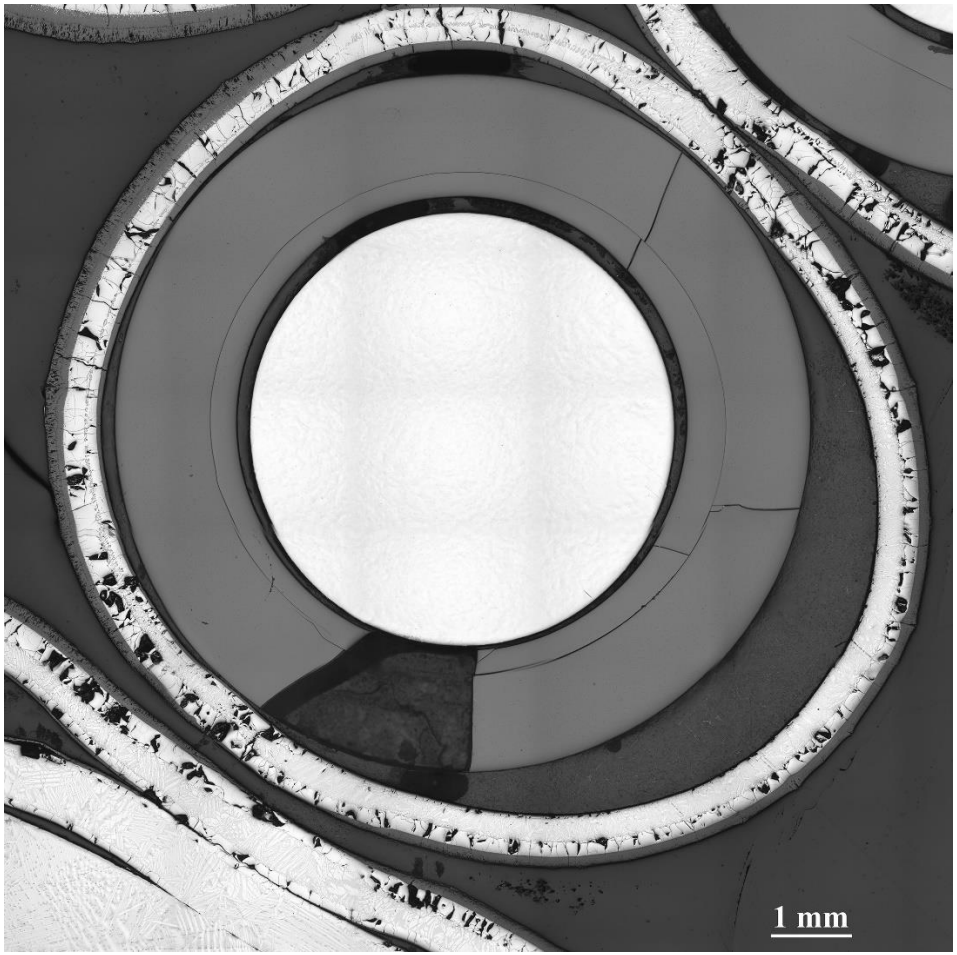

rod 21: moderately oxidized cladding with relative thick β-Zr layer; decreased cladding oxidation due to small gap between cladding and neighbour bundle elements

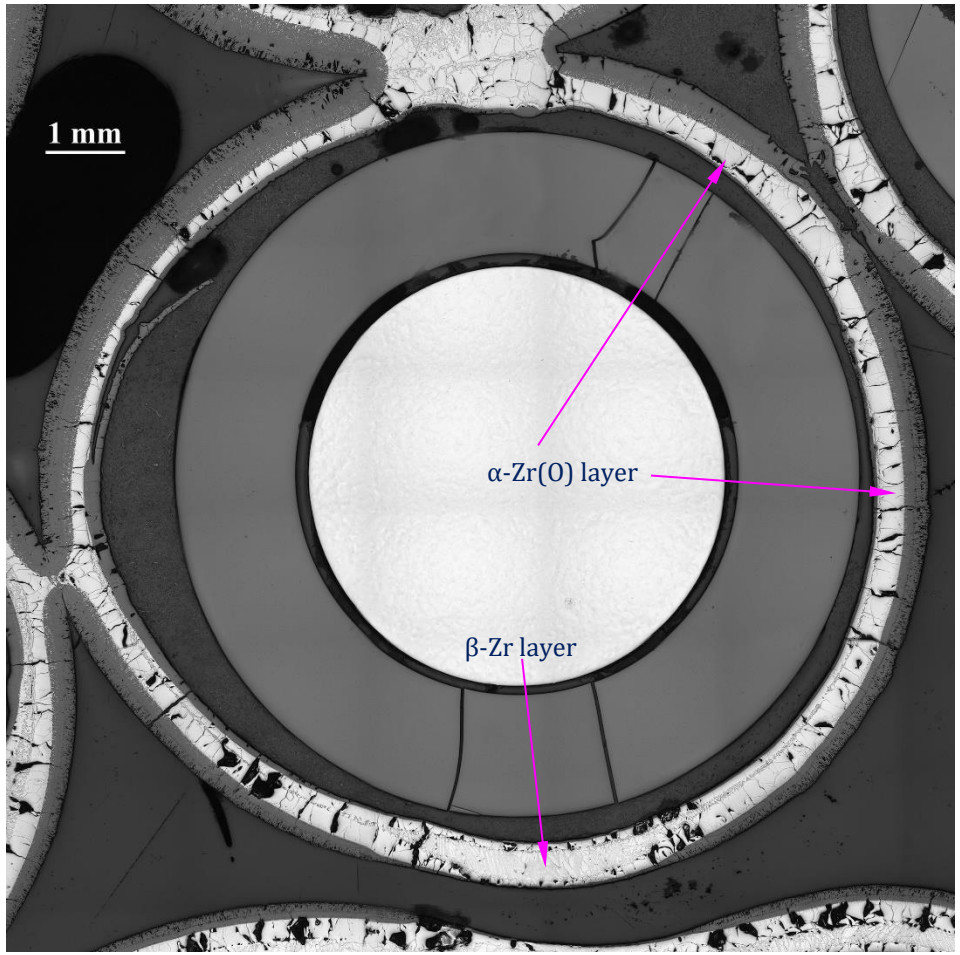

rod 22: significantly oxidized cladding with locally remaining β-Zr layer

Figure 101 QUENCH-20; Oxidation of claddings for rods #21and #22 at bundle elevation 850 mm.

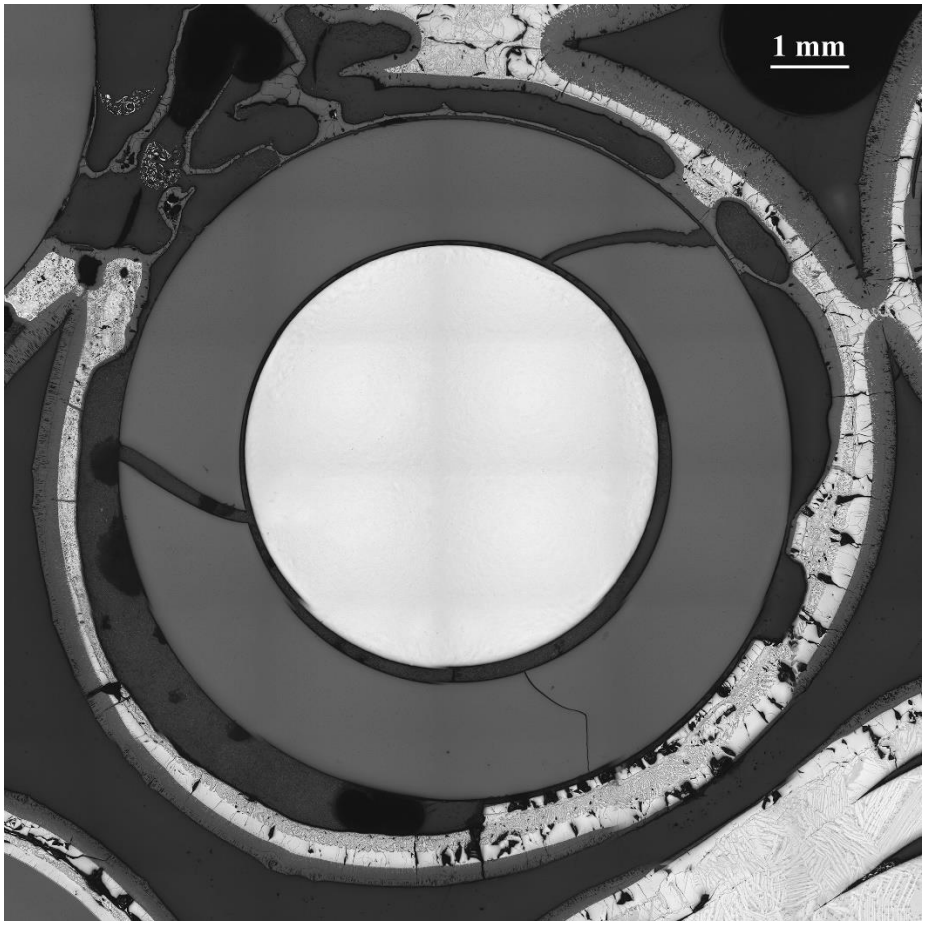

rod 23: cladding melt formed here was relocated to lower elevations

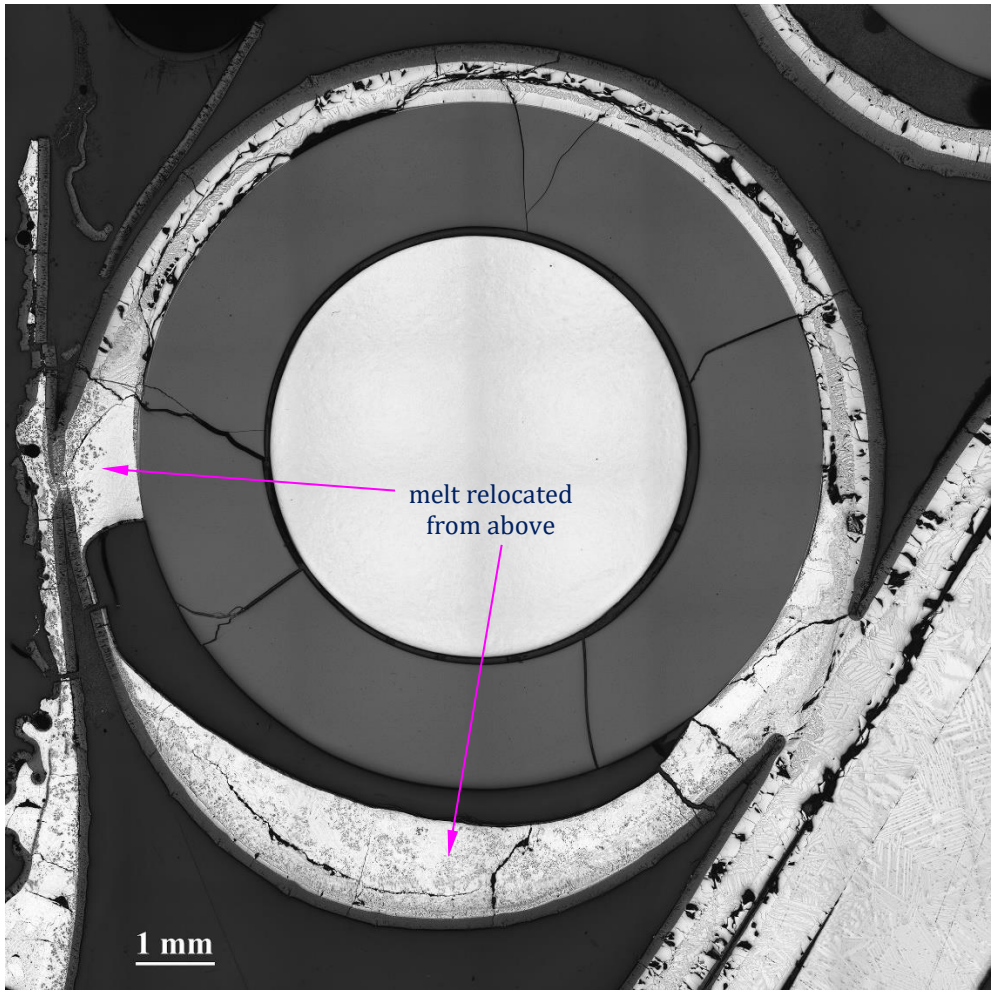

rod 24: frozen melt relocated from above inside the gap between pellet and outer oxide layer

Figure 102 QUENCH-20; Oxidation and melting of claddings for rods #23 and #24 at bundle elevation 850 mm.

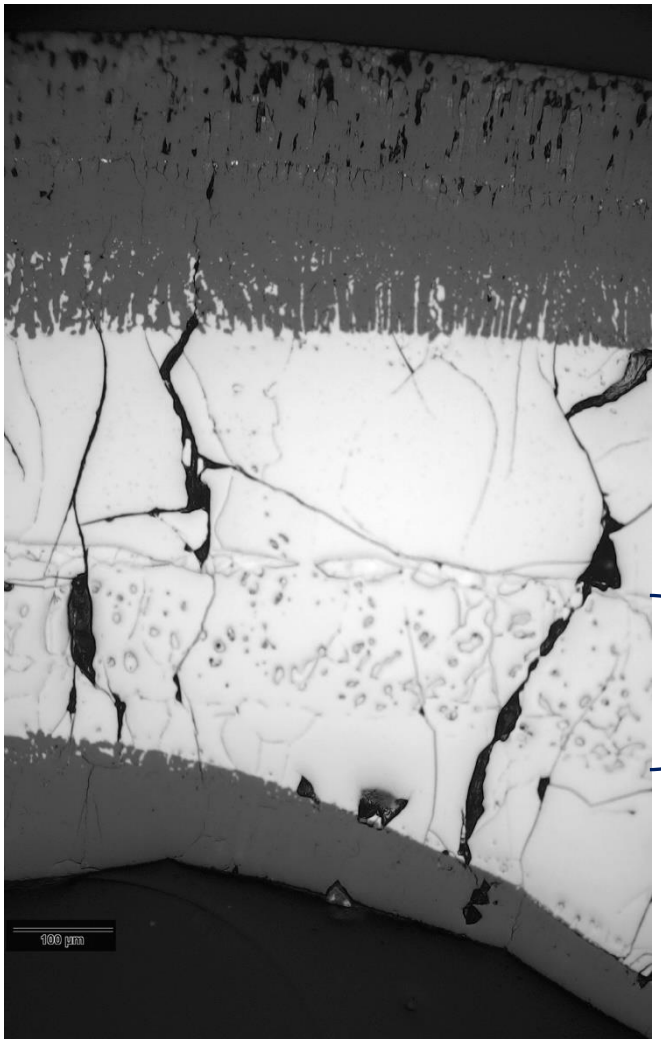

90°: beginning of melting inside the inner α-Zr(O) layer

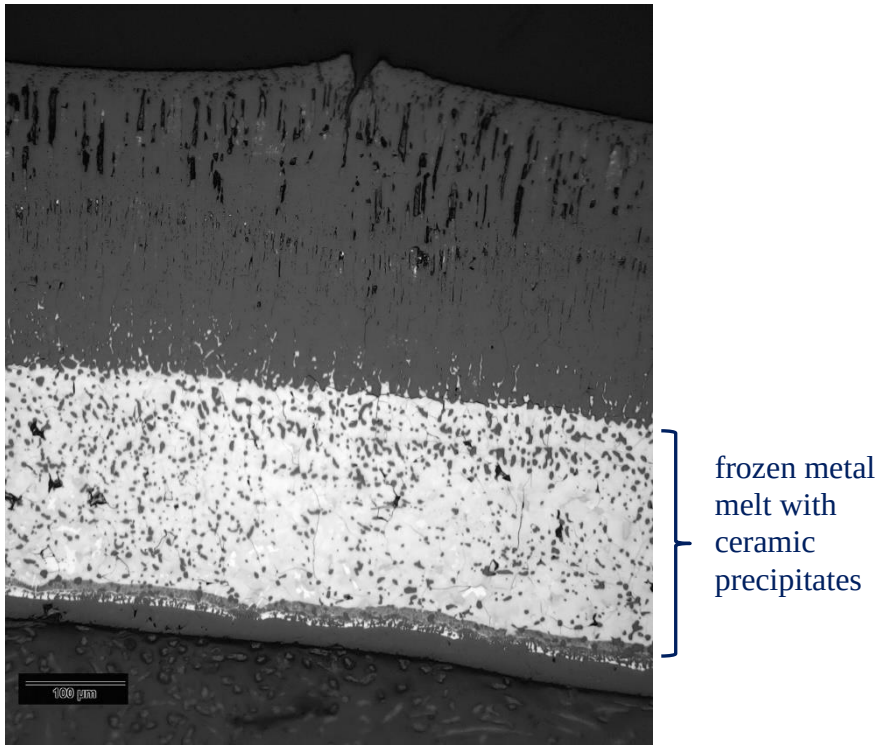

270°: partially oxidized melt between oxide layers

Figure 103 QUENCH-20; Layers of cladding #23 at bundle elevation 850 mm.

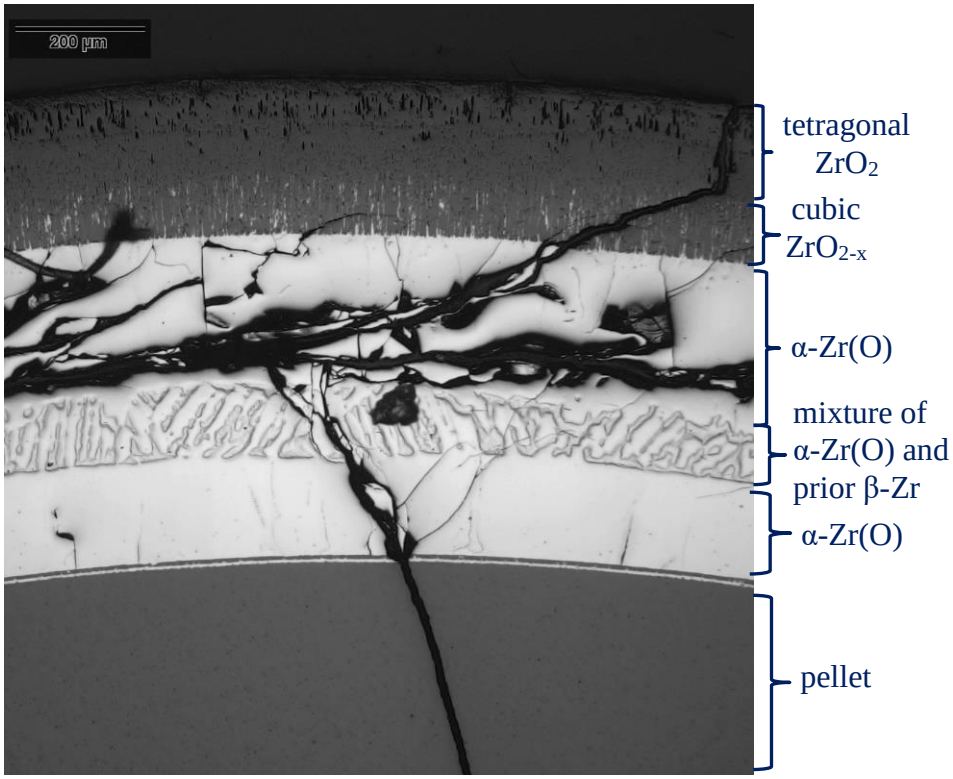

0°: not melted cladding

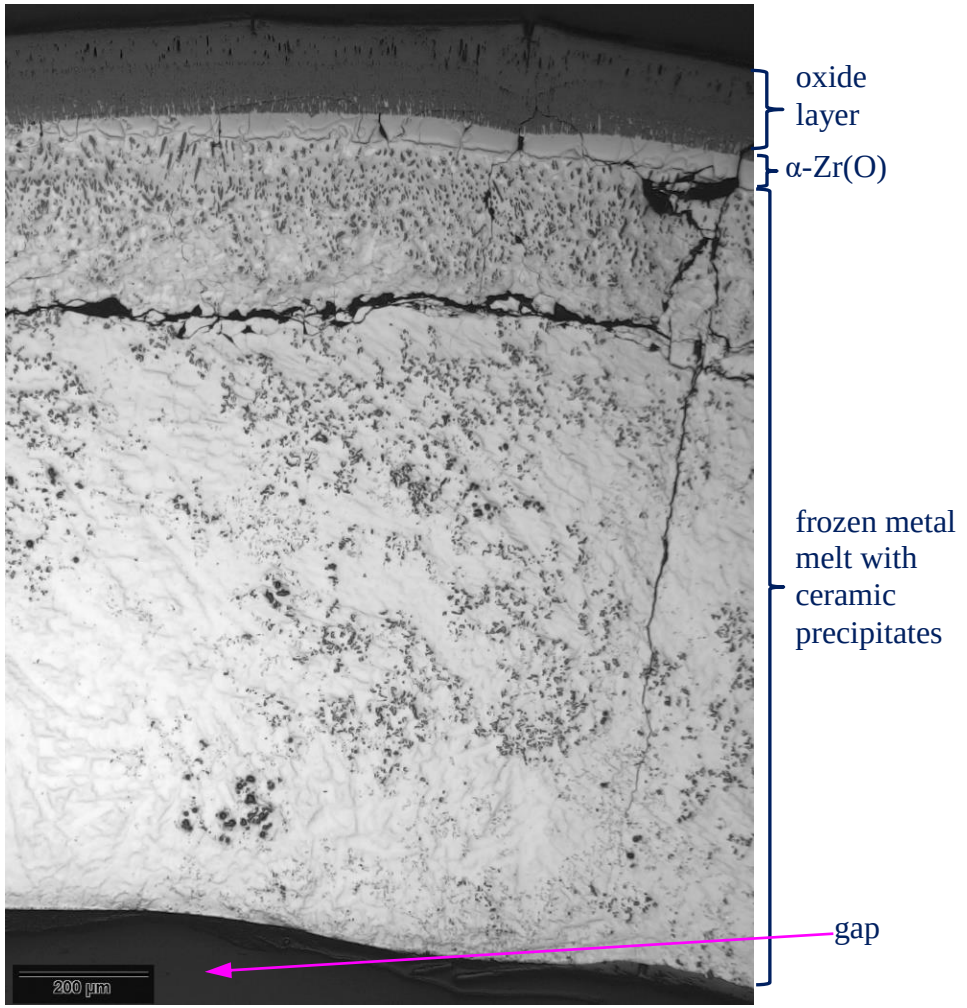

180°: partially oxidized melt relocated from above inside gap

Figure 104 QUENCH-20; Layers of cladding #24 at bundle elevation 850 mm.

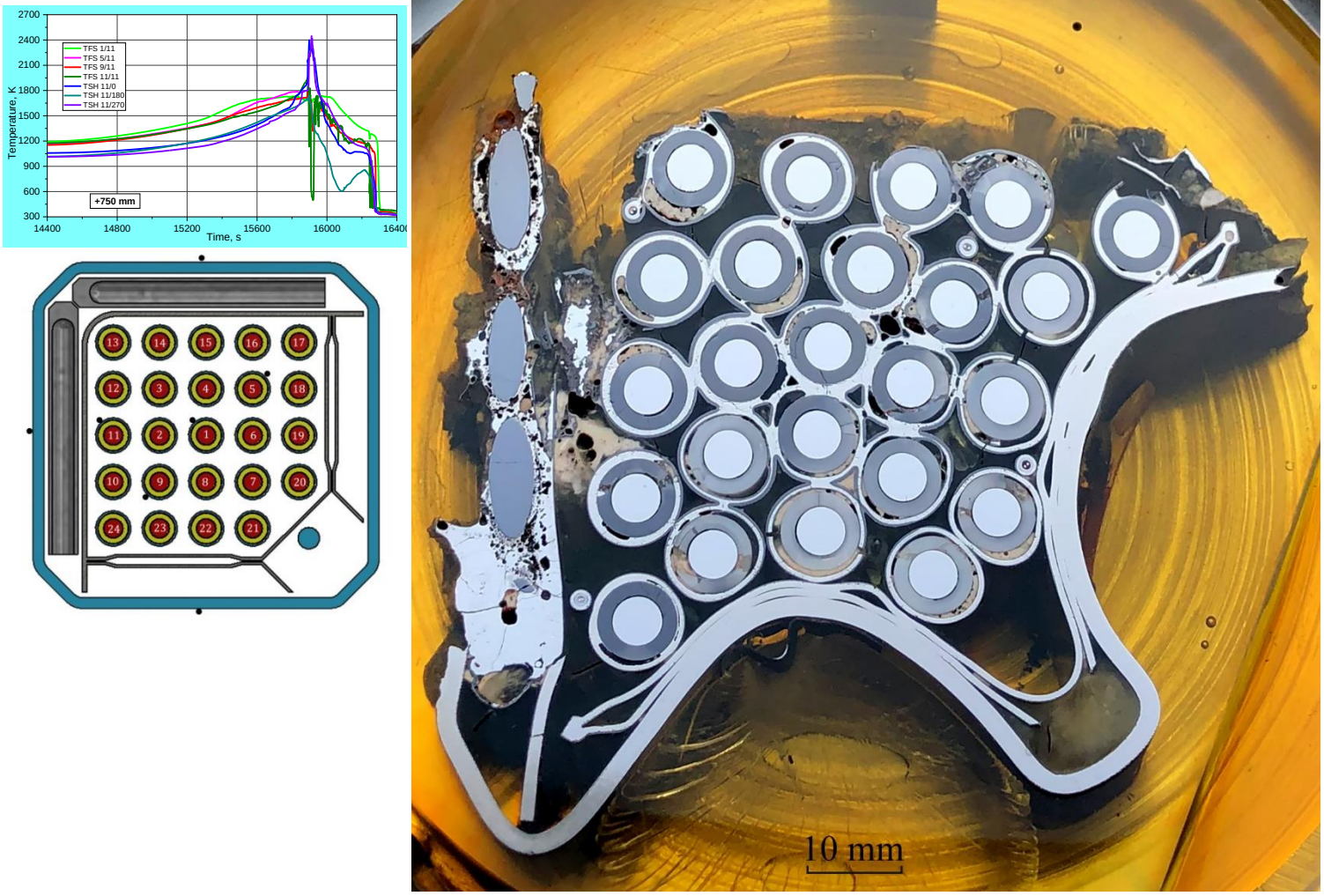

Figure 105 QUENCH-20; Bundle cross section at the elevation of 750 mm.

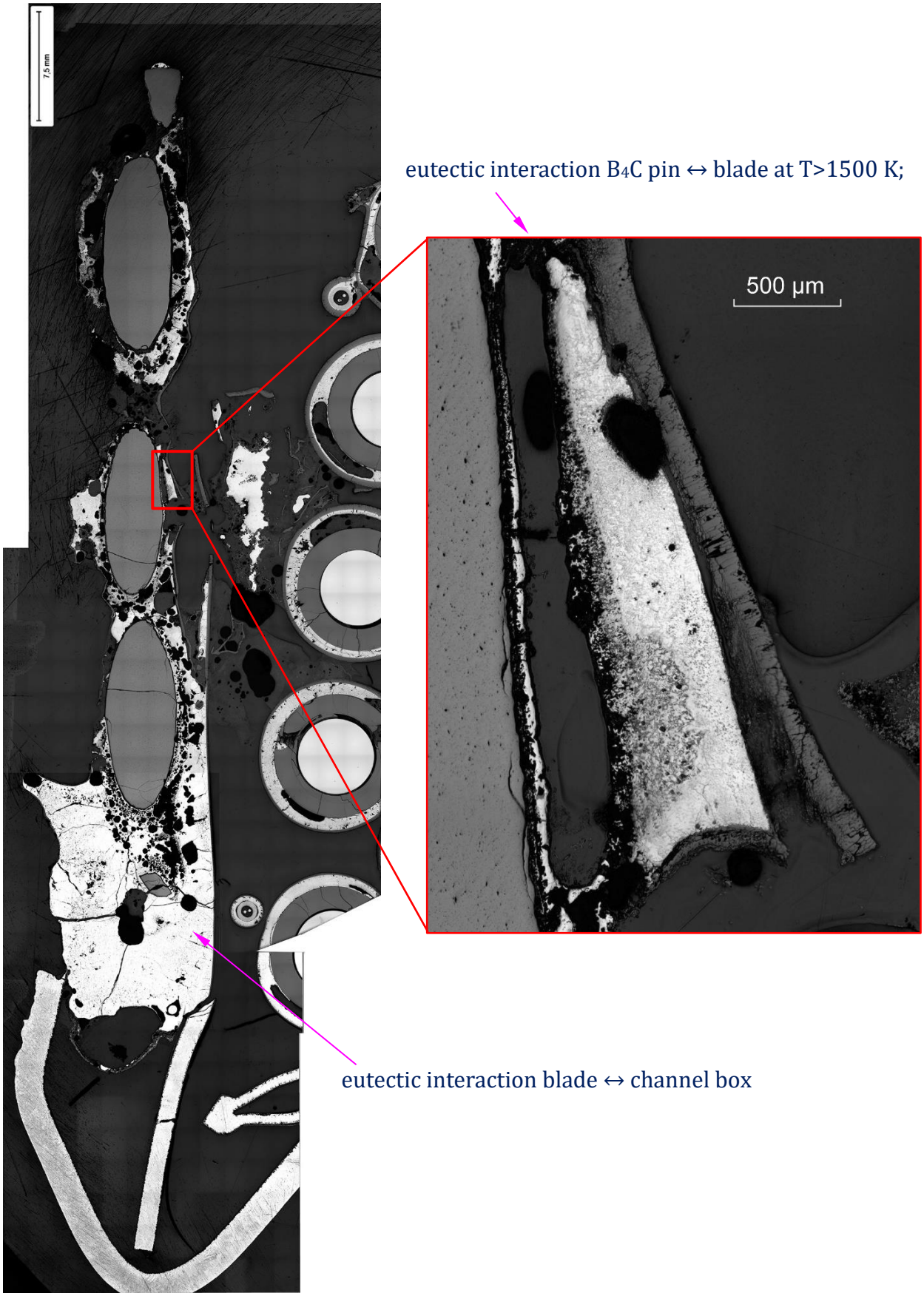

Figure 106 QUENCH-20; Interaction of stainless steel blade with B_4C and ZIRLO channel box at 750 mm.

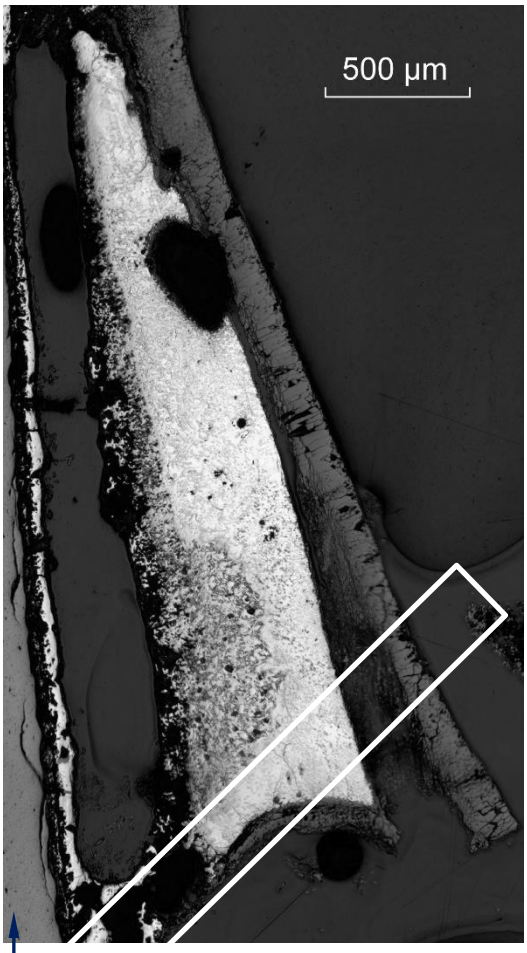

B_4C pin

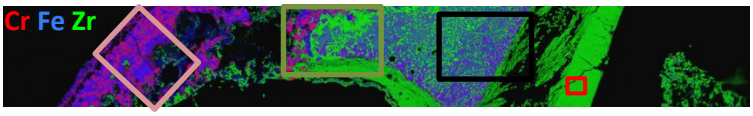

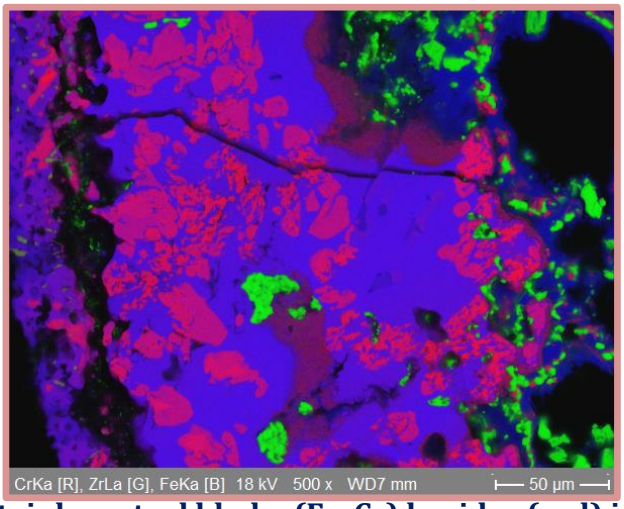

stainless steel blade: (Fe, Cr) borides (red) in steel melt (blue)

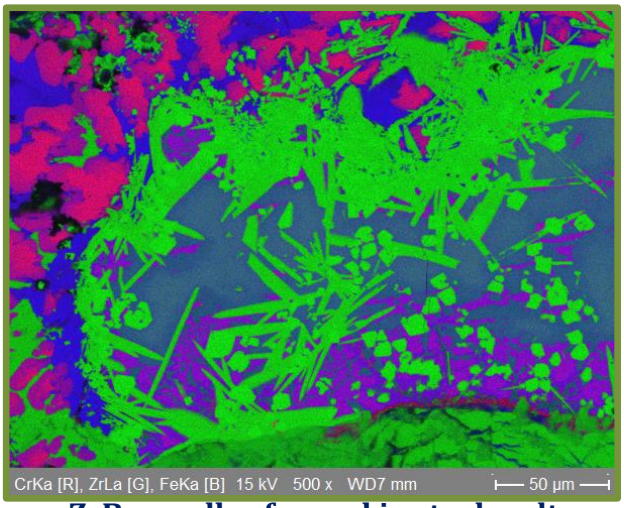

ZrB_2 needles formed in steel melt

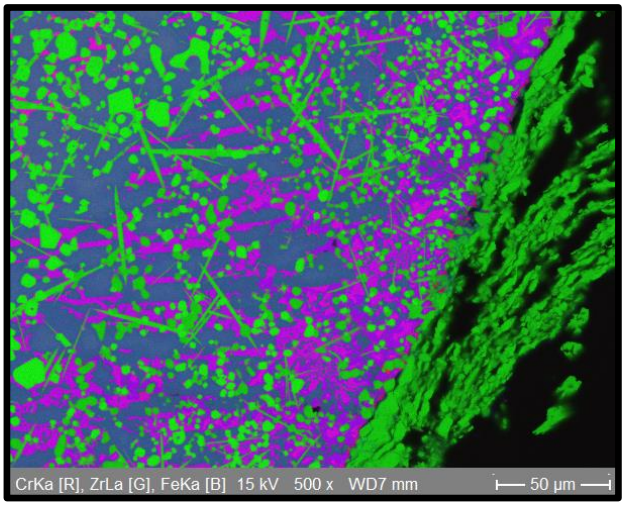

ZrB_2 needles formed in steel melt

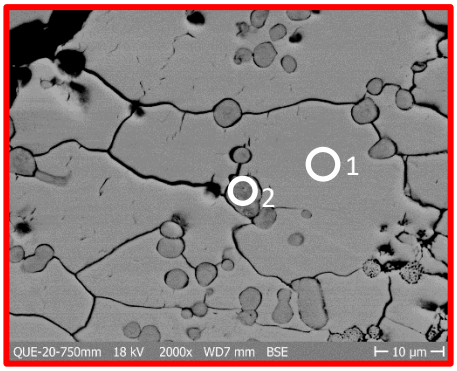

ZrO_2 layer: Spot1 O 80%, Zr 20%
Spot2 O 80%, Zr 20%

Figure 107 QUENCH-20; SEM/EDX investigation of interaction of B_4C with steel blade and ZIRLO channel box at 750 mm, formation of zirconium diboride needles in steel melt.

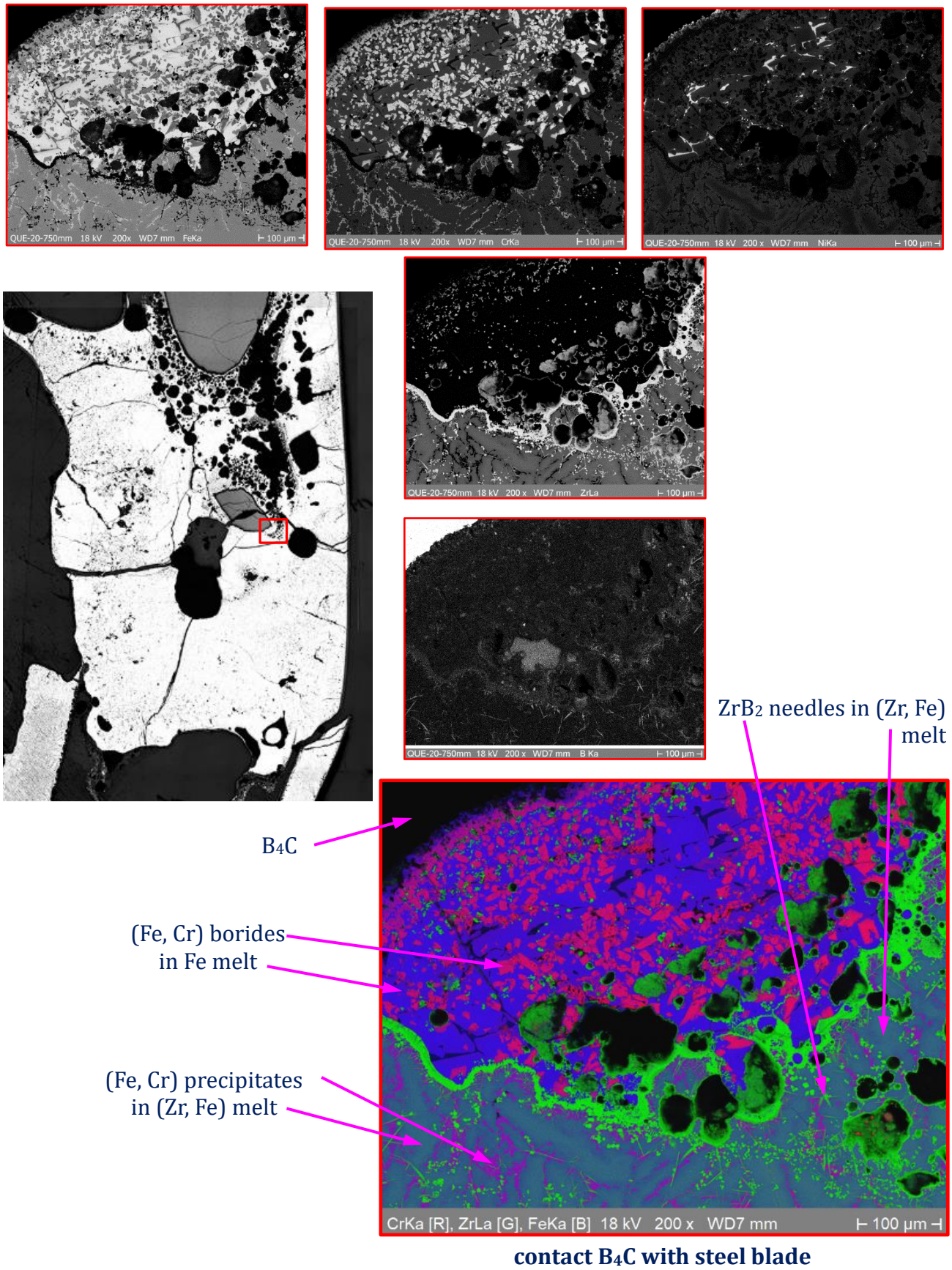

Figure 108 QUENCH-20; SEM/EDX investigation of interaction of B_4C with steel blade and ZIRLO channel box at 750 mm near to the rest of B_4C pin: mapping of different elements.

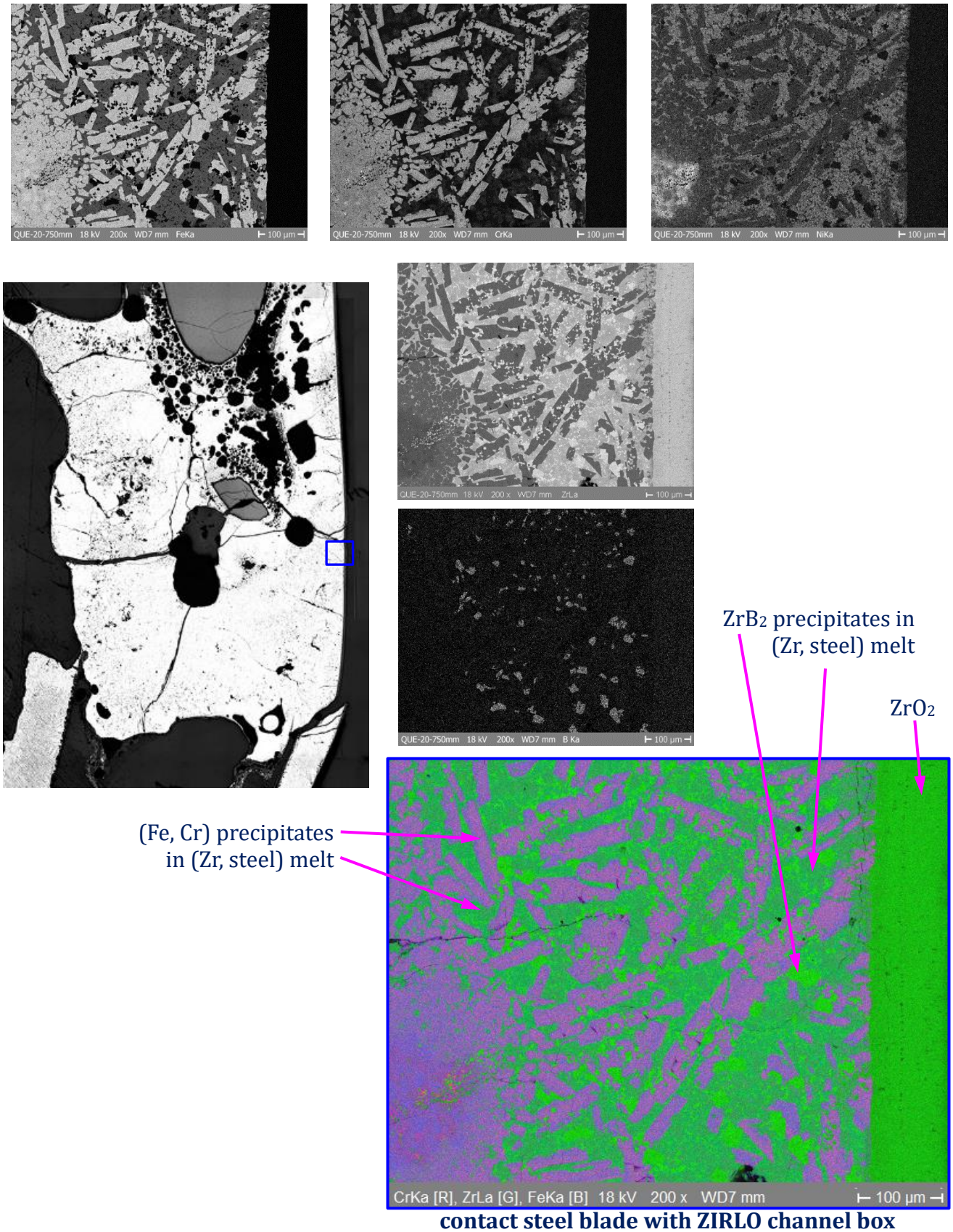

Figure 109 QUENCH-20; SEM/EDX investigation of interaction of B_4C with steel blade and ZIRLO channel box at 750 mm near to channel box: mapping of different elements.

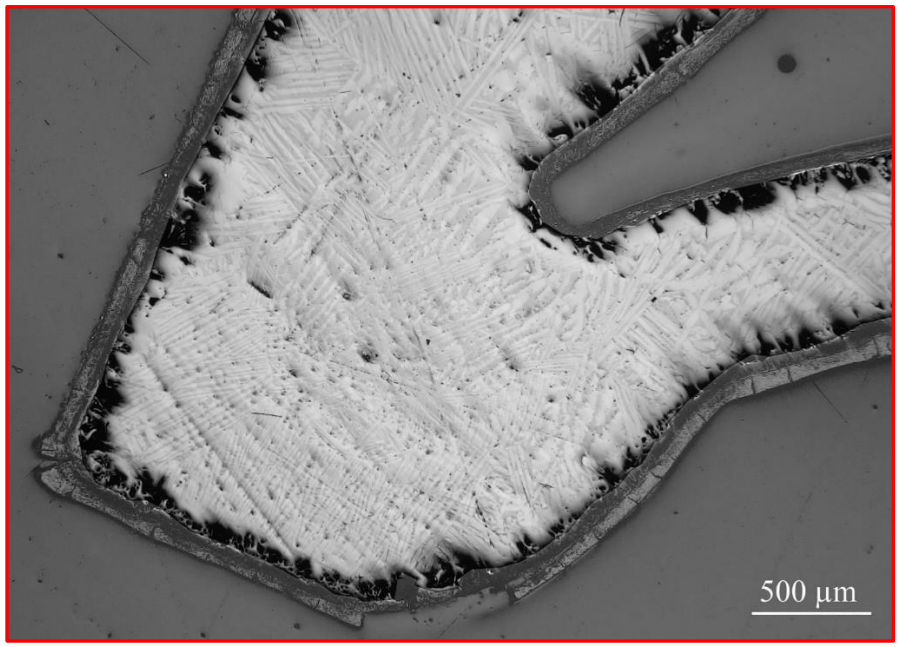

water wing; average thickness of oxide layer is 130 µm

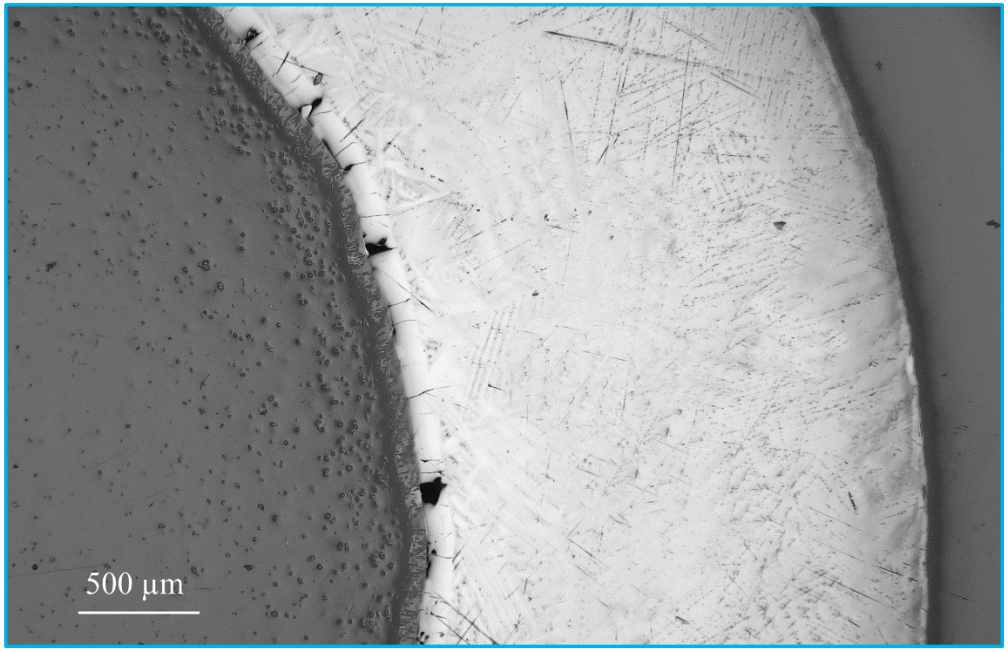

shroud; average thickness of oxide layer is 85 µm

Figure 110 QUENCH-20; Oxidation of water wings and shroud at 750 mm (left corner).

Figure 111 QUENCH-20; thicknesses of cladding layers at bundle elevation of 750 mm; for several rods, the outer ZrO_2 thickness is limited due to contact with the neighbor rod whereas the thickness of α-Zr(O) layer is limited either due to oxidized inner cladding surface or due to melting of β-Zr layer.

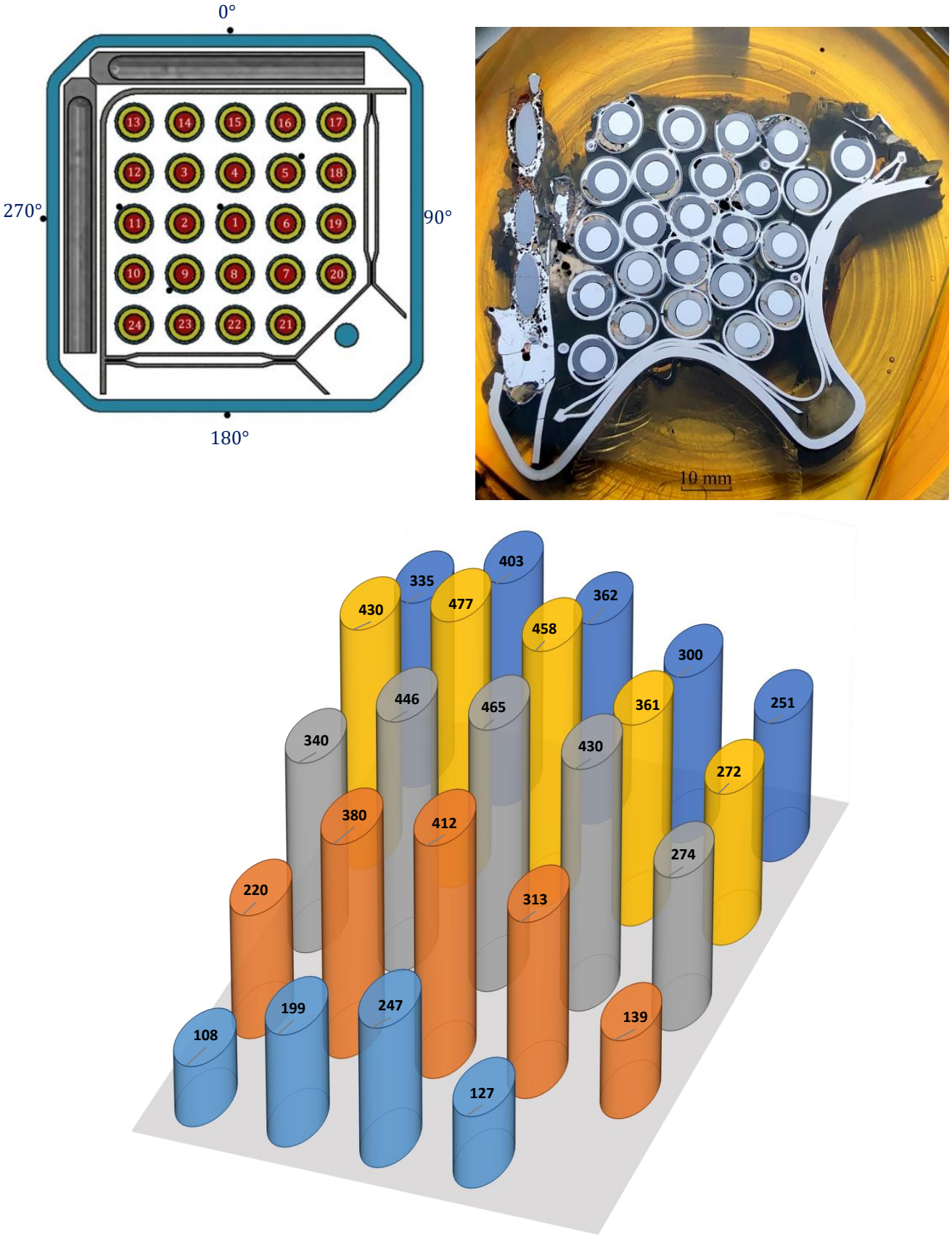

Figure 112 QUENCH-20; average thicknesses of outer ZrO_2 for each cladding at bundle elevation of 750 mm; indication of coldest bundle region at 180°.

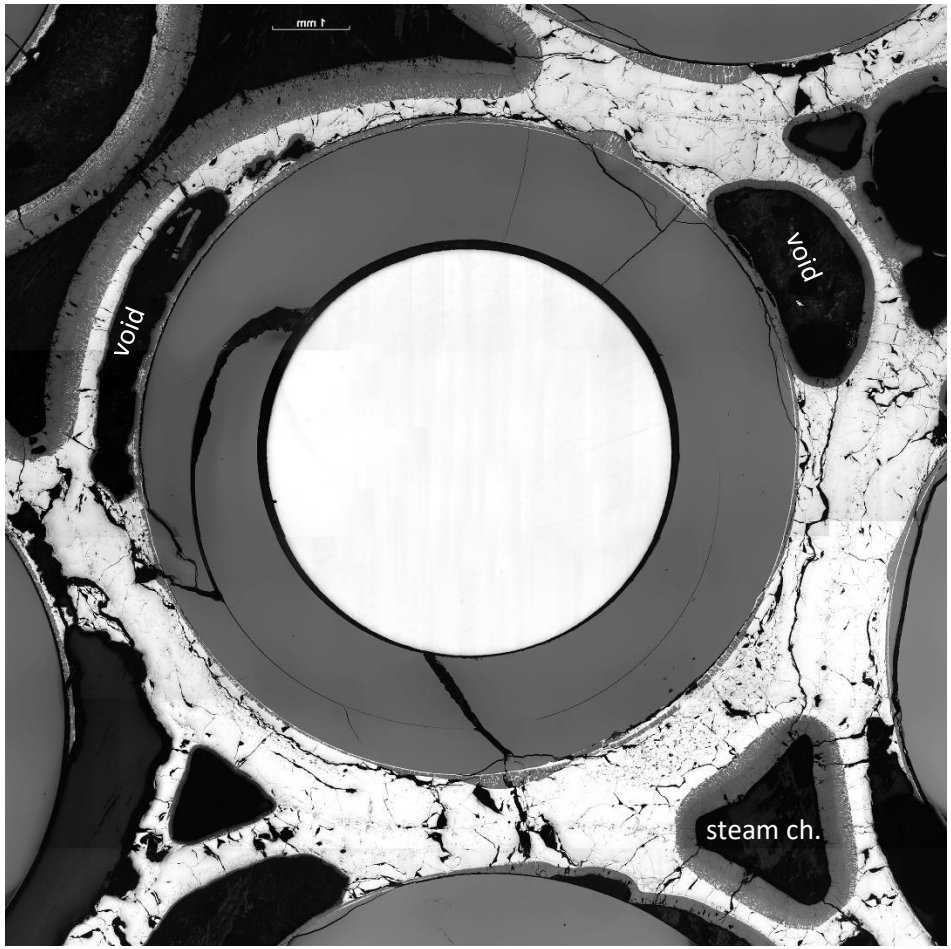

rod #1: interaction of Zr melt with outer α-Zr(O) layer and pellet; partial downwards relocation of melt (voids); formation of steam channels

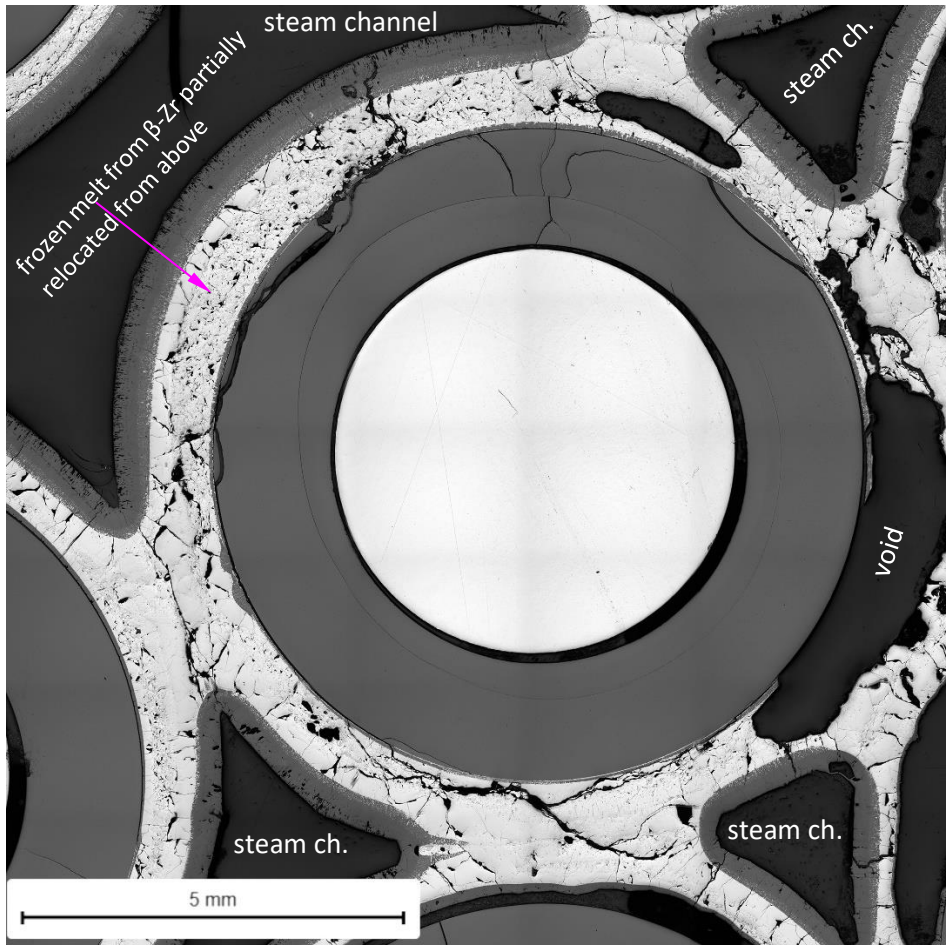

rod #2: interaction of Zr melt with outer α-Zr(O) layer and pellet; partial downwards relocation of melt (voids); formation of steam channels

Figure 113 QUENCH-20; Cladding oxidation and melting of rods #1 and #2 at bundle elevation 750 mm.

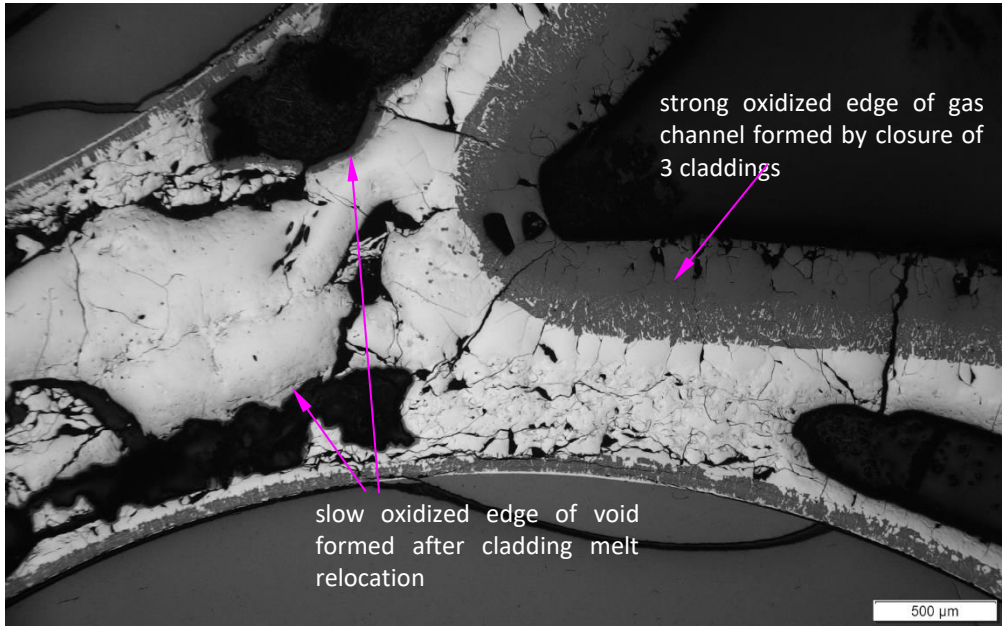

strong and slow oxidation of void edges at 45°

cladding microstructure at 315°

Figure 114 QUENCH-20; Microstructure of partially melted cladding of rod #2 at bundle elevation 750 mm.

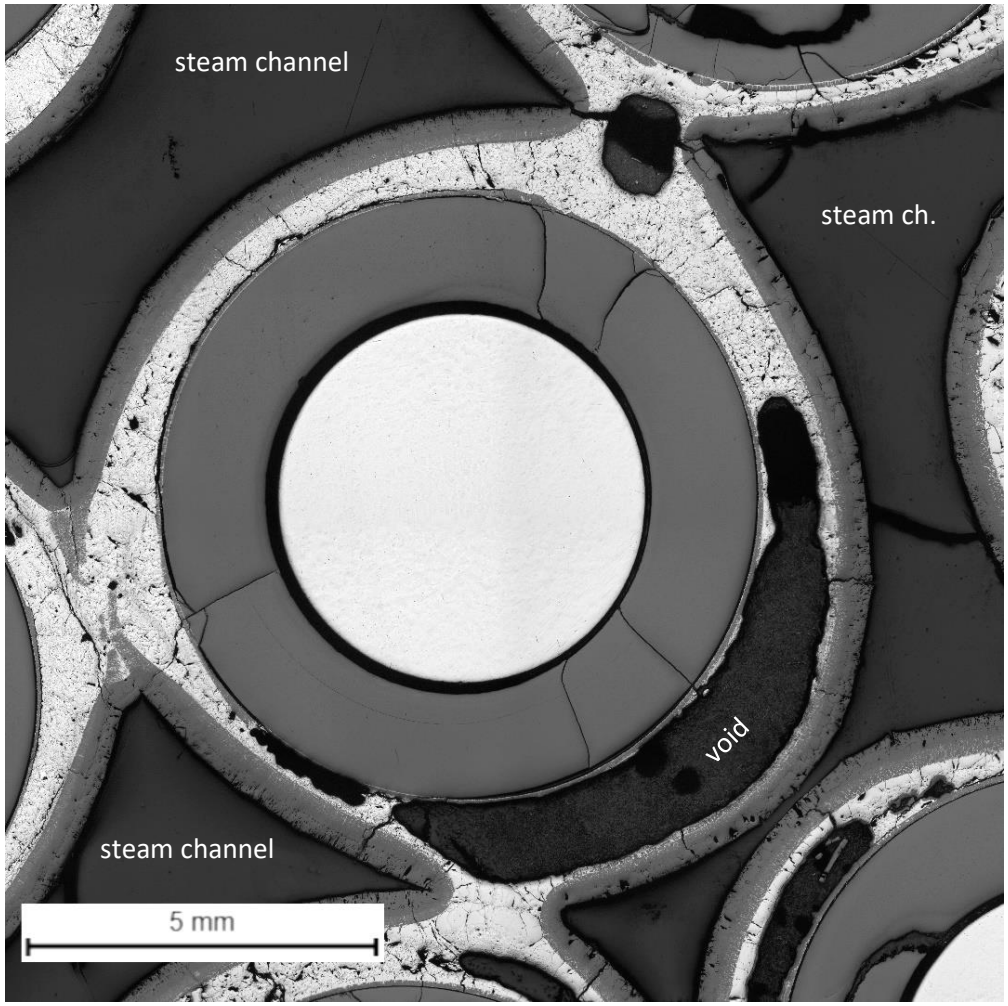

rod #3: interaction of Zr melt with outer oxide layer and pellet; partial downwards relocation of melt inside the rod(voids)

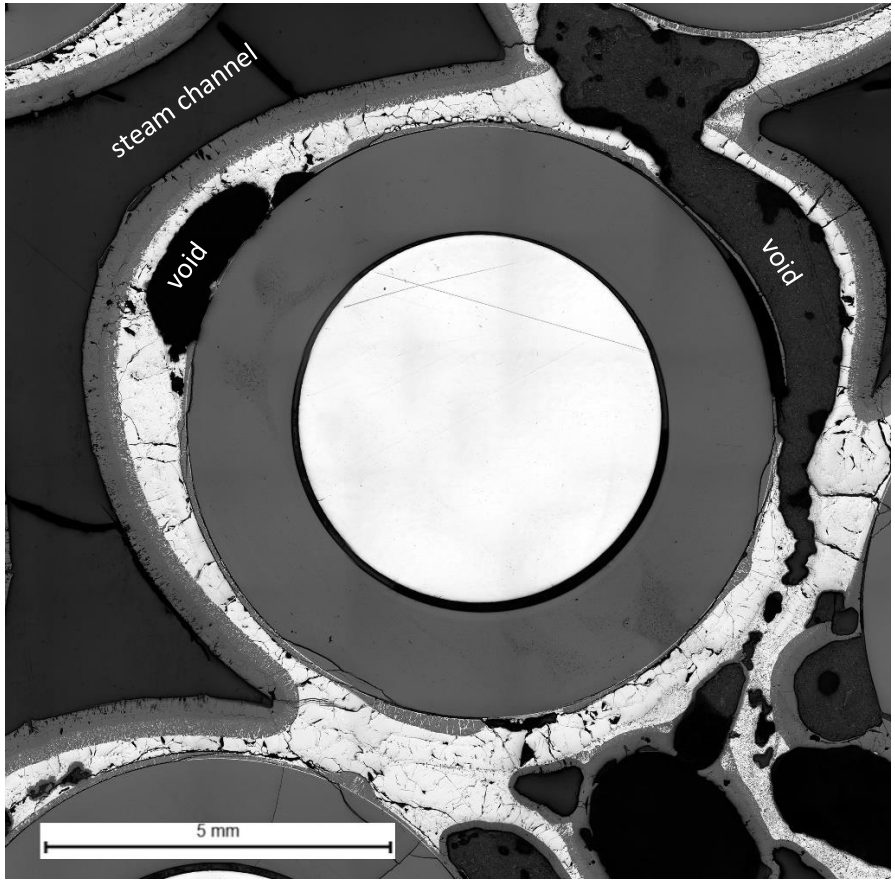

rod #4: interaction of Zr melt with outer α-Zr(O) layer and pellet; partial downwards relocation of melt (voids); formation of steam channels

Figure 115 QUENCH-20; Cladding oxidation and melting of rods #3 and #4 at bundle elevation 750 mm.

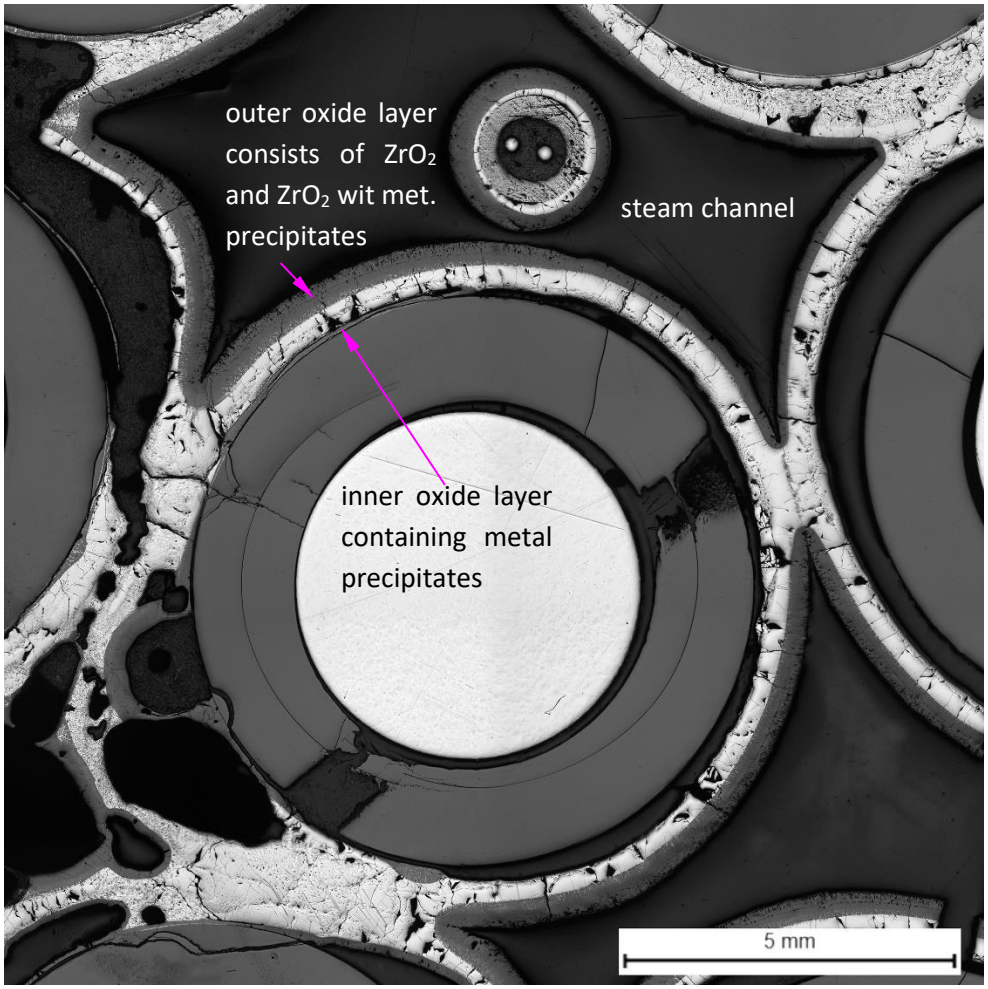

rod #5: cladding lift-off; interaction of Zr melt with outer oxide layer and pellet

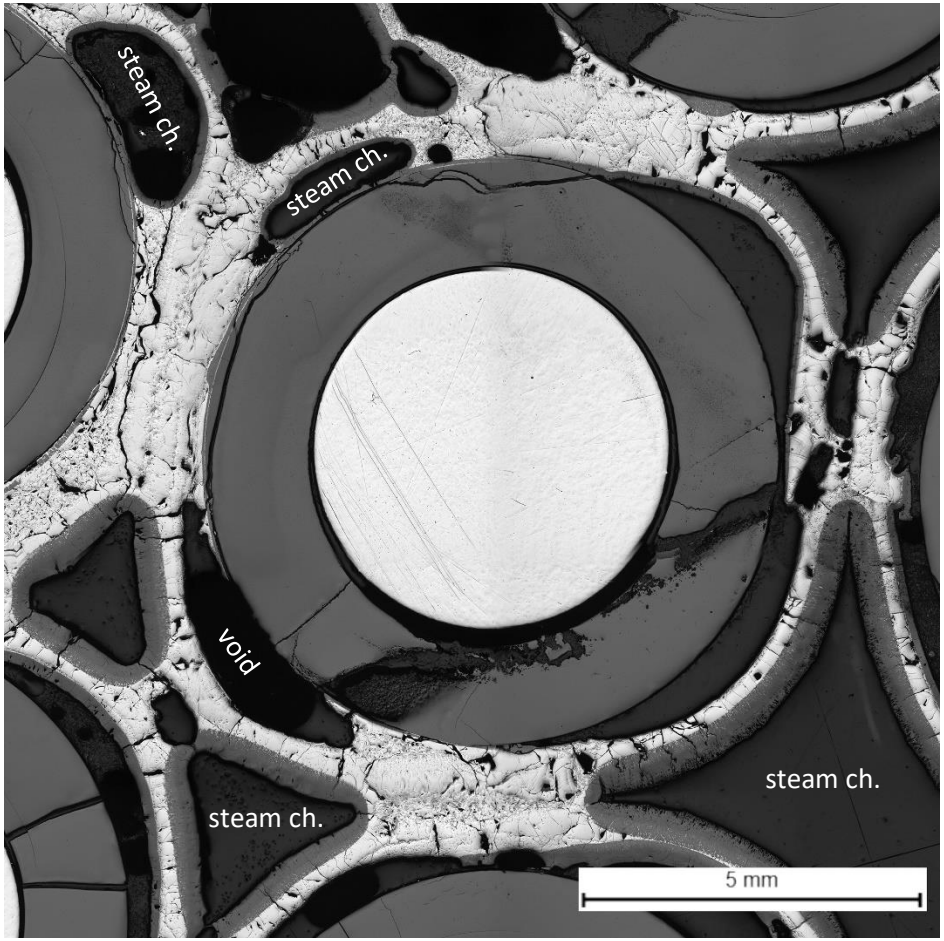

rod #6: cladding lift-off; partial downwards relocation of melt (voids); formation of steam channels

Figure 116 QUENCH-20; Cladding oxidation of rod #5 as well as oxidation and melting of rod #6 at bundle elevation 750 mm.

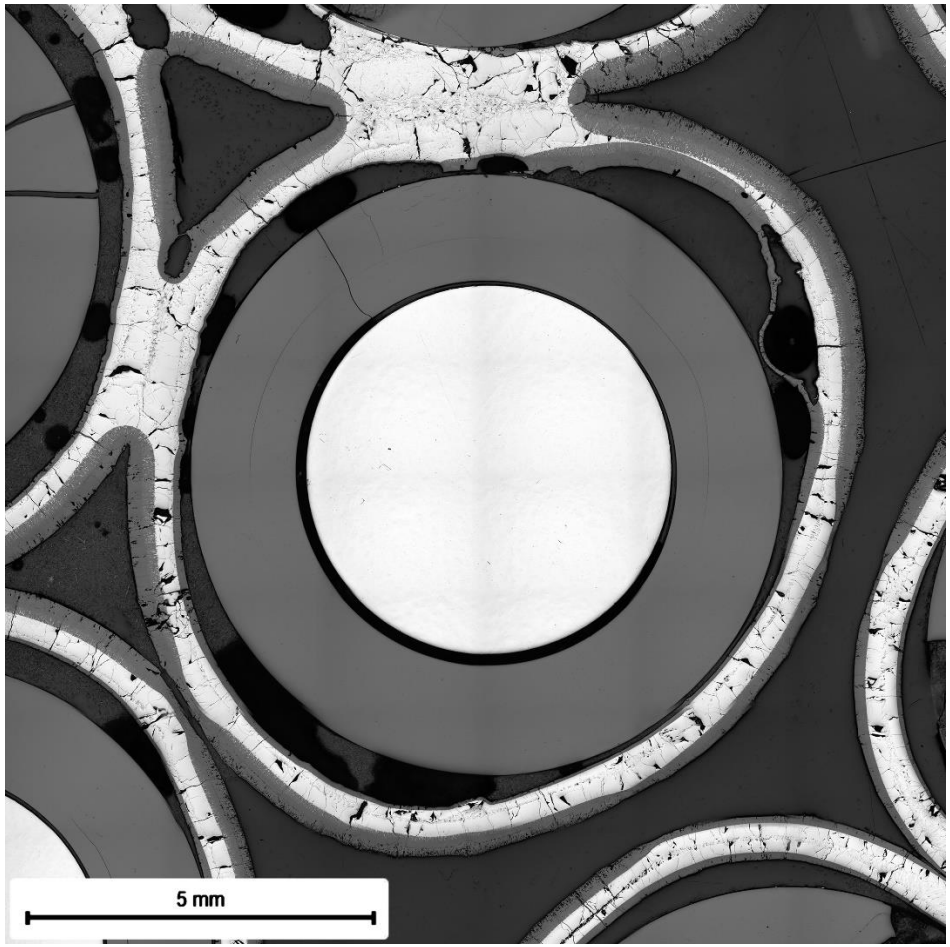

rod #7: cladding lift-off; outer and inner cladding oxidation

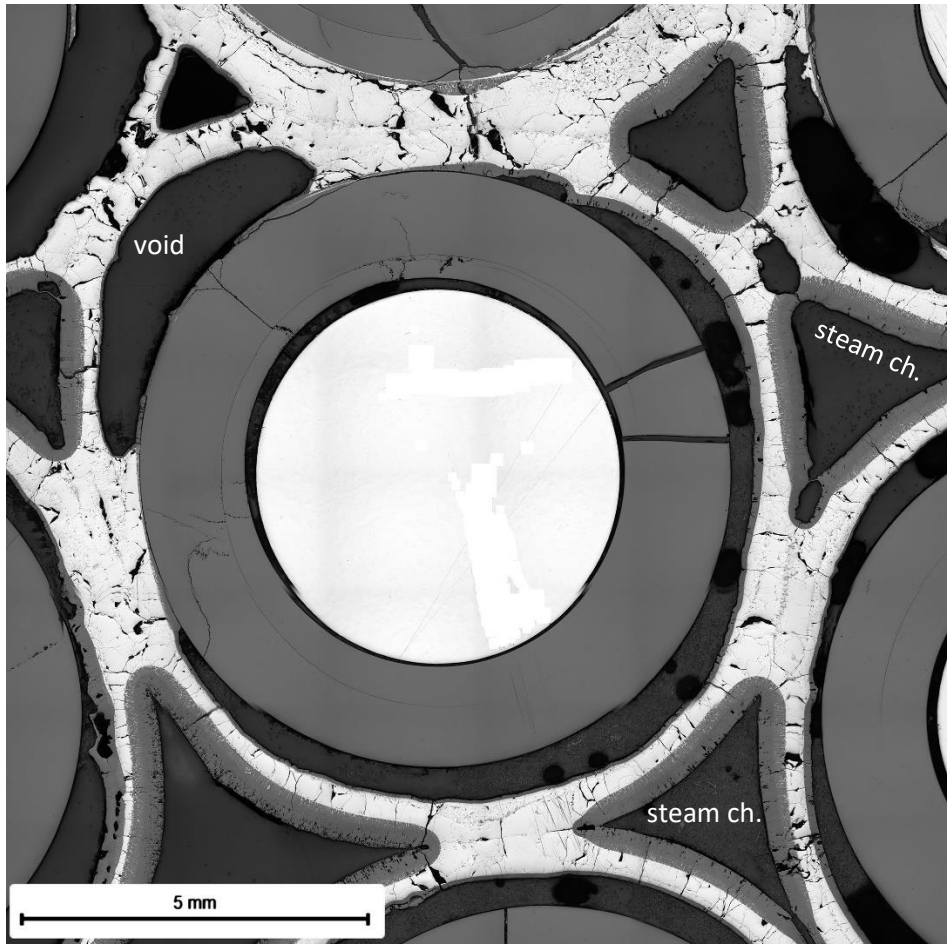

rod #8: cladding lift-off; partial downwards relocation of melt (void); formation of steam channels

Figure 117 QUENCH-20; Cladding oxidation and melting of rods #7 and #8 at bundle elevation 750 mm.

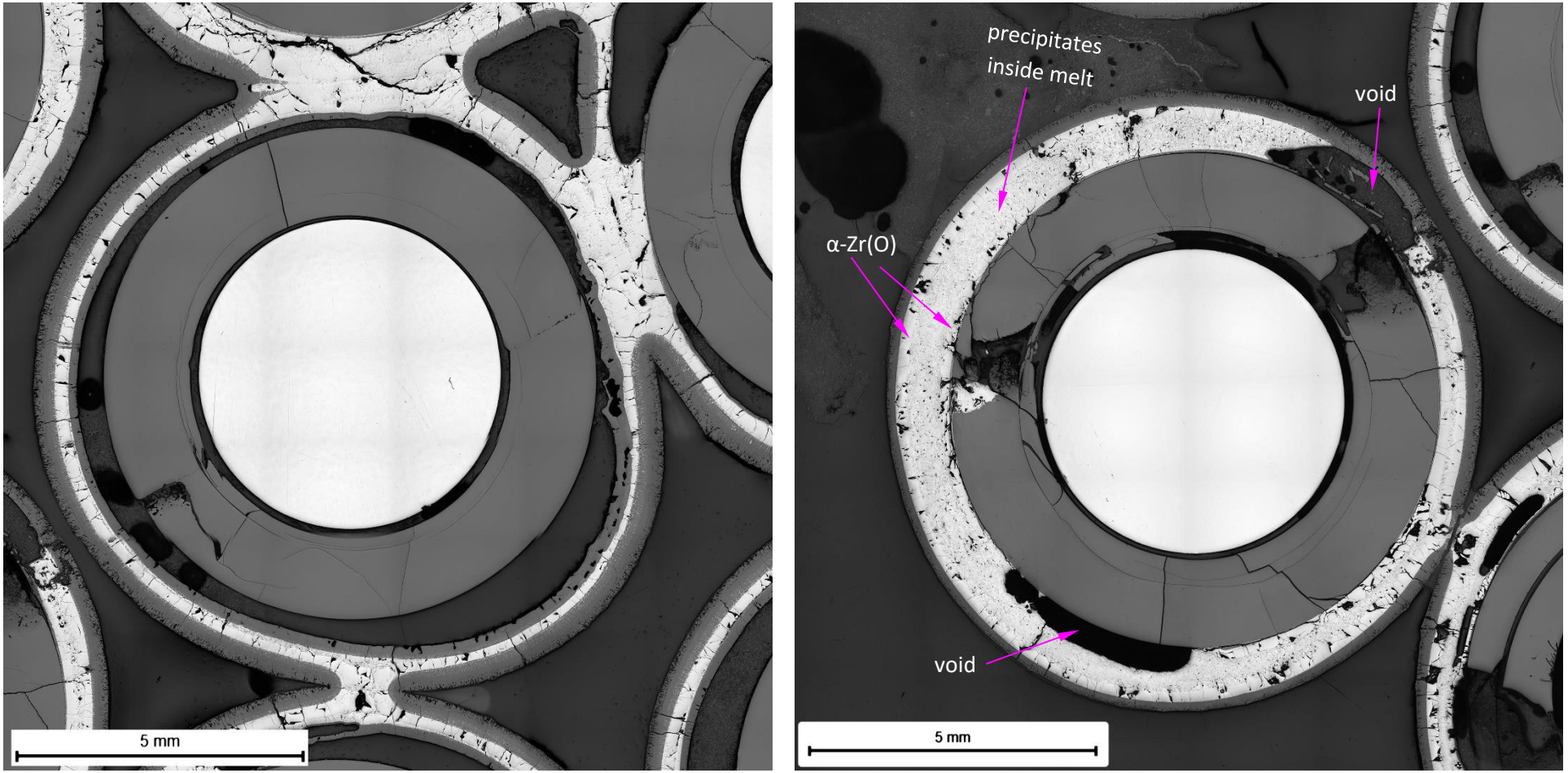

rod 9: cladding lift-off due to inner pressure

rod 10: frozen melt between oxide layer and pellet

Figure 118 QUENCH-20; Cladding oxidation and melting of rods #9 and #10 at bundle elevation 750 mm.

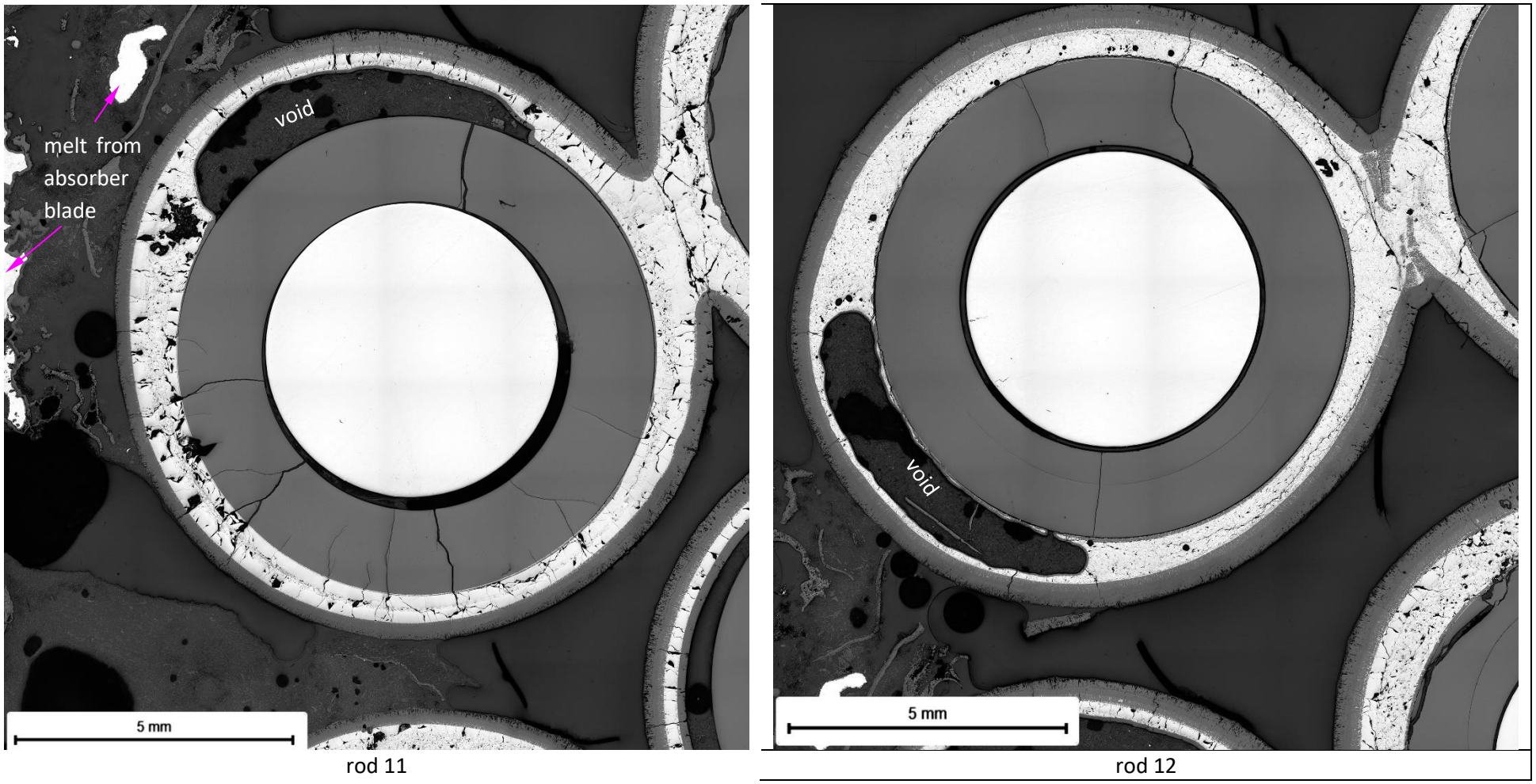

Figure 119 QUENCH-20; Cladding oxidation and melting of rods #11 and #12 at bundle elevation 750 mm.

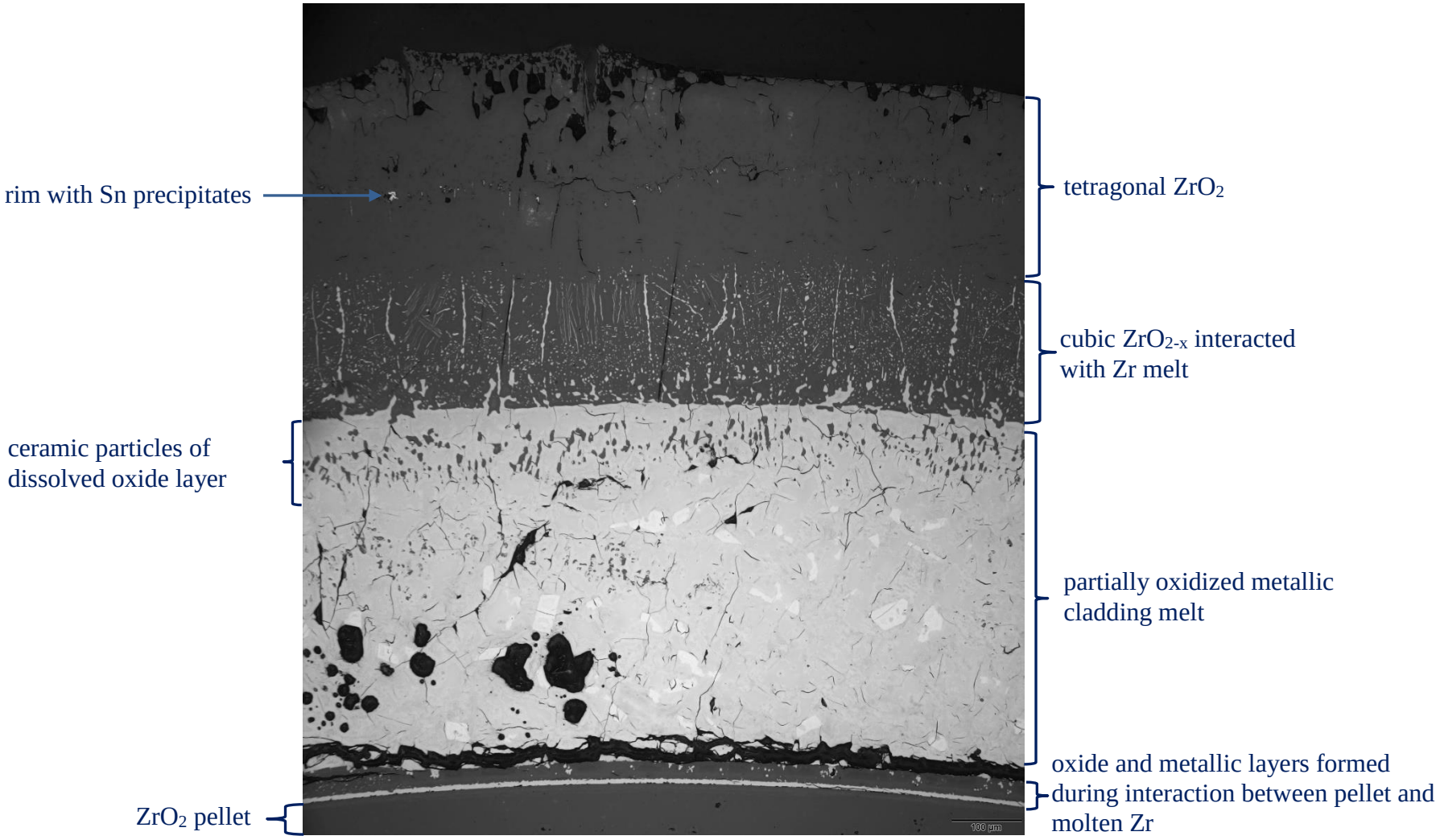

Figure 120 QUENCH-20; Microstructure of cladding (horizontally mirrored) for rod #12 at bundle elevation 750 mm, 0°.

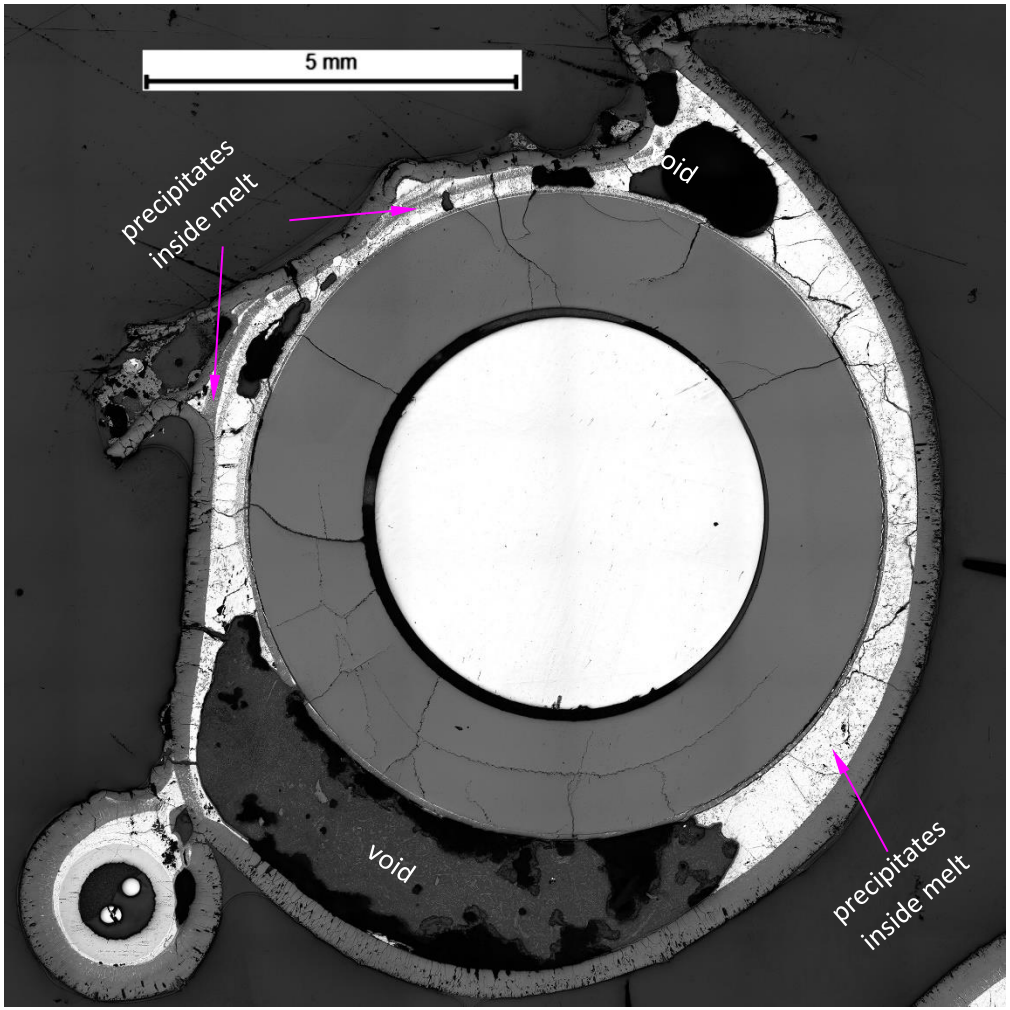

rod 13: ceramic precipitates inside metal melt

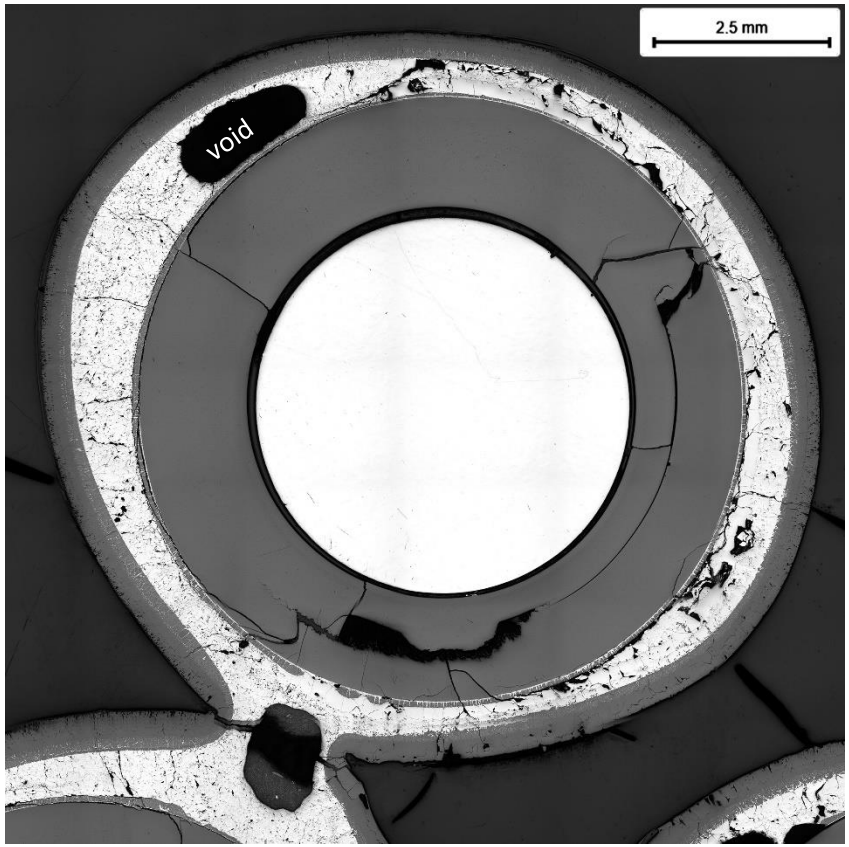

rod 14: metal melt between oxide layer and pellet

Figure 121 QUENCH-20; Cladding oxidation and melting of rods #13 and #14 at bundle elevation 750 mm.

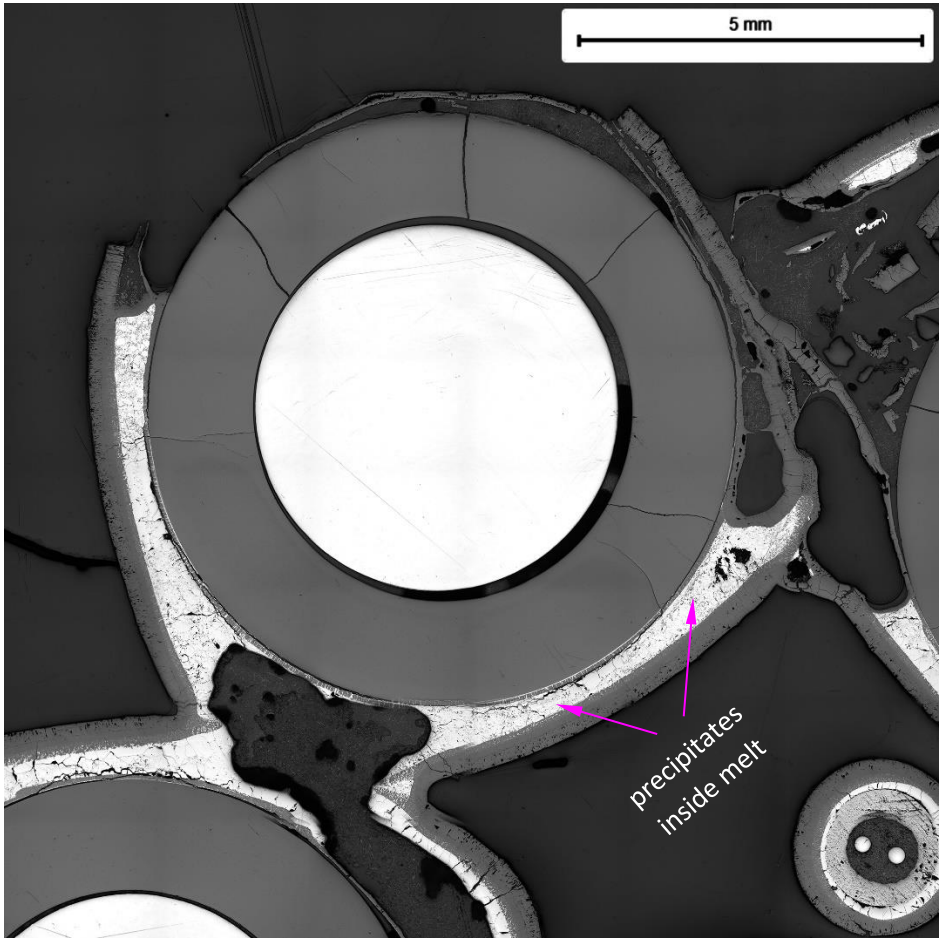

rod 15

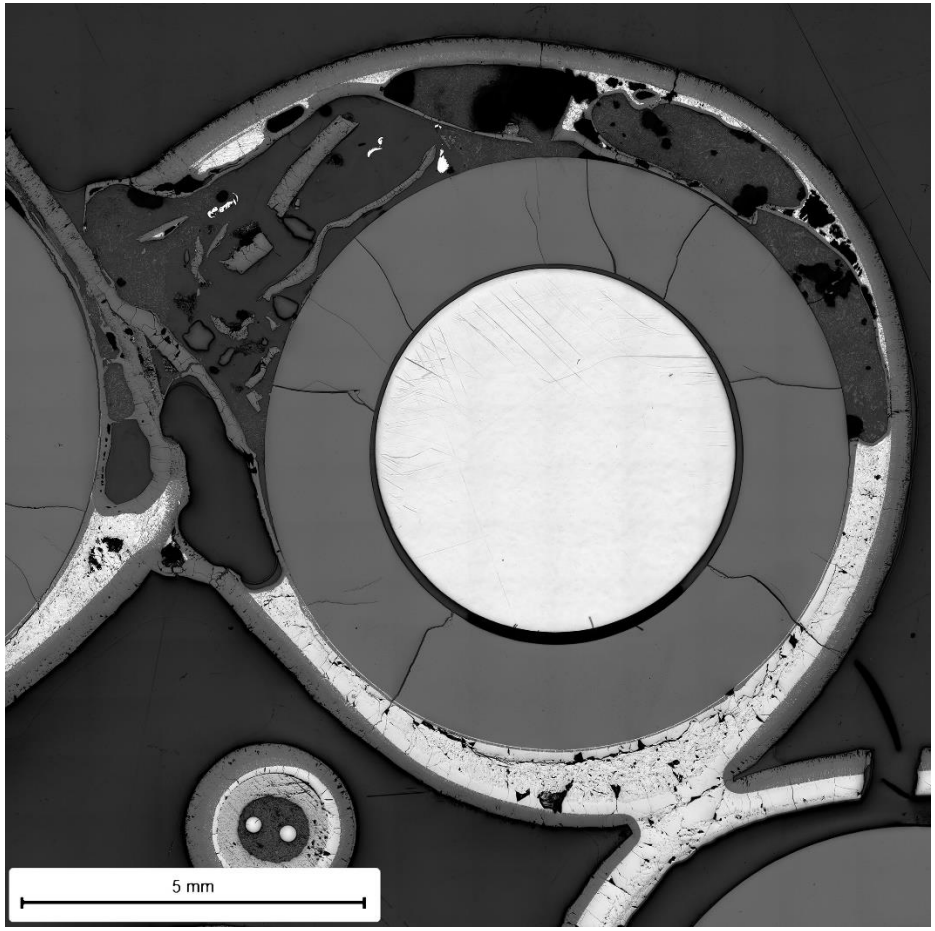

rod 16

Figure 122 QUENCH-20; Cladding oxidation and melting of rods #15 and #16 at bundle elevation 750 mm.

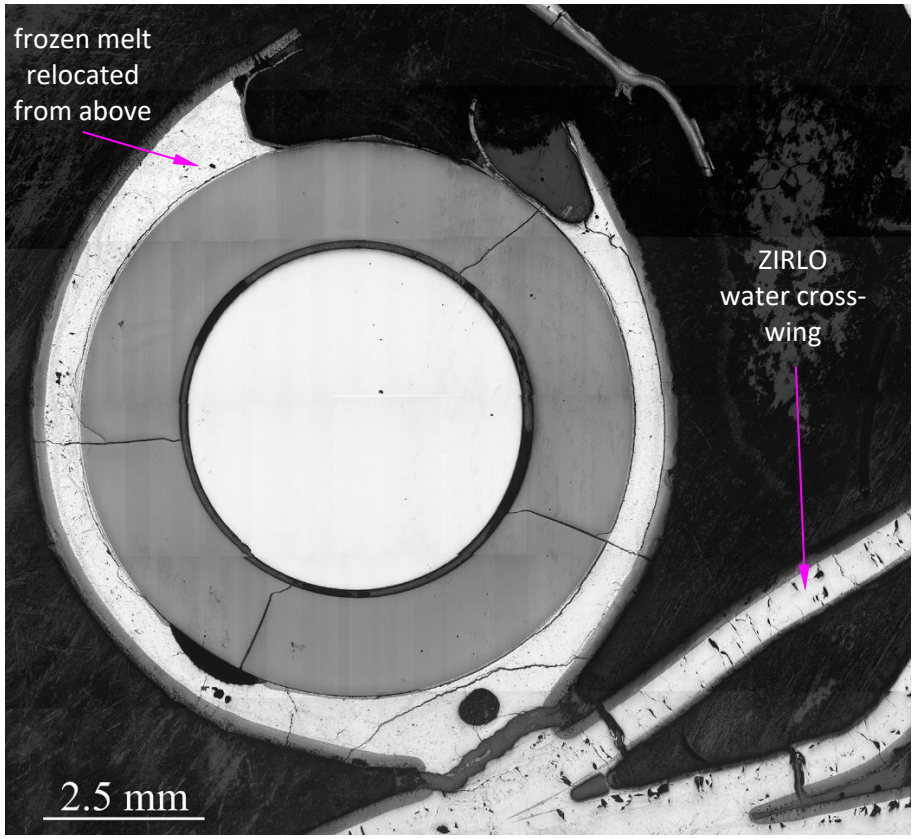

rod 17: significant cladding melting, frozen melt relocated from upper elevations

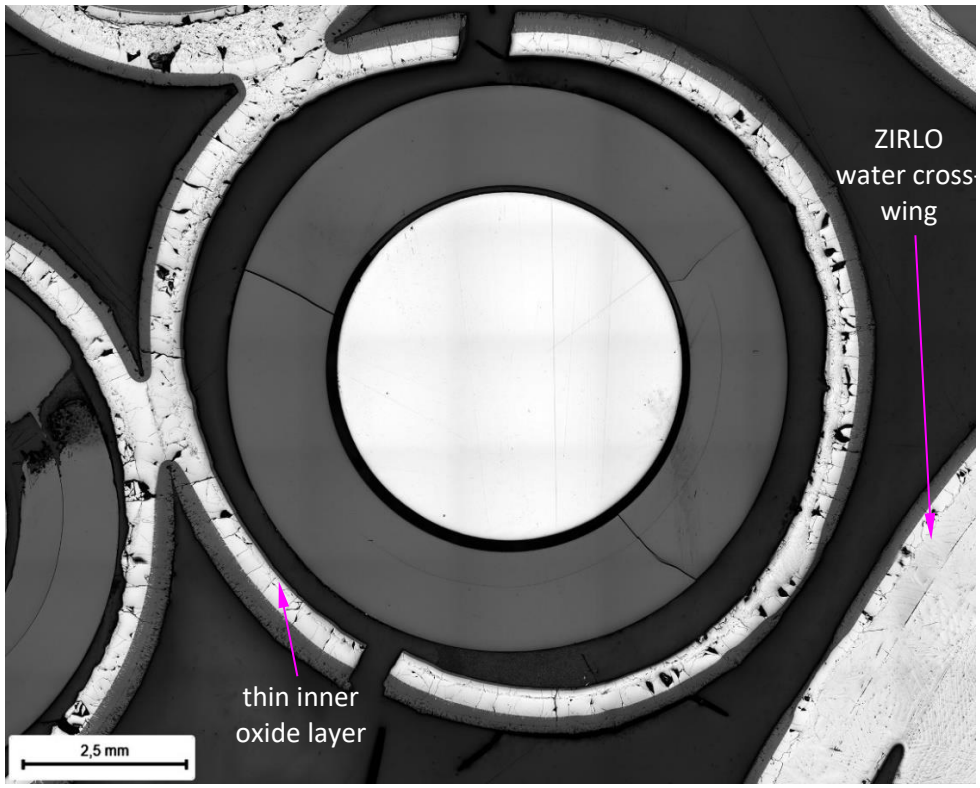

rod 18: cladding lift-off

Figure 123 QUENCH-20; Cladding oxidation and melting of rods #17 and #18 at bundle elevation 750 mm.

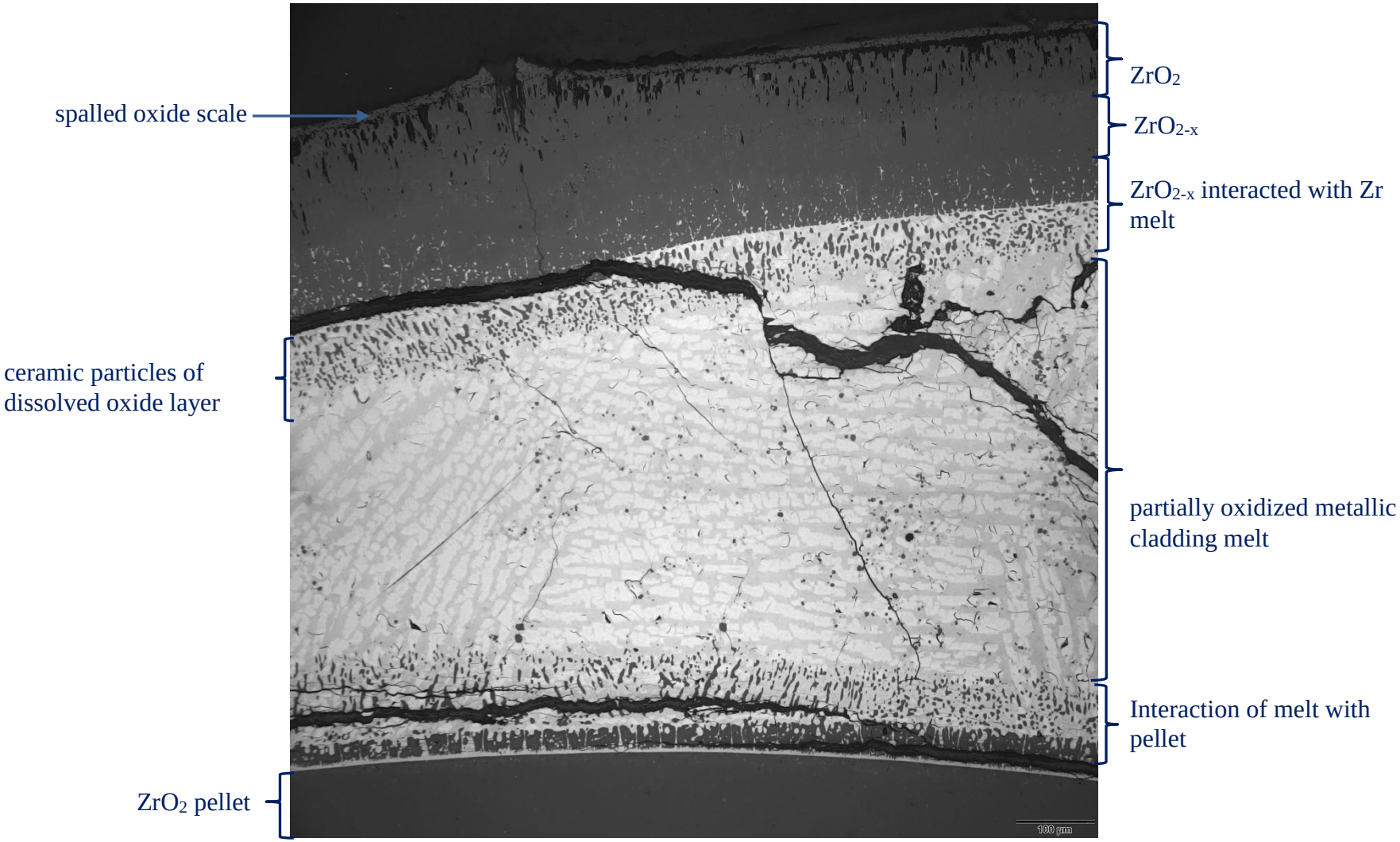

Figure 124 QUENCH-20; Microstructure of cladding for rod #17 at bundle elevation 750 mm, 45°: melt frozen between outer oxide and pellet.

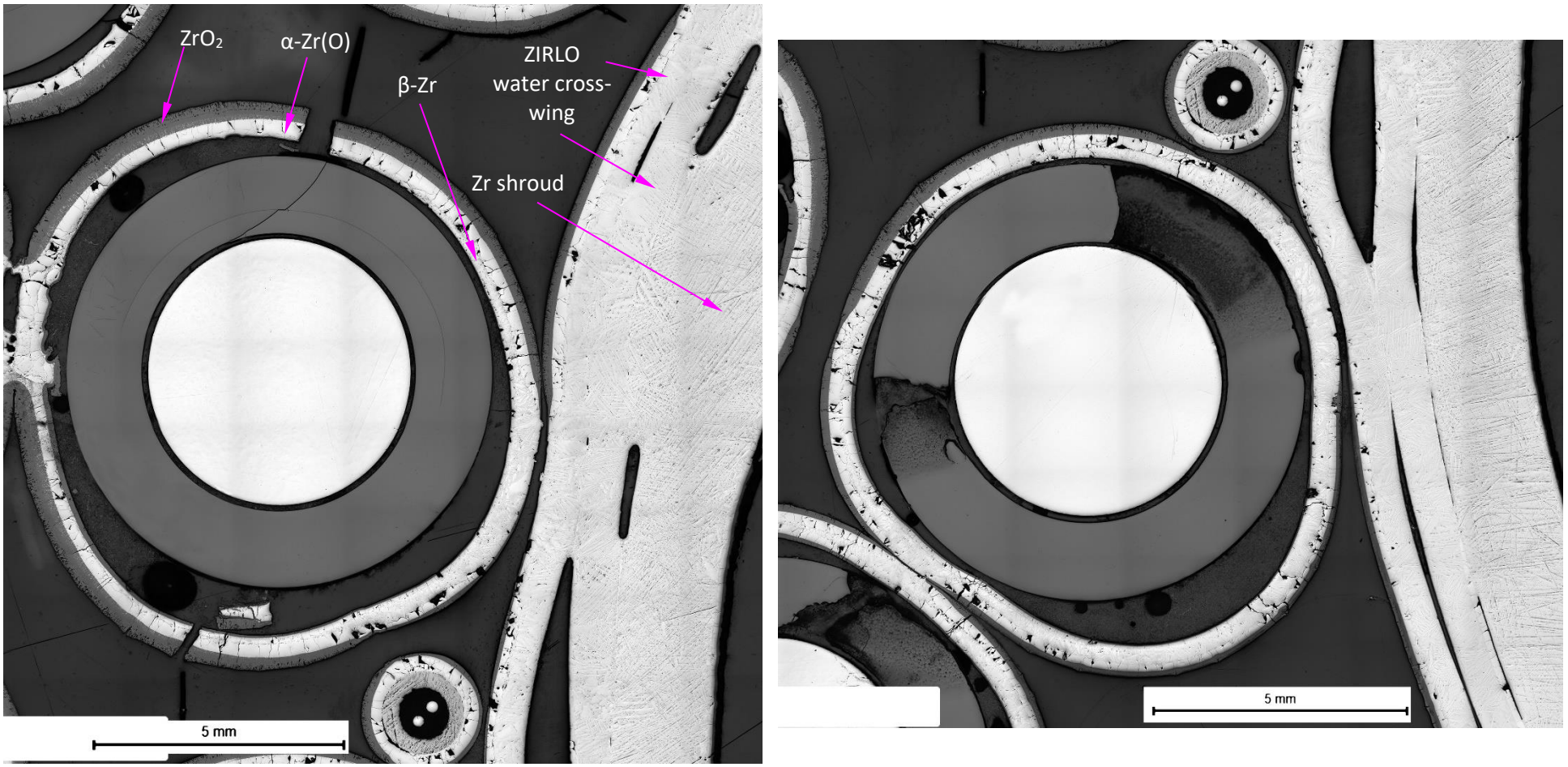

rod 19 rod 20

Figure 125 QUENCH-20; Cladding lift-off and oxidation of rods #19 and #20 at bundle elevation 750 mm.

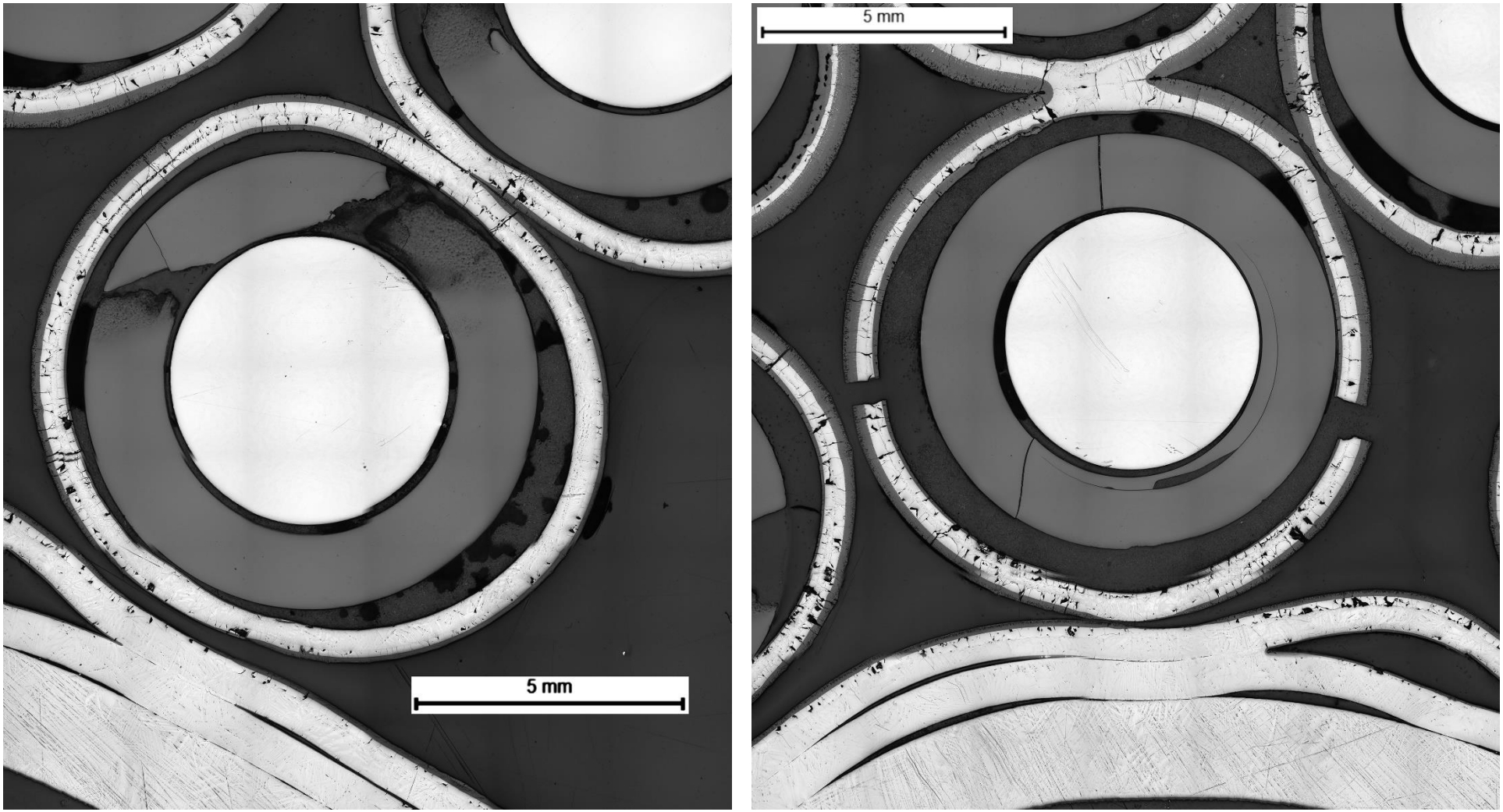

rod 21 rod 22

Figure 126 QUENCH-20; Cladding lift-off and oxidation of rods #21 and #22 at bundle elevation 750 mm.

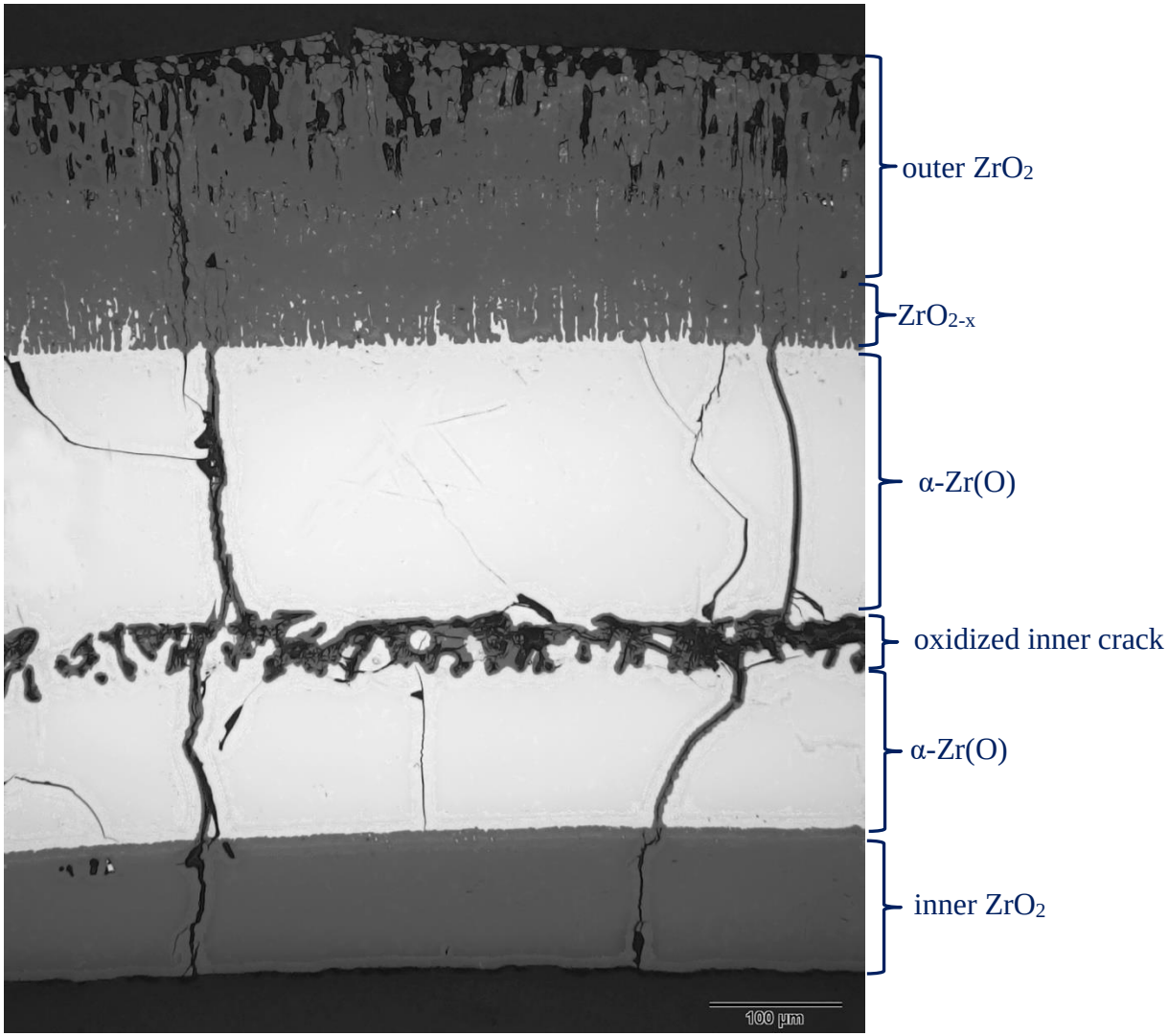

Figure 127 QUENCH-20; Microstructure of cladding for rod #21 at bundle elevation 750 mm, 315°: oxidation of cracks.

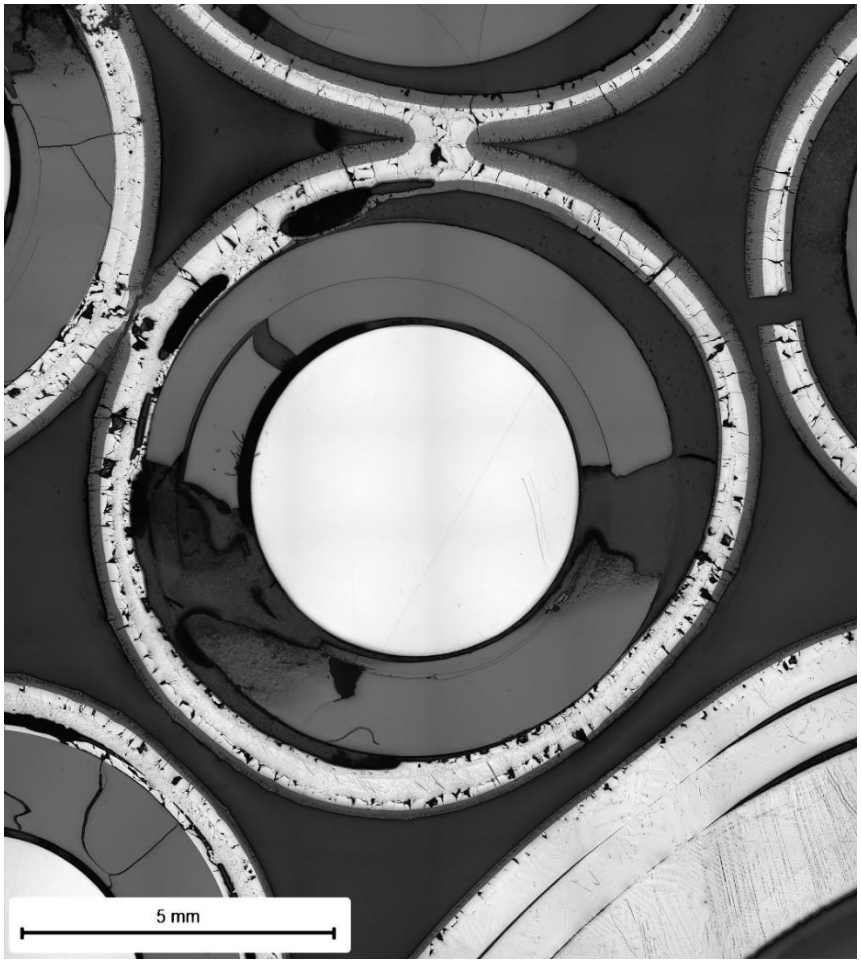

rod 23: cladding lift-off

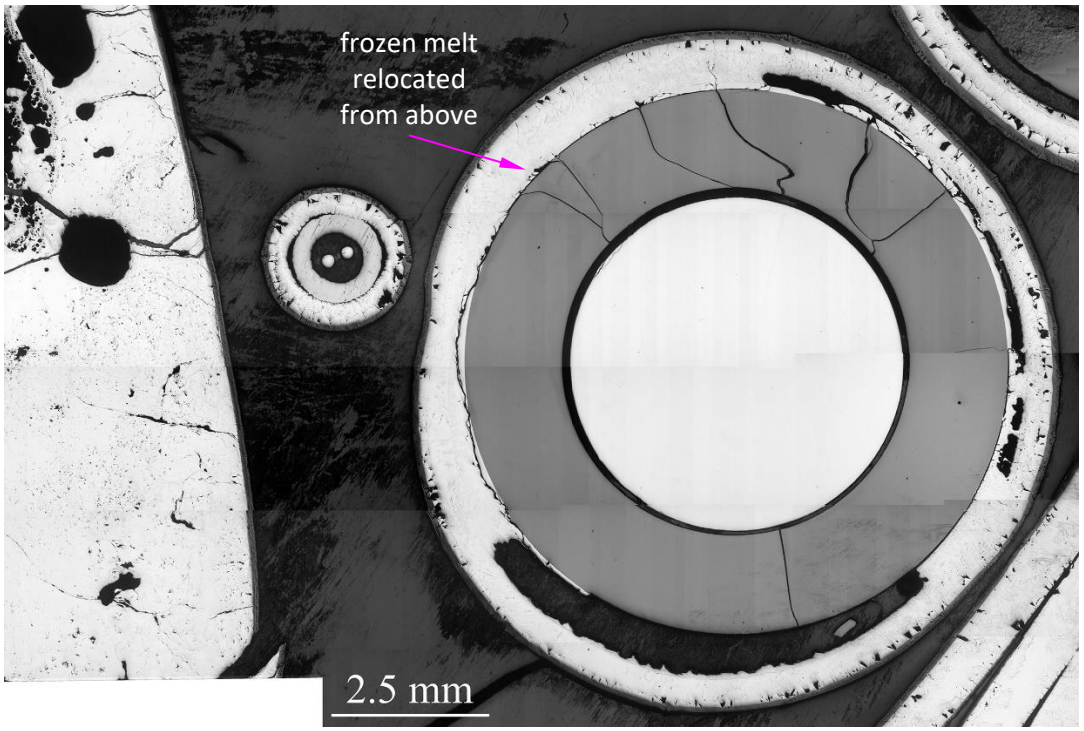

rod 24: frozen melt relocated from upper elevations, thin outer oxide layer

Figure 128 QUENCH-20; Cladding oxidation and melting of rods #23 and #24 at bundle elevation 750 mm.

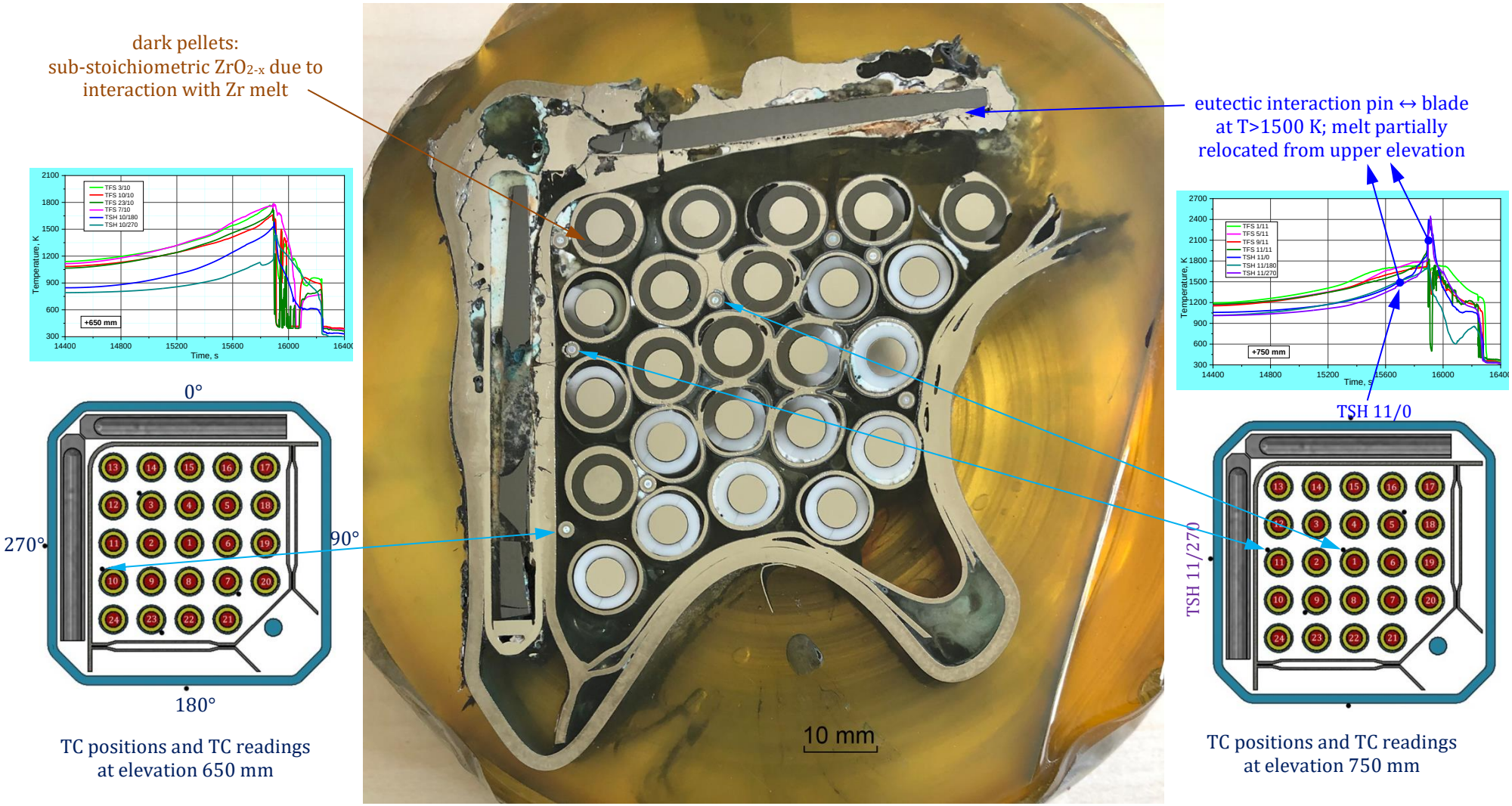

Figure 129 QUENCH-20; Bundle cross section at the elevation of 650 mm; influence of higher temperatures in the bundle centre (melting of cladding inner β-Zr layer) and at the shroud position of 0° (eutectic interaction B_4C pin with stainless steel blade); dark pellets correspond to sub-stoichiometric ZrO_{2-x} formed due to oxygen transport from pellet to surrounding melt.

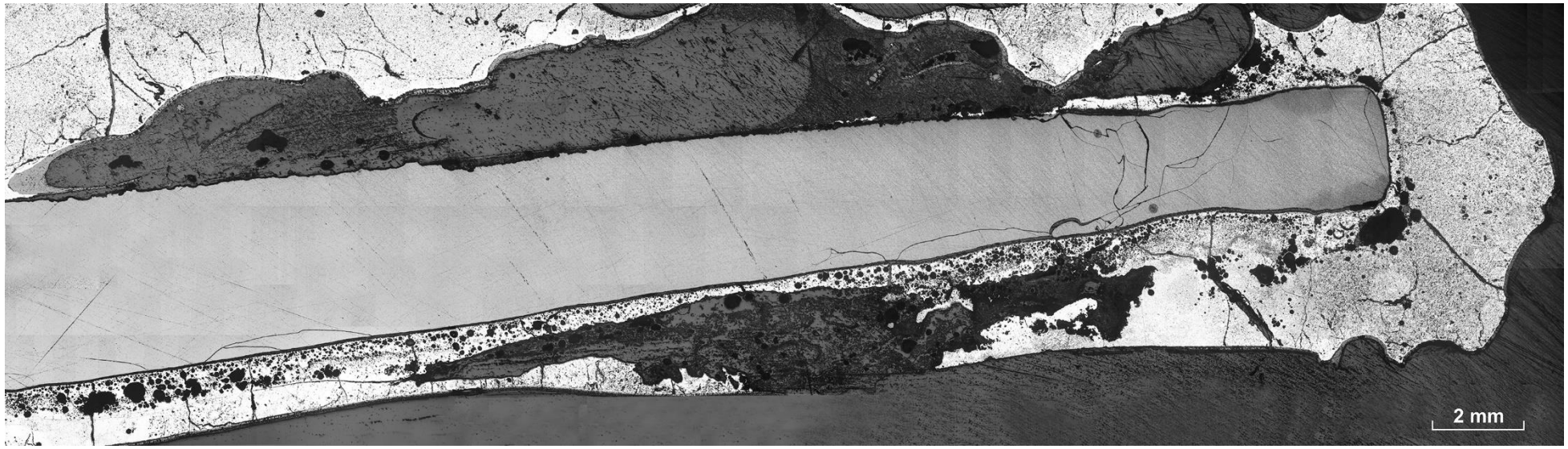

Figure 130 QUENCH-20; interaction of B_4C pin with stainless steel blade and channel box at elevation 650 mm and bundle azimuth 0° (right side of B_4C pin).

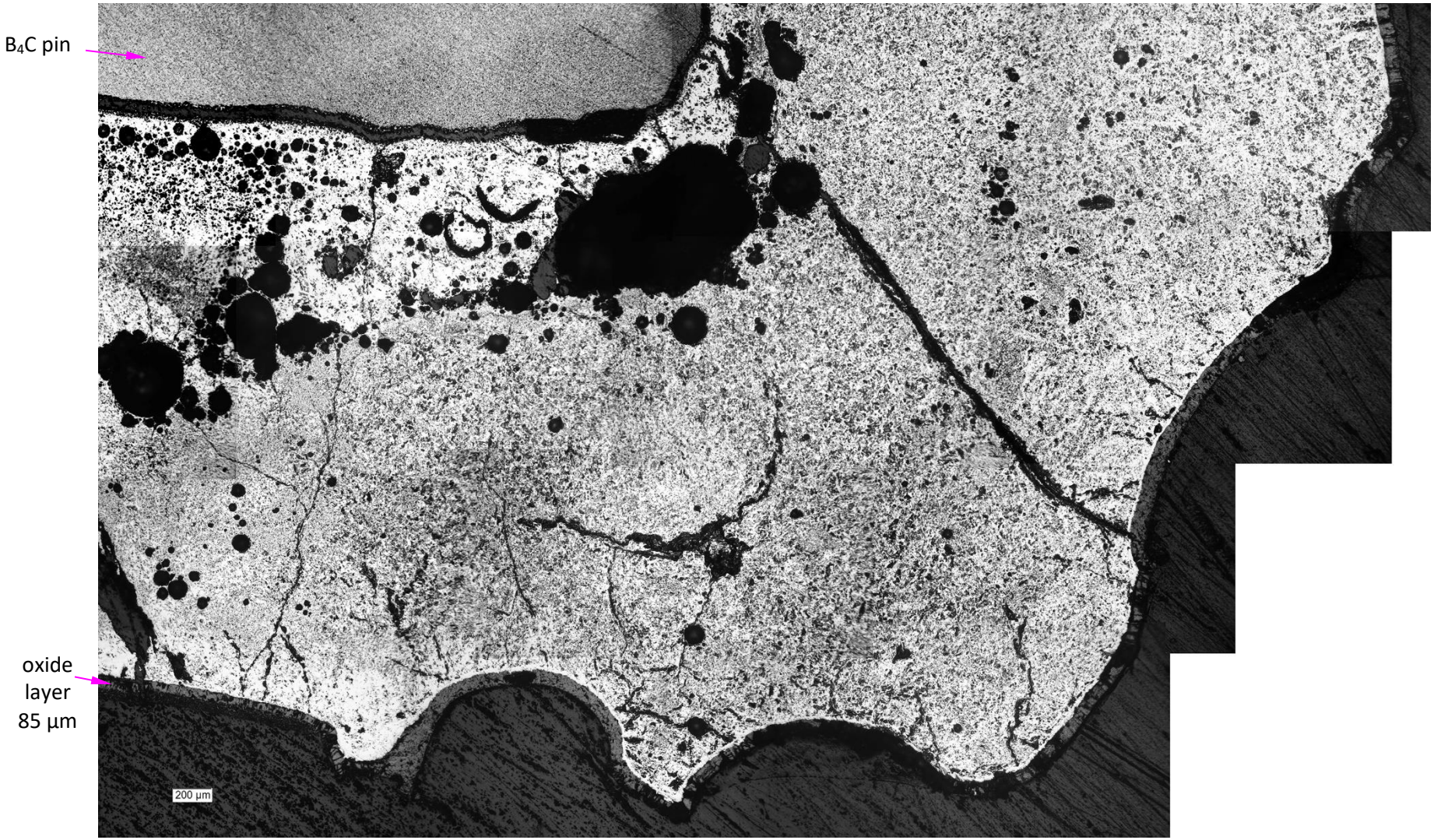

Figure 131 QUENCH-20; interaction of stainless steel blade and channel box at elevation 650 mm and bundle azimuth 0° (right side of B_4C pin).

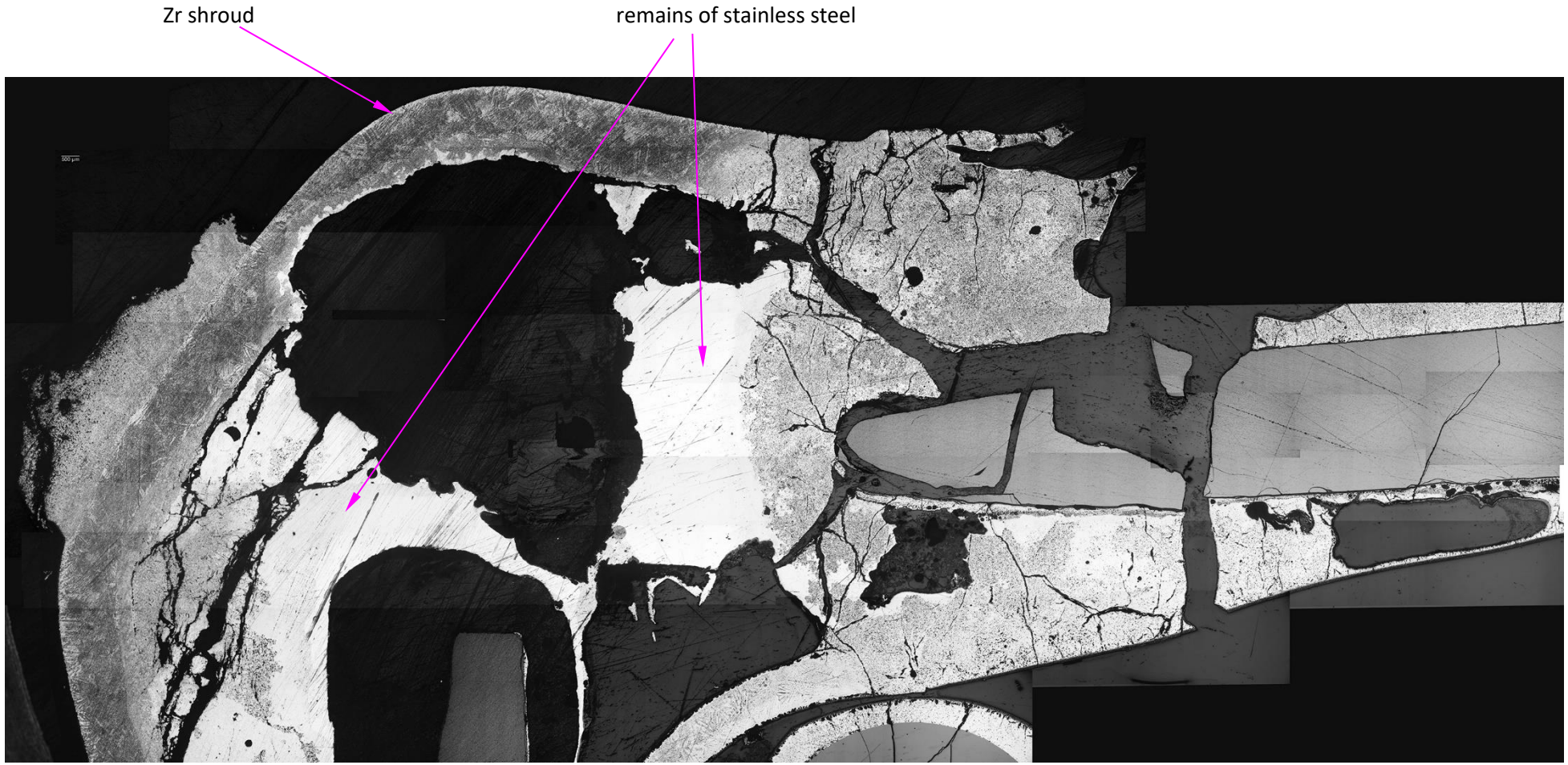

Figure 132 QUENCH-20; interaction of stainless steel blade with ZIRLO channel box and shroud at elevation 650 mm and bundle azimuth 0° (left side of B_4C pin).

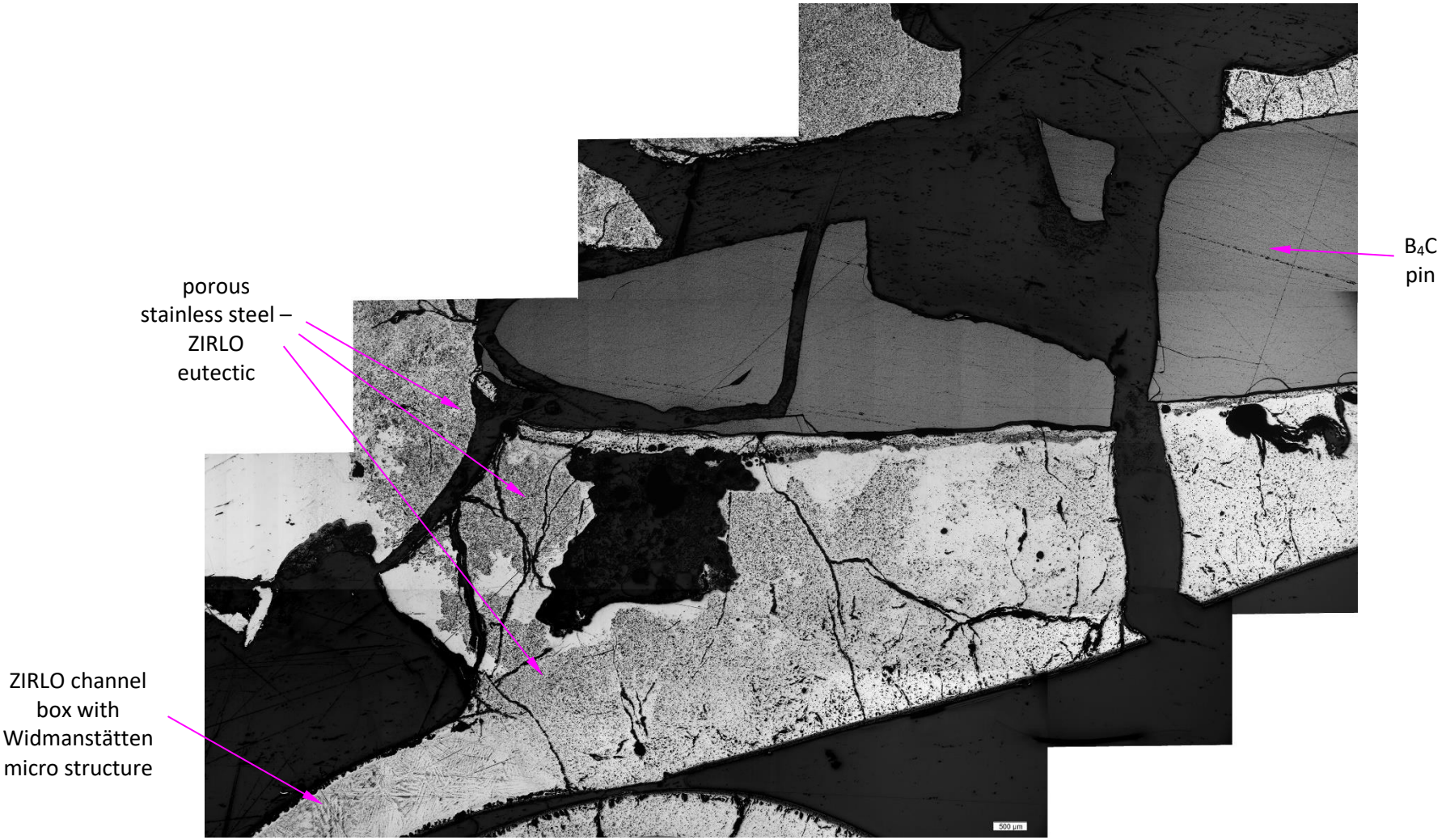

Figure 133 QUENCH-20; interaction of stainless steel blade with ZIRLO channel box at elevation 650 mm and bundle azimuth 0°.

Figure 134 QUENCH-20; thicknesses of outer ZrO_2 and outer α-Zr(O) layers at bundle elevation of 650 mm; for several rods, the outer ZrO_2 thickness is limited due to contact with the neighbor rod whereas the thickness of α-Zr(O) layer limited either due to oxidized inner cladding surface or due to melting of β-Zr layer.

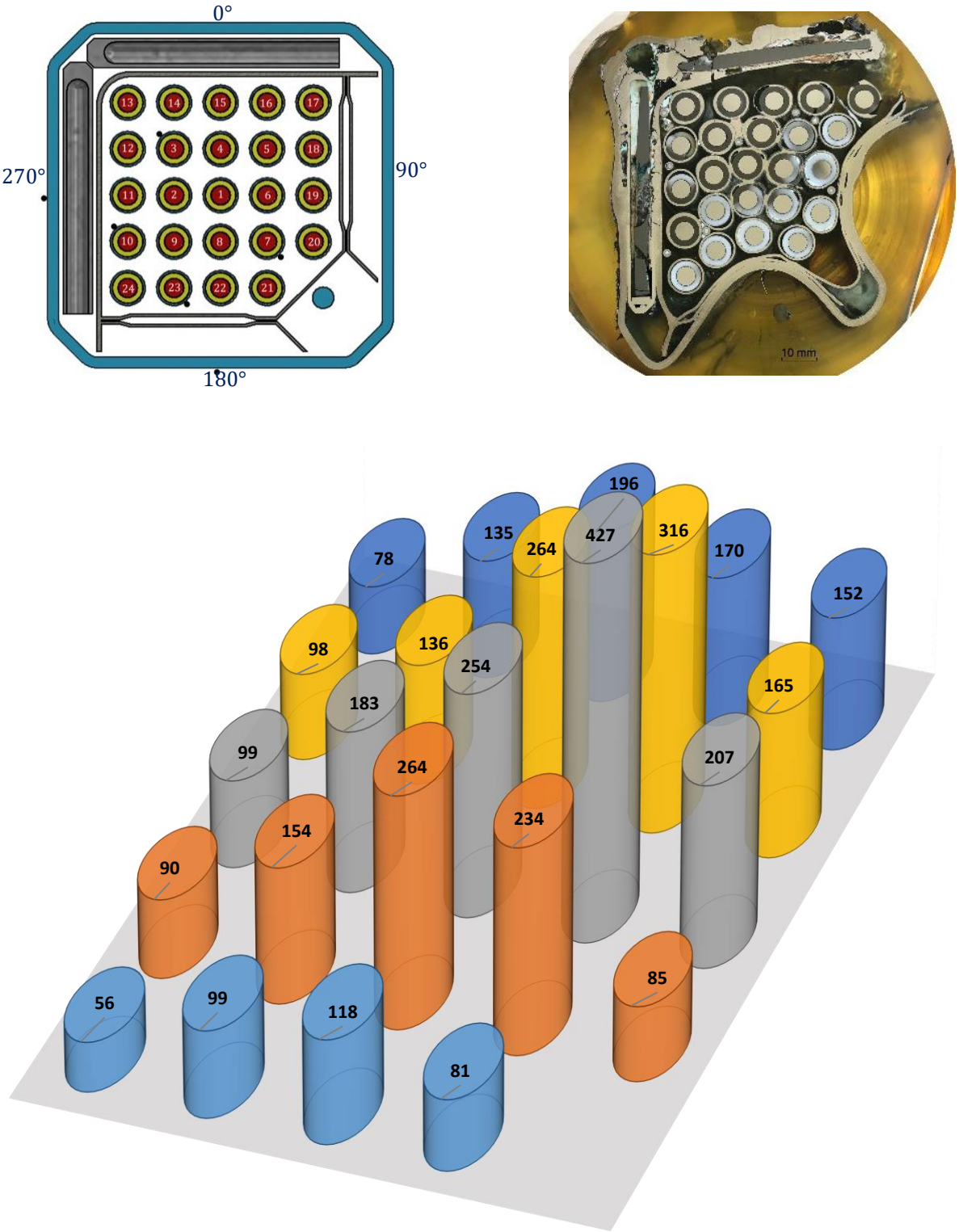

Figure 135 QUENCH-20; average thicknesses of outer ZrO_2 for each cladding at bundle elevation of 650 mm; indication of coldest bundle region at 180°.

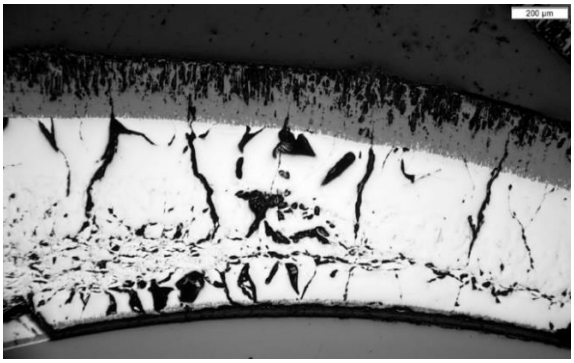

0°: outer ZrO_2 220…240 µm, α-Zr(O) 600…720 µm, inner ZrO_2 17…25 µm

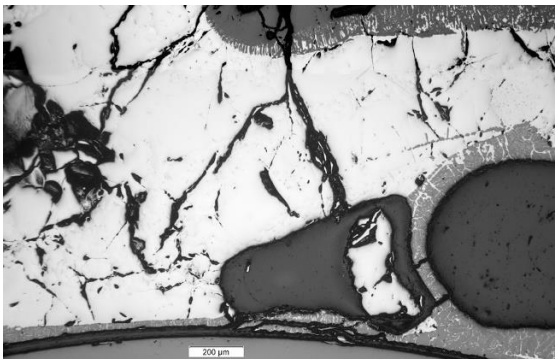

45°: no outer ZrO_2 due to contact to rods #4, #6 and dissolution of prior thin oxide; inner ZrO_2 30…90 µm; void with oxidized edges

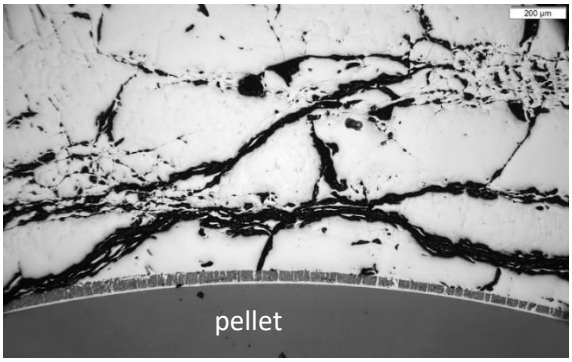

90°: no outer ZrO_2 due to contact to rod #6 and dissolution of prior thin oxide; inner ZrO_2 40 µm

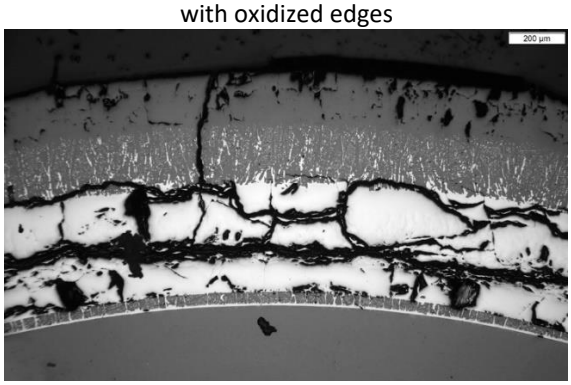

135°: outer ZrO_2 405 µm (220 prior tetr.+205 prior cub), α-Zr(O) 405 µm, inner ZrO_2 40 µm

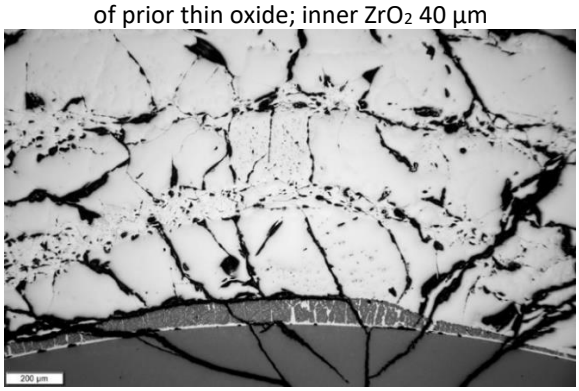

180°: no outer ZrO_2 due to contact to rod #8 and dissolution of prior thin oxide; inner ZrO_2 15…90 µm

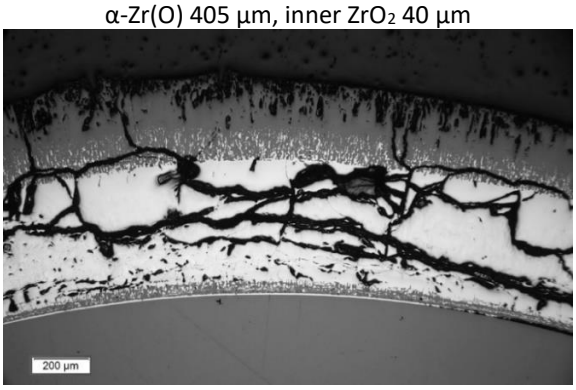

225°: outer ZrO_2 260…320 , α-Zr(O) 450 µm, inner ZrO_2 20…45 µm

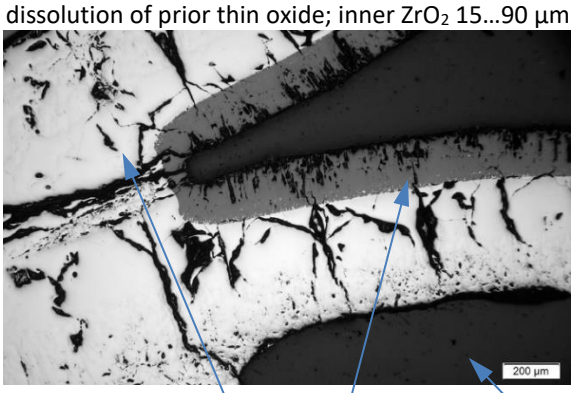

270°: contact with rod #2; outer ZrO_2 180 µm; void

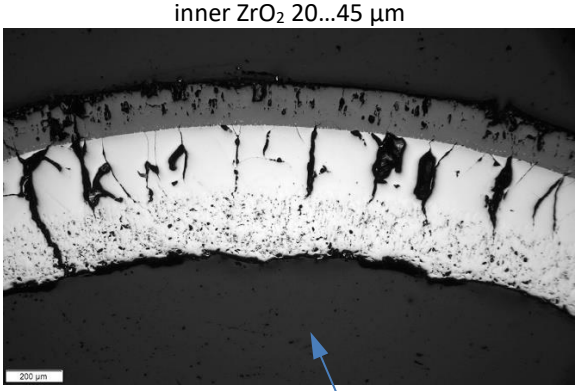

315°: outer ZrO_2 150 µm, α-Zr(O) 250 µm, melted prior β-Zr 210 µm; void

Figure 136 QUENCH-20; Cladding layer structures of rod #1 at different azimuthal positions at the bundle elevation of 650 mm: very thick α-Zr(O) layer and melted prior β-Zr.

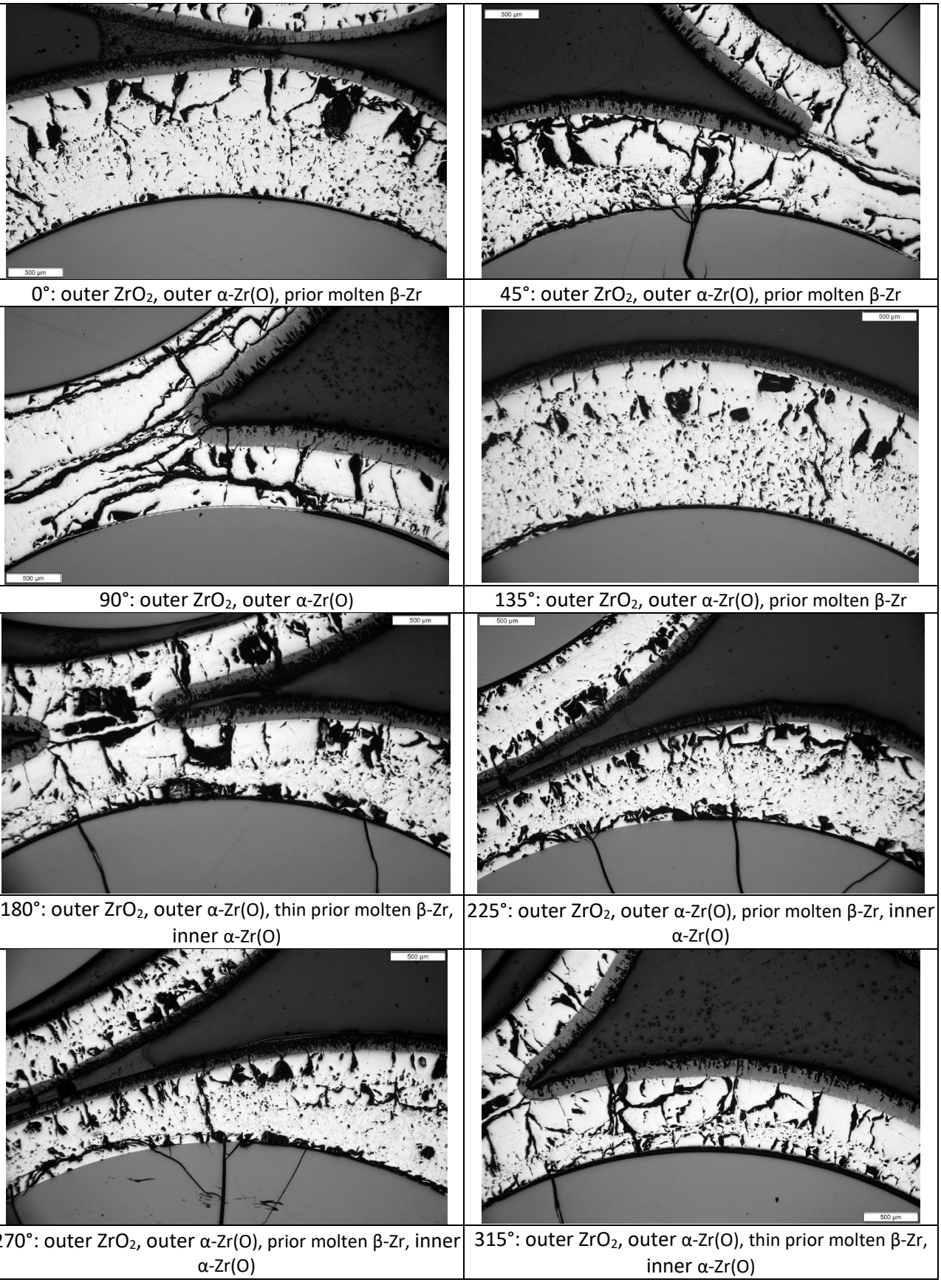

0°: outer ZrO_2, outer α-Zr(O), prior molten β-Zr

45°: outer ZrO_2, outer α-Zr(O), prior molten β-Zr

90°: outer ZrO_2, outer α-Zr(O)

135°: outer ZrO_2, outer α-Zr(O), prior molten β-Zr

180°: outer ZrO_2, outer α-Zr(O), thin prior molten β-Zr, inner α-Zr(O)

225°: outer ZrO_2, outer α-Zr(O), prior molten β-Zr, inner α-Zr(O)

270°: outer ZrO_2, outer α-Zr(O), prior molten β-Zr, inner α-Zr(O)

315°: outer ZrO_2, outer α-Zr(O), thin prior molten β-Zr, inner α-Zr(O)

Figure 137 QUENCH-20; Cladding layer structures of rod #2 (lower rod at each picture) at different azimuthal positions at the bundle elevation of 650 mm: melted prior β-Zr.

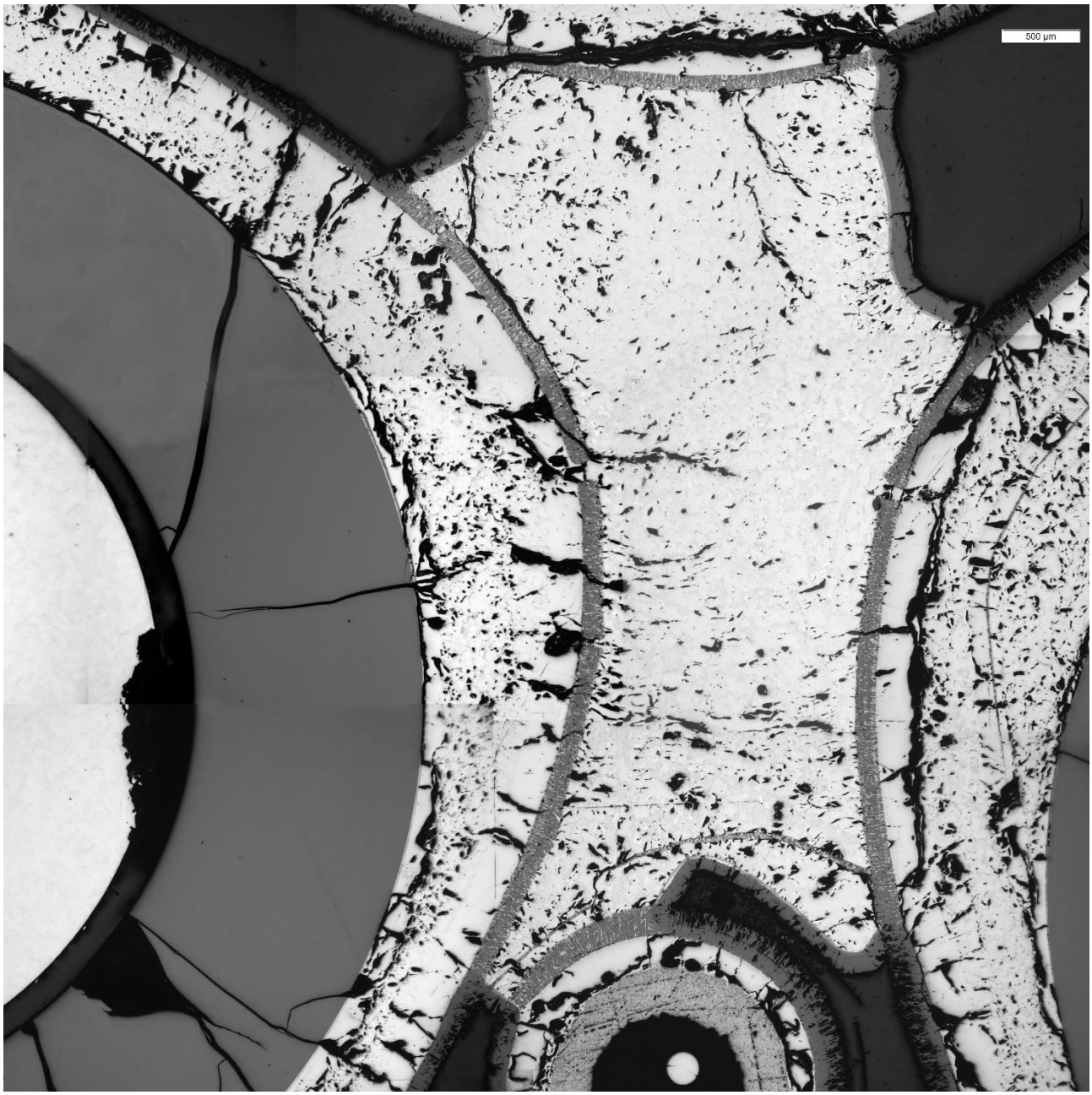

Figure 138 QUENCH-20; frozen molten pool formed at elevation 650 mm between rods #3 and #4: molten Zry-2 (prior β-Zr) was relocated from upper elevations and oxidized at the pool periphery.

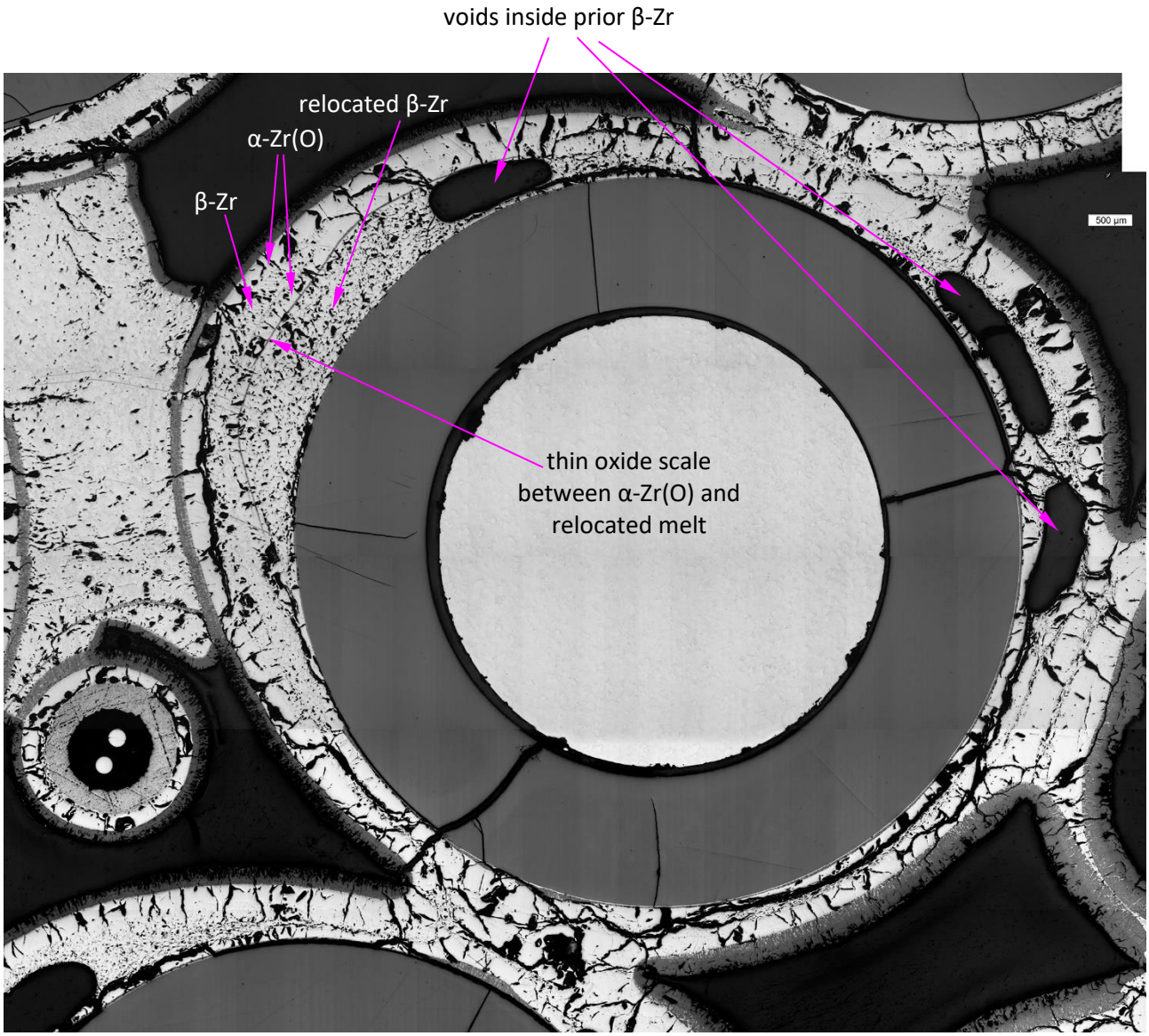

Figure 139 QUENCH-20; overview of rod #4 at elevation 650 mm: voids inside relocated prior molten β-Zr.

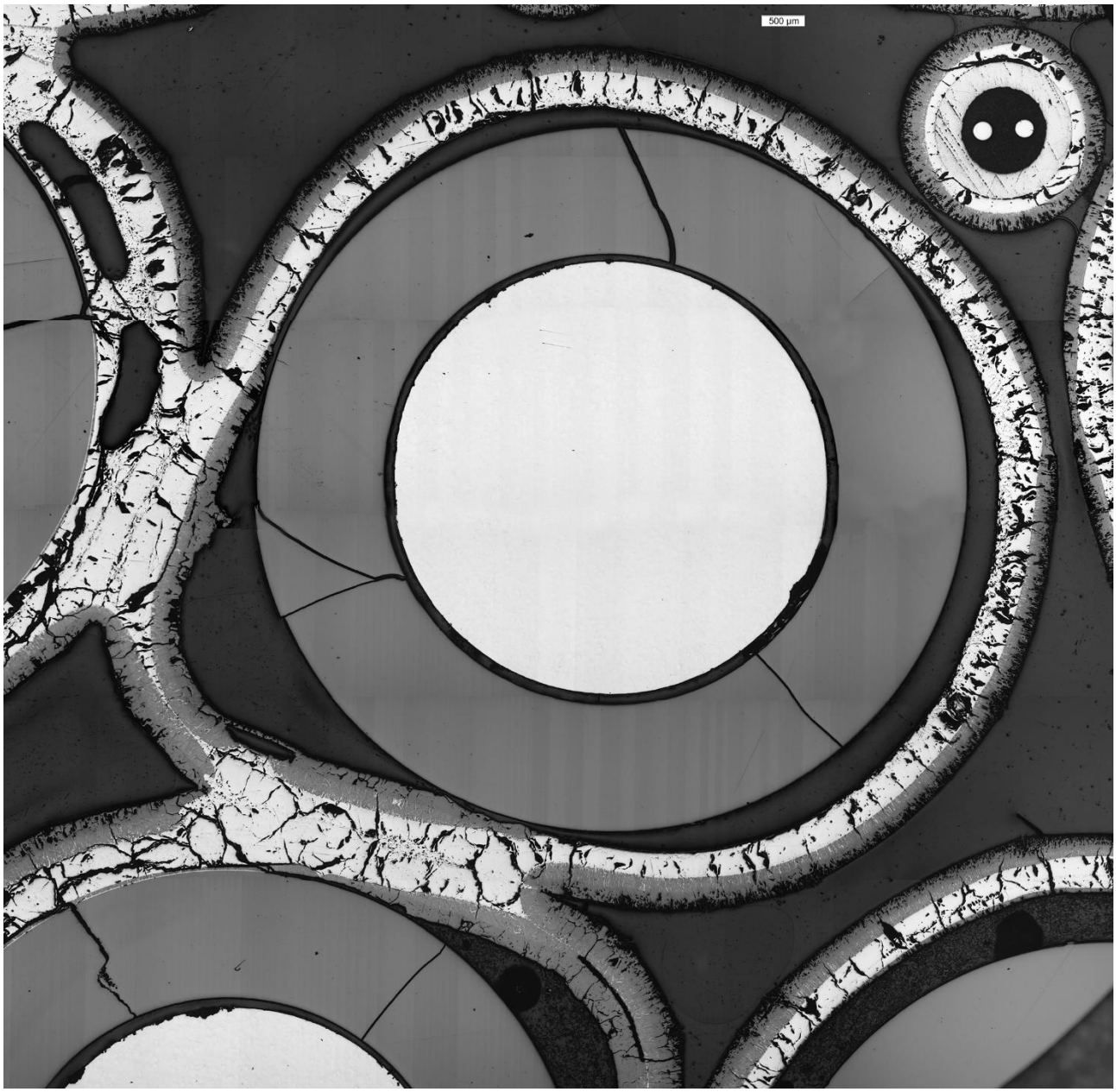

Figure 140 QUENCH-20; overview of rod #5 at elevation 650 mm: lift-off of cladding due to overpressure inside rods, oxidation of inner cladding surface due to steam penetration into the cladding-pellet gap at higher elevations.

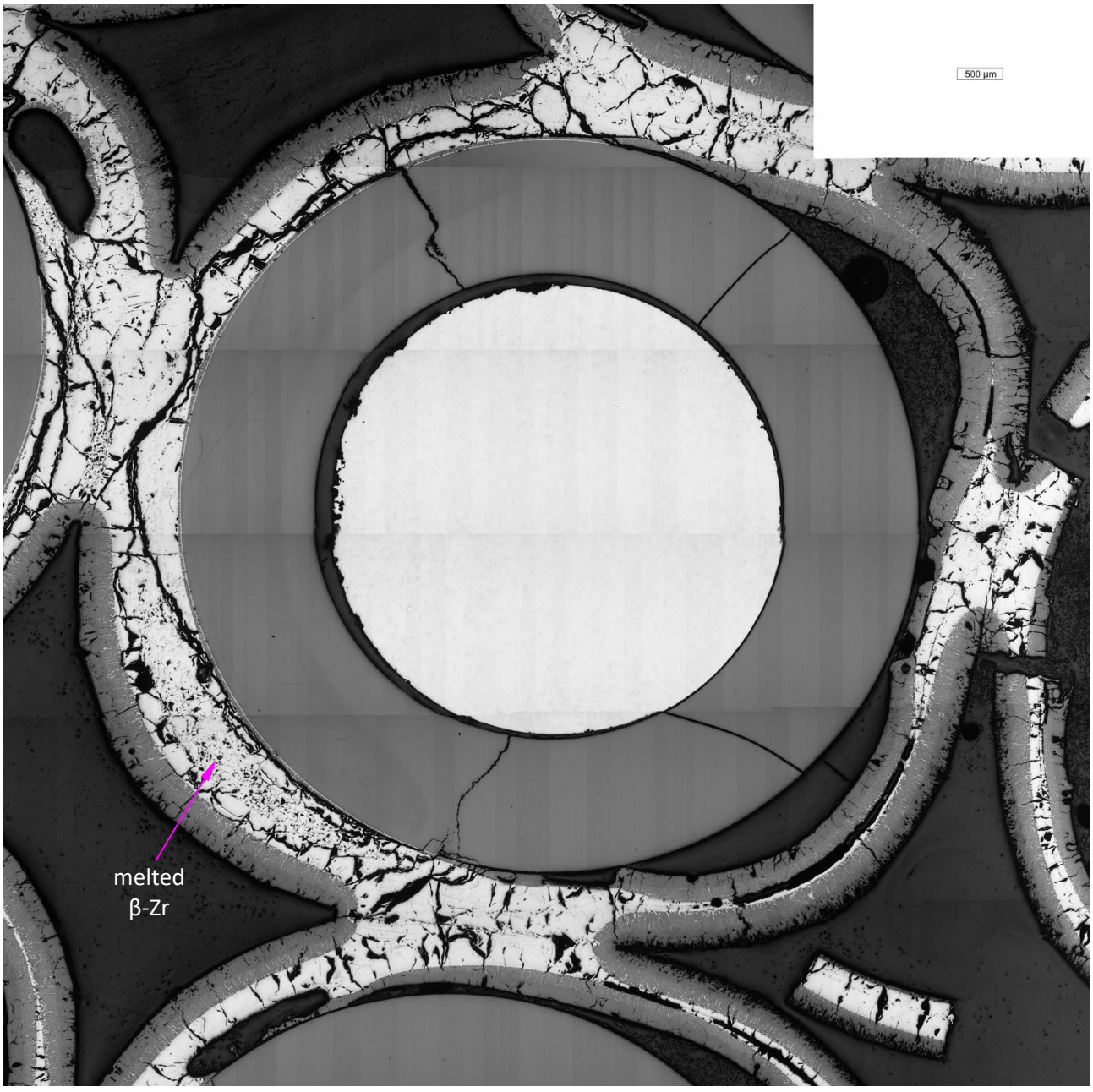

Figure 141 QUENCH-20; overview of rod #6 at elevation 650 mm: lift-off of cladding due to overpressure inside rods, oxidation of inner cladding surface due to steam penetration into the cladding-pellet gap at higher elevations, melted β-Zr near the hottest central rod.

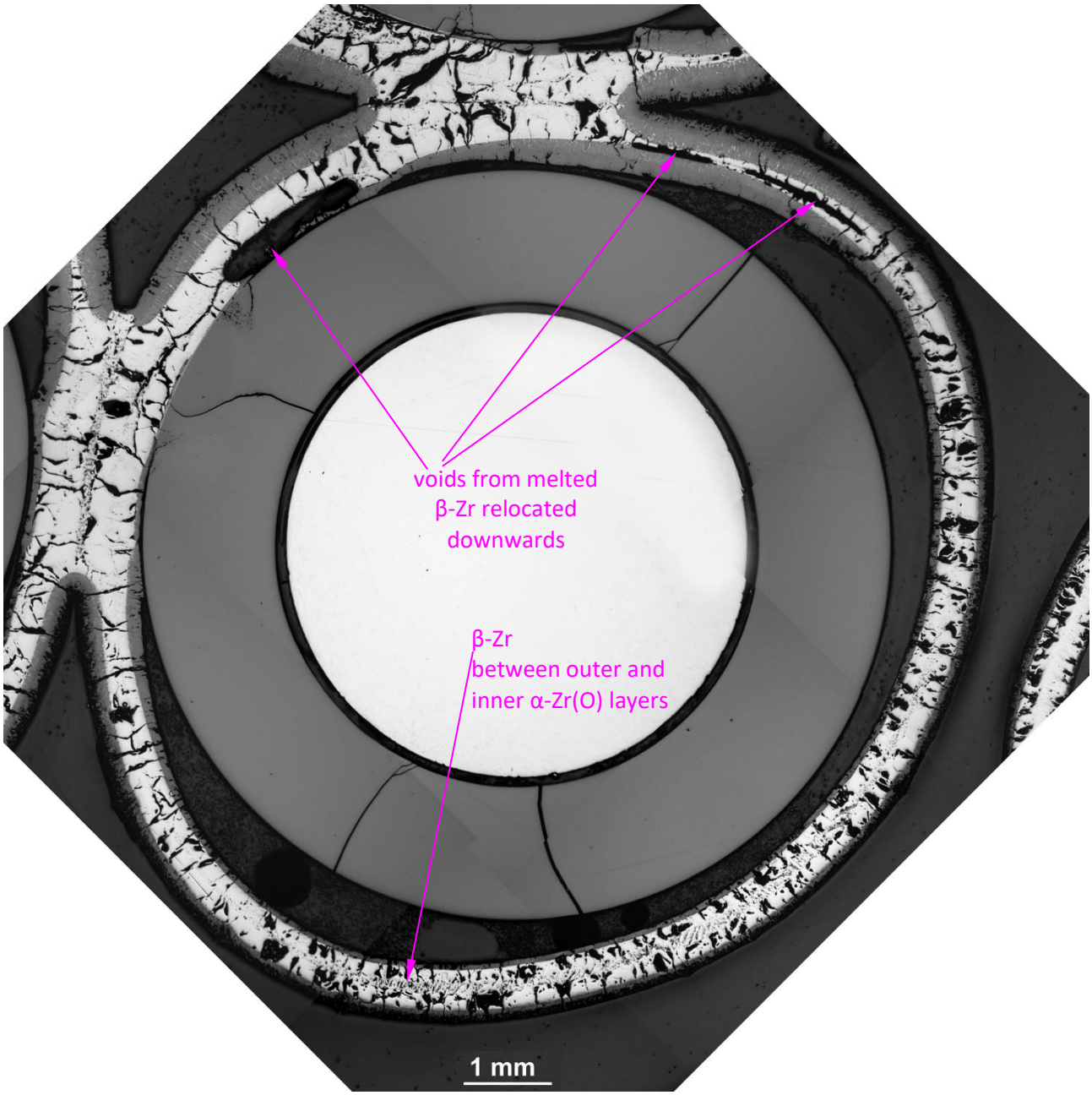

Figure 142 QUENCH-20; overview of rod #7 at elevation 650 mm: lift-off of cladding, oxidation of outer and inner cladding surfaces, melted β-Zr.

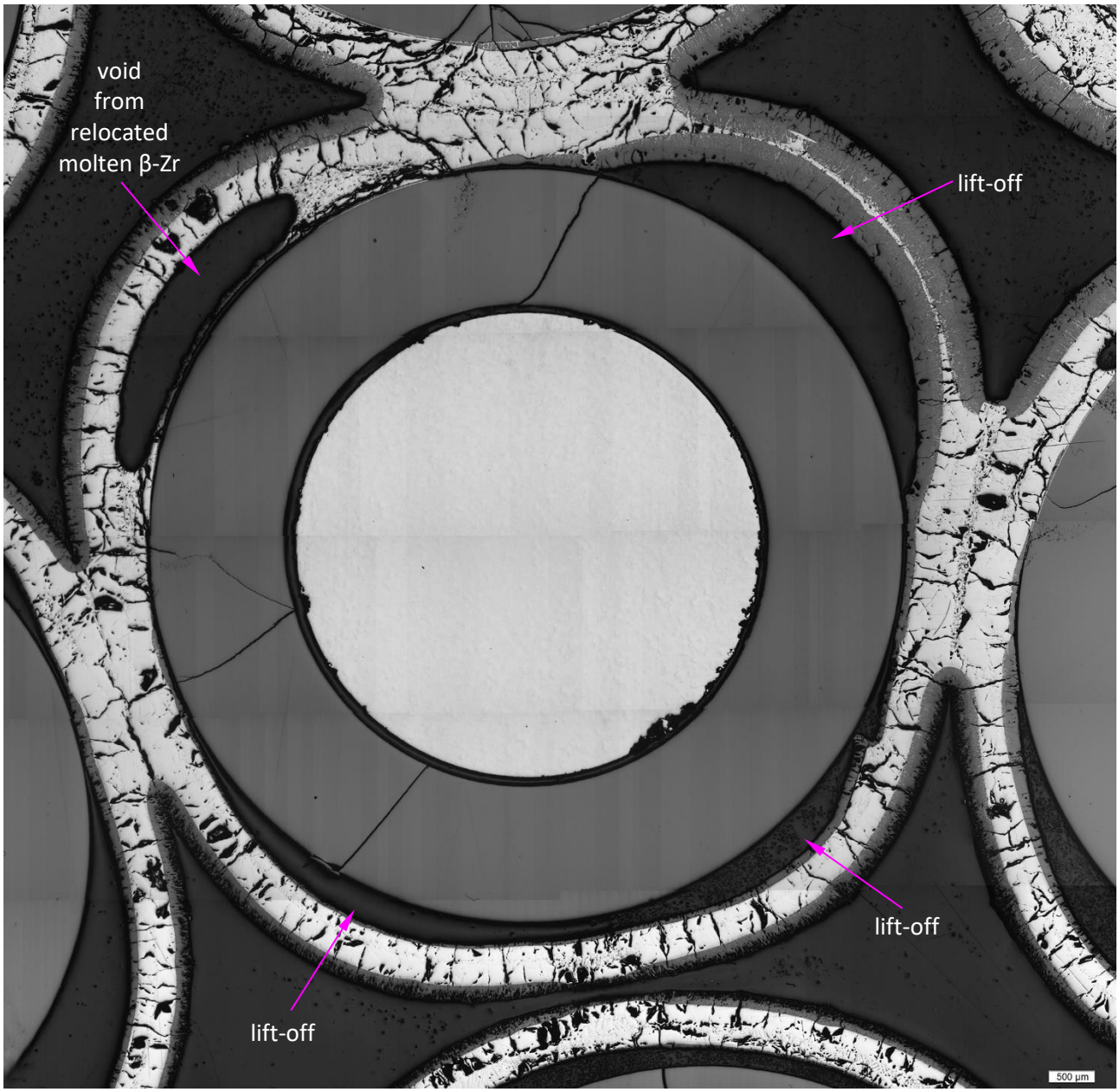

Figure 143 QUENCH-20; overview of rod #8 at elevation 650 mm: lift-off of cladding due to overpressure inside rods, oxidation of inner cladding surface due to steam penetration into the cladding-pellet gap at higher elevations, void from relocated β-Zr.

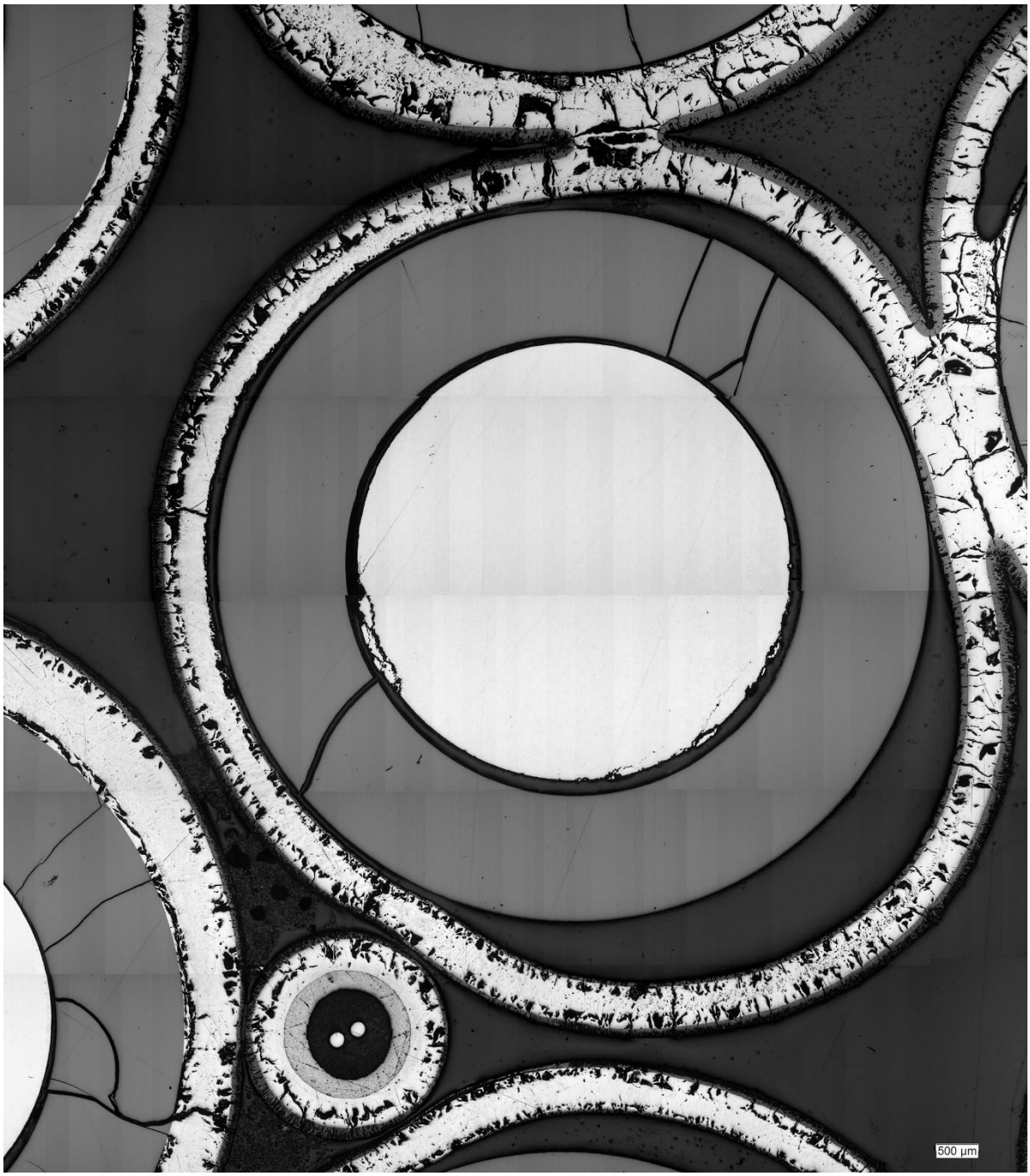

Figure 144 QUENCH-20; overview of rod #9 at elevation 650 mm: lift-off of cladding due to overpressure inside rods, oxidation of inner cladding surface due to steam penetration into the cladding-pellet gap at higher elevations.

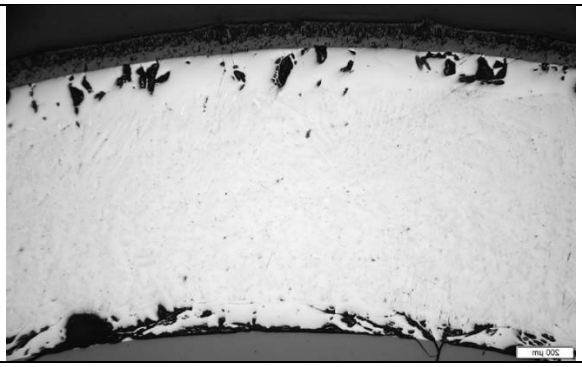

0°: ZrO_2 90 µm, outer α-Zr(O) 160 µm, prior β-Zr 770 µm (melt), inner α-Zr(O) 105 µm

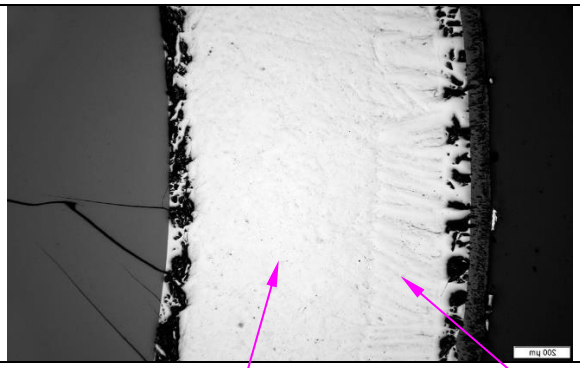

45°: ZrO_2 110 µm, outer α-Zr(O) 180 µm, prior β-Zr 570 µm (incl. melt), inner α-Zr(O) 130 µm

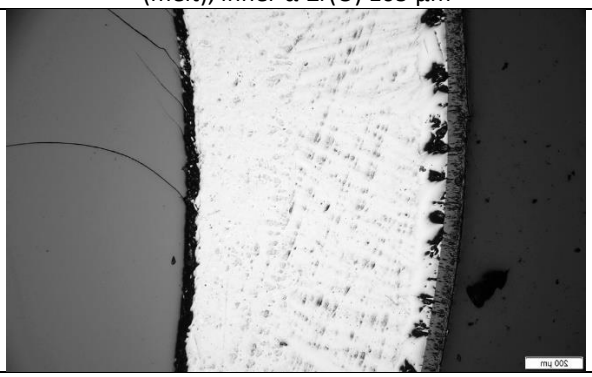

90°: ZrO_2 110 µm, outer α-Zr(O) 205 µm, prior β-Zr 220 µm, inner α-Zr(O) 160 µm; contact with TC TFS 9/10

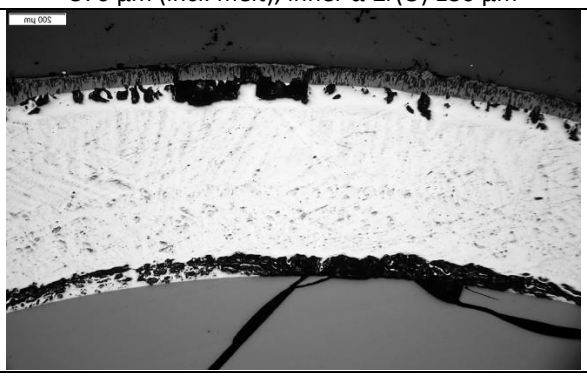

135°: ZrO_2 90 µm, outer α-Zr(O) 125 µm, prior β-Zr 250 µm, inner α-Zr(O) 120 µm

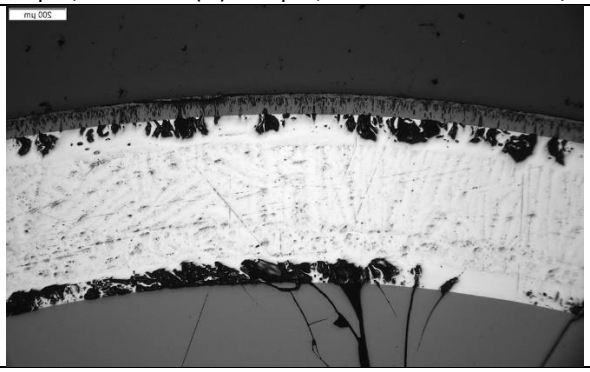

180°: ZrO_2 72 µm, outer α-Zr(O) 105 µm, prior β-Zr 405 µm, inner α-Zr(O) 95 µm

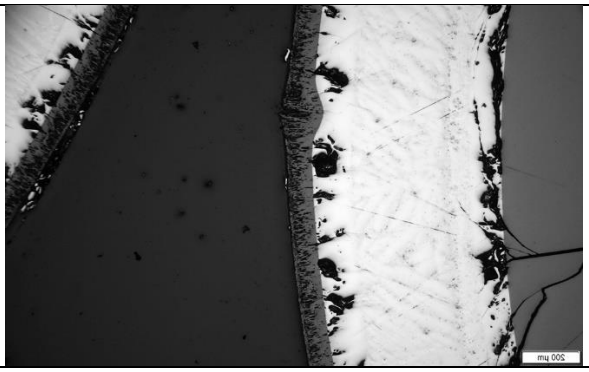

225°: ZrO_2 65 µm, outer α-Zr(O) 88 µm, prior β-Zr 515 µm, inner α-Zr(O) 87 µm

270°: ZrO_2 65 µm, outer α-Zr(O) 95 µm, prior β-Zr 760 µm, inner α-Zr(O) (loose during preparation) 45 µm

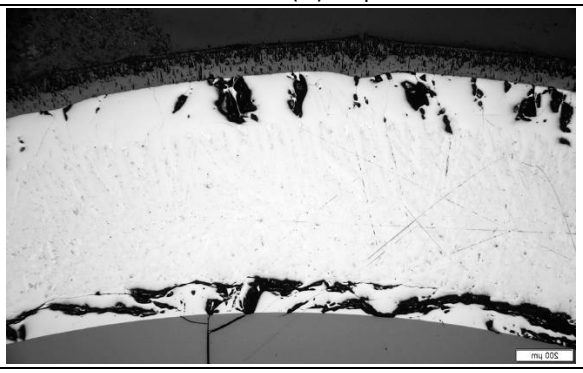

315°: ZrO_2 72 µm, outer α-Zr(O) 105 µm, prior β-Zr 255 µm, molten β-Zr 655 µm, inner α-Zr(O) 95 µm

Figure 145 QUENCH-20; Cladding layer structures of rod #10 at 650 mm: molten prior β-Zr partially relocated from upper elevations through the pellet-cladding gap.

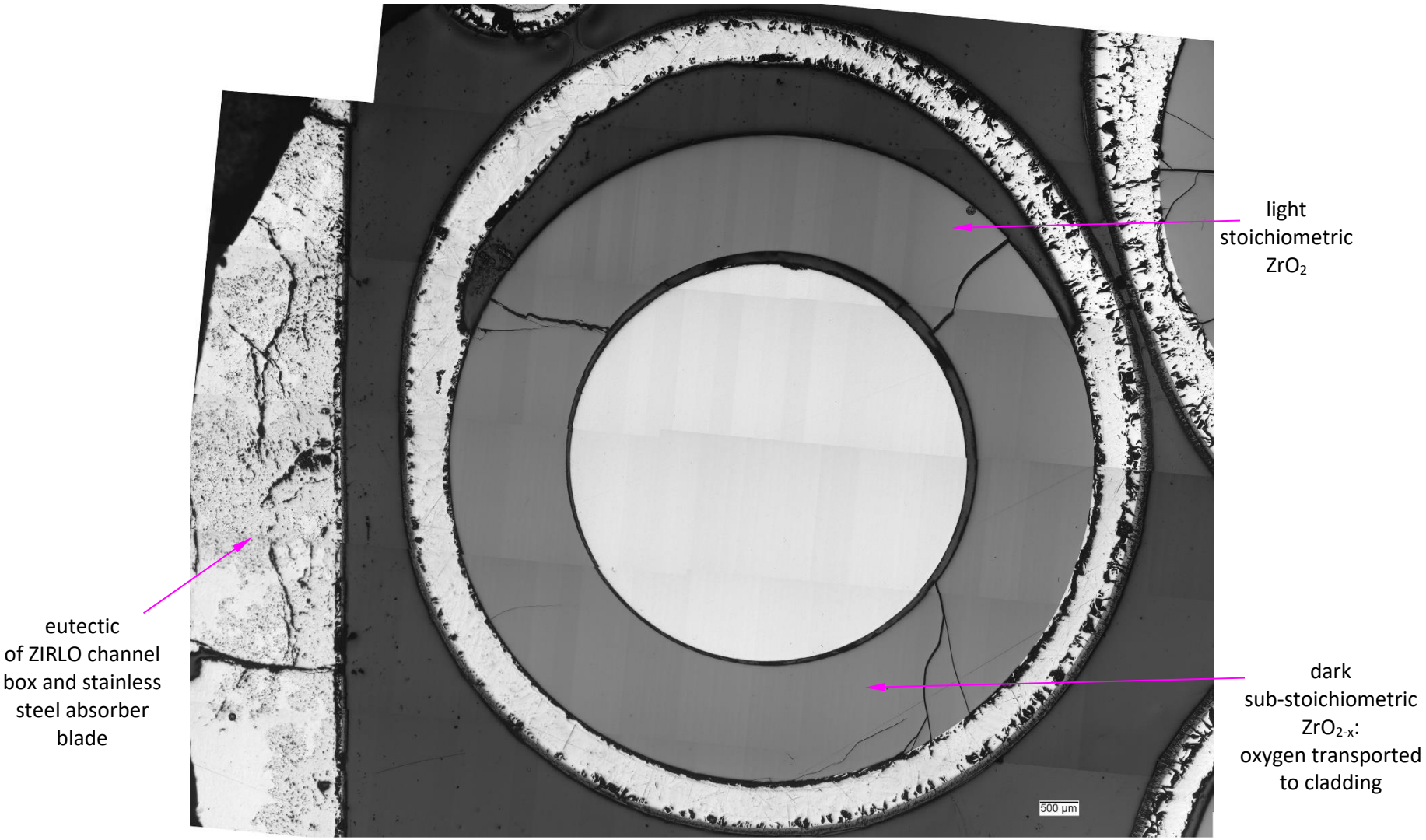

Figure 146 QUENCH-20; overview of rod #11 at elevation 650 mm: lift-off of the cladding at segment between 270° and 90° with oxidation of cladding inner surface; contact pellet-cladding between 90° and 270°.

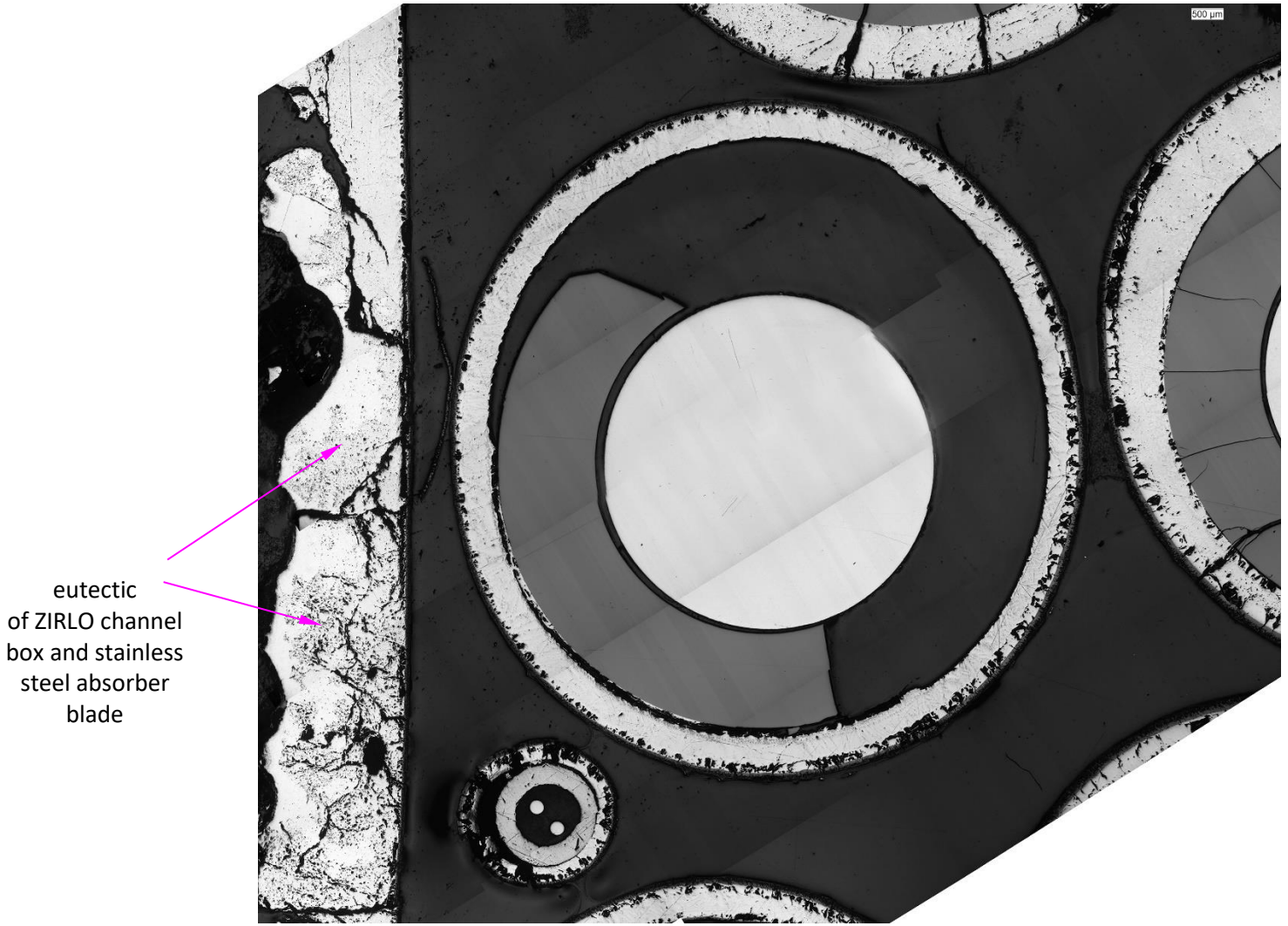

Figure 147 QUENCH-20; overview of rod #12 at elevation 650 mm: contact between pellet and cladding between 180° and 270°.

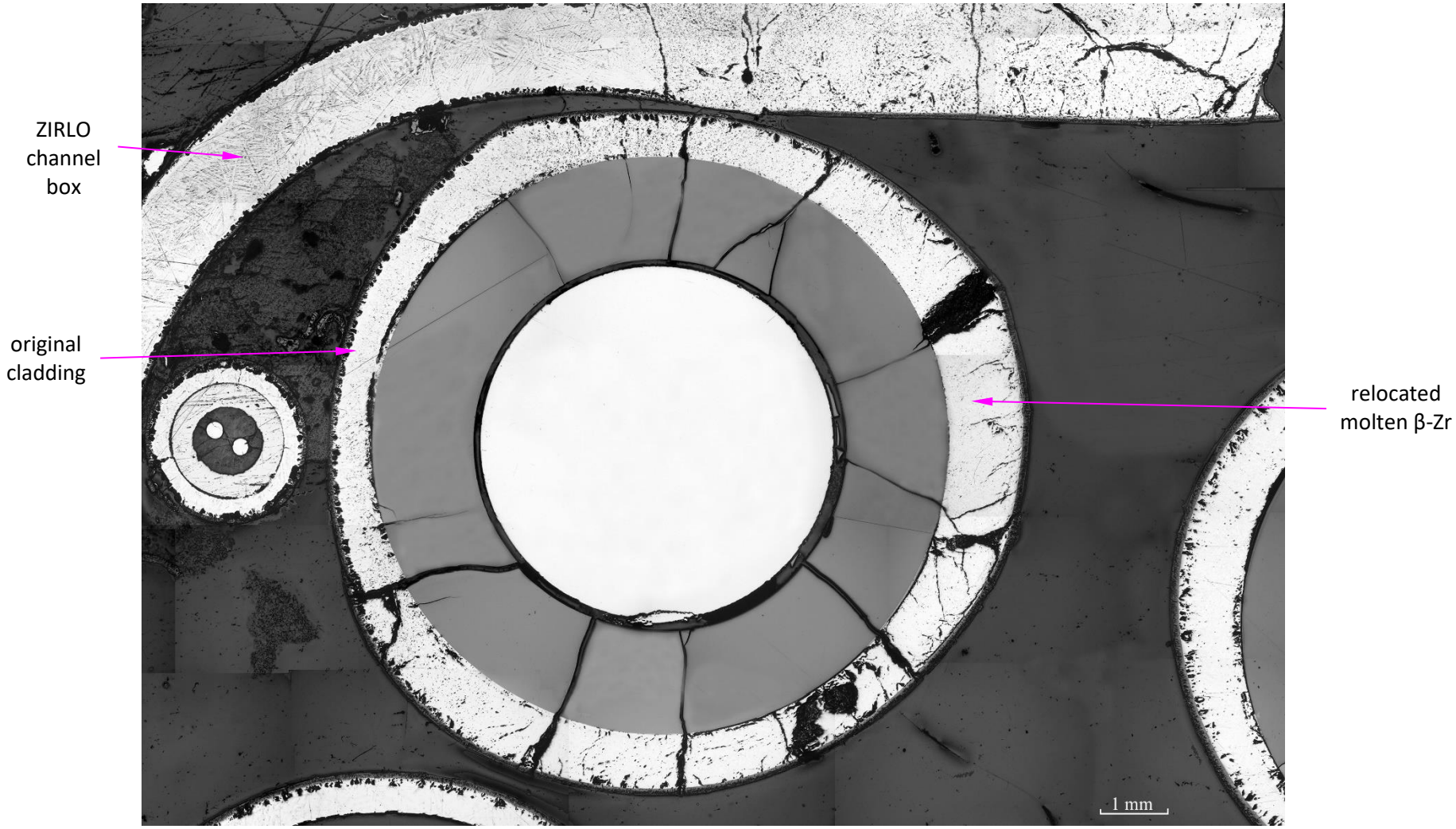

Figure 148 QUENCH-20; overview of rod #13 at elevation 650 mm: filling of the gap between pellets and outer α-Zr(O) with molten prior β-Zr from upper elevations.

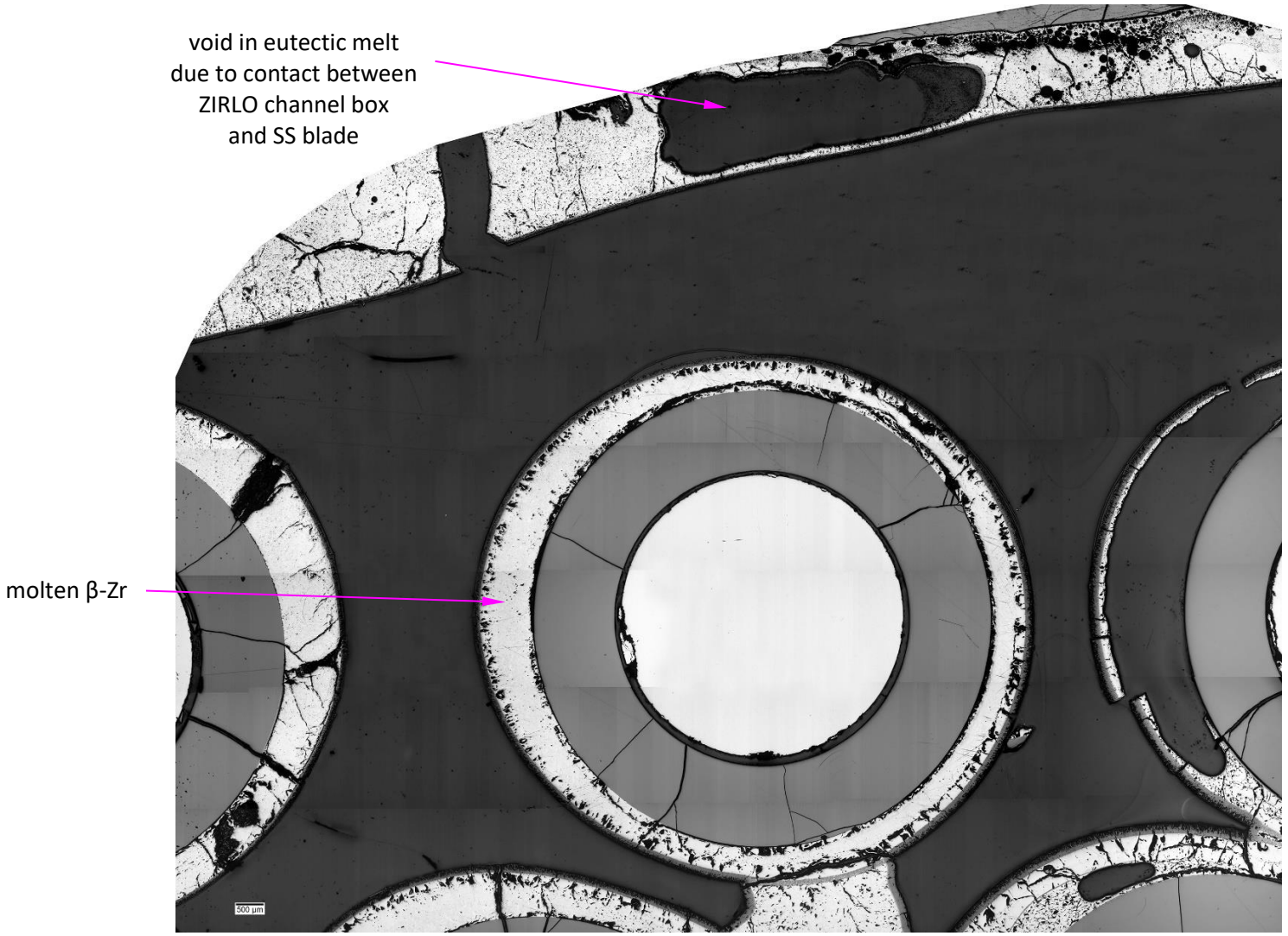

Figure 149 QUENCH-20; overview of rod #14 at elevation 650 mm: contact between pellet and cladding due to melting of β-Zr layer.

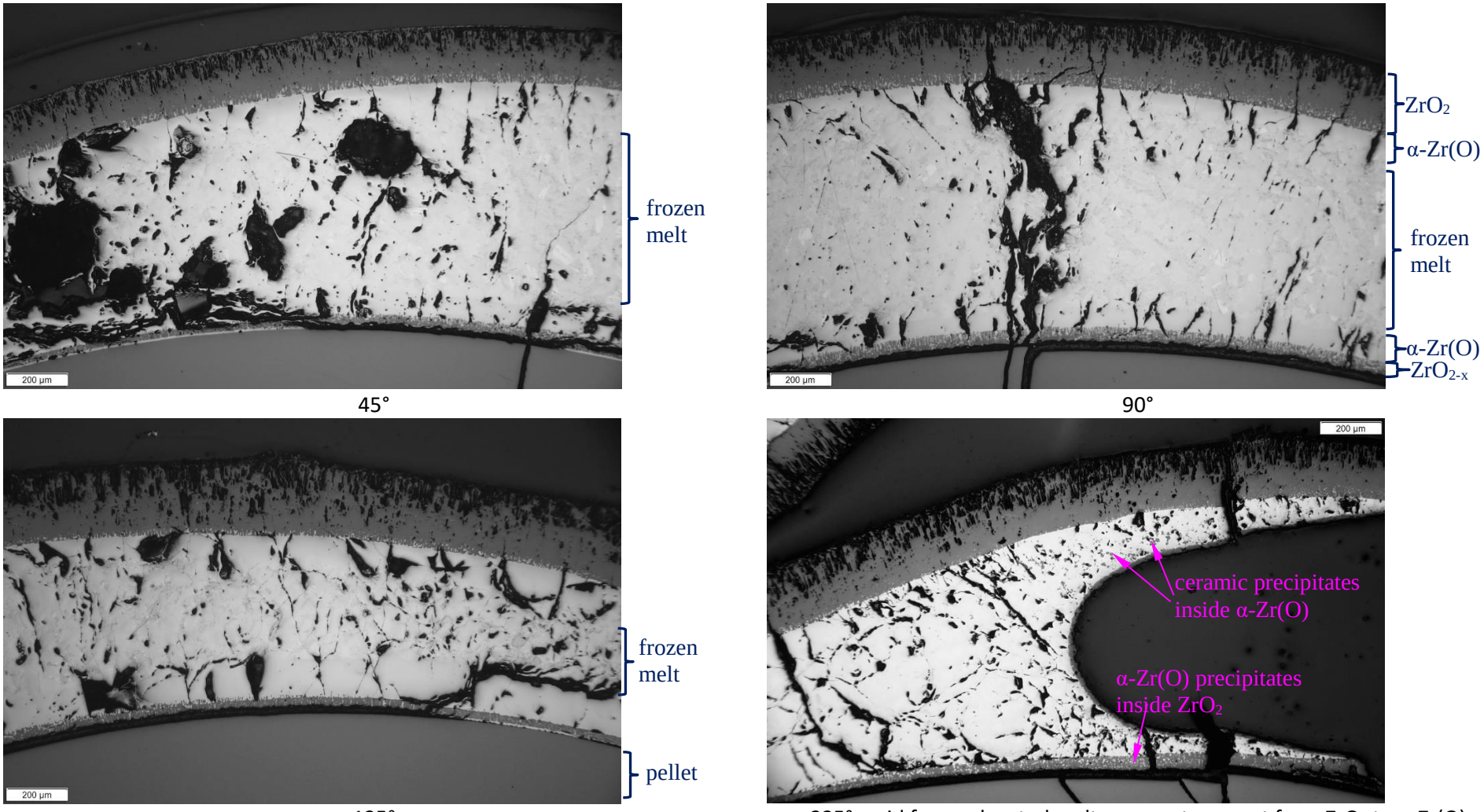

Figure 150 QUENCH-20; melt formation and relocation between pellet and outer oxide of rod #15 at 650 mm.

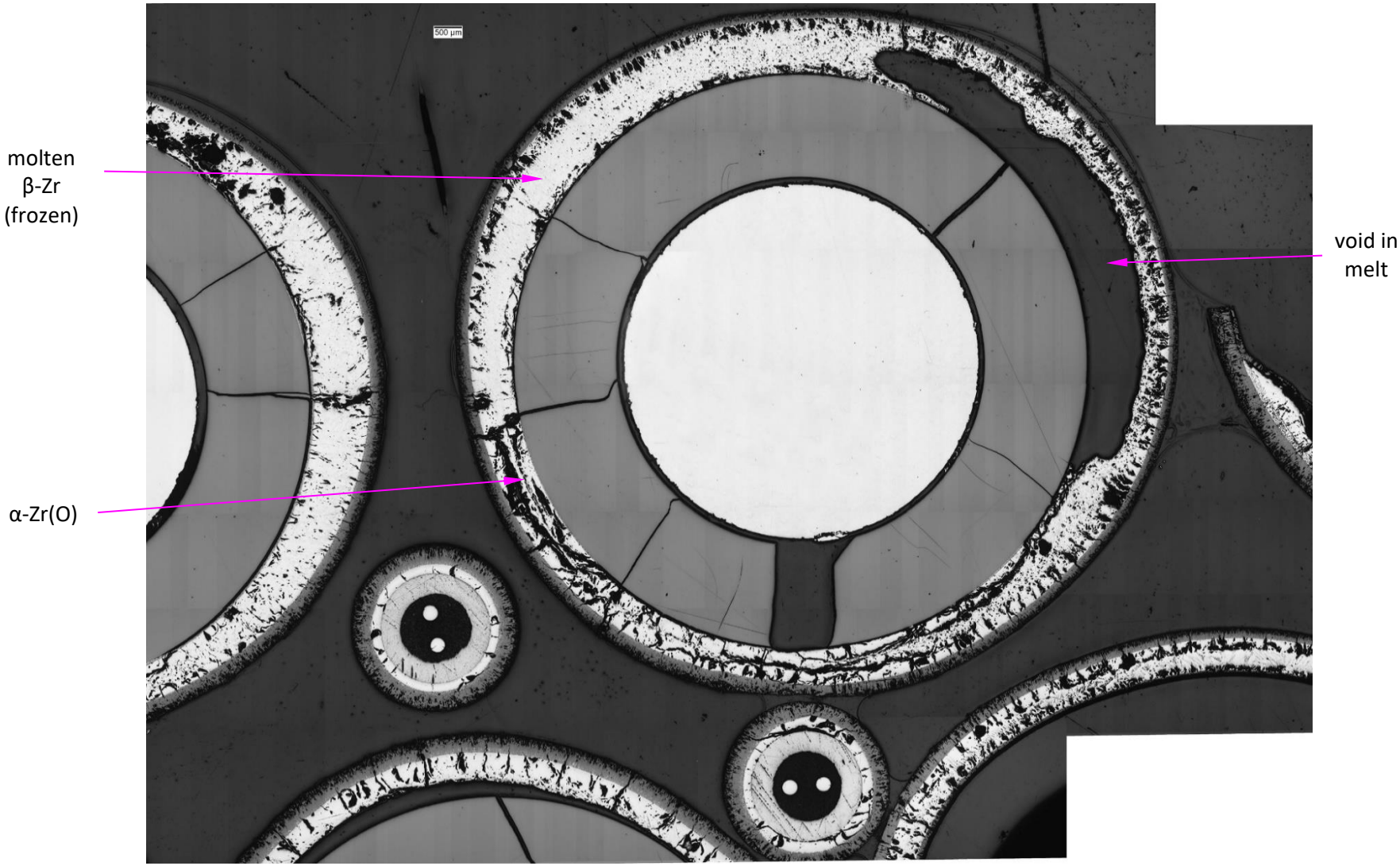

Figure 151 QUENCH-20; overview of rod #16 at elevation 650 mm: molten prior β-Zr trapped between pellet and cladding outer oxide layer.

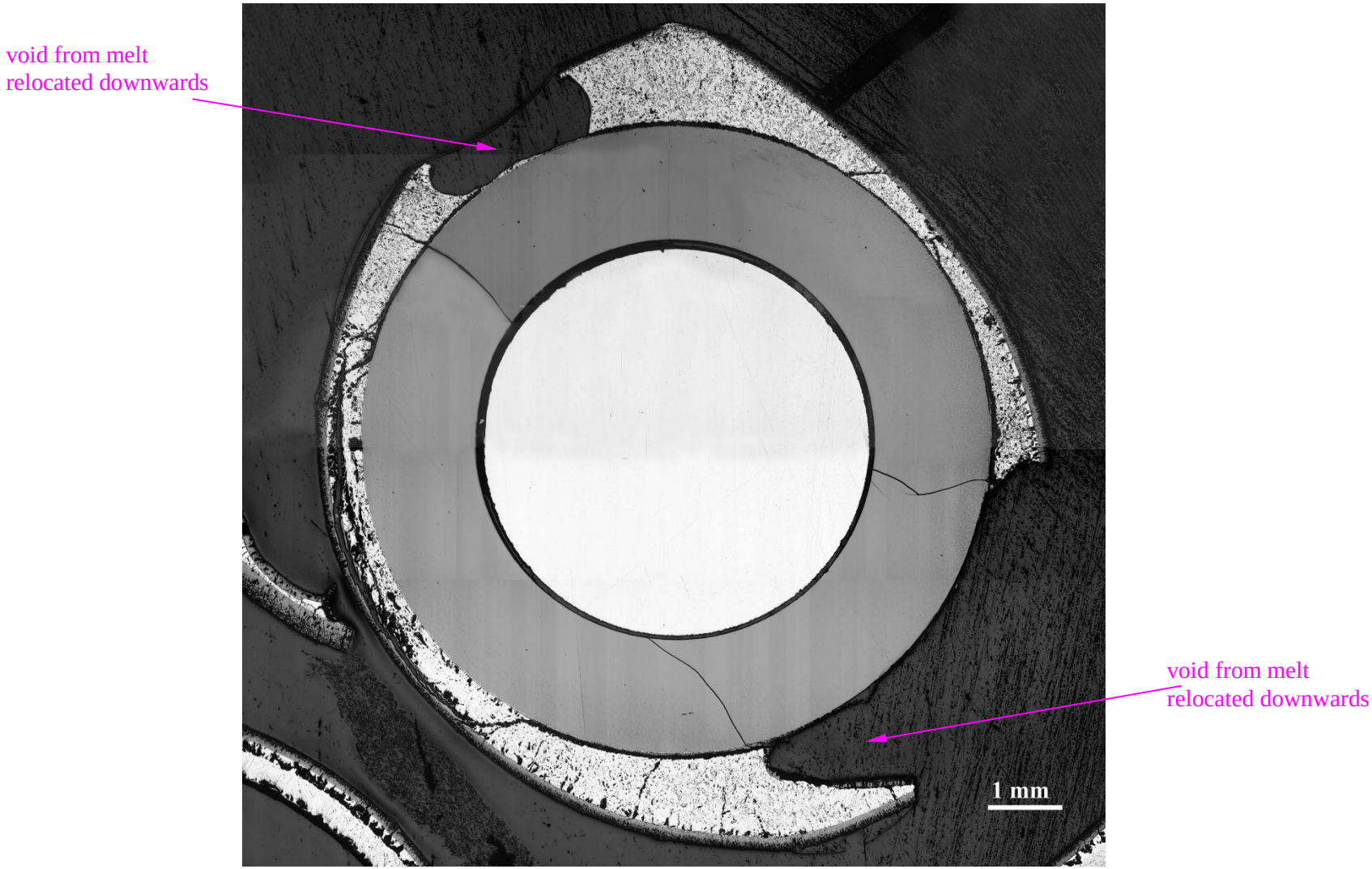

Figure 152 QUENCH-20; metal melt between the pellet and the cladding oxide layer of the rod #17 at 650 mm.

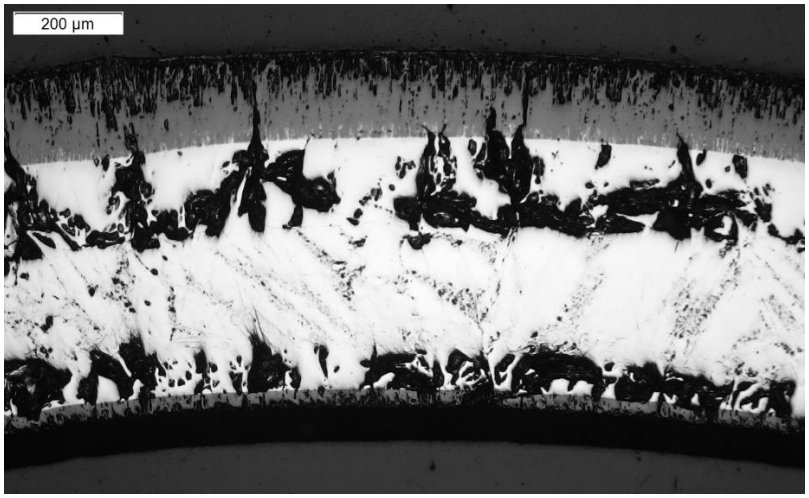

0°: thick prior β-Zr layer with thick segregated α-Zr(O) lamellas

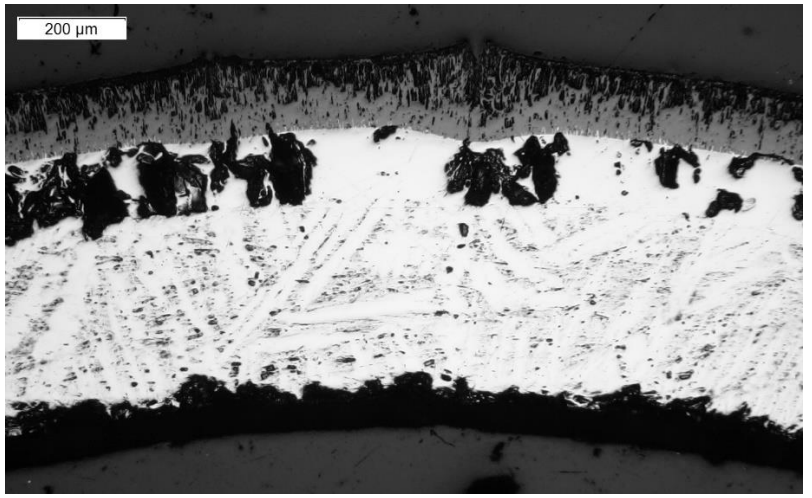

90°: no oxidation of inner cladding surface; thin α-Zr(O) lamellas inside prior β

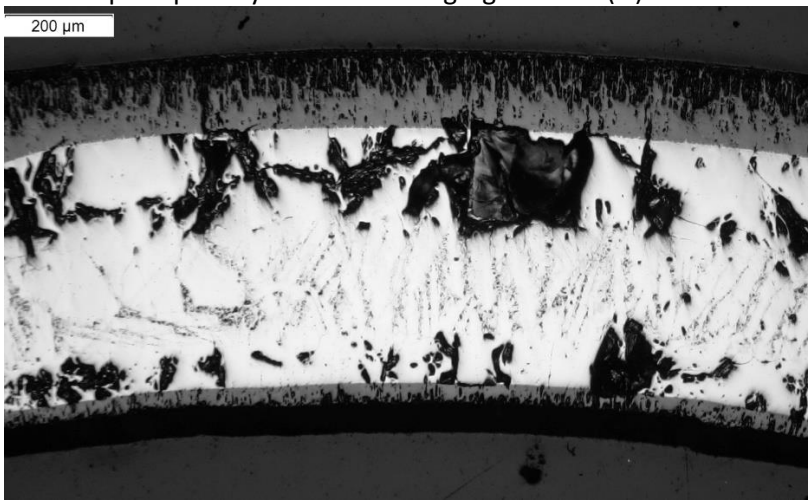

180°: thick prior β-Zr layer with thick segregated α-Zr(O) lamellas

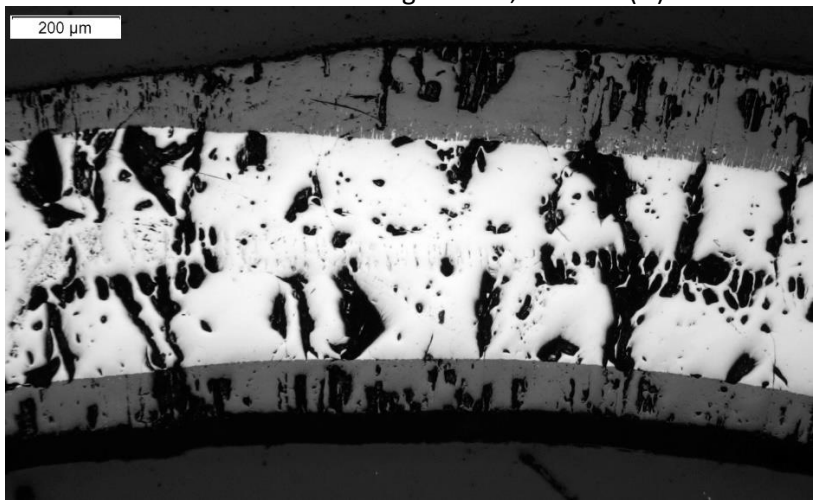

270°: strong oxidation of inner cladding surface

Figure 153 QUENCH-20; cladding layers of the rod #18 at 650 mm: no melting.

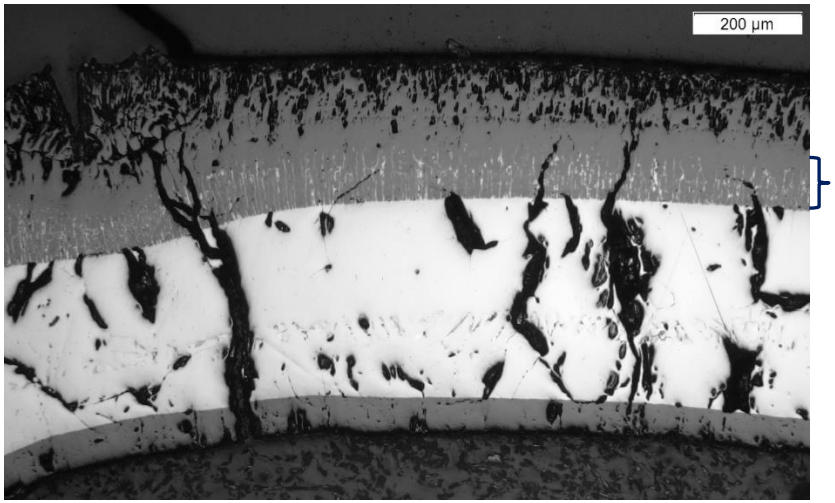

0°: thick prior cubic ZrO_{2-x} due to higher temperature

90°: thick prior β-Zr layer

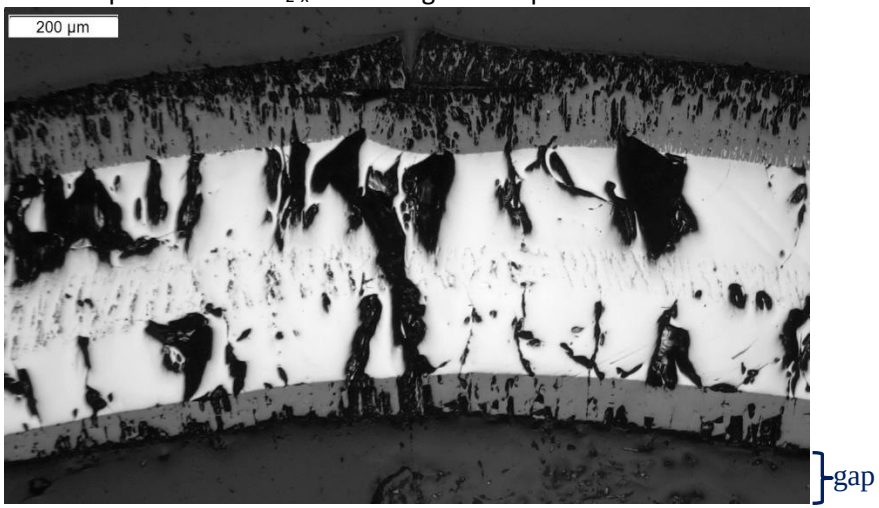

180°: crack inside outer ZrO_2; thick inner ZrO_2

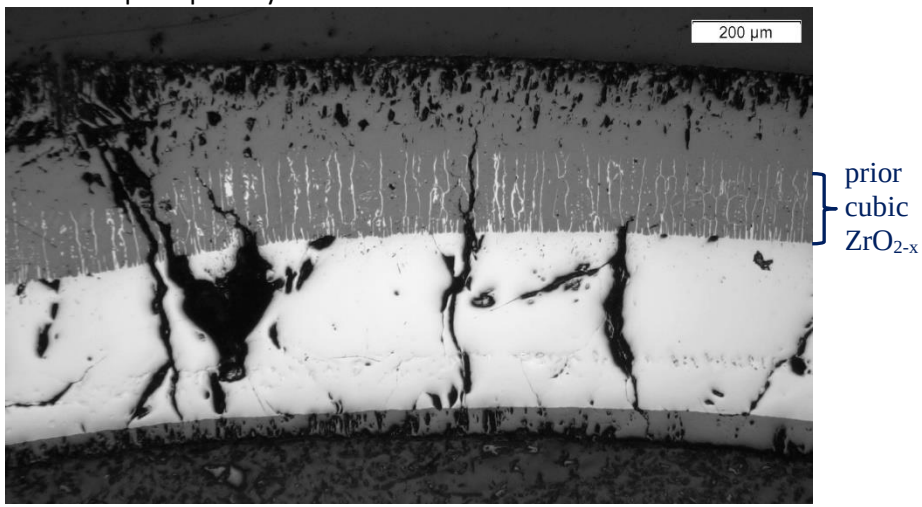

315°: thick prior cubic ZrO_{2-x} due to higher temperature

Figure 154 QUENCH-20; cladding layers of the rod #19 at 650 mm: no melting.

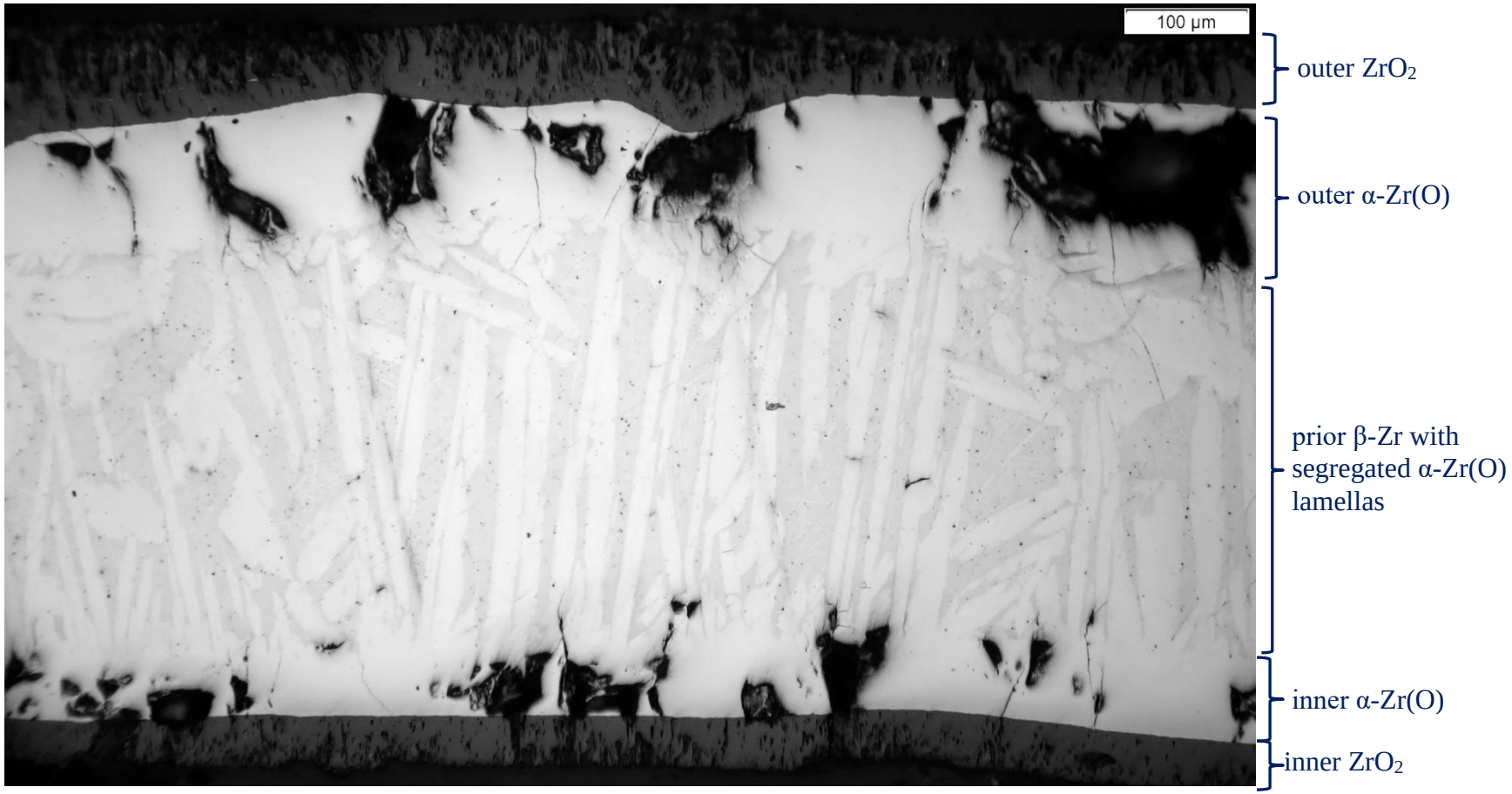

Figure 155 QUENCH-20; Cladding layer structures of rod #20 at 650 mm: formation of α-Zr(O) lamellas inside the prior β-Zr (Widmanstätten patterns) during cooling.

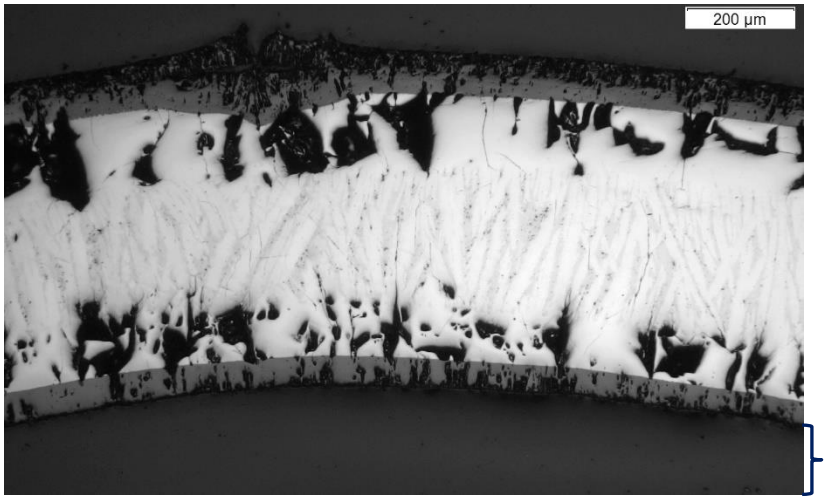

0°: significant oxidation of inner cladding surface by steam through the gap

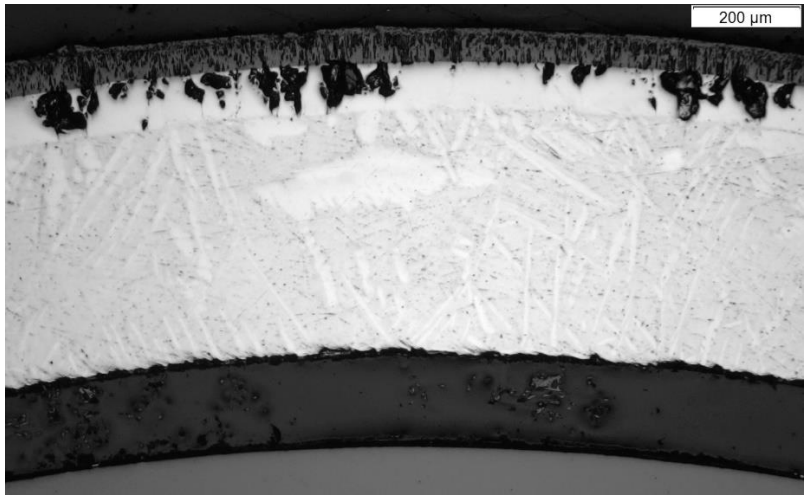

90°: no oxidation of inner cladding surface

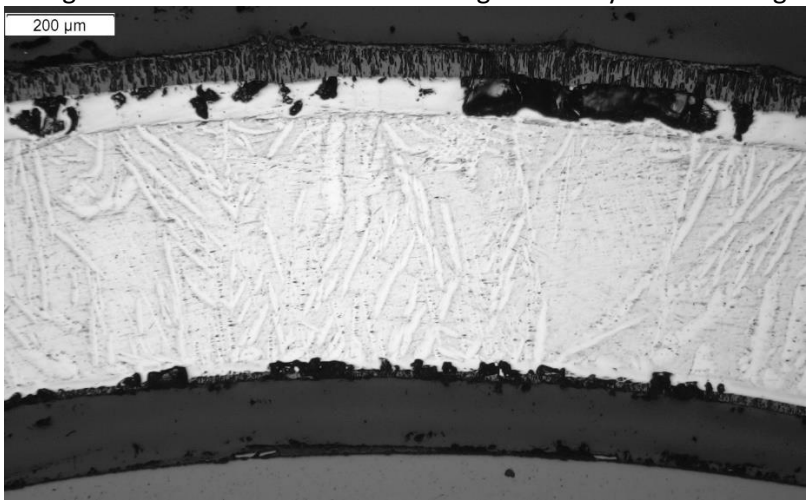

180°: slight oxidation of inner cladding surface

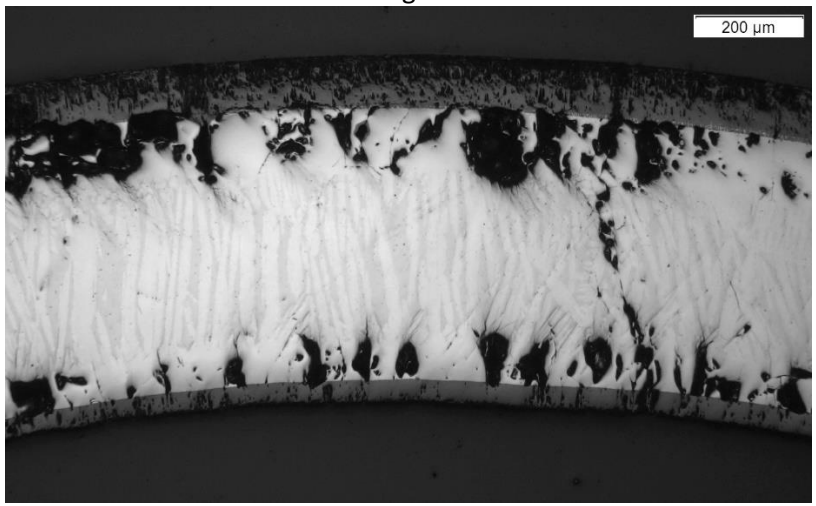

270°: significant oxidation of inner cladding surface by steam through the gap

Figure 156 QUENCH-20; cladding layers of the rod #21 at 650 mm: no melting.

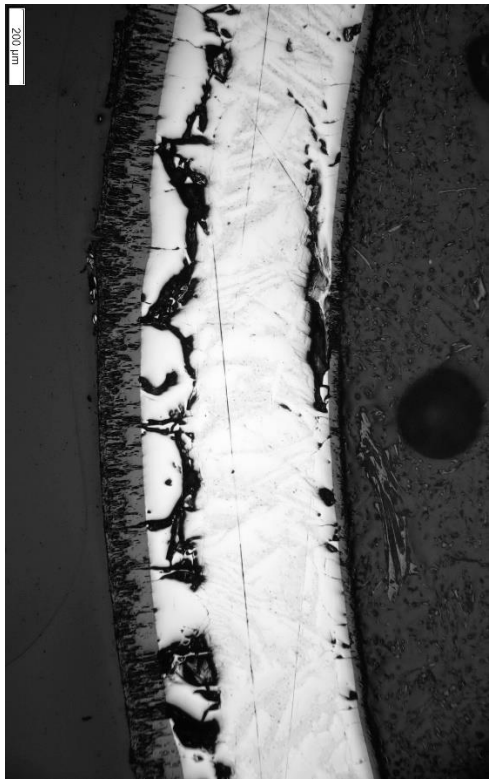

270°: outer and inner cladding oxidation

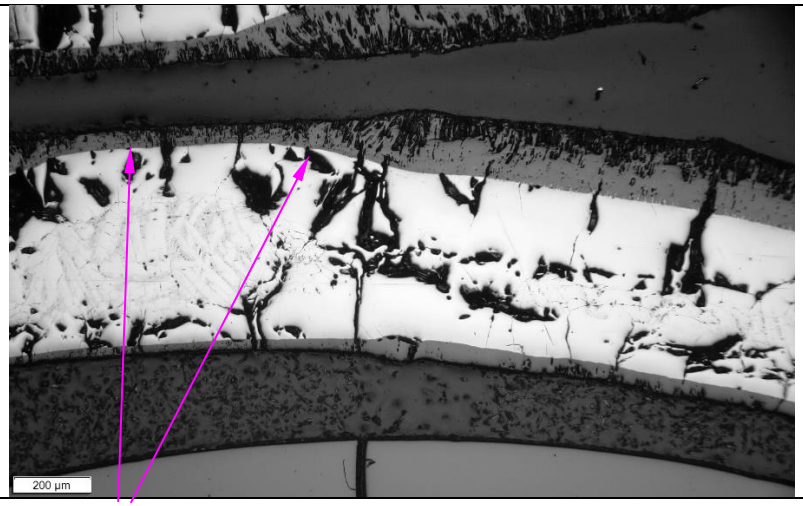

0°: decreased cladding oxidation due to narrowing of steam channel

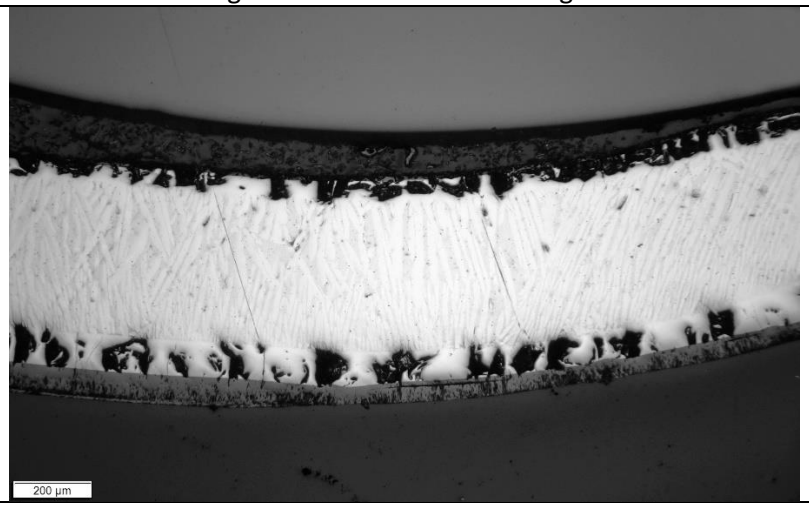

180°: slight inner oxidation

90°: outer and inner cladding oxidation

Figure 157 QUENCH-20; cladding layers of the rod #22 at 650 mm: no melting.

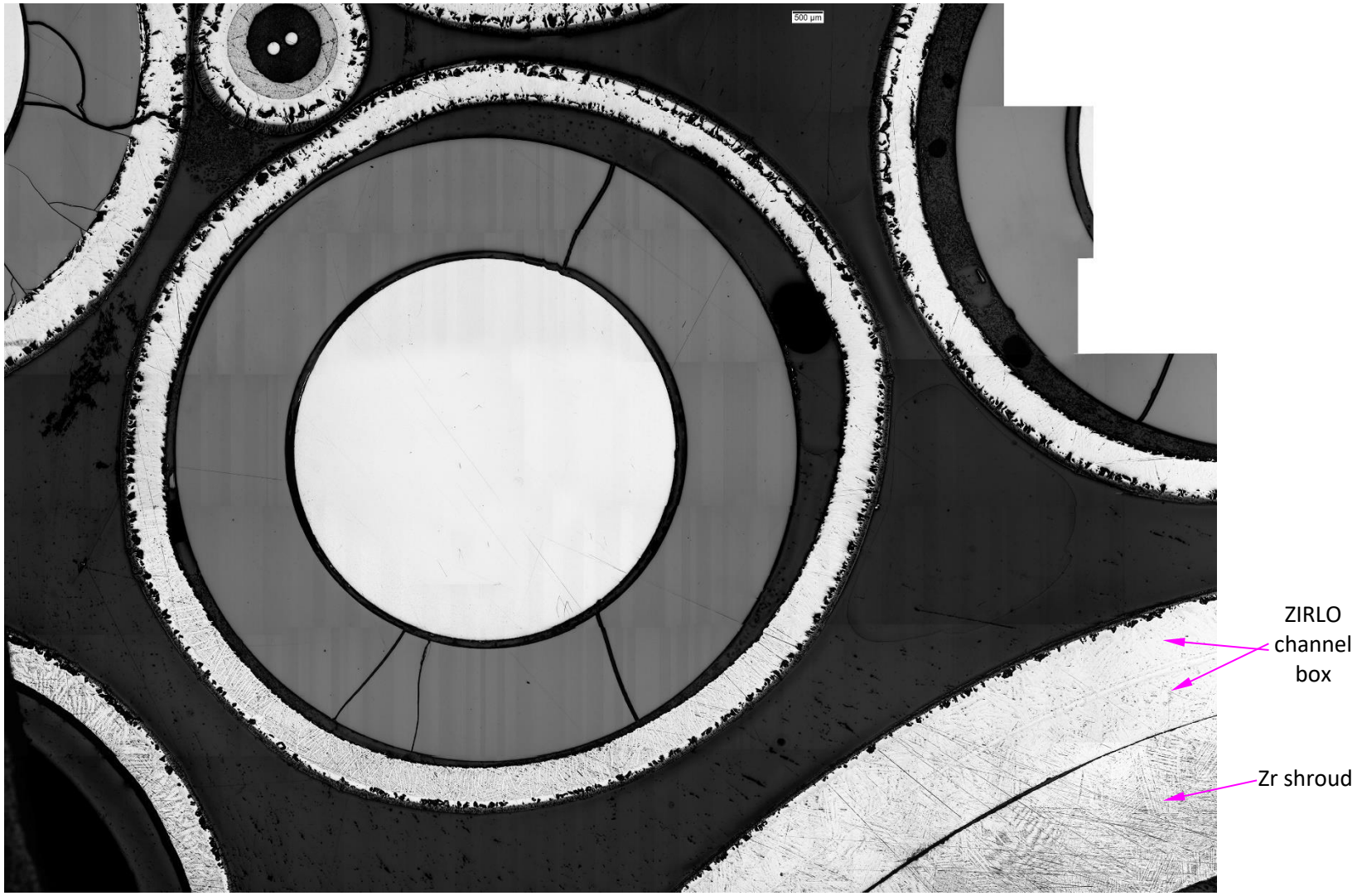

Figure 158 QUENCH-20; overview of rod #23 at elevation 650 mm: lift-off of the cladding into the hottest direction, oxidation of cladding inner surface.

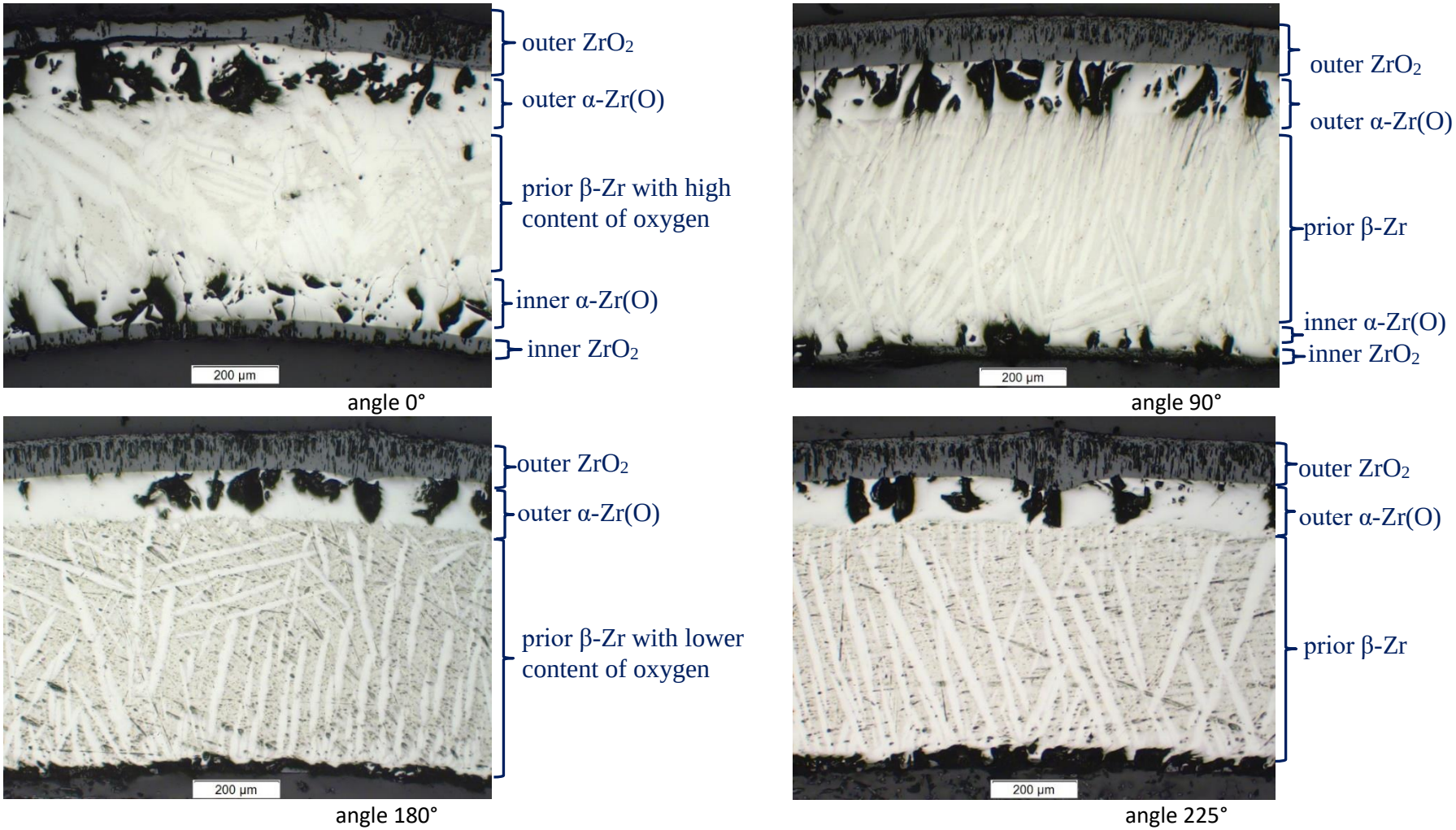

Figure 159 QUENCH-20; Cladding layer structures of rod #23 at 650 mm: formation of α-Zr(O) lamellas inside the prior β-Zr (Widmanstätten patterns) during cooling.

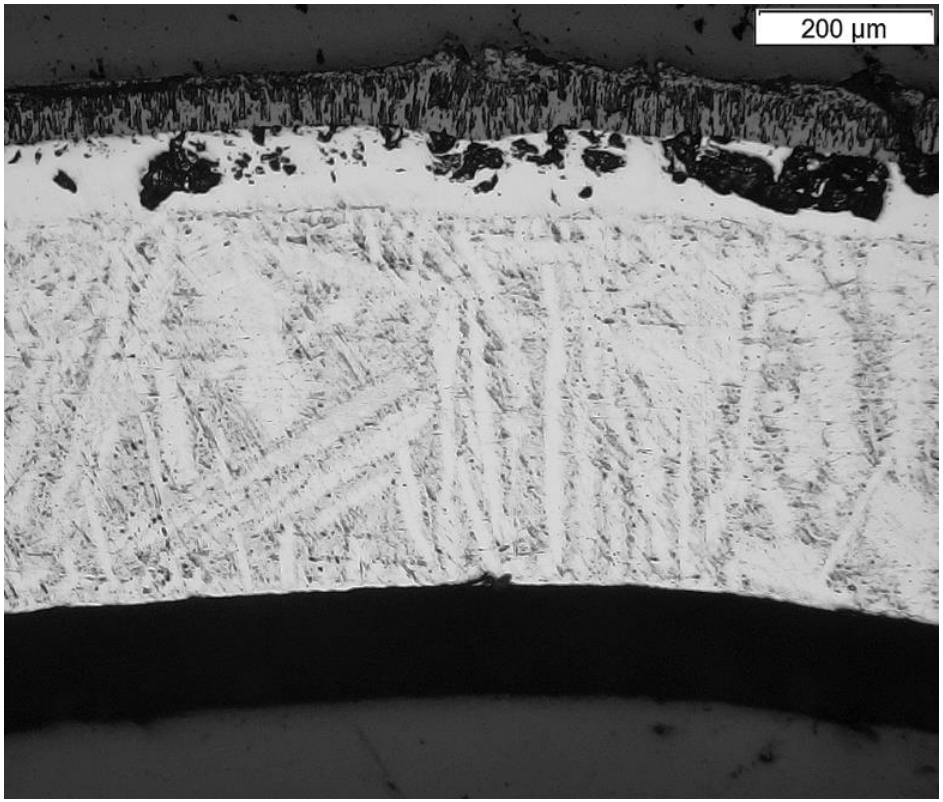

0°: thicker ZrO_2 and α-Zr(O) layers

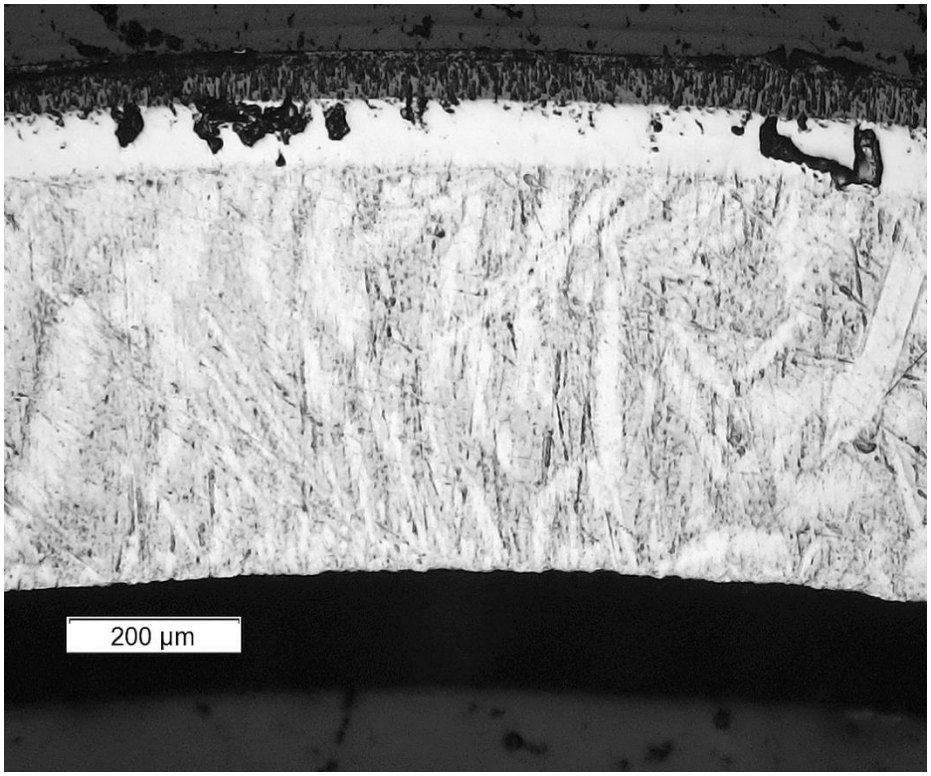

315°: thinner ZrO_2 and α-Zr(O) layers

Figure 160 QUENCH-20; Cladding layer structures of rod #24 at 650 mm: moderate outer oxidation, no inner oxidation, prior β-Zr with segregated α-Zr(O) lamellas.

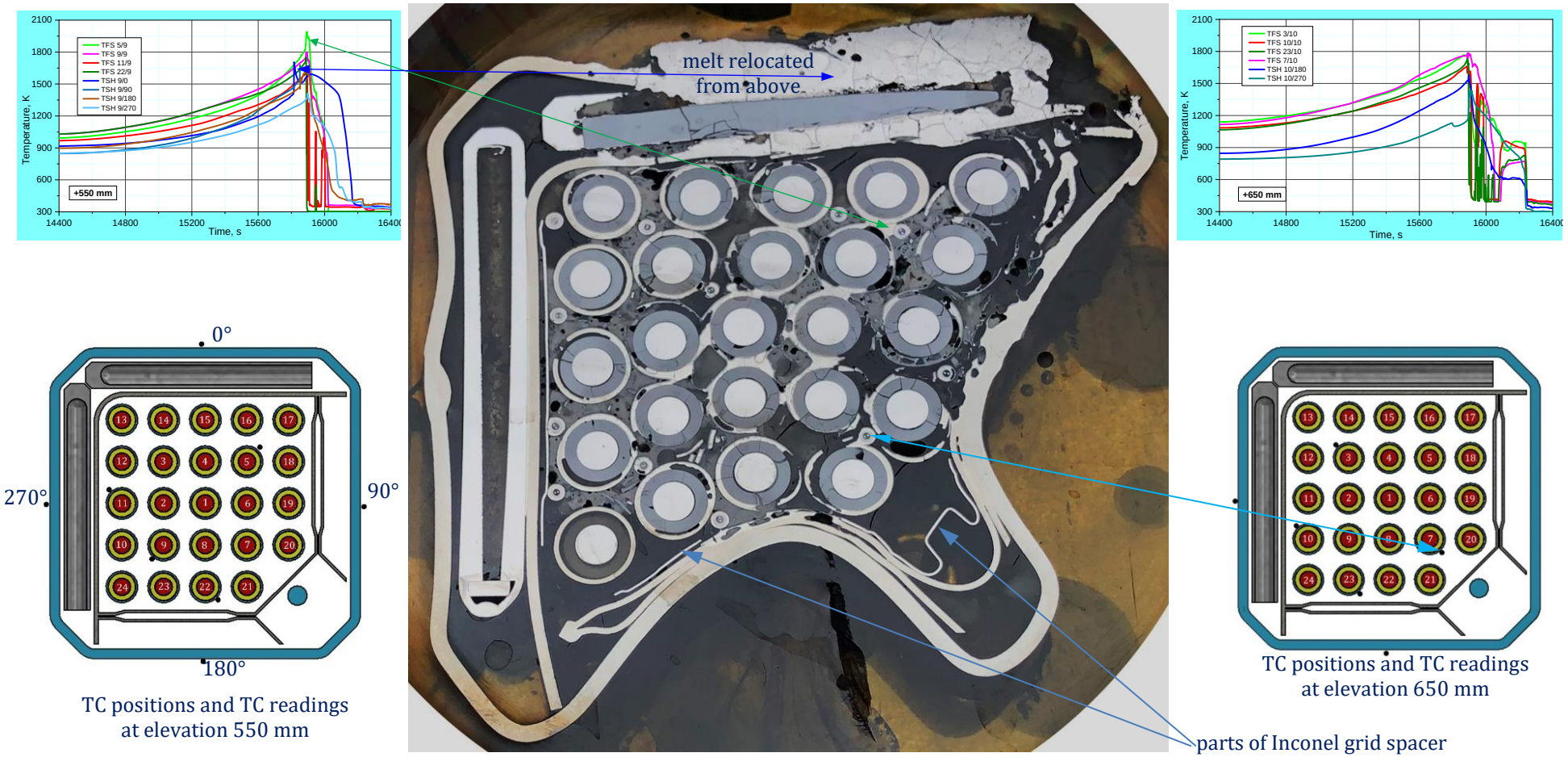

Figure 161 QUENCH-20; Bundle cross section at the elevation of 555 mm; strong cladding degradation due to eutectic interaction with the Inconel grid spacer and at the absorber position of 0° (eutectic interaction B_4C pin with stainless steel blade).

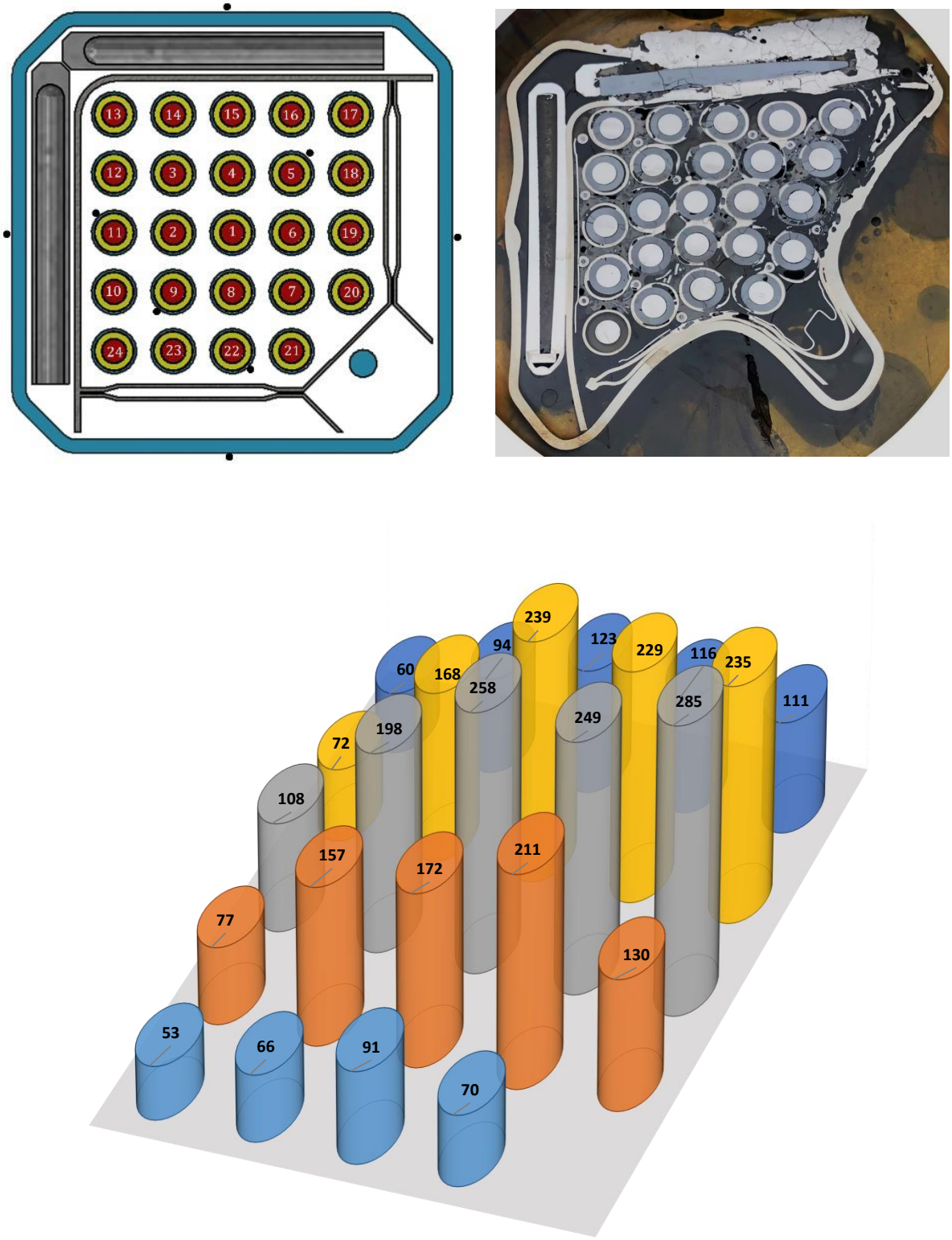

Figure 162 QUENCH-20; average thicknesses of outer ZrO_2 for each cladding at bundle elevation of 555 mm; indication of coldest bundle region at 180°.

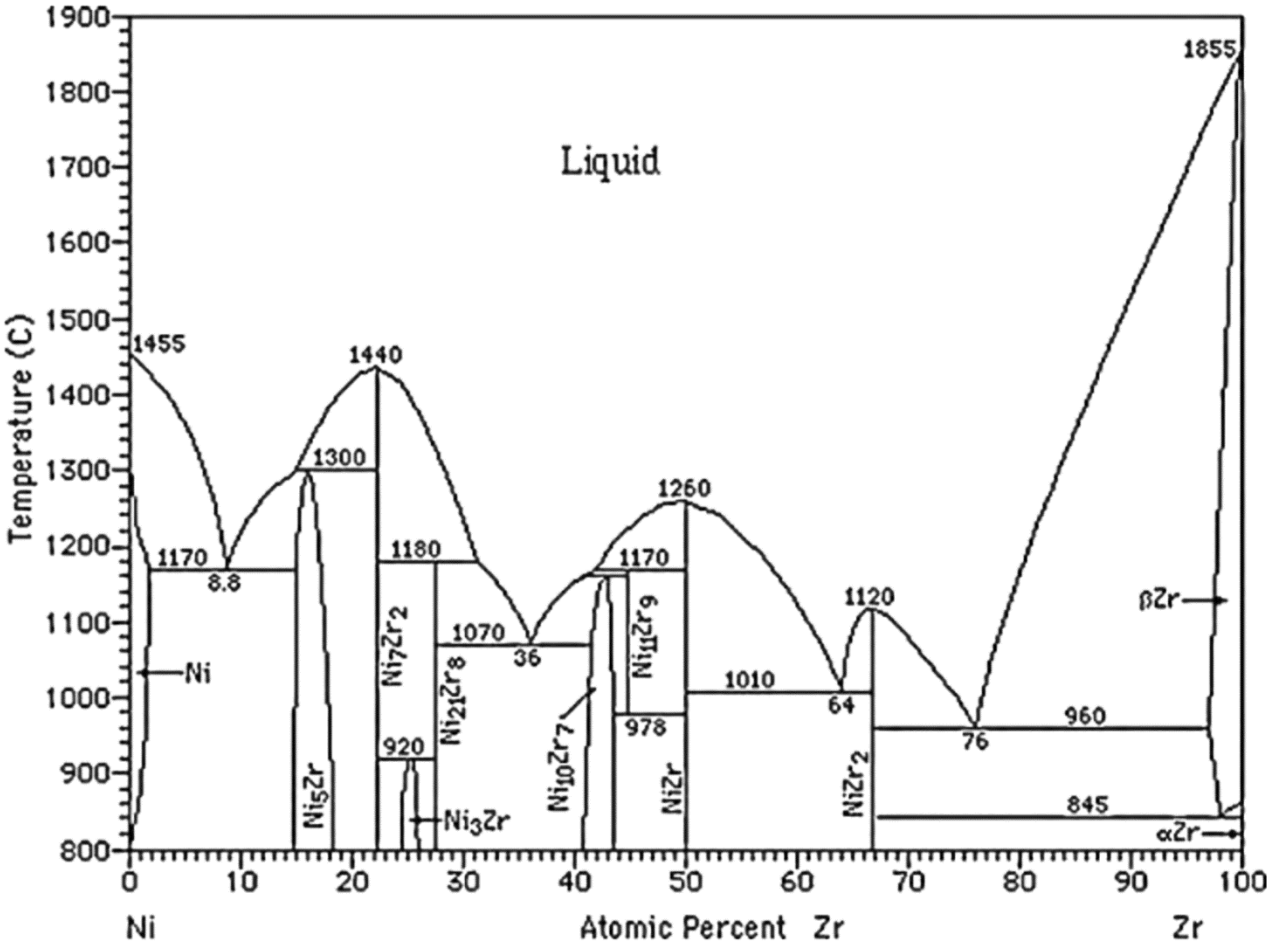

[Nash P., Jayanth C.S. (1991) Ni-Zr (Nickel-Zirconium). In: Nash P. (ed) Phase Diagrams of Binary Nickel Alloys. ASM International, Materials Park OH, pp 390-394]

Figure 163 Binary phase diagram of the Ni-Zr system: the lowest eutectic temperature 960 °C (1233 K).

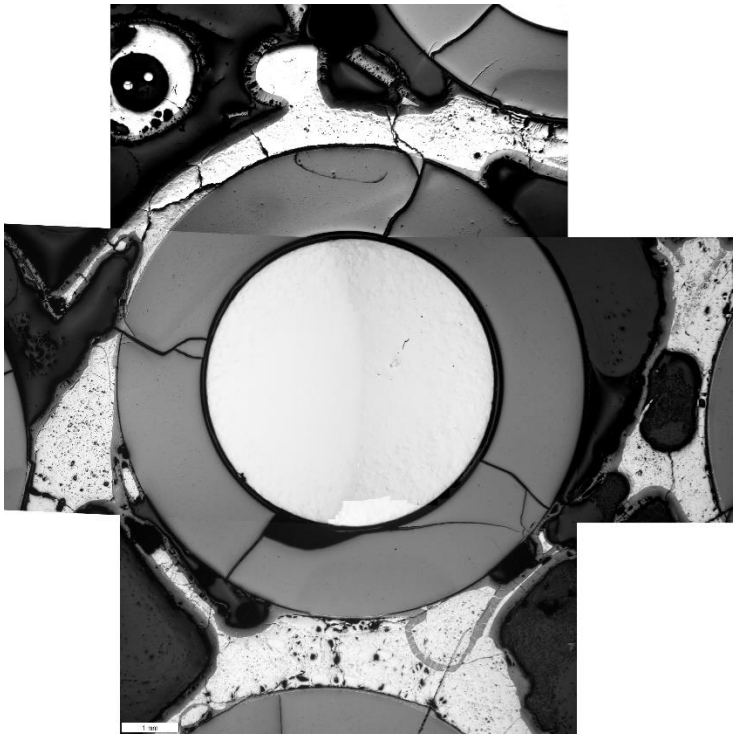

overview: molten pools around the rod

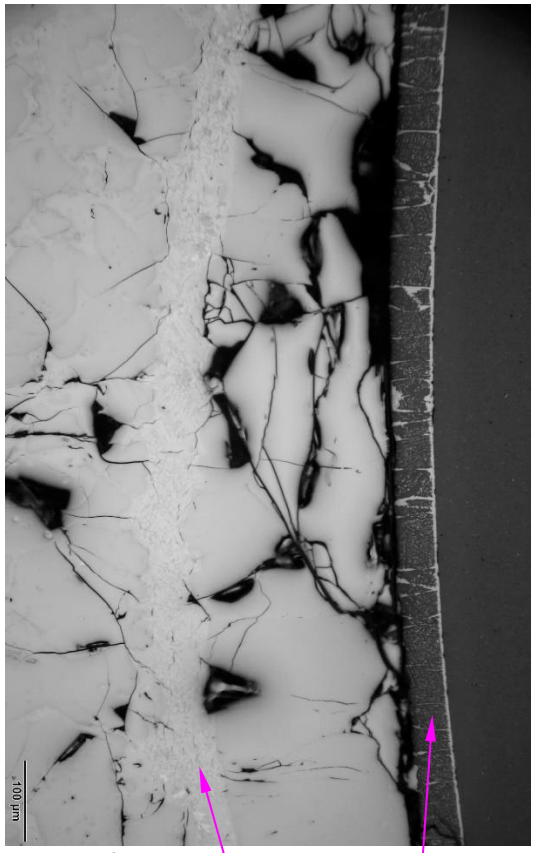

180°: frozen molten layer ; inner oxide layer at the contact with pellet

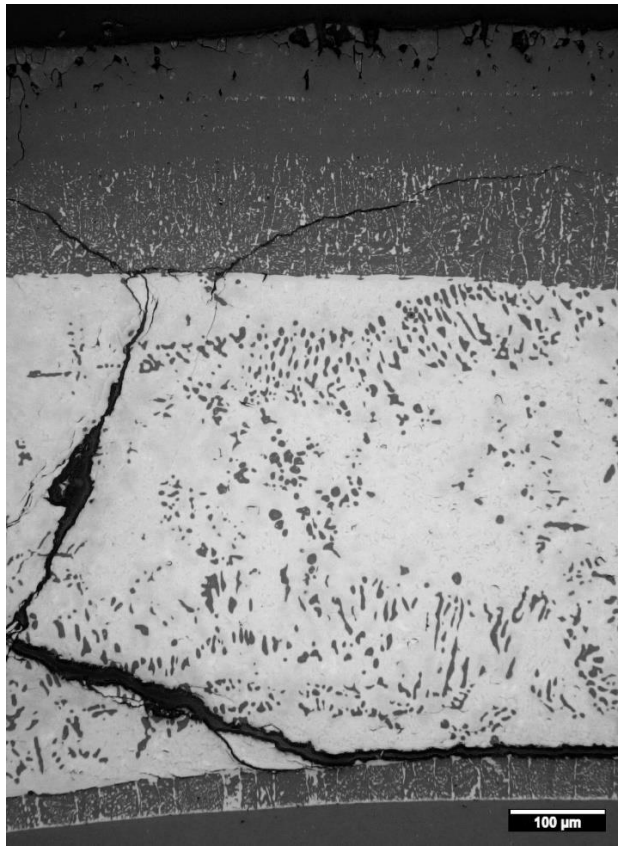

315°: ceramic precipitates in metal melt locked between outer and inner oxide layers

Figure 164 QUENCH-20; rod #1 at elevation 555 mm: strong cladding melting.

90°: melt between rods 2 (pellet down) and 1 (pellet top)

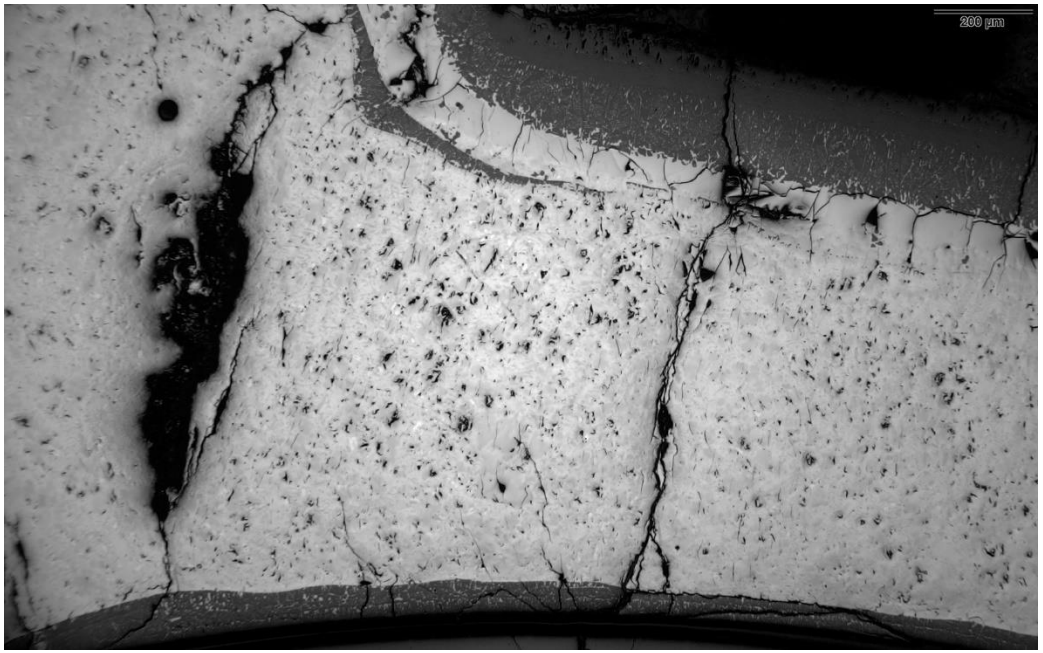

180°: melt between rods 1 (pellet down) and 9 (top)

Figure 165 QUENCH-20; rod #2 at elevation 555 mm: molten pools between neighbor rods.

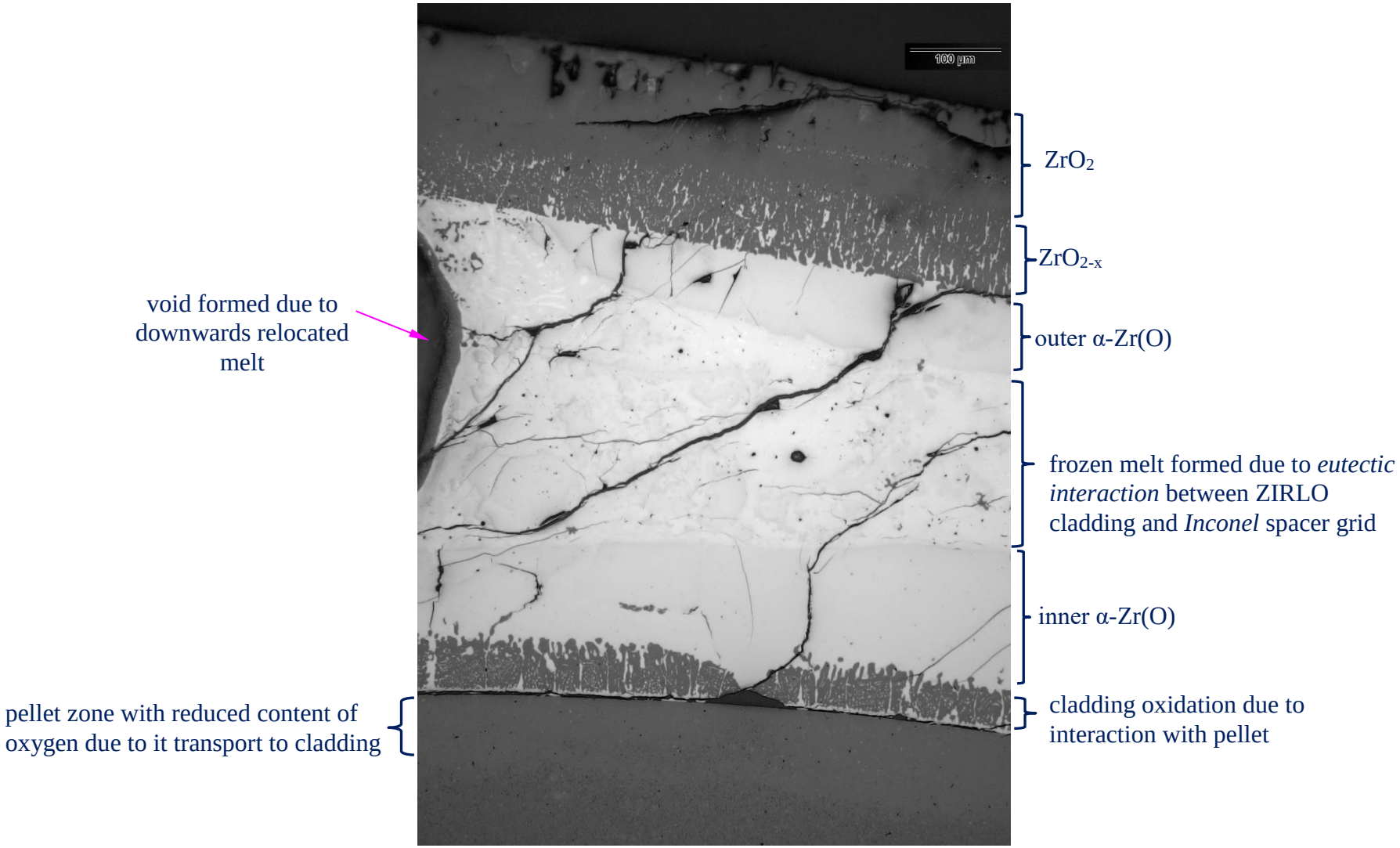

Figure 166 QUENCH-20; cladding and pellet layers of rod #3 at the bundle elevation 555 mm and angle 135°: melting of prior β-Zr.

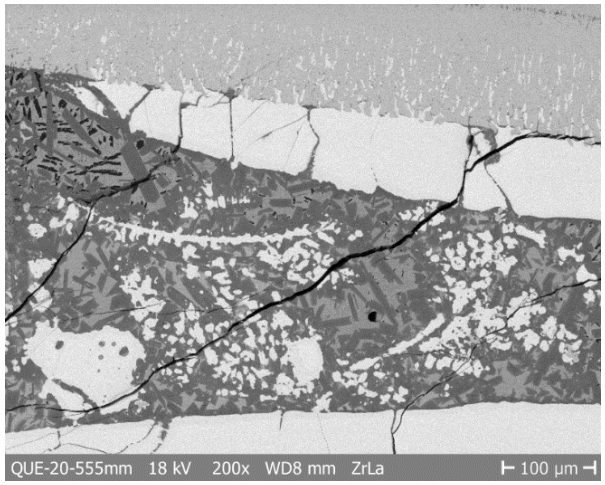

Zr distribution in oxide, α-Zr(O) and melt layers; α-Zr(O) precipitates in melt

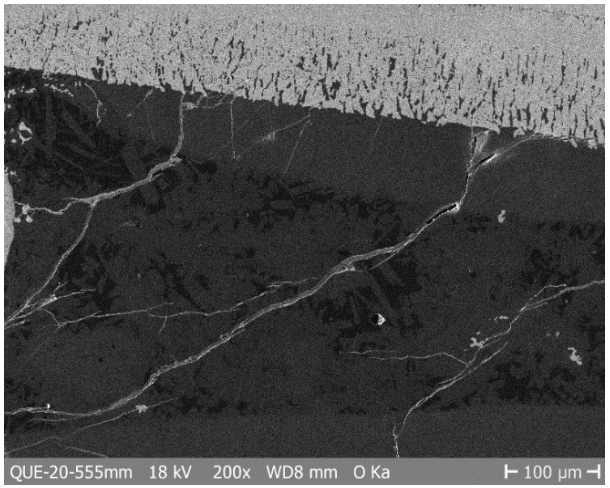

oxygen in oxide layer and in α-Zr(O) precipitates and layers

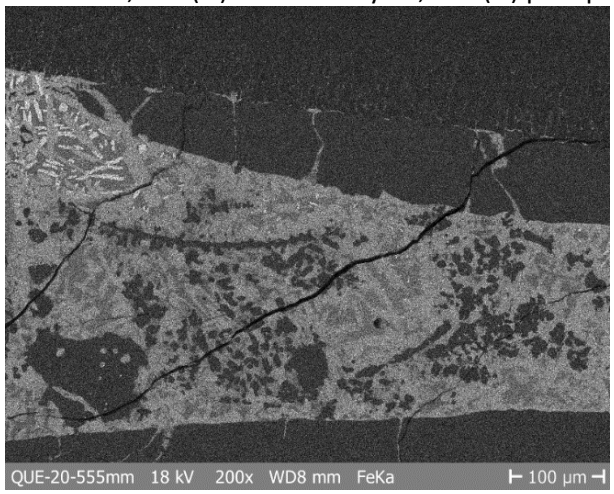

penetration of Fe (from spacer grid) into cladding melt

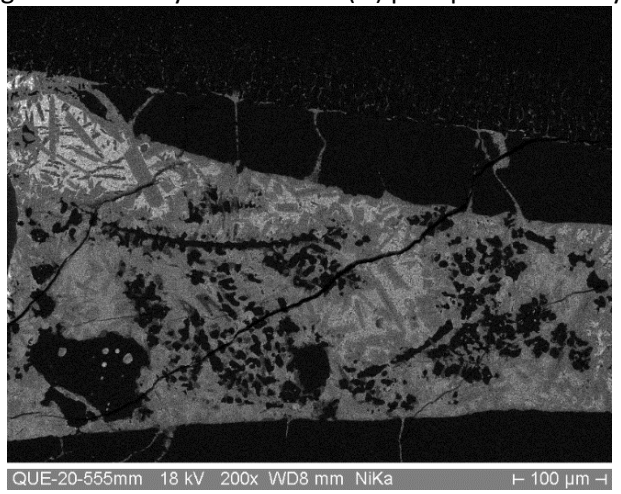

penetration of Ni (from spacer grid) into cladding melt

Figure 167 SEM/EDX element mapping of cladding #3 at bundle elevation 555 mm and angle 135°: penetration of molten spacer grid into molten cladding metal.

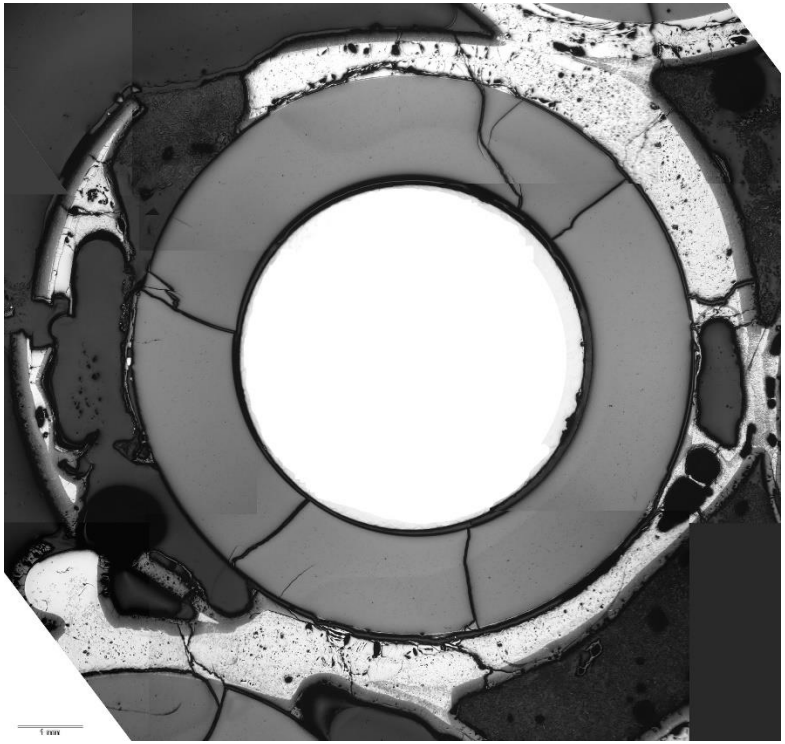

overview

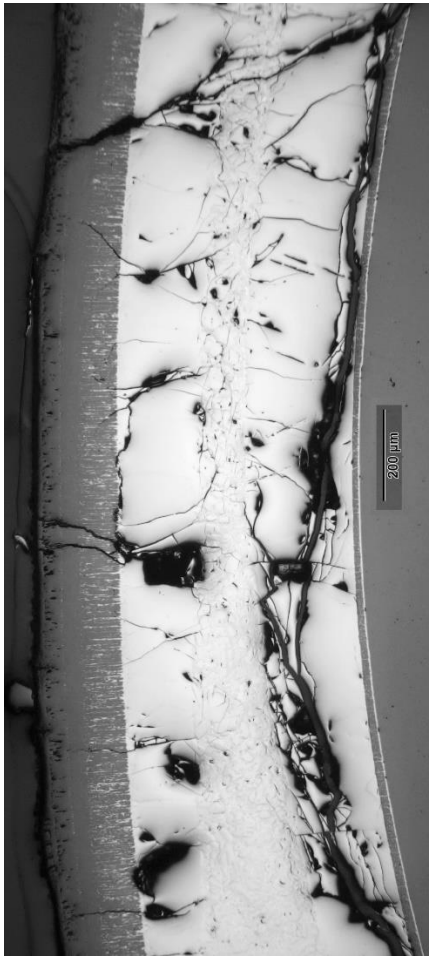

0°: melted thin prior β-Zr layer

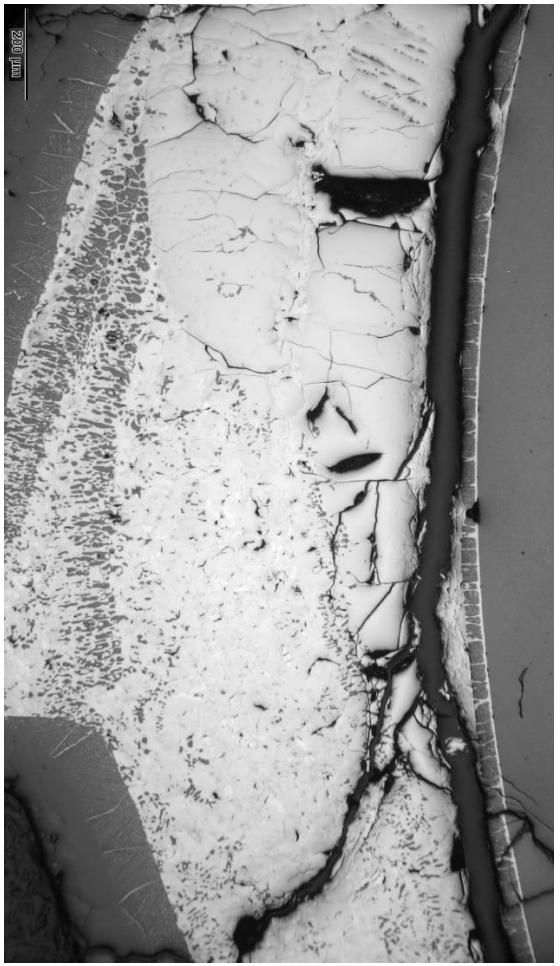

180°: cladding metal relocated from above

Figure 168 QUENCH-20; rod #4 at elevation 555 mm: mostly melted cladding.

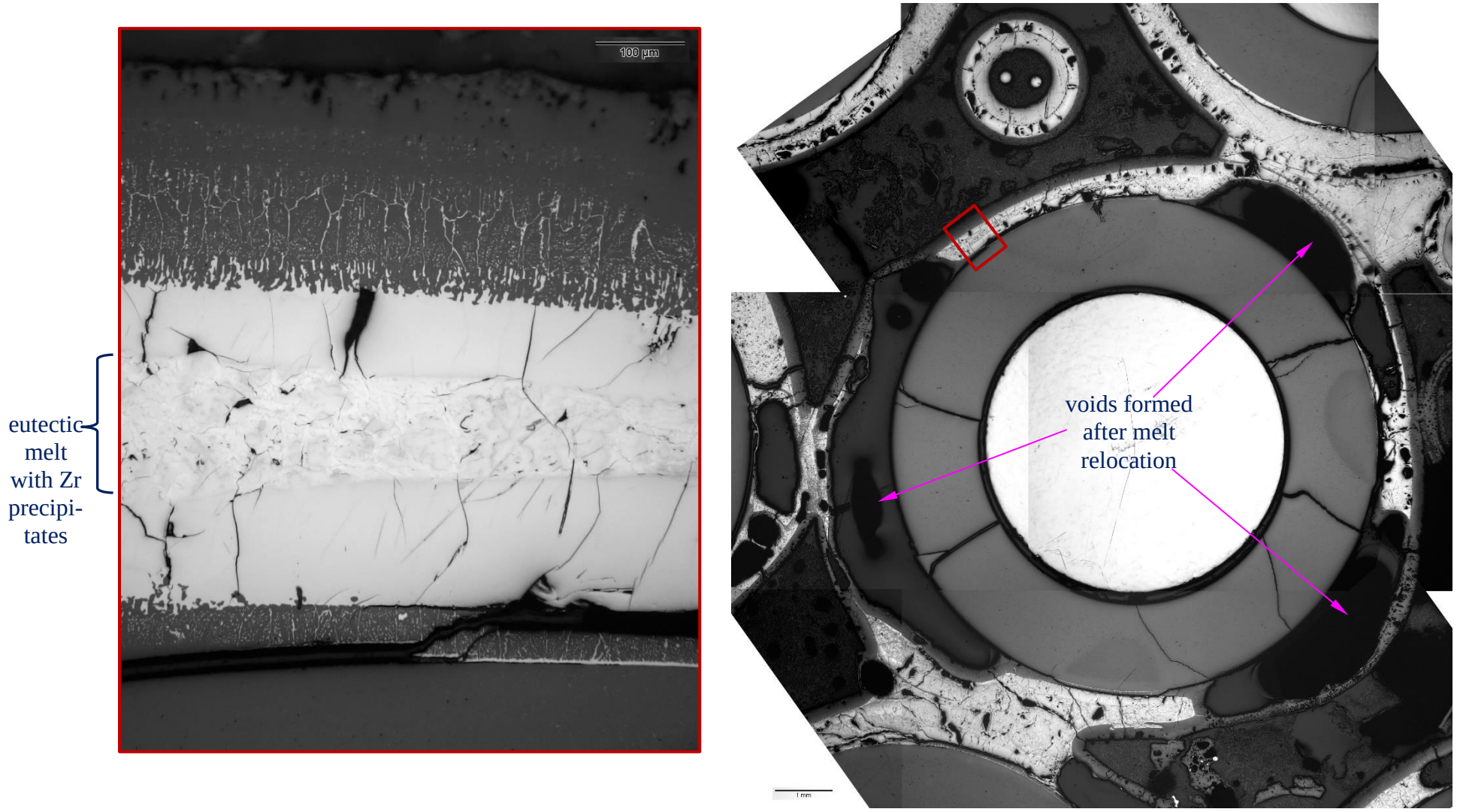

Figure 169 QUENCH-20; rod #5 at elevation 555 mm: strong cladding melting and melt relocation inside gap.

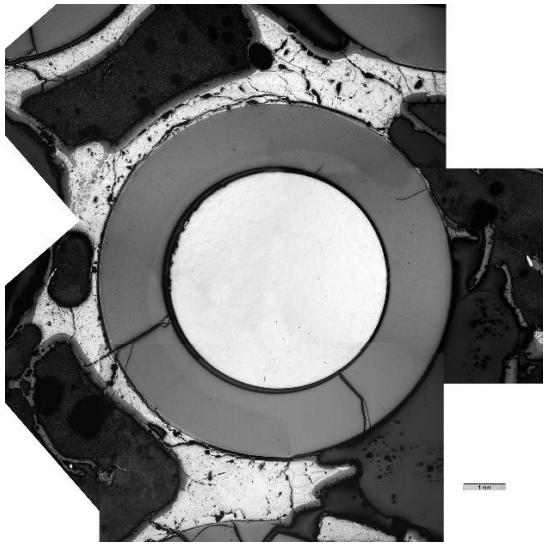

darkening of pellet (sub-stoichiometric ZrO_{2-x}) at contact with melt between 180° and 45°

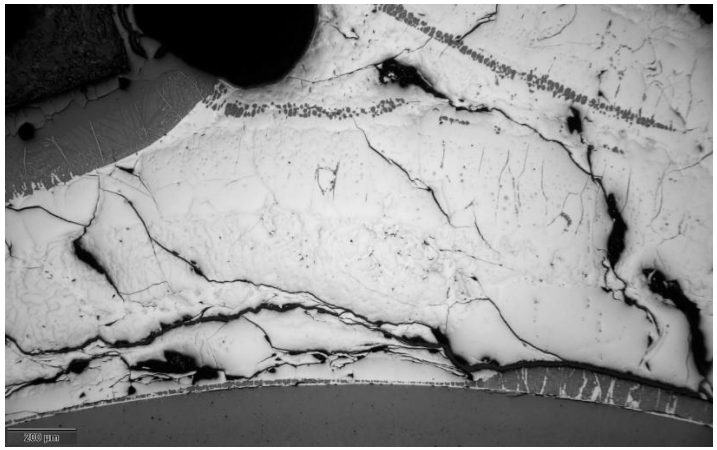

0°

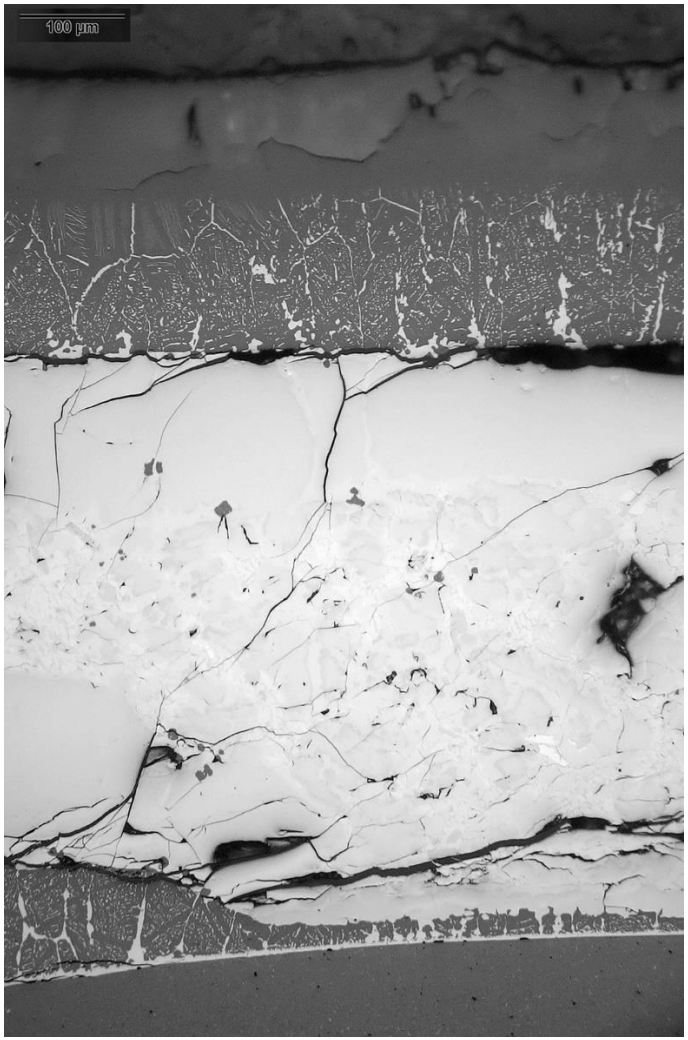

315°: eutectic melt penetrated between outer and inner α-Zr(O)

Figure 170 QUENCH-20; rod #6 at elevation 555 mm: structure of eutectic melt formed due to interaction between cladding and spacer.

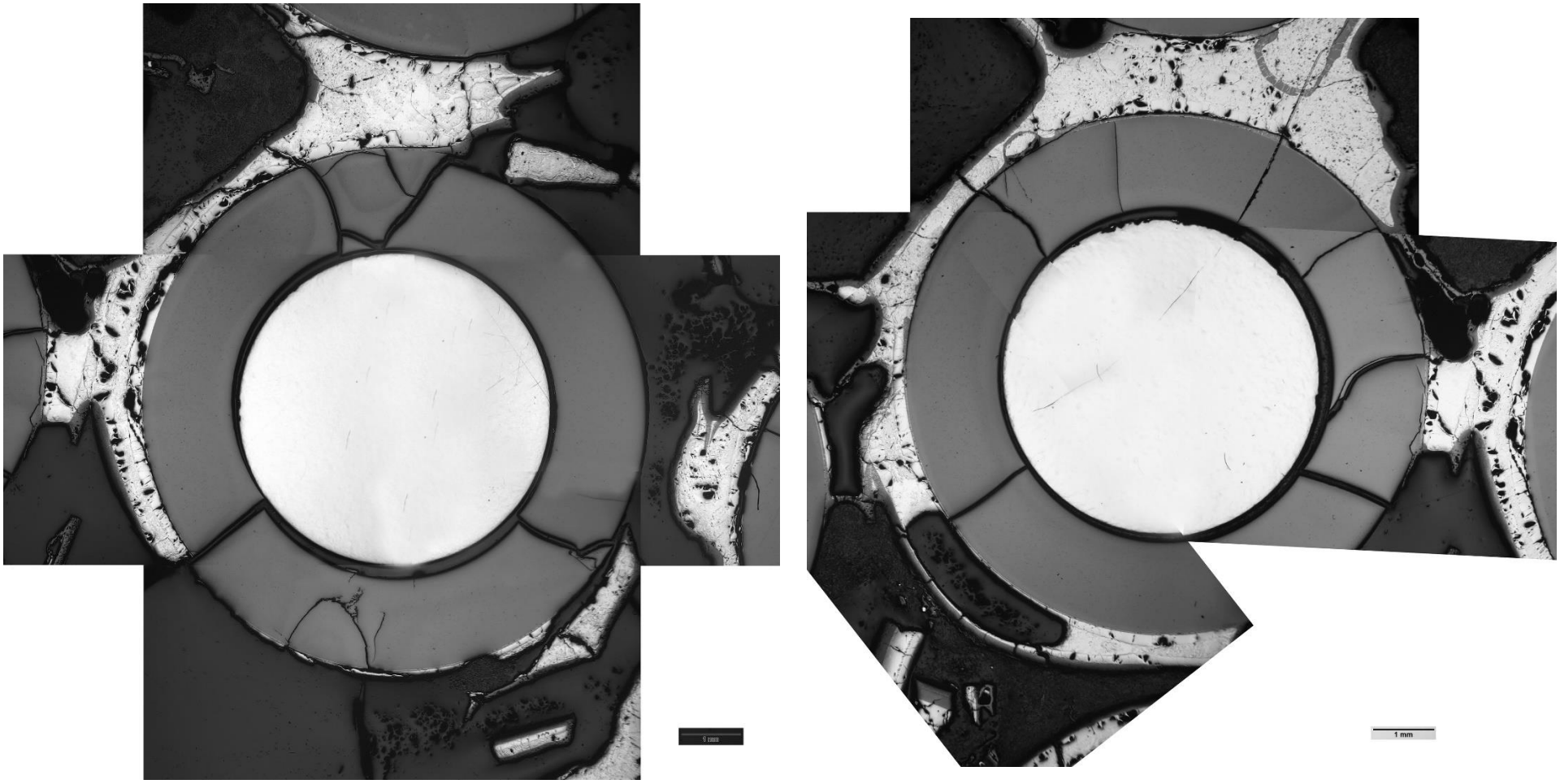

rod 7 rod 8

Figure 171 QUENCH-20; rods #7 and #8 at elevation 555 mm: eutectic melt remained around the pellets.

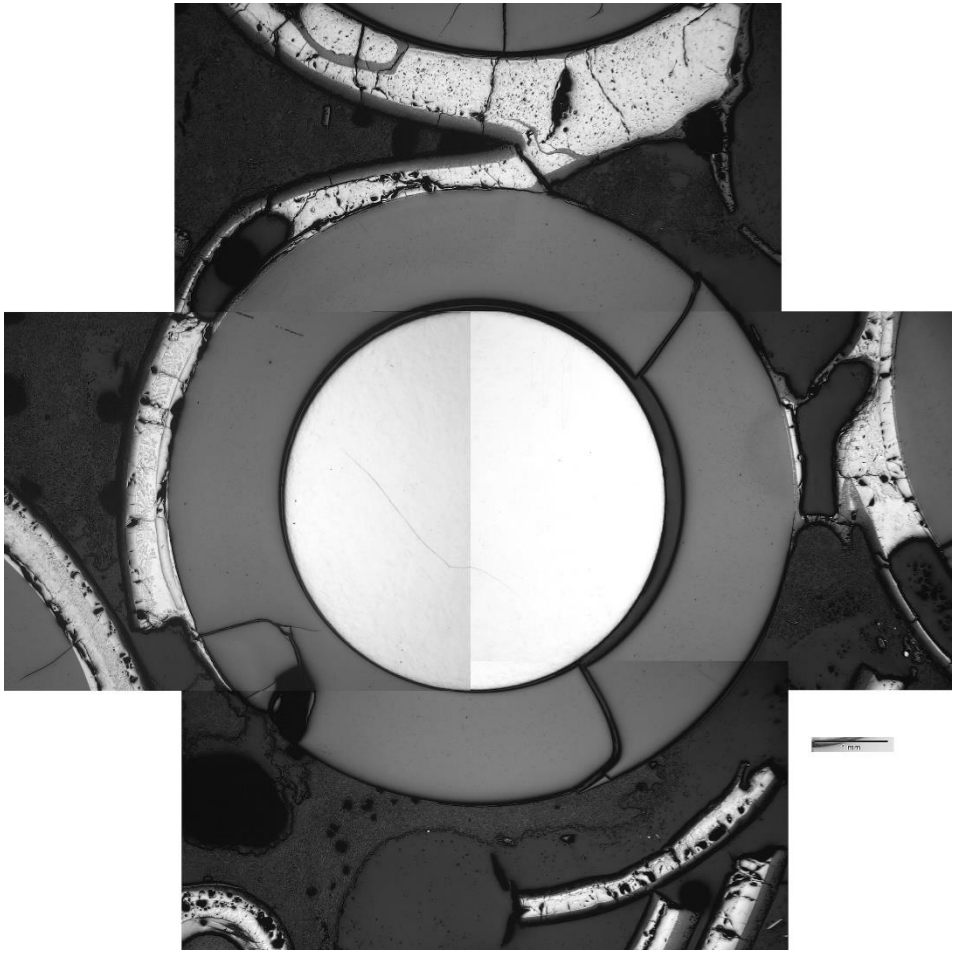

cross-section of rod

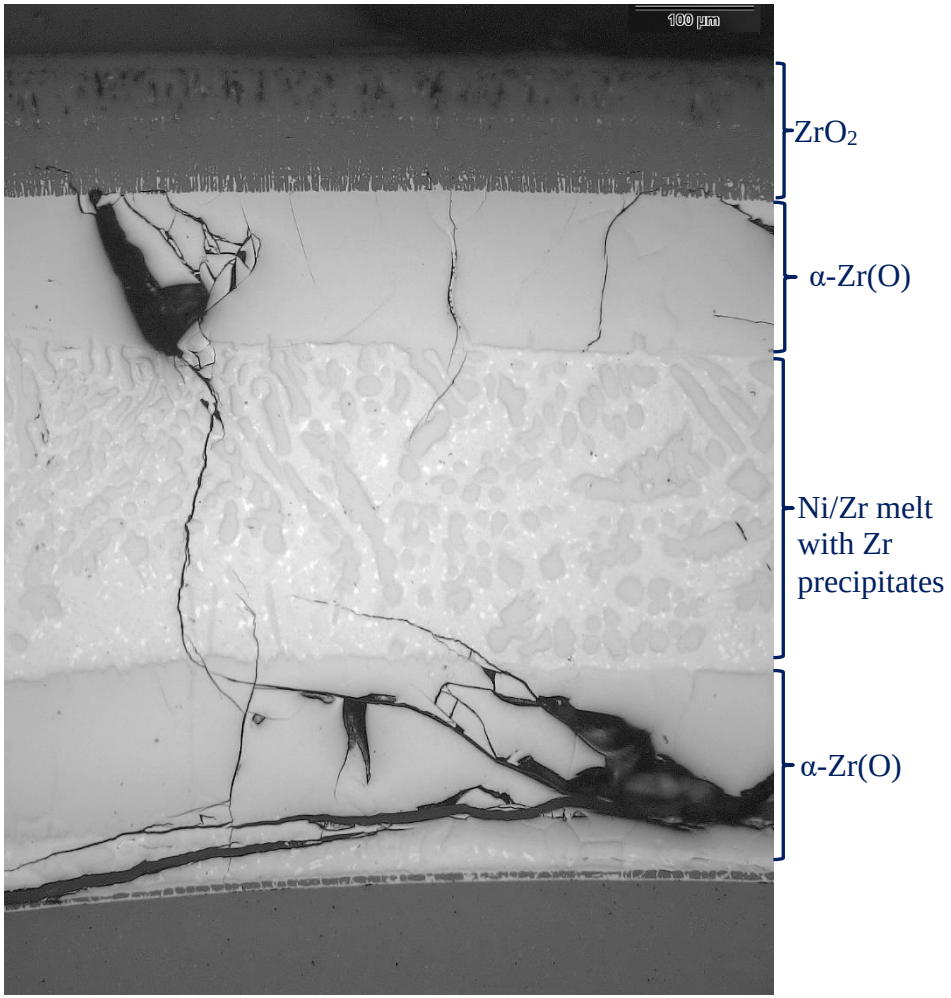

270°: melt between outer and inner α-Zr(O); Zr precipitates in Ni/Zr melt

Figure 172 QUENCH-20; rod #9 at elevation 555 mm: cladding/spacer eutectic melt remained around the pellet.

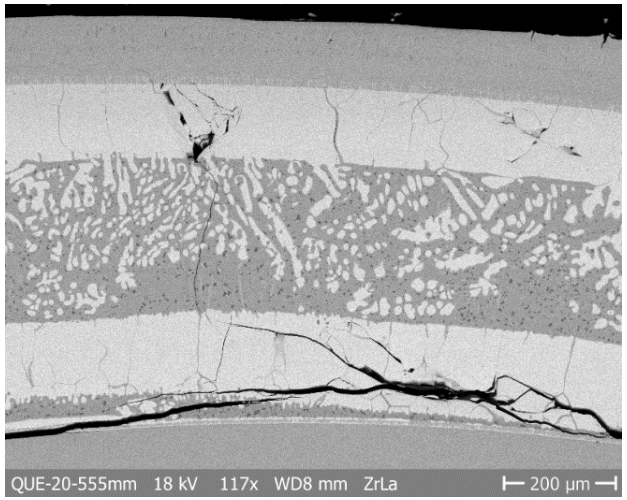

Zr distribution in oxide, α-Zr(O) and melt layers

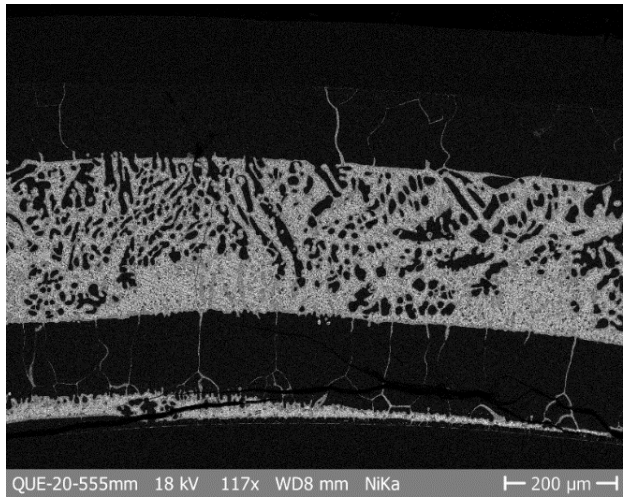

Ni from molten spacer grid in the cladding melt and in the cladding-pellet gap

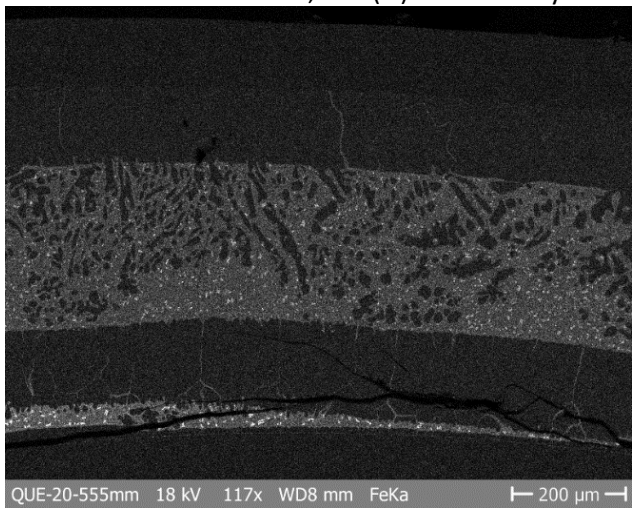

only small Fe precipitates in the melt

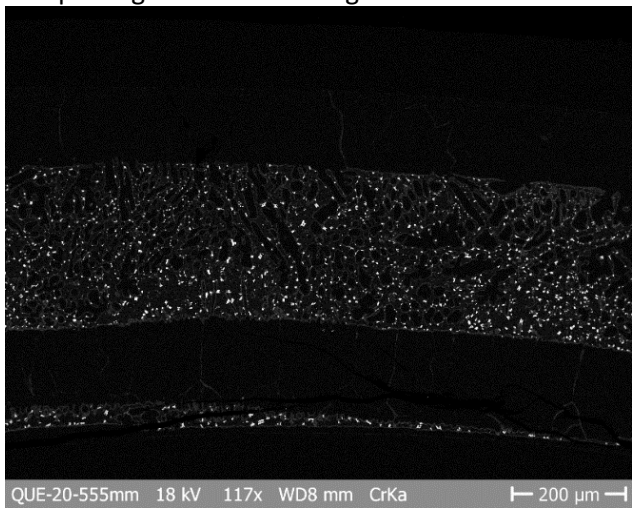

only small Cr precipitates in the melt

Figure 173 SEM/EDX element mapping of cladding #9 at bundle elevation 555 mm and angle 270°: penetration of molten spacer grid into molten cladding metal.

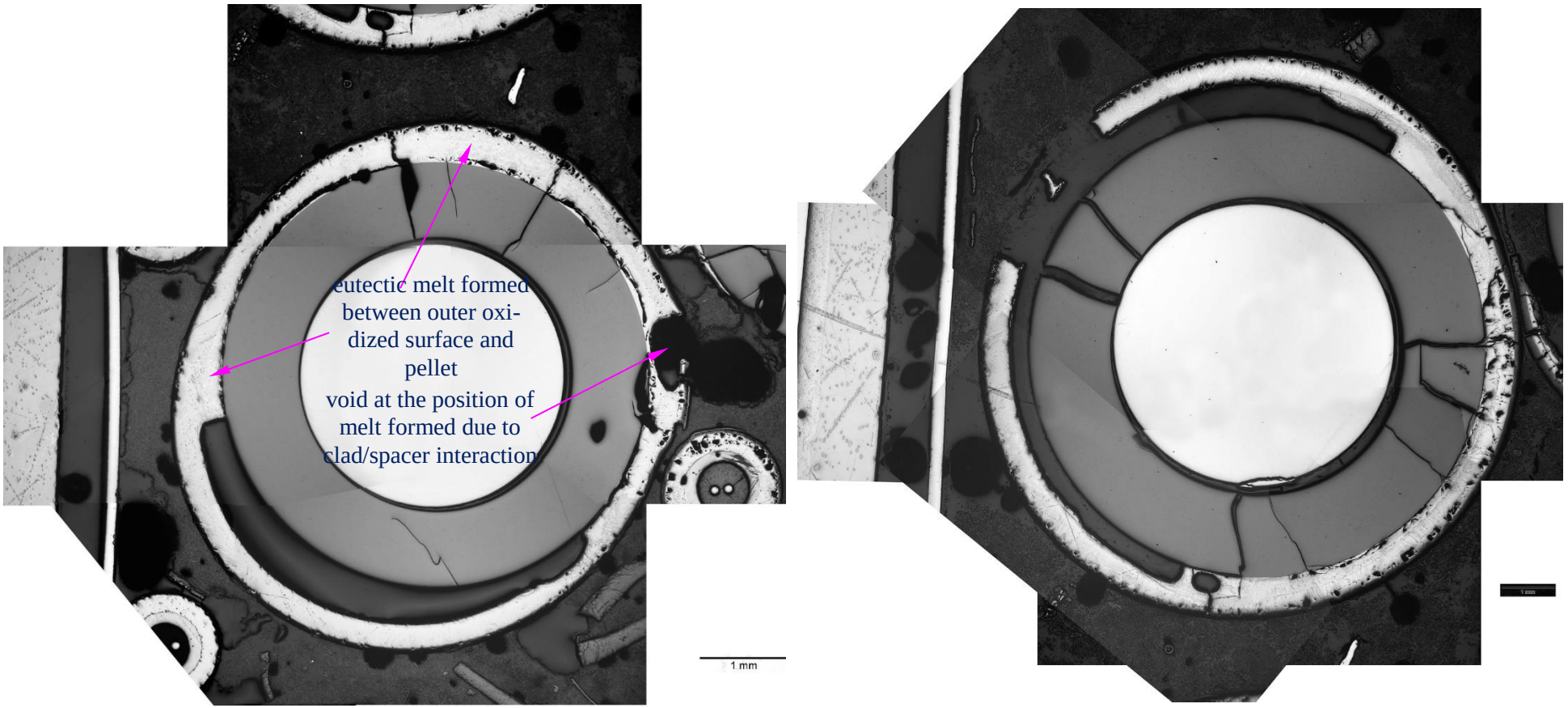

Figure 174 QUENCH-20; rods #10 and #11 at elevation 555 mm: melt relocated from 850 mm in gap between pellet and outer α-Zr(O).

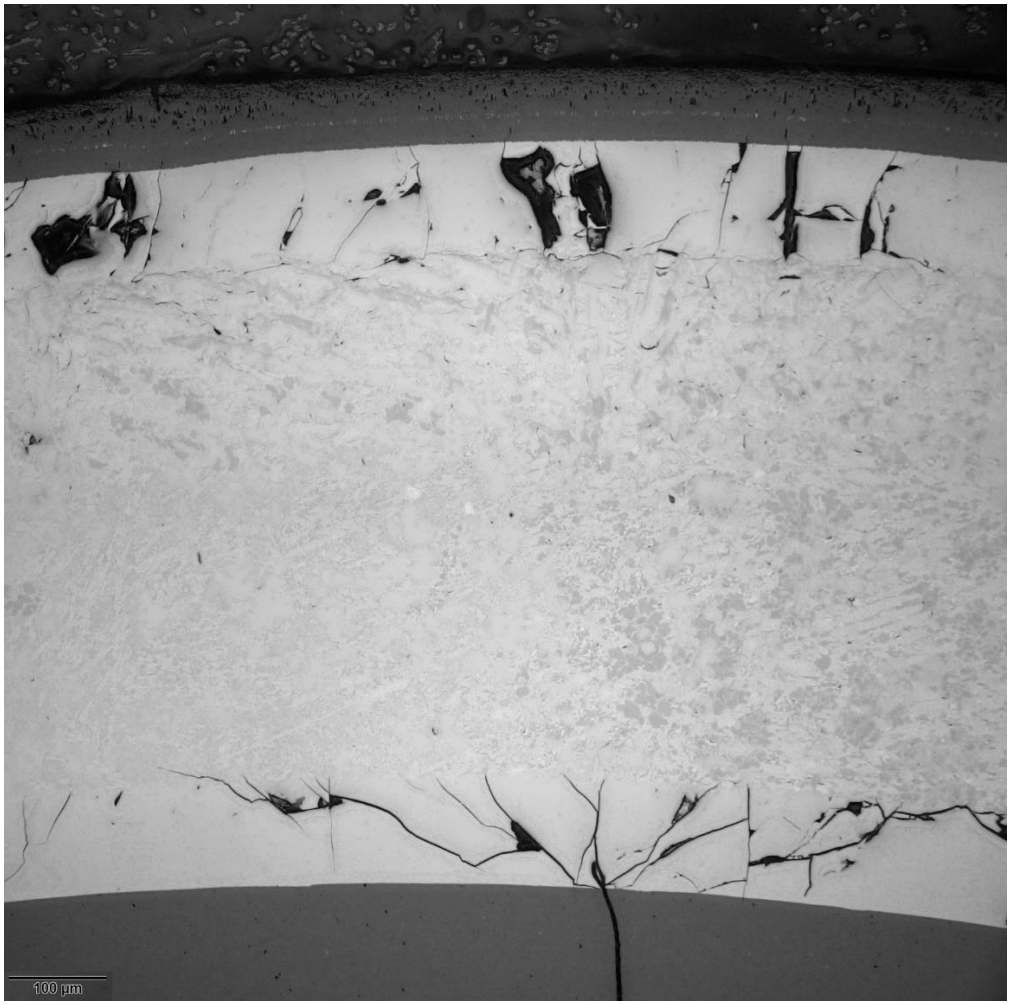

0°: melt between outer and inner α-Zr(O) layers

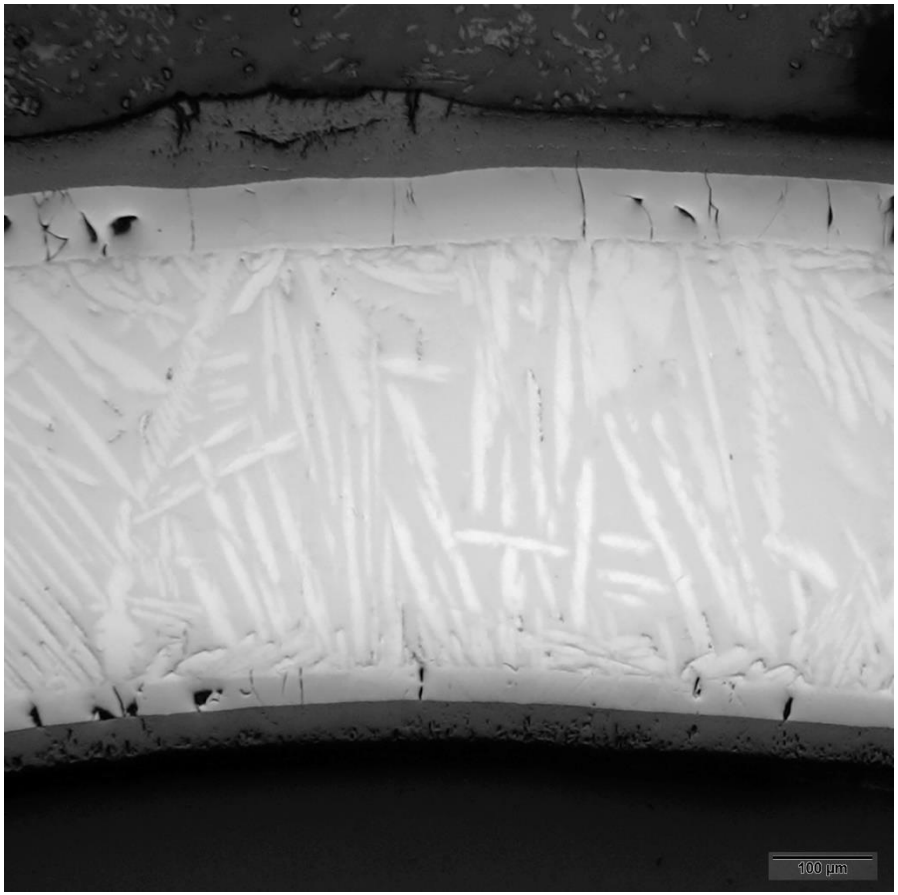

180°: prior β-Zr (with α-Zr(O) lamellas segregated during cooldown) between outer and inner α-Zr(O) layers

Figure 175 QUENCH-20; cladding micro structure of rod #10 at elevation 555 mm: melt in gap between pellet and outer α-Zr(O).

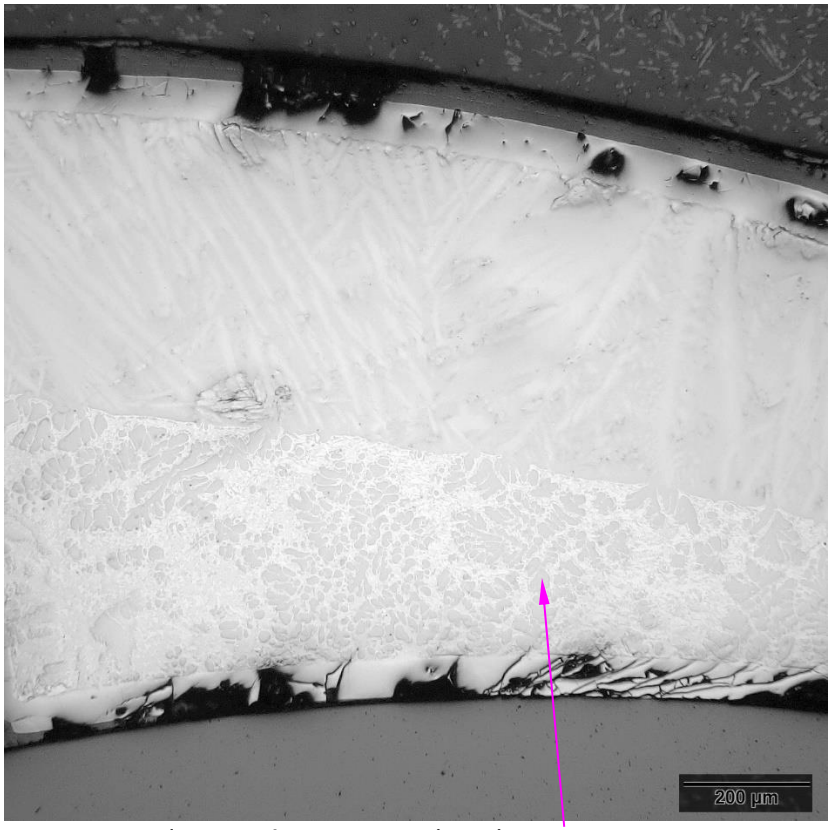

rod 10, 270°: eutectic melt with Zr precipitates

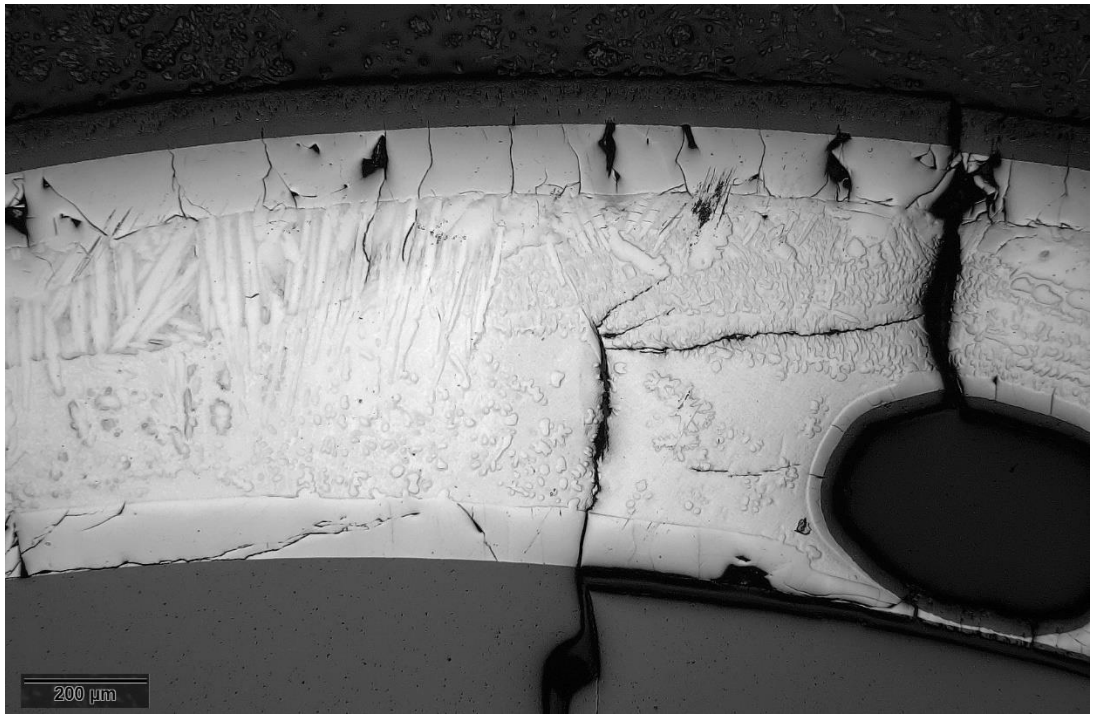

rod 11, 180°

Figure 176 QUENCH-20; cladding micro structure of rods #10 and #11 at elevation 555 mm: melt in gap between pellet and outer β-Zr layer.

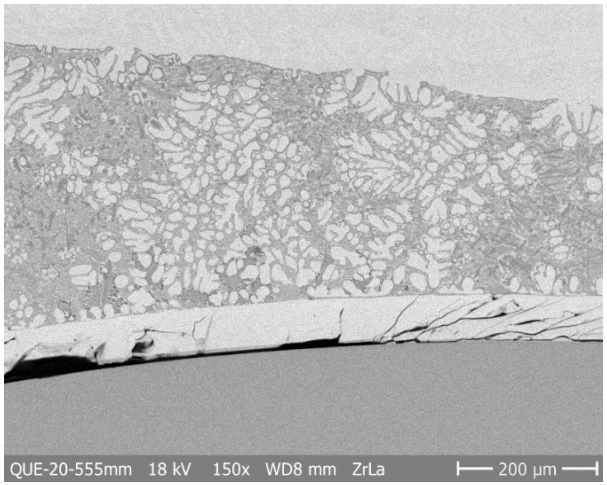

Zr distribution in oxide, α-Zr(O) and melt layers

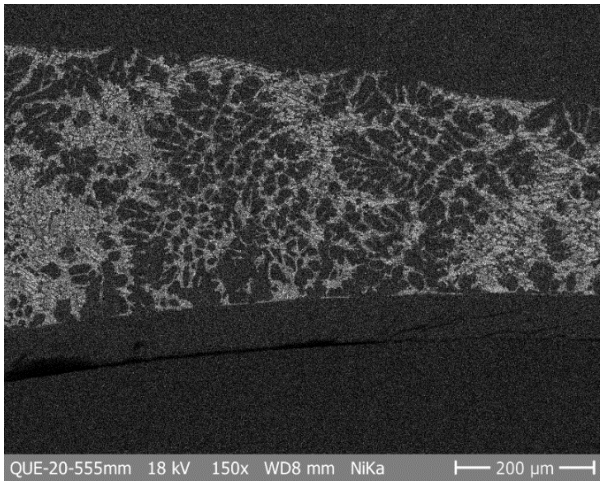

Ni from molten spacer grid in the cladding melt

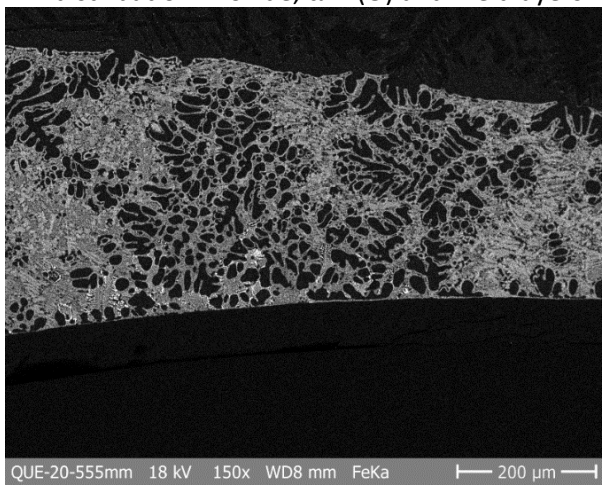

Fe from molten spacer grid in the cladding melt

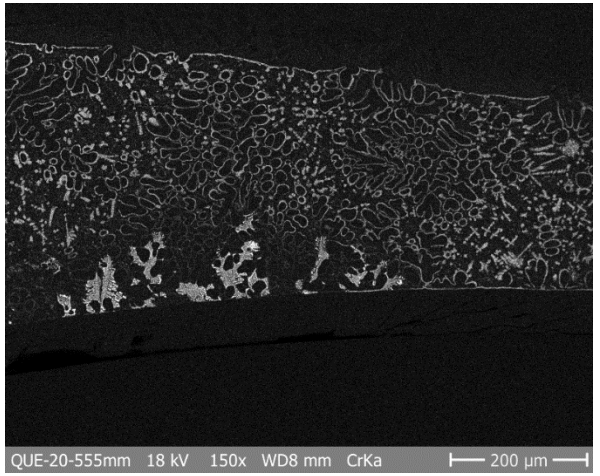

only small Cr traces in the melt

Figure 177 SEM/EDX element mapping of cladding #10 at bundle elevation 555 mm and angle 270°: penetration of molten spacer grid into molten cladding metal.

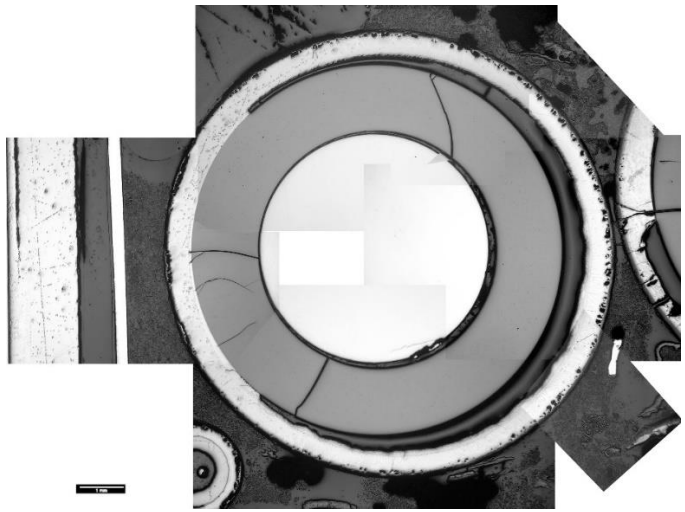

overview: melt in gap relocated from 850 mm

0°: not melted region

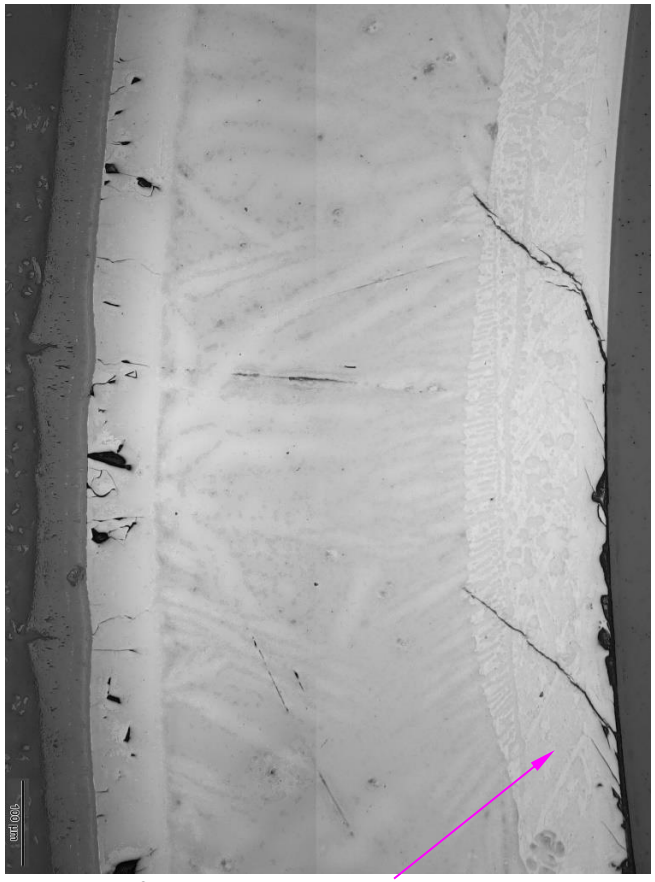

225°: gap filled with eutectic melt penetrated under cladding failed at 850 mm

Figure 178 QUENCH-20; rod #12 at elevation 555 mm: eutectic melt relocated from upper elevations.

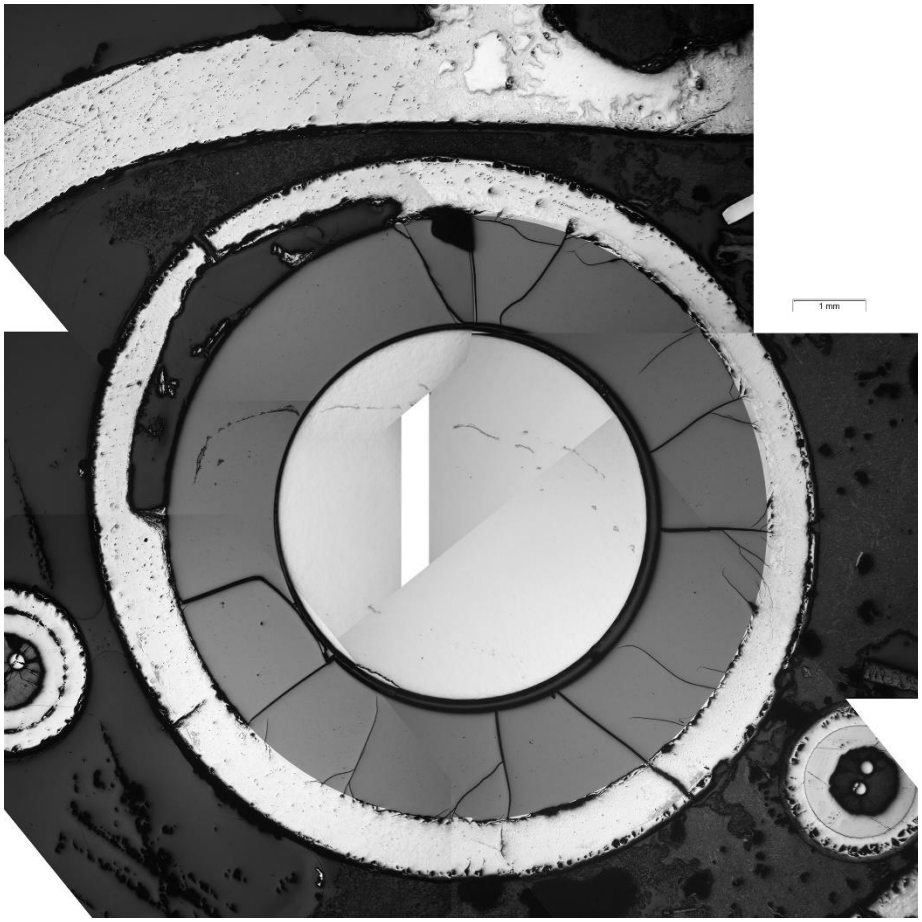

overview

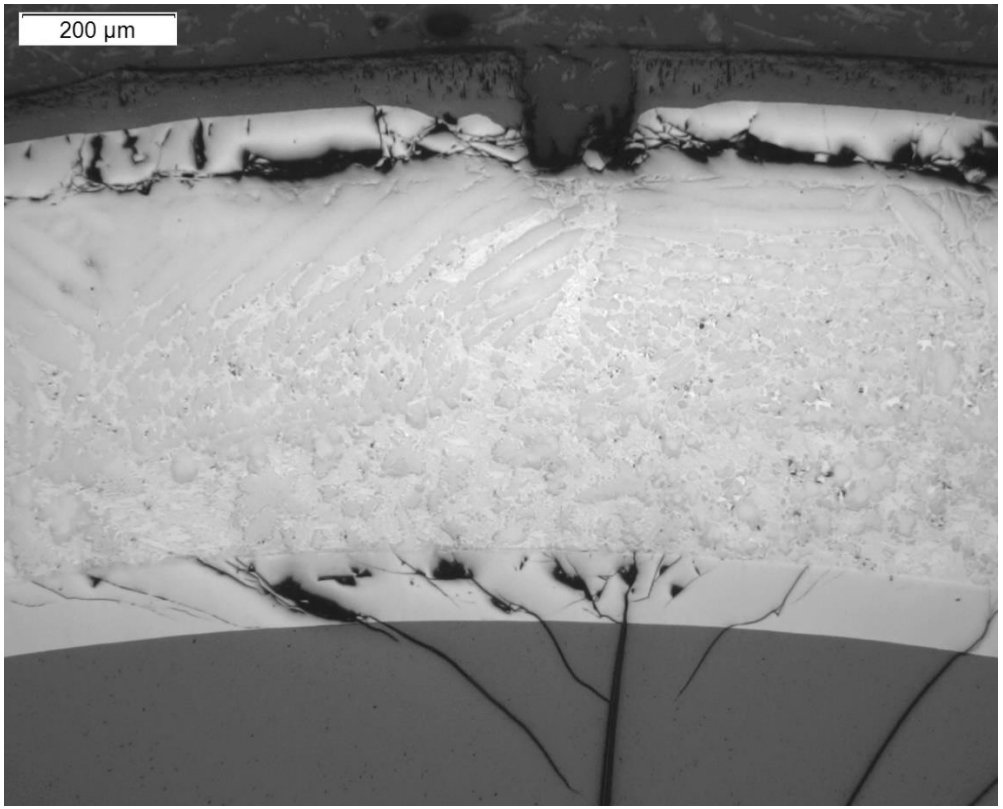

90°: partially melted prior β-Zr

Figure 179 QUENCH-20; rod #13 at elevation 555 mm: melted cladding.

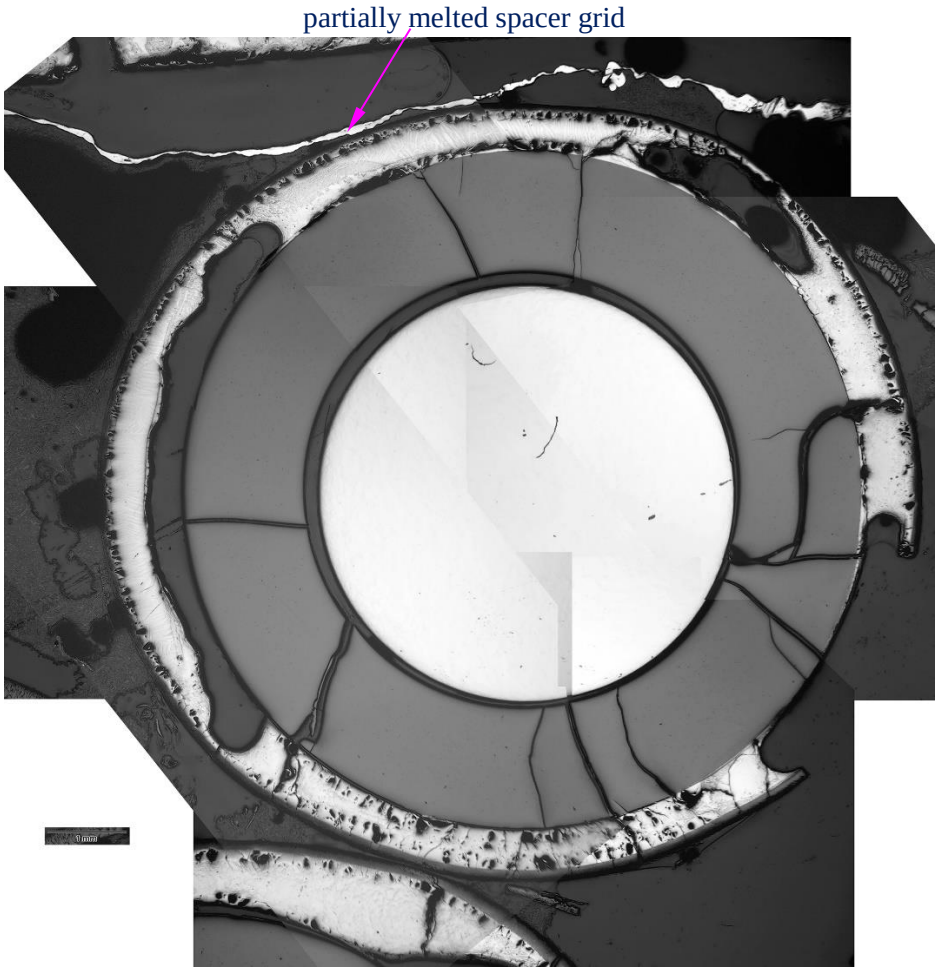

overview

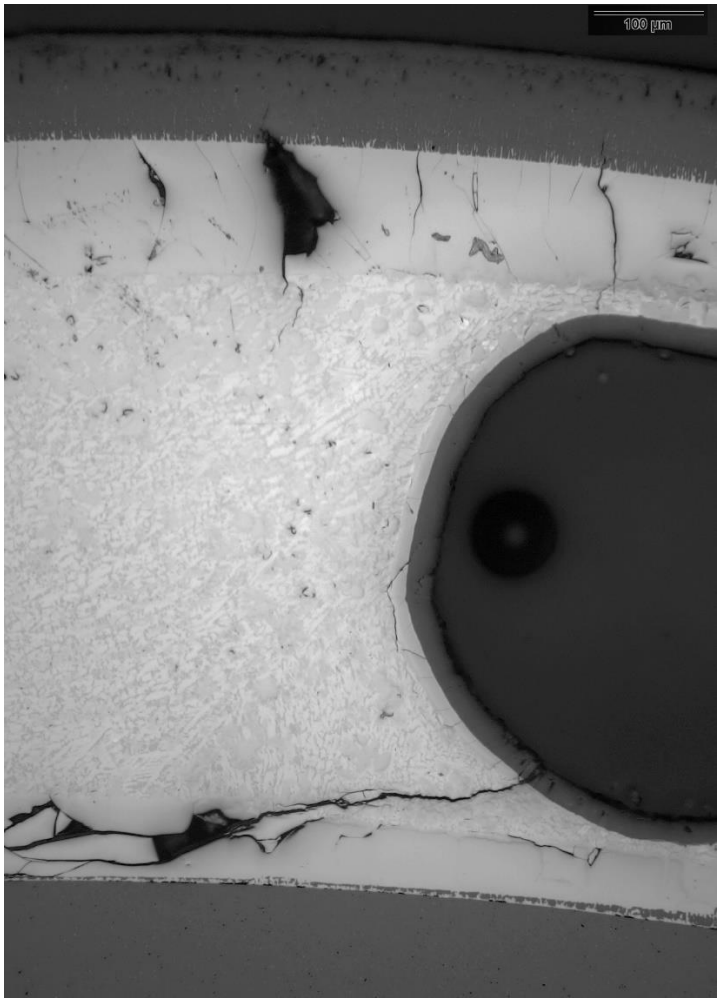

90°: melt between outer and inner α-Zr(O) layers; oxidized edge of void after melt relocation

Figure 180 QUENCH-20; rod #14 at elevation 555 mm: melted cladding and melted spacer grid.

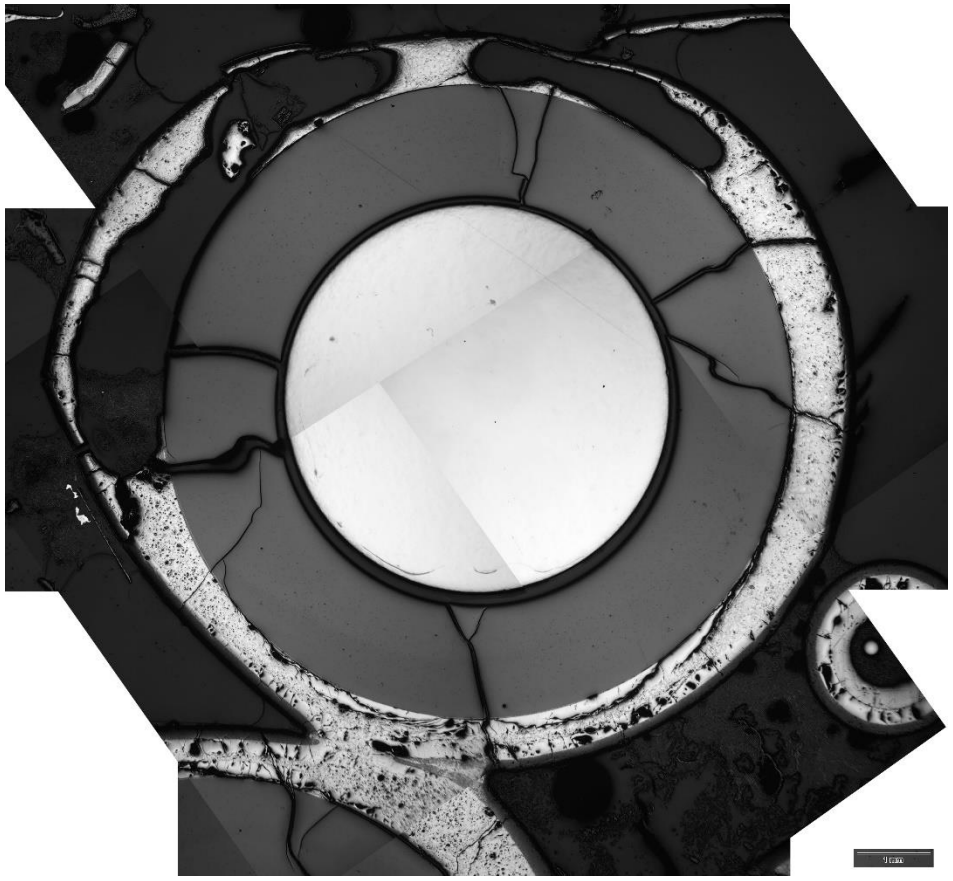

overview

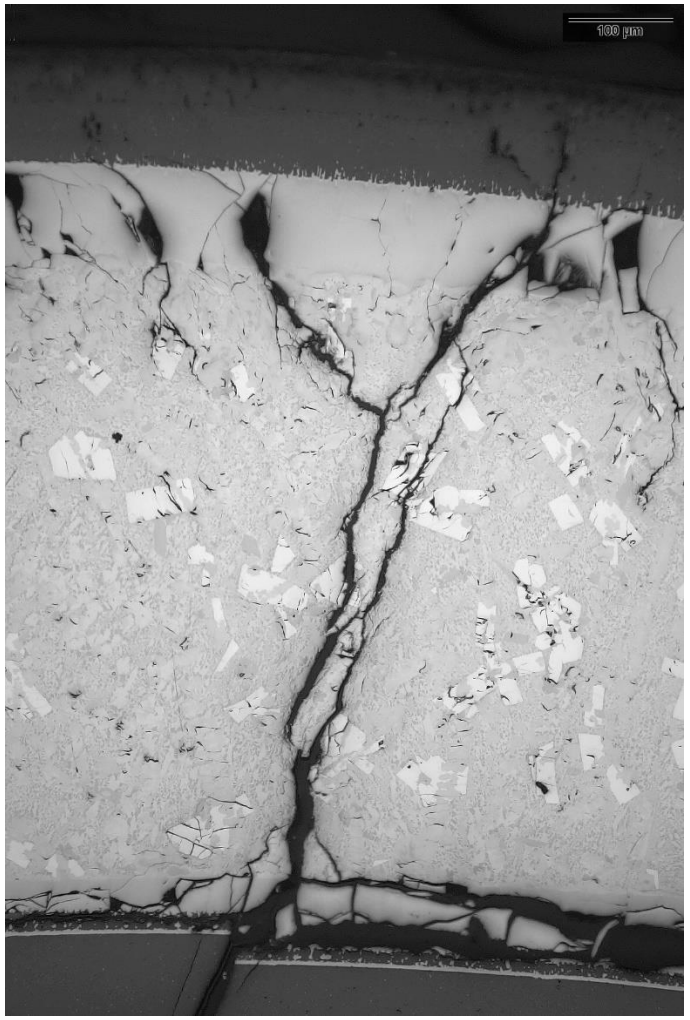

90°

Figure 181 QUENCH-20; rod #15 at elevation 555 mm: melted cladding.

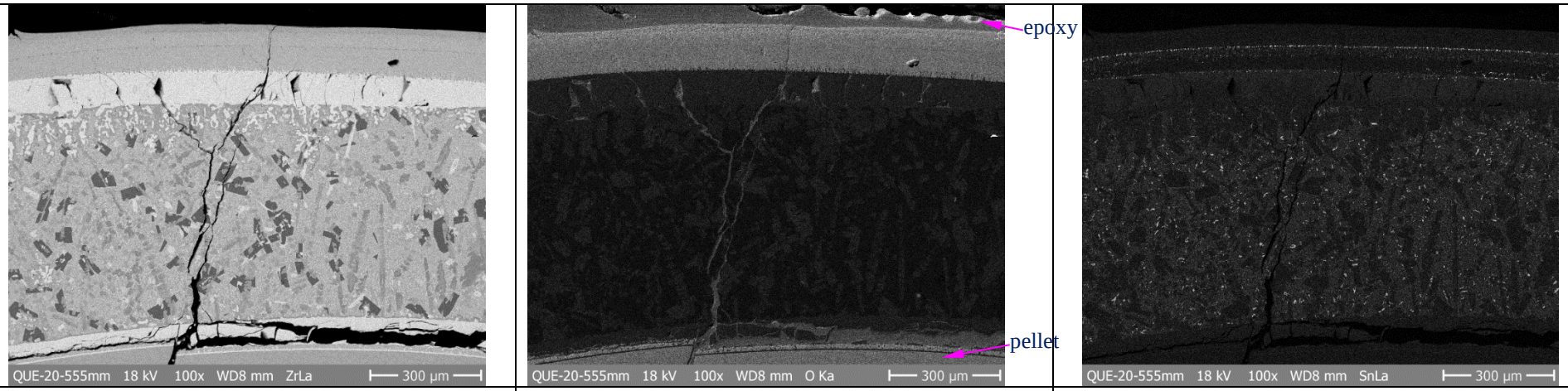

Zr distribution in oxide, α-Zr(O) and melt layers	oxygen in oxide layers and pellet	Sn precipitates inside of outer oxide layer and melt
(Fe, Cr) chunks in melt	(Fe, Cr) chunks in melt	Ni from Inconel spacer grid inside (Zr, Ni) eutectic

Figure 182 SEM/EDX element mapping of cladding #15 at bundle elevation 555 mm and angle 90°: penetration of molten spacer grid into molten cladding metal, redistribution of (Fe, Cr) chunks inside (Zr, Ni) eutectic.

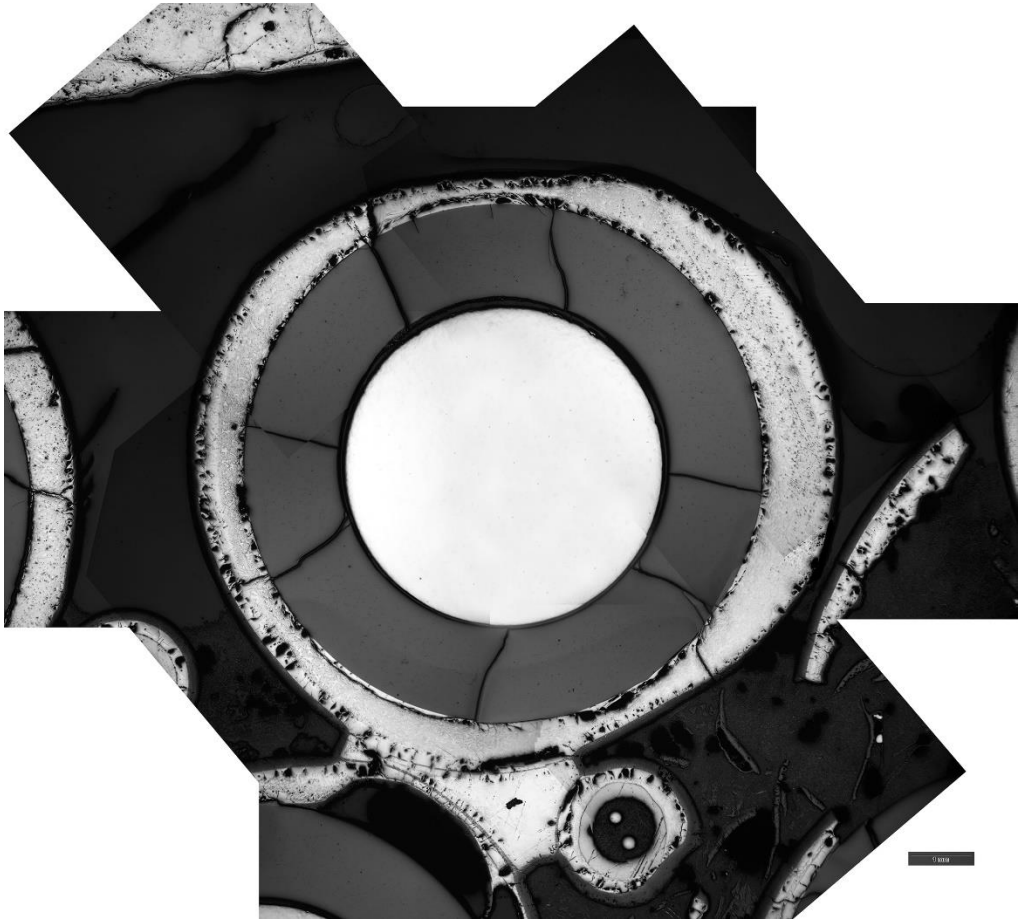

overview

315°: Zr precipitates in Zr/SS melt relocated from 750 mm

Figure 183 QUENCH-20; rod #16 at elevation 555 mm: melted cladding.

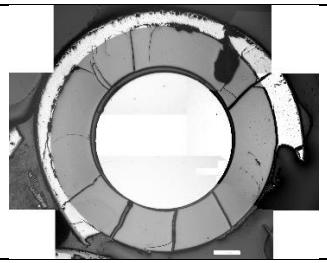

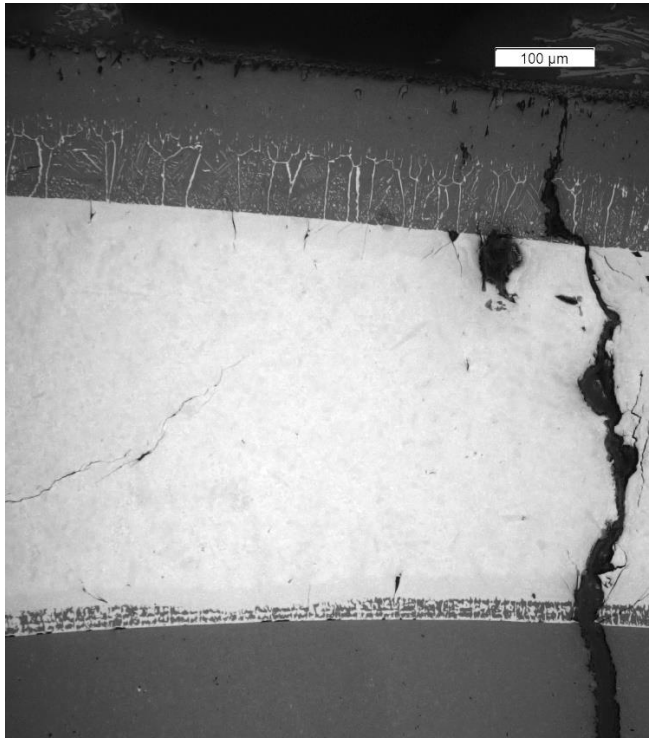

0°: ZrO_2, α-Zr(O), β-Zr, melt, α-Zr(O); pellet	225°: ZrO_2, ZrO_{2-x}, α-Zr(O), melt, interaction of melt with pellet	315°: ZrO_2, α-Zr(O), β-Zr, melt, α-Zr(O); pellet

Figure 184 QUENCH-20; rod #17 at elevation 555 mm: cladding layers; (Ni, Fe)-containing eutectic melt formed due to cladding-spacer interaction.

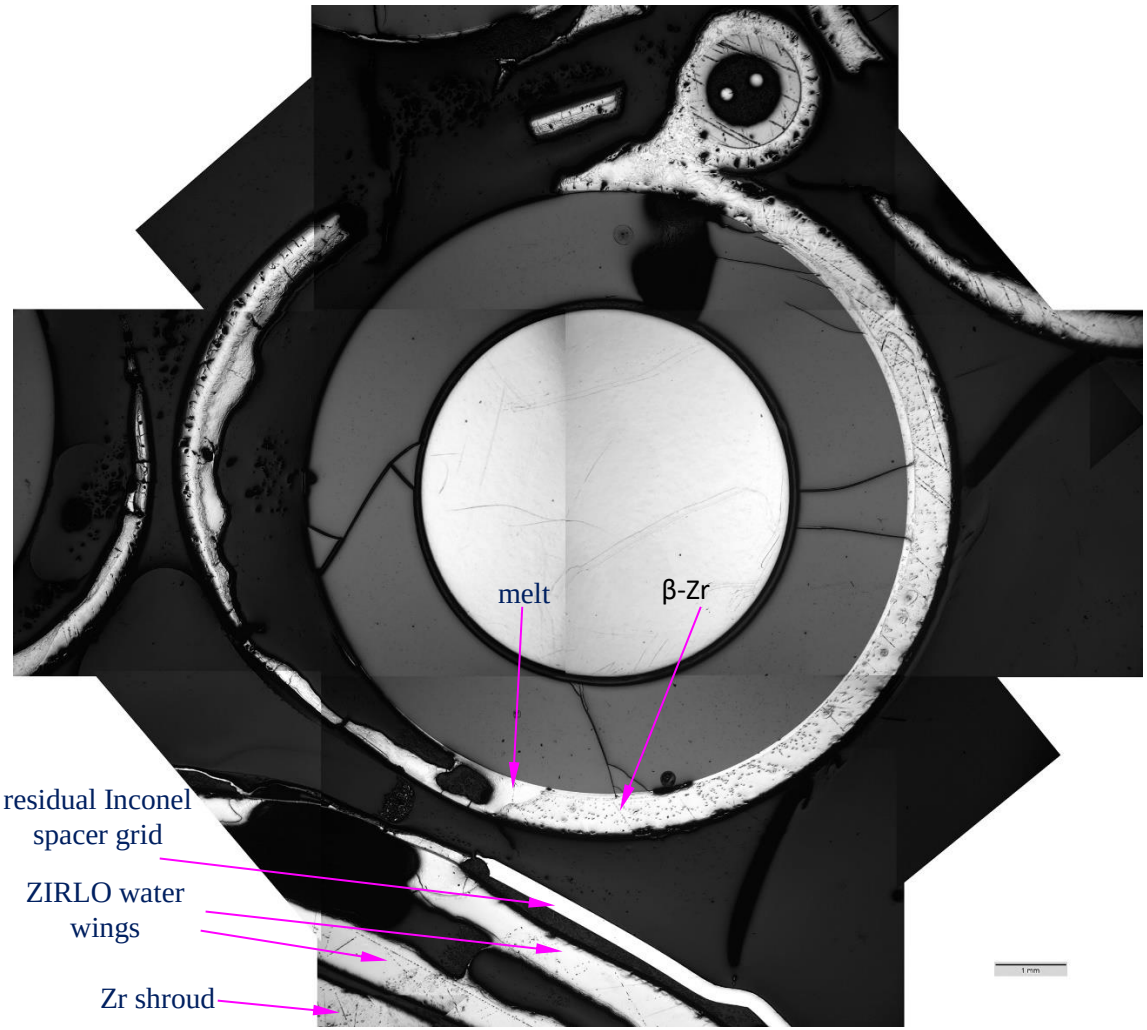

overview

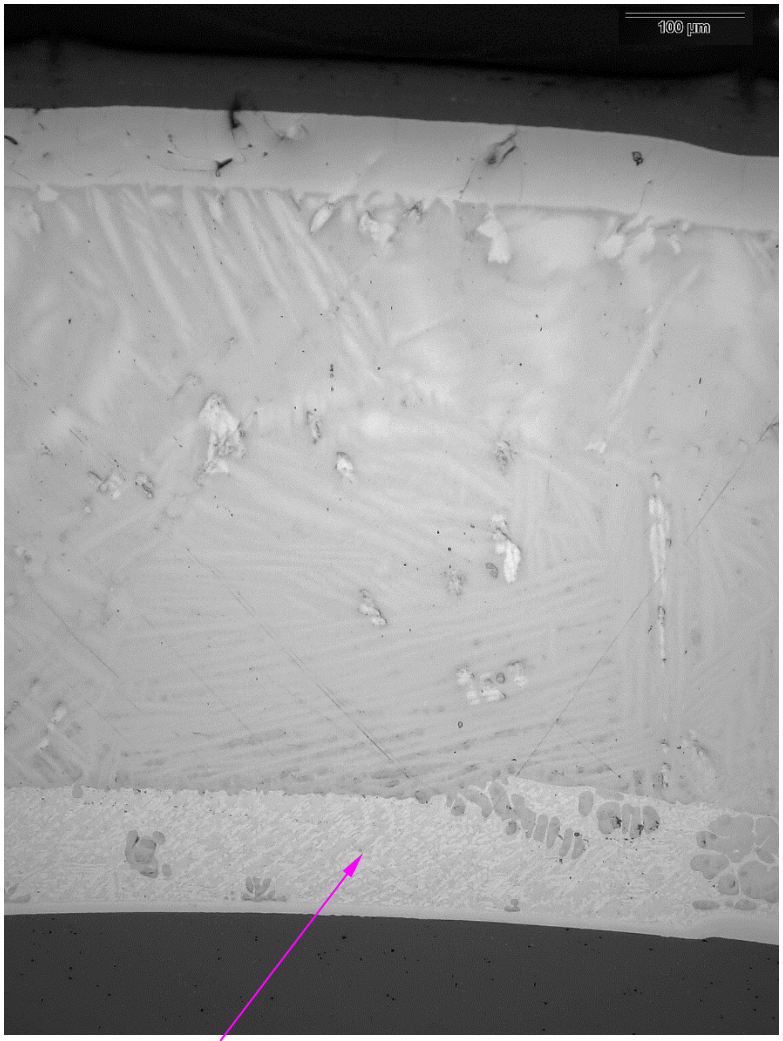

90°: melt between β-Zr and pellet

Figure 185 QUENCH-20; rod #21 at elevation 555 mm: melted cladding.

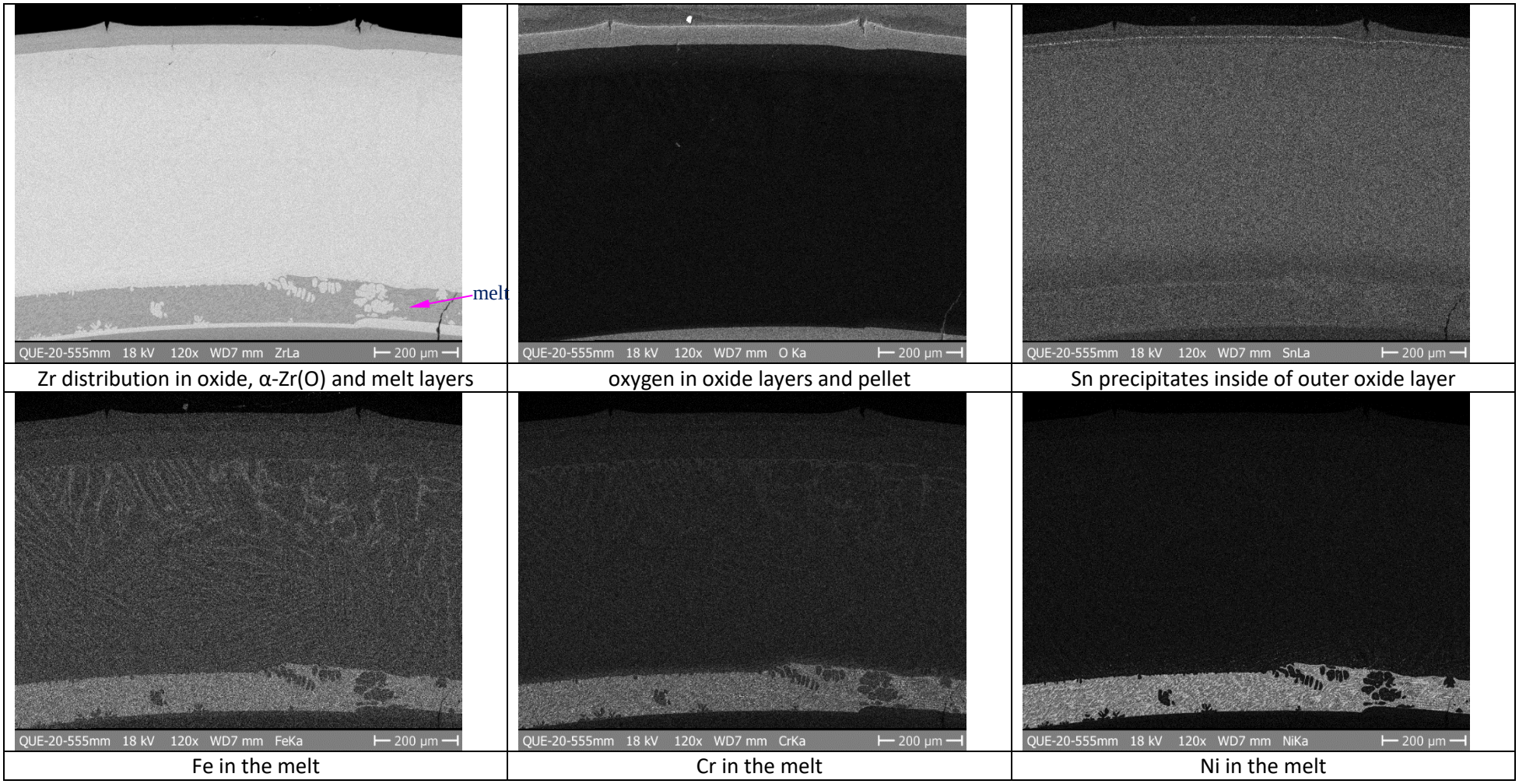

Zr distribution in oxide, α-Zr(O) and melt layers	oxygen in oxide layers and pellet	Sn precipitates inside of outer oxide layer
Fe in the melt	Cr in the melt	Ni in the melt

Figure 186 SEM/EDX element mapping of cladding #21 at bundle elevation 555 mm and angle 90°: penetration of molten spacer grid into the gap between cladding and pellet.

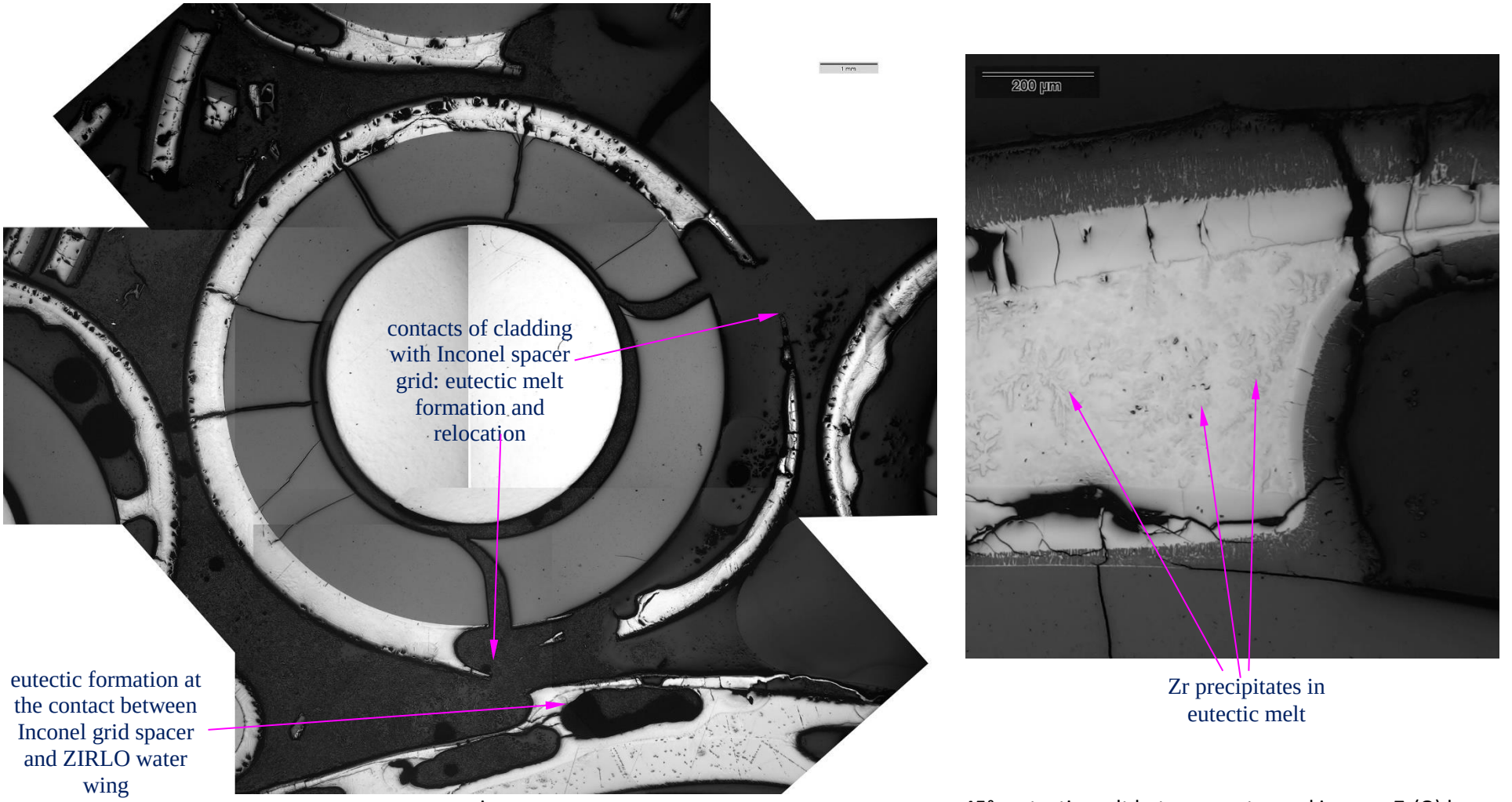

Figure 187 QUENCH-20; rod #22 at elevation 555 mm: eutectic interactions of Inconel spacer grid with cladding and water wing.

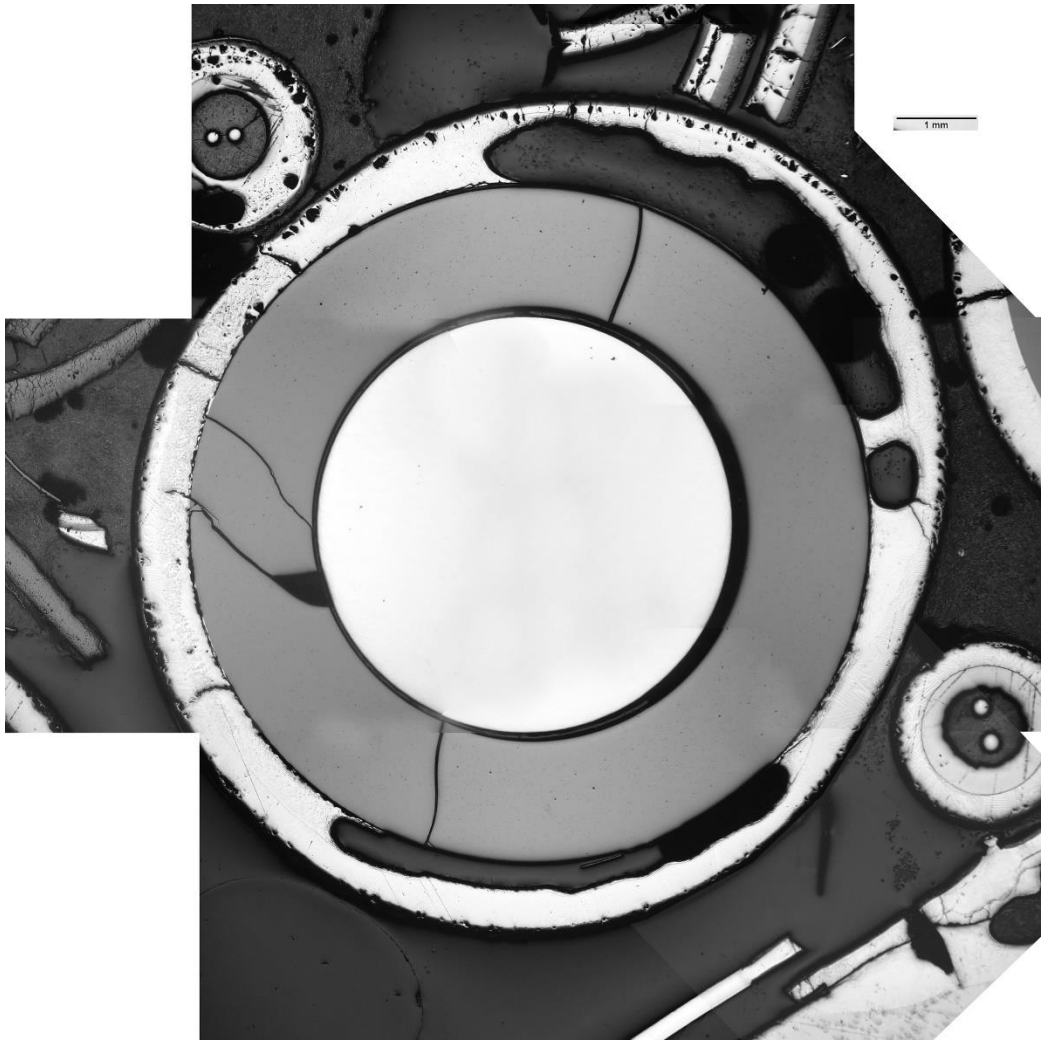

overview

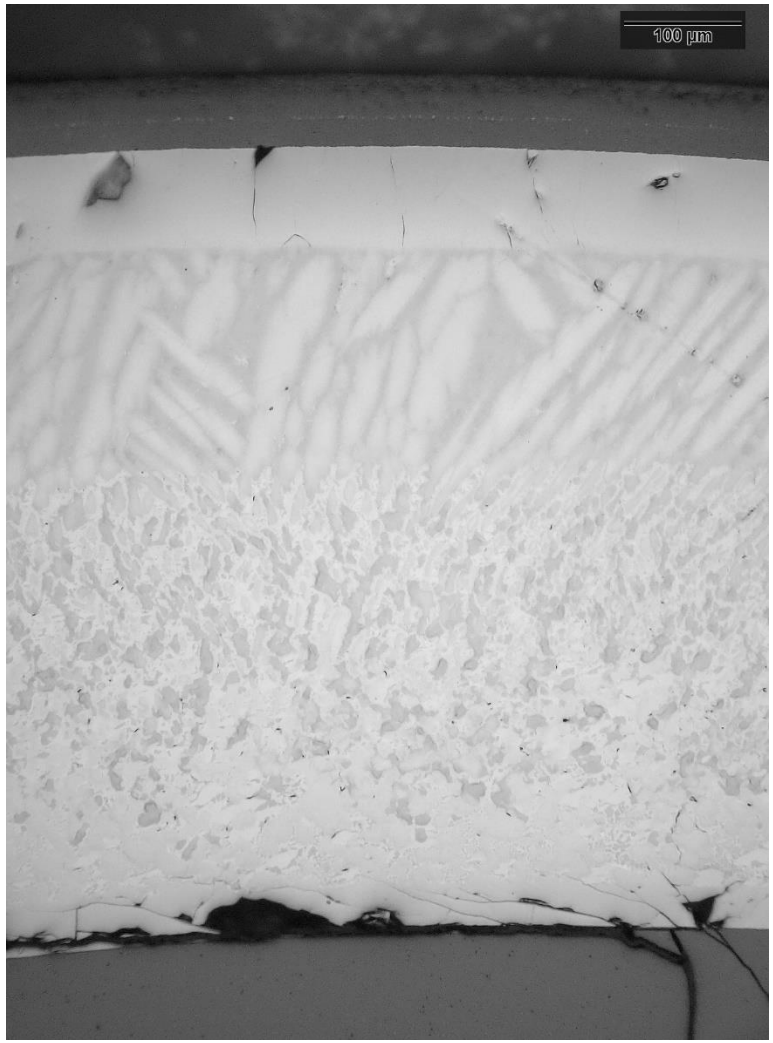

270°: melt between β-Zr and inner α-Zr(O)

Figure 188 QUENCH-20; rod #23 at elevation 555 mm: melted cladding.

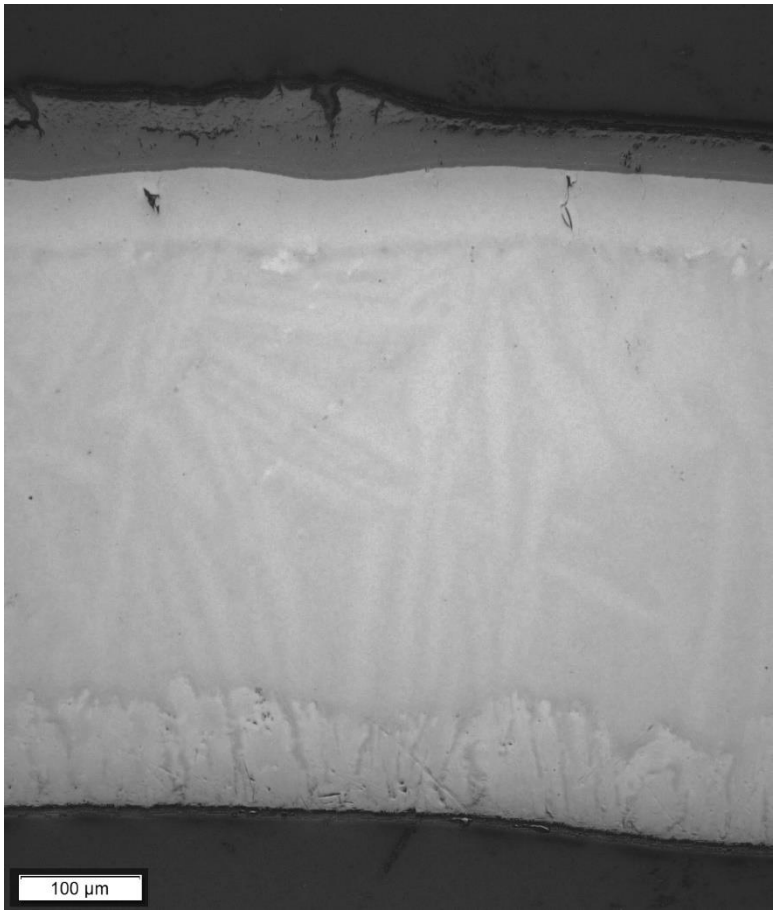

90°

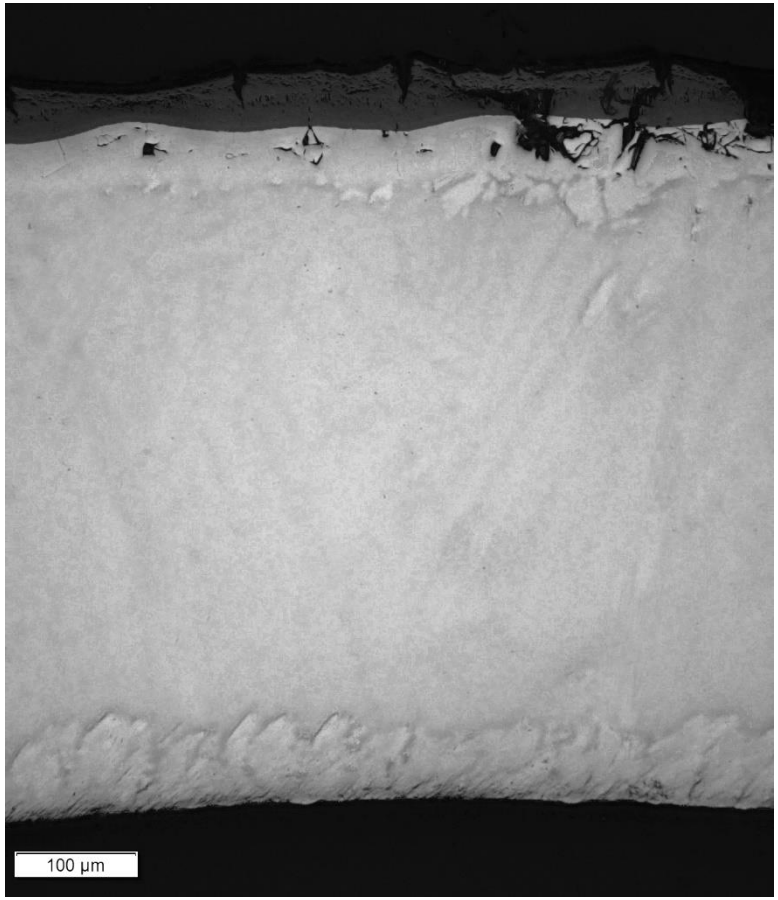

270°

Figure 189 QUENCH-20; rod #24 at elevation 555 mm: cladding structure with melt formed at inner cladding surface.

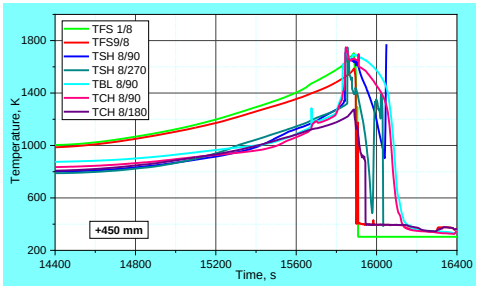

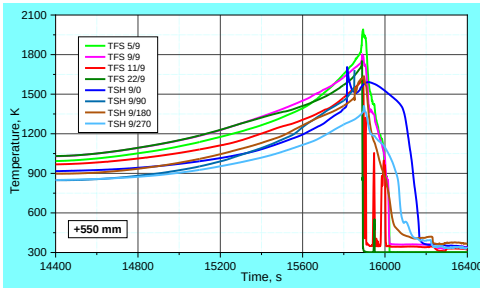

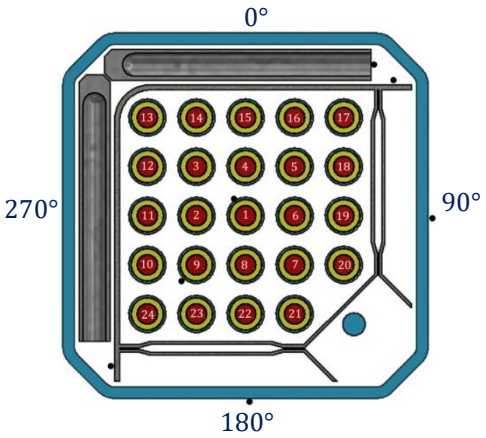

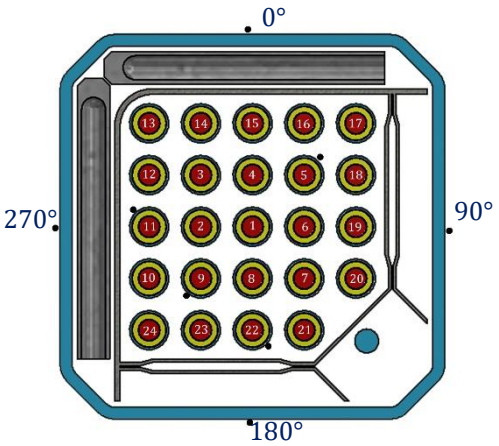

TC positions and TC readings
at elevation 550 mm

Figure 190 QUENCH-20; Bundle cross section at the elevation of 450 mm; influence of higher temperatures in the bundle (melt relocation from above and melting of cladding inner β-Zr layer) and at the shroud position of 0° (eutectic interaction B_4C pin with stainless steel blade). Not changed white pellets inside rods without melt.

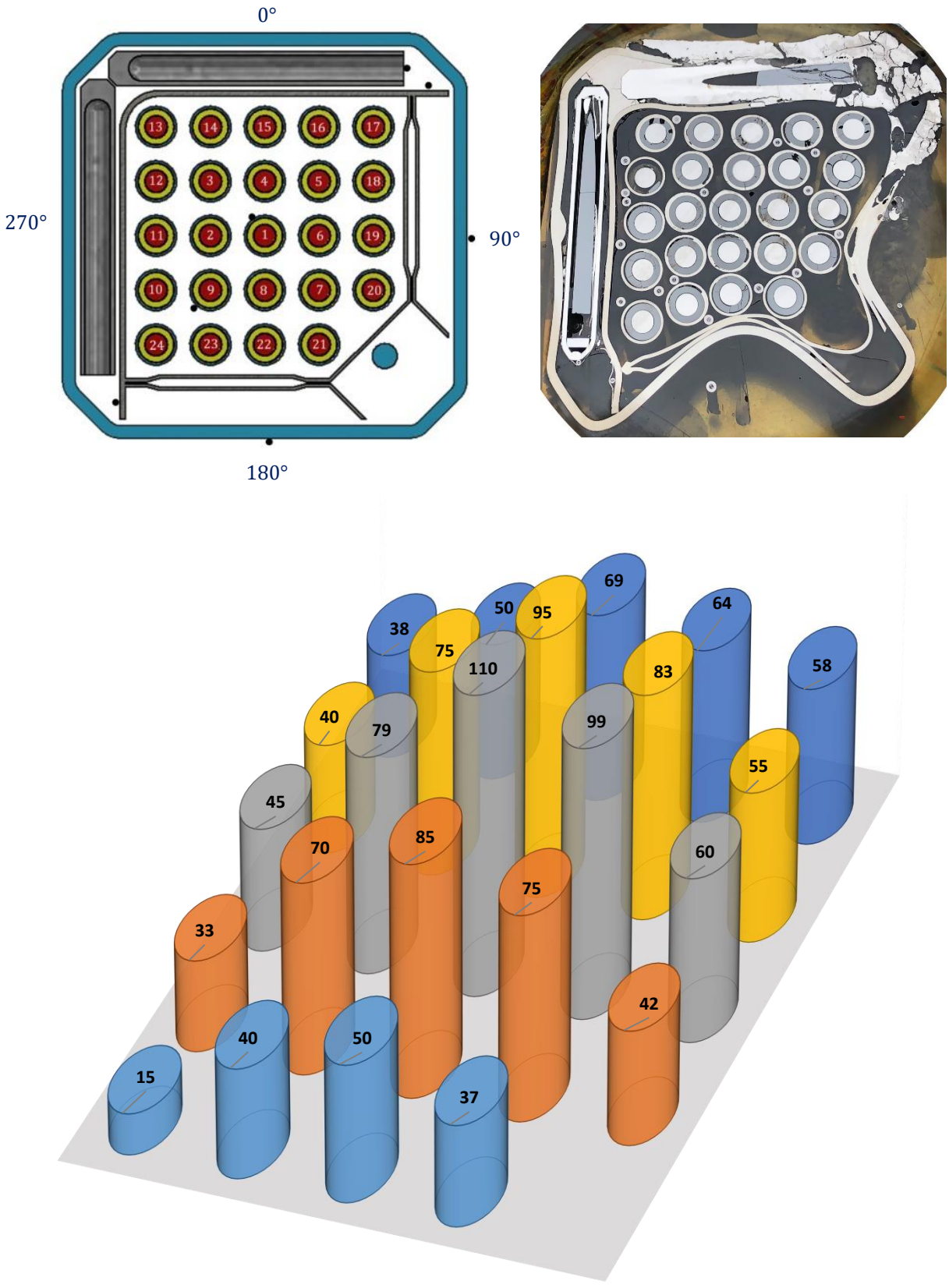

Figure 191 QUENCH-20; average thicknesses of outer ZrO_2 for each cladding at bundle elevation of 450 mm; indication of coldest bundle region at 180°.

45°: strong outer and inner oxidation;

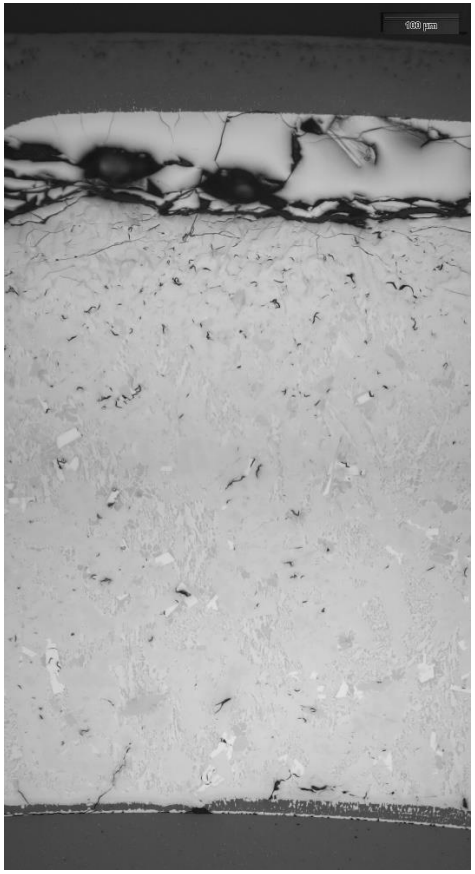

90°: very thin inner α-Zr(O)

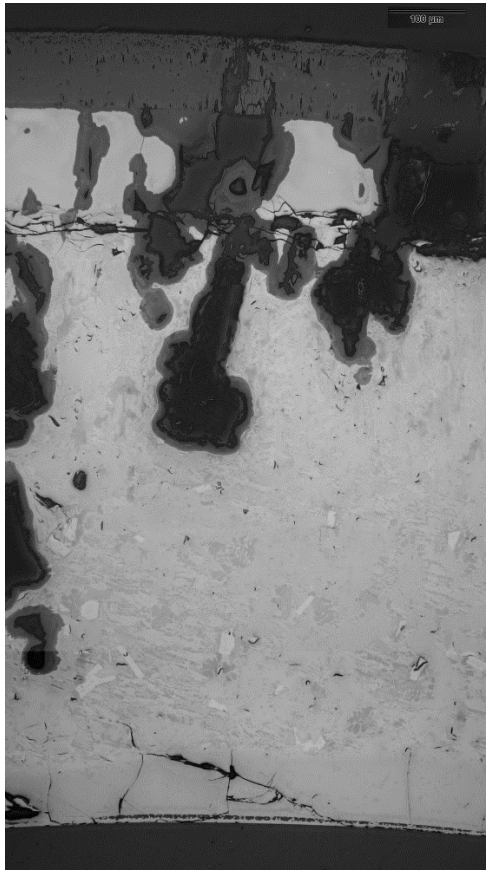

135°: penetration of oxygen through the outer cracks into metal

315°: absence of inner oxide layer

Figure 192 QUENCH-20; rod #1 at elevation 450 mm: cladding layers; inner cladding oxidation due to interaction with pellet; eutectic melt relocated from 550 mm.

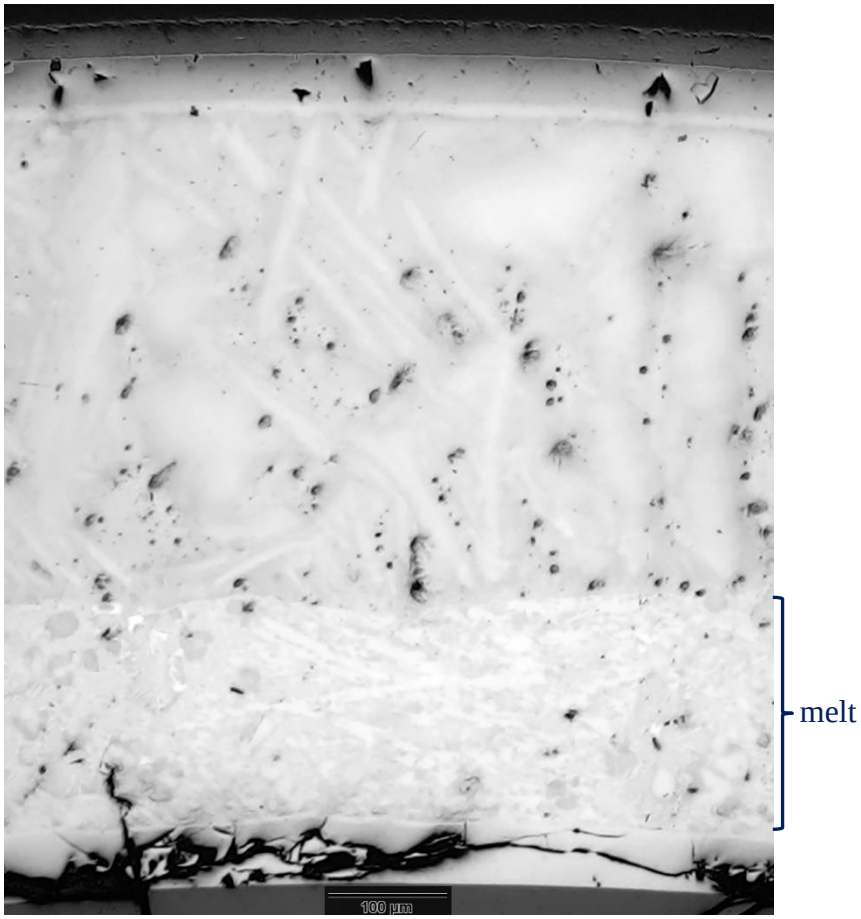

180°: lower temperatures

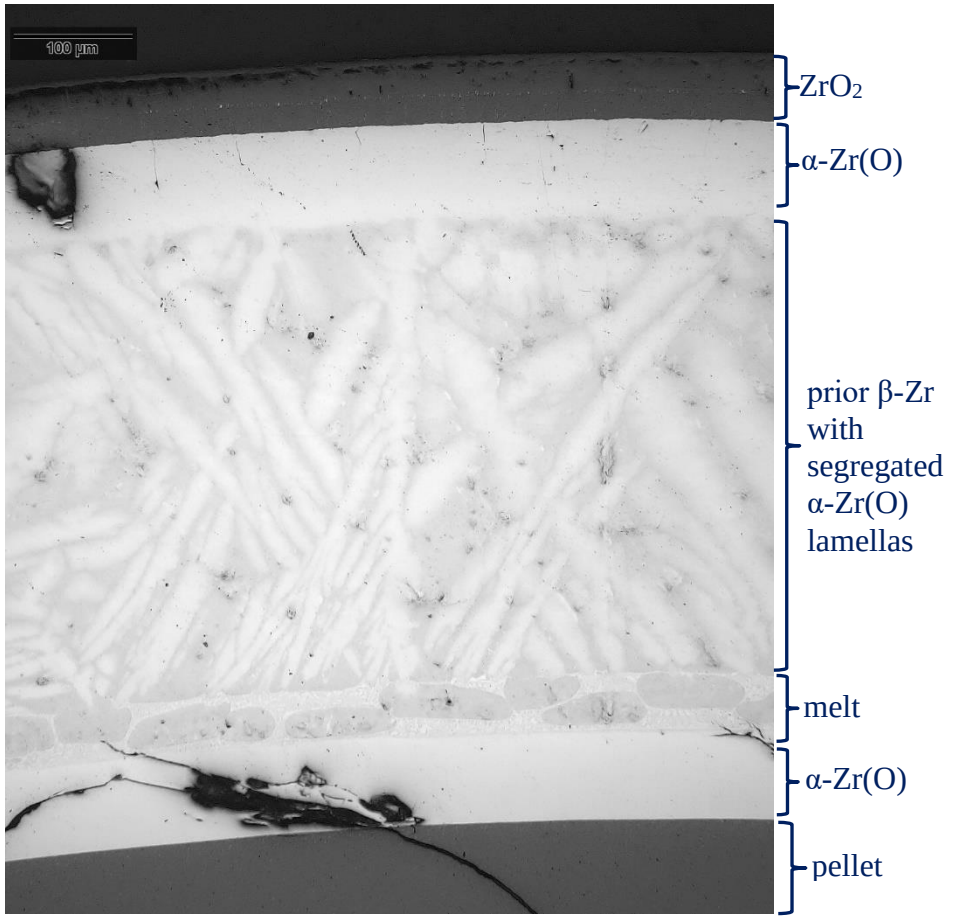

270°: higher temperatures

Figure 193 QUENCH-20; rod #20 at elevation 450 mm: cladding layers, direct contact with pellet; eutectic melt relocated from 550 mm.

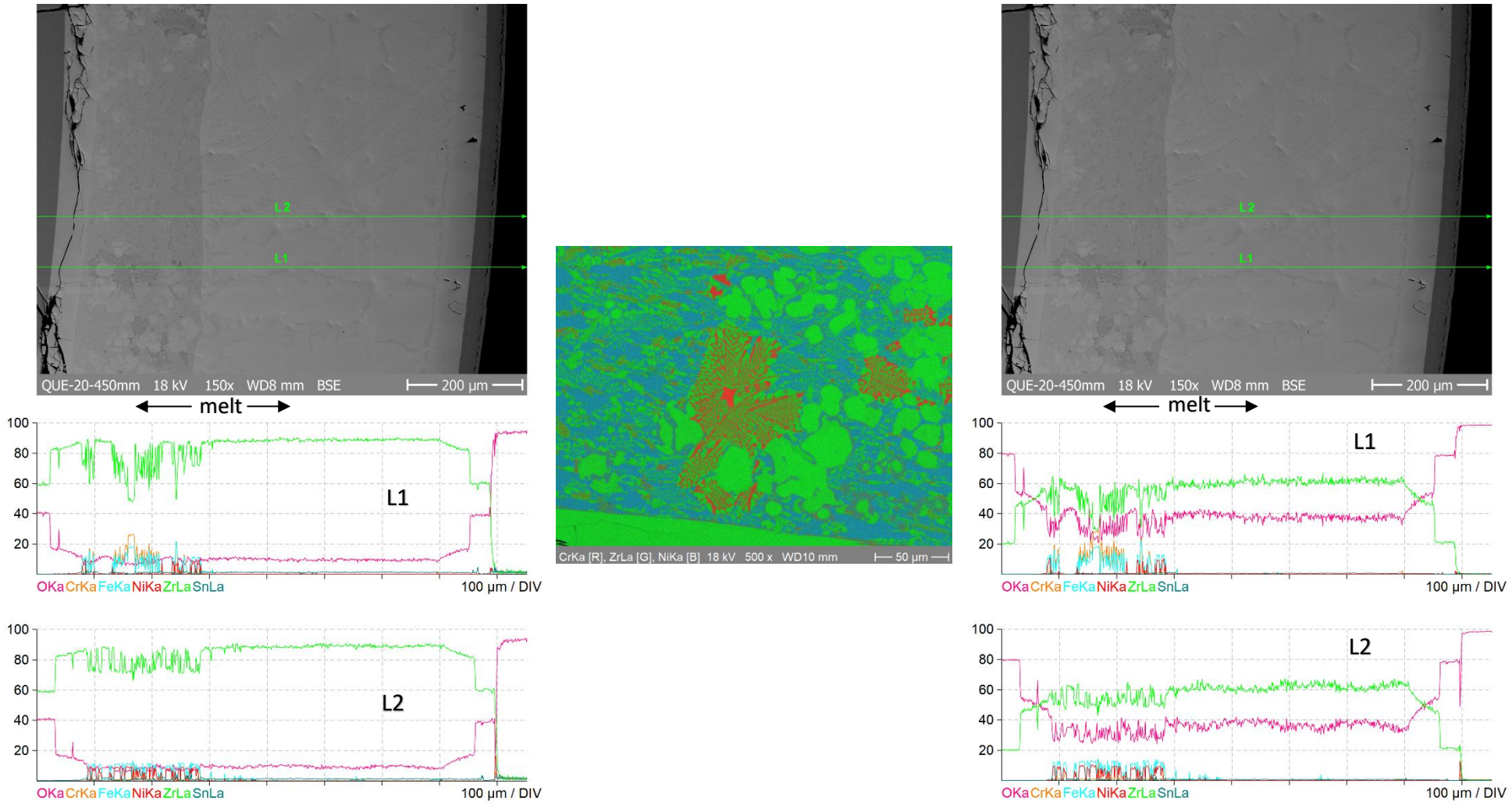

Figure 194 QUENCH-20; SEM/EDX scan of rod #20 at elevation 450 mm and angle 180°: components of the Inconel grids from the elevation 550 mm inside the frozen melt.

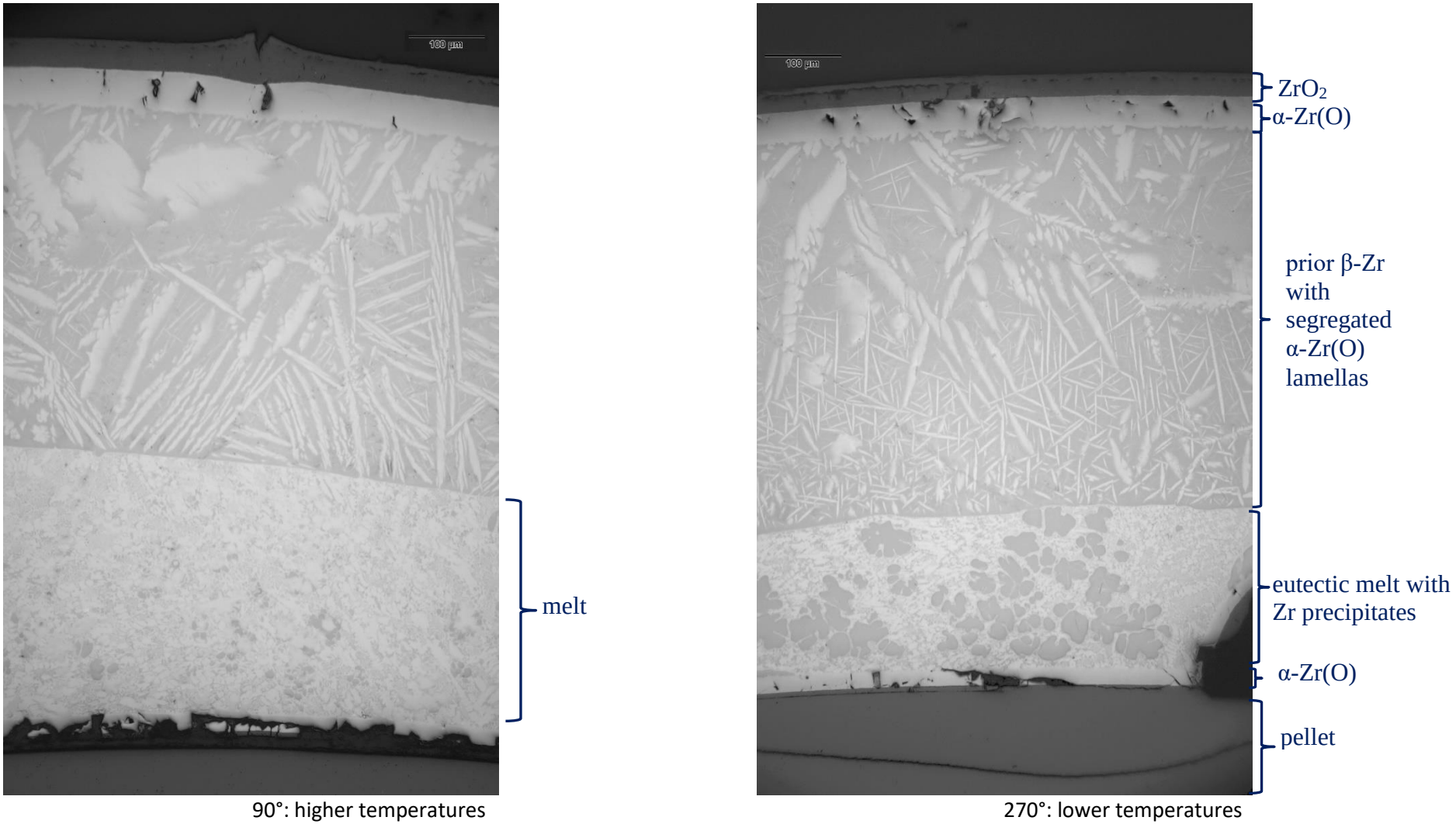

Figure 195 QUENCH-20; rod #23 at elevation 450 mm: cladding layers, contact with pellet; eutectic melt relocated from above.

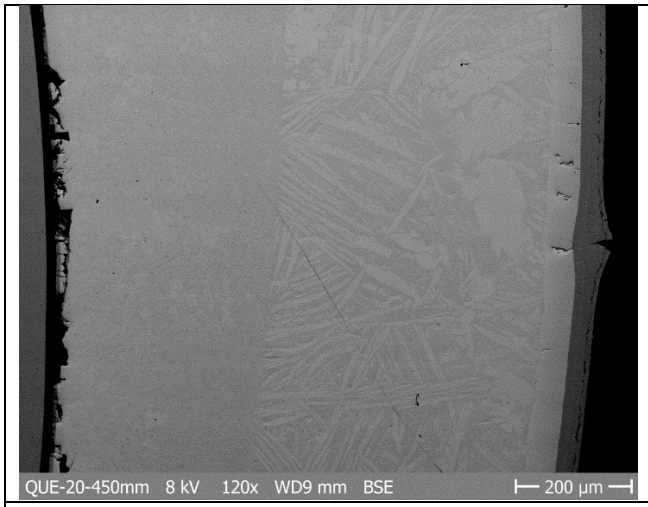

SEM image

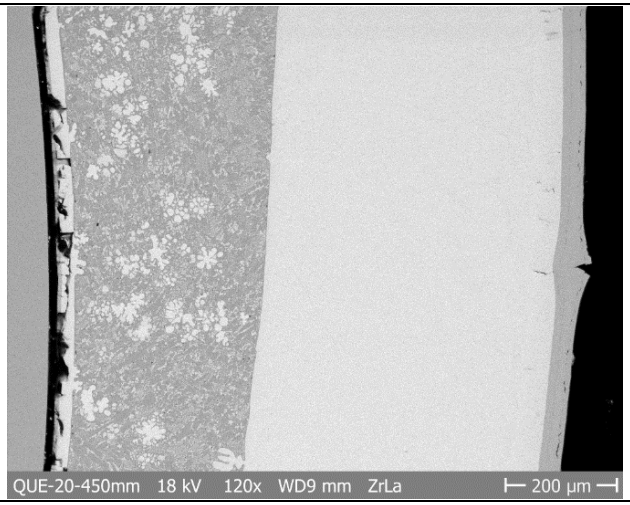

α-Zr(O)-precipitates in eutectic melt

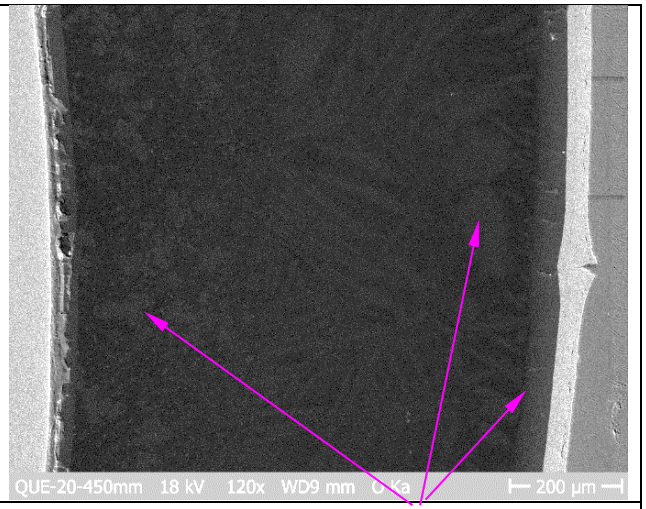

low oxygen content in α-Zr(O)

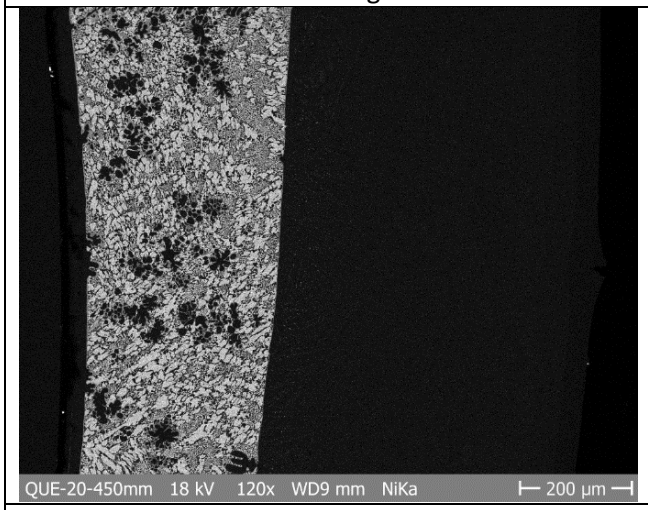

melt layer: Ni from spacer melted at 550 mm

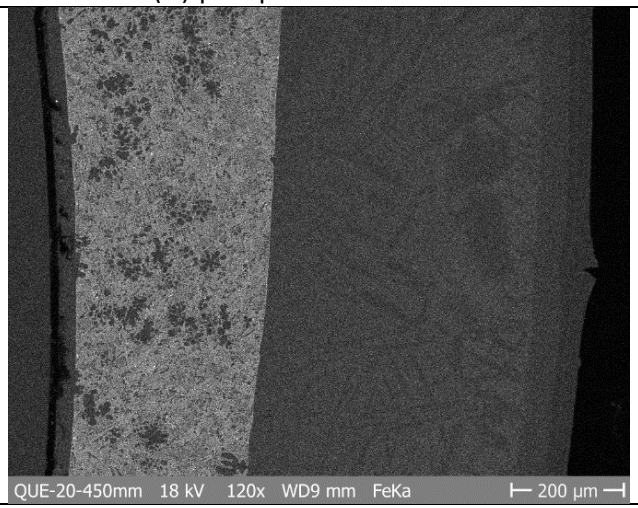

melt layer: Fe from spacer melted at 550 mm

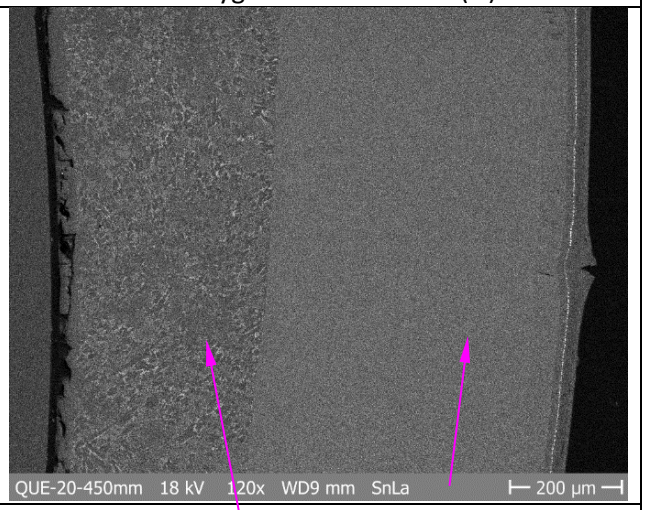

less Sn in melt than in prior β-Zr layer

Figure 196 QUENCH-20; SEM/EDX mapping of rod #23 (90°) at elevation 450 mm.

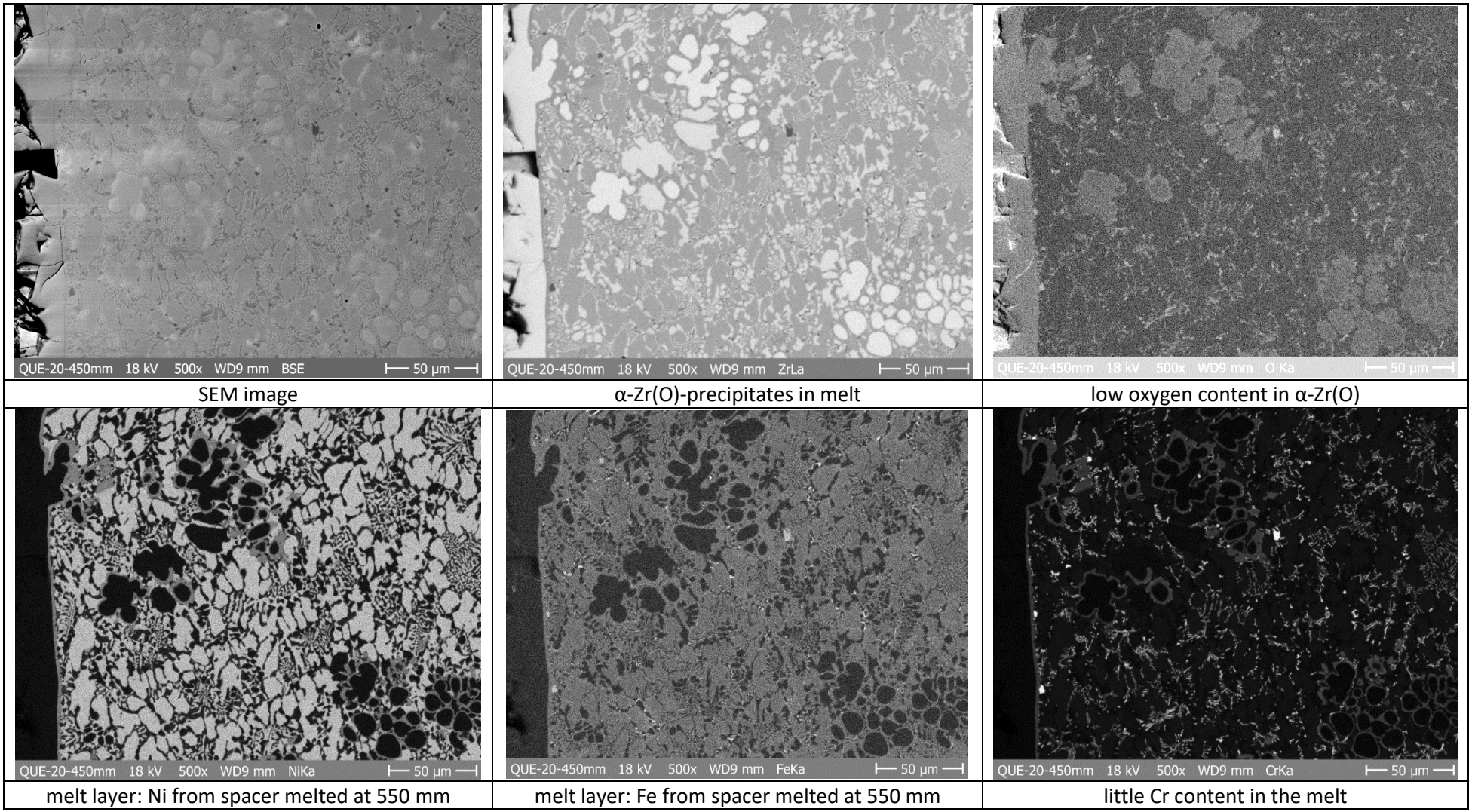

SEM image	α-Zr(O)-precipitates in melt	low oxygen content in α-Zr(O)
melt layer: Ni from spacer melted at 550 mm	melt layer: Fe from spacer melted at 550 mm	little Cr content in the melt

Figure 197 QUENCH-20; SEM/EDX melt layer mapping of rod #23 (90°) at elevation 450 mm; α -Zr(O)-precipitates in (Zr, SS) eutectic melt.

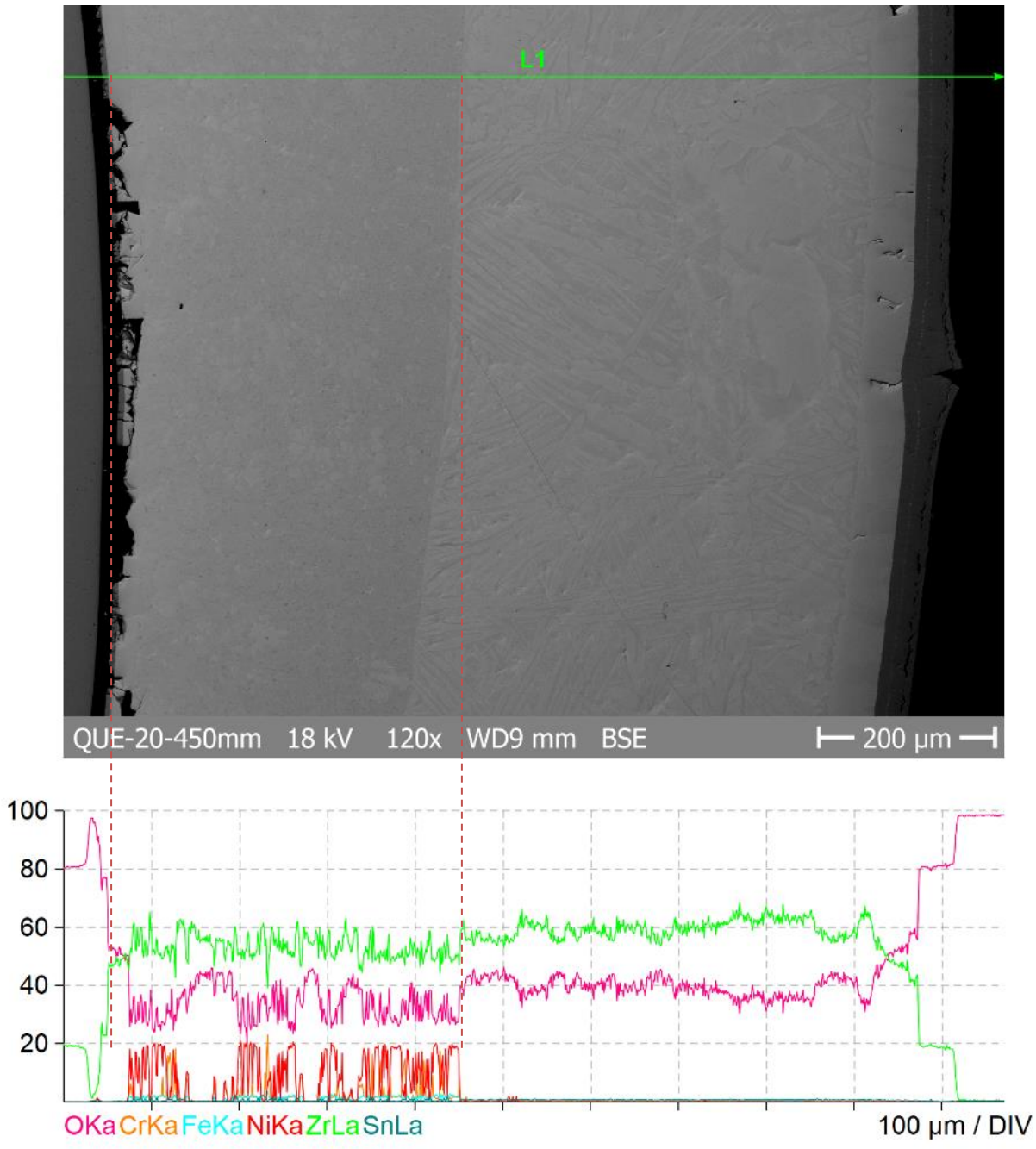

Figure 198 QUENCH-20; SEM/EDX line scan of rod #23 (90°) at elevation 450 mm (at%): high Ni content in melt.

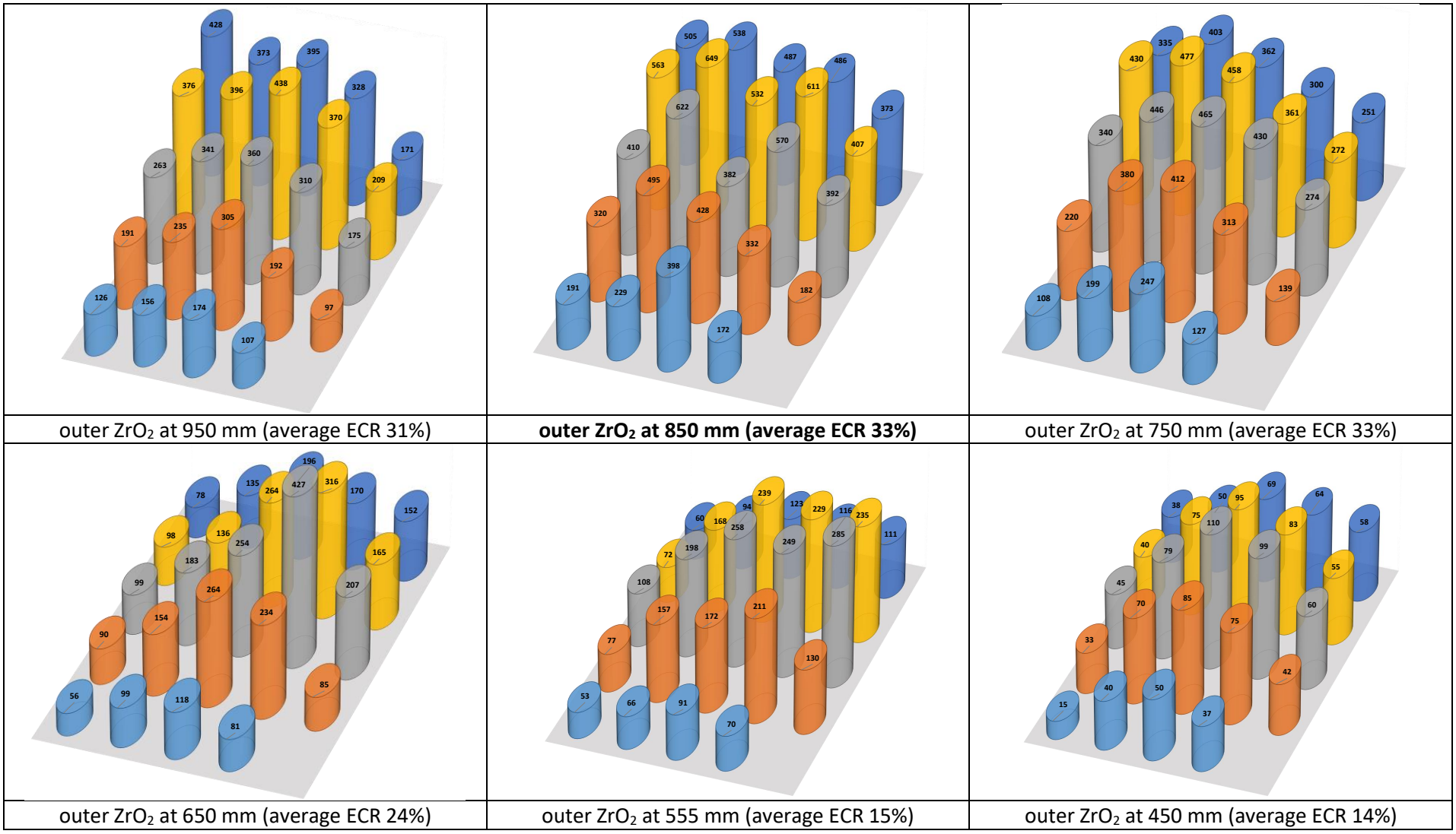

outer ZrO_2 at 950 mm (average ECR 31%)	**outer ZrO_2 at 850 mm (average ECR 33%)**	outer ZrO_2 at 750 mm (average ECR 33%)
outer ZrO_2 at 650 mm (average ECR 24%)	outer ZrO_2 at 555 mm (average ECR 15%)	outer ZrO_2 at 450 mm (average ECR 14%)

Figure 199 QUENCH-20; comparison of outer oxide thickness for different rods at different elevations.

The experiment QUENCH-20 with BWR geometry simulation bundle was successfully conducted at KIT on 9th October 2019 in the framework of the international SAFEST project. The test bundle mock-up represented one quarter of a BWR fuel assembly with 24 electrically heated fuel rod simulators and two B_4C control blades. The rod simulators were filled with Kr to an inner pressure of 5.5 bar. The pre-oxidation stage in a flowing gas mixture of steam and argon (each 3 g/s) and system pressure of 2 bar lasted 4 hours at the peak cladding temperature of 1250 K. The Zry-4 corner rod, withdrawn at the end of this stage, showed the maximal oxidation at elevations between 930 and 1020 mm with signs of breakaway. During the transient stage, the bundle was heated to a maximum temperature of 2000 K. The coolability of the bundle was decreased by its squeezing due to the shroud ductile deformation caused by an overpressure outside the shroud. The cladding radial strain and failures due to inner overpressure (about 4 bar) were observed at temperature about 1700 K and lasted about 200 s.

During the period of rod failures also the first absorber melt relocation accompanied by shroud failure were registered. The interaction of B_4C with the steel blade and the ZIRLO channel box were observed at elevations 650…950 mm with the formation of eutectic melt. The typical components of this melt are (Fe, Cr) borides and ZrB_2 precipitated in steel or in Zr-steel eutectic melt. Massive absorber melt relocation was observed 50 s before the end of transition stage. Small fragments of the absorber melt moved down to the elevation of 50 mm.

The melting point of Inconel spacer grids at 500 and 1050 mm was also reached at the end of the transition stage. The Inconel melt from the elevation 1050 mm relocated downwards through hot bundle regions to the Inconel grid spacer at 550 mm and later (during the escalation caused by quench) to 450 mm. This melt penetrated also under the damaged cladding oxide layer and formed molten eutectic mixtures between elevations 450 and 550 mm.

The test was terminated by quench water injection with a flow rate of 50 g/s from the bundle bottom. Fast temperature escalation from 2000 to 2300 K during 20 s was observed due to the strongly exothermic oxidation reactions. As result, the metal part (prior β-Zr) of the claddings between 550 and 950 mm was melted, partially released into space between rods and partially relocated in the gap between pellet and outer oxide layer to 450 mm. In this case, the positive role of the oxide layer should be noted, which does not allow the melt to completely escape into the inter-rod space. It is thereby limiting the possibility of interactions of a large amount of melt with steam, which could significantly increase the exothermic oxidation processes and the escalation of temperatures.

The distribution of the oxidation rate within each bundle cross section is very inhomogeneous: whereas the average outer ZrO_2 layer thickness for the central rod (#1) at the elevation of 750 mm is 465 µm, the same parameter for the peripheral rod #24 is only 108 µm. The average oxidation rate of the inner cladding surface (due to interaction with steam and with ZrO_2 pellets) is about 20% in comparison to the outer cladding oxidation. The bundle elevations 850 and 750 mm are mostly oxidized with average cladding ECR 33%. The oxidation of the melt relocated inside the rods was observed at elevations 550…950 mm.

The mass spectrometer measured release of CO (12.6 g), CO_2 (9.7 g) and CH_4 (0.4 g) during the reflood as products of absorber oxidation; the corresponding B_4C reacted mass was 41 g or 4.6% of the total B_4C inventory. It is significantly lower than in the PWR bundle tests QUENCH-07 and QUENCH-09 containing central absorber rod with B_4C pellets inserted into a thin stainless steel cladding and Zry-4 guide tubes (20% and 50% reacted B_4C correspondingly). Hydrogen production during the reflood amounted to 32 g during the reflood (57.4 g during the whole test) including 10 g from B_4C oxidation.